Geochemistry of Soil Radionuclides

SSSA Special Publication Number 59

Geochemistry of Soil Radionuclides

Geochemistry of Soil Radionuclides

Editors
Peng-Chu Zhang and Patrick V. Brady

Editorial Committee
Peng-Chu Zhang
Patrick V. Brady
Matthew Eick
Jeremy B. Fein
Dean L. Hesterberg
Samuel J. Traina

Managing Editor
Dave M. Kral

Editor
Marian K. Viney

SSSA Special Publication Number 59

Soil Science Society of America
Madison, Wisconsin, USA
2002

Cover Design: Pat Scullion

Soil Society of America, Inc.
677 South Segoe Road, Madison, WI 53711-1086 USA

Library of Congress Registration Number: 2002106128

Printed in the United States of America

CONTENTS

FOREWORD

As the primary source of food and fiber and major interface with the environment, soil is the reservoir on which most life on earth depends. Soil science has accomplished much, providing us with a basic understanding of the physical, chemical, and biological properties and processes essential to ecosystem integrity and function. This knowledge has helped us to understand the role of soils in enhancing human health, not only through food production, but also in controlling the transport and risk posed by toxic substances in the environment.

The editors and contributors to *Geochemistry of Soil Radionuclides* have done an excellent job in capturing the essence of important concepts in linking fundamental principles of radionuclide transport in soil. One impetus for this publication was the increased prevalence of radionuclides in soil and need for information on the processes controlling their biological availability in natural systems. Previous knowledge was not adequate to predict movement in near-surface environments and the long-term fate and impact of radionuclides to humans and ecosystems. This work builds on both basic science and empirical engineering studies to provide a mechanistic approach to facilitate risk assessment and cost-effective remediation procedures. The theories and technologies presented highlight the editors' intention for this book in advancing our understanding of the fate of radionuclides in soil, groundwater, and in potential nuclear waste repositories.

This work moves us another step forward in our common journey to *Sustain Earth and Its People* by continuing to *Translate our Science into Practice*.

JOHN W. DORAN, President
Soil Science Society of America

PREFACE

Recurring concerns about the environmental fate and potential health impacts of radionuclides such as ^{137}Cs, ^{90}Sr, and ^{99}Tc continue to focus interest on understanding the mechanisms controlling radionuclide transport in soils. At the same time, the difficulty and complexity of cleaning up radionuclide-contaminated soils highlights our inability to predict radionuclide transport in near surface environments. Nevertheless, new theories and novel analytical techniques are increasingly able to provide a picture of radiochemical reactivity in situ in soils at the molecular level. There is therefore the possibility that an atomic level view of contaminant binding to soils can provide a knowledge-based framework for choosing remedial targets, achieving cleanup, and protecting public health. Interest in such subjects led to a symposium entitled "Soil Geochemical Processes of Radionuclides" that was held at the 1999 Soil Science Society of America Annual Meeting at Salt Lake City, UT.

This special publication contains 10 chapters that are an outgrowth of the 1999 symposium. The intention of this book is to highlight theories and technologies developed in understanding the fate of radionuclides in soils, groundwater and in potential nuclear waste repositories.

Chapter 1 provides a general overview of radiochemistry, the sources of soil radionuclides, and the significance of the soil processes for radionuclide fate. Chapters 2 and 3 consider the theoretical underpinnings of radionuclide solution chemistry, sorption, and speciation—as well as the application of analytical technologies to probe the environmental reactivity of soil radionuclides. Chapter 4 outlines the application of surface complexation models to understand U(VI) adsorption. Chapter 5 describes the molecular basis for developing computer simulations of radionuclide interaction with soil materials. Chapter 6 evaluates biological controls over chromate and uranyl reduction in anaerobic soils. Chapter 7 examines the role of colloids in radionuclide transport in soils and groundwater. Chapter 8 provides a macroscopic overview of radionuclide plume behavior. Chapter 9 summarizes the potential role of mineral backfills in radionuclide retention. And Chapter 10 applies radionuclide sorption models to consider the potential performance of a proposed high-level nuclear waste repository at Yucca Mountain, Nevada.

We greatly appreciate the help of the SSSA in organizing the 1999 symposium and in supporting this special publication.

Special thanks should go to Dr. Margaret Chu, Head of the Office of Civilian Radioactive Waste Management; and Ed O'Donnell of the U.S. Nuclear Regulatory Commission for their encouragement and for the financial support of SNL and the US-NRC. We thank the editorial committee members: Dr. Matthew Eick, Department of Crop and Soil Environmental Sciences at Virginia Polytechnical Institute and State University; Dr. Jereni B. Fein, Department of Civil Engineering and Geological Sciences at Notre Dame; Dr. Dean L. Hesterberg, Department of

Soil Science at North Carolina State University; and Dr. Samuel J. Traina, School of Natural Resource at Ohio State University.

Lastly, we greatly appreciate the careful and thoughtful comments of the anonymous reviewers.

Peng-Chu Zhang, coeditor
Patrick V. Brady, coeditor
Sandia National Laboratories
Albuquerque, New Mexico

CONTRIBUTORS

F. Paul Bertetti	Center for Nuclear Waste Regulatory Analyses, Southwest Research Institute, 6220 Culebra Road San Antonio, TX 78238-5166
Patrick V. Brady	Sandia National Laboratories, MS 0750 Albuquerque, NM 87185-0750
Gabe Carr	Sandia National Laboratories, MS 0750 Albuquerque, NM 87185-0750
Steve D. Conradson	Los Alamos National Laboratory, Los Alamos, NM 87545
Randall T. Cygan	Geochemistry Department, Sandia National Laboratories, Albuquerque, NM 87185-0750
James A. Davis	U.S. Geological Survey, Menlo Park, CA 94025
Scott Fendorf	Department of Geological and Environmental Sciences, Stanford University, Stanford, CA 94305
Colleen M. Hansel	Department of Geological and Environmental Sciences, Stanford University, Stanford, CA 94305
Bruce D. Honeyman	Division of Environmental Science and Engineering, Colorado School of Mines, Golden, CO 80302
Frank Huang	Environmental Engineering Department, New Mexico Institute of Mining and Technology, Socorro, NM 87801
Calos F. Jové-Colon	Sandia National Laboratories, MS 0778 Albuquerque, NM 87185-0750
James L. Krumhnsl	Sandia National Laboratories, MS 0750 Albuquerque, NM 87185-0750
Calos F. Jové-Colon	Los Alamos National Laboratory, Los Alamos, NM 87545
Mavis Lin	Los Alamos National Laboratory, Los Alamos, NM 87545
May P. Neu	Los Alamos National Laboratory, Los Alamos, NM 87545
Roberto T. Pabalan	Center for Nuclear Waste Regulatory Analyses, Southwest Research Institute, 6220 Culebra Road San Antonio, TX 78238-5166
Timothy E. Payne	Australian Nuclear Science and Technology Organisation, Menai, NSW 2234, Australia
James F. Ranville	Department of Chemistry and Geochemistry, Colorado School of Mines, Golden, CO 80302
Wolfgang Runde	Los Alamos National Laboratory, Los Alamos, NM 87545
Donna M. Smith	Los Alamos National Laboratory, Los Alamos, NM 87545

David R. Turner Center for Nuclear Waste Regulatory Analyses, Southwest Research Institute 6220 Culebra Road San Antonio, TX 78238-5166

Craig E. VanPelt Los Alamos National Laboratory, Los Alamos, NM 87545

T. David Waite University of New South Wales, Sydney, NSW 2052, Australia

Bruce Wielinga Sheppard Miller, Inc., 3801 Automation Way, Suite 100, Fort Collins, CO 80525

Youwen Xu Los Alarnos National Laboratory, Los Alamos, NM 87545

Peng-Chu Zhang Sandia National Laboratories, MS II 3 7 Albuquerque, NM 87185-0750

Conversion Factors for SI and non-SI Units

Conversion Factors for SI and non-SI Units

To convert Column 1 into Column 2, multiply by	Column 1 SI Unit	Column 2 non-SI Units	To convert Column 2 into Column 1, multiply by
	Length		
0.621	kilometer, km (10^3 m)	mile, mi	1.609
1.094	meter, m	yard, yd	0.914
3.28	meter, m	foot, ft	0.304
1.0	micrometer, µm (10^{-6} m)	micron, µ	1.0
3.94×10^{-2}	millimeter, mm (10^{-3} m)	inch, in	25.4
10	nanometer, nm (10^{-9} m)	Angstrom, Å	0.1
	Area		
2.47	hectare, ha	acre	0.405
247	square kilometer, km^2 (10^3 m)^2	acre	4.05×10^{-3}
0.386	square kilometer, km^2 (10^3 m)^2	square mile, mi^2	2.590
2.47×10^{-4}	square meter, m^2	acre	4.05×10^3
10.76	square meter, m^2	square foot, ft^2	9.29×10^{-2}
1.55×10^{-3}	square millimeter, mm^2 (10^{-3} m)^2	square inch, in^2	645
	Volume		
9.73×10^{-3}	cubic meter, m^3	acre-inch	102.8
35.3	cubic meter, m^3	cubic foot, ft^3	2.83×10^{-2}
6.10×10^4	cubic meter, m^3	cubic inch, in^3	1.64×10^{-5}
2.84×10^{-2}	liter, L (10^{-3} m^3)	bushel, bu	35.24
1.057	liter, L (10^{-3} m^3)	quart (liquid), qt	0.946
3.53×10^{-2}	liter, L (10^{-3} m^3)	cubic foot, ft^3	28.3
0.265	liter, L (10^{-3} m^3)	gallon	3.78
33.78	liter, L (10^{-3} m^3)	ounce (fluid), oz	2.96×10^{-2}
2.11	liter, L (10^{-3} m^3)	pint (fluid), pt	0.473

Mass			
2.20×10^{-3}	gram, g (10^{-3} kg)	pound, lb	454
3.52×10^{-2}	gram, g (10^{-3} kg)	ounce (avdp), oz	28.4
2.205	kilogram, kg	pound, lb	0.454
0.01	kilogram, kg	quintal (metric), q	100
1.10×10^{-3}	kilogram, kg	ton (2000 lb), ton	907
1.102	megagram, Mg (tonne)	ton (U.S.), ton	0.907
1.102	tonne, t	ton (U.S.), ton	0.907
Yield and Rate			
0.893	kilogram per hectare, kg ha^{-1}	pound per acre, lb $acre^{-1}$	1.12
7.77×10^{-2}	kilogram per cubic meter, kg m^{-3}	pound per bushel, lb bu^{-1}	12.87
1.49×10^{-2}	kilogram per hectare, kg ha^{-1}	bushel per acre, 60 lb	67.19
1.59×10^{-2}	kilogram per hectare, kg ha^{-1}	bushel per acre, 56 lb	62.71
1.86×10^{-2}	kilogram per hectare, kg ha^{-1}	bushel per acre, 48 lb	53.75
0.107	liter per hectare, L ha^{-1}	gallon per acre	9.35
893	tonne per hectare, t ha^{-1}	pound per acre, lb $acre^{-1}$	1.12×10^{-3}
893	megagram per hectare, Mg ha^{-1}	pound per acre, lb $acre^{-1}$	1.12×10^{-3}
0.446	megagram per hectare, Mg ha^{-1}	ton (2000 lb) per acre, ton $acre^{-1}$	2.24
2.24	meter per second, m s^{-1}	mile per hour	0.447
Specific Surface			
10	square meter per kilogram, m^2 kg^{-1}	square centimeter per gram, cm^2 g^{-1}	0.1
1000	square meter per kilogram, m^2 kg^{-1}	square millimeter per gram, mm^2 g^{-1}	0.001
Density			
1.00	megagram per cubic meter, Mg m^{-3}	gram per cubic centimeter, g cm^{-3}	1.00
Pressure			
9.90	megapascal, MPa (10^6 Pa)	atmosphere	0.101
10	megapascal, MPa (10^6 Pa)	bar	0.1
2.09×10^{-2}	pascal, Pa	pound per square foot, lb ft^{-2}	47.9
1.45×10^{-4}	pascal, Pa	pound per square inch, lb in^{-2}	6.90×10^3

(continued on next page)

Conversion Factors for SI and non-SI Units

To convert Column 1 into Column 2, multiply by	Column 1 SI Unit	Column 2 non-SI Units	To convert Column 2 into Column 1, multiply by
		Temperature	
1.00 (K − 273)	kelvin, K	Celsius, °C	1.00 (°C + 273)
(9/5 °C) + 32	Celsius, °C	Fahrenheit, °F	5/9 (°F − 32)
		Energy, Work, Quantity of Heat	
9.52×10^{-4}	joule, J	British thermal unit, Btu	1.05×10^{3}
0.239	joule, J	calorie, cal	4.19
10^{7}	joule, J	erg	10^{-7}
0.735	joule, J	foot-pound	1.36
2.387×10^{-5}	joule per square meter, J m^{-2}	calorie per square centimeter (langley)	4.19×10^{4}
10^{5}	newton, N	dyne	10^{-5}
1.43×10^{-3}	watt per square meter, W m^{-2}	calorie per square centimeter minute (irradiance), cal cm^{-2} min^{-1}	698
		Transpiration and Photosynthesis	
3.60×10^{-2}	milligram per square meter second, mg m^{-2} s^{-1}	gram per square decimeter hour, g dm^{-2} h^{-1}	27.8
5.56×10^{-3}	milligram (H_2O) per square meter second, mg m^{-2} s^{-1}	micromole (H_2O) per square centimeter second, µmol cm^{-2} s^{-1}	180
10^{-4}	milligram per square meter second, mg m^{-2} s^{-1}	milligram per square centimeter second, mg cm^{-2} s^{-1}	10^{4}
35.97	milligram per square meter second, mg m^{-2} s^{-1}	milligram per square decimeter hour, mg dm^{-2} h^{-1}	2.78×10^{-2}
		Plane Angle	
57.3	radian, rad	degrees (angle), °	1.75×10^{-2}

Electrical Conductivity, Electricity, and Magnetism

10	siemen per meter, S m^{-1}	millimho per centimeter, mmho cm^{-1}	0.1
10^4	tesla, T	gauss, G	10^{-4}

Water Measurement

9.73×10^{-3}	cubic meter, m^3	acre-inch, acre-in	102.8
9.81×10^{-3}	cubic meter per hour, $m^3\ h^{-1}$	cubic foot per second, $ft^3\ s^{-1}$	101.9
4.40	cubic meter per hour, $m^3\ h^{-1}$	U.S. gallon per minute, gal min^{-1}	0.227
8.11	hectare meter, ha m	acre-foot, acre-ft	0.123
97.28	hectare meter, ha m	acre-inch, acre-in	1.03×10^{-2}
8.1×10^{-2}	hectare centimeter, ha cm	acre-foot, acre-ft	12.33

Concentrations

1	centimole per kilogram, cmol kg^{-1}	milliequivalent per 100 grams, meq 100 g^{-1}	1
0.1	gram per kilogram, g kg^{-1}	percent, %	10
1	milligram per kilogram, mg kg^{-1}	parts per million, ppm	1

Radioactivity

2.7×10^{-11}	becquerel, Bq	curie, Ci	3.7×10^{10}
2.7×10^{-2}	becquerel per kilogram, Bq kg^{-1}	picocurie per gram, pCi g^{-1}	37
100	gray, Gy (absorbed dose)	rad, rd	0.01
100	sievert, Sv (equivalent dose)	rem (roentgen equivalent man)	0.01

Plant Nutrient Conversion

	Elemental	*Oxide*	
2.29	P	P_2O_5	0.437
1.20	K	K_2O	0.830
1.39	Ca	CaO	0.715
1.66	Mg	MgO	0.602

1 Introduction to Properties, Sources and Characteristics of Soil Radionuclides

Peng-Chu Zhang, James L. Krumhansl, and Patrick V. Brady

Sandia National Laboratories
Albuquerque, New Mexico

ABSTRACT

The demands for assessing the potential impact of radionuclides produced by military and nuclear power supply applications on environmental quality and human and the desire to remediate radionuclide-contaminated site have triggered an intensive and wide range of research activities. Soil chemical reactions are critical to both environment and human health and to successful remediation. This chapter's aim is to briefly describes the physical and chemical characteristics of the most important radioactive nuclides likely to be found in soils. The primary sources of these radionuclides include the fallout from atmospheric weapon tests, release from fuel processes facilities, nuclear material storage facilities, biomedical applications, and, of course, naturally-occurring radioactive elements. The forms and interactions of the radionuclides in soil environment are subsequently discussed.

Commercial and defense applications of nuclear technology in the past several decades have had a profound impact upon sociological and ecological development and ecological quality throughout the globe. Nuclear technology has been applied in soil sciences to monitor the physical and chemical processes important to agricultural products, the effectiveness of fertilizer application, chemical metabolism soils, carbon cycling, and water content and movement in soil profiles and the subsurface environment. The benefits of nuclear technology to the soil sciences cannot be argued. Although natural radionuclides such as ^{40}K, ^{238}U, and ^{14}C have reacted with soils for millions of centuries, a large quantity of anthropogenic radionuclides that has entered soil since the min-1900s due to massive mining of radioactive mineral ore, multistep processing, and producing nuclear materials for industrial, medical, and weapon application. A direct consequences is a new mode of soil contamination—that of such unnatural isotopes and elements as ^{137}Cs, ^{90}Sr, ^{129}I, and ^{241}Am—that is distinctive of the nuclear century.

In complex soil systems, numerous geochemical, biological, and hydrological processes directly and indirectly affect bioavailability and mobility of soil radioisotopes, and ultimately, ecological quality and potentially human health. Due

 Geochemistry of Soil Radionuclides, SSSA Special Publication no. 59.

to the interlocking and often coupled nature of soil processes, the chemical controls on radioisotope fate in soils can only be understood when the effects of other biological and physical processes are taken into account. Moreover, chemical reactions typically occur in soils under largely uncontrollable conditions due to the spatial and temporal heterogeneity of mineral distribution and behavior, as well as porosity and permeability. This inevitably imparts a large uncertainty to any attempt to describe and/or model the chemical behavior of radioisotopes in soils. Although a wealth of research on soil radiochemistry has been published, a comprehensive and up-to-date summary of research and development is lacking.

This is the motivation for this special publication. Detailed soil chemical processes will be discussed in the subsequent chapters in the hopes of providing a picture of the "state of the art" to those who may not have complete familiarity with radionuclide transport in soils.

ESSENTIALS OF RADIOACTIVITY

It is beyond the scope of this special publication and this chapter to discuss radiochemistry and nuclear chemistry in details beyond those needed to understand the fate of radioisotopes in soils and groundwaters. For details, the readers are referred to more in-depth sources of Adloff and Guillaumont (1993), Choppin (1964), Choppin et al. (1995), Ehmann and Vance (1990), and Geary (1986).

Radionuclide and Radioactivity

A nuclide is an atomic species (X, the chemical symbol for an element) characterized by specific values of the atomic number (Z), and the mass number (A), and is simply represented by the symbol:

$$^{A}_{Z}X \qquad \text{or just, } ^{A}X$$

which is one of the isotopes of an element X (e.g., ^{238}U is an isotope with a mass number of 238 in the element uranium isotope family). The mass number A is the sum protons (Z) and neutrons (N) in the nucleus of the atom:

$$A = Z + N$$

Nuclear masses are represented by m and atomic masses by M. They are expressed in atomic mass unit (amu or μ)

$$1\ \mu = 1.660565 \times 10^{-27}\ \text{kg}$$

or in relation with energy

$$1\ \mu = 931.5016\ \text{MeV}/c^2$$

where MeV is one mega-electron volt (10^6 eV) and c is the speed of light ($2.997925 \times 10^8\ m\ s^{-1}$). In practice 1 μ = 931.5016 MeV is used. The mass of three atomic constituents are given below (Adloff & Guillaumont, 1993):

Proton	1.007276 μ	1.672648×10^{-27} kg	935.279 MeV
Neutron	1.008665 μ	1.674954×10^{-27} kg	939.673 MeV
Electron	5.485802×10^{-4} μ	0.910953×10^{-30} kg	0.511003 MeV

If the nuclide is radioactive, then the term radionuclide is used. Radioactivity is the spontaneous emission of particles or electromagnetic radiations from a species, either an atom or an ion, consisting of a nucleus surrounded by electrons with a total charge of *Z*.

In a nucleus the greater the number of protons, the greater the total coulombic instability. All isotopes that have more protons than neutrons are radioactive, the only exception being the simplest nucleus, $^{1}_{1}H$, which has one proton and no neutrons. Since the net nuclear force is proportional to the total number of neutrons, the presence of neutrons result in a stronger total nuclear force; however, too many neutrons decreases the stability of the nucleus. As the number of protons increases, so also do the repulsive coulomb forces in the nucleus. To overcome this, the total nuclear force must increase through the addition of more neutrons; thus the ratio of the number of neutrons over the number or protons (*N/Z*) increases above unity. The value of *N/Z* necessary for stability for any element is not unique but often covers a small range. Consequently, there are ratios of neutrons to protons that provide maximum stability to nuclei. With some exceptions, the neutron-rich isotopes will be radioactive if the *N/Z* ratio exceeds the values outlined in Table 1–1.

In general there are three components of radiation emitted by radioactive elements: alpha (α) and beta (β) particles and gamma (γ) rays (less common decay modes such as electron capture, neutron and proton emission are not included in this chapter). Alpha-radiation is identical to helium ions (^{4}He), whereas β-radiation is equivalent to electrons. Gamma-radiation has the same electromagnetic nature as x-rays but is of higher energy. The rate of radioactive decay per unit weight is fixed for any specific radioelement, no matter what its chemical or physical state is, though the rate differs greatly for different radioelements. The decay rate is typically expressed in terms of a half-life, which is the time required for the radioactivity of a radioelement to decay to one-half of its original value. Half-lives for the different radioelements vary from fractions of a second to billions of years. Although chemical transformations are typically sensitive to temperature, pressure, physical states, etc., radioactive transformations are not. Chemical reactions occur by rearrangements of outer electrons, whereas radioactive changes originate in the nucleus. Binding energies and reaction energies are so much greater for the nucleus than for ordinary chemical and physical changes—hence radioactive half-lives are insensitive to environmental variables.

Depending on the stability, nuclides can be classified into five different groups (Ehmann & Vance, 1990) as shown in Table 1–2.

Table 1–1. Limiting *N/Z* values for element stability (source Geary, 1986).

	N/Z ratio	Number of exception
Elements below Zn, ($Z = 30$)	1.25	4
Elements from Zn to Ag ($Z = 47$)	1.40	1
Elements from Ag to Os, (Z 76)	1.50	2

Table 1–2. Classes of nuclides.

Class	Sources	Characters	Example
Stable nuclides	Found in nature	No radioactive decay has been found.	^{12}C, ^{14}N, and ^{16}O
Primary natural radionuclides	Found in nature Radioactive since the origin of the solar system	About 26 found.	^{40}K ($t_{1/2} = 1.28 \times 10^9$ yr)
		Very long half-lives	^{238}U ($t_{1/2} = 4.47 \times 10^9$ yr)
Secondary natural radionuclides	Decay products of natural radionuclides	About 38 found. Short half lives	^{226}Ra ($t_{1/2} = 1600$ yr) ^{234}Th ($t_{1/2} = 24.1$ d)
Induced natural radionuclides	Products of cosmic rays' action	About 10 known	^{3}H, and ^{14}C
Artificial radionuclides	Man-made	Approximately 2000 known	^{60}Co, ^{137}Cs, and ^{24}Na

Alpha Decay

Nuclides emitting α particles decrease in A by four units and in Z by two:

$$^{238}_{92}U \rightarrow {}^{234}_{90}Th + {}^{4}_{2}He$$

Alpha radioactivity has been observed for all the elements above lead in the periodic table, as well as for a few nuclei as light as the lanthanide elements. In α decay the α-particles have discrete energies. The α-particles emitted from ^{238}U decay has the 4.18 and 4.13 MeV kinetic energy with abundance of 77 and 23%, respectively. α-particles usually have between 3 and 9 MeV of kinetic energy but, since they are relatively massive and doubly charged, they do not penetrate very far into matter. A thick sheet of paper is sufficient to completely stop α particles emitted in radioactive decay.

Beta Decay

If the ratio of neutrons to protons (N/Z) of the nucleus is too large for stability, a more stable situation can be approached by reducing the N/Z value—specifically by ejecting an electron, formed by the transformation of a neutron to a proton. The β decay processes include electron emission (β^-), positron emission (β^+), and electron capture (*EC*). This reaction can be represented:

$$n \rightarrow p^+ + e^-$$

and it is known as negatron decay or, simply, as negative β-decay. The emitted electron is called the β particle. The result is an increase in Z by one unit with no change in A, for example:

$$^{116}_{49}In \rightarrow {}^{116}_{50}Sn + \beta^-$$

Although there is no change in mass number, there is a change in mass in β-decay. In these spontaneous, exothermic processes, the heavier nuclide decays to the

lighter with the decrease in mass appearing principally as the kinetic energy of the products. Since it is very improbable that two adjacent isobars, the nuclei with the same value of A but different values of Z, would have exactly the same mass, the heavier would decay to the lighter. This provides a simple explanation of the rule on the stability of adjacent isobars. The ^{116}In reaction may be rewritten to indicate the energy change:

$$^{116}_{49}\text{In} \rightarrow {}^{116}_{50}\text{Sn} + \beta^- + Q$$

where Q is the decay energy, 2.95 MeV, carried of as kinetic translation energy by the ^{116}Sn and the β-particles. The energy would be distributed between the two in inverse proportion to their masses. Since ^{116}Sn is very much more massive than the electron, the latter is expected to carry off essentially all the decay energy.

Unlike the discrete energies from α decay, there is a broad, continuous distribution of energies, extending from almost zero to some maximum value from β decay. As an example, the energy is distributed from zero to 2.95 MeV from ^{116}In decaying to ^{116}Sn with the average β particle energy constituting approximately one-third of the 2.95 MeV calculated decay energy.

If negative β-particle emission occurs for nuclei with N/Z value too large for stability, then a reverse process might be expected to occur—specifically decay change should convert a proton to a neutron. As in negatron decay, this process may have to be repeated in several consecutive steps before a stable N/Z value is obtained. Conversion of a proton to a neutron can occur in two different ways—either by emission of a positron (positive β decay, where the reaction is $p^+ \rightarrow n + \beta^+$) or by absorption of an electron, usually from the K or L shells of the atom (electron capture, where the reaction is $p^+ + e^- \rightarrow n$). Two such reactions are:

$$^{120}_{51}\text{Sb} \rightarrow {}^{120}_{50}\text{Sn} + {}^{0}\beta^+$$

and

$$^{195}_{79}\text{Au} \xrightarrow{\text{EC}} {}^{195}_{78}Pt$$

Positive β decay and electron capture are competing processes, with the probability of electron capture increasing as Z increases. With few exceptions, unstable neutron-deficient nuclei with values of Z below 30 undergo positron decay, whereas such nuclei with Z values above 30 decay most often by electron capture. Both processes are observed for $30 < Z < 80$.

Gamma Decay

The third major type of radiation is γ rays. Unlike α- and β- decay, γ radiation causes no change in either Z or A. Gamma rays are electromagnetic radiation like x-rays, ultraviolet, and visible light, and radio waves. γ-rays are emitted from a nucleus as it undergoes transitions from its higher excited state to lower excited states, or its ground state, e.g.,

$$^{115m}_{49}\text{In} \rightarrow {}^{115}_{49}\text{In} + \gamma$$

Emitted γ-rays decrease in mass corresponding to the energy carried away by the γ- rays. For example, in decay of ^{238}U, 77% of the α particles have 4.18 MeV and 23% have 4.13 MeV of energy. Obviously, decay by emission of 4.13 MeV α particles leaves the nucleus with 0.05 MeV greater energy than do 4.18-MeV α emissions. It is found experimentally that this 0.05 MeV is carried off by ejection of a γ ray of that energy (Choppin, 1964). Emission of γ- rays occurs immediately ($\leq 10^{-12}$ s) following α- or β-decay but in some cases the nucleus may remain in the higher energy state for a measurable length of time (milliseconds or greater) and the excited state of the nucleus and its daughter state are referred as nuclear isomers.

Gamma rays are emitted with a discrete energy, like α-particles, rather than with a continuous spectrum of energies as negatron and positron decay particles are (β-decay). Since they have no mass or charge, γ-rays do not interact readily with matter and therefore possess great penetration power. Whereas a 4-MeV α particle is stopped by a film of water a few millimeters thick, a 4-MeV electron requires approximately 2 cm of water to achieve the same effect. By contrast, a beam of 4-MeV γ rays passing through 20 cm of water would retain one- half the original number of rays, and 10% would survive passage through 70 cm of water (Choppin, 1964).

Although α, β, and γ decay are the most common decay modes, several others exist, including fission, delayed neutron and proton emission, double-β decay, 2-proton decay, and decay by emission of heavier particles. Among these, fission is probably the most important in terms of its industrial and defense applications, and ancillary waste concerns.

In addition to the decay modes discussed, another decay mechanism, fission decay, should be briefly discussed for a completion of radioactive decay introduction. The products of fission are found in a number of sites as the sources of radioactive contaminants. Fission decay involved two types of process: spontaneous fission and neutron-induced fission. Spontaneous fission is a naturally occurring decay process in which a nucleus breaks into two fragments, along with the emission of two to three neutrons. An example of a spontaneous fission decay process is:

$$^{252}_{98}Cf \rightarrow {}^{98}_{38}Sr + {}^{152}_{60}Nd + 2 \text{ neutrons}$$

The neutron-induced fission process is initiated by capturing a neutron:

$$^{235}_{92}U + {}^{1}\text{n} \rightarrow {}^{140}_{56}Ba + {}^{94}_{36}Kr + 2 \text{ neutrons}$$

The nuclides formed in a fission process are called fission products. Each fissionable nuclide can produce a wide range of fission products. Many fission products are radioactive and decay in the modes described above.

It should be kept in mind that in a group of identical radionuclides, several decay modes may be observed. The competition is expressed by the branching ratios that correspond to the relative probability of occurrence of a decay mode. For example, three decay modes are known for ^{40}K (negative and positive β decay, ~99.8%, and electron capture (EC) decay, ~0.2%) and for ^{152}Eu (EC, 72%, β decay,

28%). Competition is the rule rather than an exception. When examined in full detail, the decay of a radionuclide is a very complex process. For example, the 15 isotopes of Pu with mass number from 232 to 246 have very different radioactive properties, depending on the mass number (A):

^{232}Pu to ^{235}Pu and ^{237}Pu decay by EC with a very weak α branching.
^{236}Pu, ^{238}Pu, ^{239}Pu, ^{240}Pu, ^{242}Pu, and ^{244}Pu are α emitters.
^{241}Pu is a β emitter with a very weak α branching.
^{243}Pu, ^{245}Pu, and ^{246}Pu are pure β emitters.
^{238}Pu, ^{239}Pu, and ^{241}Pu also emit γ rays with intensities below 4%.
^{238}Pu to ^{240}Pu, as well as ^{242}Pu and ^{244}Pu, also decay by spontaneous fission.

Radioactive Units

The earlier literature references and some of the older textbooks in radiochemistry naturally used the older units. Even now many practicing scientists have not adopted the SI units that were recommended as the standardization of names and symbols by many international scientific bodies. Curie and Becquerel units have be often found used exchangeably in literature for radiation activities.

The Curie unit (Ci) has been used for radioactive decay unit for many years and is still being used in some cases, but the SI unit, Becquerel (Bq), has practically replaced Curie unit and is the only unit accepted by most scientific publishers. The two are related as follows:

$$1 \text{ Becquerel (Bq)} = 1 \text{ disintegration } s^{-1}$$

$$1 \text{ Curie (Ci)} = 3.65 \times 10^{10} \text{ s}^{-1} \text{ (Bq) or } 1 \text{ Bq} = 27 \text{ } p\text{Ci } (p = 10^{-12})$$

The original definition of Ci was the number of decay per unit time and gram of ^{226}Ra, assuming its half-life to be 1599 y. This is now known not to be precisely correct but the detail of this argument is not directly important; what important is that it suggests a relationship between the mass of a radioisotope and its activity (Geary, 1986).

Specific Activity

The specific radioactivity describes the relationship between radioactivity and mass and is the decay rate (counts per unit of time) per unit mass of an element or compound—the SI unit is Bq kg^{-1}. For practical purposes specific radioactivity also is defined in dpm g^{-1} or dpm mole^{-1}. Activity concentration (or radioactive concentration) is given in Bq m^{-3} or Bq l^{-1}. For example, the total atoms in 1 g of ^{32}P ($t_{1/2}$ = 14.3 day) is:

$$\begin{aligned} 1 \text{ g} &= 1/32 \text{ moles of } ^{32}\text{P} \\ &= (6.023 \times 10^{23})/32 \text{ atoms of } ^{32}\text{P} \end{aligned}$$

From the decay equation:

$$dN/dt = -\lambda N$$

where N is the number of radioactive nuclides, t is time (s) and λ is the decay constant ($0.693/t_{1/2}$). The activity can be obtained from:

$$dN/dt = (-)\ \frac{0.693 \times 6.022 \times 10^{23}}{32 \times 14.3 \times 24 \times 60 \times 60} \text{ disintegrations s}^{-1}$$

$$= 1.055 \times 10^{16} \text{ disintegrations s}^{-1}$$

Therefore, 1 g of ^{32}P has the activity of 1.055×10^{16} Bq (or 2.853×10^5 Ci).

With the half-life of 1599 yr the specific activity per gram of ^{226}Ra is 0.988 Ci or 3.65×10^{10} Bq or 2.9×10^{12} dpm. The specific activities of some of the longer-lived naturally occurring radioactive species are: ^{40}K, 31.3 kBq kg^{-1}; ^{232}Th, 4.05 MBq kg^{-1}; and ^{238}U, 12.4 MBq kg^{-1} (Choppin et al., 1995).

SOURCES OF RADIONUCLIDES IN SOILS

Natural Radioactivity in Soils

Although much public concern is related to the dispersal of man-made radioisotopes, there are, in fact, a considerable number of sources of natural radioactivity in most soils. Some of these ultimately trace their origin to the stellar nuclear synthesis events that produced the basic elemental makeup of the solar system. Elements in U and Th decay chains (Table 1–3) fall in this class, along with a short list of lighter long lived radioisotopes: ^{190}Pt, ^{187}Re, ^{180}Ta, ^{174}Hf, ^{176}Lu, ^{156}Dy, ^{152}Gd, $^{147\text{-}149}Sm$, ^{144}Nd, ^{142}Ce, ^{138}La, ^{123}Te, ^{115}In, ^{87}Rb, ^{50}V, and ^{40}K. These lighter elements usually have minuscule abundances in nature and the isotopic percentage of the unstable nuclei is always very small. Thus, in practice, the only members of

Table 1–3. Uranium and Th decay chains—isotope, half life, and decay modes. Compiled from Weidner and Sells (1960) and General Electric Nuclear Energy Division (1970).

^{238}U decay series	^{235}U decay series	^{232}Th decay series (100%)
^{238}U, 4.51×10^9 yr, α	^{235}U, 7.13×10^8 yr, α	^{232}Th, 1.4×10^{10} yr, α
^{234}Th, 24.5 d, β	^{231}Th, 24.6 h, β	^{228}Rn, 5.6 yr, β
^{234}Pa, 1.14 min, β	^{231}Pa, 3.4×10^4 yr, α	^{228}Ac, 6.1 h, β
^{234}U, 2.48×10^5 yr, α	^{227}Ac, 21 y, α(1.2%)β(98.8%)	^{228}Th, 1.9 y, α
^{230}Th, 8.0×10^4 yr, α	^{227}Th, 18.2d, α	^{224}Ra, 3.6 d, α
^{226}Ra, 1662 yr, α	^{223}Fr, 21 min, β	^{223}Rn, 55.6 s, α
^{222}Rn, 3.8 d, α	^{223}Ra, 11.7 d, α	^{216}Po, 0.15 s, α
^{218}Po, 3.0 min,α (99.9%)β(0.03%)	^{219}Rn, 3.9 s, α	$^{212}Pβ$, 10.6 h, β
^{218}At, 2s, α	^{215}Po, 0.002 s, α	^{212}Bi, 1.0 h, β
^{214}Pb 26.8 min, β	^{211}Pb, 36.1 min, β	^{212}Po, 45 s, α
^{214}Bi, 20 min,α.(0.04%)β(99.9%)	^{211}Bi 2.16 min, α(99.7%)β(0.3%)	^{208}Pb, Stable
^{214}Po, $1.6s10^{-5}$ s, α	^{211}Po, 0.52 s, α	
^{210}Tl, 1.3 min, β	^{207}Tl, 4.8 min, β	
^{210}Pb, 22 yr, β	^{207}Pb, Stable	
^{210}Bi, 5 d, β		
^{210}Po, 140 d, α		
^{206}Pb, Stable		

this list that are of importance in the earth sciences are Nd, Sm, Rb, and K; and only K typically contributes a significant amount to the normal level of background radiation. The U and Th decay chains contain all the other natural radionuclides that are of economic (e.g., U and Th) or environmental (Ra, Rn, and Po) concern.

Because of their ancient origins, the source radioisotopes for the U and Th decay chains must both have very long half lives (on the order of billions of years); however, individual isotopes in the decay chain may have very short half-lives. This leads to a situation known as secular equilibrium in which the abundance of the different isotopes in a decay chain adjust to the rate at which an isotope appears due to the decay of the next higher member in the chain and is balanced by the rate that it disappears due to its own natural radioactive decay. To achieve this situation, however, requires that the system remain isolated for many thousands of years. If a system is open the chemical exchange with the environment it may permit removal of some element. Not only does this deplete the system in that radioisotope but it also perturbs the abundances of all the succeeding radioisotopes lower in the decay chain. The relative abundance of the resulting nonequilibrium assemblage of daughter products can provide insights into the timing and chemical environment of the disruption.

In addition to radioisotopes that persisting from supernova events predating the origin of the solar system, soils also contain detectable amounts of radioisotopes that are continually being replenished by cosmic ray bombardment of the solid earth and atmosphere. Although none occur in sufficient amounts to have an economic or environmental impact at least ^{14}C is of considerable scientific importance by virtue of its role in dating geologic and anthropogenic materials. These processes also produce minute amounts of ^{7}Be and ^{10}Be as well as ^{3}H (Friedlander et al., 1964). These isotopes also have been used to lesser degrees to deduce insights into the rates of geochemical processes.

Biomedical Radioactivity Sources

Since the advent of the atomic age radioisotopes have played a variety of important roles in what is broadly be termed the life sciences, including agricultural and soil sciences. The benefits cannot be argued. Various research activities have over the years employed almost every conceivable radioisotope, but probably the most commonly used isotopes are those employed for specific medical treatments or as tracers in biochemical investigations (Table 1–4). Of particular value are the isotopes that can be attached to particular sites in cellular matter to trace chemical processes in living tissue: ^{3}H, ^{35}S, ^{32}P, and ^{14}C. Other isotopes are used so routinely in modern medicine that the names of the tests appear in daily conversation: PET scan (tumor detection), thallium stress test (heart disease), cobalt irradiation (cancer treatment), and the like.

When they have finished their assigned tasks, however, all of the radioisotopes must eventually be disposed of. This typically involves entry into the sewers or burial in shallow trenches. In either case, these radioisotopes then have the potential of being locally dispersed in the soil column. How serious is this potential source of contamination? At ground zero caution is always advised until a radiation source has decayed to innocuous levels. Fortunately, the vast majority of these

Table 1–4. Common isotopes used in the life sciences:

Isotope	Use	Half life
^{3}H	Tracer	12.3 yr
^{11}C	PET scan	20 min.
^{14}C	Tracer	5730 yr
^{18}F	Diagnostics	1.8 h
^{32}P	Bone cancer therapy, tracer	14.3 d
^{35}S	DNA labeling	87.2 d
^{51}Cr	Blood cell survival	27.8 d
^{54}Mn	Liver diagnosis	313 d
^{57}Co	Instrument calibration	271 d
^{60}Co	Radiation therapy source	5.3 yr
^{65}Zn	Biochemistry	244 d
^{67}Ga	Biochemistry	3.3 d
^{68}Ge	Tumor imaging	3.26 d
^{75}Se	Antibody labeling	120 d
^{85}Sr	Biochemistrty	64.7 d
^{90}Y	Colon cancer therapy	29 yr
^{99}Mo	Radioimmunotherapy	2.7 d, to ^{99}Tc, 2.1×10^{5} yr
^{103}Pd	Diagnostics	17 d
^{111}In	Diagnostics and therapeutics	2.8 d
^{113}Sn	Diagnostics	115 d
^{123}I	Colon cancer therapy	13.1 h
^{125}I	SPECT brain imaging	59.7 d
^{131}I	Therapeutics	8.1 d
^{133}Xe	Diagnostics, thyroid disorders	3.3 d
^{153}Sm	Diagnostics and therapeutics	1.9 d
^{153}Gd	Bone cancer therapy	242 d
^{169}Yb	Osteoporosis	31 d
^{201}Tl	Radiography	3.0 d

isotopes decay quickly enough that many half-lives will elapse during the normal period of institutional control (several decades) that could reasonably be expected to restrict access to a disposal site. Thus, with competent packaging it is unlikely that most of this activity could ever move or present a hazard to the general public. Notable exceptions to this rule are ^{3}H, ^{14}C, ^{60}Co, ^{90}Y, and ^{99}Tc. Of this list, ^{3}H, ^{60}Co, and ^{90}Y are only problematic in a time frame measured in centuries while the others persist for millennia. Finally, it is relevant to note that the total curie content of most of most medical radwaste is small so that simple dilution considerations dictate that, at the worst, the radionuclides could only present a local hazard.

Fallout

At the undesirable end of the spectrum, both regard to dispersal and benefits to man, are the radioisotopes found in fallout dispersed around the globe. In general, these isotopes are associated with Ur or Pu fission events. Dispersal may be either intentional, as in the case of an above ground nuclear weapon test, or accidental, as when a reactor fails catastrophically. A great many different radionuclides are produced as a consequence of fission reactions but the proportions produced depend on the environment in which the process occurs. Nuclear weapons detonations do not produce radionuclides in the same proportions as are produced in the core of a reactor, and in detail, the radionuclide inventory from a power reac-

tor is different than that of a facility operated for plutonium production. Thus, fallout from an above ground test will not have quite the same radioisotope inventory as that from a reactor accident. The gross chemistry of the two types of fallout also is likely to be somewhat different. When a nuclear device is detonated above ground, the debris from the exploding device is mixed with immense amounts of dust (essentially Al–Si–Fe–Mg–Na–K–Ca oxides) at temperatures significantly above the melting points of these materials. Thus, many of the radionuclides ultimately end up incorporated into particles of fused glass or as minor constituents in crystals or refractory oxides formed from the major elements in the cloud. In a reactor accident much less admixture of incidental material occurs so the fallout is likely to more closely resemble the chemistry of components in the reactor cores.

Early in the Cold War Era a second important distinction was realized regarding the fate of different radionuclides as fallout is being formed. Certain elements, notably Cs and I, partition strongly into the vapor phase at significantly lower temperatures than most other elements. These elements tend to be highly mobile and may even reside primarily as dissolved constituents in water droplets in clouds. Alternatively, elements such as the rare earths and Pu are not readily vaporized and tend to associated with refractory solid particles. These differences can lead to significant partitioning of the different radioisotopes found in fallout. Thus, for example in seawater, 70% of the fallout Cs and 87% of the fallout Sr are in an ionic form while the ionic fractions of radioactive Ce and Ru are 2% and ~ 0% relatively. Instead, they reside primarily in the colloidal and suspended solid materials (Sereda, 1966).

Mobile radioisotopes are available to immediately interact with soil components while the others will reside in discrete fallout particles until they are released by weathering processes. There is an immense body of literatures dedicated to studying the uptake of mobile fallout Cs by clays (i.e., Poinssot et al., 1999) and the persistent but capricious retention of small amounts of fallout iodine in soils (Bors et al., 1988).

At the other end of the spectrum are refractory metallic grains found in fallout from the accident of a nuclear power plant at Chernobyl (1986, Ukraine). These particles can be traced to the metallic grains (Fe, Ni, Mo, Tc, Ru, Rh, and Pd) that segregate on grain boundaries during prolonged fuel irradiation. Such particles are insoluble even in nitric acid, constitute a major obstacle in reprocessing spent fuels, and should persist as discrete grains in a soil column for very long times (Schubert & Behrend,1987). Intermediate in availability are the radioisotopes incorporated into unstable ceramic or glassy particles during above-ground nuclear tests.

Finally, it is important to realize that not all fission by-products are of equal importance with regard to understanding the distribution of radionuclides in the soil. A literature survey of bomb fallout titles from 1970 to the present revealed that only the following radioisotopes were cited a significant number of times: $^{239\text{-}240}$Pu, ^{36}Cl, ^{129}I, ^{90}Sr, and ^{137}Cs. Including citations relating to the two large nuclear disasters in the former Soviet Union, Chernobyl and Mayak adds ^{103}Ru, ^{106}Ru, ^{60}Co, ^{99}Tc, (Schubert & Behrend, 1987) as well as Np and Am (Beasley et al., 1998) to the list.

The case of ^{36}Cl is of particular interest. It is not found in fallout at concentrations that present an environmental hazard and it is not a fission product. Rather,

it originates from the activation of normal ^{35}Cl by the intense flux of neutrons emanating from nuclear explosions. Parenthetically, these tests also produced a spike in the ^{14}C levels by the activation of natural stable ^{13}C (natural abundance 1.11%). Minute amounts of ^{36}Cl also are produced by cosmic ray bombardment in the atmosphere but above-ground testing completely overshadowed this natural production.

Since Cl^- is poorly retained by most mineral surfaces it is almost a conservative tracer in many groundwater systems. Thus, it's presence (or absence), along with ^3H from the hydrogen bomb tests, has shed a great deal of light on the rates and directions of groundwater movements during the last half-century. A host of fallout radionuclides also have been found in seawater (Preston, 1974) and, the more soluble ones such as ^{137}Cs and ^{90}Sr have provided much insight into mixing of water masses in the oceans. Most of the radioisotopes found in seawater, however, interact so strongly with mineral surfaces that they are of less utility in understanding groundwater systems than are ^{36}Cl and ^3H.

Nuclear Fuel Reprocessing

The reprocessing of nuclear fuel has produced immense concentrations of various radioisotopes at a number of localities around the world. Although essentially point sources the amounts of radioactivity concentrated at these localities are so great that the effluent has contaminated entire river systems. Thus, like aboveground nuclear tests and nuclear accidents, such sites may introduce radionuclides into soils on a regional basis. These sites reprocess fuel by dissolving it in nitric acid, recovering the valuable constituents (usually U and sometimes Pu) and discarding the residue as high-level nuclear waste. For defense applications the principal objective is to recover Pu. In the case of reprocessing of commercial fuel the idea is to separate the U from fission product "poisons" (fission products with large neutron capture cross sections). These poisons build up and quench the chain reaction long before the enriched U has actually been depleted to the point where clean material would no longer sustain a chain reaction. Reprocessing of these fuels is designed to simply remove the poisons and recycle the U back into new reactor fuel. Here, Pu is just another unwanted waste. Beyond the systematics of U or Pu recovery, the wastes from these processes typically contain the entire gambit of fission products plus at least a few of the actinides (Am and Np) that are not of commercial value. Locations where these high level wastes have spilled on the ground constitute some of the most heavily polluted soils in the planet.

To properly appreciate the issue it is necessary to consider the relative evolution over time of the radionuclide inventory in such wastes. After aging for a year, spent commercial fuel contains significant inventories of about 30 fission products but after a century the number shrinks to 20. The identity of the dominant radionuclides changes over time as well. After a century the activity from the ^{90}Sr and ^{137}Cs decay chains still completely dominate the radiation output from spent fuel. Taking a longer-term perspective, after 1000 years the identities of the most troublesome radionuclides will have changed and become more complicated: Pu, Am>Tc>Np, Nb>Se, Sn, Sb, Cs, and Sm. Whether the Pu will actually be in the waste or have been harvested for weapons development, depends on local cir-

cumstances. ^{93}Zr and ^{59}Ni (from neutron activation of reactor components) also may be of concern once the Cs and Sr have decayed away. During this period of time the total amount of radioactivity emanating from the waste also decreases dramatically. It is relevant to point out that the long-term problem elements appearing after 1000 years were always in the waste, and did not grow in as a function of time. Thus, to understand long term soil contamination issues it is necessary to look beyond Cs and Sr that can be readily detected in present day soils.

It should not be supposed that all of these radioisotopes are equally likely to appear in contaminated soils. If the acid solution typically used to dissolve the fuel rods is spilled then they will appear together, but this is a rare event. In practical application, the closest one can come to such a distribution occurred at Mayak Site in the former Soviet Union (Beasley et al., 1998) where a waste tank exploded and dispersed the contents without regard to the physical association of different radionuclides in the tank. Usually, releases to the environment arise from the far less catastrophic slow leakage of a waste storage tank. At least at Hanford, WA, the wastes are stored as highly caustic fluids. In this setting certain elements (Sr, rare earths, Sn, Sb, Nb) partition strongly into the colloidal Fe-Al hydrous oxide sludges that collect in tank bottoms. Tc, Cs, and Se, however, stay in solution, and may travel considerable distances from the source of the leak. Iodine is a special case as it was often released to the air as vapor during reprocessing, however, to the degree that it still resides in the liquid fraction it, too, will travel considerable distances before it its movement is attenuated significantly by soil minerals. Thus, in a simple leaking tank scenario the problem radionulides may be more determined by the chemistry of the fluid than the bulk inventory of the waste source for the pollution.

In summary both natural and anthropogenic sources can supply radionuclides to soils. Often, natural radioactivity is at such low levels as to constitute no apparent health risk. Rather, it is useful in providing insights into the rates of geochemical processes that would be difficult to understand by other means. Probably the least worrisome sources of artificially introduced radiation are wastes arising from research and medical purposes, which are usually low in radioactivity and often the half-lives are short. The major sources of artificial radioactivity dispersed in soils are fallout and leakage from nuclear fuel reprocessing facilities. Almost the entire surface of the earth has received at least measurable amounts of different radionuclides from these sources. The short-lived high activity isotopes such as ^{137}Cs and ^{90}Sr have received much of the attention. But, fully documenting the dispersal of radionuclides in soils may require consideration of other lower activity radioisotopes, that are not as readily detected, but will persist long after the ^{137}Cs and ^{90}Sr have decayed to innocuous levels.

ENVIRONMENTAL IMPACT OF SOIL RADIONUCLIDES

The impact of radioisotopes on human health is caused by radiation emission from both the initial decay and any subsequent decay of daughter products. Although a number of radionuclides have been employed in industrial and defense applications (see above section), only a limited number, a dozen or so, make it into soils

Table 1–5. Environmentally important radioisotopes and target organs.

Isotope	Organ
^{90}Sr	Bone marrow
^{129}I	Thyroid
^{60}Co, ^{137}Cs	Whole body
$^{234,235,238}U$	Whole body
$^{238,239,240,241}Pu$	Whole body
$^{226,228}Ra$	Bond surface
^{241}Am	Bone marrow
$^{229,230,232}Th$	Bone marrow

in the sufficient abundance to pose an appreciable environmental impact. Understanding of soil geochemical processes of radionuclides should in theory allow us to model transformation of chemical species of those isotopes and, more important, to predict whether the contaminant radionuclides in soils are transported to the point where they can impact human health.

Humans take up radionuclides by way of a number of paths, including: ingestion of contaminant-laden dust; consumption of contaminated ground or surface water; ingestion of plants that have picked up radionuclides either through roots, or on their leaves and, for the case of breathing of air contaminated with gaseous radioisotopes (e.g., ^{222}Rn and $^{14}CO_2$). Together, the chemical form, characteristic decay path, and the organ affected by a given radionuclide determine the risk posed on human health. In Table 1–5 several isotopes of environmental concern and the organ in which each of them concentrates are listed.

Radioactive isotopes of an element have similar environmental and toxicological behavior to the non-radioactive isotopes. If they are introduced into the body by inhalation ingestion, the chemical properties of the element will determine its ultimate destination in the body. For example, it is well known that strontium and radium are chemically similar to Ca and tend to deposit on bone surfaces and bone marrow with that element; tritium (^3H) becomes incorporated into water molecules and is distributed throughout the body. The main difference between radioactive and nonradioactive isotopes is that the radionuclides emit one or more types of radiation as they decay to more stable forms. The type and energy level of the emitted radiation is nuclide-specific.

Note that while radioisotopic contaminants that might be present in soil or groundwater at hazardous levels with respect to radioactivity [e.g., 10^6 disintegrations per minute (dpm) mL^{-1}], would still tend to be at such a low molar concentration to have no significant effect relative to the natural background of the stable isotopes of that element. For example, either of the dominant hazardous fission products, ^{90}Sr or ^{137}Cs, if present in groundwater at 10^6 dpm mL^{-1}, would only amount to a mass concentration of about 10^{-9} g mL^{-1}. Typically, groundwater exhibits much higher background levels of 10^{-5} and 10^{-6} g mL^{-1} of the natural stable isotopic forms of these elements. Strontium-90, at its maximum contaminant level (MCL) of 8 pCi/L (0.018 dpm mL^{-1}), represents a radioisotope concentration of $<10^{-16}$ g mL^{-1}. Thus, the behavior of most radioisotopes of an element with respect to chemical reactivity will be dominated by the stable isotopic forms.

In general, the longer-lived radionuclides decay slowly and are more persistent in the environment, however, their specific activity, the amount of activity per unit mass, is relatively low. Shorter-lived radionuclides decay more quickly to stable forms, and their specific activity is generally much higher than those of longer-lived radionuclides. The daughter products of a number of decaying radionuclides are themselves radionuclides, which also can provide significant doses of radiation. For example, ^{90}Sr decays to ^{90}Y, which in turn decays to stable ^{90}Zr. The contribution from ^{90}Y is approximately 8% of that ^{90}Sr based on drinking water contaminated with ^{90}Sr.

Overview of Selected Radionuclides

A short overview of radionuclide sources, decay paths, ingestion pathways and behaviors in soils and plants follows Brady et al. (1999) and others as cited.

Americium-241

Americium (^{241}Am) is found in daily life such as used in sealed sources (e.g., smoke detectors), but reactor operations and atomic weapons production are the primary activities that contribute ^{241}Am to soil. Americium has no stable isotopes. The half-life of ^{241}Am is 432.2 yr. It decays to ^{237}Np ($T_{1/2} = 2.14 \times 10^6$ yr) with the emission of a α particle and associated γ-rays. Americium exists primarily in the trivalent state. The soil mobility of ^{241}Am is low except the soils contain low Ca and Na. Only small quantities can be expected to migrate within the soil to the biosphere. Sorption to carbonate minerals is a known sequestration mechanism (Higgo & Rees, 1986). Lower pH values tend to destabilize the carbonate minerals and increase Am mobility (Pavlotskaya et al., 1991; Yamamoto et al., 1980). Soil Am is taken up by plant roots, though uptake varies by plant species. Chelating ligands aid plant uptake. Because ^{241}Am is primarily an α emitter, it is most dangerous in humans when it is taken into the body via inhalation of ingestion where it can interact with living tissue. The critical organs of concern in internal exposures are the bone, liver, and lung. Biological half-lives are 70 000 d for the bone and total body and 30 000 d for the liver and kidneys.

Cesium-137

Radioactive fallout from above ground nuclear weapon testing and nuclear facility accident releases are the primary source of ^{137}Cs in soil. ^{137}Cs has a half-life of 30.2 yr. Ninety-four percent of the time it decays to metastable ^{137m}Ba ($T_{1/2}$ = 153 s) with the emission of a 514 keV maximum energy β particle. The remaining 6% decays directly to stable ^{137}Ba with the emission of a 1176 KeV maximum energy β particle. The ^{137m}Ba nucleus usually (~90%) decays to stable ^{137}Ba with the emission of a 662 keV γ-ray; the remaining 10% of decays are by low energy electrons. It is the 6621 keV γ-ray emitted by the ^{137m}Ba nucleus that is of most concern from a health perspective. Plants take up Cs and uptake by fodder crops is one of the primary processes that transfers Cs to the animal and human food chain. Gastrointestinal tract absorption of Cs is the primary means Cs entering into humans. Although not strongly retained, Cs tends to accumulate in soft tissues and muscles.

The biological half-life of ^{137}Cs is approximately 100 d in adults. External exposure to ^{137}Cs from the surface of contaminated soil is typically the pathway providing the greatest dose.

Cobalt-60

The primary source of environmental ^{60}Co is low-level radioactive waste materials generated as a result of neutron activation of stable ^{59}Co present in structural components of nuclear reactor vessels. Cobalt-60 also comes from nuclear reactor operations the manufacture, use, and/or disposal of medical and industrial sources. ^{60}Co has a half-life of approximately 5.3 yr, and decays to stable ^{60}Ni with the emission of 1480 keV maximum energy β particles. The high energy γ-rays also emitted during decay (1170 and 1330 keV) means that the radiation from this radionuclide is often the limiting radiation for personnel exposure during reactor maintenance activities. In soils Co can be strongly sorbed onto Fe and Mn oxides' surfaces and loosely to soil organic matter (Bibak, 1994; Brooks & Herman, 1998). In the White Oak Creek Watershed in Oak Ridge, Cerling and Spalding (1982) found about 60% of the ^{60}Co strongly bound to the hydrous ferromanganous oxide phase of the streambed sediments. Uptake of ^{60}Co by plants is pH-dependent. Cobalt tends to preferentially accumulate in the liver. The biological half-life of ^{60}Co in the body is 9.5 d.

Iodine-129

Iodine (^{129}I) is a fission product that is found in nuclear power plant wastes, including ion-exchange resins, filter sludges, evaporator bottoms, off-gas cartridge filters, trash, and decommissioning wastes. The half-life of ^{129}I is 16 million years. It decays to stable ^{129}Xe through emitting a β particles with a maximum energy of 150 KeV. Iodide is the primary form of I in soils except under particularly arid and alkaline conditions. Although iodide typically sorbs poorly to most soil materials, it is apparently taken up by soil organic matter, some clays, and metal sulfides (Krumhansl et al., 2002, this publication). The most important ^{129}I ingestion pathway for humans is the air–vegetable–cow–milk pathway (particularly for children and infants). Accumulation in the thyroid occurs largely within the first 12 h of exposure. The biological half-life of ^{129}I is approximately 100 d for the thyroid, 14 d for the bone, and 7 d for the kidney, spleen, and reproductive organs.

Plutonium

Plutonium does not exist as a naturally occurring element with the exception that small amount of Pu generated in the natural reactors (the Oklo natural reactor in Gabon). The primary input of Pu to environment is fallout from nuclear weapon tests and accident release (e.g., the Windscale accident in 1957 and the Chernobyl accident in 1986). Three of the most common of the 15 known Pu isotopes are ^{239}Pu (94%), ^{240}Pu (6%), and ^{241}Pu (0.4%). ^{239}Pu has a half-life of 24,000 yr. Its α-decay results in production of ^{235}U ($T_{1/2}$ = 700 million yr). ^{240}Pu has a half-life of 6560 yr, emits α particles and decays to ^{236}U ($T_{1/2}$ = 20 million yr). Due to the long half-

life of ^{236}U, remaining isotopes in the decay chain are not significant to dose. ^{241}Pu has a half-life of 14.4 yr and decays to ^{241}Am ($T_{1/2}$ = 433 yr) with the emission of a β particle. Americium-241 subsequently decays to ^{237}Np ($T_{1/2}$ = 2.14 million yr) by emitting α particle. Because ^{241}Pu is difficult to measure and ^{239}Pu and ^{240}Pu cannot be differentiated, the total Pu (^{239}Pu + ^{240}Pu) is usually reported. The mobility of Pu in soils depends upon a number of soil conditions such as pH, clay content, the presence of $CaCO_2$, and organic matter (Nitsche & Silva, 1996; Ryan et al., 1998). Microbial activity may enhance the movement of Pu (Ruggiero et al., 1999). Surface contamination, rather than uptake by roots, is considered as the primary cause of accumulation of Pu in the native plants and agricultural crops (Fresquez et al., 1998; Livens et al., 1994). Most ingested Pu in human body is eventually deposited in the skeleton and the liver and tends to be immobile in these two organs (biological half-lives of respectively 84 and 73 yr).

Radium-226

Radium (^{226}Ra) has a half-life of 1600 yr and is the decay product of ^{238}U. Radium is often found in waters draining U-bearing rocks and in the U processing wastes. Radium exists in the environment typically as a divalent cation, Ra^{2+} which behaves similarly to Ba or Ca and may form aqueous complexes with sulfate ions or carbonate ions. The fate and behavior of ^{226}Ra in soil and sediment directly affects the dose of public exposure to radioactivity for the Ra decay daughter product, radon, is responsible for 55% of this type of radioactivity (NCRP, 1987). Compared with U, Ra has a higher mobility in soils and higher accessibility to the food chain. The activity ratio (AR) of $^{226}Ra/^{238}U$ in the soil is about 0.1, but ^{226}Ra greatly exceeds ^{238}U activity in most surface soil (AR up to 1.8) and in vegetation (AR up to 65; Greeman et al., 1999). Interaction between Ra and soil constituents such as clays, oxides, and soil organic matters remains relatively unknown. Investigation of adsorption of Ba, as an analog to Ra, on montmorillonite, using both batch sorption and synchrotron based x-ray absorption spectroscopy (EXAFS), Zhang et al. (2001) suggest that Ra can form both inner- and outer-surface complexes on the clay surface.

Strontium-90

Strontium (^{90}Sr) is a fission product that is common in spent fuel. Nuclear fuel processing, above ground nuclear weapons testing, and nuclear accidents are primary environmental sources of ^{90}Sr. Strontium-90 also is released by nuclear power plants, submarine propulsion reactors, and radioactive waste disposal in the oceans. ^{90}Sr has a half-life of roughly 29 yr. The decay products are ^{90}Yt ($T_{1/2}$ = 64 h, with the emission of a 546 keV maximum energy β particle) and then the stable ^{90}Zr with the emission of a 2284 keV maximum energy β particle from ^{90}Y. Infrequently (~0.02%), the ^{90}Y nucleus emits a 523 keV maximum energy β particle and produces a 1750 keV γ-ray. Plant absorption of Sr is common. Being a chemical isomorph for Ca in biogenetic material like bone, Sr tends to accumulate in the bone and bone marrow. Strontium-90 tends to dominate calculated environmental and human health risks at many contaminated sites associated with nuclear processing.

Technetium-99

Technetium (^{99}Tc) is produced by U and Pu neutron fission has a half-life of 2.1×10^5 yr. ^{99}Tc has been released into the environment through nuclear weapons testing, leaks from nuclear facilities such as spent fuel reprocessing plants, storage, and repositories. In addition, ^{99}Tc also is produced by the use of ^{99m}Tc ($T_{1/2} = 6.01$ h), which is used in nuclear medicine (Tagami & Uchida, 1999). The pertechnetate ion (TcO_4^-) is the dominant chemical form of dissolved Tc(VII) and total Tc in the environment. Adsorption of pertechnetate on mineral surfaces occurs, though it is weak and tends to be strongly affected by pH and other anions (Zhang et al., 2000). In reduced soils, pertechnetate anion can be reduced to sparingly soluble Tc(IV). Reduced Tc is readily sorbed by soil constituents and also forms complexes with organic matter (Sheppard et al., 1990; Tagami & Uchida, 1996; Yanagisawa et al., 1997). Reduced technetium is not readily reoxidized when it is exposed to aerobic conditions (Tagami & Uchida, 1999). The availability of reduced Tc to plants is much less than that of pertechnetate (Yanagisawa et al., 1997). After entering plant tissues, the mobility of pertechnetate ion decreases. Consequently, the highest Tc concentrations were found in the older tissues of the plant. Ingested ^{99}Tc localizes in the thyroid gland and the gastrointestinal tract. Within 10 h, it redistributes to the stomach and organs with excretory functions. Its biological half-life in the body is approximately 60 h.

Thorium

Thorium is about three times as abundant as U and about as abundant as Pb or Mo. Thorium is recovered commercially from the mineral monazite, which contains from 3 to 9% ThO_2 along with rare-earth minerals. Thorium has several isotopes whose atomic masses range from 212 to 236. All of the isotopes are unstable. ^{232}Th occurs naturally, has a half-life of 1.4×10^{10} yr, and decays through emission of an α particle. Six α and four β decay steps occur before ^{232}Th becomes stable ^{208}Pb. Hydroxides of thorium(IV) are the dominant species in soil and aquatic systems, although carbonate complexes also form.

Tritium

Cosmic rays produces small amount of tritium in the upper atmosphere. The relatively short half-life (12.3 yr) of tritium results only in very low natural terrestrial concentrations though. A much more significant source of tritium has been radioactive fallout and discharges from nuclear power plants. Tritium also is used in industrial thickness gauges, luminous paints, nonpowered light sources, fusion research, as a radioactive tracer in chemistry and biological experiments, and in production of nuclear weapons. The energy of the β particles from tritium decay (18.6 keV) is the lowest known. The chemical properties of tritium are the same as that of ordinary H. Tritium exists as a tritated water molecule in soil and environment. Most field studies indicate that tritium distribution coefficient (K_d) values are very low—tritium migration velocities are close to those of the accompanying groundwater. The biological half-life of tritium in the human body is ~12 d. Ingested tritiated water is assumed to be completely absorbed from the gastrointestinal tract, mixing rapidly with body water.

Uranium

Natural U consists primarily of three isotopes, ^{234}U (0.0057%), ^{235}U (0.71%), and ^{238}U (99.3%). The isotope of interest for nuclear reactors and nuclear weapons is the fissile ^{235}U. Anthropogenic sources of U include mine and mill tailings, and ^{238}U from the enrichment processes, and spent fuel from nuclear reactor. The half-life for ^{234}U is 250,000 yr. Uranium-234 decays through a series of radionuclides to the stable ^{206}Pb, simultaneously emitting α and β particles and γ rays. In the U decay chain ^{222}Rn ($T_{1/2}$ = 3.8 d) is one of the radionuclides of concern because it can easily enter the human lungs for it suspends in the gas phase. ^{235}U and ^{238}U have half-lives of 700 million and 4.5 billion yr, respectively, decaying to stable ^{207}Pb, and ^{206}Pb, respectively, while emitting α and β particles and γ rays in the process.

Although U can be found as U(IV), U(V), and U(VI), U(IV) and U(VI) are the most likely U oxidation states and they are present in reducing and oxidizing conditions, respectively. In solutions without carbonates, the soluble U(VI) species include UO^{2+}, UO_2H^+, $(UO_2)_3(OH)_5^+$, and $(UO_2)_3(OH)_7^-$. Typically, carbonate levels of in the natural solutions cause conversion of hydroxyl U(VI) species to dissolved U(VI)-carbonate species such as $UO_2CO_3^0$, $UO_2(CO_3)_2^-$, and $UO_2(CO_3)_3^{4-}$. The anionic U-carbonate species dominate at and above neutral pH and tend to cause the desorption of U(VI) from mineral surfaces and solubilization of U(VI) solids. In addition to carbonate, soluble aqueous complexes of U(VI) include sulfate, fluoride, and phosphate. Soil U taken up by plants is one of the primary pathways leading to human exposure. Uranium tends to concentrate in the bones and bone marrow. Inhaled U also can provide a significant dose to the lungs for the long half-lives of U isotopes. The biological half-life of U is 300 d for the bones and 100 d for general contamination of the body; however, the chemical toxicity of U is generally more significant than its radiotoxicity.

REFERENCE

Adloff, J.-P., and R. Guillaumont. 1993. Fundamentals of radiochemistry. CRC Press, Boca Raton, FL.

Beasley, T.M., J.M. Kelley, K.A. Orlandini, L.A. Bond, A. Aarkrog, A.P. Trapeznikov, and V.N. Pozolotina. 1998. Isotopic Pu, U, and Np signatures in soils from Semipalatinsk-21, Kazakh Republic and the southern Urals, Russia. J. Environ. Radiochemistry 39(2):215–230.

Bibak, A. 1994. Cobalt, copper, and manganese adsorption by aluminum and iron-oxides and humic-acid. Commun. Soil Sci. Plant Anal. 25:3229–3239.

Bors, J., R. Martens, and W. Kuhn. 1988. Studies on the role of natural and anthropogenic organic substances in the mobility of radio-iodine in soils. Radiochimica Acta. 44/45:201–206.

Brady, P.V., B.P. Spalding, K.M. Krupka, R.D. Waters, P. Zhang, D.J. Borns, and W.D. Brady. 1999. Site screening and technical guidance for monitored natural attenuation at DOE sites. Sandia Report SAND99-0464. Sandia Natl. Lab., Albuquerque, NM.

Brooks, S.C., and J.S. Herman. 1998. Rate and extent of cobalt sorption to representative aquifer minerals in the presence of a moderately strong organic ligand. Appl. Geochem. 13:77–88.

Cerling, T.E., and B.P. Spalding. 1982. Distribution and relationship of radionuclides to streambed gravels in a small watershed. Environ. Geol. 4:99–116.

Choppin, B. 1964. Nuclei and radioactivity. W.A. Benhamin, New York.

Choppin, G. R., J.-O. Liljennzin, and J. Rydberg. 1995. Radiochemistry and nuclear chemistry. Butterworth-Heinemann Ltd., Oxford.

Ehmann, W.D., and D.E. Vance. 1990. Radochemistry and nuclear methods of analysis. John Wiley & Sons, New York.

Fresquez, P.R., D.R. Armstrong, M.A. Mullen, and L. Naranjo. 1998. The uptake of radionuclides by beans: Squash and corn growing in contaminated alluvial soils at Los Alamos National Laboratory. J. Environ. Sci. Health Part B. 33:99–121.

Friedlander, G., J.W. Kennedy, and J.M. Miller. 1964. Nuclear and radiochemistry. 2nd ed. John Wiley & Sons, New York.

General Electric Nuclear Energy Division. 1970. The chart of the nuclides, physical constants, and conversion factors and table of equivalents. Technical Education Program of GEND, San Jose, CA.

Geary, W.J. 1986. Radiochemical methods. John Wiley & Sons, London.

Greeman, D.J., A.W. Rose, J.W. Washington, R.R. Dobos, and E.J. Ciolkosz. 1999. Geochemistry of radium in soils of the eastern United States. Appl. Geochem. 14:365–385.

Khan, S.A., Riazurrehman, and M.A. Khan. 1994. Sorption of cesium on bentonite. Waste Manage. 14:629–642.

Krumhansl, J.L., P.V. Brady, and P. Zhang. 2002. Soil mineral backfills and radionuclide retention. p. 191–209. *In* P. Zhang and P.V. Brady (ed.) Geochemistry of soil radionuclides. SSSA Spec. Publ. 59. SSSA, Madison, WI.

Livens, F.R., A.D. Horrill, and D.L. Singleton. 1994. The relationship between concentrations of plutonium and americium in soil interstitial waters and their uptake by plants. Sci. Total Environ. 155:151–159.

Nitsche, H., and R.J. Silva. 1996. Investigation of the carbonate complexation of Pu(Iv) in aqueous solution. Radiochimica Acta 72:65–72.

Pavlotskaya, F.I., Y.N. Pospelov, B.F. Myasoedov, Y.V. Kuznetsov, and V.K. Legin. 1991. Behavior of transplutonium elements in the environment. Soviet Radiochemistry 33:307–313.

Poinssot, C., B. Baeyens, and M. Bradbury. 1999. Experimental and modeling studies of caesium sorption on illite. Geochim. Cosmochim. Acta. 63(19/20):3217–3227.

Preston, A. 1974. Artificial radioactivity in the sea. p. 817–836. *In* E. Goldberg (ed.) Marine chemistry. John Wiley & Sons, New York.

Ruggiero, C.E., M.P. Neu, and L.A. Vanderberg. 1999. Plutonium and uranium interactions with siderophores of aerobic soil microbes. J. Inorganic Biochem. 74:282–282.

Ryan, J.N., T.H. Illangasekare, M.I. Litaor, and R. Shannon. 1998. Particle and plutonium mobilization in macroporous soils during rainfall simulations. Environ. Sci. Technol. 32:476–482.

Schubert, P., and U. Behrend. 1987. Investigations of radioactive particles from the Chernobyl fall-out. Radiochimica Acta. 41:149–155.

Sereda, G.A., 1966. Artificial radioactivity of the oceans. p. 55. *In* V.I. Baranov and L.M. Khitrov (ed.) Radioactive contamination of the sea. Israel Program for Scientific Translations, Jerusalem.

Sheppard, S.C., M.I. Sheppard, and W.G. Evenden. 1990. A novel method used to examine variation in Tc sorption among 34 soils: Aerated and anoxic. J. Environ. Radioactivity 11:215–233.

Tagami, K., and S. Uchida. 1996. Microbial role in immobilization of technetium in soil under waterlogged conditions. Chemosphere 33:217–225.

Tagami, K., and S. Uchida. 1999. Chemical transformation of technetium in soil during the change of soil water conditions. Chemosphere 38:963–971.

Yamamoto, M., S. Yamamori, K. Komura, and M. Sakanoue. 1980. Behavior of plutonium and americium in soils. J. Radiation Res. 21:204–212.

Yanagisawa, K., Y. Muramatsu, and T. BanNai. 1997. Behavior of technetium in paddy soils. J. Radioanalytical Nucl. Chem. 226:221–223.

Weidner, R.T., and R.L. Sells. 1960. Elementary modern physics. Allyn & Bacon, Inc., Boston.

Zhang, P., P. Brady, S. Arthur, W. Zhou, D. Sawyer, and D. Hesterberg. 2001. Barium adsorption on montmorillonite surface. Colloid Surface Sci.: Physicochem. Eng. Aspects 190:239–249.

Zhang, P., J.A. Krumhansl, and P.V. Brady. 2000. Boehmite sorbs perrhenate and pertechnetate. Radiochim. Acta 88:369–373.

2 Geochemical Interactions of Actinides in the Environment

Wolfgang Runde

Los Alamos National Laboratory
Los Alamos, New Mexico

ABSTRACT

One of the world's most serious concerns is the safe treatment, shipping, and disposal of radioactive waste originated from the nuclear weapons and energy cycles. Among the multiple constituents of radioactive waste, the actinide elements are of major importance due to their long half-lives of hundreds to hundred thousands of years, their radiation emission, and their toxicity for human health. In order to predict the environmental risk and release rates of actinides and to design meaningful remediation strategies, it is critical to understand the geochemical reactions actinides may undergo when being transported by natural (ground- and surface) waters into the environment. The range of potential reactions in natural aquifer systems is extremely broad because of the great variety of chemically active compounds in nature and the rich chemistry actinide elements exhibit. The light actinide elements, U, Np, Pu, and americium, can exist in multiple oxidation states, III–VI, with each forming behaviorally distinct molecular species that can differ by orders of magnitude in reactivity, stability, and solubility. The conditions of the aquifer, such as pH, redox potential (Eh), complexant concentrations, and colloid concentration, determine the predominant actinide species and their transport characteristics. Actinide solubility increases with the formation of the higher soluble penta- and hexavalent actinides. The geochemical processes that are most important for the actinides' fate in the environment are precipitation, complexation of dissolved species, interactions at solution-mineral interfaces, colloid formation, and the interactions with microorganisms. These reactions are discussed for the light actinides (U, Np, Pu, and Am) in their environmentally most relevant oxidation states III, IV, V, and VI.

Since the advent of nuclear weapons hundreds of tons of man-made Pu have accumulated. Large amounts of fission products and heavy radionuclides have been released to the environment from nuclear weapons production, testing, and recovery, from nuclear fuel fabrication and reprocessing of spent nuclear fuel, or from past poor disposal and interim storage practices. About 6.4 billion m^3 of contaminated soil and groundwater are estimated to exist within the U.S. Department of Energy complex (U.S. Department of Energy, 1998). Testing of nuclear weapons released approximately 3.5 t of Pu into the atmosphere and 95 kg of ^{241}Am built up

 Geochemistry of Soil Radionuclides. SSSA Special Publication no. 59.

from the β-decay of the short-lived isotope ^{241}Pu (Choppin & Stout, 1989). The annual production of 400 to 500 t of spent nuclear fuel in a 22 GWe nuclear reactor contains about 4 t of Pu (Kim et al., 1996). The majority of spent nuclear fuel (SNF) is stored at the Hanford site (2133 MTHM) and at Idaho National Engineering and Environmental Laboratory (INEEL) (270 MTHM) in underground storage tanks with a total of approximately 90 million gallons of high-level and low-level radioactive waste. Many of these tanks reached their design lifetime and radioactivity is leaching out into the surrounding environment. Approximately 20 000 Curies of actinides (including technetium) have been estimated to be in the Hanford waste tanks, including 500 to 900 kg of Pu, about 30 kg of americium, and between 50 and 100 kg of Np, that require the disposal in a high-level nuclear waste repository (Agnew et al., 1997). Ten out of 18 U.S. Department of Energy Pu production and interim storage sites are reported to have significant Pu contamination in soil or sediments and groundwater (Riley & Zachara, 1992). The quantities of actinide contaminations that are found at aging production facilities and radioactive waste storage sites are of most concern because they are neither as contained and controlled as national stockpiles nor distributed at concentrations as low as global fallout.

While most of the radionuclides produced in the nuclear fuel cycle are short lived, the long-living radionuclides, such as the actinides, formed by neutron capture reactions, are of major concern for long-term risk for human health. When entering the geosphere, the light actinide elements (U, Np, Pu, Am, and Cm) exhibit a complex and diverse chemistry that is nurtured by the particularly elaborate environmental systems with hundreds of chemically active compounds and minerals. To confound matters, some of the light actinides are likely to undergo reduction–oxidation (redox) reactions and thus may change their oxidation states under the mildest conditions or often exist simultaneously in two or more of their III, IV, V, and VI oxidation states. In each oxidation state, the actinides have a characteristic chemical reactivity and form complexes and solids of different stability and solubility (Choppin, 1983; Kim, 1993; Langmuir, 1997). Accordingly, the light actinides exhibit some of the richest and most involved chemistry in the periodic table.

As a result, the chemical interactions of actinides in the environment are inordinately complex. Figure 2–1 summarizes the most important possible reactions of actinides in environmental systems. Uraniumnderstanding this dynamic interplay between actinides and the environment is needed to predict how, and how fast, actinides might migrate through the specific environments, is critical for accurately assessing the feasibility of storing nuclear waste in geologic repositories, and it is essential for designing effective cleanup strategies. We need to characterize local conditions, including the nature of minerals and soil components, temperature and pressure profiles, and the local waters' pH, Eh, and ion concentrations. We also need a quantitative knowledge of the competing geochemical processes that affect the actinide's behavior, most of which are illustrated in Fig. 2–1. The present article provides an overview of the most important geochemical reactions of actinides in natural aquatic systems confined to precipitation and dissolution, solution speciation, colloid formation, and the interaction with surfaces and microorganisms. There is an increasingly body of literature on the various environmentally relevant reactions of actinide elements and, therefore, it is not possible to provide a comprehensive review of all aspects of this scientific research area. While we are fully

aware of additional geochemical processes, such as coprecipitation, mineralization, or diffusion, their roles on the environmental behavior of the actinides will not be discussed here in detail. We also refer to the numerous articles that are devoted to the aqueous chemistry of actinide elements with focus on natural systems (Ahrland et al., 1975, 1980; Choppin, 1983; Kim, 1993; Langmuir, 1997).

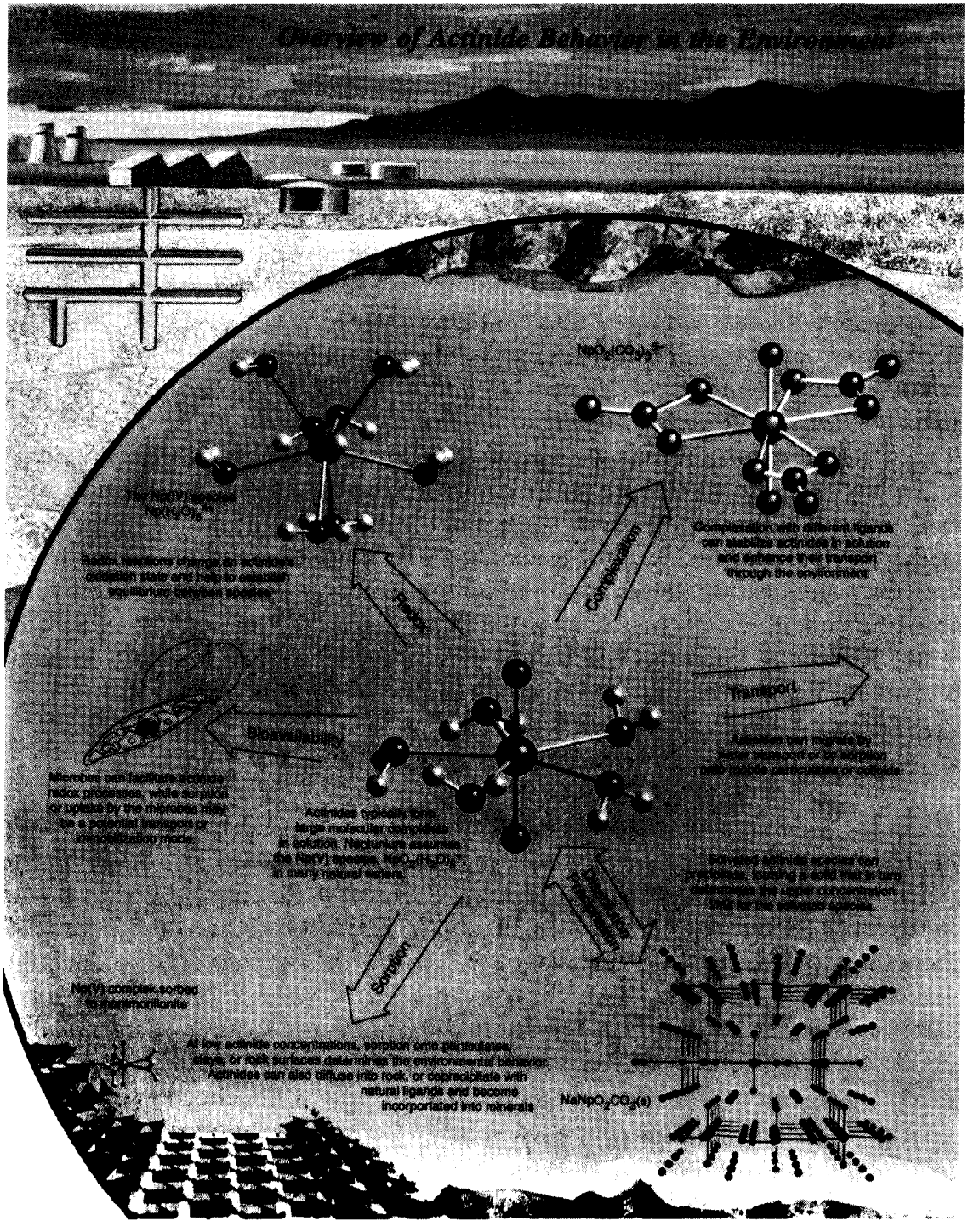

Fig. 2.1. Schematic overview of the most important reactions of actinides in a natural environment. Illustration is reproduced with permission from LA Science (2000).

SOLUTION CHEMISTRY

Water is the dominant transport medium for most elements in the environment (Stumm & Morgan, 1981). Compared with the extreme pH values and ionic strengths that can be adjusted in the laboratory, most natural waters are relatively mild, typically nearly neutral (pH 3 to 9) with a wide range of redox potentials (from −300 to 700 mV) and low salinities (ionic strength below 1 *M*) (Baas-Becking et al., 1960; Langmuir, 1997; Stumm & Morgan, 1981). Liquids that contain radionuclides and heavy metals have been released at numerous U.S. Department of Energy sites to surface soil, ponds, and pits or accidentally leaked from aging underground storage tanks, trenches, etc. In contrast to natural waters, these liquid waste streams are extreme in their chemical conditions, namely highly acidic (INEEL) or highly alkaline [Hanford or Savannah River Site (SRS)] with high amounts of inorganic or organic salt mixtures. Reactions of extreme conditioned solutes leaking from storage containers with soil constituents can alter the surface functional groups that eventually control the transport behavior of contaminants. Evaporation and precipitation of secondary minerals and waste constituents on present soil–mineral surfaces change the natural geochemical environment and may cover natural mineral surfaces with a contaminant-bearing salt layer. Consequently, the hydrogeochemical parameters of soil and mineral phases and subsequently the contaminants' interactions at the mineral–water interface may change significantly upon contact with those wastewaters.

The water conditions determine which actinide oxidation states predominate and which actinide species are stable. Groundwater conditions may change upon infiltration into the nuclear waste storage or disposal area and corrosive reactions with waste package and backfill materials. For example, corrosion of steel drums and Fe-containing materials in waste repositories produces Fe(II) that could establish reducing conditions and may change the redox potential of an infiltrating aerobic water. Reducing conditions will maintain the actinides in their low-soluble states and reduce their release rate and further transport into the environment.

Oxidation State Stability

The light actinide elements differ from their 4f analogues, the lanthanides, in their ability to exist in common solutions in oxidation states III through VI. The potential appearance of multiple oxidation states is of particular importance for the transport characteristics of redox-sensitive actinides, such as Np and Pu. Figure 2–2 shows the reported redox potentials for U, Np, Pu, and Am ions at acidic, neutral, and basic pH. For U, Np, and Am the redox potentials between the oxidation states differ sufficiently enough so that one or two states are usually favored over all others. The redox potentials of Pu in the oxidation states III, IV, V, and VI are all remarkably similar around approximately 1.0 V. Therefore, under certain conditions Pu can coexist in up to four oxidation states in the same solution. Table 2–1 summarizes the oxidation states of the actinides and highlights the environmentally most relevant ones. Some of the oxidation states listed, such as Pa(III) or Pu(VII), can be synthesized only under extreme conditions, far from those found in natural systems. In the III and IV oxidation states, the actinides form hydrated An^{3+} and An^{4+}

Table 2–1. Oxidation states of light actinides.

Th	Pa	U	Np	Pu	Am	Cm
III	III	III	III	III	**III**	**III**
IV	IV	**IV**	**IV**	**IV**	IV	IV
	V	V	**V**	**V**	V	
		VI	VI	**VI**	VI	
			VII	VII		

The environmentally most important oxidation states are bolded.

ions, respectively, in solution. The highly charged cations in the V and VI oxidation states are unstable in aqueous solution and hydrolyze instantly to form linear *trans*-dioxo (actinyl) cations, AnO_2^+ and AnO_2^{2+}, respectively. Covalent bonding between the actinide and the two (actinyl) oxygen atoms enhances the effective

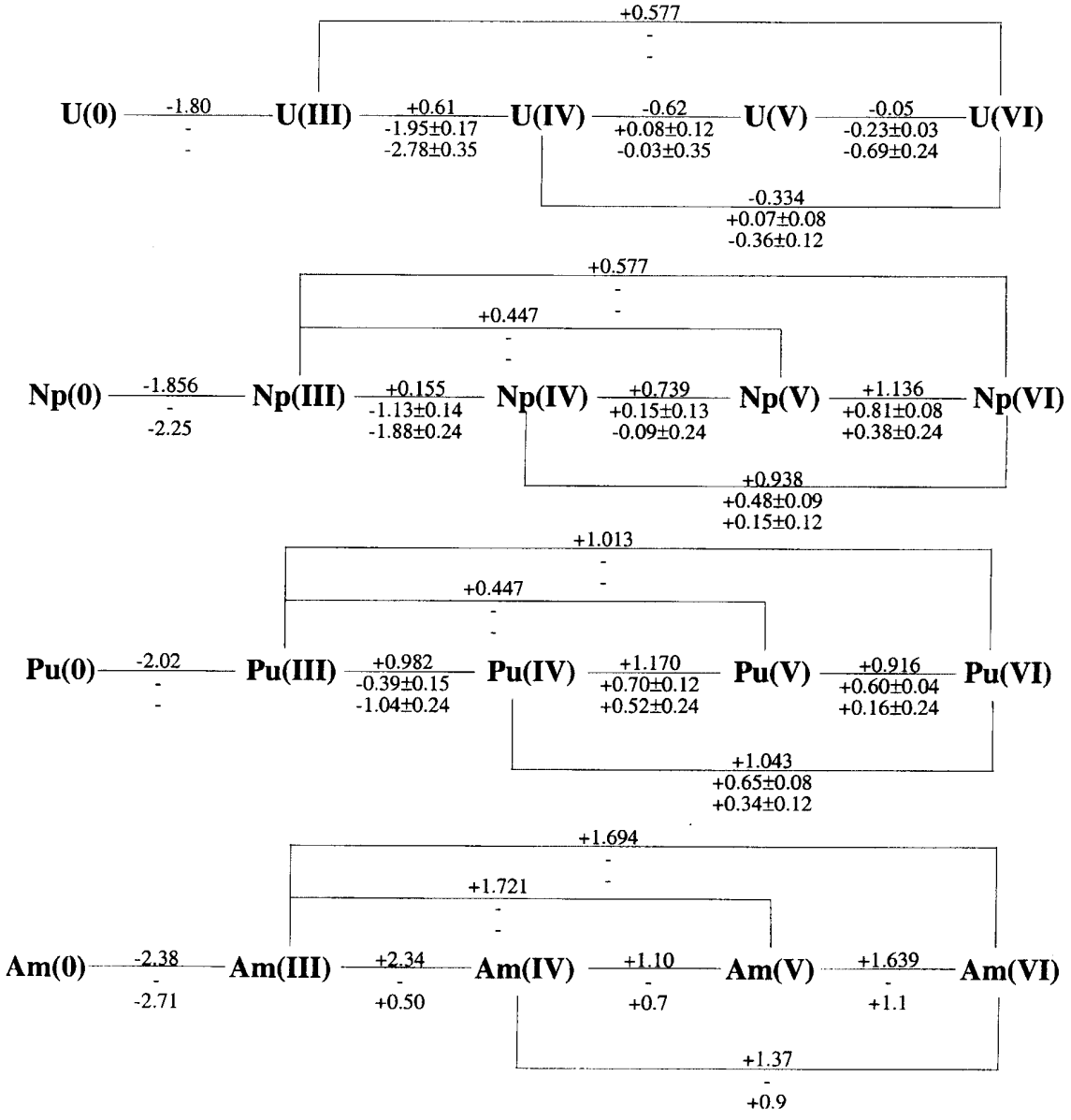

Fig. 2–2. Redox potentials in volts of U, Np, Pu, and Am in 1 *M* $HClO_4$ (top numbers), pH 8 (middle), and 1 *M* NaOH (bottom value) (Ahrland et al., 1975, 1980 and citations within).

charge of the central actinide ion to 2.3 ± 0.2 for AnO_2^+ and 3.3 ± 0.1 for AnO_2^{2+} (Choppin, 1983). The higher effective charge of An(VI) versus An(V) correlates with a stronger, hence shorter, bond to the coordinated oxygens, i.e., about 1.74 Å in Pu(VI) and 1.81 Å in Pu(V) (Conradson, 1998). The preference of actinide ions to form complexes generally follows their effective charges in the order $An^{4+} > AnO_2^{2+} = An^{3+} > AnO_2^+$. Thus, tetravalent actinides form the most stable complexes and also form the least soluble solids; conversely, An(V) complexes are the weakest among the different oxidation states and solubilities are generally the highest.

The linear trans-dioxo moiety of actinyl(V) and (VI) ions limits the structural variability in comparison to the potential coordination geometries of *tris*- and tetravalent actinide ions. For example, Am^{3+}(aq) is coordinated by nine water molecules (Matonic & Neu, 2001, personal communication), see **I** in Fig. 2–2, while UO_2^{2+}(aq) is bound by five water molecules in the equatorial plane perpendicular to the actinyl axis (Allen et al., 1997), see **II** in Fig. 2–2. The nominally higher preferred coordination number of trivalent lanthanide and actinide ions also is reflected in the coordination of four carbonate ligands to form the highly charged $Nd(CO_3)_4^{5-}$ anion (Runde et al., 2000), see **III** in Fig. 2–2, while the triscarbonato complex, $AnO_2(CO_3)_3^{4-}$ (Allen et al., 1995), see **IV** in Fig. 2–2, is known as the limiting An(VI) carbonate species.

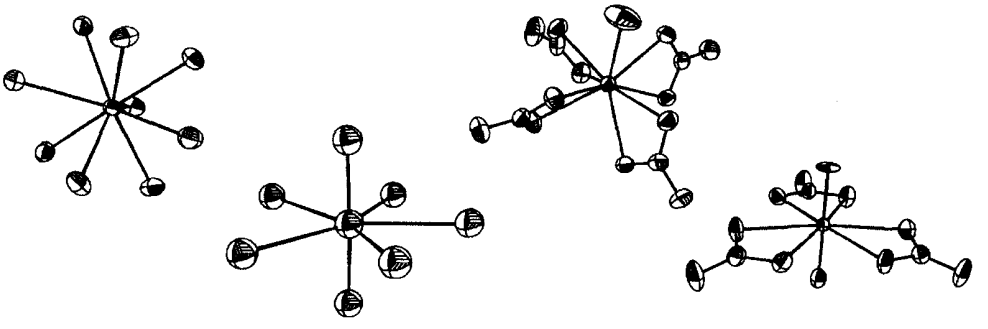

I II III IV

The conditions of a solution phase control the solution speciation of the actinides. The solution Eh governs the general stability of oxidation states that then can be enhanced by complexation reactions. Pourbaix (Eh–pH) diagrams are useful tools to illustrate oxidation state stability fields calculated from thermodynamic data. The stability region of most natural water overlaps with the stability fields of Np in the IV and V and Pu in the III, IV, V, and VI oxidation states (Fig. 2–3). In general, the lower oxidation states are more stable in acidic media, while basic conditions stabilize the higher oxidation states; however, the different complexation strengths of actinides in each oxidation state may reverse this generalized tendency (Choppin, 1983). These solution parameters are extremely important for redox-sensitive actinides, i.e., Np and Pu, which can easily alter their oxidation states. For example, aqueous tetravalent and pentavalent Np and Pu species predominate at conditions of most natural (near-neutral pH) waters. At very low redox potentials (below approximately 0.1 V), Np(IV) and Pu(IV) species are stable in solution, while increasing Eh stabilize Np(V) and Pu(V) in solution. As such, Np(V) is the most stable actinide in the pentavalent oxidation state. Disproportionation reactions of Pu(V), leading to oxidized and reduced forms simultaneously

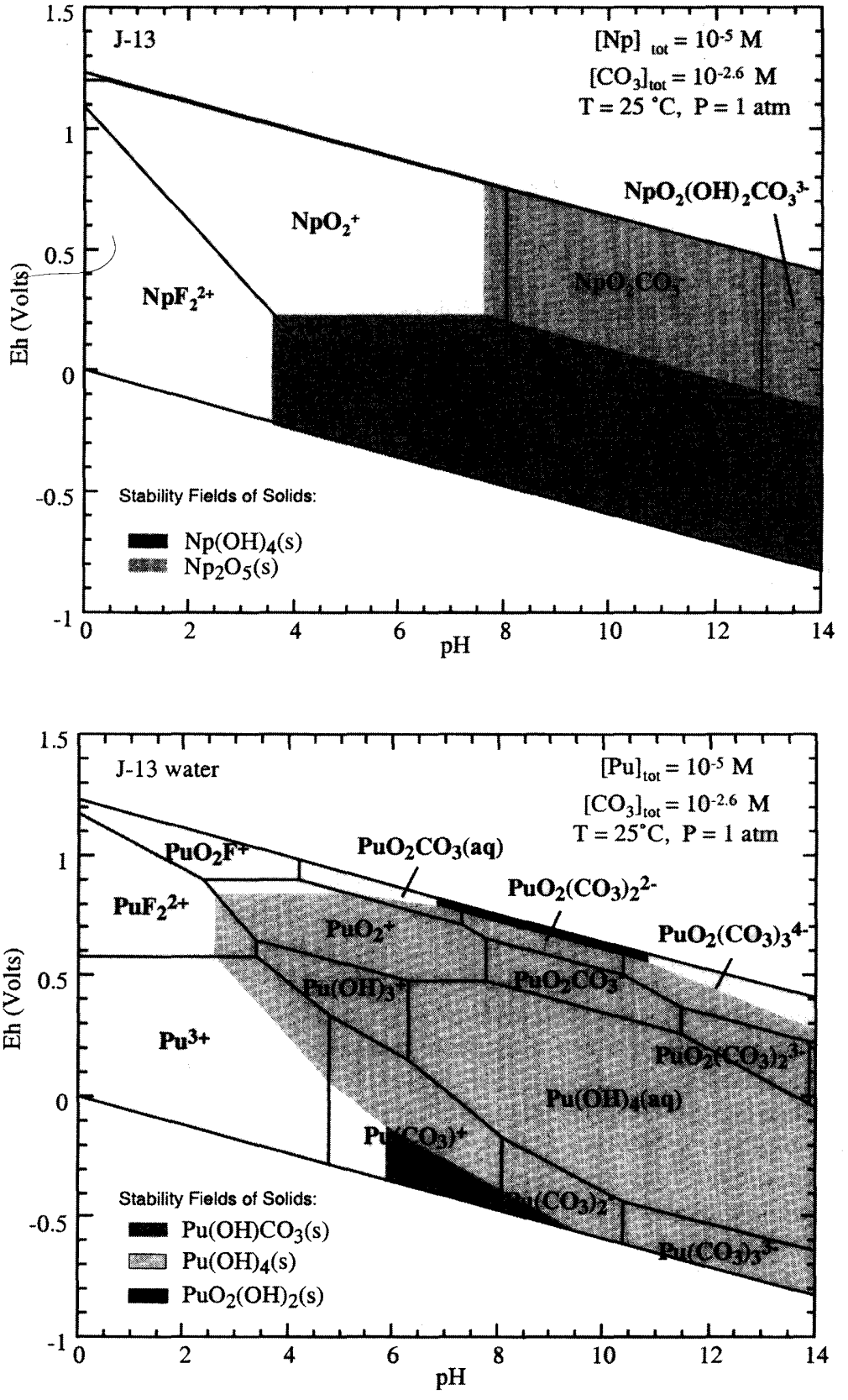

Fig. 2–3. Pourbaix (Eh vs pH) diagram for Np (top) and Pu (bottom) in water that contains hydroxide, carbonate, fluoride ions as the main coordinating ligands. The shaded areas represent stability regions of solid phases that precipitate from a 10^{-5} mol L^{-1} Np or Pu solution. Solid lines represent the stability fields for solution species. The oxidation state stabilities are enclosed by the area of water stability: above the top line, water is oxidized to oxygen and below the bottom line, water is reduced to hydrogen.

in solution, is a characteristic feature of Pu chemistry (Choppin et al., 1997); however, this reaction is favored at high concentration of Pu and is unlikely to occur at the trace concentration as found in natural waters. Plutonium(III) occurs in natural waters only at very low redox potentials (below 300 mV at pH 5 and below 0 mV at pH 7). Plutonium(VI) species reside within the Eh–pH stability field of water at very high redox potentials and therefore Pu(VI) is unlikely to persist in most geochemical systems.

While Pu can coexist in multiple valence states, the other light actinides mainly resume one or two oxidation states. Uranium is most stable in the VI oxidation state and tetravalent U can exist only under strongly reducing conditions. Americium and Cu dominate in the III oxidation states under most conditions and their chemistry is very similar to the chemistry of the predominantly trivalent lanthanides. Increasing complexity of solution composition may stabilize generally less-stable oxidation states. In fact, in concentrated chloride solutions Am(III) and Pu(IV) can be oxidized through the radiolytic formation of oxidizing species, such as hypochlorite, ClO^-. At high specific activity levels those normally stable oxidation states are oxidized to form Am(V) and Pu(VI) under the influence of (its own) α-radiation (Büppelmann et al., 1988; Magirius et al., 1985; Pashalidis & Kim, 1992; Runde & Kim, 1994). The oxidation rate is dependent on various parameters, such as the specific activity present, chloride concentration, or pH.

The concentrations of the predominant natural ligands, hydroxide and carbonate, fluctuate with changing pH and CO_2 partial pressure. As hard "acids" the actinide ions form strong complexes with oxygen-donating ligands, i.e., OH^- and CO_3^{2-} or PO_4^{3-}, and less stable complexes with F^- and SO_4^{2-}, and only weak complexes with the monovalent anions Cl^- and NO_3^-. Actinide complexes with latter ligands are only formed at significantly increased ligand concentrations (above 1 *M*), far outside the compositions of most natural waters. Although hydrolysis generally dominates the solution speciation of actinides, under ambient conditions carbonate concentrations at neutral pH are sufficient to form mixed actinide hydroxocarbonato and pure carbonato solution complexes. The resulting negatively charged solution species, such as $Am(CO_3)^{2-}$ or $UO_2(CO_3)_3^{4-}$, dominate as pH increases and are responsible for the increased actinide solubility in the more alkaline region. As an example, Fig. 2–4 shows the solution species distribution of Np and Pu in a groundwater calculated for the Eh value of 400 mV and about 2 mmol carbonate. Clearly, NpO_2^+ and $NpO_2CO_3^-$ are the most important species for the Np system and Np(IV) are orders of magnitude less stable. In contrast, $Pu(OH)_4(aq)$ is the predominant solution species under similar conditions. While Pu(IV) hydrolysis species predominate at 400mV, PuO_2^+ (at pH above 6) and the Pu(V) monocarbonato complex, $PuO_2CO_3^-$, become the most important solution species of Pu at 500 mV (Fig. 2–5). Thus, in the range of most environmental conditions even mild changes in Eh may reverse the Pu speciation and consequently its overall environmental mobility.

Solubility

While the concentration of actinide contaminants in nature is found to be low, prediction of highest soluble concentrations potentially being released is key of the safety assessment of nuclear waste repositories or long term storage facilities. The

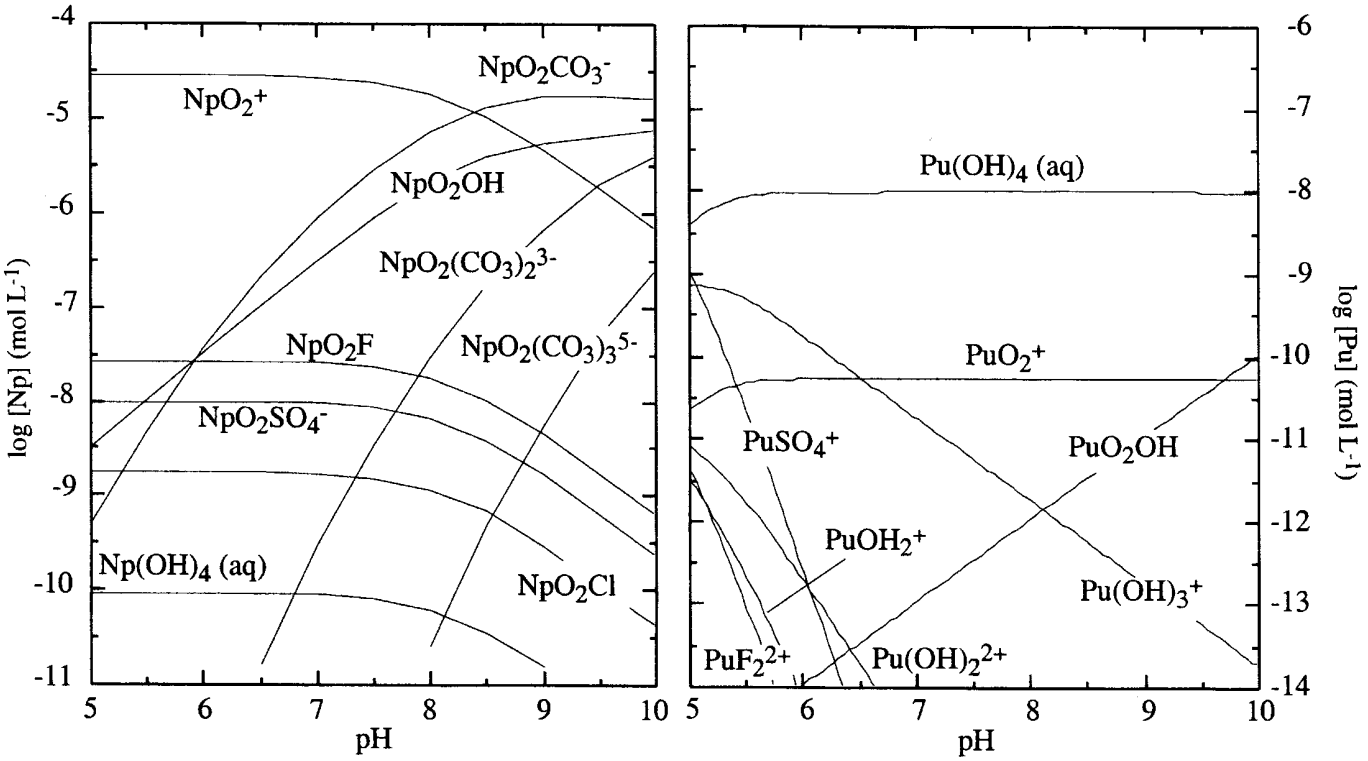

Fig. 2–4. Species distribution of Np and Pu at 400 mV in low-ionic strength (J-13) water from Yucca Mountain (calculated for a closed system with constant carbonate concentration of 2.6 mmol L^{-1}).

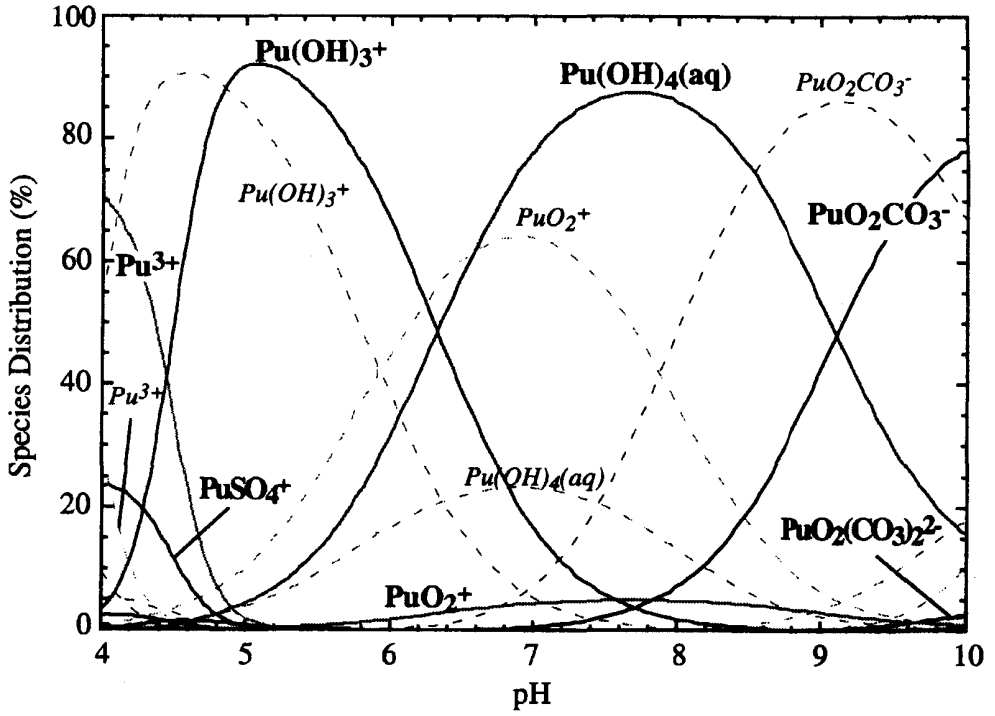

Fig. 2–5. Plutonium speciation at 400 mV (solid lines) and 500 mV(dashed lines) in J-13 water from Yucca Mountain as function of pH. The concentration ratio of the solution species $Pu(OH)_4/PuO_2^{2+}$ changes from 1:0.06 at 400 mV to about 1:2.6 at 500 mV.

maximum concentration for actinide ions in aqueous solutions is limited by the solubility of an actinide-bearing solid. To model and predict solubilities, we must understand the composition and the solubility product of the controlling solid phase, the potential complexes subsequently formed in solution and their stability constants, and the concentration of individual ligands and other cations that are competing for ligand coordination or that raise the solution ionic strength. Numerous solubility and speciation studies have been performed to investigate the thermodynamic stability of actinide solids in well-defined laboratory studies and under conditions relevant to different site-specific conditions. Figure 2–6 illustrates the concept of solid–liquid phase equilibrium studies for trivalent actinides (An = Am(III) or Cm(III)). At low pH, the aquo ion An^{3+} is the stable solution species and its soluble concentration is determined by the solubility product of the solid phase. Complexation of the An^{3+} cation occurs with increasing pH and ligand concentration, i.e., hydroxide or carbonate, stabilizing actinide ions in solution. As the pH increases and the different solution complexes form, the total An(III) concentration in solution reaches a minimum and then increases due to the formation of anionic An(III) complexes.

In most natural waters actinides are usually coordinated with hydroxide and carbonate ligands; however, waters from ancient salt formations that are proposed as disposal sites for nuclear waste, such as the Waste Isolation Pilot Plant (WIPP) in New Mexico or the Gorleben site in Germany, are saturated with chloride salts. Chloride has been shown to affect the solubility and speciation of actinides significantly compared with their chemistry in inert electrolyte solutions of similar ionic strengths. Radiolytic formation of hypochlorite in chloride brines may result in the

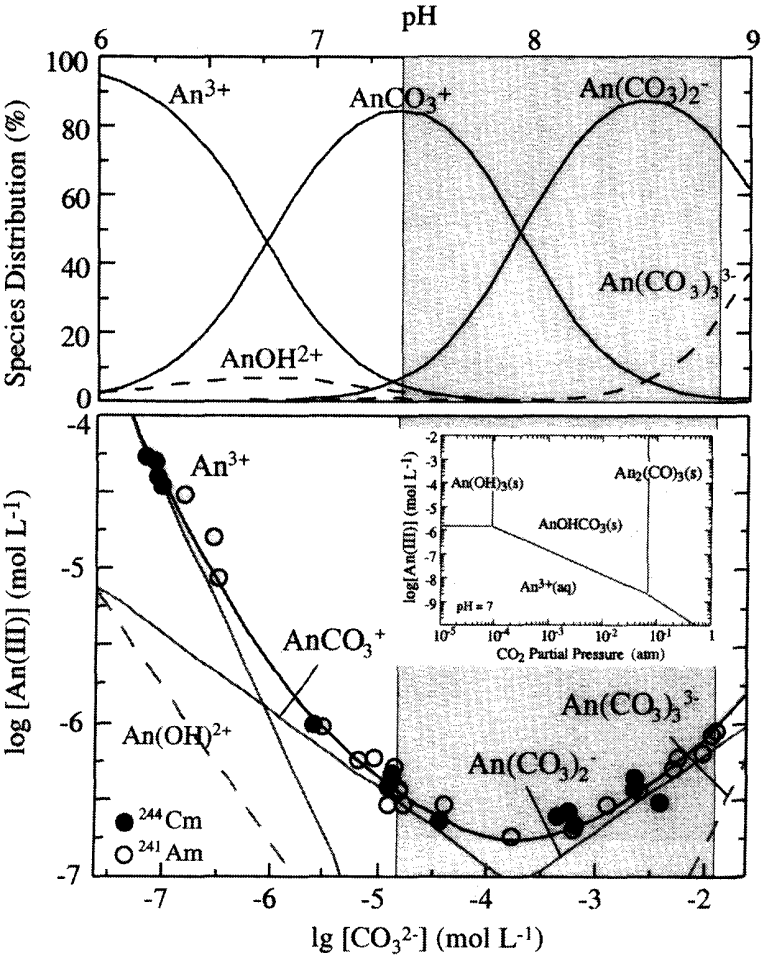

Fig. 2–6. Solution speciation (top) and solubility of Am(III) and Cm(III) with $An_2(CO_3)_3 \cdot 2\text{–}\ 3H_2O(s)$ as the equilibrium solid (bottom). Calculated concentrations for individual solution species are indicated by the gray lines that run tangent to the solubility curve. The partial pressure of CO_2 in natural waters spans about three orders of magnitude (gray area). The stability diagram (inset) shows that the An(III) hydroxocarbonate, $AnOHCO_3$ (s), is favored in most natural waters.

stabilization of actinides in higher oxidation states, i.e., Pu(VI) and Am(V) (Büppelmann et al., 1988; Magirius et al., 1985). As an example for the effect of chloride on actinide speciation and solubility, the Np(V) solubility is about one order of magnitude higher in acidic and near-neutral 5 *M* NaCl solution than in 5 *M* $NaClO_4$ because of the effect of neptunyl-chloride interactions (Fig. 2–7) (Runde et al., 1996). The hydrated ternary Np(V) carbonate, $NaNpO_2(CO_3) \cdot nH_2O$, is the solubility-controlling solid at low carbonate concentrations. Interestingly, this solid also is kinetically favored at increased carbonate, but over time it transforms to the thermodynamically stable phase $Na_3NpO_2(CO_3)_2 \cdot nH_2O$ (Neck et al., 1995).

Neptunium is one of the actinides of primary importance because it is most stable in the V oxidation state in which it is most soluble, does not easily sorb on common minerals, and thus is very mobile in the environment. In Fig. 2–8, experimentally measured total Np and Pu concentrations in J-13 water from the Yucca Mountain site are compared with solubility predictions as function of ionic strength. While theory and experiment agree well with each other for Np solubilities, a discrepancy of several orders of magnitude exist between calculated and measured Pu solubility. Overall, Np solubility is orders of magnitude higher than that of Pu be-

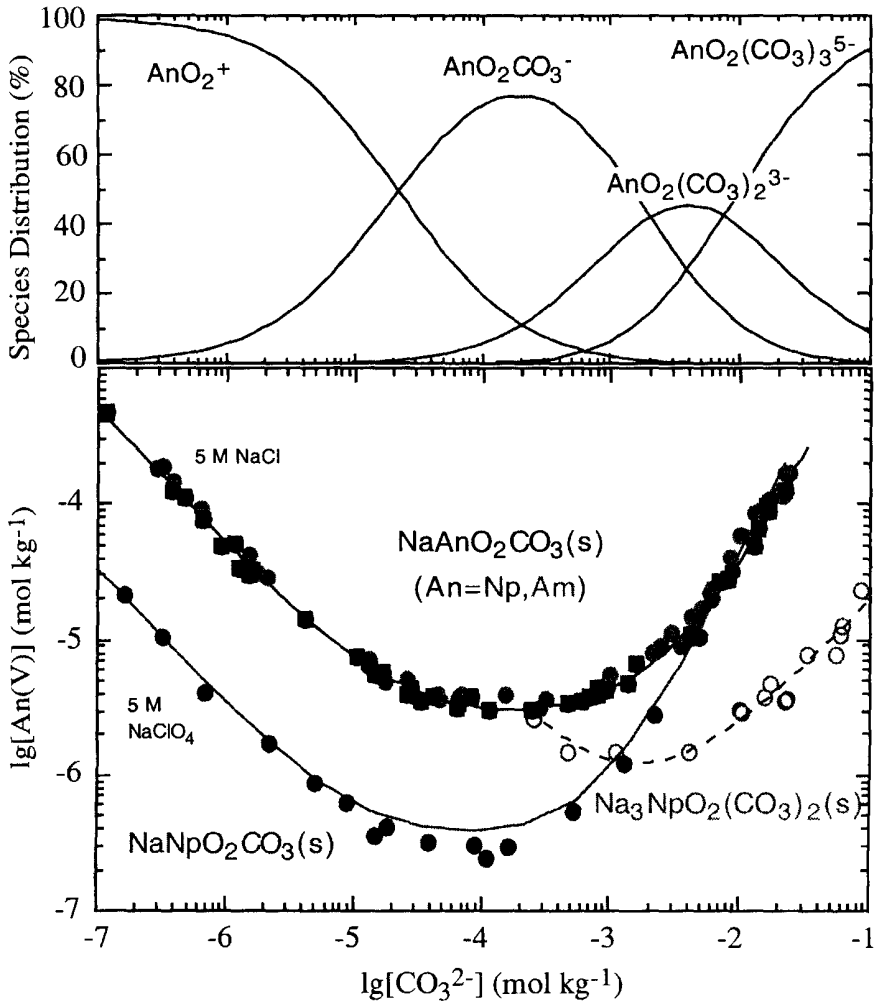

Fig. 2–7. Solution speciation (top) and solid equilibrium phase stability and solubility of Np(V) in concentrated electrolyte solutions (bottom). Under more acidic conditions, chloride increases the solubility of Np(V) whereas the Np solubility converges at increasing carbonate where the Np(V) bis- and triscarbonate species predominate.

cause of the higher stability of Np(V) versus Pu(V). In the Np system, Np(V) controls the nature of solution and solid phase, while Pu(IV) solids limit the Pu solubility.

Thermodynamics predict the oxides, PuO_2 and NpO_2, as the predominant stable solids (with solubility of about 10^{-12} mol L^{-1}) for most Eh and pH conditions that span the stability range of natural waters; however, NpO_2 has not been found to precipitate in laboratory solubility experiments conducted from oversaturation, and Np_2O_5 and $Np(OH)_4$(am) have been identified instead as the confining solids (Efurd et al., 1998; Nitsche et al., 1993). Under reducing conditions (below 0.1 V), $Np(OH)_4$(am) restricts the Np concentration to approximately 10^{-8} molar (Fig. 2–9). Redox potentials above 0.35 V stabilize Np_2O_5 at neutral pH. In the intermediate range (about 0.1–0.3V), the total Np concentration in solution is controlled by the solubility of $Np(OH)_4$(am) with varying concentration ratios of Np(IV)/Np(V) species in solution determined by the Eh and pH (Kaszuba & Runde, 1999). In this region, the soluble Np(IV) species remains constant at approximately 10^{-8} mol L^{-1}. A phase transformation to the Np(V)-bearing solid occurs at neutral pH at about

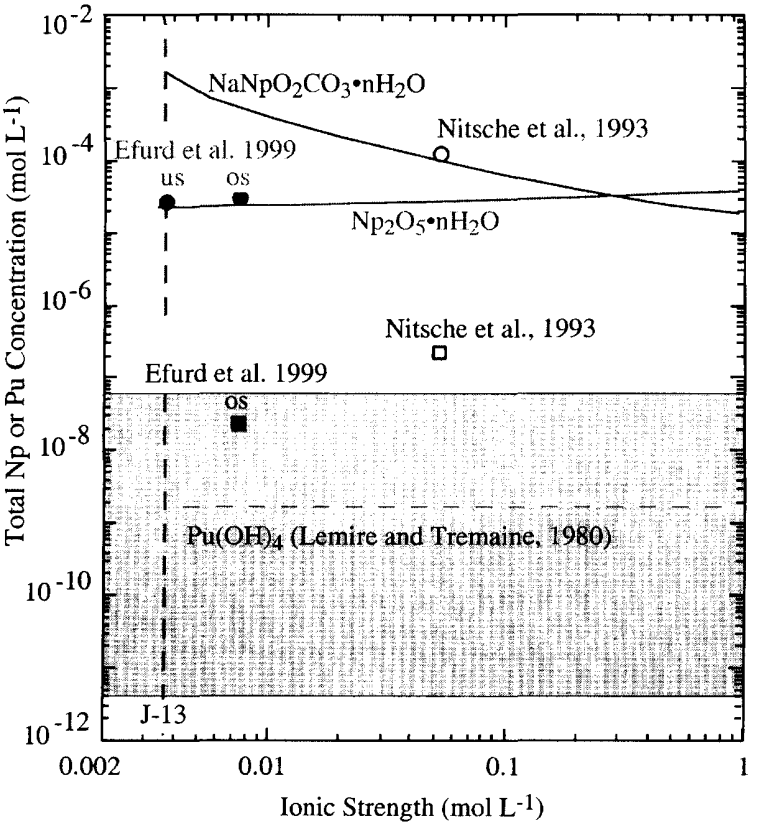

Fig. 2–8. Experimental and predicted solubilities of Np and Pu in J-13 water saturated with an corresponding actinide-bearing solid phase. The shaded area illustrates the predicted range of $Pu(OH)_4(s)$ solubility using the range of solubility products for $Pu(OH)_4(s)$ reported in the literature. us = undersaturation; os = oversaturation.

0.35 V when the soluble Np(V) concentration reaches saturation of Np_2O_5. In contrast, Pu(V) solids are calculated as too soluble to precipitate in natural systems and only solid Pu(IV) (oxy)hydroxide restrict the Pu solubility under environmental conditions (Runde et al., 2002); however, the Eh and pH of the aquatic system defines the amount of stable Pu(V) species in solution and determines the extent of soluble Pu that exceeds the thermodynamic solubility of the solid Pu(IV) (oxy)hydroxide. Thus, under the conditions in most groundwater systems (pH 5 to 8 and Eh –0.1 to 0.5 V), the soluble Np and Pu concentrations can change significantly due to a shift in the species' oxidation state stability. Clearly, evaluation of near-field radionuclide mobility in geochemical environments proximate to nuclear waste repositories must account for soluble radionuclide concentrations that are controlled by the redox potential of the system as well as the nature and solubility of relevant solid phases. Generally, oxides and hydroxides, i.e., $An(OH)_3(s)$, AnO_2 and $An(OH)_4(s)$, or $AnO_2(OH)_2 \cdot nH_2O$, are the most important actinide solids under natural conditions. In the presence of carbonate, the formation of mixed hydroxy-carbonate solids, i.e., $AmOHCO_3(s)$ or $Pu(OH)_2CO_3(s)$, and pure carbonates, i.e., $UO_2CO_3(s)$, become important. Increasing ionic strength, such as present at geologic salt formations, is critical for the formation of ternary actinide solids, i.e. $NaNpO_2CO_3 \cdot nH_2O$.

The release of radioactive material from storage or disposal sites is initiated with the corrosion of the package material and the dissolution of the original ra-

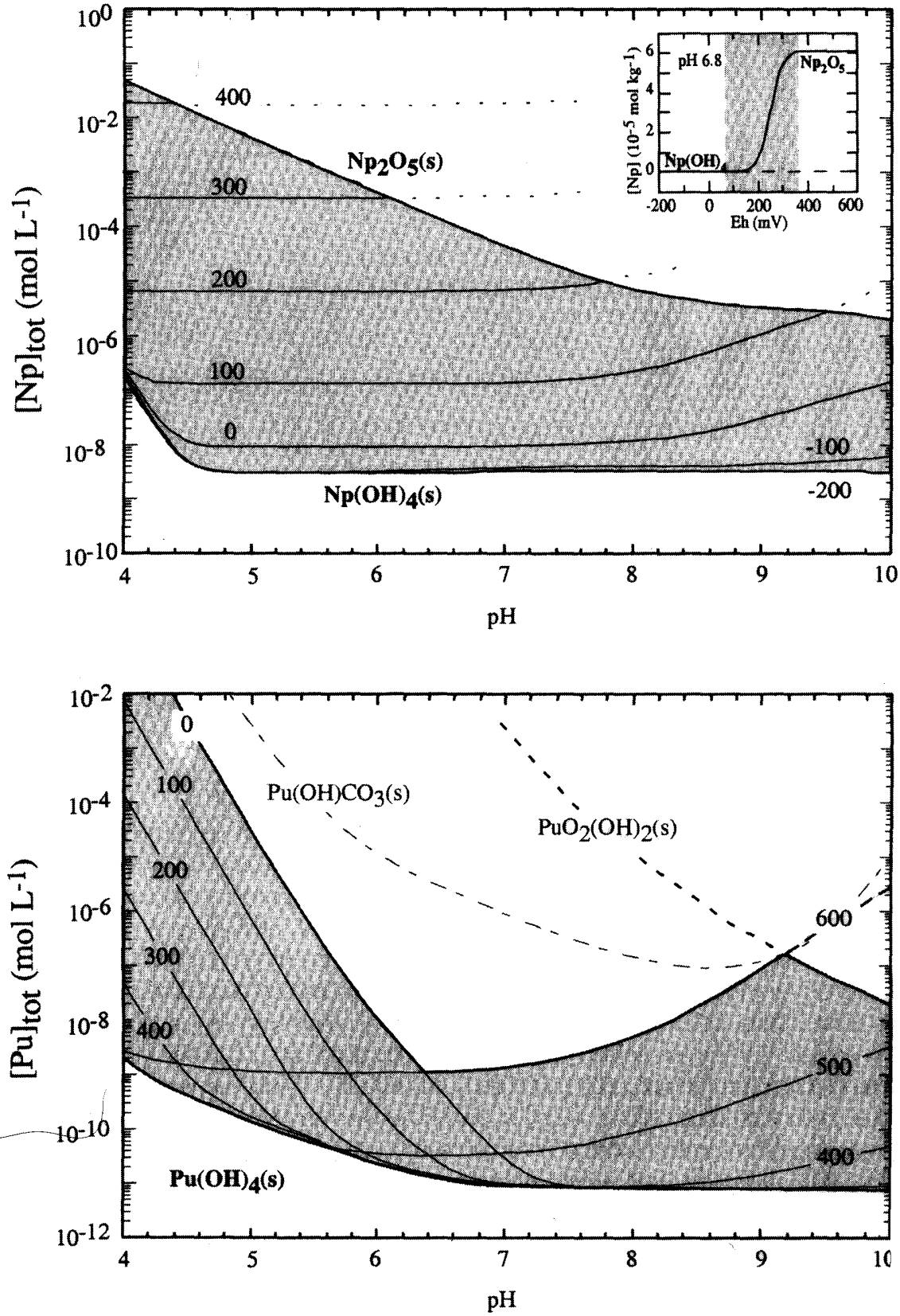

Fig. 2–9. Calculated solubility curves of Np (top) and Pu (bottom) in J-13 water at distinct Eh values of the solution. The shaded areas represent the calculated soluble concentration range for Np or Pu where $Np(OH)_4(s)$ and $Pu(OH)_4(s)$ are the solubility-controlling solid phases and oxidized species determine the solution speciation. The inset shows the redox-controlled region at neutral pH where $Np(OH)_4(s)$ is stable and Np(V) species predominate in solution.

dionuclide source term. For example, UO_2, the main component (95–99%) in spent nuclear fuel, is thermodynamically unstable in most conditions and will undergo oxidative dissolution upon contact with infiltrating water. The dissolved U(VI) ion can be complexed with inorganic and organic compounds to form soluble species or may precipitate to form a secondary solid phase. The investigation of the spent nuclear fuel alteration indicated the formation of dehydrated schoepite which, in the presence of soluble silicates, eventually converted to a paragenetic sequence of U(VI) silicate minerals, i.e., soddyite, $(UO_2)_2(SiO_4)(H_2O)_2$, uranophane, $Ca[(UO_2)(SiO_3OH)_2](H_2O)_5$, and ultimately boltwoodite $(Na,K)[(UO_2)(SiO_3OH)](H_2O)]_{1.5}$ (Wronkiewicz & Buck, 1999). These secondary phases may determine the subsequent release and mobility of key radionuclides. For example, uranyl oxyhydroxide has been demonstrated to incorporate Np into its structure (M&O, 2000). Subsequent release of Np from this metastable U(VI) phase may be assumed to be congruent to U by using a conditional solubility product of this secondary phase. On the other hand, the ultimately more stable silicate phases did not provide experimental evidence for Np incorporation to a significant degree. Hence, the release of Np from U(VI) oxyhydroxide is likely to be controlled by the infiltration rate and composition of infiltrating water and the corresponding solid phase conversion rates. Without understanding the reaction processes and phase paragenesis that may dictate actinide solubility and release, a conservative approach to geochemical modeling of their near-field behavior is unrealizable.

Colloid Formation

Actinides in the IV oxidation state have a high charge-to-radius ratio and hydrolyze more readily to form stable hydroxide complexes than in any other oxidation state. Radiocolloid formation is believed to be initiated by stepwise hydrolysis and proceed rapidly through a series of nucleation and polymerization processes. The ultimate result is a thermodynamically and kinetically stable product that can exceed thermodynamically calculated actinide solubility significantly (Rai et al., 1980). The formation of radiocolloids is dependent on the initial actinide concentration and thus is most likely to occur in the close environment of a source with significant amounts of tetravalent actinides. The sizes of Pu(IV) intrinsic colloids can vary ranging between one and hundreds of nanometers depending on the conditions during the aging process. Recent laser-induced breakdown spectroscopic studies showed that Pu does not form significant amounts of colloidal Pu(IV) with sizes smaller than 400 nm when the total Pu concentration is below 3×10^{-5} *M* (Knopp et al., 1999). Characterization of intrinsic Pu(IV) colloids revealed a variety of structural features with some similar to that of PuO_2, such as the Pu–O and Pu–Pu near-neighbor distances of 2.33 Å and 3.84 Å, respectively (Conradson, 1998; Neu et al., 1997). A number of Pu–O distances ranging between about 2.2 and 3.7 Å are suggestive of terminal Pu–OH moieties, oxo-bridged Pu atoms, and substantially varying structural subunits and terminal ligands. There is some evidence that other actinides form intrinsic colloids, i.e., U(IV) and Am(III), but the intrinsic colloids of Pu(IV) have been studied in more detail.

At the low actinide concentrations expected in surface and groundwater systems, the reactions of actinides with particulate surfaces most likely control the ac-

tinides' fate in the environment. Colloidal particulates can be produced by waste package degradation and can occur naturally in most soils and groundwater. The amount and stability of natural colloids differ for each site-specific ground- and surface waters due to their varying chemical compositions and hydrogeochemical steady states (Degueldre et al., 2000). Because of the large surface area of colloids, the extent of radionuclide interaction with colloidal matter is critical. The pseudo-colloids formed can be mobile and enhance the transport of strongly sorbing radionuclides along flow paths to the accessible environment.

For example, Fe(oxy)hydroxide-based colloids may be produced by corrosion of the Fe-based waste drum steels. Dissolution of high-level waste glass and spent nuclear fuel may generate clay (mainly smectite) and silica colloidal material (M&O, 2000). Both types of colloids generally have composition and surface characteristics similar to the immobile aquifer solids but are mobile within the aquifer. The large surface area of these colloids (10^4 to 10^5 m^2 kg^{-2}) offers significant sorption capacities for radionuclides reflected in higher sorption distribution coefficients relative to sorption onto compact geomatrix. Colloidal Fe(oxy)hydroxide sequesters Pu nearly quantitatively in an irreversible uptake mechanism and may transport Pu over long distances (Keeney-Kennicutt & Morse, 1985; Sanchez et al., 1985). On the other hand, silica and montmorillonite can release adsorbed Pu in a new environment to a significant fraction, thus potentially changing the transport mechanism with a water flow.

Macromolecular organic acids are found in most environments and can provide a variety of organic functional groups with high affinities for highly charged actinide ions (Choppin, 1992; Kim, 1991). Fulvic and humic acids have been widely studied as representatives for their strong interaction potential with actinide ions and their redox properties. Several groups reported the strong binding affinities for actinides in the III and IV oxidation states. For example, Cm(III) and U(VI) humate complexes are predicted to dominate solution speciation in some German groundwaters that are rich in humic acids (Panak et al., 1996; Zeh et al., 1999). It also has been demonstrated that humic acid can reduce higher Np and Pu oxidation states to Np(IV) and Pu(IV) (Choppin, 1992; Zeh et al., 1999). Although the structure and binding mechanisms of actinides onto colloidal material are still in debate, colloid-facilitated actinide transport could adversely affect the environmental behavior of actinides especially in the III and IV oxidation states. An illustrative example for the impact of colloids on actinide transport is the reported discovery of Pu that evidently migrated 1.3 km within 30 yr at the Nevada Test Site (Kersting et al., 1999).

INTERACTIONS AT THE MINERAL–SOLUTION INTERFACE

In the near-field of the contaminant source, the actinides may be at saturation with respect to primary or secondary solid phases, depending on the water infiltration rate. When actinides will be released and migrate in lower concentrations (by dilution) along water transport paths they will come into contact with hundreds of chemically active compounds and minerals. The intimate contact between contaminant and geologic medium provides a dominant reaction path for its retention

and immobilization. The complex actinide chemistry, the variety of mineral surface functional groups and properties, and the dynamic reorganization of mineral surfaces are the basis for a continuum of mechanisms for the interactions between actinide solution species and mineral surfaces.

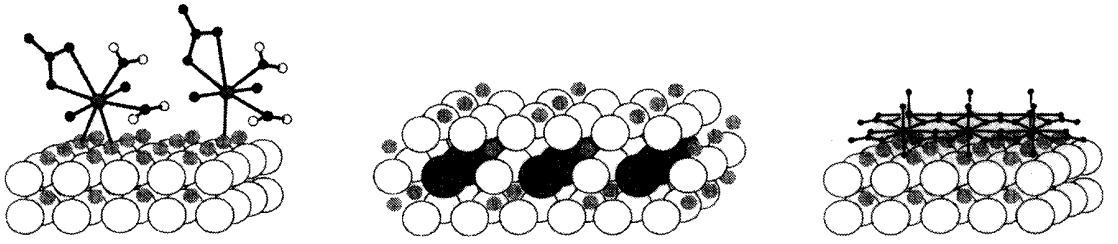

V VI VII

The actinide ion can sorb to the surface as a molecular species, **V**, or it can be embedded in the mineral structure, **VI**, or it can precipitate to form macroscale secondary phases, **VII**. Actinide sorption onto mineral surfaces depends on many factors, such as the actinide's speciation, flow rate, and the chemistry and composition of water and surrounding rocks or soil. Generally, batch-sorption experiments are performed to investigate how actinides will be retained. The sorption distribution coefficient, K_d = (ion concentration adsorbed per mass sorbent)/(ion concentration in solution) in (mL g^{-1}), has been used to parameterize uptake of contami-

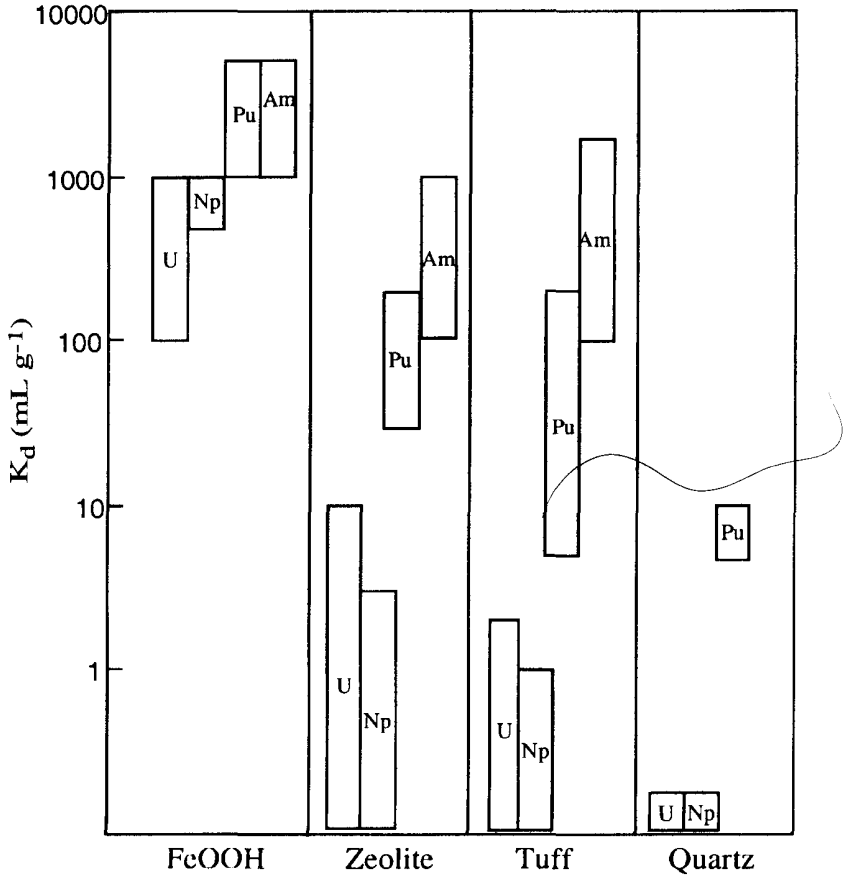

Fig. 2.10. Range of sorption distribution coefficients of light actinides and soil constituents (Triay et al., 1997).

nants onto soils and minerals (Triay et al., 1997). The K_d approach describes the distribution of the actinide ion between dissolved and solid phase and its removal from solution by all of the mentioned mechanisms combined. The measured K_d values are conditional constants valid for a given pH, solution and mineral composition, temperature, etc., and describe only the system in which they were measured. Applying a single K_d value to predict the removal of species that form strong complexes or precipitates or are subject to redox processes, such as Np and Pu, can lead to large errors of many orders of magnitude. As Fig. 2–10 shows for U, Np, Pu, and Am, the sorption data can be correlated with the main actinide oxidation states and the petrographic properties of the soil used. The sorption distribution coefficient values decrease in the sequence Fe(oxy)hydroxide>clay>> sand (quartz) and is highest for tri- and tetravalent actinides (Triay et al., 1997).

The majority of actinide uptake studies have been either batch distribution coefficient determinations or column transport studies. Both methods were not designed to distinguish between different reaction mechanisms, such as bulk precipitation versus molecular surface complexation. In recent years, more sophisticated spectroscopic techniques, i.e., x-ray absorption spectroscopy, have been applied to investigate the molecular aspects of interfacial reactions. For example, while initially time-resolved fluorescence spectroscopy revealed different U(VI) sorption complexes on (oxy)hydroxide surfaces, such as goethite, hematite, alumina and silica, x-ray absorption fine structure (EXAFS) spectroscopy studies provided additional detailed information on the local structure around the U atom (Sylvester et al., 2000). In addition to the axial U–O bond lengths of about 1.8 Å, two different equatorial shells at 2.35 and 2.50 Å were observed at low p-H suggesting the formation of mononuclear inner-sphere uranyl surface complexes. At pH above 6, U—Si distance of 3.1 Å and U—U distance of about 4.0 Å suggested the formation of an inner-sphere surface species and polynuclear surface complex or precipitate at near-neutral pH. Although the observed data at low pH reveal evidence of mononuclear inner-sphere complexation, the U—Si and U—U distances could be indicative of the precipitation of a U(VI) silicate phase.

Due to the complex redox chemistry Pu exhibits, it is important to understand the oxidation state stability of Pu at the solution–mineral interface for accurately predicting their long-term stability. Early studies showed that Pu(V) reacts far stronger with surfaces than its chemical analogue Np(V) (Fig. 2–11). Because Np(V) and Pu(V) generally behave chemically similar in solution, the higher uptake of Pu indicates a more complex interaction mechanism. In the absence of colloids, Pu(V) and Np(V) were stable in solution, and the soluble Pu concentration did not decrease due to reduction of Pu(V) to the less soluble $Pu(OH)_4(aq)$; however, in the presence of colloidal goethite, fast uptake kinetics were observed within the first 100 h with a subsequent gradual increase of sorbed Pu (Lu et al., 2000; Sanchez et al., 1985). The Pu(V) absorption approaches the colloidal uptake curve of Pu(IV) (Sanchez et al., 1985). Keeney-Kennicut and Morse (1985) reported the disproportionation reaction of PuO_2^+ on goethite to form Pu(IV) and Pu(VI). The latter is then slowly reduced to Pu(IV), leaving Pu(IV) as the dominant surface species. Different uptake kinetics also were observed for Np(IV) and Np(V) interaction with marine particulates (McCubbin & Leonard, 1997). Neptunium(IV) has a rapid initial sorption followed by desorption during long period of times, whereas

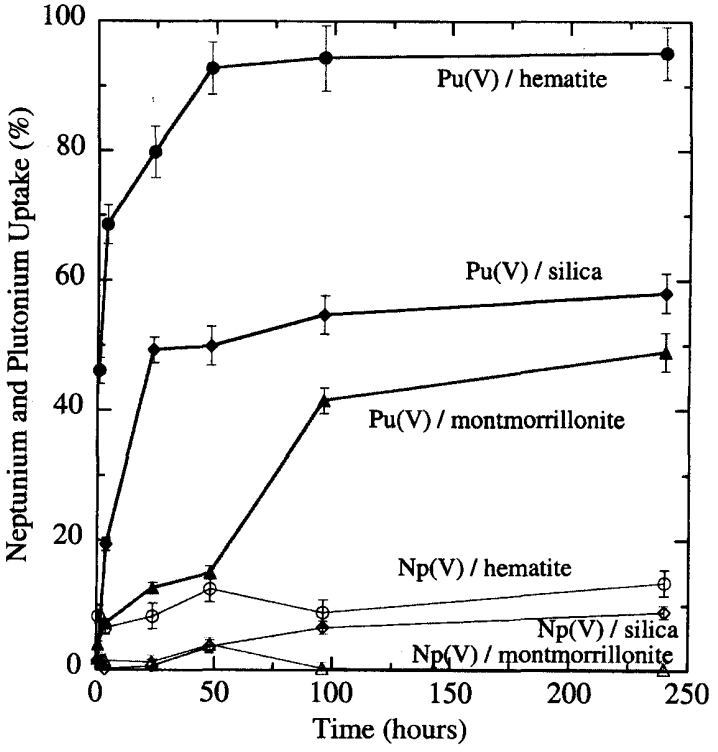

Fig. 2–11. Uptake of Np and Pu on hematite, silica, and montmorillonite (Lu et al., 2000).

the uptake of Np(V) was below 20% and occurred at a much slower rate. Consequently, reductive processes at the mineral-water interface most likely contribute to the high uptake of Pu(V), and reported K_d values represent uptake of Pu(IV) rather than Pu(V). Redox-active minerals may enhance the instability of Pu(V). MnO_2 is known to participate in electron-transfer reactions and affect the oxidation state of the sorbent. Recent XAFS investigations indicated the oxidation of Pu(V) and the existence of Pu(VI) species on MnO_2 (Smith et al., 2002). Preferred sorption to manganese oxide within a heterogeneous mixture also has been observed with Pu(V) and Pu(VI) on the surface (Duff et al., 1999). Although details of the conceptual reaction mechanisms still have to be unraveled, molecular studies clearly show that the empirical K_d approach can lead to significant misinterpretation and misleading long-term transport predictions.

Dynamic mineral surfaces, such as found on oxides and carbonates, can provide a potential sink for radionuclide uptake and a more stable long-term coordination. Incorporation of contaminants may be approached via surface dissolution and re-precipitation or via surfacial and structural diffusion of adsorbed species. The substitution effectiveness is strongly dependent on the host's crystal structure and the charge and structural limitations of the contaminant species. Sturchio et al. (1998) substituted Ca^{2+} with the U^{4+} ion in natural calcite without significant distortion of the overall structure. Recently, Reeder et al. (2000) observed different coordination stabilities of U(VI) in the two most common carbonate polymorphs, calcite and aragonite. Incorporated into aragonite, U(VI) is present in similar environment as in the dominant solution species $UO_2(CO_3)_3^{4-}$. A change in the U(VI) coordination is required for its incorporation into calcite resulting in a less ordered and less stable coordination environment. Consequently, calcite is less effective for the long-

term sequestration of U(VI). Obviously, scavenging radionuclides by incorporation into a mineral structure can provide a valuable retention mechanism that may become critical for long-term actinide mobility and bioavailability assessments.

INTERACTIONS WITH MICROBES

The importance of and potential impact of microorganisms on the environmental behavior of the actinides and the promising use of bacteria for remediating actinide-contaminated soils, groundwater, and waste streams attracts increasing attention. A wide variety of microorganisms exist in all aquifers and soils, and many survive under most extreme conditions, such as around hydrothermal vents at the bottom of the sea floor or within the hypersalinity of geologic salt beds. Microorganisms can accumulate on solid surfaces forming extended biofilms, or they may be suspended in the aquifer and thus act as mobile or self-propelled colloids. Actinides can interact with microorganisms in several ways. For example, they can sorb directly on the cell wall, be accumulated and carried into the cell interior (Panak et al., 1998), or react with microbial (extracellular polymeric) biproducts (Johnson et al., 2000). Microorganisms, especially bacteria, are also known to mediate redox processes and bioconvert actinides in their higher oxidation states to the lower less-soluble forms, i.e., U(VI) to U(IV) (Barton et al., 1996).

Given these characteristics, microbes could pose a third natural barrier to actinide transport from geologic repositories. For example, in recent WIPP-related studies Francis et al. (1998) have shown that actinides are associated only at low levels with the halophilic bacteria isolated from muck pile salts around the WIPP site. The extent of association varied with bacterial culture, actinide species, pH, and the presence of organic or inorganic complexants. The radiolytic effects on the microbial viability were found to be negligible; however, other microorganisms can concentrate metal ions to a great extent. For example, the bacteria *Pseudomonas* sp. concentrated Pu to levels that were up to about 10 000 times greater than a sterile control organism (Hersman et al., 1996). Although actual applications of bacteria in field demonstrations are rare, these examples clearly demonstrate the potential of bacteria for soil remediation strategies.

A recent, more detailed study of the microbial association mechanism included analysis of U and Pu uptake by extracellular polymers and sequestering agents. Both U(VI) and Pu(IV) ions formed soluble complexes with γ-polyglutamic acid, an exopolymer produced by B*acillus licheniformis*, at metal-to-glutamate ratios 1:100 and 1:200, respectively (Johnson et al., 2000). Active cells of B*acillus licheniformis* bonded to more than 90% of the introduced Pu(IV)-up to 8.4 mmol of Pu(IV) were added. As expected, other functional groups on the exterior cell surface (in addition to the PGA exoploymer) increase the number of binding sites and enhance metal binding. The binding strength for U(VI) and Pu(IV) is lower than for other strong ligands and chelators, such as Tiron or NTA, but on the same order as for other exopolymers or humic acids. Incorporation of actinides into the bacterial cell has been proposed that could use low-weight organic molecules that are excreted by the bacteria (siderophores) to acquire nutritional metal cations, such as Fe(III) or Zn(II). Neu et al. (Neu et al., 2000) synthesized and characterized the first complex of Pu

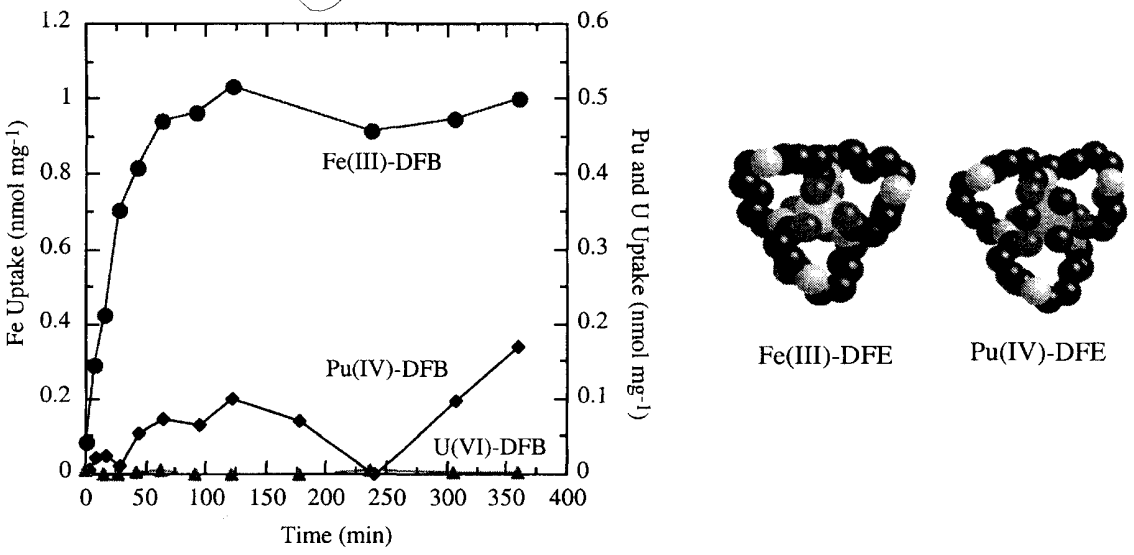

Fig. 2–12. Uptake of Fe(III), Pu(VI), and U(VI) by *M. flavescens* in nmol mg^{-1} of dry weight bacteria in the presence and absence of DFB (John et al., 2001). Uranium(VI) is not recognized and thus no uptake is observed. A comparison of the Fe(III)-DFE and Pu(IV)-DFE complexes shows the structural similarity (Neu et al., 2000). Three water molecules bind to a nine-coordinate Pu^{4+} ion that protrudes slightly from the siderophore cavity.

with desferrioxamine E, a hydroxamate-based siderophore. This complex exhibits similar structural features as the analogue Fe(III)-DFE compound. While desferrioxamine β-bound Pu is recognized by the same cell's uptake channel receptors, the DFB-mediated Pu translocation into the cell interior is slower and significantly lower than that for iron (Fig. 2–12) (John et al., 2001). These examples illustrate the dynamic interaction mechanisms of microorganisms with actinides and their potential impact on actinide biogeochemistry and mobility within the environment. Future studies will focus on understanding the mechanistic aspects of these interactions to fully exploit their potential for actinide remediation and immobilization efforts.

CONCLUSIONS

This overview illustrates the important geochemical reactions of actinides that are related to their unique existence in one or more of the III, IV, V, and VI oxidation state. The inherent characteristics of actinides in each oxidation state, such as redox activity, solubility, complexation strength, are affected by the unique local environments and site-specific conditions. The chemical conditions of aquatic systems, i.e., Eh, pH, complexant and colloid concentrations, determine the stability of actinide species and how they may migrate through the environment. To understand this complex set of interacting processes requires a strong multidisciplinary foundation in actinide and environmental chemistry, molecular science, and interfacial science and the requisite spectroscopies, subsurface testing, and laboratory experiments. To evaluate overall transport characteristics, the experimental results need to be interpreted within the context of the multicomponent natural system. Thermodynamic solubility studies may provide upper limits of soluble actinide con-

centrations when increased amounts are present, but kinetics may be in favor of metastable phases. Although thermodynamic properties of actinide compounds relevant to the environment have been of increased interest, the kinetics of complexation reactions, precipitation, and of reactions at mineral surfaces have been neglected. Ultimately, the most important processes that govern the environmental fate of all metals, including the actinides, occur at the solution–solid interfaces of minerals, microorganisms' cells, or colloidal materials. The development of more sophistic spectroscopic techniques with better sensitivity and spatial resolution allows the beginning evolution of a conceptual understanding of the actinides' bulk thermodynamics, kinetics, and phase partitioning based on molecular-scale spectroscopic characterization. As the inventory of actinides in interim storage facilities grows and storage containers age, increasing the risk of accidental releases, and as the safety of permanently storing nuclear waste in geologic repositories must be evaluated, it becomes increasingly important to understand how actinides will interact with the environment. More sophisticated theoretical models are needed to account for all the potential migration paths away from an actinide source. Theoretical and experimental scientists will be challenged for years by the demands of developing those models.

REFERENCES

Agnew, S.F., J. Boyer, R.A. Corbin, T.B. Duran, J.R. Fitzpatrick, K.A. Jurgensen, T.P. Ortiz, and B.L. Young. 1997. Hanford tank chemical and radionuclide inventories: HDW Model Rev. 4 LA-UR-96-3860. Los Alamos National Laboratory, Los Alamos, NM.

Ahrland, S., J.O. Liljenzin, and J. Rydberg. 1975. Actinide solution chemistry. *In* J.C. Bailer et al. (ed.) Comprehensive inorganic chemistry. Pergamon Press, Oxford.

Allard, B., H. Kipatsi, and J.O. Liljenzin. 1980. Expected species of uranium, neptunium, and plutonium in neutral aqueous solutions. J. Inorg. Nucl. Chem. 42:1015–1027.

Allen, P.G., J.J. Bucher, D.L. Clark, N.M. Edelstein, S.A. Ekberg, J.W. Gohdes, E.A. Hudson, N. Kaltsoyannis, W.W. Lukens, M.P. Neu, P.D. Palmer, T. Reich, D.K. Shuh, C.D. Tait, and B.D. Zwick. 1995. Multinuclear NMR, Raman, EXAFS, and x-ray diffraction studies of uranyl carbonate complexes in near-neutral aqueous solution: X-ray structure of $[C(NH_2)_3]_6[(UO_2)_3(CO_3)_6] \cdot 6.5H_2O$. Inorg. Chem. 34:4797–4807.

Allen, P.G., J.J. Bucher, D.K. Shuh, N.M. Edelstein, and T. Reich. 1997. Investigation of aquo and chloro complexes of UO_2^{2+}, NpO_{2+}, Np^{4+}, and Pu^{3+} by x-ray absorption fine structure spectroscopy. Inorg. Chem. 36:4676–4683.

Baas-Becking, L.G.M., I.R. Kaplan, and D. Moore. 1960. Limits of the natural environment in terms of pH and oxidation–reduction potentials. J. Geol. 68:243–284.

Barton, L.L., K. Choudhury, B.M. Thomson, K. Steenhoudt, and A.R. Groffman. 1996. Bacterial reduction of soluble uranium: The first step of *in situ* immobilization of uranium. Radioact. Waste Manage. Eviron. Restoration 20:141–151.

Büppelmann, K., J.I. Kim, and C. Lierse. 1988. The redox-behavior of plutonium in saline solutions under radiolysis effects. Radiochim. Acta 44/45:65.

Choppin, G.R. 1983. Solution chemistry of actinides. Radiochimica Acta 32:43–53.

Choppin, G.R. 1992. The role of natural organics in radionuclide migration in natural aquifer systems. Radiochim. Acta 58/59:113–120.

Choppin, G.R., A.H. Bond, and P.M. Hromadka. 1997. Redox speciation of plutonium. J. Radioanal. Nucl. Chem. 219:203–210.

Choppin, G.R., and B.E. Stout. 1989. Actinide behavior in natural waters. Sci. Total Environ. 83:203–216.

Conradson, S.D. 1998. Application of x-ray absorption fine structure spectroscopy to materials and environmental science. Appl. Spectroscopy 52:252A–279A.

Degueldre, C., I. Triay, J.I. Kim, P. Vilks, M. Laaksoharju, and N. Miekeley. 2000. Groundwater colloid properties: A global approach. Appl. Geochem. 15:1043–1051.

Duff, M.C., D.B. Hunter, I.R. Triay, P.M. Bertsch, D.T. Reed, S.R. Sutton, G. SheaMccarthy, J. Kitten, P. Eng, S.J. Chipera, and D.T. Vaniman. 1999. Mineral associations and average oxidation states of sorbed Pu on Tuff. Environ. Sci. Technol. 33:2163–2169.

Efurd, D.W., W. Runde, J.C. Banar, D.R. Janecky, J.P. Kaszuba, P.D. Palmer, F.R. Roensch, and C.D. Tait. 1998. Neptunium and plutonium solubilities in a Yucca Mountain groundwater. Environ. Sci. Technol. 32:3893–3900.

Francis, A.J., J.B. Gillow, C.J. Dodge, M. Dunn, K. Mantione, B.A. Strietelmeier, M.E. Pansoy-Hjelvik, and H.W. Papenguth. 1998. Role of bacteria as biocolloids in the transport of actinides from a deep underground radioactive waste repository. Radiochim. Acta 82:347–354.

Hersman, L., P. Maurice, and G. Sposito. 1996. Iron acquisition from hydrous Fe(II)-oxides by an aerobic *Pseudomonas* sp. Chem. Geol. 132:25–31.

John, S.G., C.E. Ruggiero, L.E. Hersman, C.-S. Tung, and M.P. Neu. 2001. Siderophore mediated plutonium accumulation by *Microbacterium flavescens* (JG-9). Environ. Sci. Technol. 35:2942–2948.

Johnson, M.T., L. He, D.J. Chitwood, L.A. Vanderberg, and M.P. Neu. 2000. Interactions of microbial exopolymers and whole cells with actinides. p. U370–U371. *In* 22nd ACS Natl. Meeting, Washington DC, Aug. 26–30, 2000.

Kaszuba, J.P., and W. Runde. 1999. The aqueous geochemistry of neptunium: Dynamic control of soluble concentrations with applications to nuclear waste disposal. Environ. Sci. Technol. 33:4427–4433.

Keeney-Kennicutt, W.L., and J.W. Morse. 1985. The redox chemistry of $Pu(V)O_2^+$ interaction with common mineral surfaces in dilute solutions and seawater. Geochim. Cosmochim. Acta 49:2577–2588.

Kersting, A.B., D.W. Efurd, D.L. Finnegan, D.J. Rokop, D.K. Smith, and J.L. Thompson. 1999. Migration of plutonium in ground water at the Nevada test site. Nature 397:56.

Kim, J.I. 1991. Actinide colloid generation in groundwater. Radiochim. Acta 52/53:71–81.

Kim, J.-I. 1993. The chemical behavior of transuranium elements and barrier functions in natural aquifer systems. p. 3–21. *In* Scientific basis for nuclear waste management. Vol. 294. Materials Res. Soc., Pittsburgh, PA.

Kim, J.I., K. Gompper, K.D. Closs, G. Kessler, and D. Faude. 1996. German approaches to closing the nuclear fuel cycle and final disposal of HLW. 238:1–10.

Knopp, R., V. Neck, and J.I. Kim. 1999. Solubility, hydrolysis, and colloid formation of plutonium(IV). Radiochim. Acta 86:101–108.

Langmuir, D. 1997. Aqueous environmental geochemistry. Prentice-Hall, Upper Saddle River, NJ.

Lu, N., J. Conca, G.A. Parker, P.A. Leonard, B. Moore, B. Strietelmeier, and I.R. Triay. 2000. Adsorption of actinides onto colloids as a function of time, temperature, ionic strength and colloid concentration. LA-UR-00-5121. Los Alamos National Laboratory, Los Alamos, NM.

M&O, C. 2000. Commercial spent nuclear fuel degradation in unsaturated drip tests. Input Transmittal WP-WP-99432.T. ACC: MOL.20000107.0209, Las Vegas, NV.

Magirius, S., W.T. Carnall, and J.I. Kim. 1985. Radiolytic oxidation of Am(III) to Am(V) in NaCl solutions. Radiochim. Acta 38:29–32.

McCubbin, D., and K.S. Leonard. 1997. Laboratory studies to investigate short-term oxidation and sorption behavior of neptunium in artificial and natural seawater solutions. Marine Chem. 56:107–121.

Neck, V., W. Runde, and J.I. Kim. 1995. Solid–liquid equilibria of neptunium(V) in carbonate solutions of different ionic strengths: II. Stability of the solid phases. J. Alloys Comp. 225:295–302.

Neu, M.P., J.H. Matonic, C.E. Ruggiero, and B.L. Scott. 2000. Structural characterization of a plutonium(IV) siderophore complex: Single-crystal structure of Pu-desferrioxamine E. Angew. Chem. Int. Ed. 39:1442.

Neu, M.P., R.K. Schulze, S.D. Conradson, J.D. Farr, and R.G. Haire. 1997. Polymeric plutonium(IV) hydroxide: Formation, prevalence, and structural and physical characteristics plutonium future: The science. Vol. LA-13338-C. Los Alamos Natl. Laboratory, Santa Fe, NM.

Nitsche, H., R.C. Gatti, E.M. Standifer, S.C. Lee, A. Muller, T. Prussin, R.S. Deinhammer, H. Maurer, K. Becraft, S. Leung, and S.A. Carpenter. 1993. Measured solubilities and speciations of neptunium, plutonium, and americium in a typical groundwater (J-13) from the Yucca Mountain Region. YMP Milestone Rep. 3010 LA-12562-MS. Los Alamos National Laboratory, Santa Fe, NM.

Panak, P., R. Klenze, and J.I. Kim. 1996. A study of ternary complexes of Cm(III) with humic acid and hydroxide or carbonate in neutral pH range by time-resolved laser fluorescence spectroscopy. Radiochim. Acta 74:141–146.

Panak, P., B.C. Hard, K. Pietzsch, S. Kutschke, H. Roske, S. Selenska-Pobell, G. Bernhard, and H. Nitsche. 1998. Bacteria from uranium mining waste pile: Interactions with U(VI). J. Alloys Comp. 271:262–266.

Pashalidis, I., and J.I. Kim. 1992. Chemisches verhalten des sechswertigen plutoniums in konzentrierten NaCl-lösungen under dem einfluss der eigenen alpha-strahlung RCM01092. Institut für Radiochemie, TU München, München.

Rai, D., R.J. Serne, and J.L. Swanson. 1980. Solution species of plutonium in the environment. J. Environ. Qual. 9:417–420.

Reeder, R.J., M. Nugent, G.M. Lamble, C.D. Tait, and D.E. Morris. 2000. Uranyl incorporation into calcite and araginite: XAFS and luminescence studies. Environ. Sci. Technol. 34:638–644.

Riley, R.G., and G.M. Zachara. 1992. Chemical contaminants on DOE lands and selection of contaminant mixtures for subsurface science research. DOE-ER-0547-T. U.S. Department of Energy, Office of Energy Research Subsurface Science Program, Washington DC.

Runde, W., S.D. Conradson, D.W. Efurd, N.P. Lu, and C.E. VanPelt. 2002. Solubility and sorption of redox-sensitive radionuclides (Np, Pu) in J-13 water from the Yucca Mountain site: Comparison between experiment and theory. Appl. Geochemistry 17:837–853.

Runde, W., and J.I. Kim. 1994. Chemisches verhalten von drei- und fünfwertigem americium in salinen NaCl-lösungen RCM01094. Institut für Radiochemie, TU München, München.

Runde, W., M.P. Neu, and D.L. Clark. 1996. Neptunium(V) hydrolysis and carbonate complexation: Experimental and predicted neptunyl solubility in concentrated NaCl using the Pitzer Approach. Geochim. Cosmochim. Acta 60:2065–2073.

Runde, W., M.P. Neu, C. VanPelt, and B.L. Scott. 2000. Single crystal and solution complex structure of $Nd(CO_3)_4^{5-}$. The first characterization of a mononuclear lanthanide(III) carbonato complex. Inorg. Chem. 39:1050–1051.

Sanchez, A.L., J.W. Murray, and T.H. Sibley. 1985. The adsorption of plutonium IV and V on goethite. Geochim. Cosmochim. Acta 49:2297–2307.

Smith, D.M., M.A. Ginder-Vogel, S. Skanthakumar, L. Soderholm, and M.P. Neu. 2002. Interactions of plutonium(V) and plutonium(VI) with manganese dioxide. submitted to Environ. Sci. Technol. (in press).

Stumm, W., and J.J. Morgan. 1981. Aquatic chemistry: An introduction emphasizing chemical equilibria in natural waters. 2nd ed. John Wiley & Sons, New York.

Sturchio, N.C., M.R. Antonio, L. Soderholm, S.R. Sutton, and J.C. Brannon. 1998. Tetravalent uranium in calcite. Science (Washington, DC) 281:971–973.

Sylvester, E.R., E.A. Hudson, and P.G. Allen. 2000. The structure of uranium(VI) sorption complexes on silica, alumina, and montmorillonite. Geochim. Cosmochim. Acta 64:2431–2438.

Triay, I.R., A. Meijer, J.L. Conca, K.S. Kung, R.S. Rundberg, B.A. Strietelmeier, C.D. Tait, D.L. Clark, M.P. Neu, and D.E. Hobart. 1997. Summary and synthesis report on radionuclide retardation for the Yucca Mountain site characterization project LA-13262-MS. Los Alamos National Laboratory, Los Alamos, NM.

U.S. Department of Energy. 1998. Accelerating cleanup: Paths to closure DOE-EM-0362. DOE-EM-0362, Office of Environmental Management, Washington DC.

Wronkiewicz, D.J., and E.C. Buck. 1999. Uranium mineralogy and the geologic disposal of spent nuclear fuel. p. 475–494. *In* P.H. Ribbe (ed.) Uranium: Mineralogy, geochemistry, and the environment. Vol. 38. Mineral. Soc. of Am., Washington DC.

Zeh, P., J.I. Kim, C.M. Marquardt, and R. Artinger. 1999. The reduction of Np(V) in groundwater rich in humic substances. Radiochim. Acta 87:23–28.

3 Geochemical Speciation of Actinides in Soil and Solution

Wolfgang Runde, Mary P. Neu, Steve D. Conradson, Dien Li, Mavis Lin, Donna M. Smith, Craig E. Van-Pelt, and Youwen Xu

Los Alamos National Laboratory
Los Alamos, New Mexico

ABSTRACT

The mobility and reactivity of actinides within the geosphere is depends on their aqueous speciation, the nature of solubility controlling phases, and their interaction behavior with soils and sediments. Speciation of the actinides is critical for assessing environmental risks and for monitoring and controlling contaminant transport. The actinides may undergo immobilization by (co)precipitation of secondary phases or by sorption onto corroded waste packages or mineral phases, but also may be transported into the environment as molecular solution species or sorbed onto colloidal particulates. We have used a variety of spectroscopic techniques to obtain information on the speciation of the light actinides (U, Np, Pu, Am) in different environments. Through some examples, we illustrate the application of conventional and advanced ultra-sensitive speciation techniques to determine the nature of U, Np, and P species in concentrated chloride solutions, in precipitates in J-13 water from the Yucca Mountain site, and at the solid-solution interface of synthetic samples, and in contaminated soil samples from the Rocky Flats Environmental Technology Site.

Nuclear waste management, environmental restoration, and long-term stewardship of contaminated sites rival the efforts originally invested in nuclear weapons production. Wide-spread radioactive contamination of soil and groundwater from past waste disposal, accidental releases and nuclear weapons testing, and aging interim storage facilities have resulted in potentially serious problems for the environment and human health (U.S. Department of Energy, 1998). The actinides are arguably of most concern to both the U.S. Department of Energy and the public because of their long half-lives, high toxicity, very complex chemical and physical properties, and because they are difficult and costly to handle and dispose. To complicate matters, the diversity and heterogeneity of waste and natural environments leads to a large number of actinide compounds that may form. Successful contaminant retrieval and long-term site stewardship rely on our ability to accurately characterize these species, to estimate mobility rates, and to assess risk to environmental and human health. Key components controlling the environmental transport of ac-

 Geochemistry of Soil Radionuclides. SSSA Special Publication no. 59.

tinides are solution complexes, actinide-bearing solids, and species formed at the mineral-water interface. Actinide solution complexes may occur over a wide concentration range, depending on various site-specific geochemical and source conditions (Ahrland et al., 1975; Kim, 1993; Langmuir, 1997). Historically, actinide speciation studies have been done in simple solutions that do not reflect complex media where contamination exists or repositories have been planned. Or they have been done at concentrations that are orders of magnitude higher than that relevant to most problems, and therefore may not accurately model the environmental chemistry. In addition, the stability ranges of predominant solid phases (e.g. oxides and hydroxides) that will likely govern the solubility of the actinide are not known. At lower concentrations, below the solubility product for actinide solids, native minerals or engineered barrier materials will control actinide solution concentration and mobility via interactions between actinide solution complexes and the solid surface.

There is therefore a need to study actinide speciation in complex matrices and to do so over a broad concentration range. In some cases we can gain new information by using a number of spectroscopic techniques, where only a single physical method had been used in the past. For example, it is becoming routine to characterize a binary metal-ligand system using multiple laboratory-based techniques, such as optical absorbance and vibrational spectroscopy in addition to conventional potentiometry. In other cases, synchrotron-based techniques can be used to obtain structural information and allow for contaminant characterization without chemical perturbation of an environmental sample. This chapter will illustrate, through some examples, how we have used a variety of spectroscopic and microscopic techniques to obtain important speciation data for U, Np, and Pu in the solution and solid states, and at the mineral-solution interface.

ACTINIDE SPECIATION UNDER CONDITIONS REPRESENTATIVE OF THE WASTE ISOLATION PILOT PLANT AND THE YUCCA MOUNTAIN SITES

Hexavalent Actinide Speciation in Concentrated Sodium Chloride

The disposal of nuclear waste in ancient geologic salt formations compels systematic investigation of actinide chemistry in brines to predict their behavior in these natural, highly concentrated salt environments. Actinide release scenarios from the repository involve the dissolution and transport of actinide species in brine that has intruded into the waste emplacement area. To accurately predict the amounts of radionuclides that could be released to the surrounding environment we need to know the solubility, solution speciation, and the interactions with particulate matter and mineral surfaces under these conditions. Radiolysis produces oxidants in brines and the intrinsic high anion concentration are likely to stabilize actinides in their higher oxidation states (Büppelmann et al., 1988; Magirius et al., 1985).

For the major actinides in waste, U, Np, and Pu, the formation and stabilization hexavalent Pu would have a dramatic impact on potential release considerations. Because U is easier to handle and predominates as U(VI) under most conditions,

its chemical behavior can be used to estimate the chemical behavior of Pu(VI). The aqueous chemistry of U(VI) in dilute acidic and near-neutral solutions is relatively well known (Grenthe et al., 1992). Most studies were performed in solutions containing non- or weakly interacting electrolytes, such as $NaNO_3$ and $NaClO_4$. In contrast, the aqueous chemistry of U(VI) (and all actinides) in complex multicomponent solutions is poorly understood. Toward filling this gap in our fundamental knowledge of actinide speciation, we investigated the speciation of U(VI) in concentrated chloride solution.

In low-ionic strength solutions, depending on the total U(VI) concentration, monomeric (UO_2OH^+, $UO_2(OH)_2(aq)$) and polymeric ($(UO_2)_2(OH)_2^{2+}$, $(UO_2)_3(OH)_5^+$)) hydrolysis products dominate the solution speciation in the pH range between 3 and 7 (Grenthe et al., 1992). Mononuclear complexes are significant only at U(VI) concentrations below 10^{-5} *M*, where they are below their detection limits of conventional optical absorbance spectroscopic techniques. We distinguished the uranyl hydroxo complexes by their different Raman and infrared (IR) frequencies of symmetric and asymetric uranyl stretching modes when coordinated water molecules are replaced by chloro and hydroxo ligands. The three Raman (IR) frequencies of the polynuclear species in 5 *M* $NaClO_4$ solution, 870 cm^{-1} (961 cm^{-1}) for the UO_2^{2+}(aq) ion, 852 cm^{-1} (942 cm^{-1}) for $(UO_2)_2(OH)_2^{2+}$, and 839 cm^{-1} (924 cm^{-1}) for $(UO_2)_3(OH)_5^+$, agree well with those observed in low-ionic strength solutions (Fig. 3–1). But when the chloride concentration is increased, U(VI) initially forms two inner-sphere complexes, UO_2Cl^+ and $UO_2Cl_2(aq)$, whose thermodynamic stability constants in dilute solution are known (Grenthe et al., 1992) Accordingly, the Raman (IR) frequency shifts from 870 cm^{-1} (961 cm^{-1}) in 5 *M* $NaClO_4$ to 862.4 cm^{-1} (949 cm^{-1}) in 5 *M* NaCl. In agreement with our data up to 5 *M* NaCl, Nguyen-Trung et al. (1992) used three U(VI) chloro species, UO_2Cl^+, $UO_2Cl_2(aq)$, and $UO_2Cl_3^-$, formed in 3.2 and 8.2 *M* LiCl at low pH to deconvolute the broad Raman

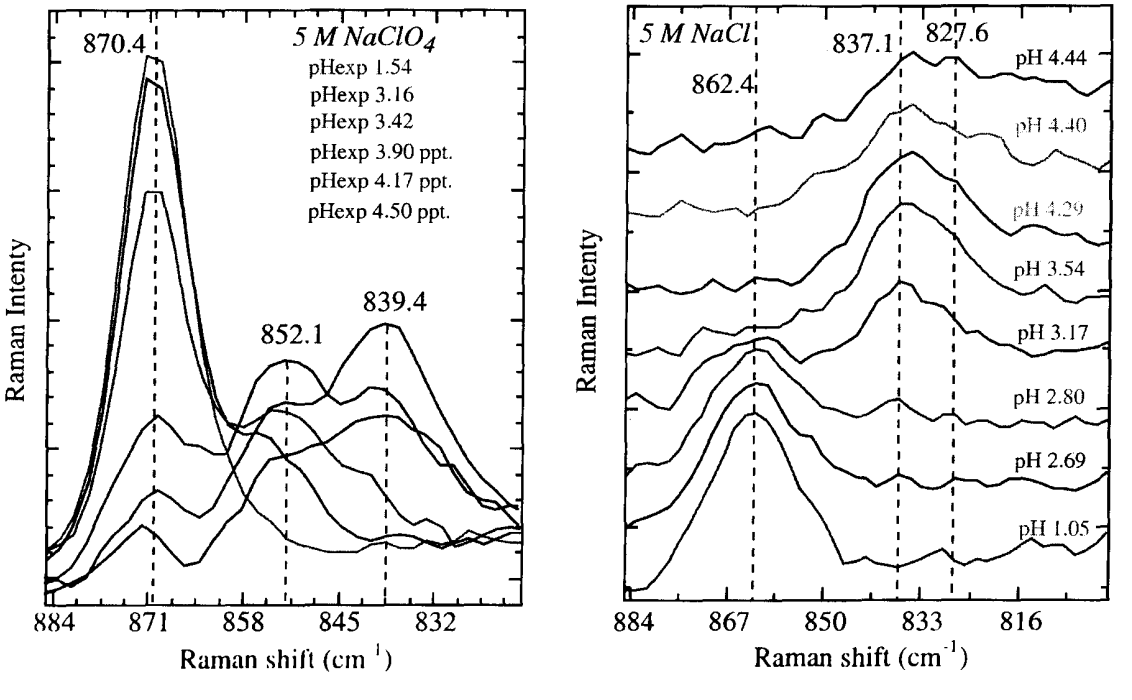

Fig. 3–1. Raman spectra of U(VI) in 5 *M* $NaClO_4$ (left) and 5 *M* NaCl (right).

bands. With increasing pH new bands appear in the Raman and IR spectra; however, the Raman (IR) band for the dimeric species, $(UO_2)_2(OH)_2^{2+}$, which forms at low ionic strength and is expected to have a Raman band at about 844 cm^{-1} (930 cm^{-1} in the IR), is missing. Instead, the first Raman band is observed at 837 cm^{-1} (822 cm^{-1} in the IR) and corresponds to the trimeric hydrolysis product, $(UO_2)_3(OH)_5^+$. At about pH 3.5, a new Raman band appears at 828 cm^{-1} (912 cm^{-1} in the IR) close in energy, 821 cm^{-1}, to that observed for the solid $K_2(UO_2)_4O_2(OH)_2Cl_4 \cdot 6H_2O$ (Perrin & Prigent, 1977) This compound is made up of μ_2–chloro- and μ_2–hydroxo-bridged tetranuclear U(VI) anionic subunits, linked together by chloride atoms to form a chain structure. The structure of $[(UO_2)_4Cl_2O_2(OH)_2(H_2O)_6] \cdot 4H_2O$ (Åberg, 1976) contains these tetranuclear units as discrete molecules that are connected through a network of hydrogen bonding. The loss of the dimeric species, $(UO_2)_2(OH)_2^{2+}$, and the increased stability of the trimer, $(UO_2)_3(OH)_5^+$, in concentrated chloride are significant speciation changes that must be included in geochemical modeling and performance assessment calculations. This set of experiments confirms the limitations of speciation data obtained in dilute solution and the importance of studying the chemistry of actinides in media more closely related to the brines surrounding repositories in salt formations such as WIPP.

Actinide Solids Precipitated from Solutions Mimicking Natural Waters from the Yucca Mountain and Waste Isolation Pilot Plant sites

In addition to the solution speciation of actinides, another critical aspect of the risk assessment of nuclear waste repositories is the determination of upper limits of radionuclide concentrations for very site-specific conditions (Nitsche et al., 1992). Solubility studies provide data that are used to calculate these upper-limit concentrations and enable a conservative predictive approach. We studied the solid phases containing U, Np, and Pu that precipitate out of aqueous solutions of compositions mimicking waters surrounding the YM and WIPP sites.

Due to the low ligand concentrations, sulfate, nitrate, phosphate, and chloride solids are generally not formed in most natural waters, and oxides and hydroxides are the primary phases (Kaszuba & Runde, 1999). For Pu, Pu(V) and Pu(VI) are undersaturated with respect to most of their solid phases in low-ionic strength waters and Pu(IV) phases are predicted to control the solution concentration. For Np, Np(V) is much more stable than the other oxidation states and Np(V) solids should predominate. In a general sense, since An(V) solids are more soluble than An(IV) solids and more Np than Pu will be in solution.

To test this model, we studied the phases formed in J-13 well water from the YM site when Np and Pu were added to the solution at concentrations believed to exceed the solubility limit of their oxides and hydroxides. Solids were separated from the solutions as a function of reaction time and temperature and were their x-ray diffraction (XRD) powder patterns were measured. The Bragg reflections of Np and Pu solids precipitated at ambient temperature are diffuse and broad, but those for solids formed from solutions at 90 °C are distinct and sharper, indicating more highly-ordered solids, and can be assigned to known crystalline phases (Efurd et al., 1998). The powder pattern of the Np solid matches the data reported for Np_2O_5,

and the diffraction pattern of all Pu solids investigated show peaks characteristic of the Fm_3m PuO_2(s) phase (Mooney & Zachariasen, 1949); however, amorphous Pu(IV) hydroxide or Pu(IV) oxyhydroxide is known to exhibit that same powder pattern. So we used x-ray absorption spectroscopy (XAS), including x-ray absorbance near-edge spectroscopy (XANES) and x-ray absorbance fine structure (XAFS), to determine the actinide oxidation states and obtain some information on the bond distances within the solids.

The XANES spectra of the Np solids match that of separately prepared NpO_2OH (Np(V)) and are shifted towards higher energy compared with the NpO_2 (Np(IV)) standard. This finding confirms the presence of Np(V) in the solid phase (Fig. 3–2a). In contrast, the XANES spectrum of the Pu solid precipitated from J-13 water is identical to that of PuO_2 with no significant differences from the high-fired PuO_2 spectrum (Fig. 3– 2b), confirming the Pu(IV) oxidation state. A number of Pu–O distances were observed in the extended x-ray absorption fine structure (EXAFS) within the range 2.3 to 3.7 Å, characteristic of colloidal Pu(IV) hydroxide (Conradson, 1998; Neu et al., 1997). The low amplitude at 2.27 Å indicates that only a small amount of short Pu–O distances, presumably corresponding to terminal Pu–OH moieties that are thought to be present in colloidal Pu(IV) materials, are present in this precipitate (Conradson, 1998; Neu et al., 1997). The intense amplitude at 3.86 Å corresponds to Pu–Pu distances that are slightly longer than those in colloidal Pu(IV) hydroxide (3.84 Å) and PuO_2(s) (3.83 Å) (Conradson, 1998; Neu et al., 1997). The Fourier Transform (Fig. 3–2, right bottom) also indicated a Pu–O distance of about 1.85 Å, which is characteristic for the plutonyl distance within aqueous PuO_2^+ (Pu(V)) complexes, and agrees well with the plutonyl bond distance of 1.81 Å measured for PuO_2^+(aq) ion in dilute acid solution (Conradson, 1998). The Pu–O bonds in Pu(VI) compounds are generally much shorter, i.e., 1.74 Å in PuO_2^{2+}(aq); however, the amount of this Pu(V) feature is sufficiently small so as to not to affect the XANES spectra, which shows only the features of Pu(IV). Thus, under similar initial solution conditions, the Np solubility was found to be governed by the Np(V) solid Np_2O_5; whereas, Pu solubility was controlled primarily by a Pu(IV) oxyhydroxide phase that is orders of magnitude more soluble than PuO_2. And a small amount of Pu(V) (<10%) may be present, which also will increase the Pu solubility above what has been calculated based on only PuO_2 forming.

We have shown that high electrolyte concentrations (NaCl), as present in saturated salt brines at the WIPP site, can cause speciation different from that in dilute solutions. Similar differences can occur in the solid state: another solid, with a corresponding (different) solubility limit, can be stabilized. In dilute aqueous solutions, like the J-13 water just described, binary actinide hydroxides and oxides control the soluble actinide concentrations. In concentrated salt solutions ternary solid actinide phases are likely to form. Examples include formation of carbonates like $NaNpO_2(CO_3) \cdot 5H_2O$ and $Na_3NpO_2(CO_3) \cdot nH_2O$ (Neck et al., 1995) and the replacement of UO_2CO_3 by $Na_4UO_2(CO_3)_3 \cdot nH_2O$ at higher pH and sodium carbonate concentrations.

Many studies on the thermodynamic properties of U oxides and hydroxides have been performed (Grenthe et al., 1992). Their structures and classification of the sheet topologies in U(VI) (oxy)hydroxides have been recently described (Burns, 1999). Several forms of hydrated UO_3(s) have been reported to form at tempera-

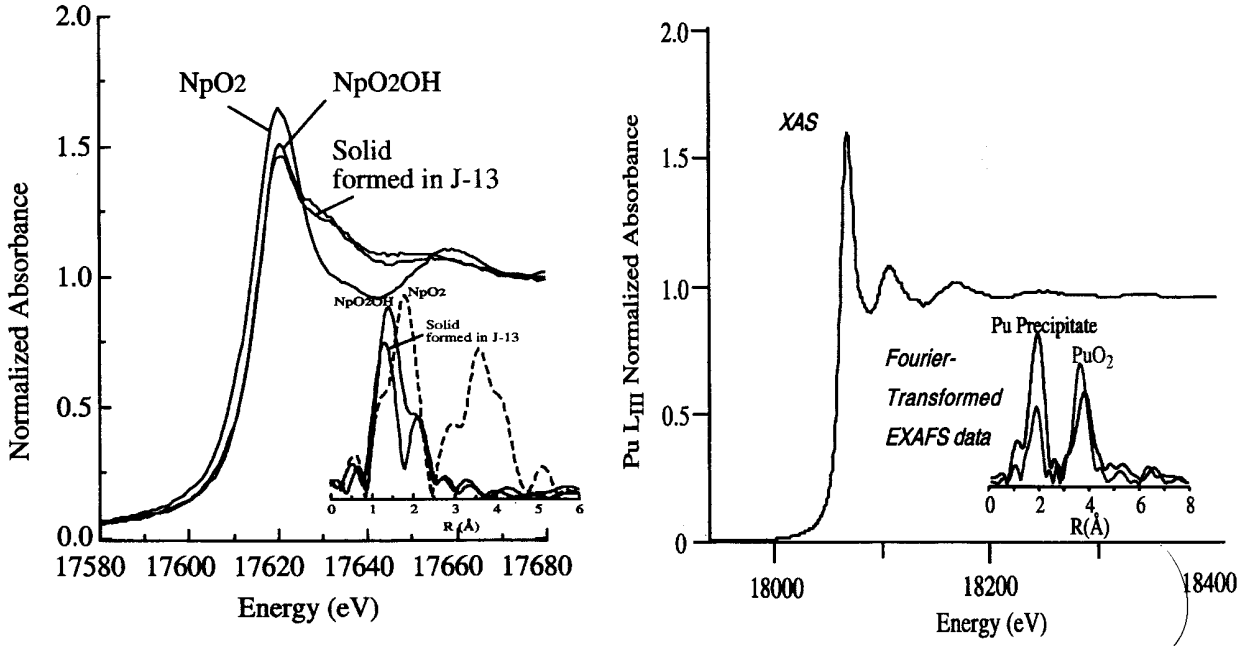

Fig. 3–2. XAS data of Np (a) and Pu (b) solid precipitated in J-13 water from the Yucca Mountain site in comparison with synthesized NpO_2 and PuO_2.

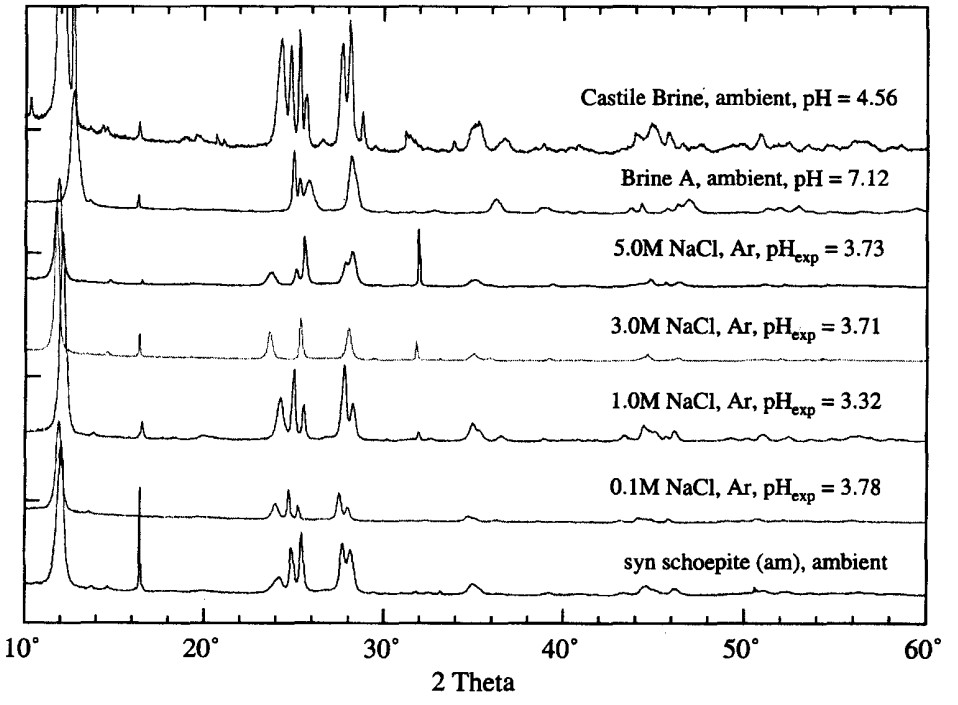

Fig. 3–3. Bragg reflections of U(VI) solid phases formed in NaCl solutions. Initial solid phase was $UO_2(OH)_2 \cdot nH_2O$.

tures below 300 °C as corrosion products of spent nuclear fuel (Finn et al., 1996). These type of solids would be placed in repositories. Should chloride brines come into contact with binary U(VI) hydroxide phases they could be transformed to ternary oxyhydroxide phases. In the presence of 1 *M* $CaCl_2$ and KCl, schoepite spontaneously transforms to becquerelite, $CaU_6O_{19} \cdot 11H_2O$, and compreignacite, $K_2U_6O_{19} \cdot 11H_2O$ (Sandino & Grambow, 1994); however, schoepite, $UO_2(OH)_2 \cdot H_2O$, appeared to be a stable phase in 1 *M* NaCl. As shown in Fig. 3–3, transformation of the solid schoepite phase occurs only at higher NaCl concentrations. A significantly different XRD powder pattern of the U(VI) solid phase is obtained for the solid equilibrated with 3 and 5 *M* NaCl, indicating the formation of a new ternary uranate phase. Since the solid phase is the primary determinant of the upper solubility of actinide ions and its composition can differ significantly if it forms in dilute or concentrated salt solutions, characterization of the solids is critical for interpreting experimental solubility data and developing accurate actinide solubility models.

ACTINIDE SPECIATION WHEN SOLUTION SPECIES ARE COMBINED WITH NATURAL MINERALS AND PROPOSED BARRIER MATERIALS

The geochemical interactions of actinides with minerals are generally most important for those containing oxo-type surface groups, such as hydroxide, silicate, carbonate, or phosphate. Understanding the speciation of surface complexes and the underlying sorption mechanism(s) is important for the determining the effectiveness and long-term retention of mineral phases and engineered reactive barrier

materials. Previous studies of actinide sorption depended heavily on macroscopic chemical and physical measurements, e.g. adsorption isotherms and sorption coefficient (K_d) values; however, these measurements provide little information about the chemical entities and sorption mechanisms. For example, the K_d approach, where one measures the difference in metal ion solution concentration with and without a mineral present, does not differentiate between surface sorption and precipitation, which may have different kinetic and thermodynamic stabilities. Spectroscopic techniques (EXAFS, XPS, TRLFS, and others) are being increasingly used to provide interfacial speciation data that are critical for meaningful modeling of actinide transport.

Uranyl Species Formed on Silicate Surfaces

We reacted silica suspended in 0.1 *M* $NaClO_4$ solutions with varying U(VI) concentrations (from 10^{-5} to 10^{-7} *M*) in the pH range 2 to 9, for 24 h. After filtration through 0.2 mm nylon membrane filters, the solution U(VI) concentration was determined using optical fluorescence spectroscopy. The uranyl fluorescence of the U-sorbed silica was measured between 450 nm and 600 nm with an excitation wavelength at 420 nm. Below pH 5 and U(VI) concentrations below 10^{-4} *M*, prominent peaks at about 502, 520, 544, and 572 nm were attributed to the uranyl ion sorbed on the silica surface, $=SiO_2UO_2$ (Fig. 3–4). These bands shift towards higher wavelength with increasing pH, indicating the formation of different uranyl surface species. At initial U(VI) concentrations of 5×10^{-5} and 5×10^{-6} *M*, the peak at 520 nm is shifted to 528 nm. The shift of the fluorescence bands in the pH region 6 to 8 was attributed to the formation of an $=SiO_2UO_2OH^-$ surface complex. The different positions of the fluorescence peaks at initial U(VI) concentration of 5×10^{-4} *M* suggest the formation of polynuclear surface species or the formation of a surface precipitate; however, the precipitation of $UO_2(OH)_2 \cdot nH_2O$ could be excluded based upon comparison with the fluorescence spectra of the pure solid phase synthesized in separate experiments.

The Fourier transform moduli of EXAFS data of three silica samples that sorbed U(VI) appeared to be very similar (Fig. 3–5). The uranyl U=O distance of 1.78 ± 0.01 Å is typical of U(VI) compounds. Shells for hydroxide coordinated in the equatorial plane appeared in the range 2.22 to 2.31 Å, while bond distances for coordinated water molecules were observed from 2.43 to 2.51 Å. The presence of a U–Si shell (between 3.1 and 3.3 Å) in all samples investigated suggests the formation of inner-sphere uranyl surface complexes, and there was no evidence for a U–U shell, which would indicate surface precipitation or polynuclear uranyl species. The short U–Si bond length of about 3.2 Å and coordination number of 1 at pH around 3 suggests bidentate complexation to a single silica atom. At pH 5, the coordination number of 2 for the Si shell suggests the coordination of the uranyl complex to two Si atoms (Sylwester et al., 2000).

Uranyl Species Formed on Phosphate Surfaces

Phosphate minerals are common in the environment and are known to scavenge heavy metals and actinides from solution. For example, U(VI) phosphates have

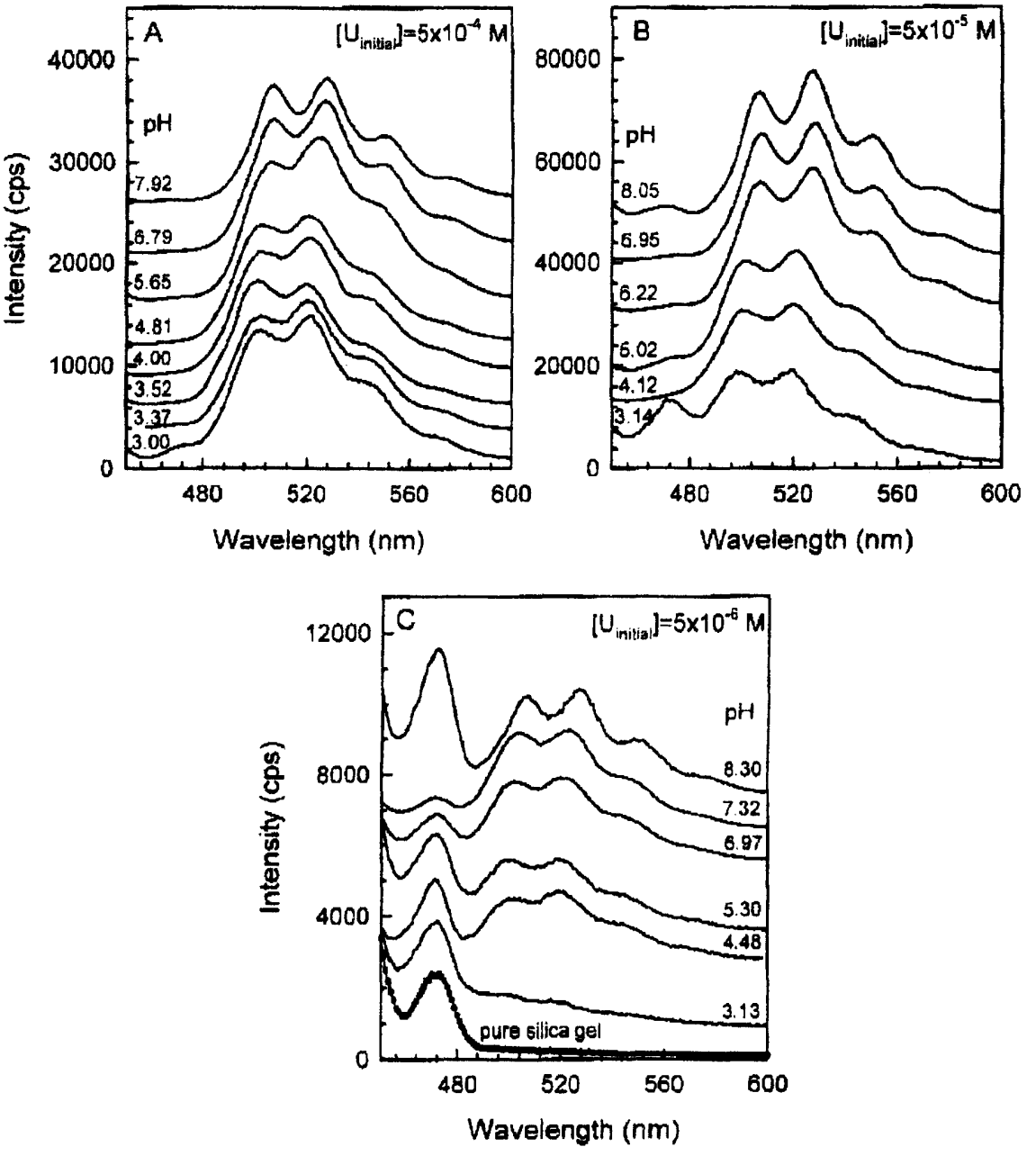

Fig. 3–4. Fluorescence spectra of U(VI) sorbed on silica at different initial U(VI) concentrations and varying pH.

been characterized in soil samples from the Fernald Site in Ohio, a former U.S. Department of Energy processing center for U (Morris et al., 1996). Reactive phosphates have been used to separate actinides, and this chemistry may be used to stabilize actinides in phosphate waste forms or to inhibit environmental actinide mobility by using phosphate-based barriers. Hydroxyapatite [$Ca_{10}(PO_4)_6(OH)_2$], which makes up the mineral of animal teeth, and phosphosilicated apatite have been used to trap heavy metals and/or radionuclides and yield a durable, insoluble waste form for long-term storage or disposal. Precipitation of U(VI) and Th(IV)-bearing solid phosphate phases, as well as distribution coefficients for sorption onto phosphate apatite, have been reported (Gauglitz et al., 1992; Murray et al., 1983; Saray et al., 1999). Predictions of the long-term barrier functions of phosphate materials have been unreliable since retention may rely on a lower solubility product of a new solid

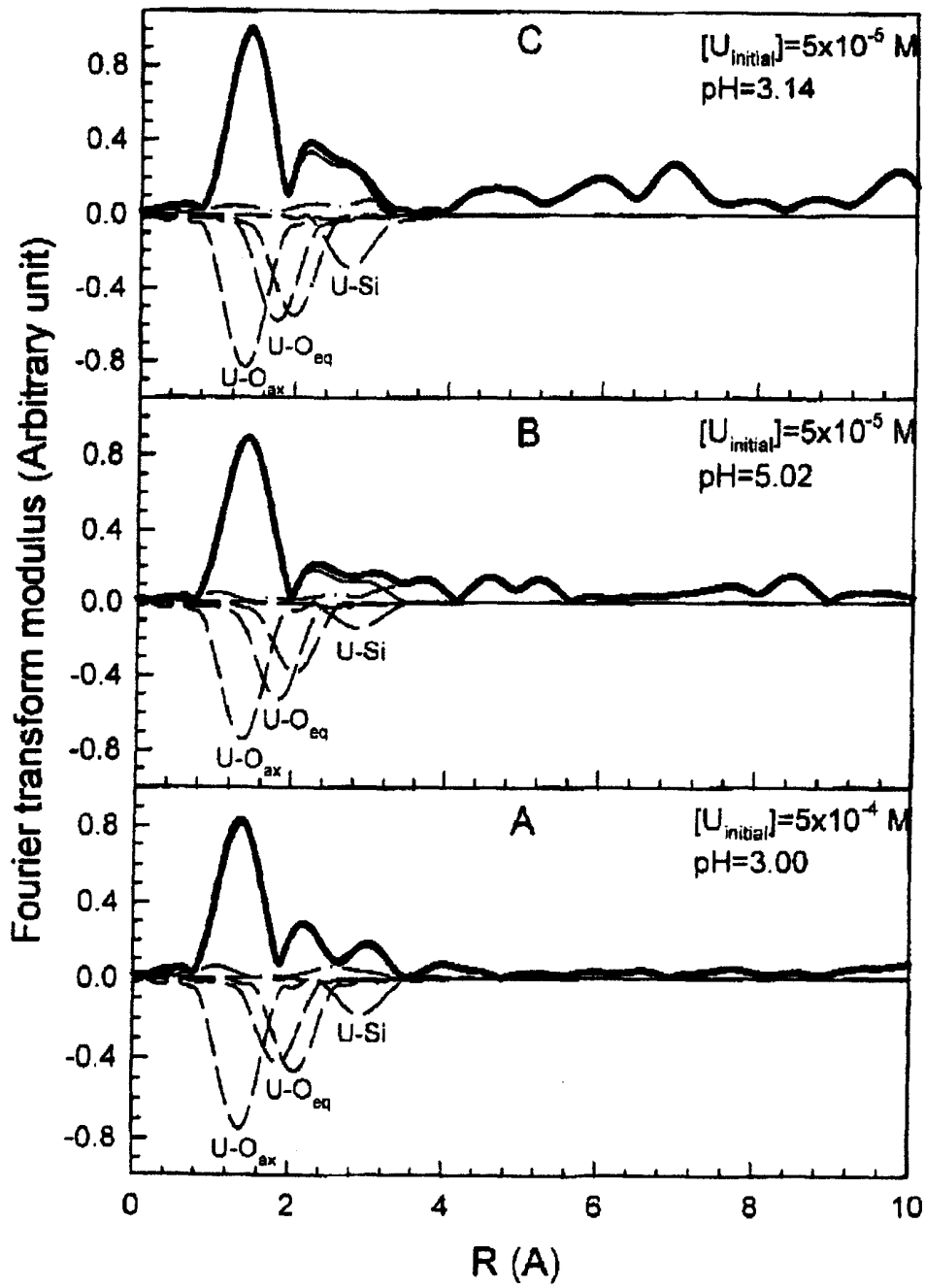

Fig. 3–5. Fourier Transform moduli of U(VI) sorbed on silica at pH 3 and 5.

or on the stability of surface-bound species. We initiated studies on the uptake of U by apatite and on the underlying reaction mechanism(s) by varying the U concentration, pH, carbonate concentration, and mineral pretreatment. We used a variety of techniques including SEM, Raman, TRLFS, and Atomic Force Microscopy (AFM), to distinguish between surface sorption and precipitation. Interaction of U(VI) on apatite depends on pH, following the general U(VI) solution complexation behavior. At low pH, sorption is low, but it increases significantly with pH (Fig. 3–6). After 9 d of reaction, about 58, 40, 11, and 0.04 % of the initial U(VI) concentration remained in solution at pH 2.5, 4.4, 8.5, and 11.7, respectively. The significantly higher K_d value at pH 11.7 indicates precipitation of U(VI).

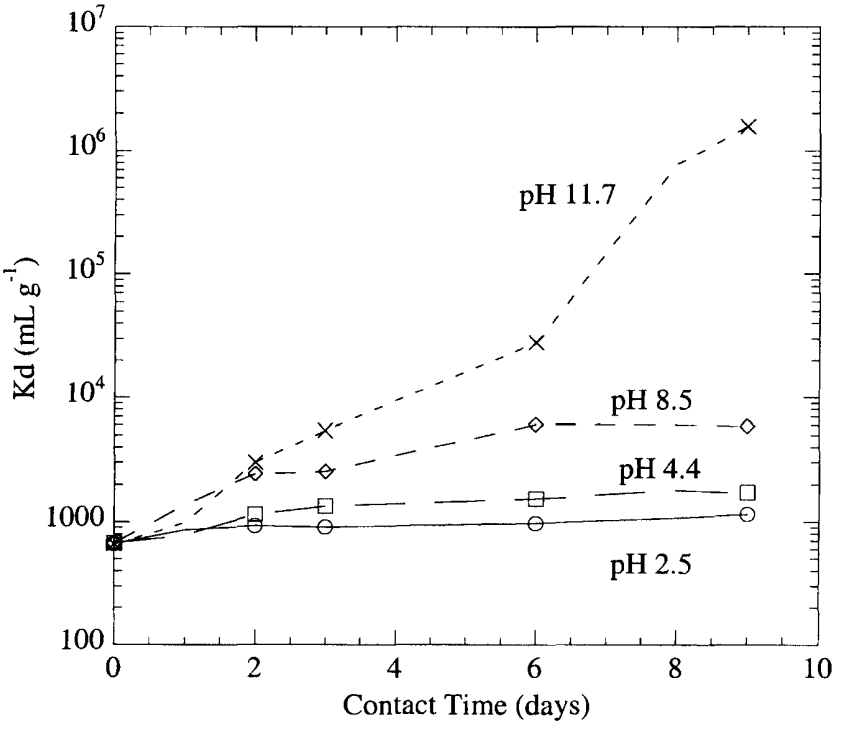

Fig. 3–6. K_d values for U(VI) uptake on apatite at different pHs.

The reaction mechanism of U(VI) with the apatite surface also depends on the total U(VI) concentration. A SEM micrograph of apatite that had been contacted with a 10^{-4} *M* U(VI) solution at pH 4 is shown in Fig. 3–7. A crystalline solid phase, containing Ca/U/P by energy dispersive spectroscopy (EDS), was detected on the surface. The fluorescence spectrum was identical in peak position and relative intensities to that obtained for synthesized $KUO_2(PO_4) \cdot nH_2O$. These characteristic features disappeared when the initial U(VI) concentration was decreased, suggesting an interfacial reaction mechanism on a molecular scale (inner-sphere sorption) rather than surface precipitation. When the apatite is pretreated with 0.1 *M* phosphoric acid, uranyl retention increases. AFM studies showed that the surface of the apatite mineral is more amorphous after being pretreated with acid. As expected, the sorption decreases with increasing carbonate concentration due to the formation of anionic, highly soluble U(VI) carbonate species in solution. $(UO_2(CO_3)_3^{4-}$ is the limiting species at carbonate concentrations above 10^{-3} *M* (Grenthe et al., 1992). The results of these studies clearly indicate the importance of the U(VI) concentration on the formation of a surface precipitate, observed at 10^{-4} *M* U(VI), and surface sorption that occurs at lower U(VI) concentrations.

Spectroscopic Analysis of Plutonium Contaminated Soil

Natural samples contaminated with actinides from accidental releases are generally extremely low in contaminant concentration. Consequently, only the total actinide concentration in soils and groundwater samples is generally measured, while contaminant speciation remains unknown. We analyzed a number of samples from the Rocky Flats Environmental Technology Site (RFETS), including sediment and

Fig. 3–7. Scanning electron microscopy of apatite surface contacted with a solution containing 10^{-4} M U(VI) at pH 4.

water samples from the drainage and settling ponds at the site. Consistently, we found very low Pu concentrations, far below concentrations necessary to obtain any detailed speciation information. Some samples from the 903 Pad area, a past waste storage area within the RFETS site, were sufficiently concentrated in Pu and provided an opportunity to determine the chemical and physical details of the Pu contamination. The soil samples were size-fractionated to reduce the amount of particles with a lower fraction of contaminant per mass. Representative samples were analyzed using XAS, autoradiography, scanning electron microscopy (SEM), and energy dispersive x-ray (EDX) analysis.

Due to previous difficulties with the presence of elements that absorb in the same energy range of the Pu LIII absorption edge, most importantly for these studies, Sr, XAS data were obtained on the soil fractions using the Pu LII absorption edge. The 0.0116 to 0.0164 inch fraction of a soil sample yielded XAS spectra that showed absorbance edges and spectral features beyond the edge into the EXAFS region (Fig. 3–8). The absorbance maximum and absorption edge features were similar to those for the standard PuO_2 and the absence of a near-edge shoulder characteristic for Pu(V) or Pu(VI) were clear indications that the sample contains Pu in

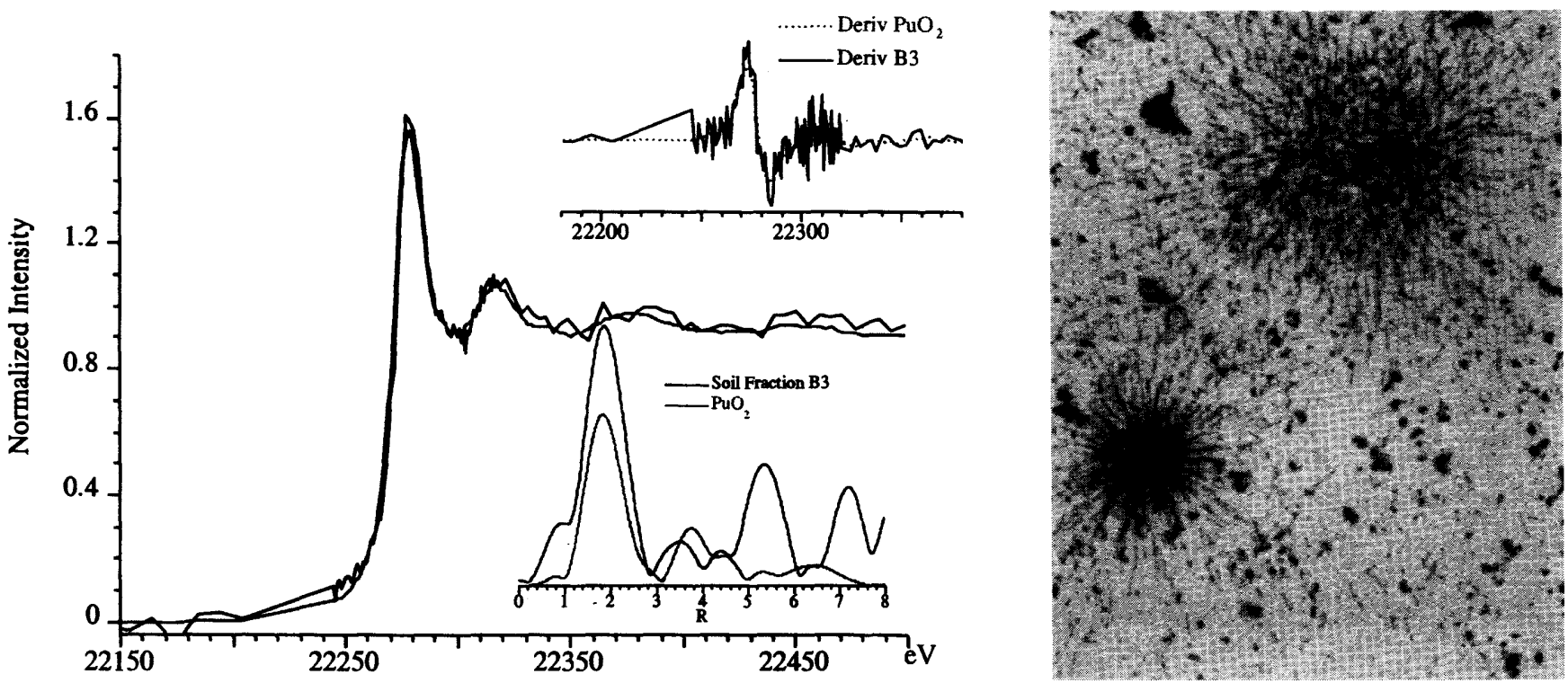

Fig. 3–8. X-ray absorption spectroscopy (left) and radiograph (right) of soil sample from Rocky Flats Environmental Technology Site contaminated with Pu. The x-ray absorption near edge structure (XANES) shows spectrum with similar Pu(IV) energy nearly identical to PuO_2. The Rocky Flats Environmental Technology Site shows that Pu(IV) in the soil sample has about 8 oxygen neighbors at 2.33 Å.

the IV oxidation state. Although the signal to noise in this spectrum of an environmental sample is far from ideal, analysis of the EXAFS data indicates approximately eight nearest neighbor atoms at a distance of 2.33 Å from the Pu in the soil sample, consistent with PuO_2. Features characteristic for other environmentally relevant Pu species, such as Pu(IV) hydroxide, colloid, or carbonate, are absent and the XAS spectrum would be significantly different if these species were present at a significant fraction of the total Pu. This first definitive spectrum of Pu in an environmental sample shows that the Pu in the most concentrated samples from the RFETS is in a highly stable and immobile form, similar or identical to PuO_2.

Particle track radiographic images were obtained for dozens of subsamples of the soil fractions with measurement times of 1 to 5 d. Nearly all radiographs showed dispersed, omni-directional tracks, indicating delocalized radioactivity. Only a small number of very small particles (<0.0116 inch) showed some localized radioactivity (Fig. 3–8). These results should be very useful to RFETS personnel tasked with addressing concerns regarding Pu migration from the site and for those tasked with remediating the site. Based on our results the Pu is more likely to be transported by physical methods, such wind erosion, than by chemical action, such as by dissolution into groundwater.

CONCLUSIONS

Speciation is a critical element needed to assess environmental risks and to predict, monitor, and control transport of actinides. Different methods can be used to determine speciation in well-controlled laboratory systems (in solution, the solid state, or at the mineral–water interface) that are similar to those in nature. The range of actinide concentration can be varied widely, allowing the use of conventional speciation techniques. However, the concentration of actinides in natural contaminated soil and groundwater is generally orders of magnitudes lower than that in synthesized samples. Advanced ultra-sensitive spectroscopic techniques are still needed to allow us to directly determine the nature of species in these samples and of actinides sorbed on mineral surfaces.

ACKNOWLEDGMENTS

This work was supported by the Yucca Mountain Site Characterization Project Office of Los Alamos National Laboratory as part of the Civilian Radioactive Waste Management Program of the U.S. Department of Energy, and by the Waste Isolation Pilot Plant, under contract no. AT-8743 with Sandia National Laboratories and the Source Term Test Project with US Department of Energy. Carlsbad Area Office, managed by R. Villareal. The characterization of Pu in soil samples were supported by the U.S. Department of Energy Environmental Management Science Program. XAS experiments were performed at the Stanford Synchrotron Radiation Laboratory, which is supported by the U.S. Department of Energy Office of Basic Energy Sciences.

REFERENCES

Åberg, M. 1976. The crystal structure of $[(UO_2)_4Cl_2O_2(OH)_2(H_2O)6] \cdot 4H_2O$, a compound containing a tetranuclear aquachlorohydroxooxo complex of uranyl(VI). Acta Chem. Scand. A 30:507–514.

Ahrland, S., J.O. Liljenzin, and J. Rydberg. 1975. Actinide solution chemistry. *In* J.C. Bailer et al. (ed.) Comprehensive inorganic chemistry. Pergamon Press, Oxford.

Büppelmann, K., J.I. Kim, and C. Lierse. 1988. The redox-behavior of plutonium in saline solutions under radiolysis effects. Radiochim. Acta 44/45:65.

Burns, P.C. 1999. The crystal chemistry of uranium. p. 23–90. *In* P.C.B.A.R. Finch (ed.) Uranium: Mineralogy, geochemistry, and the environment. Vol. 38. Mineral. Soc. of Am., Washington, DC.

Conradson, S.D. 1998. Application of x-ray absorption fine structure spectroscopy to materials and environmental science. Appl. Spectroscopy 52:252A–279A.

Efurd, D.W., W. Runde, J.C. Banar, D.R. Janecky, J.P. Kaszuba, P.D. Palmer, F.R. Roensch, and C.D. Tait. 1998. Neptunium and plutonium solubilities in a Yucca Mountain groundwater. Environ. Sci. Technol. 32:3893–3900.

Finn, P.A., J.C. Hoh, S.F. Wolf, S.A. Slater, and J.K. Bates. 1996. The release of uranium, plutonium, cesium, strontium, technetium, and iodine from spent fuel under unsaturated conditions. Radiochim. Acta 75:65–71.

Gauglitz, R., M. Holterdorf, W. Franke, and G. Marx. 1992. Immobilization of heavy metals by hydroxylapatite. Radiochim. Acta 58/59:253–257.

Grenthe, I., J. Fuger, R.J.M. Konings, R.J. Lemire, A.B. Muller, C. Nguyen-Trung, and H. Wanner. 1992. Chemical thermodynamics of uranium. North-Holland Elsevier Science Publishers, Amsterdam.

Kaszuba, J.P., and W. Runde. 1999. The aqueous geochemistry of neptunium: Dynamic control of soluble concentrations with applications to nuclear waste disposal. Environ. Sci. Technol. 33:4427–4433.

Kim, J.-I. 1993. The chemical behavior of transuranium elements and barrier functions in natural aquifer systems. p. 3–21. *In* Materials Research Society Symp. Proc. Scientific Basis for Nuclear Waste Management. Vol. 294. Materials Res. Soc., Pittsburgh, PA.

Langmuir, D. 1997. Aqueous environmental geochemistry. Prentice-Hall, Upper Saddle River, NJ.

Magirius, S., W.T. Carnall, and J.I. Kim. 1985. Radiolytic oxidation of Am(III) to Am(V) in NaCl solutions. Radiochim. Acta 38:29–32.

Mooney, R.C.L., and W.H. Zachariasen. 1949. The transuranium elements. Part II. McGraw-Hill, New York.

Morris, D.E., P.G. Allen, J.M. Berg, C.J. Chisholm-Brause, S.D. Conradson, N.J. Hess, J.A. Musgrave, and C.D. Tait. 1996. Speciation of uranium in fernald soils by molecular spectroscopic methods: Characterization of untreated soils. Environ. Sci. Technol. 30:2322–2330.

Murray, F.H., J.R. Brown, W.S. Fyfe, and B.I. Kronberg. 1983. Immobilization of U-Th-Ra in mine wastes by phosphate mineralization. Can. Mineral. 21:607–610.

Neck, V., W. Runde, and J.I. Kim. 1995. Solid–liquid equilibria of neptunium(V) in carbonate solutions of different ionic strengths: II. Stability of the solid phases. J. Alloys Comp. 225:295–302.

Neu, M.P., R.K. Schulze, S.D. Conradson, J.D. Farr, and R.G. Haire. 1997. Polymeric plutonium(IV) hydroxide: Formation, prevalence, and structural and physical characteristics. Proc. Plutonium Future: The Science. LA-13338-C. Los Alamos Natl. Laboratory, Santa Fe, NM.

Nguyen-Trung, C., G.M. Begun, and D.A. Palmer. 1992. Aqueous uranium complexes. 2. Raman spectroscopic study of the complex formation of the dioxouranium(VI) ion with a variety of inorganic and organic ligands. Inorg. Chem. 31:5280–5287.

Nitsche, H., A. Muller, E.M. Standifer, R.S. Deinhammer, K. Becraft, T. Prussin, and R.C. Gatti. 1992. Dependence of actinide solubility and speciation on carbonate concentration and ionic strength in groundwater. Radiochem. Acta 58/59:27–32.

Perrin, A., and J. Prigent. 1977. Synthesis and vibration spectra of series of tetranuclear halogen complexes of uranyl-ion, $M_2(UO_2)_4O_2(OH)_2X_4 \cdot 6H_2O$: Example of selective deuteration of hydroxo and aquo groups. Spectrochim. Acta A 33:781–785.

Sandino, M.C.A., and B. Grambow. 1994. Solubility equilibria in the U(VI)–Ca–K–Cl–H_2O system: Transformation of schoepite into becquerelite and compreignacite. Radiochim. Acta 66/67:37–43.

Saray, J.S., J.C. Seaman, and P.M. Bertsch. 1999. Immobilization of uranium in contaminated sediments by hydroxyapatite addition. Environ. Sci. Technol. 33:337–342.

Sylwester, E.R., E.A. Hudson, and P.G. Allen. 2000. The structure of uranium(VI) silica complexes on silica, alumina, and montmorillonite. Geochim. Cosmochim. Acta 64:2431–2438.

U.S. Department of Energy. 1998. Accelerating cleanup: Paths to closure. DOE-EM-0362. Office of Environmental Management, Washington DC.

4 Simulating the pH and pCO_2 Dependence of Uranium(VI) Adsorption by a Weathered Schist with Surface Complexation Models

James A. Davis

U.S. Geological Survey
Menlo Park, California

Timothy E. Payne

Australian Nuclear Science and Technology Organisation
Menai, Australia

T. David Waite

University of New South Wales
Sydney, Australia

ABSTRACT

Surface complexation models developed to simulate U(VI) adsorption by a weathered schist material in an earlier publication are extended by considering additional U(VI) surface species and a modified modeling approach. It is illustrated that the surface speciation of Component Additivity models can be different than Generalized Composite (GC) models, because of the different approaches to fitting the pH dependence of adsorption data. Collecting experimental adsorption data at more than one partial pressure of carbon dioxide was important in achieving excellent fits between U(VI) adsorption data and model simulations. Calibration of GC models across a wide pH range (4–10) with FITEQL 4.0 yields good predictions of percent U(VI) adsorbed, but appears to result in a significant overestimation of K_d values in the neutral pH range. Better agreement between the model and experimental K_d values was obtained by considering data across a narrower pH range (6–8.6), which is important for application of the GC modeling approach to field data. It is recommended that a modified optimization method be developed for calibration of surface complexation models with experimental K_d values.

Applications of the surface complexation concept to adsorption of ions by soils and sediments are relatively rare due to the complexity of natural systems. Some examples include Turner et al. (1996), Zachara et al. (1995a,b), Stollenwerk (1995),

 Geochemistry of Soil Radionuclides. SSSA Special Publication no. 59.

Davis et al. (1998), Waite et al. (2000), and Arnold et al. (2001). The surface properties of mineral phases in soil and subsurface environments are greatly altered by the accumulation of poorly crystalline phases of Fe(III) and aluminum oxyhydroxides and silicates (Padmanabhan & Mermut, 1996). Diagenesis and interactions with bacteria may cause leaching of surface layers of minerals (Hiebert & Bennett, 1992), formation of various mixed layer clays, and the deposition of extremely fine-grained, high surface area precipitates (Parfitt et al., 1992). For surface complexation modeling (SCM), the principal difficulties posed by these materials are that the identity, structure, composition, and electrical double layer properties of the wetted surface are usually not well known.

In many cases, the surface chemical properties of sediments may be completely dominated by secondary minerals or grain coatings, which usually constitute only a minor fraction of the sediment mass (Coston et al., 1995; Jackson & Inch, 1989; Davis, 1984). It has been shown that the surfaces of silica, rutile, ferrihydrite, and goethite become enriched with Al when they are mixed with poorly crystalline alumina phases or solutions containing dissolved Al (e.g., Lovgren et al., 1990). These types of surface enrichment can greatly alter the chemical and adsorptive properties of mineral surfaces (Ainsworth et al., 1989). Coston et al. (1995) showed that metal ion adsorption by an aquifer sediment was far more reactive than pure quartz surfaces because of the extensive Al- and Fe-rich surface coatings present on the quartz grains of the sediment.

The literature on SCM largely describes the results of well controlled laboratory investigations of the adsorption of ions by a variety of mineral phases (Davis & Kent, 1990). Most of these studies have been undertaken by aquatic scientists interested in developing a thermodynamic understanding of the coordinative properties of mineral surface functional groups. Such studies can benefit performance assessment modeling for nuclear waste disposal, because the chemical and physical principles that have been developed for individual mineral phases can guide studies of natural materials (Davis et al., 1998; Dzombak & Morel, 1990).

There are two major approaches for applying the SCM concept to model metal ion and radionuclide adsorption to soils and sediments (Davis et al., 1998): the component additivity approach, and the generalized composite approach.

In the component additivity (CA) approach, it is assumed that the wetted surface of a complex mineral assemblage is composed of a mixture of one or more reference mineral (or organic) phases, whose surface properties are known from independent studies of the individual phases. Model parameters are derived from the fit of a surface complexation model to experimental adsorption data for the reference phases, and then applied without further fitting to the mixed mineral assemblage based on a measurement of the composition of the assemblage or the distribution of surface areas among the components of the assemblage. Thus, in the CA approach, the modeler attempts to predict adsorption on the mixed assemblage, assuming that the contributions to adsorption by each phase are additive (Arnold et al., 2001; Waite et al., 2000; Zachara et al., 1994; Honeyman, 1984). A special case of the CA modeling approach is to assume (or prove) that one phase in the mineral assemblage dominates the sorption by the whole assemblage, and thus one can predict adsorption from the model parameters for that phase alone (Payne & Waite, 1991).

A potential problem for CA modeling is that the databases for metal ion adsorption have generally been developed using models that correct mass action equations for coulombic effects, but coulombic effects on adsorption are poorly understood in soils and sediments. For example, in the diffuse double layer (DDL) model of Dzombak and Morel (1990), a typical molecular scale reaction that describes the adsorption of divalent metal ions by Fe oxides is:

$$Me^{2+} + \equiv FeOH \overset{K_{Me}}{\leftrightarrow} \equiv FeOMe^{+} + H^{+} \quad [1]$$

where ≡FeOH refers to a structurally undefined, average ferrinol group on the surface, and K_{Me} is the intrinsic stability constant for the mass action equation. The mass law for Eq. [1] is written as follows:

$$[\equiv FeOMe^{+}]\{H^{+}\} = [\equiv FeOH]\{Me^{2+}\}K_{Me}(\exp(-F\Psi/RT)) \quad [2]$$

where { } denotes the activity of a dissolved solute, [ ] denotes the concentration of an adsorbed species, and the exponential term is the electrostatic energy for forming a surface species with a charge of +1, in which Ψ is the mean field potential at the surface (Dzombak & Morel, 1990).

Equation [1] suggests that one proton will be released per Me^{2+} adsorbed at the surface; however, the charged species formed, ≡FeOMe$^+$, increases the surface charge and mean field potential, and this promotes additional proton release due to coulombic repulsion via the following reaction,

$$\equiv FeOH \leftrightarrow \equiv FeO^{-} + H^{+} \quad [3]$$

With correction to Eq. [1] for coulombic effects, calculations with the DDL model suggest that a macroscopic release of 1.7 to 2.0 protons per Me^{2+} adsorbed should be observed experimentally, depending on the pH and ionic strength of the solution (Dzombak & Morel, 1990). This point emphasizes the importance of the magnitude of electrostatic correction terms in SCM.

Since it is difficult to assess the actual surface potential at mineral surfaces in complex mixtures of phases, it will usually not be possible to determine the appropriate description of the electrical double layer (EDL) that is required for more complex SCM, such as the DDL or the triple layer model (TLM) (Davis et al., 1998; Bolt & van Riemsdijk, 1987). It is known that the surface charge of mineral phases in natural waters is very different from that observed in simple electrolyte solutions. For example, the adsorption of major ions in natural waters (e.g., Mg^{2+}, Ca^{2+}, SO_4^{2-} and silicate) and the formation of organic coatings are known to cause large changes in the point-of-zero-charge (pH_{PZC}) and isoelectric point (pH_{IEP}) of mineral phases (Davis & Kent, 1990).

The simplest of all SCM models uses the nonelectrostatic model (NEM), which considers surface equilibria strictly as chemical reactions, without explicit correction for electrostatic attraction or repulsion. In the NEM, the pH-dependent coulombic energy contribution to the mass action equation is included within the apparent binding constant. The apparent binding constants and the stoichiometry

of the mass action equations are derived by fitting the macroscopic dependence of ion adsorption as a function of pH. As a consequence, the mass action equations that describe ion adsorption in an NEM are not expected to provide accurate representations of the stoichiometry of the reactions at the molecular scale, however, the surface reactions can still be coupled with aqueous geochemical models to provide accurate simulations of metal ion adsorption. The NEM has been applied in relatively few instances in the literature (Davis et al., 1998; Bradbury & Baeyens, 1997; Zachara et al., 1994, 1995a; KoB, 1988), but because of its simplicity, this approach may be the most appropriate for performance assessment modeling of sites with radionuclide contamination.

In the generalized composite (GC) approach, it is assumed that the surface composition of the mineral assemblage is inherently too complex to be quantified in terms of the contributions of individual phases to adsorption. Instead, it is assumed that the adsorptive reactivity of the surface can be described by SCM equilibria written with generic surface functional groups, with the stoichiometry and formation constants for each SCM mass law determined by fitting experimental data for the mineral assemblage (Davis et al., 1998; KoB, 1988; Westall et al., 1995). This approach is simplified by fitting the pH dependence of adsorption without explicit representation of electrostatic energies. When using the NEM in GC modeling, the stoichiometric coefficients of surface reactions, e.g., Eq. [1], typically will be different from that used in models with an EDL term. For example, because a macroscopic release of 1.7 to 2.0 protons per Me^{2+} adsorbed is observed experimentally for metal adsorption on hydrous oxides, an NEM model generally needs to include the following equation to fit the experimental data:

$$Me^{2+} + \equiv FeOH + H_2O \overset{K_{MeOH}}{\leftrightarrow} \equiv FeOMeOH + 2H^+ \qquad [4]$$

An illustration of the effect of proton stoichiometry on fitting data for Zn^{2+} adsorption on quartz is given in Davis et al. (1998).

In this chapter we present CA and GC modeling approaches for simulating U(VI) adsorption by a weathered schist material from Australia. Calculations that simulate U(VI) adsorption by the Fe oxide component of the schist using the CA modeling approach are illustrated. The main purpose of the chapter, however, is to demonstrate the important role of data range in the parameterization of GC models. Previously, Waite et al. (2000) presented preliminary CA and GC models for U(VI) adsorption on the schist material in systems equilibrated with air. Despite reasonable agreement between the model and data when plotted as % U(VI) adsorbed, both the CA and GC models were not entirely satisfactory because the simulations overestimated experimental K_d values by up to one order of magnitude in the pH range from 5 to 8 (Waite et al., 2000). Since the groundwater at the field site falls within this pH range and in situ field estimations of K_d values support the laboratory adsorption data (Payne et al., 2001), further investigations of CA and GC model performance within the circumneutral pH range were warranted. Here we extend the modeling to examine the effect on GC model parameterization of including data for U(VI) adsorption in systems equilibrated with an atmosphere containing 1% CO_2. Other U(VI) surface species than those used by Waite et al. (2000)

are considered and the effect on model fitting of excluding U(VI) adsorption data outside a given pH range is evaluated. It is shown that an advantage of the semi-empirical GC modeling approach is that good agreement among model simulations and experimental data can be achieved for relevant field conditions. In addition, the possibility that model calibration might be changed by optimizing fits to experimental K_d values rather than adsorption density is briefly discussed.

METHODS AND MATERIALS

Characterization of Schist Samples

Weathered schist materials used in the study were obtained in the vicinity of the Koongarra U ore deposit in Australia (Payne; 1999; Davis, 2001; Waite & Payne, 1993). The Koongarra U deposit lies 225 km east of the city of Darwin and 25 km south of the town of Jabiru in the Northern Territory of Australia. The ore deposit lies near the land surface and the top 25 to 30 m of the subsurface consist of a highly weathered zone derived from the upper portion of the primary ore body. Deeper, within the unweathered zone of the primary ore body, the ore consists of lenses containing coalescing veins of uraninite within steeply dipping host Cahill quartz-chlorite schists. Secondary mineralization is present in the weathered schists, from below a surficial sand cover to the base of weathering. This mineralization has been derived from decomposition and leaching of the primary mineralized zone and forms a tongue-shaped fan of ore grade material dispersed downslope for about 80 m to the southeast (Payne, 1999; Davis, 2001). Alteration of uraninite at the (hydrologic) upgradient edge of the primary ore zone has produced a variety of secondary minerals, particularly the uranyl silicates kasolite, sklodowskite, and uranophane (Snelling, 1990). Above the ore body the secondary mineralization in the weathered schists is characterized by uranyl phosphates, particularly saleeite, metatorbernite, and renardite. Further away from the primary ore zone, U is dispersed in the weathered schists and adsorbed onto clays and Fe oxides (Payne et al., 2001; Waite & Payne, 1993). Groundwater chemistry at the site is summarized in Yanase et al. (1995).

Cores were obtained from a number of locations (W1, W2, and W7) in the weathered zone using a cable-tool rig. The W1 core consisted of a highly weathered schist from above the upstream edge of the orebody—a region considered to be the former upward extension of the primary ore. W2 was collected near the leading edge of the dispersion fan approximately 50 m downgradient from the primary ore zone. W7 was obtained about 100 m further downgradient, and the U content of the solid phase was only slightly elevated relative to background (Table 4–1).

A fine fraction for adsorption experiments (approximately <10 mm) was obtained from each of these samples using sieving and sedimentation, following the procedure described in Payne (1999). The resulting slurry contained a suspension of fine particles that could be reproducibly subsampled by vigorous agitation, followed by removal of an aliquot of known volume. The fine fractions were characterized by SEM/EDS and XRD and all found to be dominated by kaolinite with a minor component of mica. Iron was found as coatings on clay particles and as abun-

Table 4–1. Characteristics of fine fractions (<10 mm) of Koongarra soil samples used in U(VI) adsorption experiments.

Sample name	Depth	Total U content	TAO extractable U content†	BET surface area
	m	μg g^{-1}		m^2 g^{-1}
W1	13.0–13.2	356	42.6	24.6
W2	14.0–14.2	426	225.0	52.3
W7	13.0–13.2	10.4	1.0	51.9

†TAO, Tamm's acid oxalate.

dant fine particles about 1 mm in size. The W1 sample had greater amounts of hematite, as evidenced by its brick-red color. In contrast, the W2 and W7 samples were yellow/brown. The minor components P, Ti, and Mn were only observed in particles rich in Fe, indicating a possible association of these elements. The BET surface areas of the fine fractions of the W2 and W7 samples were somewhat higher than W1 (Table 4–1).

The samples used in the adsorption studies were subjected to a five-stage sequential extraction scheme (Davis, 2001). Solutions obtained from each extraction step were analyzed for their elemental and U isotopic concentrations. As previously described (Payne, 1999; Payne & Waite, 1991), U(VI) in the relatively weak extractions (acetate buffer and Tamm's acid oxalate, referred to as TAO) can be considered accessible to the groundwater. The U(VI) released in these extractions is of importance in quantifying the total amount of U(VI) that may participate in adsorption equilibria when the soil minerals are bathed in aqueous solutions. The quantification of the accessible U(VI) in each of the samples by the extractions was also supported by excellent agreement with that determined by U(VI) isotopic exchange (Payne, 1999; Payne & Waite, 1991; Davis, 2001).

The $^{234}U/^{238}U$ ratio in each soil extract was also determined. For all samples, the readily leachable U(VI) in the acetate buffer and TAO extractions had a much lower $^{234}U/^{238}U$ isotope ratio than in the stronger extractions (Davis, 2001). The $^{234}U/^{238}U$ ratio in the weaker extractions was significantly below 1.0, and this ratio was very similar to the $^{234}U/^{238}U$ isotope ratio in groundwater samples from the weathered zone. This adds to the evidence that the U(VI) released in the weak extractions can be used to estimate the total amount of U(VI) that participates in adsorption equilibria when the soils minerals are bathed in aqueous solutions.

Most of the Fe in the soil samples was only extracted to a significant extent by citrate/dithionite reagent or 6 *M* HCl, indicating that it was probably present as crystalline Fe oxides. About 1% of the Fe in the samples was extracted with TAO, and can thus be considered poorly crystalline.

Protocol for Adsorption Experiments

The experimental procedures are given in detail in Payne (1999) and Davis (2001). Batch experiments were carried out in polypropylene centrifuge tubes and were equilibrated with air or a nitrogen–carbon dioxide–air gas mixture. Aliquots containing known weights of the soil fine fractions were transferred to 25 mL polypropylene centrifuge tubes, and suspended in 0.1 *M* $NaNO_3$. Each tube had a

Table 4–2. Experimental conditions for U(VI) adsorption.

Soil sample	Solid–liquid ratio	Natural U(VI)† participating in adsorption equilibria	Added U(VI)	Total U(VI) participating in adsorption equilibria	Gas phase
	$g\ L^{-1}$		μM		
W1	20	3.6	0.1	3.7	Air or 1% CO_2
W1	4	0.72	0.01	0.73	Air
W2	4	3.8	0.1	3.9	Air or 1% CO_2
W7	4	0.017	0.01	0.03	Air
W7	4	0.017	1.0	1.02	Air

†Assumed to equal the U extracted by the TAO reagent.

2 mm hole in the lid to permit air equilibration without loss of sample during agitation. For studies at pH >7.0, sufficient $NaHCO_3$ was added to ensure pH stability and to fix the carbonate content of the system at the concentration in equilibrium with the gas phase. U(VI) was added after a 24 h pre-equilibration, during which the system was allowed to come to equilibrium. U(VI) was added to the systems either as ^{236}U or ^{238}U, depending on the experimental U(VI) concentration range.

In most experiments the adsorption results are based on the distribution of the tracer ^{236}U at steady state (Payne, 1999); however, most of the U(VI) involved in the adsorption equilibria is derived from U(VI) already present in the schist sample (predominantly ^{238}U), and thus, the total U(VI) in the experiment is greater than the amount of ^{236}U added. The labile amount of U(VI) was assumed to participate in the adsorption equilibria, which was estimated by sequential extraction and isotopic exchange techniques (Payne, 1999; Davis, 2001), and this quantity is given in Tables 4–1 and 4–2.

The experimental tubes were gently shaken in a water bath at 25°C for 48 h, with the pH being checked and adjusted after 24 h. Immediately prior to sampling the pH was measured and the aqueous phase was separated by high speed centrifugation [relative centrifugal force (RCF) > 6500 *g*] for 30 min. U(VI) concentrations in the supernatant were determined using kinetic phosphorescence analysis or by alpha spectrometry (see Payne, 1999). While most data were collected under atmospheric conditions, some investigations were performed in a glove box at a partial pressure of carbon dioxide (pCO_2) of 0.01 atm (Table 4–2).

SUMMARY OF EXPERIMENTAL RESULTS

The experimental data used for the U(VI) surface complexation modeling are shown in Fig. 4–1, with the data presented as K_d values ($mL\ g^{-1}$) and K_a values ($mL\ m^{-1}$), the latter defined as the K_d value divided by the specific surface area of the sample. The decrease in adsorption at alkaline pH values is due to the formation of aqueous U(VI)-carbonate complexes (Davis, 2001; Barnett et al., 2000; Waite et al., 1994). Normalizing the adsorption data to surface area (Fig. 4–1b) decreases the scatter in the K_d plot (Fig. 4–1a) somewhat, especially in the pH ranges from 4 to 6 and from 7.5 to 10.

Similarities of U(VI) adsorption on the schist material, ferrihydrite, quartz, and hematite as a function of pH can be seen clearly in Fig. 4–2, which compares K_a values for systems equilibrated with air. Although the K_d values for U(VI) ad-

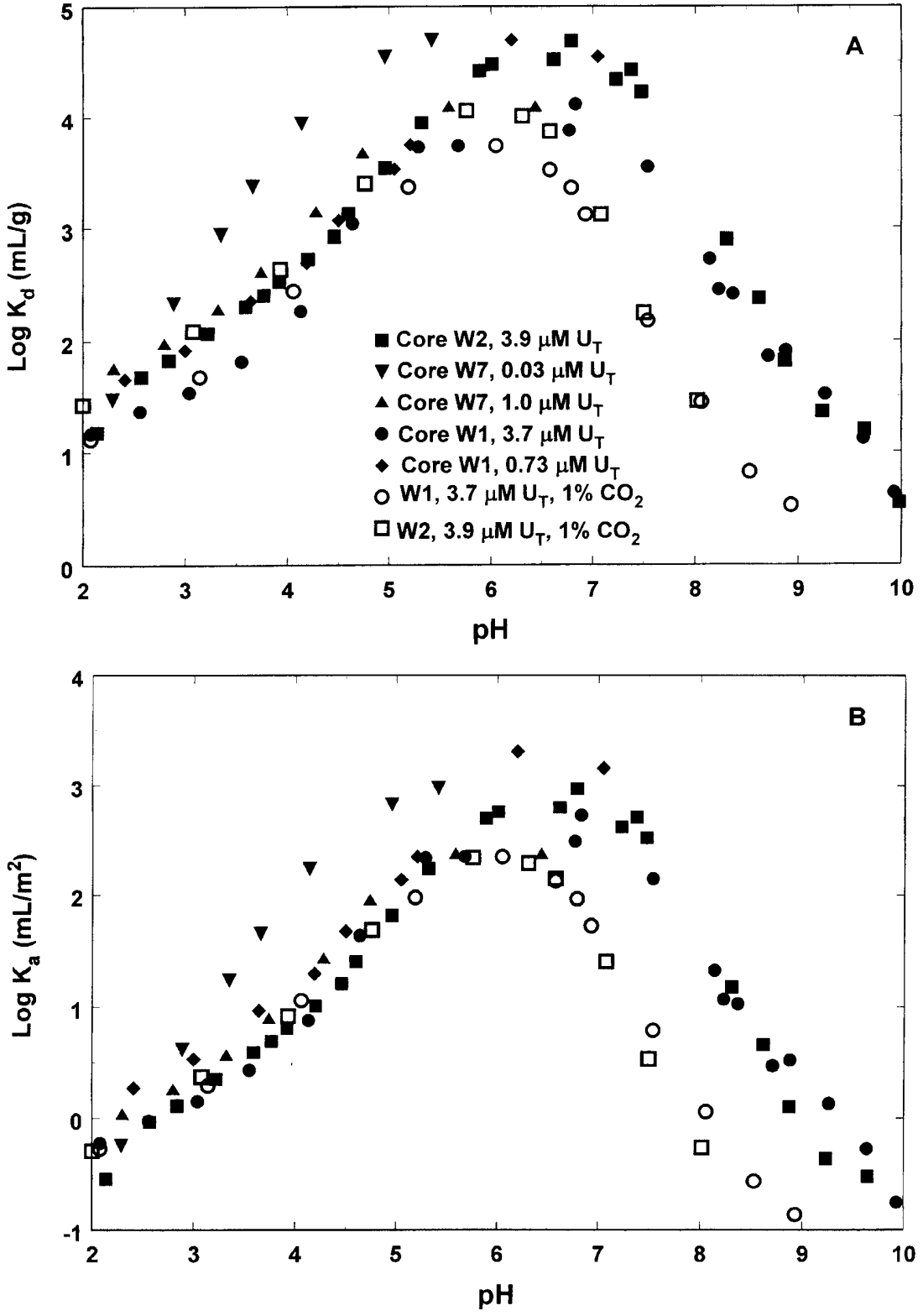

Fig. 4–1. U(VI) adsorption onto Koongarra soil samples expressed as K_d (mL g^{-1}) and K_a (mL m^{-2}) values as a function of pH and the partial pressure of CO_2. Filled symbols are for systems equilibrated with air and open symbols are for systems equilibrated with a 1% CO_2/99% N_2 gas mixture. Experimental conditions are given in Table 4–2. Data from Payne (1999).

sorption on these mineral phases differ by several orders of magnitude, the differences among the mineral phases are relatively small after normalization to the BET specific surface area. This is due to the strong and rigid character of the U–O bonds in UO_2^{2+}, even at mineral surfaces (Bargar et al., 2000). A similar finding has been reported by Pabalan et al. (1998) for aluminosilicate phases; our results extend their finding by comparing soil samples with additional mineral phases. The K_d values are particularly close in the pH range from 4 to 5.5, but exhibit greater scatter across the pH range from 5.5 to 9 (Fig. 4–2). The reason for this scatter is unknown, but may be due to the formation of ternary U(VI)-carbonate complexes on the Fe oxides (Bargar et al., 2000), while additional ternary complexes, such as U(VI)-phosphate or -silicate complexes, might exist on the schist surfaces. In addition, there could be problems in assessing the (adsorptive) reactive surface of the schist materials by the BET gas adsorption method (Davis & Kent, 1990).

Adsorption of U(VI) on the W7 sample was greater than on the other two samples (Fig. 4–1) in the experiments at low total U (U_T) concentration. Since the mineralogy and surface area of the W7 sample was not much different than the other samples, it is likely that the stronger adsorption on the W7 sample was solely due to the lower U_T concentration. Stronger adsorption in experiments with lower U_T is attributed to the presence of a small number of strong binding sites on the surfaces of the natural substrates (Davis, 2001; Davis et al., 1998).

The partial pressure of carbon dioxide (pCO_2) in Koongarra ground waters ranges from 0.004 to 0.05 atm (Yanase et al., 1995). In experiments carried out with 1% CO_2 (0.01 atm CO_2), U(VI) adsorption was significantly reduced at pH >6, relative to experiments carried out in air (Fig. 4–1). This is due to the greater dominance of aqueous U(VI)-carbonate complexes at higher pCO_2 (Duff & Amrhein, 1996; Waite et al., 1994). Adsorption of U(VI) at pH <6, where aqueous U(VI)-car-

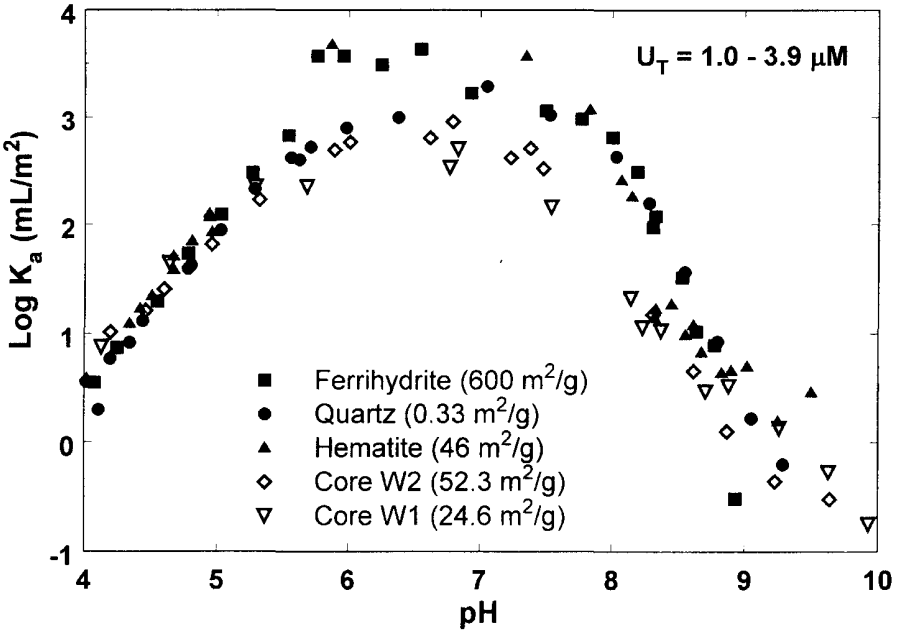

Fig. 4–2. Comparison of K_a (mL m^{-2}) values as a function of pH for ferrihydrite, quartz, hematite, and Koongarra soil samples. Total U concentration participating in adsorption equilibria (U_T) ranged from 1 to 3.9 µ*M*. Ferrihydrite data from Waite et al. (1994), quartz data from Davis (2001), and hematite data from Reitmeyer et al. (1999).

bonate complexes are not important, was not significantly affected by the higher pCO_2. The laboratory adsorption data have been shown to be very relevant to the in situ partitioning of U(VI) in the shallow aquifer at Koongarra, particularly when laboratory experiments are conducted at the appropriate pCO_2 (Payne et al., 2001).

SURFACE COMPLEXATION MODELING

Component Additivity Modeling

Two example CA model calculations for the W1 sample are presented here, in order to illustrate some modeling issues and the difference with the GC modeling approach. High-resolution TEM studies indicate that the surficial U in the schist materials is principally associated with iron oxide phases (Lumpkin et al., 1999; Sato et al., 1997). A TAO extract of the W1 sample dissolved 0.88 mg Fe g^{-1} of sample (Davis, 2001). Assuming that the Fe was derived from a poorly crystalline iron oxide phase similar to ferrihydrite, one can estimate a total surface site concentration for the sample from the relationship of 0.875 moles of sites per mole of Fe in ferrihydrite (Waite et al., 1994). Assuming the presence of weak and strong U(VI) binding sites ($\equiv W(OH)_2$ and $\equiv T(OH)_2$, respectively) as previously described by Waite et al. (1994), and with stability constants for solution and surface equilibria as shown in Tables 4–3 and 4–4, one can make predictive diffuse double layer (DDL) model calculations for U(VI) adsorption by the ferrihydrite in the W1 sample.

The calculated U(VI) adsorption is considerably less than that observed experimentally for the W1 sample (Fig. 4–3), although the predicted adsorption by ferrihydrite near pH 6 was significant. The calculations carry the assumption that

Table 4–3. Formation constants for selected aqueous species used in surface complexation modeling (Davis, 2001).

Reaction	Log K ($I = 0$)
$UO_2^{2+} + H_2O \Leftrightarrow UO_2OH^+ + H^+$	−5.20
$UO_2^{2+} + 2H_2O \Leftrightarrow UO_2(OH)_2^0 + 2H^+$	−11.50
$UO_2^{2+} + 3H_2O \Leftrightarrow UO_2(OH)_3^- + 3H^+$	−20.00
$UO_2^{2+} + 4H_2O \Leftrightarrow UO_2(OH)_4^{2-} + 4H^+$	−33.00
$2UO_2^{2+} + H_2O \Leftrightarrow (UO_2)_2OH^{3+} + H^+$	−2.70
$2UO_2^{2+} + 2H_2O \Leftrightarrow (UO_2)_2(OH)_2^{2+} + 2H^+$	−5.62
$3UO_2^{2+} + 4H_2O \Leftrightarrow (UO_2)_3(OH)_4^{2+} + 4H^+$	−11.90
$3UO_2^{2+} + 5H_2O \Leftrightarrow (UO_2)_3(OH)_5^+ + 5H^+$	−15.55
$3UO_2^{2+} + 7H_2O \Leftrightarrow (UO_2)_3(OH)_7^- + 7H^+$	−31.00
$4UO_2^{2+} + 7H_2O \Leftrightarrow (UO_2)_4(OH)_7^+ + 7H^+$	−21.90
$2UO_2^{2+} + 3H_2O + H_2CO_3 \Leftrightarrow (UO_2)_2CO_3(OH)_3^- + 5H^+$	−17.543
$UO_2^{2+} + H_2CO_3 \Leftrightarrow UO_2CO_3^0 + 2H^+$	−7.013
$UO_2^{2+} + 2H_2CO_3 \Leftrightarrow UO_2(CO_3)_2^{2-} + 4H^+$	−16.426
$UO_2^{2+} + 3H_2CO_3 \Leftrightarrow UO_2(CO_3)_3^{4-} + 6H^+$	−28.449
$UO_2^{2+} + NO_3^- \Leftrightarrow UO_2NO_3^+$	0.30
$H^+ + CO_3^{2-} \Leftrightarrow HCO_3^-$	6.354
$2H^+ + CO_3^{2-} \Leftrightarrow H_2CO_3^0$	16.683

Table 4–4. Stability constants for surface equilibria used in iron oxide component additivity modeling approach.

Reaction	Log K (I = 0.1)
$TOH + H^+ \Leftrightarrow TOH_2^+$	6.51
$WOH + H^+ \Leftrightarrow WOH_2^+$	6.51
$TOH \Leftrightarrow TO^- + H^+$	−9.13
$WOH \Leftrightarrow WO^- + H^+$	−9.13
$T(OH)_2 + UO_2^{2+} \Leftrightarrow TO_2UO_2^0 + 2H^+$	−2.57
$W(OH)_2 + UO_2^{2+} \Leftrightarrow WO_2UO_2^0 + 2H^+$	−6.28
$T(OH)_2 + UO_2^{2+} + H_2CO_3 \Leftrightarrow TO_2UO_2CO_3^{2-} + 4H^+$	−13.031
$W(OH)_2 + UO_2^{2+} + H_2CO_3 \Leftrightarrow WO_2UO_2CO_3^{2-} + 4H^+$	−17.103

† A total site density of 16.38 μmoles m^{-2} and relative concentrations of strong to weak sites of 0.21% was assumed, i.e., $[TOH]_T = 0.0021[WOH]_T$. Constants are identical to those derived for U(VI) adsorption on ferrihydrite by Waite et al. (1994) using the Diffuse Double Layer model.

the surface properties of the poorly crystalline Fe oxide phases in the W1 sample are identical to those of the 2-line ferrihydrite synthesized in the experiments of Waite et al. (1994). Perhaps the most important assumption of this modeling approach, though, is that the surface properties of the Fe oxides are not changed by the adsorption of organic acids, silicate, and other solutes present in the groundwater. Adsorbed organic material and other surface coatings would be expected to significantly alter the EDL on ferrihydrite (Davis & Kent, 1990; Davis, 1982; Tipping, 1981), and thus, influence the adsorption of U(VI).

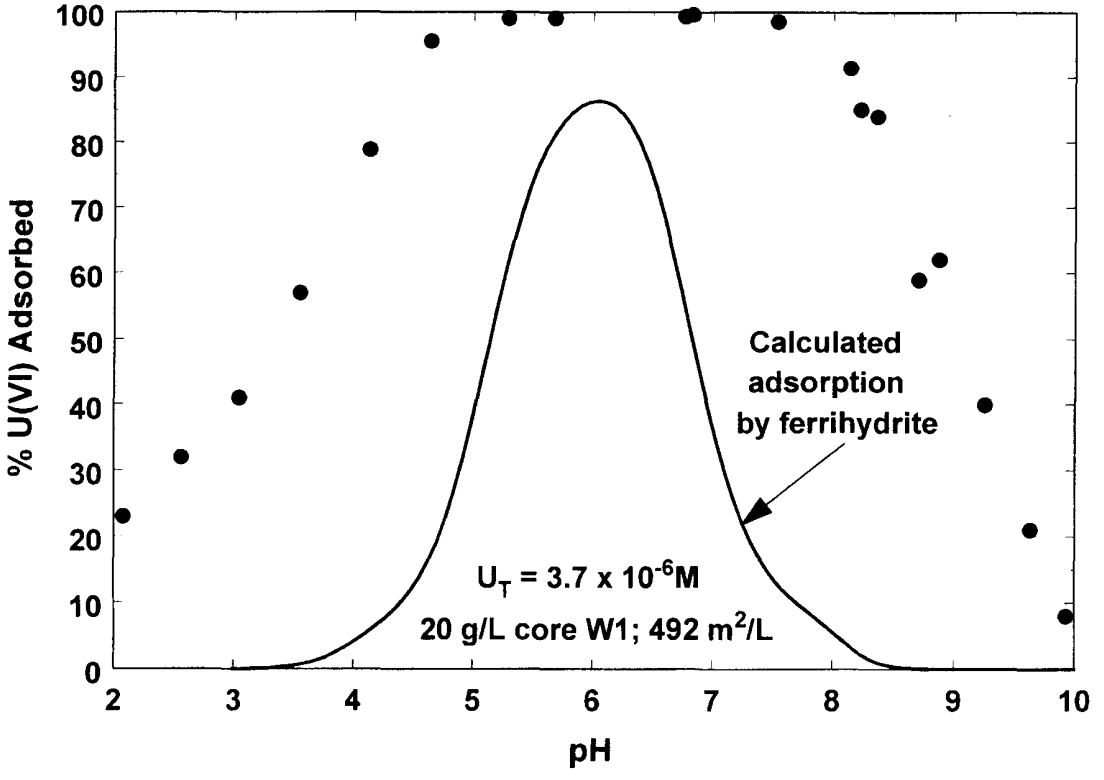

Fig. 4–3. Component additivity model calculation of U(VI) adsorption by ferrihydrite mineral present in the Koongarra W1 sample compared with experimental data for U(VI) adsorption.

Dithionite-citrate and HCl extractions of the W1 sample dissolved 70.4 mg Fe g^{-1} of sample, probably present as goethite and hematite. Assuming a composition of Fe_2O_3, this corresponds to 100.7 mg of Fe_2O_3 g^{-1} of sample. Submicron sized Fe oxide particulates typically have surface areas from 20 to 50 m^2 g^{-1}; a 50 m^2 g^{-1} value is equivalent to a crystalline Fe oxide surface area of 5.04 m^2 g^{-1} within the W1 soil sample, roughly 20% of the total surface area of the sample. The predicted U(VI) adsorption on the crystalline Fe oxide component of the schist material using this surface area is shown in Fig. 4–4, with the assumption that the U(VI) binding constants and the site densities are the same as observed for ferrihydrite (Table 4–4). As was found for ferrihydrite (Fig. 4–3), the calculated U(VI) adsorption is less than that observed experimentally for the W1 sample, but the prediction is much improved.

Waite et al. (2000) made a similar CA modeling calculation with the assumption that the entire surface area of the W1 sample had U(VI) binding constants identical to that observed for ferrihydrite. The results yielded a modeling curve similar in shape to that shown in Fig. 4–4, but with the adsorption edges displaced to lower and higher pH values. The model calculations were in reasonably good agreement with the % U(VI) adsorbed data at pH values greater than approximately 4. This result was encouraging and it supports the observation that many minerals adsorb U(VI) in a similar manner when normalized to surface area (Fig. 4–2), since other phases than Fe oxides would be expected to contribute surface area to the sample. The calculations also suggest that surface coatings on larger mineral grains in soils and sediments may exhibit site densities per unit mass similar to ferrihydrite, even though present as fine-grained crystalline material. A similar result was observed for an aquifer sand by Davis et al. (1998).

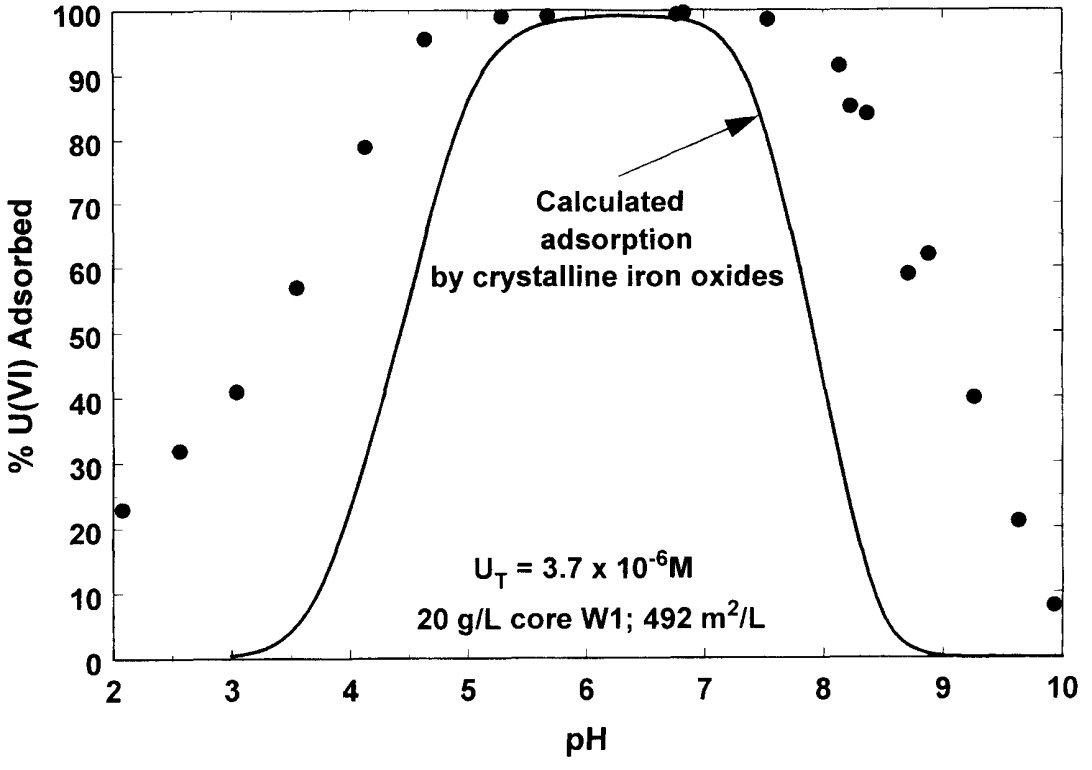

Fig. 4–4. Component additivity model calculation of U(VI) adsorption by crystalline Fe oxides present in the Koongarra W1 sample compared with experimental data for U(VI) adsorption

Generalized Composite Modeling

In this section we illustrate the application of GC modeling to the schist materials and discuss the role of data range and surface speciation in the parameterization of GC models. Previously, Waite et al. (2000) developed a two-site GC model for the U(VI) adsorption data for systems equilibrated with air; however, the GC model calculations of Waite et al. (2000) assumed that only the surface species, SO_2UO_2 and $SO_2UO_2CO_3^{2-}$, were present (where S denotes a generic surface site, strong or weak), based on the earlier ferrihydrite DDL model of Waite et al. (1994). Because the GC model calculations presented here are performed with an NEM model, it is possible that different surface species may yield a better fit to the experimental data than those found in a DDL model, because of the effect of the EDL terms on adsorption calculations (Dzombak & Morel, 1990).

The GC modeling results presented here examine several issues simultaneously. First, the issue of data selection is evaluated to ascertain the importance of data range (pH, pCO_2) in model calibration and data fitting. This was accomplished by calibrating a GC model with U(VI) adsorption data over a narrow or wide pH range, and by inclusion–exclusion of data for systems equilibrated with 0.01 atm CO_2. Secondly, the issue of surface species selection in GC modeling is examined. Finally, the significance of the optimization method used is briefly discussed in terms of its impact on fitting absolute or relative measurements of adsorption (e.g., K_d values are relative because the adsorbed quantity is divided by a dissolved quantity).

In order to simplify the modeling and provide a basis for comparison, the following modeling choices were made: (i) a nonelectrostatic model was used because no quantitative information of coulombic effects at the surface was available, (ii) a single-site model was adopted since there was little variation in the U_T concentration in the experiments (most points were determined at a U_T concentration in the range from 1 to 3.9 μM), (iii) adsorption data for pH <4 were not considered because of potential problems associated with sample dissolution under acidic conditions, (iv) a site density equal to that used by Waite et al. (1994) (16.38 μmoles m^{-2}) was assumed in calculating the surface site concentrations, and (v) no more than three U(VI) surface species were used to describe the experimental data. The latter constraint was arbitrary, but was adopted to address criticism that surface complexation models have too many independent parameters (the complex aqueous speciation of U(VI) notwithstanding). In general, a goal of the semi-empirical GC modeling approach is to develop the simplest model possible that describes the major features of adsorption as chemical conditions are varied over field-relevant ranges (Davis et al., 1998).

Ideally, spectroscopic data would be available to constrain the possible choices of surface species (in both CA and GC modeling); however, no x-ray absorption (XAS) data were collected that describe U(VI) speciation at the surface of the schist materials because the U concentrations were below EXAFS detection limits. XAS and FTIR spectroscopic studies have indicated that U(VI) forms strong, edge-sharing, bidentate bonds with the surfaces of ferrihydrite and hematite and that the attached uranyl cation may then form ternary surface complexes with carbonate anions (Bargar et al., 1999, 2000). At least nine monomeric U(VI) sur-

Table 4–5. Surface reactions considered in generalized composite modeling.

Number	Reaction
1	$S(OH)_2 + UO_2^{2+} = SO_2HUO_2^{+} + H^+$
2	$S(OH)_2 + UO_2^{2+} = SO_2UO_2 + 2H^+$
3	$S(OH)_2 + UO_2^{2+} + H_2CO_3 = SO_2UO_2H_2CO_3 + 2H^+$
4	$S(OH)_2 + UO_2^{2+} + H_2CO_3 = SO_2UO_2HCO_3^{-} + 3H^+$
5	$S(OH)_2 + UO_2^{2+} + H_2CO_3 = SO_2UO_2CO_3^{2-} + 4H^+$
6	$S(OH)_2 + UO_2^{2+} + 2H_2CO_3 = SO_2UO_2H_2CO_3HCO_3^{-} + 3H^+$
7	$S(OH)_2 + UO_2^{2+} + 2H_2CO_3 = SO_2UO_2(HCO_3)_2^{2-} + 4H^+$
8	$S(OH)_2 + UO_2^{2+} + 2H_2CO_3 = SO_2UO_2CO_3HCO_3^{3-} + 5H^+$
9	$S(OH)_2 + UO_2^{2+} + 2H_2CO_3 = SO_2UO_2(CO_3)_2^{4-} + 6H^+$

face reactions are possible in a uranyl–carbonate–iron oxide system (Table 4–5). Other U(VI) surface ternary complexes seem plausible in natural samples, including phosphate and silicate ternary complexes, but these were not considered here because their existence has not yet been confirmed in model systems. Bargar et al. (2000) observed multimeric surface ternary complexes of U(VI) in the carbonate–hematite system, however, these were only present within a very narrow pH range (8 to 8.5) and at high adsorbed concentrations (>0.4 μmoles m^{-2}), and therefore, these were not considered here. Multimeric U(VI) surface complexes also seem unlikely across much of the pH range and U(VI) adsorption density studied because of the trends observed as a function of U(VI) concentration (Davis, 2001).

FITEQL 4.0 (Herbelin & Westall, 1999) was used to determine the best fit of various reactions or combinations of reactions in Table 4–5 to subsets of the experimental data shown in Fig. 4–1. The Davies equation was used for activity correction of aqueous species. The method recommended by Herbelin and Westall (1999) for formulating the problem for fitting adsorption data was used, in which adsorbed U(VI) was defined as a Type II *dummy* component. The optimization procedure minimizes the difference between experimental and calculated values of adsorbed U(VI). Relative errors of 1% in the concentrations of surface sites, total U(VI), and adsorbed U(VI), and relative errors of 5% in log $[H^+]$ and log $[H_2CO_3]$ were used as FITEQL inputs.

GC models were calibrated using three different subsets of the data for U(VI) adsorption on the schist materials. Model 1 was calibrated using all data points (n = 58) with pH >4. Model 2 was calibrated with a smaller set of experimental data (n = 17), including only data for systems equilibrated with air and with pH values from 6 to 8.6. Model 3 was calibrated with an intermediate set of experimental data (n = 29), including all data with pH values from 6 to 8.6 (air and 1% CO_2). In all cases, only single-site models were used and the only surface species considered were those in Table 4–5. All major U(VI) aqueous chemical species were included (Table 4–3).

Model 1

In the first step, FITEQL was used to determine which single reaction (Table 4–5) would provide the best fit to the experimental data. FITEQL output includes

Table 4–6. Summary of generalized composite models.

Model 1	Data considered: All data for pH > 4 (n = 58, fit = 33)
Reaction	
2	$S(OH)_2 + UO_2^{2+} = SO_2UO_2 + 2H^+$
5	$S(OH)_2 + UO_2^{2+} + H_2CO_3 = SO_2UO_2CO_3^{2-} + 4H^+$
8	$S(OH)_2 + UO_2^{2+} + 2H_2CO_3 = SO_2UO_2CO_3HCO_3^{3-} + 5H^+$
Model 2	Data considered: 6 < pH < 8.6, air only (n = 17, fit = 1)
Reaction	
1	$S(OH)_2 + UO_2^{2+} = SO_2HUO_2^+ + H^+$
7	$S(OH)_2 + UO_2^{2+} + 2H_2CO_3 = SO_2UO_2(HCO_3)_2^{2-} + 4H^+$
8	$S(OH)_2 + UO_2^{2+} + 2H_2CO_3 = SO_2UO_2CO_3HCO_3^{3-} + 5H^+$
Model 3	Data considered: 6 < pH < 8.6, air only and 1% CO_2 (n = 29, fit = 7)
Reaction	
2	$S(OH)_2 + UO_2^{2+} = SO_2UO_2 + 2H^+$
4	$S(OH)_2 + UO_2^{2+} + H_2CO_3 = SO_2UO_2HCO_3^- + 3H^+$
8	$S(OH)_2 + UO_2^{2+} + 2H_2CO_3 = SO_2UO_2CO_3HCO_3^{3-} + 5H^+$

a goodness-of-fit parameter, WSOS/DF, the weighted sum of squares of the difference in value among model simulations and experimental data points, divided by the degrees of freedom (Herbelin & Westall, 1999). Lower values of WSOS/DF mean the proposed model is a better fit to the data; WSOS/DF will be referred to as *fit* below. Representing the data for U(VI) adsorption at pH >4 with a single reaction produced poor fits, with the best fit provided by Reaction 2 (fit = 312).

The second step in model development was to consider combinations of Reaction 2 with the other eight reactions, i.e., to determine how well the experimental data set could be represented by two reactions, with one being Reaction 2. The fit to the data was considerably improved in some cases, with the best combination being Reactions 2 and 8 (fit = 36).

Finally, the best third reaction was found by considering combinations of Reactions 2 and 8 with the other reactions. Only a small improvement to the fit was made by adding a third reaction (fit = 33), with the best combination being Reactions 2, 5, and 8 (Table 4–6). Fits of Model 1 to some of the experimental data are shown in Fig. 4–5 to 4–8; however, the model was derived by obtaining the best fit to all of the experimental data at pH >4, not just the data shown in Fig. 4–5 to 4–8.

Model 2

Model 2 was calibrated with a subset of the experimental data (n = 17), including only data for systems equilibrated with air and in the pH range from 6 to 8.6. Representing these data with a single reaction produced some good fits, with the best fit provided by Reaction 4 (fit = 8.4). Other good fits included Reactions 2 and 6 (fits = 10 and 8.5, respectively).

Next, combinations of Reaction 4 with the other eight reactions were considered. The fit to the data was improved in several cases, with the best combination being Reactions 4 and 1 (fit = 5.7). Other good combinations were Reactions 4 and 2 and 4 and 3 (fits = 5.9 for each case).

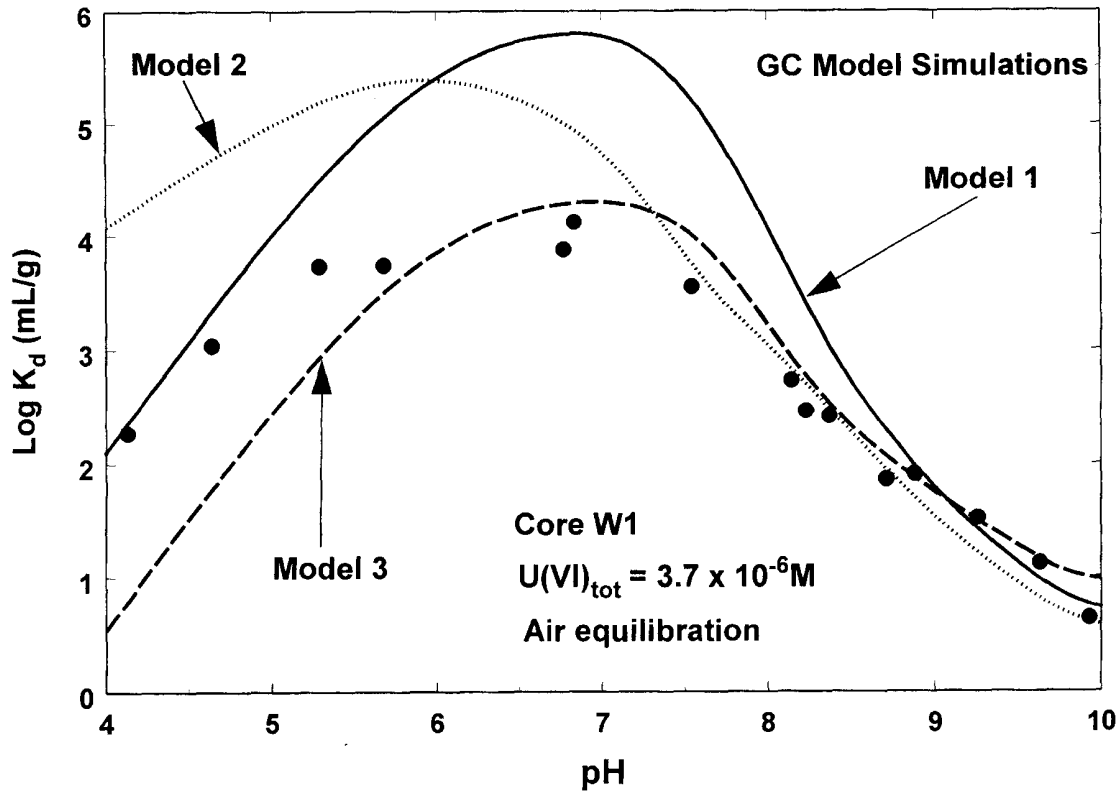

Fig. 4–5. Generalized composite model calculations of U(VI) adsorption by the Koongarra W1 sample equilibrated with air compared with experimental data. Model 1 calibrated to all Koongarra schist adsorption data in the pH range from 4 to 10. Model 2 calibrated to Koongarra schist adsorption data in the pH range from 6 to 8.6 for systems equilibrated with air. Model 3 calibrated to Koongarra schist adsorption data in the pH range from 6 to 8.6 for systems equilibrated with air and 1% CO_2.

A significant improvement to the fit was made by adding a third reaction to Reactions 1 and 4. The best improvement was made by adding Reaction 5 (fit = 1.8); however, it also was discovered that a different set of three reactions (1, 7, and 8) provided an even better fit (Table 4–6, fit=1.0). Fits of Model 2 to some of the experimental data are shown in Fig. 4–5 to 4–8.

Model 3

Model 3 was calibrated with a larger subset of experimental data (n = 29), using the same pH range constraint as in Model 2, but also including the data for systems equilibrated with 1% CO_2. Representing these data with a single reaction produced relatively poor fits, with the best fit provided by Reaction 6 (fit = 101).

Next, combinations of Reaction 6 with the other reactions were considered. The fit to the data was improved somewhat by adding a second reaction, with the best combination being Reactions 6 and 8 (fit = 59) or 6 and 9 (fit = 65).

Significant improvements to the fit were made by adding a third reaction to Reactions 6 and 8. The best improvement was made by adding Reaction 2 (fit = 5.2). Another combination of reactions that provided almost as good a fit was Reactions 2, 4, and 8 (fit = 6.6). The latter combination of three reactions (2, 4, and 8) was preferred on the basis of chemical plausibility and is referred to as Model 3

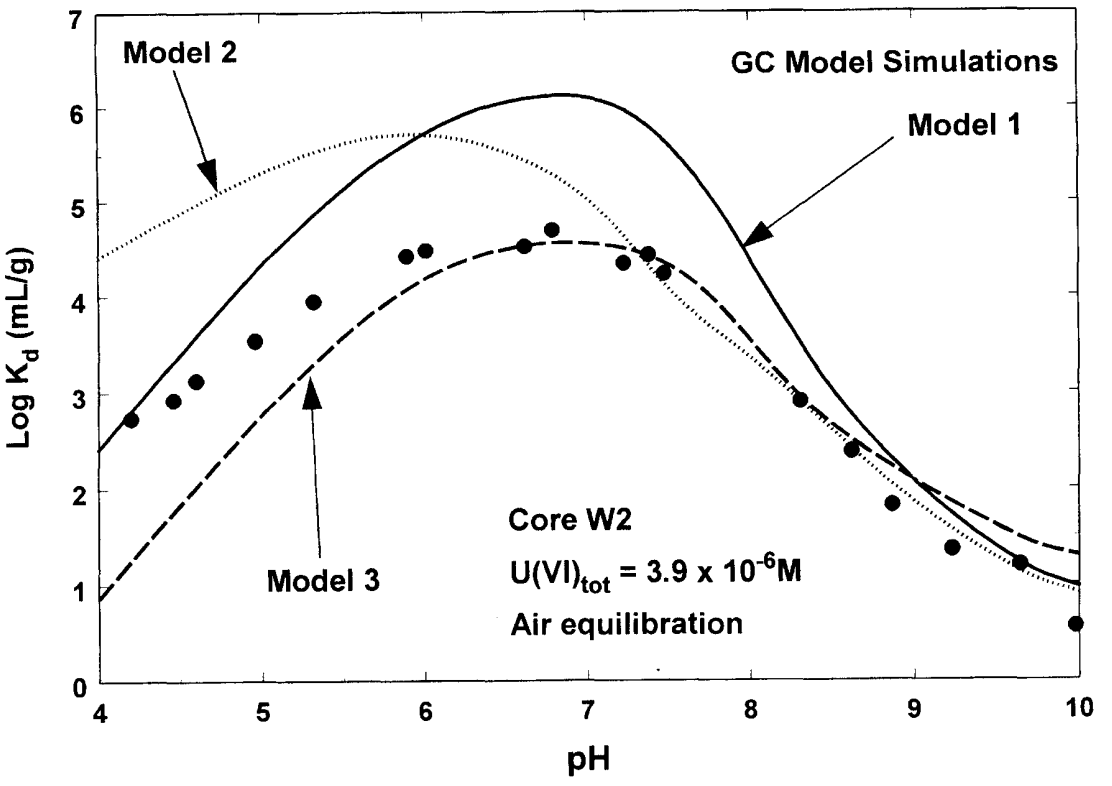

Fig. 4–6. Generalized composite model calculations of U(VI) adsorption by the Koongarra W2 sample equilibrated with air compared with experimental data. Model 1 calibrated to all Koongarra schist adsorption data in the pH range from 4 to 10. Model 2 calibrated to Koongarra schist adsorption data in the pH range from 6 to 8.6 for systems equilibrated with air. Model 3 calibrated to Koongarra schist adsorption data in the pH range from 6 to 8.6 for systems equilibrated with air and 1% CO_2.

(Table 4–6). Fits of Model 3 to some of the experimental data are shown in Fig. 4–5 to 4–8.

DISCUSSION

The variability of pH in groundwater, even in contaminated aquifers, is often limited in comparison to the range of variable pH examined in laboratory studies of metal ion adsorption by hydrous oxides. With respect to the assessment of radionuclide transport in natural systems, most applications are in the circumneutral pH range. Studying the adsorption of radionuclides across a wide pH range in research studies with single mineral phases is useful for interpreting surface reaction stoichiometry and system behavior; however, interpreting the results of adsorption experiments with soils and sediments in acidic and alkaline solutions is complex, due to the confounding effects of mineral dissolution on the kinetics and equilibria of adsorption reactions (Davis & Kent, 1990). In these cases it can advantageous to constrain the variability of pH (and other solute concentrations) to the range observed in the natural system that is to be modeled (e.g., Kent et al., 2000; Davis et al., 1998). In addition, an SCM might fit data adsorption well across one pH range, but not another (as in the high calculated K_d values of Waite et al. (2000) at circumneutral pH). Confining the pH range of data collection, though, raises a ques-

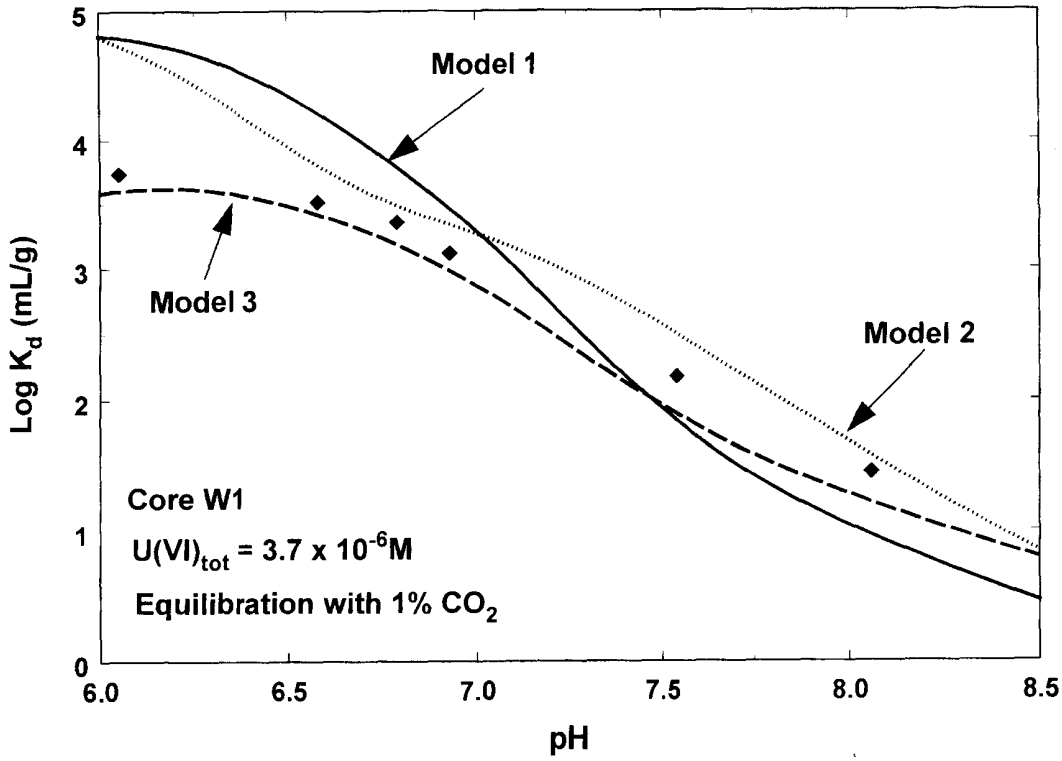

Fig. 4–7. Generalized composite model calculations of U(VI) adsorption by the Koongarra W1 sample equilibrated with 1% CO_2 compared with experimental data. Model 1 calibrated to all Koongarra schist adsorption data in the pH range from 4 to 10. Model 2 calibrated to Koongarra schist adsorption data in the pH range from 6 to 8.6 for systems equilibrated with air. Model 3 calibrated to Koongarra schist adsorption data in the pH range from 6 to 8.6 for systems equilibrated with air and 1% CO_2.

tion: Can an SCM be properly calibrated when data are collected across a narrow range relevant to a field system?

The comparison of results obtained for Models 1, 2, and 3 demonstrate that the range of chemical variables (pH, pCO_2) across which experimental data are collected can have a significant effect on GC model parameters and goodness-of-fit. Model 1 overestimated K_d values of experimental data, particularly in the pH range from 5 to 7.5 (Fig. 4–5 and 4–6). In attempting to achieve the best fit to all of the experimental data with pH > 4, better agreement between the calculated and experimental K_d values was achieved at the upper and lower ends of the pH range. Figure 4–9 shows the distribution of the three surface species as a function of pH. The calculated adsorption was dominated by the binary uranyl surface complex, SO_2UO_2, at pH values <8. The ternary uranyl-carbonate surface complexes were only important between pH 8 and 9.5.

Another factor that contributed to the quality of the fit of Model 1 were the high K_d values for the W7 sample at low U_T concentration and in the pH range from 4 to 6. Higher K_d values are expected at lower U_T concentrations (Davis, 2001). One set of data for the W7 core material was collected at 0.03 μM total U(VI), a concentration about two orders of magnitude lower than most of the other experimental systems. Because the data at this low U_T concentration were only collected in the low pH range, calculated adsorption in the low pH range was slightly skewed higher to achieve the best fit to all of the experimental data. This dependence of surface complexation parameters on adsorbate concentration is generally addressed

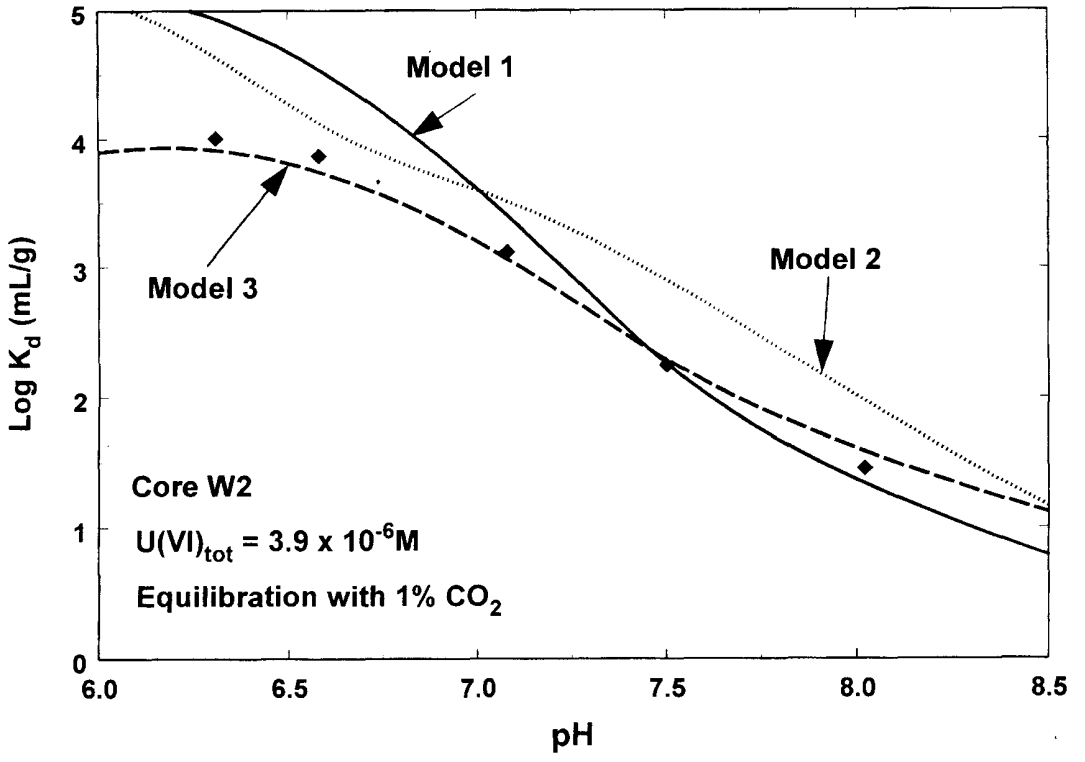

Fig. 4–8. Generalized composite model calculations of U(VI) adsorption by the Koongarra W2 sample equilibrated with 1% CO_2 compared with experimental data. Model 1 calibrated to all Koongarra schist adsorption data in the pH range from 4 to 10. Model 2 calibrated to Koongarra schist adsorption data in the pH range from 6 to 8.6 for systems equilibrated with air. Model 3 calibrated to Koongarra schist adsorption data in the pH range from 6 to 8.6 for systems equilibrated with air and 1% CO_2.

by using a two-site model (Waite et al., 1994), however, in this case there were insufficient data at the low U_T concentration to warrant the inclusion of a second site.

Models 2 and 3 were calibrated only with experimental data in the pH range from 6 to 8.6. Model 2 was calibrated with experimental data for systems equilibrated with air, whereas Model 3 used data for systems equilibrated with air and 1% CO_2. It can be seen clearly in Fig. 4–7 and 4–8 that Model 3 provided a better simulation of the K_d values in the systems equilibrated with 1% CO_2. The result indicates that it is important to collect experimental data at more than one partial pressure of CO_2 if the surface species include ternary carbonate complexes. In addition, this is an important issue for radionuclide performance assessment calculations for ground waters, as most aquifers are characterized by partial pressures of CO_2 greater than present in air. Thus, experiments in air can significantly overestimate K_d values for U(VI) (Payne et al., 2001), and perhaps other actinides, causing a non-conservative error in performance assessment calculations.

Models 2 and 3 simulations were in much better agreement with experimental K_d values in the pH range from 5 to 7.5 than was Model 1 (Fig. 4–5 and 4–6). The better agreement between Models 2 and 3 and experimental data should be expected given the narrower pH range of data used to calibrate the models, however, this is important if the purpose of the model calibration is to develop a predictive tool to be used for simulations only within a relatively narrow, field-relevant pH range (e.g., 1 or 2 pH units). Since the simpler GC modeling approach is most likely to be used for field applications and the model is semi-empirical, it is probably more impor-

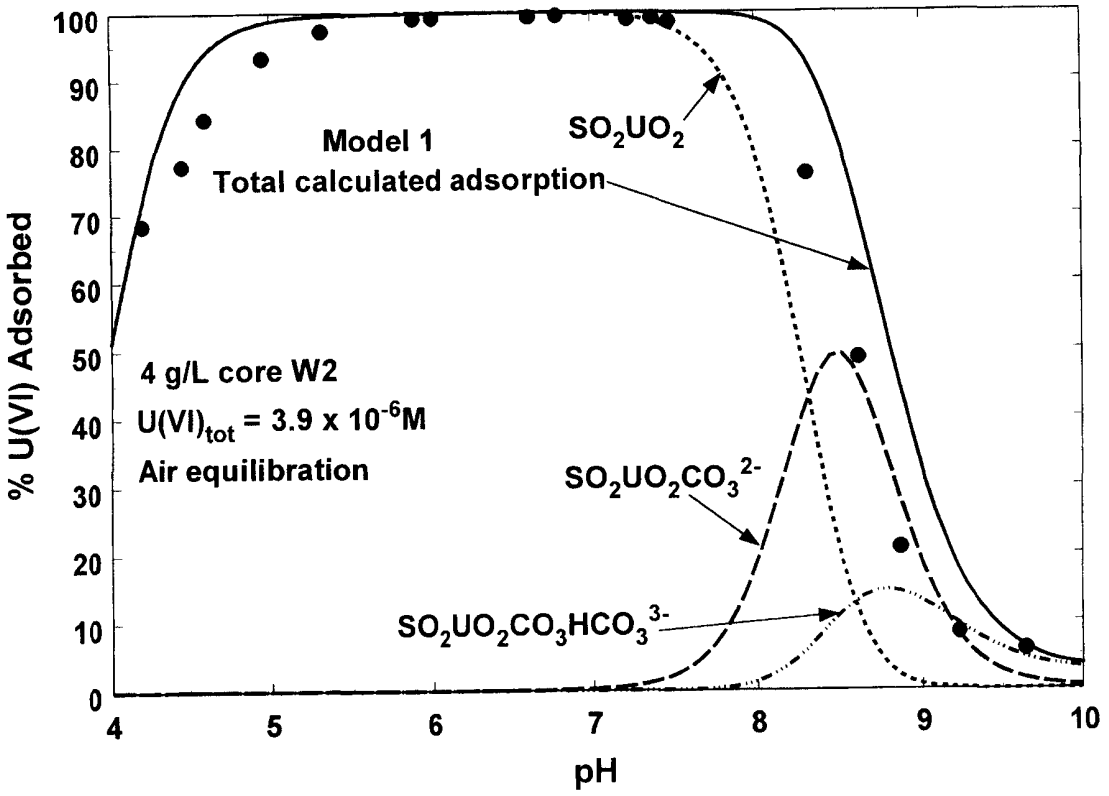

Fig. 4–9. Model 1 GC calculations of U(VI) adsorption by the Koongarra W2 sample equilibrated with air compared with experimental data. Distribution of surface species as a function of pH. Model 1 was calibrated to all Koongarra schist adsorption data in the pH range from 4 to10.

tant to collect more high-quality radionuclide adsorption data in the relevant range of pH (or other chemical variable) than to study a large pH range; however, it always should be remembered that such models may simulate data poorly when extended outside the range of model calibration. For example, the poor agreement of Model 2 with the data for pH <6 is caused by calculated adsorption of the species, SO_2HUO_2, at low pH values (Fig. 4–10). This species was not selected in Model 1 because it did not represent the experimental data well at low pH values.

The surface speciation in Model 3 simulations for systems equilibrated with air and 1% CO_2 is shown in Fig. 4–11 and 4–12. The ternary carbonate complexes in Model 3 were of greater importance in comparison to Model 2. This emphasizes again the significance of collecting adsorption data as a function of the partial pressure of CO_2, in order to accurately represent the effect of carbonate complexation on both aqueous and surface speciation. Model 3 speciation better represented the experimental data not only as a function of CO_2, but also as a function of pH in the pH range from 5 to 7.

In view of the Model 1 results (Fig. 4–5 and 4–6), we conclude that the lack of agreement of the GC model of Waite et al. (2000) with experimental K_d values at circumneutral pH could not be improved substantially by considering other U(VI)- or U(VI)-carbonate ternary species. Better agreement of the GC model was only obtained by considering experimental data collected across a narrower pH range. The lack of agreement seems larger than experimental error or scatter, and the laboratory K_d values agree well with field-estimated values (Payne et al., 2001).

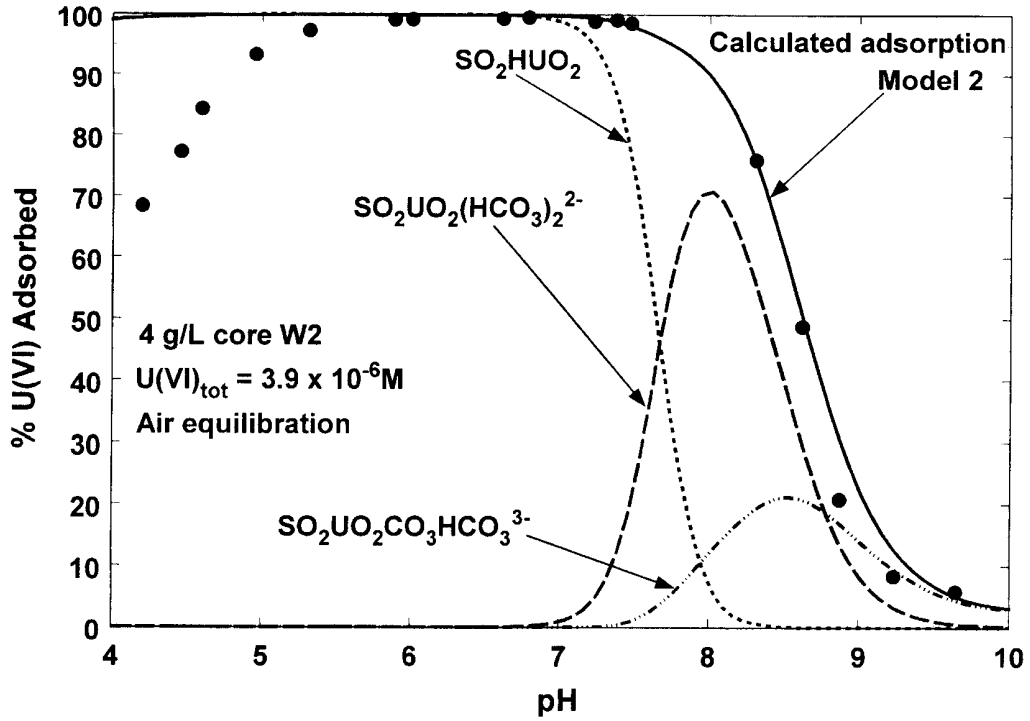

Fig. 4–10. Model 2 GC calculations of U(VI) adsorption by the Koongarra W2 sample equilibrated with air compared with experimental data. Distribution of surface species as a function of pH. Model 2 was calibrated to Koongarra schist adsorption data in the pH range from 6 to 8.6 for systems equilibrated with air.

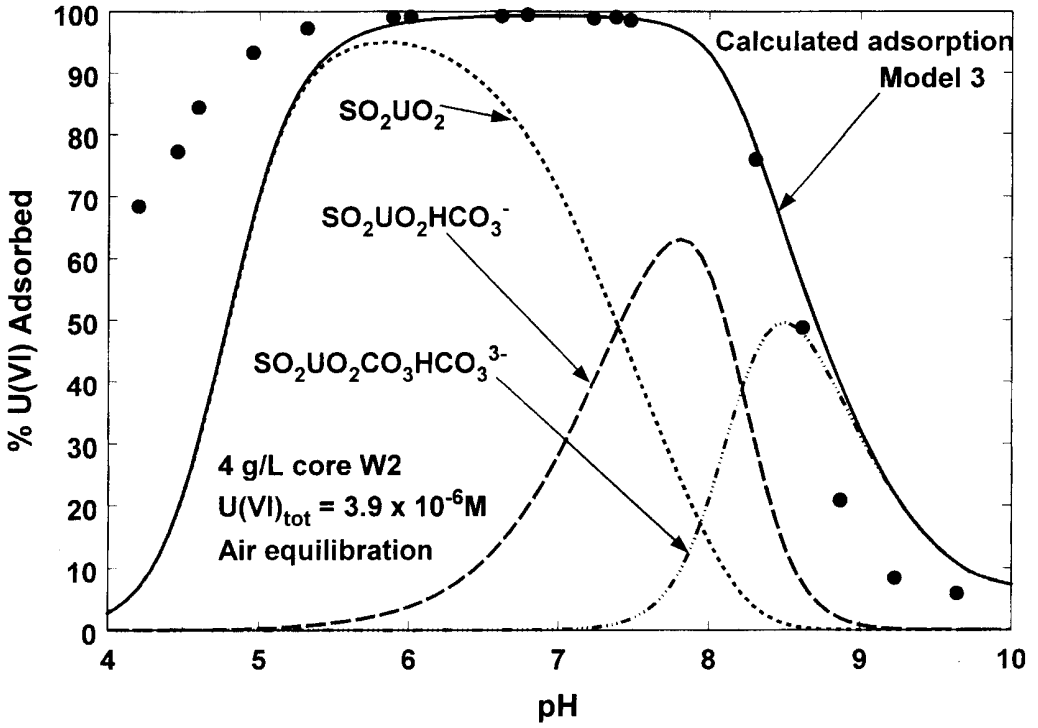

Fig. 4–11. Model 3 GC calculations of U(VI) adsorption by the Koongarra W2 sample equilibrated with air compared with experimental data. Distribution of surface species as a function of pH. Model 3 was calibrated to Koongarra schist adsorption data in the pH range from 6 to 8.6 for systems equilibrated with air and 1% CO_2.

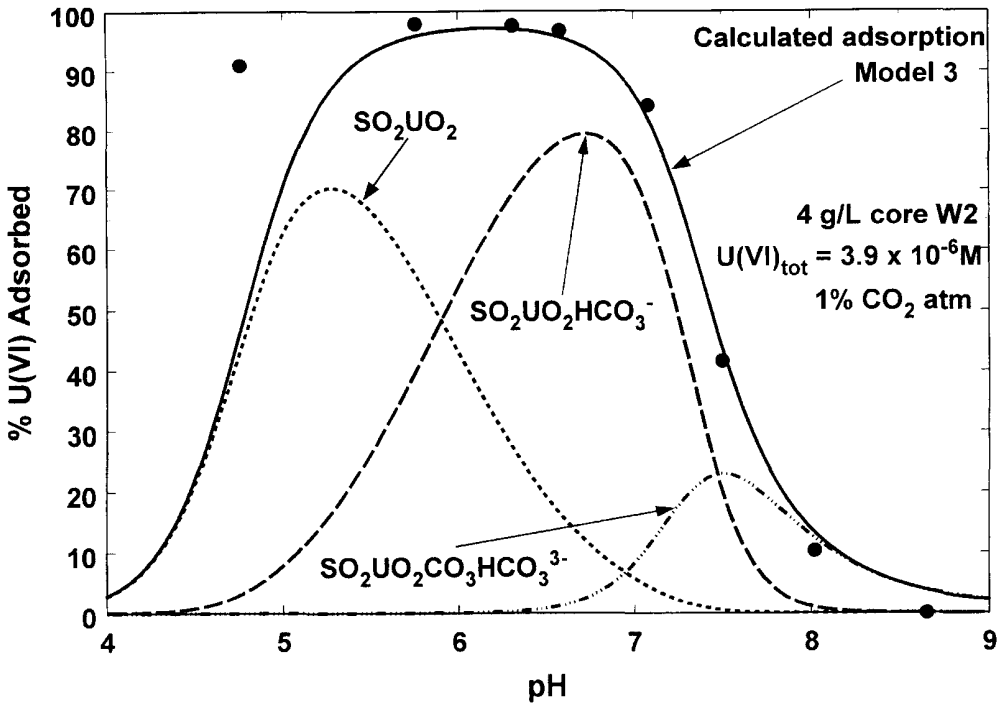

Fig. 4–12. Model 3 GC calculations of U(VI) adsorption by the Koongarra W2 sample equilibrated with 1% CO_2 compared with experimental data. Distribution of surface species as a function of pH. Model 3 was calibrated to Koongarra schist adsorption data in the pH range from 6 to 8.6 for systems equilibrated with air and 1% CO_2.

Although the possibility of other U(VI) ternary surface complexes in the circumneutral pH range might be the cause of the disagreement of Model 1, another question arises in considering the optimization method. Because the comparison of calculated and experimental adsorption is plotted as percentage of U(VI) adsorbed in Fig. 4–9, it appears that the greatest difference among these quantities occurs not in the pH range from 5 to 7.5 (where adsorption is near 100%), but rather in the upper and lower ends of the pH range. This is in contrast to the K_d plots that suggest the greatest error is in the pH range from 5 to 7.5 (Fig. 4–5 and 4–6), as also was observed by Waite et al. (2000). This appears to be related to the optimization method used (example 10 of the FITEQL 4.0 manual, Herbelin & Westall, 1999), which minimized the differences between the experimental and calculated values of adsorption density (in moles L^{-1} of adsorbed U(VI)). Using this method, a small difference between calculated and experimental data (e.g., 0.9% adsorbed) contributes the same to the optimization of model parameters whether that difference occurs at 50 or 99% adsorbed; however, because K_d is a relative quantity (U(VI) adsorption density/dissolved U(VI)), the difference between 99.0% and 99.9% has a very large effect on K_d values, while the difference between 50 and 50.9% has little effect. This has the unintended effect of giving less weight to fitting the dissolved U(VI) data at high K_d values and contributes greatly to the difference between the calculated and experimental values for K_d in Model 1, especially in the pH range from 5 to 7.5 (Fig. 4–5 and 4–6). It would be in the interest of the radioactive waste community that either a new version of FITEQL or a new method of using FITEQL is developed that allows optimization of surface complexation model parameters explicitly to K_d values.

The CA and GC modeling approaches can differ in the selection of surface species to fit experimental data. Surface speciation in the CA modeling approach is normally fixed by a previous fit of an SCM to a reference mineral phase, such as ferrihydrite (Waite et al., 1994; Dzombak & Morel, 1990). Ideally, spectroscopic data (XAS, FTIR, and others) are used to constrain the selection of surface species in CA models for reference minerals, so that molecular scale details of the bonding are included within the model as well as EDL terms; however, as is illustrated in the CA model calculations presented here and elsewhere (Waite et al., 2000; Davis et al., 1998), application of CA models to soils and sediments is not straightforward. Without very detailed characterization of the physical and chemical characteristics of the surface, several assumptions need to be made to apply a CA model.

The EXAFS and FTIR results of Bargar et al. (1999, 2000) were used to constrain the U(VI) surface species considered in the GC models to those in Table 4–5. Because of the lack of an EDL term in the GC modeling, however, the actual reactions chosen were based on the best fit of the data (Table 4–6) and probably do not have the same stoichiometry as the microscopic reactions occurring at the surface. Instead, the reactions were chosen based on their best fit of the macroscopic dependence of U(VI) adsorption on pH and pCO_2. Thus, GC modeling is semi-empirical in nature and should be expected to include surface reactions that are different than those used in the CA modeling approach because EDL terms are excluded. Because of this, the utility of the GC modeling approach is more closely aligned with meeting the objectives of field applications (Kent et al., 2000) than with understanding details of molecular scale bonding at mineral–water interfaces.

CONCLUDING REMARKS

Geochemical modeling of the fate and transport of radionuclides in aquifers requires an understanding of the variation of key chemical parameters [pH, redox status (Eh), major ion groundwater composition] within the spatial and temporal domains of the natural system. Variability in the geochemical composition of the system can strongly influence the adsorptive reactivity of radionuclides along migration pathways. Thermodynamic models that include SCM allow simultaneous consideration of both the geochemical variability of the system and its influence on radionuclide adsorption, thereby providing support for the selection and estimation of uncertainty for radionuclide K_d values (Nuclear Energy Agency, 2001).

A great deal of effort has been invested in experimentally determining K_d values for radionuclides on a wide variety of geological solids (Nuclear Energy Agency, 2001). It is now recognized that a K_d measured for a given radionuclide/solid phase combination under one set of chemical conditions cannot generally be used to predict a K_d for another set of conditions (Kohler et al., 1996). In contrast, an SCM modeling approach allows predictions of radionuclide partitioning across a wider range of system conditions because it quantifies the fundamental parameters responsible for radionuclide partitioning and couples adsorption calculations with aqueous speciation (Davis et al., 1998).

Although the GC modeling approach is semi-empirical, it can be constrained to consider plausible surface species that are supported by ancillary spectroscopic

studies. One limitation of the approach is that the mass action equations and associated stability constants are valid only for site-specific materials; a database that is transferable to other mineral assemblages is not expected. The GC approach can be preferable to completely empirical approaches, such as a constant K_d model or adsorption isotherms, because the important linkage between surface and aqueous species is retained in the modeling through the coupling of mass action equations. With only three surface species, a one-site GC model (Model 3) without EDL terms was able to accurately simulate K_d values for U(VI) adsorption on the schist material as a function of pH and pCO_2.

The results with both the GC and CA modeling approaches indicate that the surface complexation concept can be applied to model radionuclide adsorption by soils and sediments, and that models without an EDL can be useful for that purpose. The GC approach requires less information and laboratory data, and is probably more useful for immediate and practical applications.

ACKNOWLEDGMENT

The authors wish to thank B. Honeyman for his critical review and J. Westall for technical discussions. This research was supported by the U.S. Nuclear Regulatory Commission (RES-93-012) and the U.S. Geological Survey Toxic Substances Hydrology program.

REFERENCES

Ainsworth, C.C., D.C. Girvin, J.M. Zachara, and S.C. Smith. 1989. Chromate adsorption on goethite: Effects of aluminum substitution. Soil Sci. Soc. Am. J. 53:411–418.

Arnold, T., T. Zorn, H. Zanker, G. Berhard, and H. Nitsche, H. 2001. Sorption behavior of U(VI) on phyllite: Experiments and modeling. J. Contam. Hydrol. 47:219–231.

Bargar, J.R., R. Reitmeyer, and J.A. Davis. 1999. Spectroscopic confirmation of uranium(VI)-carbonato adsorption complexes on hematite. Environ. Sci. Technol. 33:2481–2484.

Bargar, J.R., R. Reitmeyer, J.J. Lenhart, and J.A. Davis. 2000. Characterization of U(VI)-carbonato ternary complexes on hematite: EXAFS and electrophoretic mobility measurements. Geochim. Cosmochim. Acta 64:2737–2749.

Barnett, M.O., P.M. Jardine, S.C. Brooks, and H.M. Selim. 2000. Adsorption and transport of uranium(VI) in subsurface media. Soil Sci. Soc. Am. J. 64:908–917.

Bolt, G.H., and W.H. van Riemsdijk. 1987. Surface chemical processes in soil. p. 127–164. *In* W. Stumm (ed.) Aquatic surface chemistry. John Wiley & Sons, New York.

Bradbury, M.H., and B. Baeyens. 1997. A mechanistic description of Ni and Zn sorption on Na-montmorillonite. II: Modelling. J. Contam. Hydrol. 27:223–248.

Coston, J.A., C.C. Fuller, and J.A. Davis. 1995. Pb^{2+} and Zn^{2+} adsorption by a natural Al-and Fe-bearing surface coating on an aquifer sand. Geochim. Cosmochim. Acta 59:3535–3547.

Davis, J.A. 1982. Adsorption of natural dissolved organic matter at the oxide–water interface. Geochim. Cosmochim. Acta 46:2381–2393.

Davis, J.A., 1984. Complexation of trace metals by adsorbed natural organic matter. Geochim. Cosmochim. Acta 48: 679–671.

Davis, J.A., 2001. Surface complexation modeling of uranium(VI) adsorption on natural mineral assemblages. NUREG/CR-6708. U.S. Nuclear Regulatory Commission, Washington, DC.

Davis, J.A., J.A. Coston, D.B. Kent, and C.C. Fuller. 1998. Application of the surface complexation concept to complex mineral assemblages. Environ Sci. Technol. 32:2820–2828.

Davis, J.A., and D.B. Kent. 1990. Surface complexation modeling in aqueous geochemistry. p. 177–260. *In* Mineral–water interface geochemistry. Mineral. Soc. of Am., Washington, DC.

Duff, M.C., and C. Amrhein. 1996. Uranium(VI) adsorption on goethite and soil in carbonate solutions. Soil Sci. Soc. Am. J. 60:1393–1400.

Dzombak, D.A., and F.M.M. Morel. 1990. Surface complexation modeling: Hydrous ferric oxide. John Wiley & Sons, New York.

Herbelin, A.L., and J.A. Westall. 1999. FITEQL: A computer program for the determination of chemical equilibrium constants from experimental data. Version 4.0. Rep. 99-01. Oregon State Univ., Corvallis.

Hiebert, F.Z., and P.C. Bennett. 1992. Microbial control of silicate weathering in organic-rich ground water. Science (Washington, DC) 258:278–281.

Honeyman, B.D. 1984. Cation and anion adsorption at the oxide/solution interface in systems containing binary mixtures of adsorbents: An investigation of the concept of adsorptive additivity. Ph.D. diss. Stanford Univ., Stanford, CA.

Jackson, R.E., and K.J. Inch. 1989. The in situ adsorption of ^{90}Sr in a sand aquifer at the Chalk River Nuclear Laboratories. J. Contam. Hydrol. 4:27–50.

Kent, D.B., R. H. Abrams, J.A. Davis, J.A., Coston, and D.R. LeBlanc. 2000. Modeling the influence of variable pH on the transport of zinc in a contaminated aquifer using semi-empirical surface complexation models. Water Resour. Res. 36:3411–3425.

Kohler, M., G.P. Curtis, D.B. Kent, and J.A. Davis. 1996. Experimental investigation and modeling of uranium(VI) transport under variable chemical conditions. Water Resour. Res. 32:3539–3551.

KoB, V. 1988. Modeling of U(VI) sorption and speciation in a natural sediment–groundwater system, Radiochim. Acta 44/45:403–406.

Lovgren, L., S. Sjoberg, and P.W. Schindler. 1990. Acid/base reactions and Al(III) complexation at the surface of goethite. Geochim. Cosmochim. Acta 54:1301–1306.

Lumpkin, G.R., T.E. Payne, B.R. Fenton, and T.D. Waite. 1999. Preferential association of adsorbed uranium with mineral surfaces: A study using analytical electron microscopy. Mater. Res. Soc. Proc. 556:1067–1074.

Nuclear Energy Agency (NEA). 2001. Using thermodynamic sorption models for guiding radioelement distribution coefficient (K_d) investigations: A status report. OECD Nuclear Energy Agency, Paris.

Pabalan, R.T., D.R. Turner, F.P. Bertetti, and J.D. Prikryl. 1998. Uranium(VI) sorption onto selected mineral surfaces: Key geochemical parameters. p. 99–130. *In.* E.A. Jenne (ed.) Adsorption of metals by geomedia. Academic Press, San Diego, CA.

Padmanabhan, E., and A.R. Mermut. 1996. Submicroscopic structure of Fe-coatings on quartz grains in tropical environments. Clays Clay Minerals 44:801–810.

Parfitt, R.L., S.J. Van der Gaast, and C.W. Childs. 1992. A structural model for natural siliceous ferrihydrite. Clays Clay Minerals 40:675–681.

Payne, T.E. 1999. Uranium (VI) interactions with mineral surfaces: Controlling factors and surface complexation modeling. Ph.D. Diss. Univ. of New South Wales, Australia.

Payne, T.E., R. Edis, B.R. Fenton, and T.D. Waite. 2001. Comparison of laboratory uranium sorption data with in situ distribution coefficients at the Koongarra uranium deposit, Northern Australia. J. Environ. Radioactivity 57:35–55.

Payne, T.E., and T.D. Waite. 1991. Surface complexation modelling of uranium sorption data obtained by isotope exchange techniques. Radiochim. Acta 52/53:487–493.

Reitmeyer, R., J.R. Bargar, and J.A. Davis. 1999. A spectroscopic approach to surface complexation modeling of uranyl carbonates on Fe-oxide surfaces. Extended Abstracts of the Environ. Chem. Div., Am. Chem. Soc., Anaheim, CA.

Sato, T., T. Murakami, N. Yanase, H. Isobe, T.E. Payne, and P.L. Airey. 1997. Iron nodules scavenging uranium from groundwater. Environ. Sci. Technol. 31:2854–2858.

Snelling, A.A. 1990. Koongarra uranium deposits. p. 807–812. *In* F.E. Hughes (ed.) The geology of the mineral deposits of Australia and Papua New Guinea. The Australasian Inst. of Mining and Metallurgy, Melbourne, Australia.

Stollenwerk, K.G. 1995. Modeling the effects of variable groundwater chemistry on adsorption of molybdate. Water Resour. Res. 31:347–357.

Tipping, E. 1981. The adsorption of aquatic humic substances by iron oxides. Geochim. Cosmochim. Acta 45:191–199.

Turner, G.D., J.M. Zachara, J.P. McKinley, and S.C. Smith. 1996. Surface-charge properties and UO_2^{2+} adsorption of a subsurface smectite. Geochim. Cosmochim. Acta 60:3399–3414.

Waite, T.D., J.A. Davis, B.R. Fenton, and T.E. Payne. 2000. Approaches to modelling uranium(VI) adsorption on natural mineral assemblages. Radiochimica Acta 88:687–693.

Waite, T.D., J.A. Davis, T.E. Payne, G.A. Waychunas, and N. Xu. 1994. Uranium(VI) adsorption to ferrihydrite: Application of a surface complexation model. Geochim. Cosmochim. Acta 58:5465–5478.

Waite, T.D., and T.E. Payne. 1993. Uranium transport in the subsurface environment: Koongarra: A case study. p. 349–410. *In* H. Allen et al. (ed.) Metals in groundwater. Lewis Publ., Ann Arbor, MI.

Westall, J.C., J.D. Jones, G.D. Turner, and J.M. Zachara. 1995. Models for association of metal ions with heterogeneous environmental sorbents: 1. Complexation of Co(II) by leonardite humic acid as a function of pH and $NaClO_4$ concentration. Environ. Sci. Technol. 29:951–959.

Yanase, N., T.E. Payne, and K. Sekine. 1995. Groundwater geochemistry in the Koongarra ore deposit, Australia: I. Implications for uranium migration. Geochemical J. 29:1–29.

Zachara, J.M., C.T. Resch, and S.C. Smith. 1994. Influence of humic substances on Co^{2+} sorption by a subsurface mineral separate and its mineralogic components. Geochim. Cosmochim. Acta 58:553–566.

Zachara, J.M., P.L. Gassman, S.C. Smith, and D. Taylor. 1995a. Oxidation and adsorption of Co(II)$EDTA^{2-}$ complexes in subsurface materials with iron and manganese oxide grain coatings. Geochim. Cosmochim. Acta 59:4449–4464.

Zachara, J.M., S.C. Smith, and L.S. Kuzel. 1995b. Adsorption and dissociation of Co-EDTA complexes in iron oxide-containing subsurface sands. Geochim. Cosmochim. Acta 59:4825–4844.

5 Molecular Models of Radionuclide Interaction with Soil Minerals

Randall T. Cygan

Sandia National Laboratories
Albuquerque, New Mexico

ABSTRACT

Experimental attempts to develop a fundamental understanding of the physiochemical processes that control the interactions of radionuclide species with soil minerals are often fraught with difficulties. Soil phases, including clays and other hydrous compounds, are typically characterized by submicron grain size, complex and multicomponent compositions, isomorphic substitutions, heterogeneous structures, large unit cells, low symmetry, site disorder, defects, lack of long-range order, variable hydration states, and complex surface speciation. It is therefore not surprising that these phases are far from the ideal state needed to provide quality and unambiguous results from standard characterization and spectroscopic methods. Fortunately, molecular modeling methods, in recent years, have matured to an extent where they can provide significant benefit to the soil scientist and geochemist in the evaluation of sorption and interactions of radionuclides with soil phases. Molecular simulation techniques provide controlled procedures to discriminate among various competing models to explain the macroscopic observations of experiment and field studies. Computer modeling allows the soil chemist to reduce the complex nature of a sorption process to several possible structural models that can be tested using several molecular modeling tools to evaluate the local geometry, binding energy, potential reactions, transition states, and even produce diffraction patterns, and vibrational and other spectra. Results of the various structural models can then be compared with each other and with the results from experimental observations to form a more detailed conceptual model of sorption. Assuming a valid and accurate molecular model, it is even possible to model the behavior of soil phases at conditions that are not achievable by experimental means or are not observable in the field. Ultimately, any success in applying molecular modeling in these research areas must rely on a thorough understanding of the theory and knowledge of the limits of each method. Furthermore, the modeler must provide suitable validation of the models through numerous tests and applications. It is important to remember that a model may be right or wrong, but it also might be irrelevant.

This chapter provides an overview of the theory and methods of molecular modeling and molecular simulation, and reviews applications involving soil minerals. The first section includes a review of the basic theory and then describes the mo-

 Geochemistry of Soil Radionuclides. SSSA Special Publication no. 59.

lecular modeling methods that are in common use today. The second part of the chapter presents a review and discussion of several examples in which molecular models were used to evaluate the interactions of various radionuclides with commonly-occurring soil phases. Although a detailed review of molecular modeling methods is beyond the scope of this chapter, the reader is directed to the comprehensive and thorough reviews provided by Clark (1985) and Allen and Tildesley (1987), and the books by Frenkel and Smit (1996) and Leach (1996). The recent volume by Cygan and Kubicki (2001) is of particular interest in presenting a broad review of molecular modeling methods and providing numerous examples relating to mineralogical and geochemical processes.

THEORETICAL METHODS AND MODELING TOOLS

Molecular modeling methods rely on an accurate description of the potential energy of a chemical system. The energy forcefield may involve an empirical parameterization based on either experimental observables or on the results of quantum mechanical calculations. An analytical description of potential energy as a function of geometry typically requires the input of atomic structure and physical properties to be used to parameterize the coefficients of the energy expression. Alternatively, the energy forcefield may rely solely on the explicit calculation of energy through quantum calculations performed throughout a dynamics simulation. The latter approach, often referred to as quantum dynamics, or Carr-Parinello approach, is extremely costly and practical only in applications of limited size systems (see Hass et al., 1998); however, molecular modeling of the complex nature of soil phases, especially clay minerals, requires models of bulk structures or representative surfaces that often incorporate hundreds if not thousands of atoms. In these cases, and even with access to some of the most advanced supercomputers, first principles quantum methods are impractical. Therefore, almost all molecular modeling studies of soil minerals to date involve the use of energy forcefields to describe the potential energy of the system.

Potential Energy

The total potential energy of a chemical system is typically represented by the following energy components:

$$E_{\text{Total}} = E_{\text{Coul}} + E_{\text{VDW}} + E_{\text{Bond Stretch}} + E_{\text{Angle Bend}} + E_{\text{Torsion}} \quad [1]$$

where E_{Coul} and E_{VDW} represent the Coulombic and van der Waals energy and collectively are referred to as the nonbonded energy of the system. The last three terms represent the bonded energy components associated with bond stretching, angle bending, and dihedral torsion, respectively. The Coulombic energy, or electrostatics energy, is described by the classical description of interacting charged particles and varies inversely with the distance r_{ij}:

$$E_{\text{Coul}} = (e^2/4\pi\varepsilon_0) \sum_{i \neq j} (q_i q_j / r_{ij}) \quad [2]$$

Here, q_i and q_j represent the charge on the two ions, e is the electron charge, and ε_0 is the permittivity of a vacuum. The summation ensures that all atom–atom interactions are counted while avoiding duplication. As expected, Eq. [2] provides negative energies for the attraction of atoms (ions) of opposite charge, and positive energy for repulsion of atoms (ions) having charges of like sign. Atoms are effectively treated as single point charges, which in practice is equivalent to having the atoms behave as spherical-shaped and rigid bodies.

Due to the long-range nature of Eq. [2], the electrostatics contribution to the total energy must be properly determined to provide convergence for the case of materials having long-range order. This is problematic for crystalline compounds where the $1/r$ term is nonconvergent except for the most simple and highly symmetric crystals. Typically, molecular modeling techniques employ the Ewald method (Ewald, 1921; Tosi, 1964) for periodic systems in which the inverse function is replaced by a Laplace transform that is decomposed into real space and reciprocal space components that combined provide rapid convergence of the Coulombic energy. The need for an accurate determination of the Coulombic energy component is paramount in the analysis of radionuclide–substrate interactions due to the dominant role of electrostatics in controlling sorption processes. The covalent bonding associated with most molecules such as organic compounds—as opposed to the predominantly ionic bonding of minerals—requires the evaluation of the electrostatics as some partial charge character is maintained on atom centers. This is especially important for the proper evaluation of molecule–molecule interactions in liquid, solution, or even within the interlayer of a clay. In these cases, the Coulombic energy can be evaluated by direct summation using Eq. [2] without resorting to an Ewald summation.

The second nonbonded energy term involves the van der Waals interactions as represented by the Lennard-Jones expression:

$$E_{VDW} = \sum_{i \neq j} D_0[(R_0/r_{ij})^{12} - 2(R_0/r_{ij})^6] \qquad [3]$$

where D_0 and R_0 are empirically-derived parameters that relate to the dissociation energy and the equilibrium distance, respectively. This function includes the short-range repulsion that occurs as two atoms approach each other ($1/r^{12}$ term), and the attractive force (London dispersion) associated with the fluctuations in electron density on adjacent atoms ($-1/r^6$ term). Several equivalent forms of Eq. [3] are used in the molecular modeling literature based on the choice of fitting parameters. Additionally, other functional forms for the short-range interactions exist including the 9-6 function (two parameter) and the exponential-6 function (three parameter). Fundamentally, the exact form of these short-range energy functions are not critical as long as the resulting energy accurately describes the atomic interactions. An excellent discussion of the various forms of the van der Waals energy expression is provided by Halgren (1992).

A further refinement of the nonbonded energy terms that is often implemented in the modeling of ionic solids—where the first two terms of Eq. [1] are sufficient for describing the total energy—is the incorporation of a shell model (Dick & Overhauser, 1958). This approach introduces a polarization energy term to account for

the shift in the electronic cloud of an ion as induced by the local electrostatic field. The shell model uses two point charges joined by a harmonic spring to represent the polarization as a negatively-charged shell is shifted away from a positively-charged core. This refinement dramatically helps to improve the modeling of the structures and properties of various oxides and silicate phases having significant covalent character (e.g., Lewis & Catlow, 1986), and is useful for the evaluation of certain surface structures, and elastic, dielectric, defect, and diffusion properties of materials.

The addition of bonded energy terms to the total potential energy is important for molecular models of compounds characterized by strong covalent bonds. Models of organic compounds typically incorporate one of several functions to describe the energy as a bond compresses or stretches about an equilibrium distance. A simple quadratic expression is typically used:

$$E_{\text{Bond Stretch}} = k_1 (r - r_0)^2 \quad [4]$$

where r is the atom–atom separation distance, r_0 is the equilibrium bond distance, and k_1 is an empirical force constant. The potential well also describes the energy constraints associated with the vibration of atoms about the equilibrium bond distance, and often vibrational spectra are used to derive the force constant. More refined models for bond stretching interactions include the Morse potential in which the physical dissociation of a bond is allowed at large separation distances:

$$E_{\text{Morse}} = D_0 [1 - \exp\{1 - \alpha(r - r_0)\}]^2 \quad [5]$$

D_0 is the equilibrium dissociation energy and α is a parameter related to the vibrational force constant. The bond stretch energy also will be important in periodic systems in which covalent bonds occur, for example, organic solids or inorganic compounds involving molecular anions such carbonate, nitrate, or phosphate phases. In addition, soil minerals where water or hydroxyl groups exist will often require Eq. [4] or Eq. [5] to accurately describe O–H behavior. To date, only a few studies have modeled water behavior in soil minerals. These include the analysis of the bulk structure and swelling of clay minerals (Cygan et al., 2002) and the sorption and swelling of layered hydroxides including hydrotalcite (Kalinichev et al., 2000; Wang et al., 2001).

Additional bonded terms for the total energy include expressions for angle bend and torsion to assist in controlling the geometries for, respectively, three-body and four-body interactions:

$$E_{\text{Angle Bend}} = k_2 (\theta - \theta_0)^2 \quad [6]$$

$$E_{\text{Torsion}} = k_3 (1 + \cos 3\phi) \quad [7]$$

Here, θ is the bond angle for a triad of sequentially-bonded atoms, θ_0 is the equilibrium bond angle, ϕ is the dihedral angle for a quartet of sequentially-bonded atoms, ϕ_0 is the equilibrium dihedral angle, and k_2 and k_3 are empirical force constants. These two terms effectively maintain bond geometries for various atom hy-

bridization such as tetrahedral sp^3 carbons in alkanes, or planar sp^2 carbons in alkenes. Additionally, these terms are often used to describe angle bending for metal hydroxyl groups or out-of-plane torsion for carbonate groups. More complex potential energy expressions, often incorporating cross-term coupling of the bonded terms, can be incorporated into the total potential energy expression (e.g., Dauber-Osguthorpe et al., 1988). The functionality of these forcefields will only be limited by the quality and accuracy of the data used to parameterize the potential functions, which often is lacking for the more complex nature of soil phases.

An important part of the potential energy forcefield is the assignment of partial charges for each atom type. Purely ionic models incorporate the formal charge of the atom as would be expected for the localization of charge on the atom center; however, most chemical systems are nonionic and require the partitioning of charges among the constituents. There are various schemes available to assign partial charges, one of the more common being the charge equilibration scheme of Rappé and Goddard (1991). This approach incorporates bond geometry, ionization potentials, electron affinities, and radii of the component atoms to derive partial charges, and can be applied in a dynamic fashion throughout a molecular simulation. Other simpler empirical schemes involve coordination, connectivity, and bond order to assign partial charges. Deformation electron densities derived from high-resolution x-ray diffraction analysis (e.g., Coppens, 1992; Spasojevicde-Bire & Kiat, 1997) can provide accurate partial charge assignments for inorganic solids; however, one of the most convenient approaches is to use quantum mechanics to derive Mulliken (Mulliken, 1955) or electrostatic potential (ESP) charges (Breneman & Wiberg, 1990; Chirlian & Francl, 1987). The significance of partial charge assignments cannot be overstated—accurate charges are critical in the evaluation of sorption processes where electrostatic dominate and control the behavior of radionuclides interactions with soil minerals.

Forcefields

Although the scientific literature has several general energy forcefields available for the molecular simulation of organic molecules (e.g., Dauber-Osguthorpe et al., 1988; Maple et al., 1994; Sprague et al., 1987; Weiner et al., 1984), only a few of the forcefields have been parameterized to model inorganic compounds, mostly aluminosilicate zeolite materials used in catalysis applications (e.g., Hill et al., 1994; Hill & Sauer, 1995; Rappé et al., 1992). Unfortunately, of the latter, none of the energy forcefields are satisfactory for the molecular simulation of complex oxides such as clays and associated soil minerals. The structures and physical properties of layered compounds are not included in the database used in the parameterization scheme for the forcefield. Furthermore, clays and other layered soil phases are unique in having aluminum in octahedral coordination. Their low symmetry and anisotropic electrostatic fields are not necessarily compatible with the forcefields derived for the more symmetric structures of the zeolite materials. For example, most theoretical studies of clay mineral structures and interlayer dynamics to date rely on maintaining a fixed or rigid clay layers during the simulation (Chang et al., 1995; Greathouse & Sposito, 1998; Karaborni et al., 1996; Skipper et al., 1995a,b; Smith, 1998). Unfortunately, these molecular models are unable to

allow full relaxation of all atoms and conserve the energy and momentum during dynamical simulations.

Recently, Teppen et al. (1997), recognizing the failings of previous forcefields for simulating clays, developed a set of potentials suitable for the simulation of dioctahedral clay minerals and related compounds. Based on the valence format (bonded model) originally developed by Hill and Sauer (1994,1995), Teppen et al. (1997) reparameterized nonbonded terms and developed a unique O–Al–O angle bend potential based on the experimental refinements of representative clay minerals. In addition, improved partial charge assignments were derived from ESP charges of quantum mechanic calculations of cluster models, and from deformation electron densities derived from x-ray diffraction studies of oxide compounds. The modified forcefield provided accurate models of the heavy element structure of various phyllosilicate phases, and, using molecular dynamics techniques, produced an excellent model of the sorption of hexadecyltrimethylammonium ions ($HDTMA^+$) in the interlayer of the dioctahedral clay beidellite (Teppen et al., 1997).

A more recent forcefield designed for application to clays and other hydrous phases was developed by Cygan et al. (2002) to simulate the bulk and surface structures and dynamics of hydroxides, oxyhydroxides, layered double hydroxides, and clays. The forcefield was designed specifically for the large-scale simulation of large simulation cells (up to tens of thousands of atoms), and therefore was based on a nonbonded interatomic potential (Eq. [2] and Eq. [3]) for the interaction of heavy atoms. The simplified nonbonded forcefield provides a computationally-efficient means for evaluating a significant number of configurational energies during large-scale simulations. Water and hydroxyl potentials from previous bonded and flexible potentials (Berendsen et al., 1981; Teleman et al., 1987) were used to provide a general and fully flexible hydrous forcefield. The forcefield provides similar structures of clays compared to the Teppen et al. (1997) that are in very good agreement with experimental structures. There is improvement in the disposition and behavior of hydroxyls in the clay structures compared with the previous clay forcefield.

Molecular Mechanics

The classical-based modeling methods are most attractive due to their relative efficiency in calculating total energies for various molecular configurations, especially in comparison to more sophisticated quantum chemical methods. The energetics and relative stabilities of various compounds can be assessed in this manner. Molecular mechanics includes those modeling methods that evaluate the energies through classical energy forcefield descriptions.

Conformational Analysis

Conformers represent various arrangements of a particular molecular geometry that can be converted from one to another by rotation about a single bond, typically with energy barriers between stable and metastable configurations. Typical applications include the analysis of organic molecules and rotations about single C–C bonds. Cygan (2001) discusses conformational analysis in detail and presents an example for the energy contributions for the various conformers of

dichloroethane. More complex configurations for large organic molecules and large periodic systems can be easily examined using this technique.

Energy Minimization

Geometry optimizations of molecules and periodic systems are achieved through the use of efficient energy minimization techniques. The procedure involves the repeated sampling of the potential energy surface for various system configurations until the potential energy minimum is obtained corresponding to a geometry where the forces on all atoms are zero. The energy of an initial configuration is first determined then the atoms and cell parameters (for periodic systems) are adjusted using derivatives of the potential energy to obtain a lower energy configuration. This procedure is repeated until suitable tolerances are obtained for the energy differences and derivatives between successive steps of the minimization. Repeated optimizations based on different initial configurations help to ensure the identification of a global minimum configuration rather than a structure for a local minimum. An excellent description of the various minimization methods and algorithms is provided by Leach (1996).

An illustrative example of an energy minimum configuration is provided in Fig. 5–1 for the simple interaction of two rigid ions A and B of opposite charge. The plot presents the potential energy of the system as a function of bond distance r_{AB} based on an interaction potential described by a Buckingham potential (Lewis & Catlow, 1986):

$$E_{AB} = (q_A q_B / r_{AB}) + A \exp(-r_{AB}/\rho) - (C/r_{AB}^6) \quad [8]$$

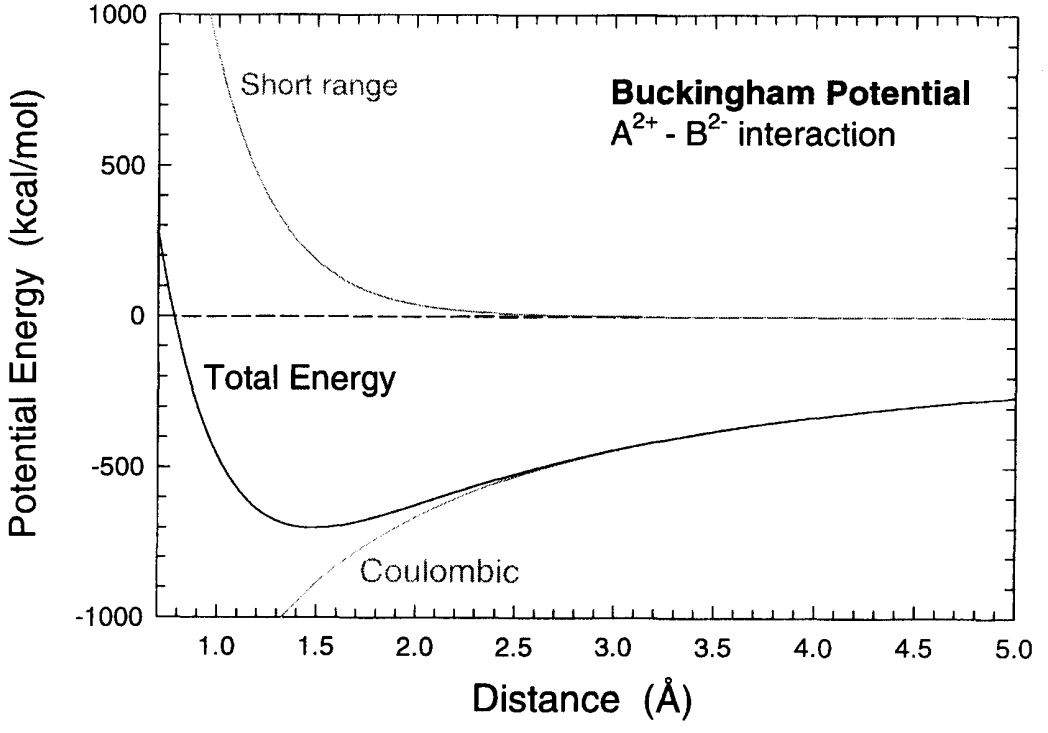

Fig. 5–1. Potential energy as a function of distance described by a Buckingham potential for the interaction of A–B ions. The total energy curve exhibits an energy minimum corresponding to the equilibrium separation distance

The A, ρ, and C are empirical parameters and the ions are assigned two electron charges each. The short-range contribution to the potential energy is positive and rapidly increases at short distances; the dispersion term is ignored ($C = 0$) for this example and therefore does not contribute to the total interaction energy. In contrast, the attractive Coulombic energy for the oppositely charged ions is negative and leads to stabilization as the two ions approach each other. The summation of the two energy terms leads to an energy minimum in the total potential curve that corresponds to the equilibrium separation distance (1.48 Å) for the ions. Alternatively, a Lennard-Jones expression (Eq. [3]) could be used to describe the short-range interactions.

This simple example demonstrates the approach used in more sophisticated methods to derive an energy-minimized configuration; however, rather than just examine two interacting atoms the optimization procedure will require tens to hundreds to perhaps thousands of interacting atoms. Special constraints can be imposed during the energy optimization. Molecular and crystallographic symmetry can be constrained or the atomic positions fixed. Periodic systems can have all cell parameters vary to simulate constant pressure conditions so that no net force occurs on the cell boundaries. Energy minimization procedures also are used in quantum mechanics to obtain optimized configurations. The algorithms are similar to those discussed above but rather than obtain system energies using analytical forcefield methods the energies are obtained through one of several quantum-based calculations.

Monte Carlo Methods

Stochastic analysis in molecular modeling usually entails the application of Monte Carlo methods to the analysis of the relative energies of a large number of possible structural configurations. Typically, a random sampling of the potential energy surface is performed in order to obtain a more practical selection of possible energy configurations. Energy-based criteria are used in the sampling process and includes an option to accept configurations that still might lead to a reasonable configuration for further analysis. The so-called Metropolis Monte Carlo method (Metropolis et al., 1953) has been successfully used in a variety of applications including the disposition of various species in zeolites: cation sites (Newsam et al., 1996), small organic molecules (Freeman et al., 1991), and inorganic gases (Douguet et al., 1996; Shen et al., 1999). There also has been substantial use of Monte Carlo methods to examine the interlayer of clay minerals. Much of this effort has been used to derive the structure and dynamics of interlayer water molecules and solvated cations due to the difficulty in obtaining this information through conventional experimental methods (e.g., Bridgeman & Skipper, 1997; Chang et al., 1995, 1997; Delville, 1991, 1992; Greathouse & Sposito, 1998; Skipper et al., 1991; Sposito et al., 1999).

Molecular Dynamics

Molecular dynamics (MD) simulations provide a deterministic approach for evaluating the equilibrium and transport properties of a chemical system based on

a classical description of the atomic interactions. Newton's equations of motion involving forces and velocities are iteratively solved to provide an evolving description of a large number of interacting atoms. A Boltzman distribution of velocities is imparted onto all or some of the atoms, and then velocities are scaled to provide the mean kinetic energy for the system to meet the target temperature for the simulation. Forces are calculated based on the implemented forcefield, and then the motion equations are integrated over the selected time interval, usually one femtosecond or less. A Verlet algorithm (Verlet, 1967), or similar method, is used to calculate the new atomic positions and velocities that are then use to loop through the integration for the next time step. This procedure is then repeated for many interactions, typically on the order of several hundred thousand steps (tens to hundreds of picoseconds of simulation time), to obtain an equilibrium configuration. Allen and Tildesley (1987) and Frenkel and Smit (1996) provide details of the various approaches used in MD simulations. Quantum dynamics, or *ab initio* MD, methods are becoming increasingly common in the literature due to advances in computer platforms and faster supercomputers. Rather than use a classical forcefield, quantum dynamics incorporates, as the name implies, a quantum method to directly obtain the energy of the system (Car & Parrinello, 1985, 1987; Tuckerman & Martyna, 2000). The high computation cost involved in these methods restricts their use to short simulation times, usually less than several picoseconds.

There are several excellent theoretical studies of clays that have used MD methods to examine the structure and dynamics of water, interlayer cations, and environmental contaminants (e.g., Greathouse et al., 2000; Hartzell et al., 1998; Kawamura et al., 1999; Miller et al., 2001; Shroll & Smith, 1999; Smith, 1998; Teppen et al., 1998a, 1997; Yu et al., 2000). The agreement of theoretical swelling curves for various clay compositions with the results of experimental studies provides significant validation for the use of the simulations as predictive tools (Cygan, 2001; Smith, 1998). Molecular dynamics simulations of double layered hydroxide materials also have been successfully completed to quantify the dynamic behavior of interlayer water and anions (Aicken et al., 1997; Kalinichev et al., 2000; Wang et al., 2001) and sorbed species on external surfaces (Kalinichev et al., 2000). These latter studies are of special interest in evaluating a variety of candidate anion-sorbing materials being considered for isolating radionuclide species such as the pertechnetate anion ($^{99}TcO_4^-$), or for the treatment of arsenic in drinking water where it typically occurs as the arsenate anion (AsO_4^{3-}).

Quantum Mechanics

Quantum methods attempt to solve the Schrödinger equation by approximate means in order to evaluate the electronic structure of large and complex systems. These methods provide a fundamental approach that surpasses the limitations imposed by a classical description of atomic interactions involving the ball and spring model of molecular mechanics. Quantum calculations can provide a first principles determinations of energies, molecular and periodic structures and properties, electrostatic potentials, spectroscopic and thermodynamic values, details of reaction mechanisms, kinetic parameters, and even evaluate nonequilibrium structures. Electronic structure calculations also provide a useful means to examine chemical

reactivity by providing molecular orbitals that map out the redistribution of electrons among the system atoms. The Schrödinger eigenfunction equation ($\boldsymbol{H}\psi = E\psi$) includes the Hamiltonian differential operator $\boldsymbol{H}$, the wavefunction ψ, and the total energy of the chemical system E. The time-independent form of this relation is evaluated for a Hamiltonian comprised of kinetic and potential energy components. The solution to the Schrödinger equation ultimately relies on the methods used to obtain appropriate wavefunctions that successfully describe the molecular orbitals for the distribution of electrons in the compound.

Among the more common quantum approaches are the *ab initio* Hartree-Fock methods and their correlated extensions (see Hehre et al., 1986), density functional theory (DFT) methods (see Jones & Gunnarsson, 1989), and semi-empirical methods (see Pople & Beveridge, 1970). Briefly, Hartree-Fock methods use an antisymmetric determinant of one-electron orbitals to define the total wavefunction. Electrons are treated individually assuming the distribution of other electrons is frozen and represented by their average distribution as part of the potential. The wavefunction orbitals and their coefficients are refined through an iterative process until the calculation reaches a steady result know as a self-consistent field. The correlated Hartree-Fock methods introduce a term in the Hamiltonian that corrects for local distortion of an orbital in the vicinity of another electron. Standard Hartree-Fock methods provide favorable equilibrium geometries compared with correlated or DFT methods, but the lack of electron correlation typically produces inaccurate spatial distributions of electrons and therefore erroneous force constants and vibrational frequencies. DFT methods incorporate exchange and correlation functionals of the electron density based on a homogeneous electron gas, and evaluated for the local density of the molecule or crystal. The density of the electrons rather than the wavefunction is used in the DFT methods to describe the energy of the system. DFT methods are efficient and convenient to use in the calculation of electronic structures for large periodic systems. Semi-empirical methods, as the name implies, incorporate empirical or experimentally-derived parameters to reduce the computational cost of evaluating all components of the *ab initio* methods. Because of the recent success of DFT methods and the improvements in computer power, plus the inaccuracies associated with the approach, semi-empirical methods are no longer as common as they were 20 years ago.

Excellent discussions of quantum theory and the methods used to obtain solutions to the Schrödinger equation are available in several review articles and texts. Noteworthy of these for applications relating to inorganic and crystalline materials are the books by Hehre et al. (1986), Labanowski and Andzelm (1991), Springborg (1997), and Cook (1998). Gibbs (1982) and Lasaga (1992) provide helpful discussions on the use of Hartree-Fock methods for mineralogical applications, while the recent review of Milman et al. (2000) covers the use of DFT methods to examine large periodic systems and includes several examples of calculations on minerals.

The use of quantum mechanics in the analysis of the structure and energetics of complex soil phases is a nontrivial task and often involves several ambiguous interpretations of the results. There are, however, a handful of studies that have successfully applied quantum methods to the analysis of layered aluminosilicate phases. Among the more useful of these quantum studies involving periodic calculations are those of Hess and Saunders (1992) and Hobbs et al. (1997) of kaoli-

nite, Bridgman et al. (1996) of talc and pyrophyllite, and Rosso et al. (2001) of muscovite (also see next section below). Often small cluster models representative of the clay structure are evaluated to assess site energies and particular coordinations (e.g., Chatterjee et al., 1998; Teppen et al., 1998b). As with classical forcefield methods, quantum methods can provide a single point energy for these structure or can be used to obtain a partially- or fully-relaxed optimized geometry.

MODELS OF RADIONUCLIDE SORPTION

Unfortunately, the soil science and mineralogical literature have few examples of the use of molecular simulation for modeling the mechanisms of radionuclide sorption on soil minerals. In part, this is due to the relatively recent advances in molecular modeling software and advanced hardware needed to examine the large and complex systems associated with soil and mineral systems. Although the published models may not accurately represent the true process for radionuclide–mineral interactions, the simulations often provide an opportunity to examine candidate mechanisms and allow the modeler, in concert with the experimentalist, to make comparisons of the possible structures and energies that may exist. In this fashion, molecular modeling provides a relatively inexpensive means to assess competitive mechanisms. This leads to further refinements of the candidate models that ultimately must survive further scrutiny and validation to be accepted as an accurate model. In this section, we examine several recent studies that have sought to develop models for metal sorption on the selected surfaces of an oxyhydroxide and exchange of metals in the interlayer of a layered aluminosilicate phase. First, however, is an example of a relatively simple modeling approach for identifying preferred sites for metal sorption.

Surface Sorption Maps

The computer simulation of clay minerals or other complex soil phases is often limited by the large unit cells and supercells required to properly represent the bulk or surface structure of the sorbing material. Furthermore, multicomponent substitutions in the structure, especially for clay minerals, lead to complex disordered systems that are not amenable to molecular simulation based on a simple unit cell to represent the system. Recently, Cygan and Kirkpatrick (2002) determined the sorption sites of several complex clay phases based on the forcefield method of Pattabiraman et al. (1985). This approach allows for the evaluation of the fundamental atomistic properties that control the sorption of molecules, metals, and anions onto the internal or external surface of clays. It is possible to evaluate the influence of crystallography, cleavage surface, composition, isomorphic substitution, and surface protonation state on the relative sorption energy.

Forcefield methods, as noted above, can employ various functional forms to describe the energy of interatomic interactions. One of the most convenient forms is that based on a nonbonded model in which all of the interatomic interactions are incorporated in the long-range electrostatics term and short-range van der Waals term:

$$E_{\text{nonbond}} = \sum_{i>j} (q_i q_j / r_{ij}) + \sum_{i>j} [(A_{ij}/r_{ij}^{12}) - (B_{ij}/r_{ij}^{6})] \quad [9]$$

Here, the first term is the usual Coulomb description of interacting charges and the second summation includes a different, yet equivalent, description of the van der Waals interactions (compare with Eq. [3]). The A_{ij} and B_{ij} terms represent the Lennard-Jones parameters for short-range interactions between atoms i and j. For sorption process, the electrostatics term dominates whereas the short-range energy term typically represents <20 % of the total energy. Pattabiraman et al. (1985) recognized that computational costs for the evaluation of sorption energies could be substantially reduced if the energy components of a large molecule were defined separate of the smaller sorbate molecule (or metal cation). The van der Waals interaction parameters needed to be defined as geometric means of the values for the individual atoms:

$$A_{ij} = (A_i A_j)^{1/2} \quad [10]$$

$$B_{ij} = (B_i B_j)^{1/2} \quad [11]$$

This approach effectively removes all of the energy parameters for the substrate component from the first summation and leads to a one-time calculation to fully evaluate the substrate material. Eq. [6] can be rewritten with the j molecule (sorbate) removed from the inner summation:

$$E_{\text{nonbond}} = \sum_j q_j \sum_i q_i / r_{ij} + \sum_j \sqrt{A_j} \sum_i \sqrt{A_i} / r_{ij}^{12} - \sum_j \sqrt{B_j} \sum_i \sqrt{B_i} / r_{ij}^{6} \quad [12]$$

Although originally employed for the analysis of drug receptor sites on macromolecules for pharmaceutical applications (Pattabiraman et al., 1985), this approach is applicable to the evaluation of sorbate–substrate interactions such as the sorption of a metal cation onto a mineral surface. The energy component for the large substrate molecule is initially evaluated over a large grid volume and the smaller sorbate or metal cation is moved to possible sorption sites where the energy is evaluated in real time. It is necessary to incorporate general or universal forcefields that are parameterized with geometric means and combination rules to describe the diagonal van der Waals energies. The consistent valence forcefield (CVFF) (Dauber-Osguthorpe et al., 1988), universal forcefield (UFF) (Rappé et al., 1992), and consistent forcefield (CFF) (Maple et al., 1994) forcefields represent several common forcefields that incorporate this convention.

A cluster model (nonperiodic) of illite was developed by Cygan and Kirkpatrick (2002) based on the structural refinement of Lin and Bailey (1984). The cluster is comprised of about 660 atoms or about 12 unit cells. The size of the cluster was optimized so as to provide suitably-sized cleavage surfaces and minimize edge effects. Cleavage was chosen to occur along the (100), (010), and (001) crystal planes with termination designed to preserve complete metal coordination by oxygens. Potassium ions were positioned on two external basal surfaces and within the interlayer. Aluminum is substituted for silicon in the tetrahedral sheet allowing for a disordered structure with aluminum avoidance and to provide the appropriate Si/Al

composition. Only aluminum occupies the dioctahedral sheet. Protonation of the illite surfaces was designed to represent surface species expected to exist at pH values of 6, 8, and 10. The CVFF forcefield (Dauber-Osguthorpe et al., 1988) was used to assign interaction parameters for all atoms and to obtain a geometry optimization of the surface hydrogens. All heavy atoms were kept constrained to positions based on the observed crystallographic structure. A sorption energy grid of 42 000 points covering the extents of the illite cluster with an additional 3 Å border zone was then generated based on the evaluation of Eq. [12]. Assuming a test sorbate characterized by unit values for the interactions parameters (i.e., fictive univalent metal cation) provides a means to compare the relative energies of the illite sorption sites.

The results of the sorption energy calculations for illite are presented in Fig. 5–2. The sorption energy map provides a convenient means to assess the relative variation in energy as a function of the illite crystallography, cleavage, pH, and local composition. Three-dimensional contours indicate the most energetically-favored sites for metal sorption. The increase in sorption energy (more negative energy values) with pH is related to the increased negative surface charge that occurs with deprotonation. The optimum sorption sites for the pH 6 cluster are clearly controlled by the coordinated location of tetrahedral aluminum sites. The aluminums on the left hand side of the (010) surface are opposite each other across the interlayer region where the contour is most prominent. Similar energy contours occur on the same surface for the deprotonated aluminol sites associated with the octahedral aluminums. The right hand (010) surface of the same cluster model does not have the concerted tetrahedral aluminums nor is there any effect of a local octahedral vacancy. Small localized sorption sites are visible near the aluminum vacancy on both illite layers for the (100) surface. The sorption map for pH 8 indicates enhanced sorption at the same sites as that for pH 6 but the right hand (010) cleavage now has enhanced sorption capability. Deprotonated silanol groups are able to contribute to the sorption energy and help to stabilize the interlayer sorption site. This sorption site is analogous to the frayed site model originally suggested by Jackson (1963) to describe the initial sorption site of a metal cation prior to incorporation of the metal into the clay interlayer. The fully-deprotonated illite cluster at pH 10 is char-

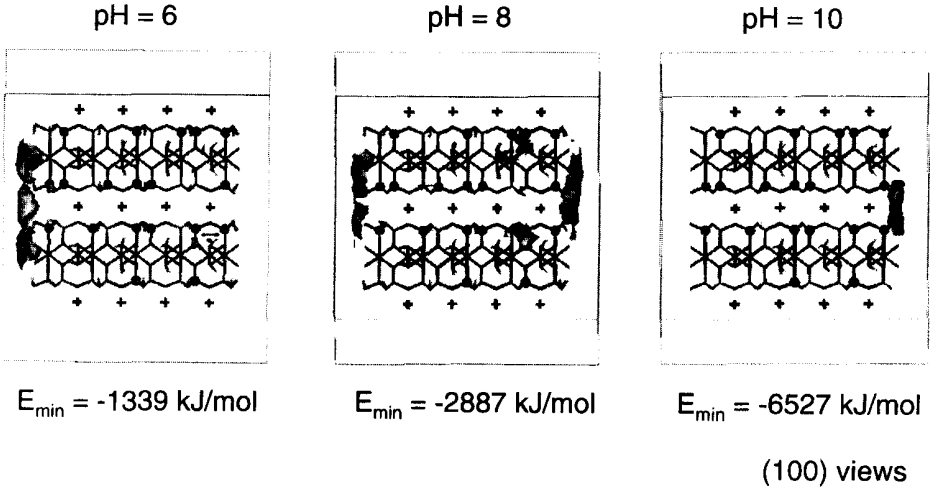

Fig. 5–2. Sorption energy maps of a molecular cluster representation of illite as a function of pH. The contour surface represents an energy value above the minimum interaction energy for the calculation (E_{min} + 335 kJ mol^{-1}). Modified from Cygan and Kirkpatrick (2002).

acterized by an interlayer that is the dominant sorption site. Tetrahedral aluminol sites are now able to coordinate to the sorbing metal. A similar analysis of sorption on kaolinite surfaces is presented by Cygan and Kirkpatrick (2002).

The sorption energy maps provide a unique insight into identifying the optimal sites for sorption on the external surfaces of clays. Notwithstanding the simple assumptions of the model, the sorption energy maps provide a relatively cost-effective means to gauge the relative importance of various surface sites given the complex nature of clays with their low symmetry, order-disorder behavior, varied composition, stacking disorder, and protonation state (function of pH). Modeling approaches involving both metal cation sorbate and the external surface of the phyllosilicate (Cygan et al., 1998; Purton et al., 1997) provide a more detailed description of the relative binding energy and surface geometry associated with the sorbed metals or radionuclides such as ^{137}Ce.

Sorption of Radium on Goethite

Iron oxide and iron oxyhydroxide minerals are commonly found in a variety of soils, various geological environments, and in numerous industrial applications (Tan, 1994). Due to the relatively high specific surface areas (>200 $m^2\ g^{-1}$ for goethite), these phases represent a large fraction of available surface area even when they are volumetrically minor phases. Hydrous oxides, in particular, can sorb a host of chemical species and are the dominant sorbents in nature due to their tendency to occur as finely dispersed phases and as coatings on various mineral substrates. Metal sorption on these phases, especially onto goethite (FeOOH) or the amorphous ferrihydrite ($FeOOH \cdot H_2O$), is an important process that needs to be critically evaluated for the safe isolation of radioactive waste materials (Lu et al., 1998; Moyes et al., 2000; Turner & Sassman, 1996). In this effort, it is desirable to use molecular modeling methods as a way to effectively evaluate the mechanisms of radionuclide sorption. The models not only offer a fundamental perspective on the controlling factors of radionuclide sorption, but also provide a convenient and relatively inexpensive means to complement direct experimental analyses that are often costly, inexact, and potentially dangerous when dealing with selected radioisotopes.

Molecular dynamics methods are particularly attractive in the analysis of radionuclide sorption mechanisms where the dynamical behavior of aqueous solution and solvated species will be important in the analysis of the substrate-fluid interface. There have been few applications of such techniques to soil phases, these being mostly for the analysis of the structure and intercalation of clay mineral systems (e.g., Cygan, 2002; Hartzell et al., 1998; Teppen et al., 1997). Models of hydrous Fe oxide phases—being similar to clay minerals having fine grain sizes, the existence of hydroxyl groups, and extensive H bonding—have been modeled in a few studies (Felmy & Rustad, 1998; Jones et al., 2000; Rustad et al., 1996a,b). Rustad et al. (1996a) demonstrated the significance of using molecular modeling tools to derive an improved model of the solvated (110) surface of goethite in which the surface hydroxylation reactions can occur. Also of significance is the recent study of Randall et al. (1999) in which the sorption of Cd to various surfaces of Fe oxyhydroxide phases was examined by synchrotron-based spectroscopy combined

with quantum DFT calculations on molecular clusters designed to represent the mineral surface. In general, these studies provide an atomistic perspective on surface speciation and metal sorption that can be linked to the macroscopic description associated with using a surface complexation model approach (see Dzombak & Morel, 1990).

The following section presents an example of using a MD approach to examine the possible mechanisms of ^{226}Ra interaction with goethite surfaces based on the recent work of Liang and Cygan (2002). Radium-226, with a half-life of 1600 yr, is the decay product of U and Th, either through natural decay processes or by discharge from uranium processing facilities (Wang et al., 1993). Unfortunately, except for a few limited bulk studies of Ra sorption in soils (Nathwani & Phillips, 1979a,b), the mechanisms of the interactions between Ra and soil minerals are unknown. The Liang and Cygan (2002) model involves the simulation of Ba, as an analog of the radioactive Ra, in order to correspond with a recent experimental and synchrotron study of Ba sorption on goethite (Westrich et al., 2000).

The interaction potentials for the goethite–water system were modified from the forcefield parameters developed for the simulation of clay minerals (Cygan et al., 2002). A nondissociative, but flexible, water model (Berendsen et al., 1981; Teleman et al., 1987) allows for the full dynamic behavior of the water molecules in the solution and for the solvation of the Ba cation. The water model includes partial charge assignments appropriate for the dipole moment of water, a harmonic bond stretch term, and a harmonic angle bend term. Nonbonded interactions are described by a Lennard-Jones 12-6 potential as described in a previous section. In order to compare the common cleavage surfaces of goethite, four substrate surfaces were generated, each with single protonation of the dangling oxygens formed during the cleavage of the bulk goethite crystal based on the refinement of Szytula et al. (1986). The (020) and (110) surfaces of goethite represent the common columnar surfaces of the needle-shaped growth morphologies, while the (101) and (021) surfaces occur as terminal faces. The termination of the goethite surface with hydroxyls represents an acidic environment (approximately pH = 4) corresponding to conditions moderately below the point of zero charge for goethite (Hayes & Leckie, 1987). Any excess positive charge created by the protonation scheme was balanced by appropriately reducing the partial charges on the Fe atoms located in the central part of the goethite slab. This procedure allowed the goethite substrate to remain charge neutral but yet provide the appropriate localized charges on the exposed cleavage surface.

The simulation cell incorporates a goethite substrate combined with a previously equilibrated Ba solution corresponding to a concentration of approximately 0.01 *M*. Molecular dynamics simulations were completed at constant particle, volume, and temperature conditions (NVT canonical ensemble) using the thermal bath method of Hoover (1985) to maintain a temperature of 300 K. All atoms of the cell were allowed to freely translate during the MD simulations except for the central region of the goethite slab; goethite atoms within 5 Å of the interface were allowed to relax. This procedure allowed for MD simulations to be run up to 100 psec with 1 fsec time steps. Depending on the surface being simulated, the simulation cells comprised anywhere from 2700 atoms to 3100 atoms.

An analysis of the energy and dynamics of Ba sorption on each of the four major goethite surfaces provided a comparison of the various geometries and relative binding strengths for sorption. Fig. 5–3 presents three simulation cells examined for Ba interacting on the columnar (110) surface as an inner sphere complex, outer sphere complex, or fully solvated by waters. Energies were obtained for each case after full equilibration of the system, and binding enthalpies were calculated as the energy difference between the sorbed and water solvated states. The results indicate the preference of a strongly bound inner surface complex for each of the four surfaces having no intermediate solvating waters between the Ba and the goethite substrate. The (101) and (110) surfaces exhibit the greatest sorbing capacity for Ba as an inner sphere, whereas none of the four surfaces show a statistical energy gain while sorbed as an outer sphere complex. The equilibrated energies for the outer sphere complexes fall within the variation of the total energy for the fully solvated cases. No transition between outer sphere and inner sphere complexes was observed on the time scale of the molecular dynamics simulations suggesting some kinetic limitation on this process.

The (101) goethite surface exhibits a greater affinity for Ba than the other surfaces. The sorption energy is about five times larger than that observed for the (110) surface. Barium sorption as an inner sphere complex on the (020) and (021) surfaces is relatively weak compared with the other two surfaces. In part, this comparison of binding strengths is related to the local geometry of the Ba on each of the surfaces. Liang and Cygan (2002) suggest that the relatively strong (101) binding is related to Ba being coordinated to 9.7 oxygens while bound to the surface, of which 3.0 of the oxygens are from the goethite and 6.7 are associated with the solvating waters. The fractional number of oxygens reflects the dynamical behavior of the sorption process on the time scale of the MD simulations-water molecules come and go while coordinating to the Ba from above while the Ba exhibits some

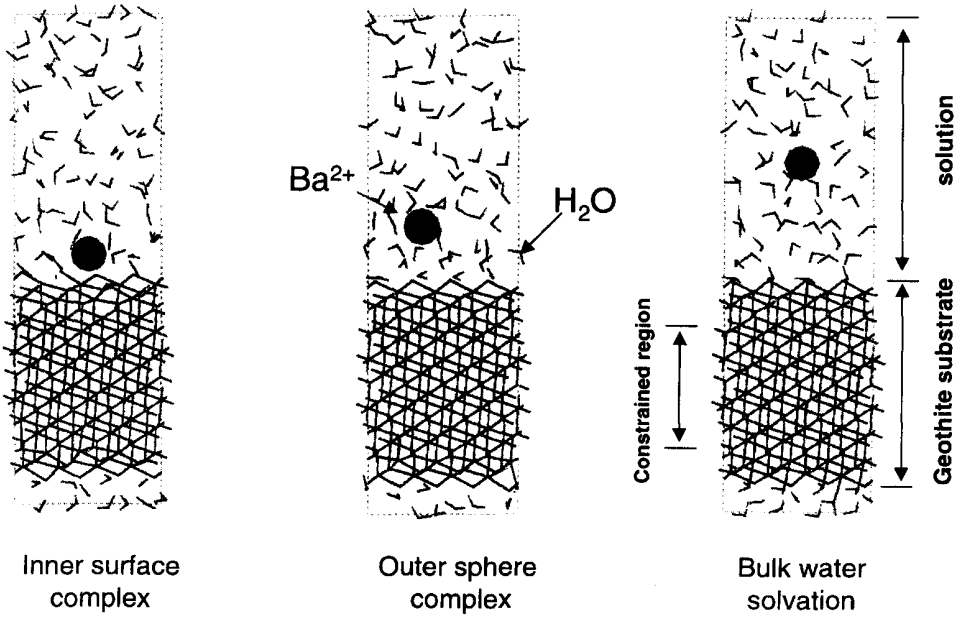

Fig. 5–3. Simulation cells used in the molecular dynamics analysis of the sorption of Ba to various goethite surfaces. Configurations represent Ba sorbed on the (110) goethite surface as an inner sphere complex, outer sphere complex, and fully solvated solution species. Modified from Liang and Cygan (2002).

movement on the goethite surface coordinating to various surface oxygens. Additionally, the (101) surface has both hydroxyls and bridging oxygens that coordinate to the inner sphere Ba complex. In contrast, the (020) surface is dominated by hydroxyls that have less influence on the binding of the Ba.

Cesium-Potassium Exchange in Muscovite

The isolation of radioactive ^{137}Cs in layered silicate minerals is of considerable environmental importance, especially in the ability of selected clay minerals to remove Cs preferentially from contaminated subsurface fluids and prevent further transport of it through the environment (Comans & Hockley, 1992; Koivula & Lehto, 1998). Recently, Rosso et al. (2001) investigated the structure and energetics of exchanging Cs ion for K ion in the interlayer of muscovite using a DFT quantum approach. Muscovite ($KAl_2(AlSi)_3O_{10}(OH)_2$) provides a relatively simple and well-characterized layered structure that is representative of the more complex smectite and illite clay phases. This work is significant in that the authors performed fully-relaxed optimizations of the primitive unit cell of muscovite in which all 42 atoms and cell parameters were allowed to vary. A plane wave pseudopotential method (Payne et al., 1992) with a generalized gradient approach (Perdew & Wang, 1992) was used in the study. The authors chose several competing structural models for the $2M_1$ polytype of muscovite based on whether hydrogens (hydroxyls) were present, and on the aluminum-silicon substitution in the tetrahedral site relative to the two possible K exchange sites in the interlayer. The choice of models led to three different charge states for the 2:1 layers of the mica. The DFT approach provided a systematic means to determine the charge distribution, structural changes, and energetics of this system as a function of layer charge, tetrahedral substitution, and the interlayer structure. This modeling approach is fundamentally different from the previously described molecular mechanics simulations. The quantum-based DFT method evaluates the electronic structure of the chemical system rather than the atomic interactions described by classical mechanics, and therefore incorporates any potential for reaction and the movement of electrons among atoms.

The exchange reaction was simulated by setting up several DFT calculations for the initial and final states of the exchange process: an initial state with K in the interlayer of the muscovite and hydrated Cs at infinite separation, and a final state with interlayer Cs and hydrated potassium at infinite separation (see Fig. 5–4). Experimental hydration enthalpies and ionization potentials were incorporated to obtain the appropriate energies for the designated states. The results of this exchange model (Rosso et al., 2001) indicate the Cs–K exchange reaction to be fairly isoenergetic and that the incorporation of Cs is favored by increasing layer charge of the model structure. The calculated exchange energies vary from –9.9 to 5.8 kJ mol^{-1} (per primitive unit cell) for, respectively, the doubly-charged and neutral simulation cells. Corresponding increases in the interlayer spacing with the incorporation of the Cs vary from 0.06 Å for the neutral cell to 0.42 Å for the doubly-charged model. The simulations also suggest that Al/Si substitution in the muscovite leads to local tetrahedral rotations and a reduction in the size of the interlayer cavity, and therefore less favored exchange for Cs. The authors conclude that the driving force for the exchange reaction is therefore quite small and that the exchange will be con-

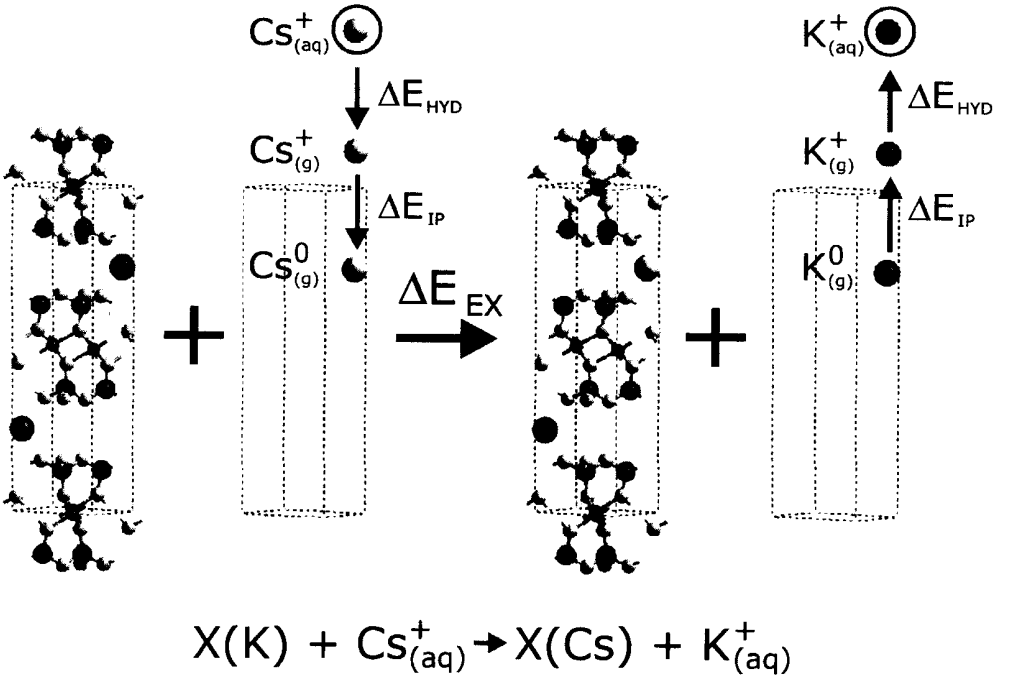

Fig. 5–4. Primitive unit cell of muscovite (doubly-charged layer model) and a schematic representation of energy calculations required to model the Cs–K exchange reaction. Modified from Rosso et al. (2001).

trolled by diffusion kinetics rather than thermodynamics. The modeling supports the frayed edge model of clays (Jackson, 1963; Sawhney, 1966; Tamura & Jacobs, 1960) where unsaturated charges and large interlayer spacings are available to promote Cs sorption.

CONCLUSION

Although not all the fundamental aspects associated with understanding the interactions of radionuclides with soil minerals are known, molecular modeling methods provide a convenient tool for evaluating the significance of various interaction mechanisms. Theoretical methods complement recent advances in materials characterization based on x-ray and neutron diffraction studies, surface spectroscopies, and synchrotron-based x-ray absorption and fluorescence methods. In combination with experiment and spectroscopic methods, molecular modeling methods can be used to develop new insights into the mechanisms of radionuclide sorption, intercalation, and reactivity with soil minerals. If properly validated and supported by experimental observation, the molecular models may ultimately be used to predict the interaction of radioactive wastes with selected soils phases that may not be amenable to experimental technique. This is especially significant if unique properties of a soil-like compound are required for specific radionuclide retention or isolation, and that may lead to the synthesis of an engineered compound to provide a solution for an important environmental waste problem.

ACKNOWLEDGMENTS

The content of this chapter greatly benefitted from the reviews provided by Patrick Brady, Brian Teppen, Henry Westrich, and the editorial board of the Soil Science Society of America. The author is appreciative of funding provided by the U.S. Department of Energy, Office of Basic Energy Sciences, Geosciences Research and the U.S. Nuclear Regulatory Commission, Office of Nuclear Regulatory Research. Sandia is a multiprogram laboratory operated by Sandia Corporation, a Lockheed Martin company, for the U.S. Department of Energy under contract DE-AC04-94AL85000.

REFERENCES

Aicken, A.M., I.S. Bell, P.V. Coveney, and W. Jones. 1997. Simulation of layered double hydroxide intercalates. Adv. Material. 9:496–500.

Allen, M.P., and D.J. Tildesley. 1987. Computer simulation of liquids. Oxford University Press, Oxford.

Berendsen, H.J.C., J.P.M. Postma, W.F. van Gunsteren, and J. Hermans. 1981. Interaction models for water in relation to protein hydration. p. 331 – 342. *In* B. Pullman (ed.) Intermolecular forces. D. Reidel, Dordrecht, the Netherlands.

Breneman, C.M., and K.B. Wiberg. 1990. Determining atom-centered monopoles from molecular electrostatic potentials: The need for high sampling density in formamide conformational analysis. J. Comput. Chem. 11:361–373.

Bridgeman, C.H., A.D. Buckingham, and N.T. Skipper. 1996. Ab-initio total energy study of uncharged 2:1 clays and their interaction with water. Molec. Phys. 89:879–888.

Bridgeman, C.H., and N.T. Skipper. 1997. A Monte Carlo study of water at an uncharged clay surface. J. Physics 9:4081–4087.

Car, R., and M. Parrinello. 1985. Unified approach for molecular dynamics and density functional theory. Phys. Rev. Lett. 55:2471–2474.

Car, R., and M. Parrinello. 1987. The unified approach to density functional and molecular dynamics in real space. Solid State Comm. 62:403–405.

Chang, F.C., N.T. Skipper, and G. Sposito. 1995. Computer simulation of interlayer molecular structure in sodium montmorillonite hydrates. Langmuir 11:2734–2741.

Chang, F.C., N.T. Skipper, and G. Sposito. 1997. Monte Carlo and molecular dynamics simulations of interfacial structure in lithium-montmorillonite hydrates. Langmuir 13:2074–2082.

Chatterjee, A., T. Iwasaki, H. Hayashi, T. Ebina, and K. Torii. 1998. Electronic and structural properties of montmorillonite: A quantum chemical study. J. Molec. Catal. 136:195–202.

Chirlian, L.E., and M.M. Francl. 1987. Atomic charges derived from electrostatic potentials: A detailed study. J. Comput. Chem. 8:894–905.

Clark, T. 1985. A handbook of computational chemistry: A practical guide to chemical structure and energy calculations. John Wiley & Sons, New York.

Comans, R.N.J., and D.E. Hockley. 1992. Kinetics of cesium sorption on illite. Geochim. Cosmochim. Acta 56:1157–1164.

Cook, D.B. 1998. Handbook of computational quantum chemistry. Oxford University Press, Oxford.

Coppens, P. 1992. Electron density from x-ray diffraction. Annu. Rev. Phys. Chem. 43:663–692.

Cygan, R.T. 2001. Molecular modeling in mineralogy and geochemistry. p. 1–35. *In* R.T. Cygan and J.D. Kubicki (ed.) Reviews in mineralogy and geochemistry: Molecular modeling theory and applications in the geosciences. Geochemical Soc., Washington DC.

Cygan, R.T. 2002. Molecular models of metal sorption on clay minerals. *In* J.D. Kubicki and W.F. Bleam (ed.) Molecular modeling of clays. Clay Minerals Soc., Boulder, CO.

Cygan, R.T., and R.J. Kirkpatrick. 2002. Sorption energy maps of clay mineral surfaces. Am. Mineral. (in press).

Cygan, R.T., and J.D. Kubicki. 2001. Molecular modeling theory: Applications in the geosciences. Geochemical Soc., Washington, DC.

Cygan, R.T., J.-J. Liang, and A.G. Kalinichev. 2002. Molecular models of hydroxide, oxyhydroxide, and clay phases and the development of a general forcefield. J. Phys. Chem. (in press).

Cygan, R.T., K.L. Nagy, and P.V. Brady. 1998. Molecular models of cesium sorption on kaolinite. p. 383–399. *In* E.A. Jenne (ed.) Sorption of metals by earth materials. Academic Press, New York.

Dauber-Osguthorpe, P., V.A. Roberts, D.J. Osguthorpe, J. Wolff, M. Genest, and A.T. Hagler. 1988. Structure and energetics of ligand-binding to proteins: Escherichia-coli dihydrofolate reductase trimethoprim, a drug-receptor system. Proteins: Struct. Func. Gen. 4:31–47.

Delville, A. 1991. Modeling the clay–water interface. Langmuir 7:547–555.

Delville, A. 1992. Structure of liquids at a solid interface: An application to the swelling of clay by water. Langmuir 8:1796–1805.

Dick, B.G., and A.W. Overhauser. 1958. Theory of the dielectric constants of alkali halide crystals. Phys. Rev. 112:90–103.

Douguet, D., R.J.M. Pellenq, A. Boutin, A.H. Fuchs, and D. Nicholson. 1996. The adsorption of argon and nitrogen in silicalite-1 zeolite: A grand canonical Monte-Carlo study. Molec. Sim. 17:255–288.

Dzombak, D., and F.M.M. Morel. 1990. Surface complexation modeling: Hydrous ferric oxide. John Wiley & Sons, New York.

Ewald, P.P. 1921. Die Berechnung optishcer und elektrostatischer Gitterpotentiale. Anna. Phys. 64:253–287.

Felmy, A.R., and J.R. Rustad. 1998. Molecular statics calculations of proton binding to goethite surfaces: Thermodynamic modeling of the surface charging and protonation of goethite in aqueous solution. Geochim. Cosmochim. Acta 62:25–31.

Freeman, C.M., C.R.A. Catlow, J.M. Thomas, and S. Brode. 1991. Computing the location and energetics of organic molecules in microporous adsorbents and catalysts: A hybrid approach applied to isomeric butenes in a model zeolite. Chem. Phys. Lett. 186:137–142.

Frenkel, D., and B. Smit. 1996. Understanding molecular simulation. Academic Press, San Diego.

Gibbs, G.V. 1982. Molecules and models for bonding in silicates. Am. Mineral. 67:421–450.

Greathouse, J.A., K. Refson, and G. Sposito. 2000. Molecular dynamics simulation of water mobility in magnesium-smectite hydrates. J. Am. Chem. Soc. 122:11459–11464.

Greathouse, J., and G. Sposito. 1998. Monte Carlo and molecular dynamics studies of interlayer structure in $Li(H_2O)_3$-smectites. J. Phys. Chem. B 102:2406–2414.

Halgren, T.A. 1992. Representation of van der waals (vdw) interactions in molecular mechanics forcefields: Potential form, combination rules, and vdw parameters. J. Am. Chem. Soc. 114:7827–7843.

Hartzell, C.J., R.T. Cygan, and K.L. Nagy. 1998. Molecular modeling of the tributyl phosphate complex of europium nitrate in the clay hectorite. J. Phys. Chem. A 102:6722–6729.

Hass, K.C., W.F. Schneider, A. Curioni, and W. Andreoni. 1998. The chemistry of water on alumina surfaces: Reaction dynamics from first principles. Science (Washington DC) 282:265–268.

Hayes, K.F., and J.O. Leckie. 1987. Modeling ionic strength effects on cation adsorption at hydrous oxide–solution interfaces. J. Colloid Interface Sci. 115:564–572.

Hehre, W.J., L. Radom, P.v.R. Schleyer, and J.A. Pople. 1986. Ab initio molecular orbital theory. John Wiley & Sons, New York.

Hess, A.C., and V.R. Saunders. 1992. Periodic ab initio Hartree-Fock calculations of the low-symmetry mineral kaolinite. J. Phys. Chem. 96:4367–4374.

Hill, F.C., G.V. Gibbs, and M.B. Boisen. 1994. Bond stretching force constants and compressibilities of nitride, oxide, and sulfide coordination polyhedra in molecules and crystals. Struct. Chem. 5:349–355.

Hill, J.R., and J. Sauer. 1994. Molecular mechanics potential for silica and zeolite catalysts based on ab initio calculations: 1. Dense and microporous silica. J. Phys. Chem. 98:1238–1244.

Hill, J.R., and J. Sauer. 1995. Molecular mechanics potential for silica and zeolite catalysts based on ab-initio calculations: 2. Aluminosilicates. J. Phys. Chem. 99:9536–9550.

Hobbs, J.D., R.T. Cygan, K.L. Nagy, P.A. Schultz, and M.P. Sears. 1997. All-atom ab initio energy minimization of the kaolinite crystal structure. Am. Mineral. 82:657–662.

Hoover, W.G. 1985. Canonical dynamics: Equilibrium phase-space distributions. Phys. Rev. A 31:1695–1697.

Jackson, M.L. 1963. Interlaying of expansible layer silicate in soils by chemical weathering. Clays. Clay Miner. 11:29–46.

Jones, F., A.L. Rohl, J.B. Farrow, and W. van Bronswijk. 2000. Molecular modeling of water adsorption on hematite. Phys. Chem. Chem. Phys. 2:3209–3216.

Jones, R.O., and O. Gunnarsson. 1989. The density functional formalism, its applications and prospects. Rev. Mod. Phys. 61:689–746.

Kalinichev, A.G., R.J. Kirkpatrick, and R.T. Cygan. 2000. Molecular modeling of the structure and dynamics of the interlayer and surface species of mixed-metal layered hydroxides: Chloride and water in hydrocalumite (Friedel's Salt). Am. Mineral. 85:1046–1052.

Karaborni, S., B. Smit, W. Heidug, J. Urai, and v. Oort. 1996. The swelling of clays: Molecular simulations of the hydration of montmorillonite. Science (Washington DC) 271:1102–1104.

Kawamura, K., Y. Ichikawa, M. Nakano, K. Kitayama, and H. Kawamura. 1999. Swelling properties of smectite up to 90 degrees C: In situ x-ray diffraction experiments and molecular dynamic simulations. Eng. Geol. 54:75–79.

Koivula, R., and J. Lehto. 1998. Ion exchange of radionuclides on natural and modified mica minerals. Radiochemistry 40:507–510.

Labanowski, J.K., and J.W. Andzelm. 1991. Density functional methods in chemistry. Springer-Verlag, New York.

Lasaga, A.C. 1992. Ab initio methods in mineral surface reactions. Rev. Geophys. 30:269–303.

Leach, A.R. 1996. Molecular modeling principles and applications. Addison Wesley Longman Limited, Essex.

Lewis, G.V., and C.R.A. Catlow. 1986. Potential models for ionic oxides. J. Phys. C: Solid State Phys. 18:1149–1161.

Liang, J.-J., and R.T. Cygan. 2002. Molecular dynamics simulation of barium sorption on goethite surfaces. Am. Mineral. (in press).

Lin, C.Y., and S.W. Bailey. 1984. The crystal structure of paragonite-$2M_1$. Am. Mineral. 69:122–127.

Lu, N., C.R. Cotter, H.D. Kitten, J. Bentley, and I.R. Triay. 1998. Reversibility of sorption of plutonium-239 onto hematite and goethite colloids. Radiochim. Acta 83:167–173.

Maple, J.R., M.J. Hwang, T.P. Stockfisch, U. Dinur, M. Waldman, C.S. Ewig, and A.T. Hagler. 1994. Derivation of class-II force-fields: 1. Methodology and quantum force-field for the alkyl functional-group and alkane molecules. J. Comput. Chem. 15:162–182.

Metropolis, N., A.W. Rosenbluth, M.N. Rosenbluth, A.H. Teller, and E. Teller. 1953. Equation of state calculations by fast computing machines. J. Chem. Phys. 21:1087–1092.

Miller, D.M., B.J. Teppen, C.H. Yu, and L. Schafer. 2001. Molecular dynamics simulation of adsorption processes at the clay mineral–aqueous solution interface. p. 257–280. *In* H.M. Selim and D.L. Sparks (ed.) Physical and chemical processes of water and solute transport/retention in soil. SSSA Spec. Publ. 56. SSSA, Madison, WI.

Milman, V., B. Winkler, J.A. White, C.J. Pickard, M.C. Payne, E.V. Akhmatskaya, and R.H. Nobes. 2000. Electronic structure, properties, and phase stability of inorganic crystals: A pseudopotential plane-wave study. Int. J. Quantum Chem. 77:895–910.

Moyes, L.N., R.H. Parkman, J.M. Charnock, D.J. Vaughan, F.R. Livens, C.R. Hughes, and A. Braithwaite. 2000. Uranium uptake from aqueous solution by interaction with goethite, lepidocrocite, muscovite, and mackinawite: An x-ray absorption spectroscopy study. Environ. Sci. Technol. 34:1062–1068.

Mulliken, R.S. 1955. Electronic population analysis on LCAO-MO molecular wave functions. J. Chem. Phys. 23:1833–1846.

Nathwani, J.S., and C.R. Phillips. 1979a. Adsorption of Ra-226 by soils: 1. Chemosphere 8:285–291.

Nathwani, J.S., and C.R. Phillips. 1979b. Adsorption of Ra-226 by soils in the presence of Ca^{2+} Ions: 2. Specific adsorption. Chemosphere 8:293–299.

Newsam, J.M., C.M. Freeman, A.M. Gorman, and B. Vessal. 1996. Simulating non-framework cation location in aluminosilicate zeolites. Chem. Comm. 16:1945–1946.

Pattabiraman, N., M. Levitt, T.E. Ferrin, and R. Langridge. 1985. Computer graphics in real-time docking with energy calculation and minimization. J. Comput. Chem. 6:432–436.

Payne, M.C., M.P. Teter, D.C. Allan, T.A. Arias, and J.D. Joannopoulos. 1992. Iterative minimization techniques for ab initio total-energy calculations: Molecular dynamics and conjugate gradients. Rev. Mod. Phys. 64:1045–1097.

Perdew, J.P., and Y. Wang. 1992. Accurate and simple analytic representation of the electron-gas correlation-energy. Phys. Rev. B: Condens. Matter 45:13244–13249.

Pople, J.A., and D.L. Beveridge. 1970. Approximate molecular orbital theory. McGraw-Hill, New York.

Purton, J.A., N.L. Allan, and J.D. Blundy. 1997. Impurity cations in the bulk and the {001} surface of muscovite: An atomistic simulation study. J. Mat. Chem. 7:1947–1951.

Randall, S.R., D.M. Sherman, K.V. Ragnarsdottir, and C.R. Collins. 1999. The mechanism of cadmium surface complexation on iron oxyhydroxide minerals. Geochim. Cosmochim. Acta 63:2971–2987.

Rappé, A.K., C.J. Casewit, K.S. Colwell, W.A. Goddard, and W.M. Skiff. 1992. UFF, a full periodic table force field for molecular mechanics and molecular dynamics simulations. J. Am. Chem. Soc. 114:10024–10035.

Rappé, A.K., and W.A. Goddard. 1991. Charge equilibration for molecular dynamics simulations. J. Phys. Chem. 95:3358–3363.

Rosso, K.M., J.R. Rustad, and E.J. Bylaska. 2001. The Cs/K exchange in muscovite interlayers: An ab initio treatment. Clays. Clay Miner. 49:500–513.

Rustad, J.R., A.R. Felmy, and B.P. Hay. 1996a. Molecular statics calculations for iron oxide and oxyhydroxide minerals: Toward a flexible model of the reactive mineral–water interface. Geochim. Cosmochim. Acta 60:1553–1562.

Rustad, J.R., A.R. Felmy, and B.P. Hay. 1996b. Molecular statics calculations of proton binding to goethite surfaces: A new approach to estimation of stability constants for multisite surface complexation models. Geochim. Cosmochim. Acta 60:1563–1576.

Sawhney, B.L. 1966. Kinetics of cesium sorption by clay minerals. Soil Sci. Soc. Am. Proc. 30:565–569.

Shen, D.M., S.R. Jale, M. Bulow, and A.F. Ojo. 1999. Sorption thermodynamics of nitrogen and oxygen on CaA zeolite. Stud. Surf. Sci. Catal. 125:667–674.

Shroll, R.M., and D.E. Smith. 1999. Molecular dynamics simulations in the grand canonical ensemble: Application to clay mineral swelling. J. Chem. Phys. 111:9025–9033.

Skipper, N.T., F.C. Chang, and G. Sposito. 1995a. Monte Carlo simulation of interlayer molecular structure in swelling clay minerals: 1. Methodology. Clays. Clay Miner. 43:285–293.

Skipper, N.T., K. Refson, and J.D.C. McConnell. 1991. Computer simulation of interlayer water in 2:1 clays. J. Chem. Phys. 94:7434–7445.

Skipper, N.T., G. Sposito, and F.C. Chang. 1995b. Monte Carlo simulation of interlayer molecular structure in swelling clay minerals: 2. Monolayer hydrates. Clays. Clay Miner. 43:294–303.

Smith, D.E. 1998. Molecular computer simulations of the swelling properties and interlayer structure of cesium montmorillonite. Langmuir 14:5959–5967.

Spasojevicde-Bire, A., and J.M. Kiat. 1997. Electron deformation density studies of perovskite compounds. Ferroelectrics 199:143–158.

Sposito, G., S.H. Park, and R. Sutton. 1999. Monte Carlo simulation of the total radial distribution function for interlayer water in sodium and potassium montmorillonites. Clays. Clay Miner. 47:192–200.

Sprague, J.T., J.C. Tai, Y. Yuh, and N.L. Allinger. 1987. The MMP2 calculational method. J. Comput. Chem. 8:581–603.

Springborg, M. 1997. Density-functional methods in chemistry and materials Science. John Wiley & Sons, Chichester.

Szytula, A., A. Burewicz, K. Dimitrijevic, S., H. Rzany, J. Todorovic, A. Wanic, and W. Wolksi. 1986. Neutron diffraction studies of a-FeOOH. Physica Status Solidi 26:429–434.

Tamura, T., and D.G. Jacobs. 1960. Structural implications in cesium sorption. Health Phys. 2:391–398.

Tan, K.H. 1994. Environmental soil science. Marcel Dekker, New York.

Teleman, O., B. Jonsson, and S. Engstrom. 1987. A molecular dynamics simulation of a water model with intramolecular degrees of freedom. Molec. Phys. 60:193–203.

Teppen, B.J., K. Rasmussen, P.M. Bertsch, D.M. Miller, and L. Schafer. 1997. Molecular dynamics modeling of clay minerals. 1. Gibbsite, kaolinite, pyrophyllite, and beidellite. J. Phys. Chem. B101:1579–1587.

Teppen, B.J., C. Yu, D.M. Miller, and L. Schafer. 1998a. Molecular dynamics simulations of sorption of organic compounds at the clay mineral–aqueous solution interface. J. Comput. Chem. 19:144–153.

Teppen, B.J., C.H. Yu, S.Q. Newton, D.M. Miller, and L. Schafer. 1998b. Ab initio investigations pertaining to aluminum in tetrahedral versus octahedral sites of clay minerals. J. Molec. Struct. 445:65–88.

Tosi, M.P. 1964. Cohesion of ionic solids in the Born model. Solid State Phys. 131:533–545.

Tuckerman, M.E., and G.J. Martyna. 2000. Understanding modern molecular dynamics: Techniques and applications. J. Phys. Chem. B 104:159–178.

Turner, D.R., and S.A. Sassman. 1996. Approaches to sorption modeling for high-level waste performance assessment. J. Contam. Hydrol. 21:311–332.

Verlet, L. 1967. Computer 'experiments' on classical fluids: I. Thermodynamical properties of Lennard-Jones molecules. Phys. Rev. 159:98–103.

Wang, J., A.G. Kalinichev, R.J. Kirkpatrick, and X. Hou. 2001. Molecular modeling of the structure and energetics of hydrotalcite hydration. Chem. Mater. 13:145–150.

Wang, R.S., A.S.Y. Chau, F. Liu, H. Cheng, P. Nar, X.M. Chen, and Q.Y. Wu. 1993. Studies on the adsorption and migration of radium in natural minerals. J. Radioanal. Nucl. Chem. 171:347–364.

Weiner, S.J., P.A. Kollman, D.A. Case, U.C. Singh, C. Ghio, G. Alagona, S. Profeta, and P. Weiner. 1984. A new force field for molecular mechanical simulation of nucleic acids and proteins. J. Am. Chem. Soc. 106:765–784.

Westrich, H.R., H.L. Anderson, S.E. Arthur, P.V. Brady, R.T. Cygan, J.-J. Liang, P. Zhang, and N. Yee. 2000. Prediction of metal sorption in soils. Sect. 1–12. *In* Proc. of the Waste Management Conf., Tucson, AZ. Feb. 27–Mar. 2, 2000. WM Symposia, Tucson, AZ.

Yu, C.H., S.Q. Newton, D.M. Miller, L. Schafer, and B.J. Teppen. 2000. Molecular dynamics simulations of the adsorption of methylene blue at clay mineral surfaces. Clays. Clay Miner. 48:665–681.

6 Operative Pathways of Chromate and Uranyl Reduction within Soils and Sediments

Scott Fendorf and Colleen M. Hansel

Stanford University
Stanford, California

Bruce Wielinga

Sheppard Miller, Inc.
Fort Collins, Colorado

ABSTRACT

Toxic heavy metals and long-lived radionuclides such as Cr and U are problematic environmental contaminants—they cannot be degraded to innocuous species. Remediation efforts must therefore focus on means to limit their availability to target organisms (i.e., diminish their risk). Chromium and U are both redox active elements in which the hexavalent states are most susceptible to transport and biological uptake. Their reduced counterparts, Cr(III) and U(IV), have limited solubilities and bind tenaciously to soil particles. As a consequence, reactions that promote reduction of Cr and uranyl may lead to the stabilization of these hazardous elements. Here we consider the kinetics for known reduction reactions and infer operating pathways in natural environments. Additionally, experimental data for competing or complimentary side-reactions are presented. On the basis of known rates, chromate reduction will proceed via chemical reduction by either ferrous Fe or sulfide in anaerobic soils and sediments. The importance of biological factors should not, however, be over looked inasmuch as reduction of chromate in aerobic environments will probably proceed through enzymatic means, and even in anaerobic systems microbial metabolites may be responsible for the chemical pathways. For example, we demonstrate bacterially facilitated reduction of chromate by biogenically formed ferrous Fe. By contrast, uranyl reduction is likely to occur directly through bacterially mediated reactions. Reduction of uranyl by metal reducing bacteria during respiration is common; unfortunately, alternate terminal electron acceptors may therefore compete with U(VI). Amorphous and short-range order ferric hydroxides and nitrate, for example, may retard the reduction of uranyl. Nevertheless, reductive stabilization of both U and Cr appear commonplace in soils and sediments under anaerobic conditions, a desirable situation from an environmental perspective.

Radionuclides and heavy metals pose a threat to environmental quality. Due in part to historical waste disposal methods, large quantities of these materials now con-

 Geochemistry of Soil Radionuclides. SSSA Special Publication no. 59.

taminate soils and have migrated to surface and groundwater systems. For example, the disposal of toxic metals and radioactive wastes generated at the U.S. Department of Energy facilities has historically involved shallow land burial via pits, trenches, and cribs. Since much of this waste was not encapsulated with physical or chemical barriers, there followed unimpeded migration of contaminants into the surrounding soils and groundwaters. Of particular concern are the redox sensitive radionuclide U and the redox sensitive metal Cr (National Research Council, 1974; U.S. Environmental Protection Agency, 1978; Riley & Zachara, 1992). These contaminants are classified as priority pollutants in soils and groundwaters at most U.S. Department of Energy sites because of the large inventory present, the health risk associated with each contaminant, and their mobility with respect to primary waste sources. As a consequence, there is a defined interest in the remediation of these redox sensitive contaminants within surface and subsurface plumes (U.S. Department of Energy, 1995). Because U and Cr contamination of soils is widespread and extensive, in situ approaches for remediation are desirable. It has therefore become important to identify processes that can stabilize such contaminants and thus limit their environmental risk.

Uranium and Cr exist in more than one oxidation state in the surface- and near-surface environment—the different oxidation states having markedly different properties. Cr(VI) exists in one of the protonation states of the chromate anion ($HCrO_4^-$ or CrO_4^{2-}) within soils. The speciation of U(VI) is complex; the uranyl cation (UO_2^{2+}) is the central species with hydroxy and carbonato derivatives. Fredrickson et al. (2000) provides data regarding the speciation of uranyl within environmental settings. Despite the variable speciation, the fully oxidized species of Cr and U have a high solubility in soils and sediments, and consequently they tend to be mobile in the environment. Chromate also is subject to biological uptake, a factor that contributes to its toxicity (Turner & Rust, 1971; Venitt & Levy, 1974). In contrast, the reduced form of Cr, Cr(III), has a limited hydroxide solubility and forms strong complexes with soil minerals; it is therefore less mobile and has a lower availability than Cr(VI) (Sass & Rai, 1987; Fendorf et al., 1992). Similarly, the oxidized forms of U have a greater solubility (Smith & Martell, 1982) and hence exhibit greater mobility in soils and subsurface environments than either U(IV) or U(V) (Duff et al., 1999). We may conclude that oxidized forms of these radionuclides and metals are subject to enhanced migration through surface and subsurface environments relative to their reduced counter parts. Reductive stabilization is therefore a desirable pathway for removing these elements form the aqueous phase and minimizing their risk.

In situ remediation of contaminants presents an attractive alternative to ex situ methods due to the lower cost and the potential for achieving remediation objectives. To enhance the efficiency and the effectiveness of in situ plume stabilization, techniques involving microbiological reduction of contaminant metals have attracted considerable attention (see for example Lovley, 1991; Lovley & Phillips, 1992; Rusin et al., 1994; Shen & Wang, 1994; Wang & Shen, 1995; Wang & Xiao, 1995; Zhang et al., 1996; Abdelouas et al., 1998; Fredrickson et al., 2000). Anaerobic bacteria can mediate the reduction of redox sensitive elements either directly, by using them as terminal electron acceptors in the absence of O, or indirectly through reaction with the reduced products of microbial metabolism (e.g., H_2S, Fe(II), and

many organic chemicals such as ascorbate). Ferric iron and sulfate are two of the principal terminal electron acceptors that lead to reactive, reduced products that may have a profound impact on contaminant dynamics. Thus, it is likely that anaerobic microbial activity can effectively alter the redox state of toxic metals and radionuclides to render them immobile. In fact, the reductive stabilization of U by indigenous groundwater bacteria has recently been demonstrated (Abdelouas et al., 1998).

The speciation and mobility of Cr and U in surface and subsurface environments depends not only on biological activity of anaerobic organisms but also on the reactivity of reduced chemical constituents. We should consider that contaminant reduction may occur directly through microbial enzymatic reduction (i.e., electron transfer from the organism directly to the contaminant) or indirectly through reaction with microbial metabolites. Fostering the latter reduction pathway is a shift in the soil's mineralogical framework toward solids bearing reduced constituents such as ferrous Fe and sulfide. For example, a number of Fe(II) biogenic minerals have been identified as metabolic end products of microbial respiration on ferric iron (e.g., Fredrickson et al., 1998; Zachara et al., 1998) that may react with uranyl or chromate.

The oxidation state of contaminants, such as U and Cr, dictate their fate and transport within the environments. The mobility and, hence, risk associated with U(VI) and Cr(VI) decreases upon reduction due to increased adsorption and precipitation capacity of their reduced states. The fate of each element will depend on the kinetics and thermodynamics of microbial and chemical processes within soils. By impeding the spread of contaminants in the environment, remediation strategies can focus on source areas thereby accelerating clean-up activities at reduced effort and cost. Moreover, enhancing our knowledge of redox processes will improve modeling efforts aimed at predicting the fate of contaminants in surface and subsurface environments.

EXPERIMENTAL APPROACH

We begin our evaluation of uranyl and chromate reduction by considering published reaction rates for both biological and chemical reduction. Subsequent to this initial assessment, we provide data from studies conducted using *Shewanella alga* strain BrY (ATCC no. 51181, hereafter referred to as BrY) as a model dissimilatory Fe-reducing bacterium (DIRB). BrY is a well-characterized, facultative anaerobic bacterium with the demonstrated ability to couple the oxidation of organic acids and H_2 to the reduction of Fe(III), Mn(IV), and U(VI) under anoxic conditions (Caccavo et al., 1992). BrY was grown and harvested as described previously (Wielinga et al., 2000). Cell suspensions were transferred to sterile, anaerobic pressure tubes having a headspace of N_2 gas, capped with a thick butyl rubber stopper, and stored on ice for <15 min before inoculation of reaction chamber (flow cell or serum vial). Heat-killed cells were prepared by holding the cell suspension at 80°C for 20 min.

Standard methods for culture of anaerobic bacteria and preparation of anoxic media were used throughout. Media and buffers were made anoxic by boiling and cooling under a stream of O_2-free N_2 or N_2:CO_2 (80:20) gas. All reactions were performed in an anaerobic chamber (Coy Laboratories, Inc., Grass Lake, MI) with an

N_2(90%):H_2(10%) atmosphere. Hematite (Fe_2O_3; 5 $m^2\ g^{-1}$) and goethite (α-FeOOH; 15 $m^2\ g^{-1}$) were purchased from Strem Chemicals, Newburyport, MA. Ferrihydrite (nominally $5Fe_2O_3 \cdot 9H_2O$; 200–600 $m^2\ g^{-1}$) was synthesized by the titration of $Fe(NO_3)_3 \cdot 9H_2O$ (0.4 *M*) with 1 *M* NaOH to pH 7 (see Wielinga et al., 2000 for details). The resulting ferrihydrite was washed with ultra pure H_2O and then either used immediately or freeze-dried and ground to a fine powder. Surface area of the freeze-dried material was determined using a BET isotherm.

Uranyl Reduction

Uranium reduction studies were conducted in batch cultures under non-growth conditions in 60 mL serum vials containing 50 mL modified bicarbonate medium (Lovley & Phillips, 1986) with Fe (as a hydroxide or oxyhydroxide) at the equivalent of about 10 μ*M* final concentration. The medium contained the following components (in g L^{-1}): $NaHCO_3$, 2.5; NH_4Cl, 1.5; KCl, 0.1; $CaCl_2$, 0.05; and 10 mL of each vitamin and mineral solutions (Lovley & Phillips, 1986). Phosphate was eliminated from the medium. Serum vials were purged with N_2:CO_2 at a ratio of 80:20, sealed with thick butyl rubber stoppers and autoclaved (121°C, 15 min). After sterilization, uranyl acetate and lactate were added from sterile anaerobic stock solutions to give final concentrations of 400 to 1000 μ*M* and 10 μ*M*, respectively. Media were inoculated with 1 to 4×10^7 CFU mL^{-1} (colony forming units) on TSA and incubated at 25 2°C in the dark without agitation.

Chromium(VI) Reduction Flow Experiments

Hydrodynamic conditions prevail within natural environments and may alter reaction pathways owing to finite residence times and removal of soluble products. In order to simulate alteration in reaction progression induced by dynamic flow conditions, we investigated the reduction of chromate within systems undergoing active bacterial reduction of ferric Fe in flow cells. Iron/Cr reduction reactions were performed in polycarbonate stirred-flow reactors containing 100 mL of either 30 μ*M* HEPES or 10 μ*M* sodium bicarbonate buffered medium that also contained the following ingredients (in g L^{-1}): NaCl, 2.5; NH_4Cl, 1.5; KCl, 0.1; $CaCl_2$, 0.1; $MgSO_4$, 0.1; and 10 mL of each vitamin and mineral solution (Balch et al., 1979). Lactate was added as an electron donor at a final concentration of 10 μ*M* unless otherwise stated. In experiments testing the ability of BrY to directly reduce Cr(VI) and gain energy for growth in this process, media was amended with 0.6 g L^{-1} KH_2PO_4.

Reactions were initiated by adding cell suspension (final cell concentration ~2×10^7 cells mL^{-1}) and Fe (hydr)oxide (surface area of 100 $m^2\ L^{-1}$) to each reactor and bringing the volume to approximately 100 mL with Cr-free medium. The initial flow rate of media into the cell before Cr addition varied between 10 and 11 mL h^{-1}. Following Cr addition, the pump speed was decreased until a steady-state Fe(II) concentration was maintained in the effluent. The flow-rate varied from about 1.5 to 4.5 mL h^{-1} at steady-state conditions depending on both Fe mineral and buffer conditions, yielding retention times that ranged from 22 to 67 h. Samples collected were analyzed for soluble Fe and Cr as described below.

Analytical Methods

Solution-Phase Analysis

Soluble Cr(VI), Fe(II), and U(VI) were monitored spectrophotometrically, Cr at 540 nm using the s-diphenyl carbazide method (Bartlett & James, 1979), Fe(II) at 562 nm using the ferrozine assay (Stookey, 1970), and U at 575 nm using 2-(5-Bromo-2-pyridylazo)-5-diethylaminophenol (Johnson & Florence, 1971). Total dissolved Cr, U, and Fe were determined by flame atomic absorption spectroscopy (AAS) or by inductively coupled plasma (ICP) optical emission spectroscopy.

Solid-Phase Analysis

At the conclusion of each experiment, solids were collected for Cr and Fe speciation and quantification. Total Cr and Fe in the solid-phase were determined by microwave assisted total acid digestion and ICP analysis. A 5 mL aliquot of well-mixed suspension was combined with 4 mL concentrated, trace metal-grade nitric acid, 1 mL concentrated hydrofluoric acid and digested following U.S. Environmental Protection Agency Method no. 3052. The oxidation states of Cr (see Patterson et al., 1997) and Fe (see LaForce et al., 2000) in the solid-phase were determined using x-ray absorption near-edge structure (XANES) spectroscopy, which was conducted at the Stanford Synchrotron Radiation Laboratory (SSRL). Detection limits are approximate 3% for Cr(VI) and 5% for Fe(II) at the concentrations investigated here.

REDUCTION PROCESSES OF CHROMIUM(VI)

Biological versus Chemical Reduction: Numerous surface and subsurface environments contain active communities of metal-reducing bacteria that enzymatically couple the reduction of multivalent metals, including toxic metals and radionuclides, to the oxidation of organic matter or other accessible electron sources (Lovley, 1993). Many of these metal-reducing bacteria have been isolated and grown in pure culture. Biological reduction of Cr(VI) to Cr(III) has been demonstrated for a number of bacterial strains, with aerobes (Gopalan & Veeramani, 1994; Garbisu et al., 1998; Park et al., 2000) and many anaerobes (Romananko & Korenkov, 1977; Lebedeva & Lyalikova, 1979; Kvasnikov et al., 1985; Gvozdyak et al., 1986; Wang et al., 1989, 1991; Lovley & Phillips, 1994; Turick et al., 1996; Tebo & Obraztsova, 1998) able to reduce Cr(VI); additionally, specific enzymes responsible for chromate reduction have been purified (e.g., Lojou et al., 1998; Park et al., 2000). In many cases, chromate reduction appears to be incidental to the organism, possibly occurring as a detoxification mechanism; recent evidence, however, suggests that some bacteria can grow using Cr(VI) as the sole electron acceptor in respiration (Tebo & Obraztsova, 1998). Despite the different microbial processes responsible for enzymatic reduction of chromate, the resulting reduction rates are surprisingly similar (Table 6–1). Measured reduction rates of chromate by different cultures, both mixed and pure, vary by less than a factor of 15, with average reduction rates on the order of 10^{-4} M h^{-1} when normalized to a cell density of ap-

Table 6–1. Bacterial reduction rates (initial) of chromate by isolated and mixed cultures.

Organism	Rate × 10^{-4}, M h^{-1}†	Reference
Pseudomonas putida	0.60	Ishibashi et al., 1990
Desulfovibrio vulgaris	2.9	Lovley & Phillips, 1994
Agrobacterium radiobacter	0.83	Llovera et al., 1993
Pseudomonas sp.	0.26	Gopalan & Veeramani, 1994
Comamonas testosteroni	0.27	Cooke et al., 1995
Enterobacter cloacae	1.4	Hardoyo et al., 1991
SRB-III	7.6	Fude et al., 1994
Shewanella alga, strain BrY-MT	0.20	Caccavo & Olson, 1999, unpublished data
Bacillus subtilis	0.20	Garbisu et al., 1998
PNNL culture	0.19	Schmieman et al., 1997)
Desulfotomaculum reducens	0.40	Tebo & Obraztsova, 1998

† Cumulative rate, normalized to a cell density of 10^9 cells mL^{-1}.

proximately 10^9 cells mL (Table 6–1). Using rate data for microbial reduction of chromate allows for a comparison with measured chemical reduction rates discussed in the succeeding section.

A multitude of constituents in soil and subsurface environments are capable of chemically reducing Cr(VI). These include Fe(II) (aq), sulfide, Fe(II)-bearing minerals, and dissolved organic molecules (Bartlett & Kimble, 1976; James & Bartlett, 1983; Eary & Rai, 1988, 1989, 1991; Masscheleyn et al., 1992; Losi et al., 1994; Anderson et al., 1994; Deng & Stone, 1996; Fendorf & Li, 1996; Patterson et al., 1997; Peterson et al., 1997; Buerge & Hug, 1999). Thus, both chemical and biological processes can reduce Cr(VI) or U(VI). Although in either case the toxic metal is reduced to a less hazardous form, the stability of the reaction product may differ appreciably depending upon the reduction mechanism. As a consequence, it is important to define by which pathways Cr(VI) or U(VI) will be reduced and the resulting products.

The reduction of Cr(VI) can lead to two general types of products: soluble Cr(III)-organic complexes (Cr(III)-DOC) or Cr hydroxide precipitates. Biological reduction or reduction by organic molecules such as L-cysteine have the potential to form soluble Cr(III)-organic complexes (Brauer et al., 1996; Lay & Levina, 1996). Reduction of chromate by ferrous iron, sulfide, and in some cases biological activity will result in a precipitate with the general formula $Cr_{1-x},Fe_x(OH)_3$. Biological or sulfide induced reductive precipitation will generate a solid with $x = 0$ while Fe(II) will give values of $x > 0$; a value of $x = 0.75$ has been hypothesized (Eary & Rai, 1989) and observed (Patterson et al., 1997) for Cr(VI) reduction by aqueous Fe(II). The importance of the reaction products is that the likelihood of Cr reoxidation corresponds to the solubility of Cr(III). For the Cr(III)-hydroxide precipitates, the solubility is proportional to the ratio of Cr/Fe, with increased quantities of Fe(III) stabilizing the solid (Fig. 6–1). Thus, soluble organic complexes have the greatest probability of reoxidation and $Cr_{0.25}Fe_{0.75}(OH)_3$ precipitates the least.

Kinetic factors will dictate the dominant mechanism of Cr(VI) or U(VI) reduction. We have tabulated cumulative reduction rates for bacterial reduction of chromate (Table 6–1), with rates normalized to cell densities of 10^9 cells mL^{-1}. These

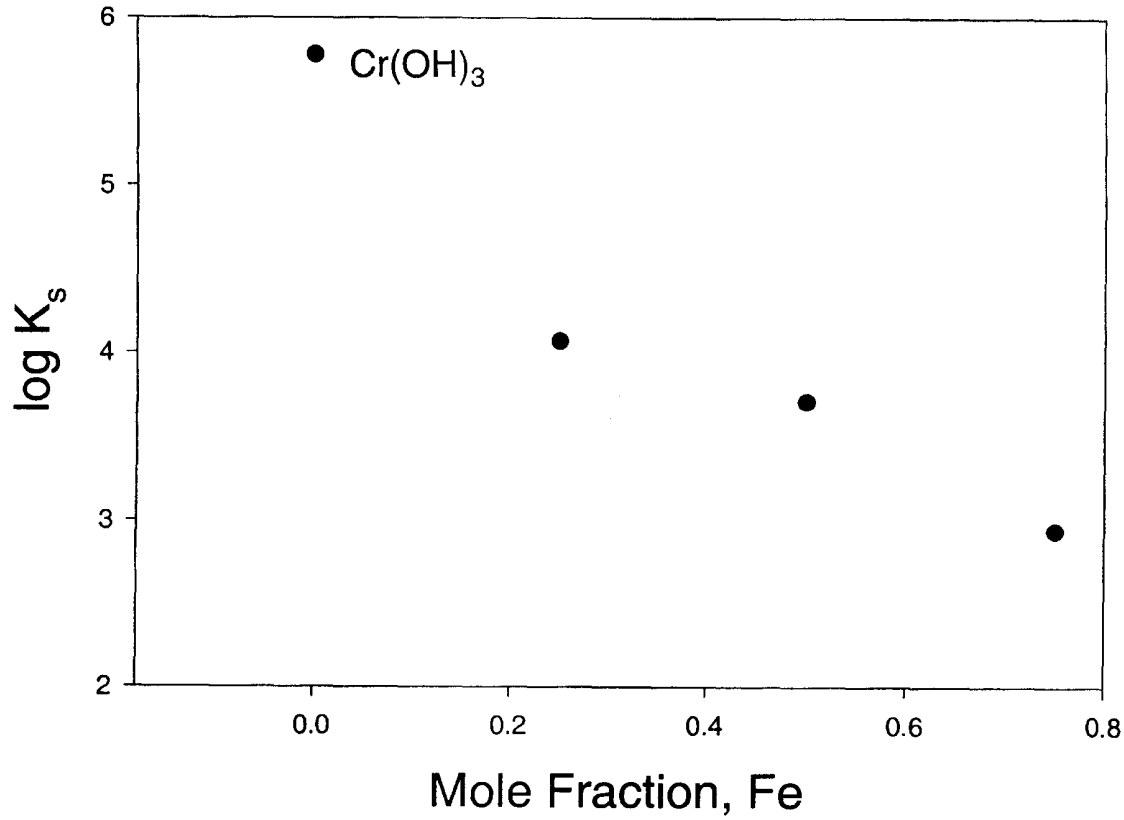

Fig. 6–1. Changes in the solubility constant for the solid $Cr_xFe_{1-x}(OH)_3$ as a function of Fe (mole fraction) incorporation (data are from Sass & Rai, 1987).

biological studies have generally been conducted at near-neutral pH values and at temperatures between 25 and 30°C. Explicit rate expressions for the reduction of chromate by Fe(II) and H_2S have been developed that allow for a predicted reaction rate depending on reactant concentration, pH, and temperature (e.g., Pettine et al., 1994; Pettine et al., 1998). Using the rate expressions for chromate reduction, we can chart the expected reduction rate under conditions likely to exist in anaerobic surface or subsurface environments (Fig. 6–2). Our calculations are based on an infinite pool of Fe(II) and S(-II) buffered at 30 μM and 10 μM, respectively (i.e., we assume that the total quantities of ferrous Fe or dissolved sulfide are in excess of the contaminant). Superimposing the measured rates for biological reduction of chromate then allows us to predict the dominant reduction pathway for this contaminant. We have plotted only the result for *D. vulgaris* since it has the greatest reaction rate reported for pure cultures (Table 6–1).

The dominant reductant of chromate at pH > 5.5 is Fe(II); at pH < 5.5 dissolved sulfide would be the dominant reductant. Since rate data are only available for biological reduction at pH 7, our comparison of chemical to biological pathways is limited. Nevertheless, one notes that the chemical (i.e., ferrous Fe) mechanisms are more than 100 times faster than the biological rate. Thus, it seems likely that chemical reduction pathways will be the major avenues by which chromate is reduced within anaerobic environments where ferrous Fe and sulfide are abundant. One must, however, bear in mind that the generation of reductant pools (e.g., Fe(II) or sulfide) depends on microbial activity, inasmuch as Fe(III) and SO_4^{2-} reduction occurs via dissimilatory reduction pathways (Lovley et al., 1991; Lovley, 1991).

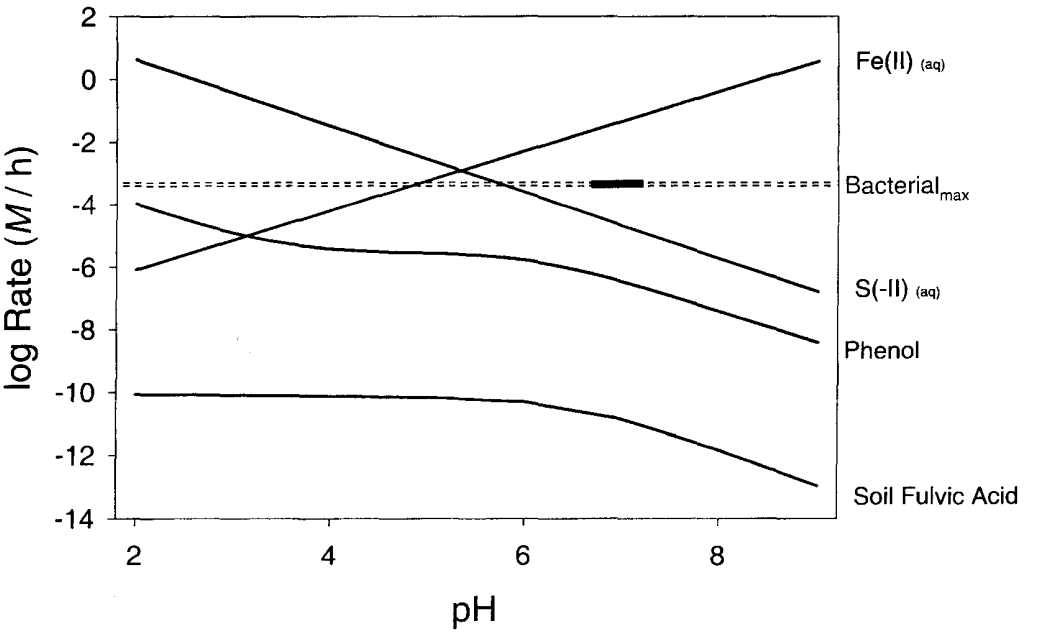

Fig. 6–2. Predicted and measured reduction rates for the reduction of chromate by chemical constituents having expanded rate expressions. For calculated rates, initial [Cr(VI)] = 100 μ*M*, [Fe(II)] = 30 μ*M*; [S(-II)] = 10 μM. Rate expressions for sulfide and ferrous Fe are from Pettine et al. (1994, 1998); for soil fulvic acid from Wittbrodt and Palmer (1995); and for 2,6-dimethoxyphenol from Elovitz and Fish (1995). Bacterial reduction is represented by data for *D. vulgaris* from Lovley and Phillips (1994)—the most rapid reductant of chromate isolated in pure culture.

Thus, in determining the mechanism of chromate or uranyl reduction, one must consider the microbial selection of terminal electron acceptor(s) and the resulting concentration of competing chemical reductants such as Fe(II) or S(-II).

In addition to dissolved reductants of chromate, a number of biogenic solids also may be instrumental reductants. Recent investigations have identified a set of Fe-bearing biogenic minerals formed by the microbial reduction of Fe (hydr)oxides; phases identified include siderite, vivianite, magnetite, and green rust (Fredrickson et al., 1998; Zachara et al., 1998); a host of Fe sulfides also may be produced in environments generating both ferrous Fe and sulfide (see for example Morse et al., 1987). Using calculated rates based on dissolved concentration of ferrous Fe for a system controlled exclusively (and individually) by, and in equilibrium with, the solids green rust 1 (hydroxy), siderite (open and closed systems), and mackinawite, for which dissolved sulfide also was determined, we can estimate the contributions of each to the reduction of chromate compared with expected, microbial enzymatic pathways (Fig. 6–3). Within these assessments, we ignore the unknown contribution of surface reactions and concentrate instead strictly on dissolution of the reductant; only single solids are considered (i.e., our assessment does not consider the minerals simultaneously). Reduction on ferrous bearing surfaces will, however, probably be a major contributor to chromate reduction as Fe(II) on metal hydroxide surfaces is a potent and facile reductant of chromate (Buerge & Hug, 1999).

At no point does the maximum rate of microbial reduction (*D. vulgaris*, Table 6–1), exceed the rates induced by dissolved Fe(II) resulting from the combination of these three solids. Bacterial reduction would only exceed that of dissolved Fe(II)

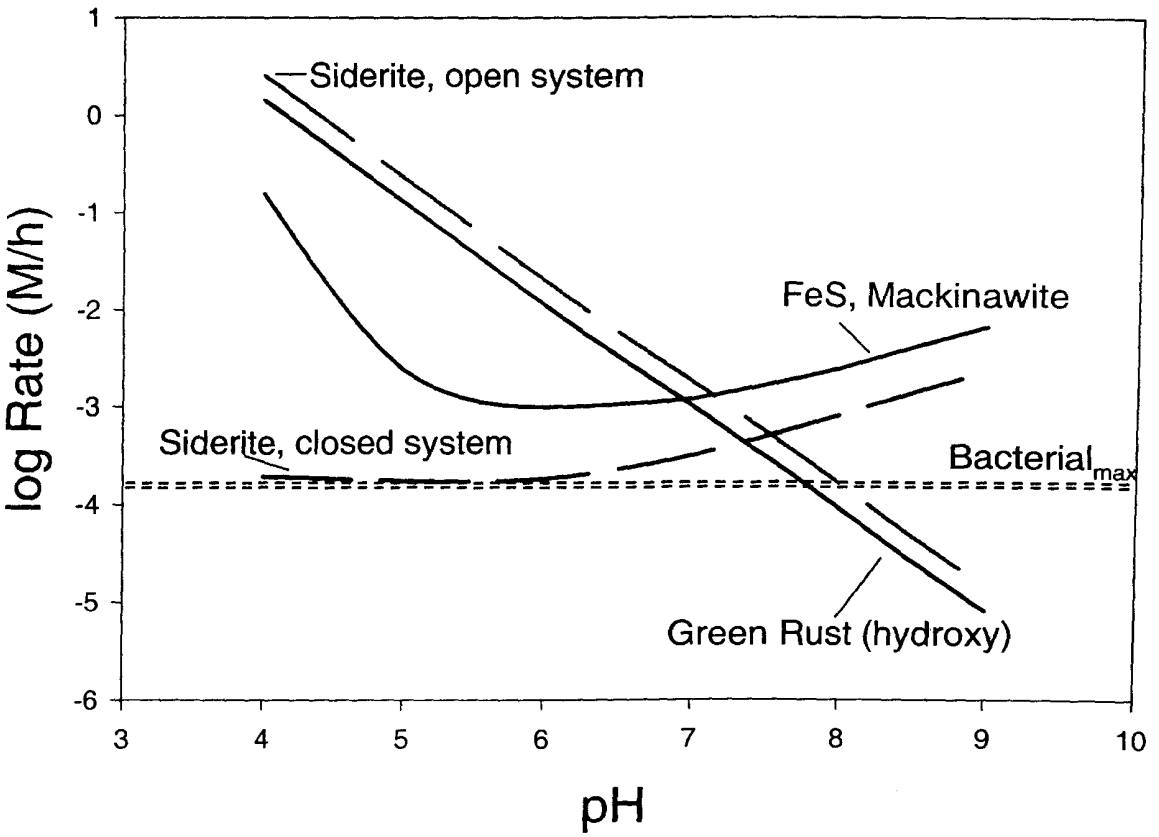

Fig. 6–3. Chromate reduction rates predicted for 100 μ*M* Cr(VI) encountering solutions in equilibrium with the solids siderite, green rust (hydroxy), and mackinawite; calculations are based in individual minerals and not combined suspensions. For siderite, both open ($PCO_2 = 10^{-3.5}$ atm) and closed systems were evaluated. Ferrous Fe was the operating reductant except in the case of mackinawite where dissolved sulfide also served as a reducing agent.

in association with green rust if maximum biological reduction rates could be sustained at pH > 8. While other sinks for Fe(II) exist (e.g., cation exchange sites), dissolved concentrations of Fe(II) in equilibrium with hydroxy green rust have been noted in many anaerobic soils (Ponnamperuma et al., 1967; Bourrie et al., 1999). Furthermore, if one considers the probable acceleration in rates noted for surface associated Fe(II) (Buerge & Hug, 1999), abiotic pathways will probably account for the majority of Cr(III) generated in anaerobic soils. Moreover, in subsurface environments, diminished cell densities coupled with high site density of Fe(II) (or sulfide) should further encourage the abiotic pathway relative to enzymatic reduction.

Chromate Reduction by Biogenic Iron(II)(aq)

On the basis of measured reaction rates, it appears chemical pathways will dominate chromate reduction in anaerobic environments—ferrous Fe at high pH and dissolved sulfide at low pH. Given the ubiquitous distribution of Fe and Fe reducing bacteria, ferrous Fe generated during Fe(III) reduction may serve as a means to reduce chromate and thus control the dissolved concentration of this hazardous species in the majority of anaerobic environments. We examined this premise by conducting flow experiments using a dissimilatory iron reducing bacterium

(DIRB) *S. alga* (BrY) that does not sustain chromate reduction directly (Wielinga et al., 2000).

Ferrous iron generated by BrY during respiration on ferrihydrite should serve as an efficient reductant of chromate. We therefore examined the impact of biogenically produced Fe(II) on chromate reduction under dynamic flow conditions. Prior to the introduction of Cr(VI) to the flow reactor, aqueous concentrations of ferrous Fe increased. Upon continuous addition of chromate to the reaction cell (addition rate equal to one third the initial rate of Fe(II) production), solution concentration of ferrous Fe decreases rapidly (Fig. 6–4); all of the chromate is removed from solution. Increasing the injection rate of chromate until a steady-state of aqueous Fe(II) is achieved provides the maximum sustainable rate of chromate reduction (see regression lines in Fig. 6–4). In systems without the addition of chromate the rate of ferrous Fe production also decreases with time before reaching a plateau at 40 h. Cessation of reduction may be invoked by Fe(II) deposition on reactive sites of ferrihydrite or Fe(II) adsorption on cell surfaces; recent evidence suggests the latter is the operating mechanism of inhibition (Urrutia et al., 1998; Roden et al., 2000).

There are two factors that complicate the assumption of reaching a steady-state in Fe(II) (aq) concentration as a proxy to the chromate reduction rate. First, it is difficult to monitor the concentration of Fe(II) and Cr(VI) present in the solid-phase during the reaction; however, the concentration of $Fe(II)_{(aq)}$ and 0.5 M HCl extractable Fe(II) at the end of the experiment were equivalent, suggesting that Fe(II) was not appreciably sequestered as a surface phase during the reaction. Additionally, neither Fe(II) nor Cr(VI) were detected in the solid-phase using XANES spectroscopy (data not shown). A second complication is the possibility that BrY could reduce chromate directly. In batch reactions, when BrY is added to bicarbonate buffered medium ($\approx 1 \times 10^8$ cells mL^{-1}) containing 0.075 μM chromate, Cr(VI) is

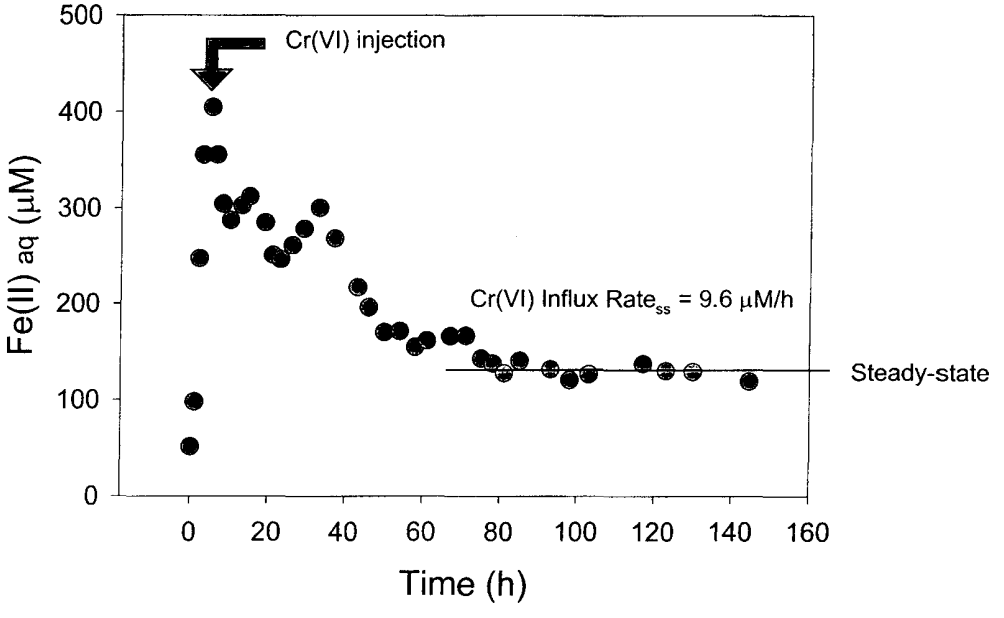

Fig. 6–4. Reduction of chromate by ferrous iron generated from the Fe reducing bacterium *Shewanella alga* BrY in the presence of ferrihydrite. Chromate was continuously injected into the flow cell after ferrous Fe was produced; increasing the rate of injection until a steady-state Fe(II) level was achieved provided a measure of the maximum sustainable reduction rate (steady state regression line).

removed from solution in approximately 0.6 h. When the systems are spiked with additional chromate (0.10 μ*M*), Cr(VI) is again removed from solution in about 1.5 h. Initial Cr(VI) reduction rates calculated under these conditions averaged 1×10^{-4} M h^{-1}, in close agreement with values previously published for bacterial chromate reduction (Fendorf et al., 2000), and considerably slower (by a factor $>10^2$) than those observed for Cr(VI) reduction by Fe(II) (Pettine et al., 1998). The slower reaction kinetics observed for direct Cr(VI) reduction by BrY in conjunction with the dramatic decrease in effluent Fe(II) strongly suggests that Fe(II) is the primary reductant under these conditions.

During the reduction of chromate, ferrous Fe is oxidized back to the ferric state. The reaction sequence for chromate reduction is therefore cyclic in nature. Thus, even limited quantities of reducible ferric Fe in a system may drive the fate of Cr. In fact, Wielinga et al. (2001) demonstrated that Fe can be cycled in the reduction of Cr.

URANIUM REDUCTION REACTIONS

Biologically Induced Uranyl Reduction

Several organisms common to soil and subsurface environments have now been identified that can enzymatically reduce U(VI) to U(IV) under anoxic conditions; rates for many of these organisms are provided in Table 6–2. These include dissimilatory metal-reducing bacteria (DMRB) *Geobacter metallireducens* (Lovley et al., 1991; Gorby & Lovley, 1992), *Shewanella putrefaciens* (Lovley et al., 1991), and *Shewanella alga* strain BrY (Caccavo et al., 1992) as well as sulfate-reducing bacteria (SRB) *Desulfovibrio desulfuricans* (Lovley & Phillips, 1992), *D. vulgaris* (Lovley et al., 1993), and *Desulfotomaculum reducens* sp. nov. strain MI-1 (Tebo & Obraztsova, 1998). Organisms from both groups (i.e., DMRB and SRB) have been shown to obtain energy to support growth via electron transport to U(VI) (Lovley et al., 1991; Tebo & Obraztsova, 1998).

Rates of U(VI) reduction found in the literature for both pure cultures and microbial consortia (Table 6–2) are similar to those reported for Cr(VI) reduction (Table 6–1) and vary from each other by less than a factor of 15; however, one should note that the chemical reduction rates for chromate and uranyl vary appreciably-with chromate reduction being much more rapid. Uranyl reduction rates determined for both *G. metallireducens*, and *S. putrefaciens* (Lovley et al., 1992) also have been compared and are similar to the reduction rate observed with BrY (Truex et al.,

Table 6–2. Bacterial reduction rates (initial) of uranyl by pure and mixed cultures.

Organism	Rate $\times 10^{-4}$, *M* h^{-1}†	Reference
Shewanella alga strain BrY	11.9	Truex et al., 1997
Desulfovibrio desulfuricans	1.5	Spear et al., 1999
SRB consortia	1.2	Spear et al., 1999
Desulfotomaculum reducens	0.74	Tebo & Obraztsova, 1998

† Cumulative rate.

Table 6–3. Maximum velocities obtained for the reduction of chromate and uranyl by different bacterial strains using the Monod approach (data from Gorby, 2000, personal communication).

Metal	*Bacterial strain*	V_{max}, $M\ h^{-1}$, $\times 10^{-4}$
Cr(VI)	CN-32†	0.84
	GS-15‡	0.90
	MR-1§	3.1
	BrY¶	1.3
U(VI)	CN-32†	1.5
	GS-15‡	1.6
	MR-1§	1.8
	BrY¶	1.8

† CN-32, *Shewanella putrefaciens.*
‡ GS-15, *Geobacter metallireducens.*
§ MR-1, *Shewanella putrefaciens.*
¶ BrY, *Shewanella alga.*

1997). Monod kinetic parameters obtained for the reduction of uranyl and chromate (Table 6–3), using lactate as the electron donor, provide maximum enzyme velocities (V_{max}) that are surprising similar (i) to maximum rates for other experimental conditions noted in Table 6–1 and 6–2, and (ii) between different organisms and different electron acceptors—V_{max} differs by less than a factor of four for different organisms and for different TEAs (Gorby, 2000, personal communication).

Thus, it appears that in situ immobilization of toxic metals and radionuclides by microbial reduction is a plausible pathway for contaminant stabilization (Lovley & Phillips, 1992); however, mineral surfaces and the production of biogenic materials may dictate the effectiveness of bacterially mediated metal-reduction processes or the operating mechanism (Tripathi, 1984; Hsi & Langmuir, 1985; Zachara et al., 1989; Mesuere & Fish, 1992; Kent et al., 1994, 1995; Chisholm-Brause et al., 1994; McKinley et al., 1995; Weng et al., 1996). Thus, there exists a need to study the intricate coupling of microbiological and geochemical processes on contaminant reduction.

Chemical Pathways of Uranium(VI) Reduction

The reduction pathways for uranyl contrast with those of chromate. While thermodynamically viable, neither aqueous Fe(II) nor H_2S effectively reduce U(VI) (Liger et al., 1999); however, Fe(II) associated with mineral surfaces (either adsorbed or as a component of the bulk solid) has a more pronounced influence on uranyl reduction. In a recent study, Liger et al. (1999) noted that while dissolved concentrations of uranyl were unchanged in the presence of aqueous Fe(II) during an 80 h reaction period, Fe(II) adsorbed on hematite resulted in complete removal of U(VI) via reduction within 60 h. Using the rate expression developed by Liger et al. (1999), coupled with the most optimistic conditions (saturation of high surface area hematite with ferrous Fe at a pH value of 7.5), we estimate the maximum initial rate of uranyl reduction to be $1.2 \times 10^{-4}\ M\ h^{-1}$; more realistic reaction parameters lead to a predicted rate $<1 \times 10^{-5}\ M\ h^{-1}$. In comparison to microbial reduction rates of uranyl (Table 6–2), hematite catalyzed reduction of uranyl by Fe(II) would result in rates comparable with, but lower than, biological pathways. Well

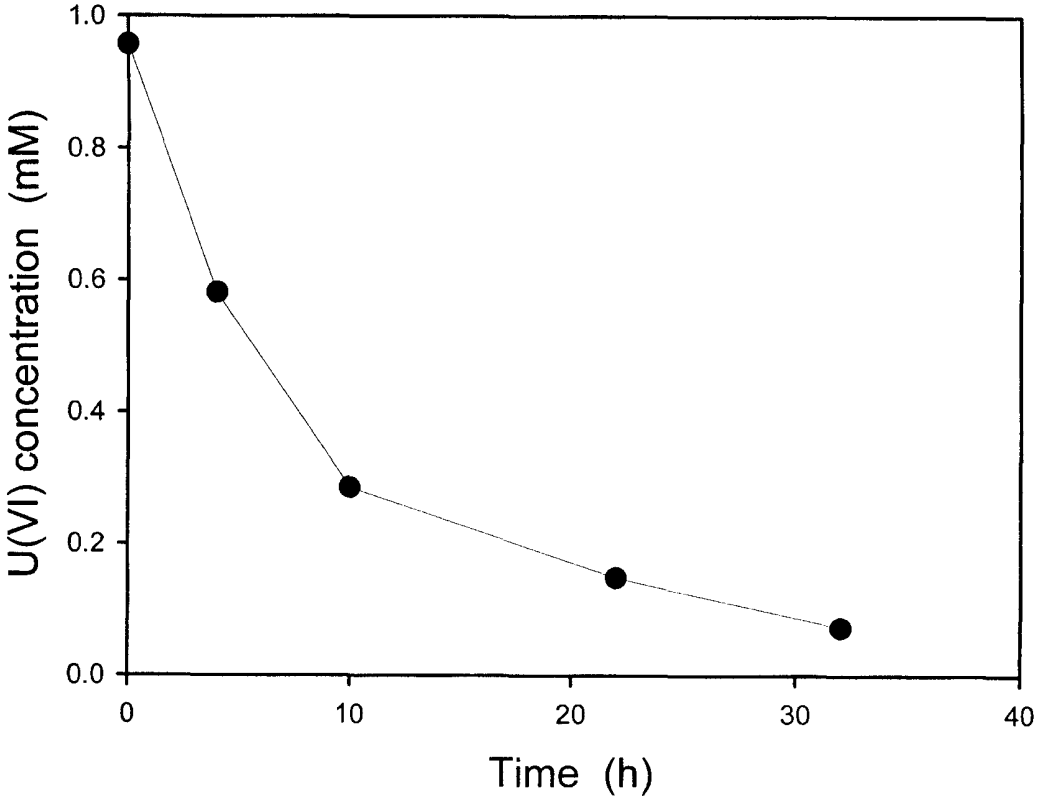

Fig. 6–5.Time-dependent reduction of uranyl in cell suspensions of *Shewanella alga*, strain BrY. Results are means of triplicate cultures; error bars are one standard deviation.

crystallized pyrite and galena, both of geologic origin, also have demonstrated the capacity to reduce U(VI) to U_3O_8 (Wersin et al., 1994). As may be expected for such materials, the reduction rate of both minerals is slow, occurring at rates of approximately 5×10^{-6} and 1×10^{-7} M h^{-1} at pH 5 (initial [U(VI)] = 200 μM, surface area = 50 m^2 dm^{-3}) for pyrite and galena, respectively (Wersin et al., 1994) Therefore, chemical reduction via Fe(II) may contribute to, but is unlikely to dominate, the reduction of uranyl. With that said, it is not inconceivable that a reactive Fe(II)-bearing solid such as green rust or amorphous FeS might provide a more favorable kinetic pathway.

Competing Electron Acceptors

On the basis of the proceeding discussion, it appears that direct biological reduction of uranyl will dominate in natural environments, with absorbed Fe(II) being a potential contributor. A consequence of dissimilatory reduction is the reductive stabilization via formation of the sparingly soluble uraninite phase. The bacterium *Shewanella alga*, strain BrY, typifies the bacterially promoted reductive stabilization process, readily reducing uranyl and forming a U(IV) precipitate (Fig. 6–5; Wielinga et al., 2000); however, one should note that reduction of uranyl by BrY is dependent on U(VI) acting as a terminal electron acceptor and that in natural environments other terminal electron acceptors may be present.

When cell suspensions of BrY encounter uranyl acetate (400 μM) alone or in combination with goethite (1.2 g L^{-1}; ≈11.1 μM U m^{-2} solid), aqueous U(VI) concentrations decreased to <5% of their initial values within 10 h (Fig. 6–6). In con-

trast, when ferrihydrite is present (1.0g L^{-1}; ca. 0.67 μM U m^{-2} solid) a large fraction of the initial U(VI) remained in solution after 10 h (52%), which continues to decline with further reaction (only 35% remains after 46 h). Moreover, increasing the ratio of ferrihydrite relative to goethite promotes Fe reduction relative to uranyl reduction (Wielinga et al., 2000). Under conditions where surface area is equated for the different ferric (hydr)oxides studied, uranyl reduction is again retarded in the presence of ferrihydrite relative to systems with no Fe oxide or with just goethite. Thus, ferric Fe within the short-range order mineral ferrihydrite is used preferentially to uranyl as a terminal electron acceptor by BrY and may impede re-

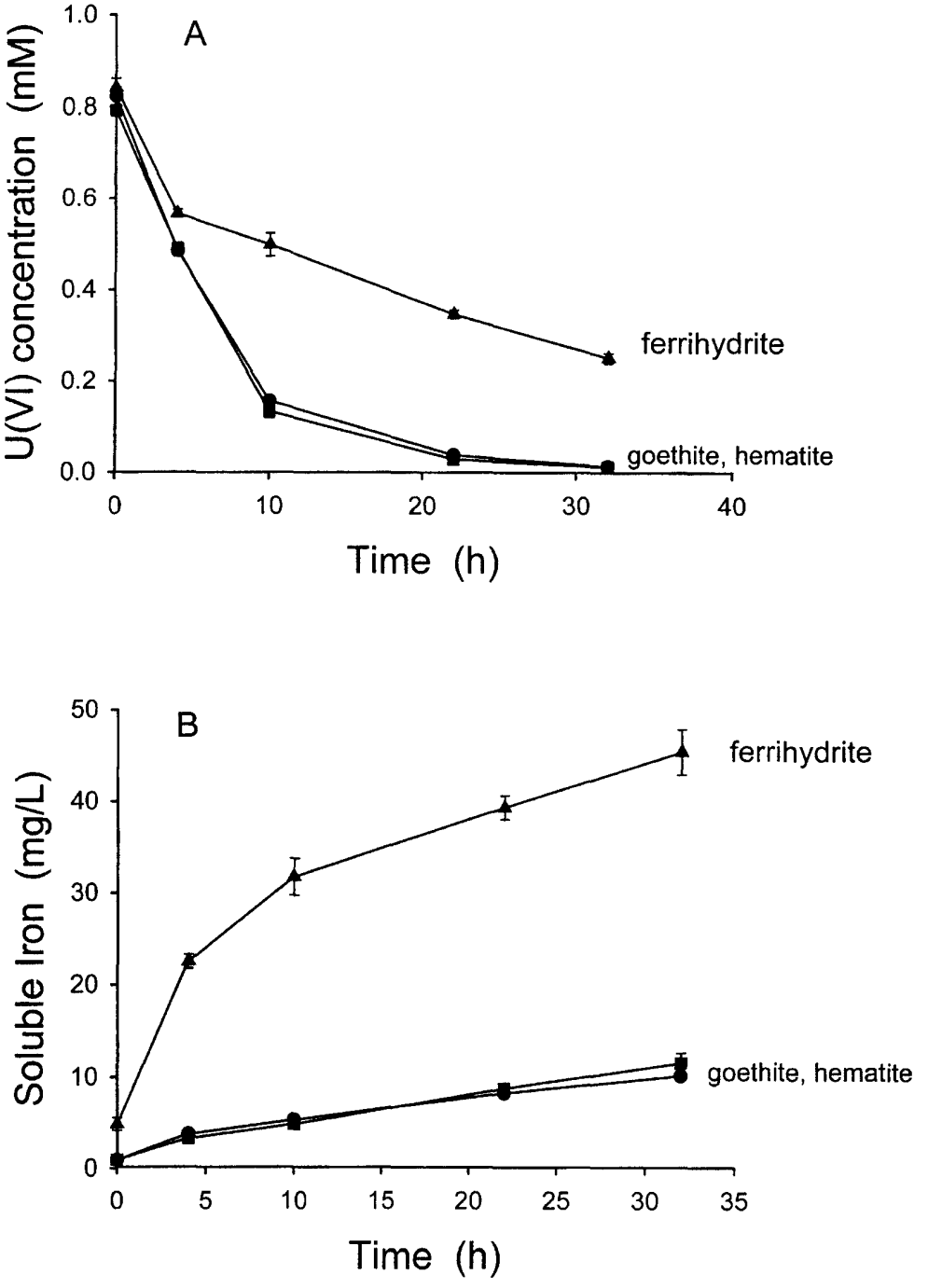

Fig. 6–6. Uranyl reduction by BrY in the presence of the ferric (hydr)oxides ferrihydrite, goethite, and hematite. Data points are the average of three replicates and error bars denote one standard deviation.

ductive stabilization of U; this is not the case for more crystalline solids such as goethite. Thus, although microbially induced reduction of uranyl should transpire, leading to the formation of uraninite, competitive inputs of other electron acceptors such as Fe(III) must be appreciated. The competitive impact of nitrate also has been realized (Achtnich et al., 1995). To ensure reductive stabilization, one must therefore account for the electron accepting capacity of other system constituents that may include molecular O_2, Fe(II I), Mn(IV/III), and nitrate.

CONCLUSIONS

Both biological and chemical (abiotic) pathways exist for the reduction of chromate and uranyl; however, the reaction kinetics for the two broad classes differ appreciably. Reduction of chromate will probably occur through chemical means, albeit that the chemical reactant may result from microbial processes, in anaerobic environments; ferrous Fe will dominate the reduction of chromate at mildly acidic to alkaline pH values while sulfide will dominate at lower pH values given equal availability. The microbial reduction of Fe (hydr)oxides promotes reduction of Cr(VI) to Cr(III)—the result of a coupled, two-step, biotic-abiotic reaction pathway in which Fe(II) produced during Fe respiration catalyzes the reduction of Cr(VI). Thus, attenuation of chromate in saturated soil environments may be in large part attributable to dissimilatory Fe reduction. Enhancing Fe reduction may therefore promote the reductive stabilization of Cr.

In contrast to chromate, biological reduction of uranyl is more rapid and, hence, more pronounced than most of the measured abiotic, naturally occurring reductants. Numerous microorganisms have demonstrated the capacity to reduce uranyl including dissimilatory metal-reducing and sulfate-reducing bacteria; however, reduction is dependent on uranyl acting as the terminal electron acceptor and thus other possible TEAs may compete, limiting the effective reduction of this hazardous element. For example, amorphous Fe hydroxides can compete with uranyl as TEAs and thereby retard its reduction in the case of Fe reducing bacteria. By contrast, sulfate reduction does not inhibit the enzymatic reduction of uranyl by *Desulfovibrio desulfurican* (Lovley & Phillips, 1992). Nevertheless, one needs to consider not only the operating reaction pathways in pristine systems but also completing reactions within complex natural environments.

ACKNOWLEDGMENTS

This research was funded by the Natural and Accelerated Bioremediation Research (NABIR) program, Biological and Environmental Research (BER), U.S. Department of Energy (grant no. DE-FG03-00ER63029).

REFERENCES

Abdelouas A., Y. Lu, W. Lutze, and H.E. Nuttal. 1998. Reduction of U(VI) to U(IV) by indigenous bacteria in contaminated ground water. J. Contam. Hydrol. 35:217–233.

Achtnich, C., F. Bak, and R. Conrad. 1995. Competition for electron donors among nitrate reducers, ferric iron reducers, sulfate reducers, and methanogens in anoxic paddy soil. Biol. Fertil. Soils 19:65–72.

Anderson, L.D., D.B. Kent, and J.A. Davis. 1994. Batch experiments characterizing the reduction of Cr(VI) using suboxic material from a mildly reducing sand and gravel aquifer. Environ. Sci. Technol. 28:178–185.

Balch, W.E., G.E. Fox, L.J. Magrum, C.R. Woese, and R.S. Wolfe. 1979. Methanogens: Reevaluation of a unique biological group. Microbiol. Rev. 43:260–296.

Bartlett R.J., and B. James. 1979. Behavior of Chromium in soils: III. Oxidation. J. Environ. Qual. 8:31–35.

Bartlett, R.J., and J.M. Kimble. 1976. Behavior of chromium in soils: II. Hexavalent forms. J. Environ. Qual. 5:383–386.

Bourrie, G., F. Trolard, J.-M.R. Genin, A. Jafrezic, V. Maitre, and M. Abdelmoula. 1999. Iron control by equilibria between hydroxy-green rusts and solutions in hydromorphic soils. Geochim. Cosmochim. Acta. 63:3417–3428.

Brauer, S.L., A.S. Hneihen, K.E. Wetterhahn. 1996. Chromium(VI) forms thiolate complexes with gamma-glutamylcysteine, N-acetylcysteine, cysteine, and the methyl ester of n-acetylcysteine. Inorg. Chem. 35:373.

Buerge, I.J., and S.J. Hug. 1999. Influence of mineral surfaces on Cr(VI) reduction by iron(II). Environ. Sci. Technol. 33:4285–4291.

Caccavo, F., Jr., R. P. Blakemore, and D. R. Lovley. 1992. A hydrogen-oxidizing, Fe(III)-reducing microorganism from the Great Bay Estuary, New Hampshire. Appl. Environ. Microbiol. 58:3211–3216.

Chisholm-Brause, C., S.D. Conradson, C.T. Buscher, P.G. Eller, and D.E. Morris. 1994. Speciation of uranyl sorbed at multiple binding sites on montmorillonite. Geochim. Cosmochim. Acta. 58:3625–3631.

Cooke, V.M., M.N. Hughes, R.K. Poole. 1995. Reduction of chromate by bacteria isolated from the cooling water of electricity generating station. J. Indust. Microbiol. 14:323–328.

Deng, B., and A.T. Stone. 1996. Surface-catalyzed Cr(VI) reduction: Reactivity comparisons of different organic reductants and different oxide surfaces. Environ. Sci. Technol. 30:2484–2494.

Duff, M.C., D.B. Hunter, P.M. Bertsch, and C. Amrhein. 1999. Factors influencing uranium reduction and solubility in evaporation pond sediments. Biogeochemistry 45:95–114.

Eary, L.E., and D. Rai. 1988. Chromate removal from aqueous wastes by reduction with ferrous ion. Environ. Sci. Technol. 22:972–977.

Eary, L.E., and D. Rai. 1989. Kinetics of chromate reduction by ferrous ions derived from hematite and biotite at 25°C. Am. J. Science 289:180–213.

Eary, L.E., and R. Rai. 1991. Chromate reduction by subsurface soils under acidic conditions. Soil Sci. Soc. Am J. 55:676–683.

Elovitz, M.S., and W. Fish. 1995. Redox interactions of Cr(VI) and substituted phenols: Products and mechanism. Environ. Sci. Technol. 29:1933–1943.

Fendorf, S.E., M. Fendorf, D.L. Sparks, and R. Gronsky. 1992. Inhibition mechanisms of Cr(III) oxidation by manganese oxides. J. Colloid Interface Sci. 148:37–54.

Fendorf, S.E., and G.C. Li. 1996. Kinetics of chromate reduction by aqueous Fe(II). Environ. Sci. Technol. 30:1614–1617.

Fendorf, S., B.W. Wielinga, and C.M. Hansel. 2000. Chromium transformations in natural environments: The role of biological and abiological processes in chromium(VI) reduction. Int. Geol. Rev. 42:691–701.

Fredrickson, J.K., J.M. Zachara, D.W. Kennedy, H. Dong, T.C. Onstott, N.W. Hinman, and S.-M. Li. 1998. Biogenic iron mineralization accompanying the dissimilatory reduction of hydrous ferric oxide by groundwater bacterium. Geochim. Cosmochim. Acta 62:3239–3258.

Fredrickson, J.K., J.M. Zachara, D.W. Kennedy, M.C. Duff, Y.A. Gorby, S.M.W. Li, and K.M. Krupka. 2000. Reduction of uranium(VI) in goethite (α-FeOOH) suspensions by a dissimilatory metal-reducing bacterium. Geochim. Cosmochim. Acta 64:3085–3098.

Fude, L., B. Harris, M.M. Urrutia, and T.J. Beveridge. 1994. Reduction of chromium(VI) by a consortium of sulfate-reducing bacteria (SRB III). Appl. Environ. Microbiol.60:1525–1531.

Garbisu, C., I. Alkorta, M.J. Llama, and J.L. Serra.1998. Aerobic chromate reduction by *Bacillus subtilis*. Biodegradation 9:133–141.

Gopalan, R., and H. Veeramani. 1994. Studies on microbial chromate reduction by *Pseudomonas sp.* in aerobic continuous suspended growth cultures. Biotech. Bioeng.43:471–476.

Gorby, Y.A., and D.R. Lovley. 1992. Enzymatic uranium precipitation. Environ. Sci. Technol. 26:205–207.

Gvozdyak, P.I., N.F. Mogilevich, A.F. Ryl'skii, and N.I. Grishchenko. 1986. Reduction of hexavalent chromium by collection strains of bacteria. Mikrobiologiya 55:962–965.

Hardoyo, J. Kato, and H. Ohtake. 1991. Effects of heavy metal cations on chromate reduction by Enterobacter cloacae HO1. J. Gen. Appl. Microbiol. 37:519–522.

Hsi, C.K.D., and D. Langmuir. 1985. Adsorption of uranyl onto ferric oxyhydroxides: Application of the surface complexation site-binding model. Geochim. Cosmochim. Acta.49:1931–1941.

Ishibashi, Y., C. Cervantes, and S. Silver. 1990. Chromium reduction in *Pseudomonas putida*. Appl. Environ. Microbiol. 56:2268–2270.

James, B.R., and R.J. Bartlett. 1983. Behavior of chromium in soils: VII. Adsorption and reduction of hexavalent forms. J. Environ. Qual. 12:177–181.

Johnson, D.A., and T. Florence. A specific and quantitative colorimetric measurement for hexavalent uranium. 1971. M. Anal. Chim. Acta. 53:73–79.

Kent, D.B., J.A. Davis, L.C.D. Anderson, and B.A. Rea. 1994. Transport of chromium and selenium in the suboxic zone of a shallow aquifer: Influence of redox and adsorption reactions. Water Resour. Res. 30:1099–1114.

Kent, D.B., J.A. Davis, L.C.D. Anderson, and B.A. Rea. 1995. Transport of chromium and selenium in a pristine sand and gravel aquifer: Role of adsorption processes. Water Resour. Res. 31:1041–1050.

Kvasnikov, E.I., V.V. Stepanyuk, T.M. Klyushnikova, and N.S. Serpokrylov. 1985. New gram–variable bacterium which reduces chromium and has a mixed type of flagellation. Mikrobiologiya. 54:83–88.

LaForce, M.J., and S. Fendorf. 2000. Solid-phase iron characterization during common selective sequential extractions. Soil Sci. Soc. Am. J. 64:1608–1615.

Lay, P.A., and A. Levina. 1996. Kinetics and mechanism of chromium(VI) reduction to chromium(III) by L-cysteine in neutral aqueous solutions. Inorg. Chem. 35:7709–7715.

Lebedeva, E.V., and N.N. Lyalikova. 1979. Reduction of crocoite by *Pseudomonas chromatophila* species *nova*. Mikrobiologiya. 48:517–522.

Liger, E., L. Charlet, and P. van Capppellen. 1999. Surface catalysis of uranium(VI) reduction by iron(II). Geochim. Cosmochim. Acta 63:2939–2955.

Llovera, S., R. Bonet, M.D. Simon-Pujol, and F. Congregado.1993.Chromate reduction by resting cells of *Agrobacterium radiobacter* EPS-916. Appl. Environ. Microbiol. 59:3516–3518.

Losi, M.E., C. Amrhein, and W.T. Frankenberger, Jr. 1994. Bioremediation of chromate-contaminated groundwater by reduction and precipitation in surface soils. J. Environ. Qual. 23:1141–1150.

Lojou, E., P. Bianco, and M. Bruschi. 1998. Kinetic studies on the electron transfer between bacterial c-type cytochromes and metal oxides. J. Electroanal. Chem. 452:167–177.

Lovley, D.R. 1991. Dissimilatory Fe(III) and Mn(IV) reduction. Microbiol. Rev. 55:259–287.

Lovley, D.R. 1993. Dissimilatory metal reduction. Annu. Rev. Microbiol. 47:263–290.

Lovley, D.R., and E.J.P. Phillips. 1986. Organic matter mineralization with reduction of ferric iron in anaerobic sediments. Appl. Environ. Microbiol. 51:683–689.

Lovley, D.R., and E.J.P. Phillips. 1992. Bioremediation of uranium contamination with enzymatic uranium reduction. Environ. Sci. Technol. 26:2228–2234.

Lovley, D.R., and E.J.P. Phillips. 1994. Reduction of chromate by *Desulfovibrio vulgaris* and its c_3 cytochrome. Appl. Environ. Microbiol. 60:726–728.

Lovley, D.R., E.J. Phillips, and D.L. Lonergan. 1991. Enzymatic versus nonenzymatic mechanisms for Fe(III) reduction in aquatic sediments. Environ. Sci. Technol. 25:1062–1067.

Masscheleyn, P.H., J.H. Pardue, R.D. DeLaune, and W.H. Patrick, Jr. 1992. Chromium redox chemistry in a lower Mississippi valley bottomland hardwood wetland. Environ. Sci. Technol. 26:1217–1226.

McKinley, J.P., J.M. Zachara, S.C. Smith, and G.D. Turner. 1995. The influence of uranyl hydrolysis and multiple site-binding reactions on adsorption of U(VI) to montmorillonite. Clays Clay Mineral. 43:586–598.

Mesuere, K., and W. Fish. 1992. Chromate and oxalate adsorption on goethite: 1. Calibration of surface complexation models. Environ. Sci. Technol. 26:2357–2364.

Morse, J.W., F.J. Millero, J.C. Cornwell, and D. Rickard. 1987. The chemistry of the hydrogen sulfide and iron sulfide systems in natural waters. Earth Sci. Rev. 24:1–42.

National Research Council. 1974. Committee on biologic effects of atmospheric pollutants. Natl. Academy of Sci., Washington, DC.

Park, C.-H., M. Keyhan, B. Wielinga, S. Fendorf, and A. Matin. 2000. Purification to homgeneity and characterization of a novel *Pseudomonas putida* chromate reductase. Appl. Environ. Microbiol. 66:1788–1795.

Patterson, R.R., S.E. Fendorf, and M.J. Fendorf. 1997. Reduction of chromate by amorphous iron sulfide. Environ. Sci. Technol. 31:2039–2044.

Peterson, M.L., A.F. White, G.E. Brown, Jr., and G.A. Parks. 1997. Surface passivation of magnetite by reaction with aqueous Cr(VI):XAFS and TEM results. Environ. Sci. Technol. 31:1573–1576.

Pettine, M., F.J. Millero, and R. Passino. 1994. Reduction of Cr (VI) with hydrogen sulfide in NaCl media. Mar. Chem. 46:335–344.

Pettine, M., L.D. Ottone, L. Campanella, F.J. Millero, and R. Passino. 1998. The reduction of Cr (VI) by iron (II) in aqueous solutions. Geochim. Cosmochim. Acta 62:1509–1520.

Ponnamperuma, F.N, E.M. Tianco, and T. Loy. 1967. Redox equilibria in flooded soils: The hydroxide systems. Soil Sci. 103:374–381.

Riley, R.G., and J.M. Zachara. 1992. Chemical contaminants on DOE lands and selection of contaminant mixtures for subsurface science research. DOE/ER-0547T. U.S. Gov. Print. Office, Washington, DC.

Roden, E.E., and M.M. Urrutia. 2000. Ferrous iron removal promotes microbial reduction of crystalline iron (III) oxides. Environ. Sci. Technol. 34:1847–1853.

Romananko, V.I., and V.N. Korenkov. 1977. A pure culture of bacteria utilizing chromates and bichromates as hydrogen acceptors in growth under anaerobic conditions. Mikrobiologiya. 46:414–417.

Rusin, P.A., L. Quintana, J.R. Brainard, B.A. Strietelmeier, C.D. Tait, S.A. Ekberg, P.D. Palmer, T.W. Newton, and D.L. Clark. 1994. Solubilization of plutonium hydrous oxide by iron-reducing bacteria. Environ. Sci. Technol. 28:1686–1690.

Sass, B.M., and D. Rai. 1987. Solubility of amorphous Cr(III)-iron(III) hydroxide solid solutions. Inorg. Chem. 26:2228–2232.

Schmieman, E.A., J.N. Petersen, D.R. Yonge, D.L. Johnstone, Y. Bereded-Samuel, W.A. Apel, and C.E. Turick.1997. Bacterial reduction of chromium. Appl. Biochem. Biotechnol. 63–65:855–864.

Shen, H., and Y.T. Wang. 1994. Biological reduction of Cr by *E. coli*. J. Environ. Eng. 120:560–572.

Smith, R.M., and A.E. Martell. 1982. Critical stability constants. Vol. 5. First Supplement. Plenum Press.

Spear, J.R., L.A. Figueroa, and B.D. Honeyman. 1999. Modeling the removal of U(VI) from aqueous solutions in the presence of sulfate reducing bacteria. Environ. Sci. Technol. 33:2667–2675.

Stookey, L.L. 1970. Ferrozine: A new spectrophotometric reagent for iron. Anal. Chem. 42:779–781.

Tebo, B.M., and A.Y. Obraztsova. 1998. Sulfate-reducing bacterium grows with Cr(VI), U(VI), Mn(IV) and Fe(III) as electron acceptors. FEMS Microbiol. Letters 162:193–198.

Tripathi, V.S. 1984. Uranium (VI) transport modeling: Geochemical data and submodels. Ph.D. Diss. Stanford Univ., Stanford, CA.

Truex, M.J., B.M. Peyton, N.B. Valentine, and Y.A. Gorby. 1997. Kinetics of U(VI) reduction by a dissimilatory Fe(III)-reducing bacterium under non-growth conditions. Biotechnol. Bioeng.55:490–496.

Turner, M.A., and R.H. Rust. 1971. Effects of chromium on growth and mineral nutrition of soybeans. Soil Sci. Soc. Am. Proc. 35:755–758.

Turick, C.E., W.A. Apel, and N.S. Carmiol. 1996. Isolation of hexavalent chromium-reducing anaerobes from hexavalent-chromium-contaminated and noncontaminated environments. Appl. Microbiol. Biotechnol. 44:683–688.

Urrutia, M.M., E.E. Roden, and J.M. Zachara. 1998. Microbial and surface controls on reduction of synthetic Fe(III) oxide minerals by the dissimatory iron-reducing bacterium shewanella alga. Geomicrobiol. J. 15:269–276.

U.S. Department of Energy, Office of Environmental Management.1995.Technology summary reports. Contaminant Plumes Containment and Remediation. DOE/EM-0248. U.S. Department of Energy, Washington, DC.

U.S. Environmental Protection Agency. 1978. Review of the environmental effects of pollutants: III. USEPA Rep.600/1-78-023. U.S. Dep. of Commerce, Springfield, VA.

Venitt, S., and L.S. Levy. 1974. Mutagenicity of chromates in bacteria and its relevance to chromate carcinogenesis. Nature 250:493–495.

Wang, P., T. Mori, K. Komori, M. Sasatsu, M. Toda, and H. Ohtake. 1989. Isolation and characterization of an *Enterobacter cloacae* strain that reduces hexavalent chromium under anaerobic conditions. Appl. Environ. Microbiol. 55:1665–1669.

Wang, P.C., M. Toda, H. Ohtake, I. Kusaka, and I. Yabe. 1991. Membrane-bound respiratory system of *Enterobacter cloacae* strain HO1 grown anaerobically with chromate. FEMS Microbiol. Lett. 78:11–16.

Wang, Y.T., and H. Shen. 1995. Bacterial reduction of hexavalent chromium. J. Ind. Microbiol.14:159–163.

Wang, Y.T., and C. Xiao. 1995. Factors affecting hexavalent chromium reduction in pure cultures of bacteria. Wat. Res. 29:2467–2474.

Weng, C.H., C.P. Huang, H.E. Allen, P.B. Leavens, and P.F. Sanders.1996.Chemical interactions between Cr(VI) and hydrous concrete particles. Environ. Sci. Technol. 30:371–376.

Wersin, P., M.F. Hochella Jr., P. Persson, G. Redden, J.O. Leckie, and D.W. Harris. 1994. Interaction between aqueous U(VI) and sulfide minerals: Spectroscopic evidence for sorption and reduction. Geochim. Cosmochim. Acta 58:2929–2943.

Wielinga, B.W., B. Bostick, R.F. Rosenzweig, and S. Fendorf.2000.Inhibition of bacterially promoted U reduction: Ferric (hydr)oxides as competitive electron acceptors. Environ. Sci. Technol. 34:2190–2195.

Wielinga, B.W., M.M. Mizuba, C.M. Hansel, and S. Fendorf. 2001. Iron catalyzed reduction of chromate by dissimilatory iron-reducing bacteria. Environ. Sci. Technol. 35:522–527.

Wittbrodt, P.R., and C.D. Palmer. 1995. Reduction of chromium(VI) in the presence of excess fulvic acid. Environ. Sci. Technol. 29:255–263.

Zachara, J.M., C.C. Ainsworth, C.E. Cowan, and C.T. Resch. 1989. Adsorption of chromate by subsurface soil horizons. Soil Sci. Soc. Am. J. 53:418–428.

Zachara, J.M., J.K. Fredrickon, S.-M. Li, D.W. Kennedy, S.C. Smith, and P.L Gassman. 1998. Bacterial reduction of crystalline Fe^{3+} oxides in single phase suspensions and subsurface materials. Am. Mineral. 83:1426–1443.

Zhang, C., S. Lui, and T.J. Phelps. 1996. Enhancement of Fe(III), Co(VI), and Cr(VI) reduction at elevated temperatures and by a thermophilic bacterium. Appl. Biochem. Biotechnol. 57/58:923–932.

7 Colloid Properties and Their Effects on Radionuclide Transport through Soils and Groundwaters

Bruce D. Honeyman

Colorado School of Mines
Golden, Colorado

James F. Ranville

Colorado School of Mines
Golden, Colorado

ABSTRACT

The transport of colloids through soils and groundwaters has been well established through both laboratory and field studies; however, while the potential transport of contaminants by colloids has been the subject of much speculation, such transport in the field has not been unequivocally demonstrated. This chapter describes the conditions necessary for colloid-facilitated contaminant transport to exist, given that colloid transport, itself, is occurring. The focus of this chapter is on the colloid-facilitated transport of contaminants that are, at least in principle, capable of partitioning among phases (i.e., pseudocolloids vs. intrinsic colloids). The discussion in this chapter shows that the range of three-phase system (immobile, colloid, and aqueous phases) properties required to foster colloid-facilitated contaminant transport is quite narrow. Consequently, colloid-facilitated contaminant transport will occur only under relatively rare geochemical conditions.

The idea that colloidal forms of contaminants may exhibit enhanced transport through geologic media, relative to dissolved forms, has been the subject of much concern and debate for the last 15 or so years. It is interesting that a phenomenon so generally accepted in principle, and subjected to such intense scrutiny, should have yielded so little incontrovertible evidence at scales of interest, i.e., the field.

The colloid problem is composed of a number of elements, including: (i) the identification, isolation, and characterization of colloidal materials from target environments; (ii) the development of predictive models for colloid release, transport, and deposition; (iii) the characterization of interactions between radionuclides and colloids (sorptive processes for pseudocolloids, radionuclide solubility for intrin-

 Geochemistry of Soil Radionuclides. SSSA Special Publication no. 59.

sic colloids); (iv) the acquisition of data and a theoretical framework for radionuclide transport in three-phase systems (i.e., colloidal, immobile, and aqueous phases); (v) the development of methodologies for upscaling radionuclide and colloid transport parameters from the scale of experiment to environmentally-appropriate scales; and (vi) the planning and execution of colloid–radionuclide transport experiments at intermediate scales (e.g., 10–100 m). These aspects contributing to colloid-mediated radionuclide retention–transport are understood to varying degrees.

During the last five or so years, several excellent review articles have been published on the behavior of colloids in subsurface systems. Of particular note are reviews by Ryan and Elimelech (1996) and Kretzchmar et al. (1999). Our goal in writing this chapter is not to provide an exhaustive review of the most recent literature but to explore some characteristics of the phenomena of colloid-facilitated contaminant transport and to arrive at a general assessment as to the system conditions under which colloid-facilitated contaminant transport is likely to take place. Although we will be focusing on radionuclides as contaminants, the general conclusions of this chapter should be applicable to nonradioactive metal-ions and organic contaminants.

PRINCIPLES OF COLLOID-FACILITATED CONTAMINANT TRANSPORT

While many details of colloid-facilitated contaminant transport need to be resolved, several principles of the phenomena can be outlined (modified from Kretzschmar et al., 1999):

1. Colloids must be able to effectively compete against immobile-phase solids for the contaminant;
2. Colloids must be transported over substantial distances (i.e., slow deposition rates); and,
3. Because transport by colloids will be limited, the contaminant must have adverse health effects at low concentrations–activities.

Point one has two subprinciples:

1a. Colloids must be present in sufficient concentrations; and,
1b. Contaminants must strongly sorb to, and slowly desorb from, colloids.

The following sections describe some of the attributes of Points 1 and 2, above. Point 3 is not considered, here. It should be noted that in the following we will be providing some general arguments regarding the nature of colloid-facilitated contaminant transport. Again, our aim is not to be exhaustive in covering the literature but to provide some additional perspectives on the problem.

RADIONUCLIDE PARTITIONING IN TWO- AND THREE-PHASE SYSTEMS

In a simple two-phase system (Fig. 7–1), the mobility of a contaminant depends on the distribution of the contaminant between an immobile phase (e.g.,

aquifer solids) and a mobile aqueous phase. Numerous books and articles describe this process. At its simplest, the transport of a contaminant in such a two-phase system can be described by the following expression

$$(\overline{v}_w/\overline{v}_c) = R_f = 1 + (K_d\rho/\theta) \quad [1]$$

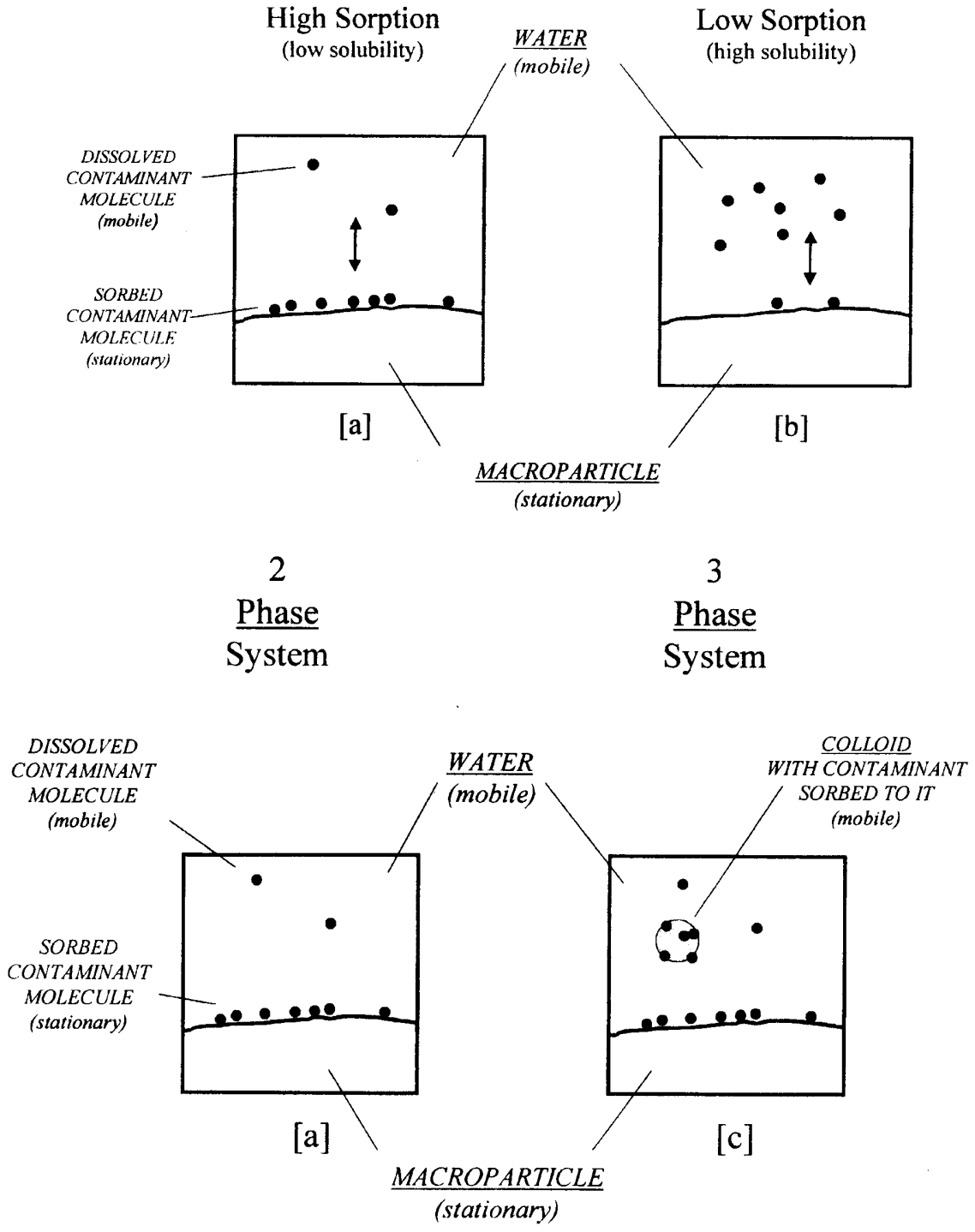

Fig. 7.1. Comparison of two- and three-phase systems. (a) Two-phase system: high K_d element; (b) two-phase system: low K_d element; (c) three-phase system: the presence of the colloidal particles acts to enhance the mobile concentration of the low K_d element (Honeyman, 1996).

where $\overline{v}_w$ and $\overline{v}_c$ are the average groundwater and contaminant velocities, respectively, and ρ and θ are the bulk density and porosity of the immobile phase (IP). K_d is a sorption parameter with the dimensions of reciprocal bulk density (e.g., $L\,kg^{-1}$). As is clear from Eq.[1], a substance that interacts with the immobile phase (i.e., that resides for some time on the immobile phase), will have an average velocity less than the average velocity of the mobile aqueous phase. That is, it will be retarded. The more strongly a contaminant interacts with the IP (1a vs. 1b) the smaller the average contaminant velocity.

The implication of a second mobile phase, i.e., a colloidal phase, came from the need to reconcile observations of the apparent accelerated transport of strongly sorbing contaminants with expectations of transport based on two-phase partitioning (e.g., McCarthy & Zachara, 1989; Buddemeier & Hunt, 1988). Evaluating the system as a whole with respect to contaminant transport, the presence of a colloid has the effect of increasing the mobile concentration of the contaminant. If the colloid phase is undetected, which was the case for many years when simple operational definitions of dissolved and sorbed were routinely used (e.g., see Honeyman & Santschi, 1989), colloids have the effect of decreasing the *apparent* value of the sorption coefficient, K_d (and apparently enhanced contaminant transport).

Figure 7–2 is a schematic illustration of the sorption interactions that we will be considering for our simple three-phase system. For illustration here, the system

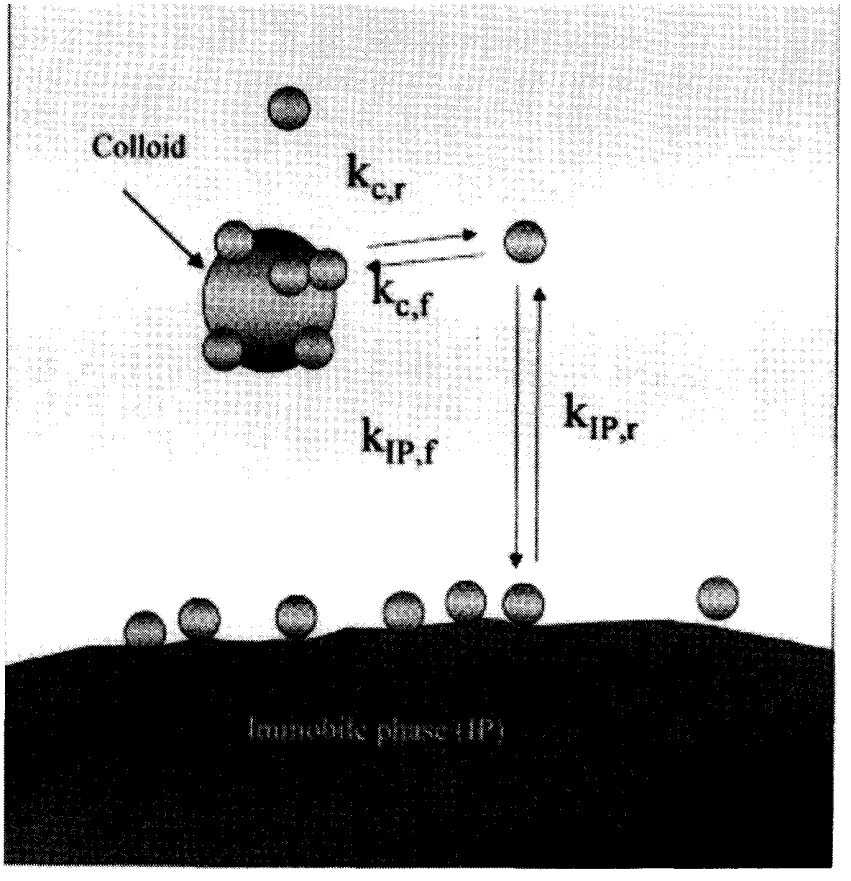

Fig. 7–2. Schematic illustration of the interactions relevant for Point 1 of the Principles of Colloid Facilitated Contaminant Transport. The small spheres represent a target radionuclide and the large sphere is a colloid. Subscripts *f* and *r* designate forward and reverse rate constants, respectively. Colloid deposition is not considered in this diagram.

consists of three phases: (i) an immobile phase consisting of soil or aquifer materials, (ii) an aqueous phase, and (iii) the colloid phase. $k_{IP,f}$ and $k_{IP,f}$ represent sorption and desorption rate constants, respectively, for the contaminant interacting with the immobile phase. The analogous constants for the sorption and desorption of the contaminant with respect to the colloid phase are $k_{c,f}$ and $k_{c,f}$. Initially we will consider radionuclide partitioning in systems at sorptive equilibrium. Thus, the sorption coefficients for the interaction of the target contaminant with the immobile- and colloid-phases are K_{IP} and K_c, respectively.

As will be discussed in more detail later, most evidence suggests that the chemical nature of the colloids and the immobile phases is similar (e.g., McCarthy & Degueldor, 1993), at least for most natural systems. Similarity of colloids and immobile phase sorptive properties in a three-phase system we define here as a *symmetrical* system. It is likely, though, that processes occurring in a waste repository (e.g., corrosion of waste containers) will result in the generation of colloids with physicochemical properties markedly different from those of the immobile phase. Such a system is defined accordingly an *asymmetrical* system.

Partitioning Calculations: Examples of Symmetrical and Asymmetrical Systems

Partitioning in Batch Systems

Figure 7–3 compares radionuclide partitioning to colloids in hypothetical symmetrical (Fig. 7–3a) and asymmetrical (Fig. 7–3b) systems (Honeyman, 1999a). The geometric characteristics of the two systems are identical; only the chemical identity of the immobile phase (IP) is different (Table 7–1). The radionuclide–colloid partitioning parameter is dimensioned in terms of reciprocal area concentration (Pabalan et al., 1998) (e.g., L m^{-2}).

The analysis is based on a mass balance for metal-ion partitioning in a three-phase system:

$$M_T = [M_c] + [M_{IP}] + [M_d] \qquad [2]$$

$$f_c = \frac{[M_c]}{M_T = [M_c] + [M_{IP}] + [M_d]} = \frac{K_c S_c}{1 + K_c S_c + K_{IP} S_{IP}} \qquad [3]$$

where f_c is the fraction of M (the target metal ion) associated with the colloid phase. The subscripts IP, c and d represent the immobile-, colloid-, and dissolved-phases, respectively. K_c and K_{IP} are metal-ion partitioning coefficients (dm^3 m^{-2}) and S is surface area concentration (m^2 dm^{-3}). If, for a given surface type, K_c and K_{IP} are not dependent on system geometry, then f_c will solely be a function of the ratio of S_c to S_{IP}. For many systems, the crucial factor in determining the amount of M associated with colloids is the colloid concentration. In the case of intrinsic colloids (e.g., $PuO_2(s)$), $f_c = 1$ (or $[M_{IP}]$ and $[M_d] = 0$).

The sorbates in Fig. 7–3 range from Th(IV) to Cs. Th(IV) is considered to be one of the strongest sorbing of the light actinides, with K_d values often exceeding 10^6 l kg^{-1} (Honeyman et al., 1988); Cs typically has K_d values in the range from

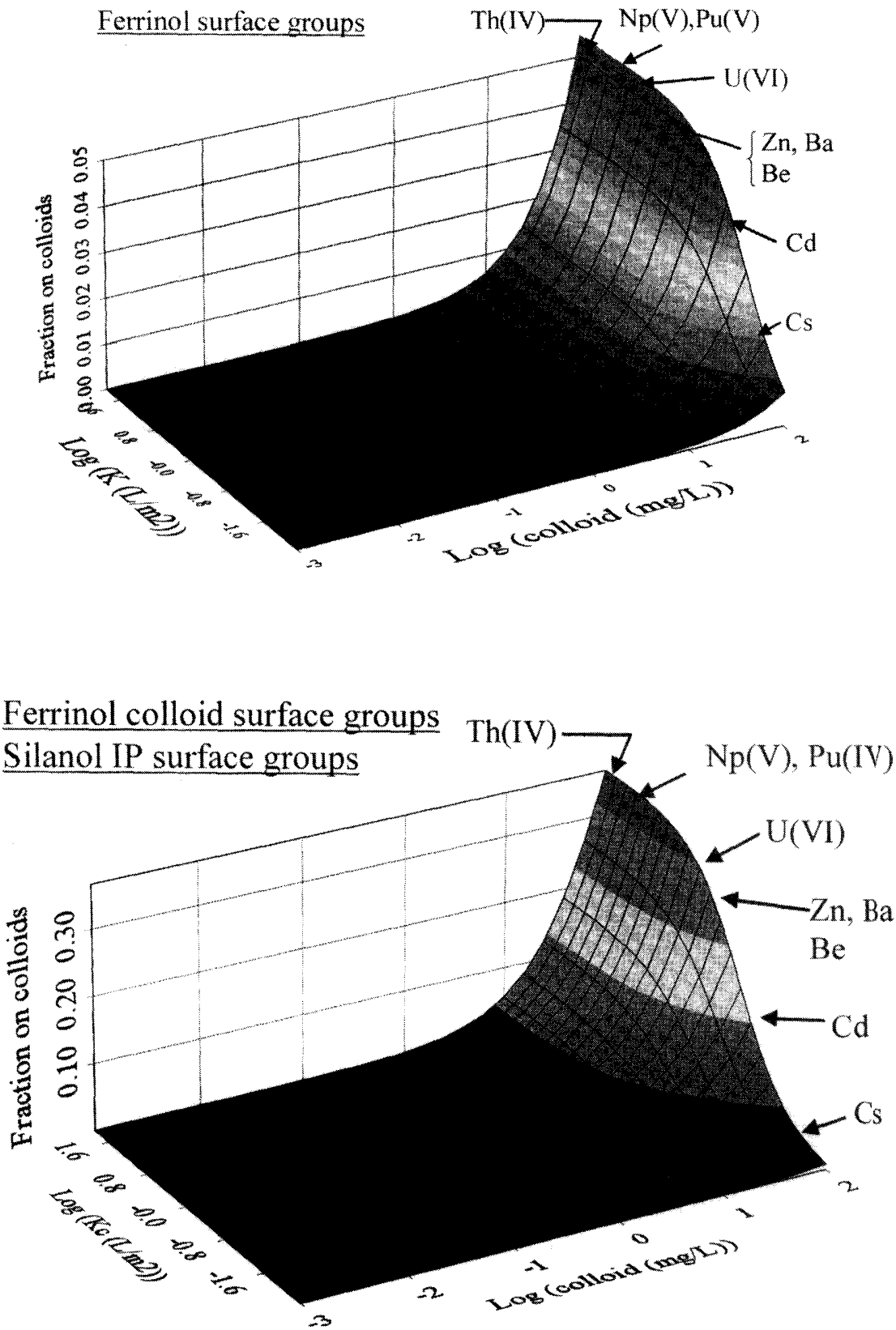

Fig. 7–3. Hypothetical partitioning (Honeyman, 1999a) of selected metals between a stationary aquifer phase (porosity = 0.4, particle size = 0.3 mm, surface area 30 $m^2\ m^{-3}$) and a colloid phase (17 $m^2\ g^{-1}$, colloid diameter = 70 nm). (a) The site types for both the immobile- and colloid-phase surfaces are ferrinol. For this example, the partitioning coefficient (K: $m^2\ L^{-1}$) is written as normalized to surface area rather than mass. (b) Ferrinol colloid sites; silanol IP sites. Data for the calculations are given in Table 7–1.

Table 7–1. System characteristics for three-phase partitioning calculations.

Figure	Ac	Immobile phase	Colloid phase	Porosity	d_p	S_{IP}	d_c	S_c	V	C
				[–]	mm	$m^2\ g^{-1}$	nm	$m^2\ g^{-1}$	$mm\ h^{-1}$	M
3a	Th(IV)	Hematite	Hematite	0.4	0.3	30	66	17.4	N/A	10^{-14}
3b	Th(IV)	Silica	Hematite	0.4	0.3	30	66	17.4	N/A	10^{-14}
4a	U(VI)	Silica	Silica	0.4	0.3	30	50	2.4×10^{-6} moles dm^{-3}	1	10^{-10}
4b	Th(IV)	Hematite	Silica	0.4	0.3	30	50	2.4×10^{-6} moles dm^{-3}	1	10^{-10}

10^2 to 10^3 l kg^{-1}. In the case of the symmetrical system (Fig. 7–3a; Table 7–1), $K_c = K_{IP}$ and the colloid phase is relatively unimportant in the distribution of the radionuclides, even in the case of the most surface-active elements. While groundwater colloid concentrations may on occasion exceed 100 mg L^{-1}, typical values are much smaller, e.g., 1 mg L^{-1} or less (Kingston & Whitbeck, 1991; Degueldre et al., 2000). This analysis is consistent with the experimental results of Vilks and Baik (2001) who showed that the extent of colloidal transport of Am and Sr through granite fractures was consistent with their K_d values: Am, with the higher K_d value, exhibited greater colloid transport than did Sr.

Figure 7–3b shows radionuclide partitioning in the asymmetrical system. In this hypothetical scenario, the colloids are hematite and the immobile-phase is dominated by quartz (silanol) surfaces. In this case, the ferrinol sites are considered to be better complexants for the radionuclides than are silanol sites (quartz): K_c values are shown on the x-axis; $K_{IP} = 0.1\ K_c$. In response to the asymmetry, the radionuclides exhibit enhanced partitioning to the colloids compared with the symmetrical case. As a consequence, Fig. 7–3b shows enhanced partitioning of the metal ions to the colloidal phase than in the symmetrical case (Fig. 7–3a).

Partitioning in Flow Systems

Figure 7–4 shows the results of simulations of colloid-facilitated radionuclide transport for two different systems: (i) a symmetrical system with U(VI) and (ii) an asymmetrical system with Th(IV). Table 7–1 contains a description of the hypothetical systems. Simulations were created using the model LEHGC (Yeh et al., 1995). In both sets of simulations, colloids and the radionuclide were injected simultaneously and the injected dissolved radionuclide concentration was equal to the total radionuclide concentration. Local equilibrium was assumed. The relative radionuclide concentration on the y-axis represents the total mobile radionuclide concentration, i.e., $M_c + M_d$.

In the symmetrical case (Fig. 7–4a) the dissolved U(VI) concentration represents about 30% of the total mobile U concentration. Thus, although colloids do contribute to the majority of the U transport, the dissolved component is significant.

For Th(IV), two cases were simulated: (i) a symmetrical case in which both the immobile and colloidal phases were composed of ferrinol surfaces; and (ii) the asymmetrical case described in Table 7–1 and the results presented in Fig. 7–4b. In the first case, no Th emerged from the mathematical column for the duration of

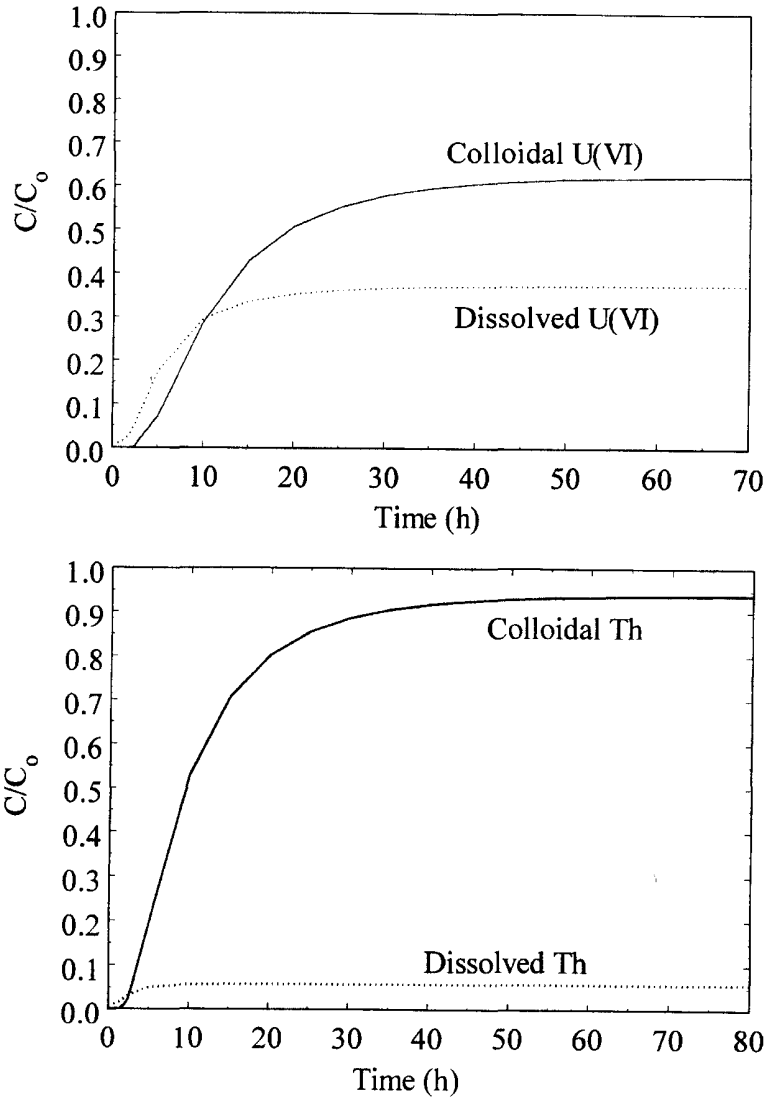

Fig. 7–4. Examples of radionculide transport in hypothetical (a) symmetrical and (b) asymmetrical systems. Data for the sorption of U(VI) by quartz from Kohler et al. (1996); Th/silica: Östhols (1995); Th/hematite (α-Fe_2O_3): Quigley et al. (1996). Calculations were performed using LEHGC (Yeh et al., 1995). Data for the calculations are given in Table 7–1.

the simulated transport experiment (70 h). In contrast, colloid forms of Th dominate Th transport in the asymmetrical simulation. It is interesting to note, however, that even in the case where there is significant colloidal transport of Th (i.e., about 90% of the mobile Th is colloidal), the vast proportion of total Th (i.e., Eq. [2]) remains associated with the immobile phase (>99%).

Colloid Transport as a Rate-Limiting Radionuclide-Transport Process

A recent analysis of the role of colloid transport of radionuclides for performance assessment (Contardi et al., 2001) provides another illustration of the limitations of colloids as a mechanism for contaminant transport. The analysis by Contardi et al. (2001) is based on a modification of the standard retardation equation (Eq. [1]), as proposed by Vilks et al. (1998) and Ryan and Elimelech (1996):

$$R_{F,eff} = 1 + \frac{(1 - \theta)\rho K_d}{\theta(1 + CFK_d)} \quad [4]$$

θ, ρ, and K_d are as defined previously (recall that K_d has the dimensions of L kg^{-1}). C is the colloid concentration and F is defined as

$$F = (K_{d,colloid}/K_{d,IP}) = (A'_{colloid}/A'_{IP}) \quad [5]$$

where $A'_{colloid}$ and A'_{IP} are specific surface areas and have the dimensions of m^2 g^{-1}. From this reasoning, it follows that, if the partitioning coefficients were written in terms of surface area rather than mass, the partitioning coefficients for the colloids and immobile phase would have the same value, assuming that they are composed of the same geological material.

Three assumptions are part of the Contardi et al. (2001) analysis: (i) the system is symmetrical; (ii) the colloids are stable with respect to deposition; and (iii) the system is in sorptive equilibrium. Thus, it is a conservative model with respect to colloid transport. A comparison of Eq. [4] with Eq. [1] shows that the consideration of colloids in the retardation equation has the effect of lowering the value of the contaminant's apparent system partitioning coefficient: as C $\rightarrow$ 0, Eq. [4] becomes Eq. [1].

For their analysis, Contardi et al. (2001) used water chemistry and colloid data from Kingston and Whitbeck (1991) for springs in the National Test Site (NTS) area. K_d values for the radionuclides were calculated by Contardi et al. (2001) using a diffuse layer model (DLM). For the suite of spring systems considered in their evaluation, the ratio of immobile-phase to colloid surfaces areas ranged from 63 to 3.2 $\times$ 10^4 [–]. For comparison, the ratio of immobile-phase to colloid surface areas considered in the examples of the Partitioning in Flow Systems section range from 1.7 $\times$ 10^6 to 17 [–].

Figure 7–5 shows $R_{F,eff}$ plotted as a function of K_d and colloid concentration, C. Colloid data are from Kingston and Whitbeck (1991). For a given K_d, increasing C lowers the value of effective retardation coefficient. In other words, for a given radionuclide, increasing C results in a shift in the distribution of the radionuclide to the mobile phases (i.e., $[M_c]$ and $[M_d]$ increase in value; Partitioning in Flow Systems section). Also illustrated in Fig. 7–5 is that, at a set value of C, increasing the value of K_d (or considering radionuclides of greater surface-active character) has, after some point, no effect on $R_{F,eff}$. Or, the effect of colloids on radionuclide transport has reached a limiting value.

Figure 7–6 shows the log K_d values derived by Contardi et al. (2001) and the colloid concentration data of Kingston and Whitbeck (1991) plotted in three-dimensional space. The y-axis is a calculation of the fraction of the mobile radionuclide pool that is associated with the colloid phase (e.g., Honeyman & Santschi, 1989)

$$f_{c/d} = [M_c]/([M_c] + [M_d]) \quad [6]$$

As $f_{c/d}$ reaches a value of 1.0, the capacity of colloids to carry radionuclides reaches a maximum, i.e., colloid facilitation of radionuclide transport reaches its limit. An

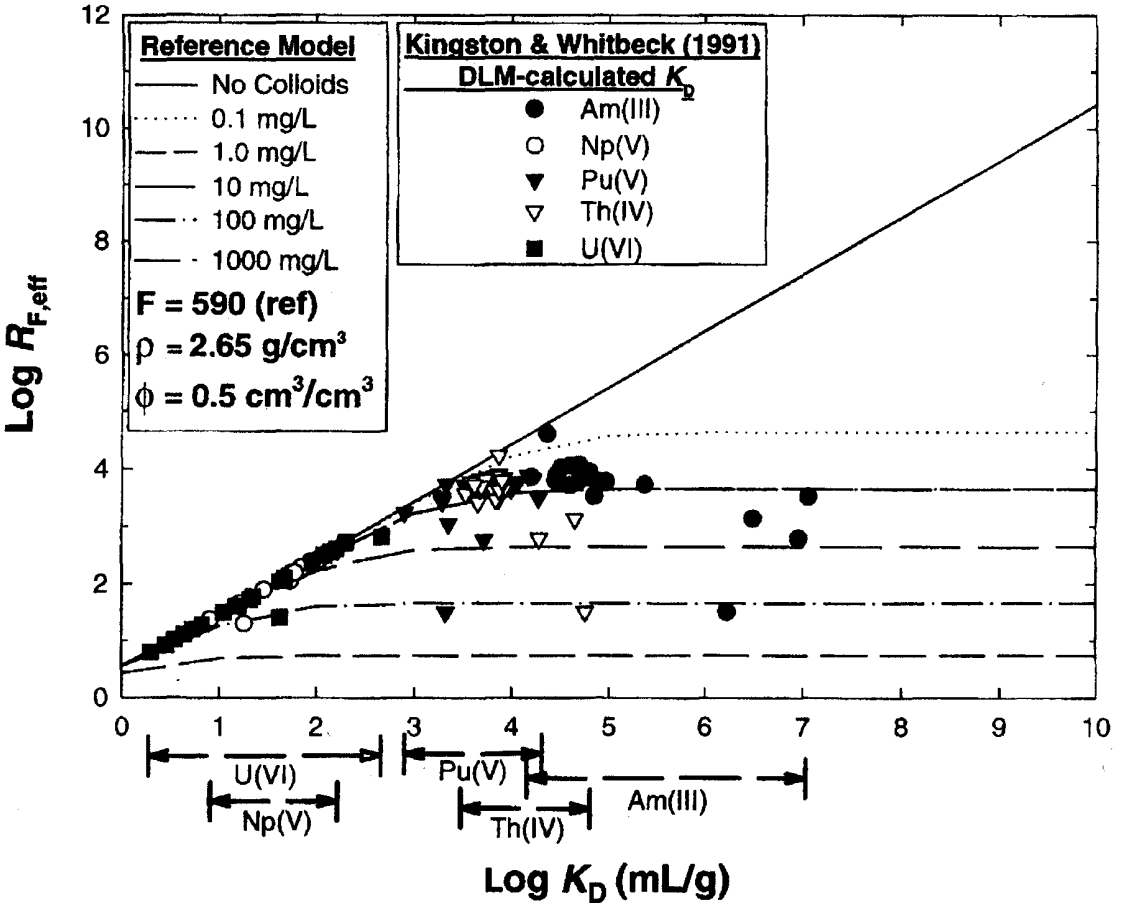

Fig. 7–5. Effective retardation factors, $R_{F,eff}$, calculated by Contardi et al. (2001) for groundwaters from the Yucca Mountain area, as a function of K_d (L kg^{-1}) and colloid concentration, C.F is defined by Eq. [5].

$f_{c/d}$ of unity can be approached through several paths (e.g., increasing K_d at constant C, or the converse) but for the most surface-active of the radionuclides the capacity of colloids to transport sorbed radionuclides is quite limited. It is crucial to note, for the systems discussed here, that even in the case of Am, the radionuclide that has the greatest potential of colloid-facilitated transport, at most 0.001% of the total Am is colloidal (Eq. [2]): the vast bulk of the Am remains with the immobile phase.

The refinement of colloid sampling techniques in recent years has yielded a number of accurate estimates of colloid concentrations in a range of systems (e.g., Ryan & Elimelech, 1996; Degueldre et al., 2000). There is enormous variation in colloid concentrations between systems. While most systems of interest for radioactive waste disposal exhibit relatively low colloid concentrations (i.e., <10 mg L^{-1}), concentrations exceeding 100 mg L^{-1} are not uncommonly reported (Kingston & Whitbeck, 1991). Of course, the important aspect of colloid concentration is not simply its absolute value but its value relative to immobile-phase sites. As noted above, Contardi et al. (2001) derived immobile phase–colloid surface area ratios ranging from 63 to 3.2×10^4 using the data of Kingston and Whitbeck (1991); however, when the strongest sorbing radionuclides are considered (e.g., Am(III)), the effect of colloids on radionuclide transport is maximized even at colloid concen-

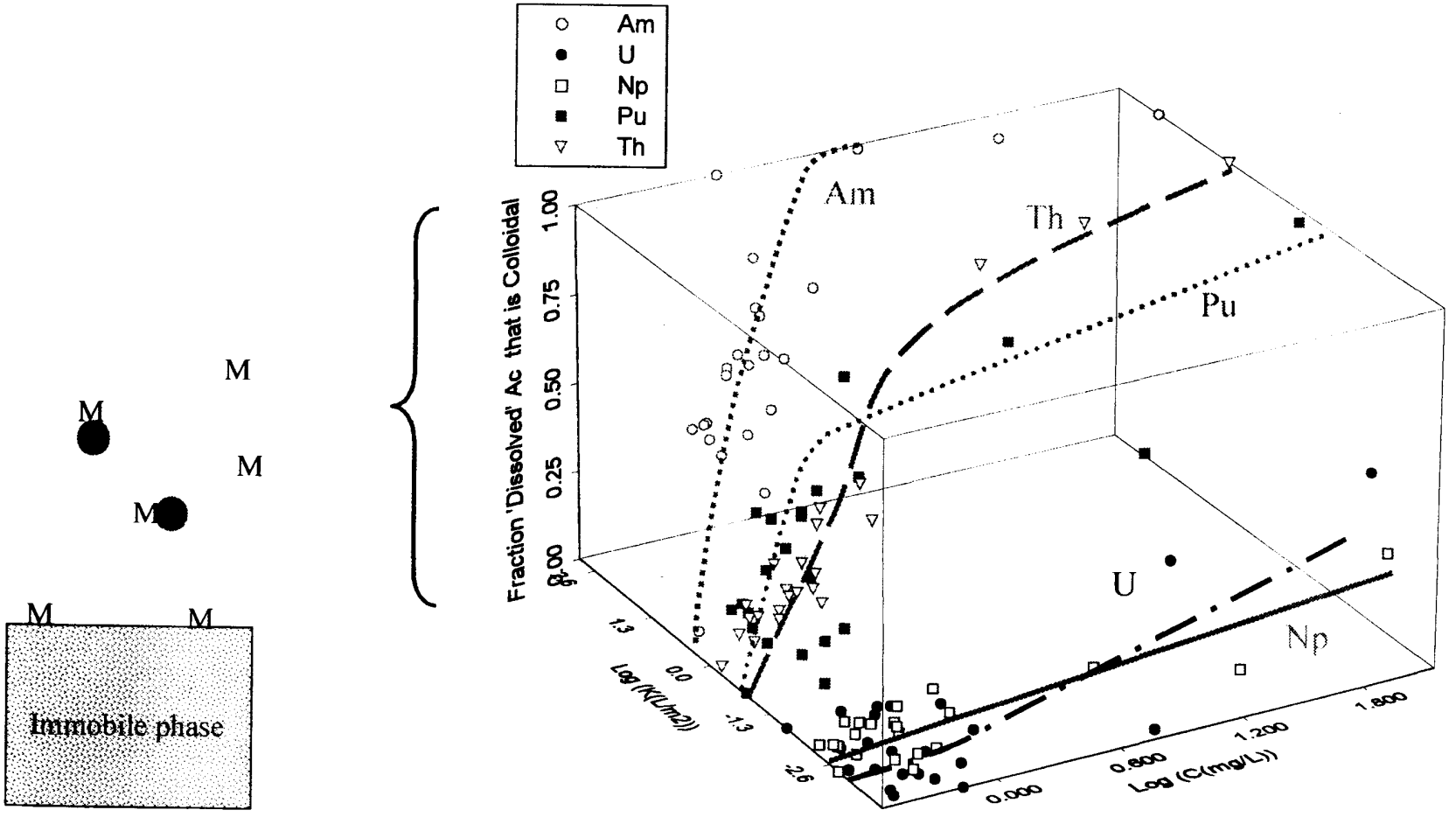

Fig. 7–6. Recalculation of the data from Contardi et al. (2001) illustrating the principle that colloids have a limited potential to transport contaminants. The *y*-axis is the fraction of dissolved (= $[M_c]$ + $[M_d]$) actinide that is associated with colloids, $f_{c/d}$ (Eq. [6]).

trations as low as 1 mg L^{-1} or less. It is interesting to note that the colloid data for the Yucca Mountain area (Fig. 7–7) is normally distributed for concentrations <1 mg L^{-1} (with the exception of the lowest concentrations); several of the highest concentrations also are not normally distributed with the bulk of the colloids.

Sorption–Desorption Kinetics

A final point with respect to the competition issue is made here and that is desorption kinetics. Thus far, this discussion has focused on colloid–IP competition under equilibrium conditions; however, the effect of colloidal species on radionuclide transport can be enhanced if the desorption of the radionuclide from the colloid is kinetically slow. This aspect of colloid-facilitated contaminant transport has been explored in several articles; the simulation results shown in Fig. 7–8 are characteristic of computational results found in the literature.

The simulation results of Fig. 7–8 (Corapcioglu et al., 1999) show that, for this case, the presence of colloids enhances contaminant transport relative to the colloid-free case. If K_{sm}, the first-order rate constant for the desorption of the contaminant from the mobile colloids, is small in value, the simulation results for the local equilibrium assumption (LEA) case and the kinetic case are the same. In the case of an intrinsic colloid, K_{sm} will be the rate of dissolution of the colloid; however, if the rate of desorption of the contaminant is relatively slow (in these cases 0.012 s^{-1} vs. 0.0005 s^{-1}), desorption kinetics has the effect of enhancing colloid-facilitated contaminant transport. Note that in the case of intrinsic colloids, K_{sm} would ~ 0.

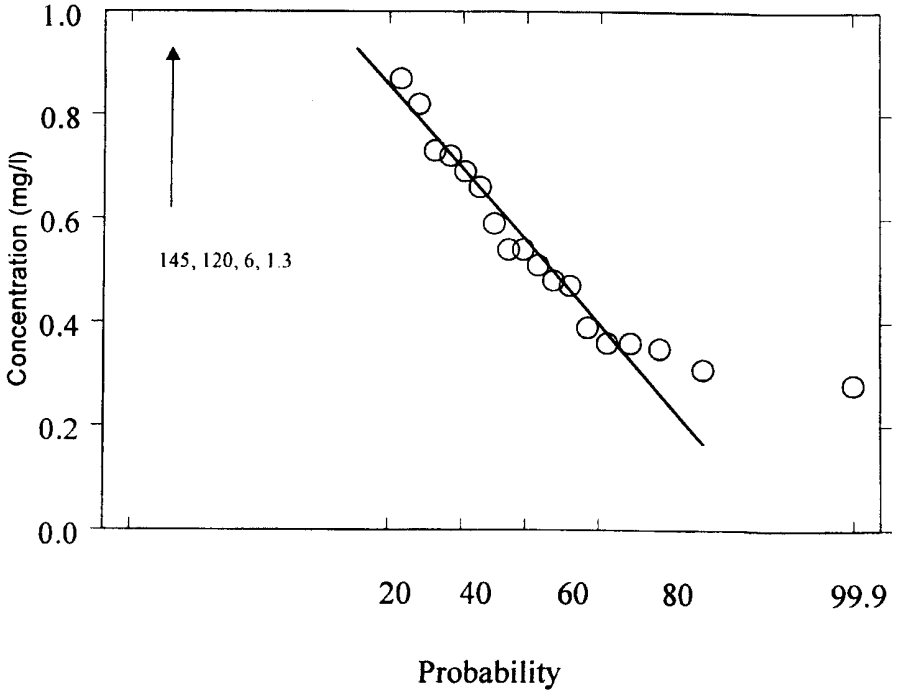

Fig. 7–7. Probability distribution plot of groundwater colloid data reported in Kingston and Whitbeck (1991).

CHEMICAL NATURE OF COLLOID- AND IMMOBILE-PHASE SURFACES

The discussion in the previous section focuses on four basic system properties that contribute to the process of colloid-facilitated radionuclide transport: (i) the physicochemical nature of colloidal species; (ii) the amount of colloids pres-

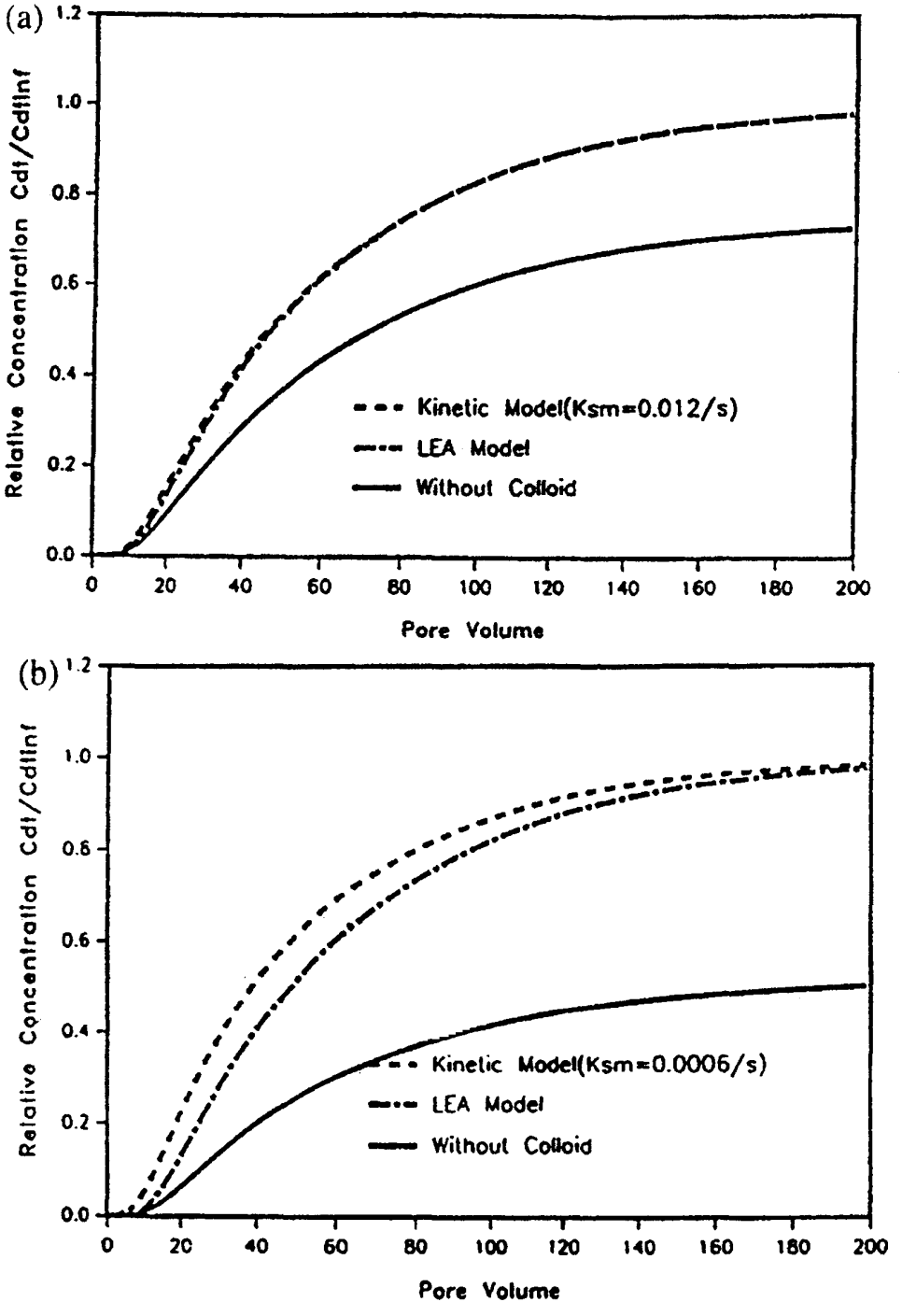

Fig. 7-8. Evaluation of the effect of local equilibrium and kinetic formulations on colloid-facilitated one-dimensional contaminant transport in porous media (Corapcioglu et al., 1999). The *y*-axis is the relative total mobile contaminant concentration at the outlet of the mathematical column. LEA is the local equilibrium assumption and K_{sm} is the first-order release rate for the contaminant form the colloids.

ent; (iii) the physicochemical nature of the immobile phase; and (iv) the concentration and distribution of immobile-phase sites for radionuclide complexation (sorption). Following is a brief review of the literature on colloid sampling and characterization.

Sampling of Colloids

The analysis of groundwater colloids depends on careful sampling that minimizes hydrodynamic disturbance of the samples. The effects of sampling on the abundance of groundwater colloids have received only limited attention (Backhaus et al., 1986; Puls et al., 1990). Puls et al. (1991) found that bailed samples contained significantly higher concentrations of particulate Cr and Ar than pumped samples, presumably due to resuspension of particles in the bottom of the well or from the surrounding aquifer. Furthermore, Puls et al. (1991) found that bladder pumps produced significantly fewer colloids than submersible pumps. Light-scattering and turbidity measurements have shown that many more well casing volumes must be purged to reach a stable particulate concentration than is required for stabilization of dissolved groundwater chemical parameters such as pH, dissolved O_2, temperature, and redox potential (Ryan & Geschwend, 1990; Puls et al., 1991). Collectively these studies suggest that groundwater samples should be taken at low pumping rates (~100 mL min^{-1}) and that particle-sensitive parameters such as turbidity should be monitored to determine required purge volume.

Exposure of groundwater samples to the atmosphere also can result in alteration of the colloid population. Formation of ferric oxyhydroxide precipitates and their subsequent flocculation are common occurrences when reducing waters are exposed to air. A study of the colloid-facilitated groundwater transport of radionuclides in the Gorleben aquifer (FDR) avoided this problem by transferring samples directly into resin coated aluminum drums equipped with an N_2 atmosphere (Lieser & Hill, 1992; Deerlove et al., 1991; Kim et al., 1992). Alteration in the partial pressure of CO_2 during sampling can cause precipitation of carbonates (Harnish et al., 1994).

Colloid Characterization Techniques

Numerous techniques exist to determine the abundance and characteristics of groundwater colloids (McCarthy & Degueldre, 1993; Kretzschmar et al., 1999). The simplest characterizations are gravimetric and/or chemical analysis of the bulk colloids obtained by filtration or centrifugation. More detailed colloid characterization is obtained using methods that are generally based on variants of light-scattering, particle counting or separation techniques. The advantage of the separation techniques is that unlike the first two techniques, size distributions of colloid composition can be obtained from chemical analysis of separated fractions.

Figure 7–9 shows data from the Grimsel Colloid Exercise (Deguelder et al., 1989) in which colloids were analyzed by a suite of methods in an intercomparison of analytical techniques (gravimetry, scanning electron microscopy, transmission electron microscopy, and single particle counting). The results show a favorable comparison between the methods; however, two caveats need to be mentioned.

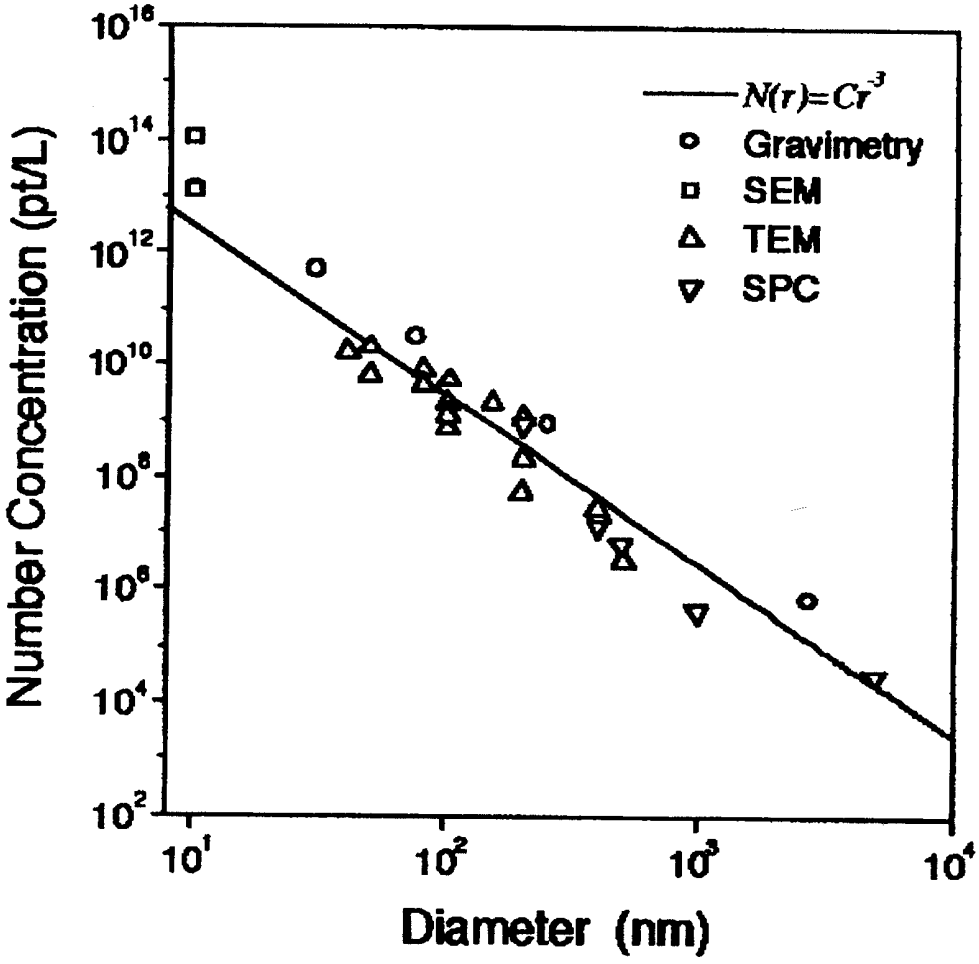

Fig. 7–9. Colloid number concentration (particles L^{-1}) as a function of diameter and analysis technique (from Deguelder et al., 1989).

First, differences in the results can be somewhat masked by the fact that the plots are on a log–log scale. Secondly, number-based distributions always favor the smallest particles, often produce similar-looking plots and under represent the importance of larger particles when considering the mass distribution of colloids. Recently, Dawson et al. (2001) compared a number of methods for a series of soil size fractions obtained by centrifugation. Although the samples represented four fractions having different size ranges, as computed by the centrifugation conditions, most methods gave somewhat similar number distributions. In contrast, clear differences in the volume distributions were observed. This distinction between number and volume-based distributions becomes important when one considers how colloids are detected and why colloid transport may be important. If colloid mass concentration is determined, or if contaminants are present as an integral component of the colloid, then a volume (mass)-based distribution is most important. If contaminants are sorbed to particle surfaces, then a surface area-based distribution, which can be computed from a number distribution if particle shape is known, may be most important. Borkovec et al. (1993) show that soil particle numbers (N) are proportional to r^{-v}, where r is the particle radii and $2.6 < v < 3.0$. In the case of the Grimsel data, $v = 3.0$.

Photon Correlation Spectroscopy (PCS), also known by the more general term Dynamic Light Scattering (DLS), is the only light scattering method commonly applied to natural water samples (Schurtenberger & Newman, 1993). DLS provides a size distribution based on the diffusion coefficients of the colloids. The advantage of DLS is that it can be directly applied to samples without pretreatment. It has been shown, however, to be difficult to apply DLS to polydisperse samples. Results can be improved by allowing larger particles to settle out of the sample prior to DLS analysis (Buffle & Leppard, 1995).

A number of techniques fall under the general category of the particle counting approach. In this approach each particle in an aliquot of the sample is individually counted and sized, and from this data a number-based distribution is constructed. The more traditional methods of particle counting are based on electrozone sensing (Coulter counter), light blockage/scattering, scanning electron microscopy (SEM), or transmission electron microscopy (TEM) (Degueldre et al., 2000). A promising new method of sizing and counting individual colloids in groundwater is Laser Induced Breakdown Detection (LIBD) (Bundschuh et al., 2001).

SEM and TEM are useful techniques for examining colloids (Nomizu et al., 1988) and their application to natural waters has been reviewed by Leppard (1992). Microscopy is the most direct of all methods for sizing particles, but is very time consuming and care must be taken to avoid artifacts. Automated methods have improved the accuracy and efficacy of the technique for producing number-based size distributions (Seaman, 2000). Qualitative chemical information for major elements is provided by energy-dispersive x-ray analysis (EDAX) commonly available with SEM instruments.

Filtration through micro-porous membranes, dialysis, and centrifugation at high gravity's have been the traditional size separation methods employed for natural waters (Batley, 1990). Filtration through successively smaller pore sizes has most commonly been used to give size distributions of colloidal-sized particles in natural waters (Kennedy et al., 1974; Salbu et al., 1985; Tanizaki et al., 1992). Factors affecting the results of filtration were carefully examined by Buffle et al. (1992) including such variables as filter type, filter loading, and flow rates. The most important physiochemical processes occurring during filtration were concentration polarization at the membrane surface, which promotes coagulation and alteration of the size distribution, and membrane exclusion effects, which inhibit the passage of very small particles through pores with similar diameters. Honeyman and Santschi (1991) documented the failure of 0.25 μm ^{59}Fe-hematite particles to pass a 0.40 μm membrane filter as a result of aggregation at the filter surface. The study of Buffle et al. (1992) illustrated how dependent the results of filtration are on procedural technique and suggests that any interpretation of particle size measurements based on filtration must be carefully examined within the context of how the filtration was performed.

Cross-flow filtration is a promising filtration method that may overcome some of the aforementioned problems associated with filtration (Gutman, 1987). In tangential or cross-flow filtration, a high tangential flow rate is maintained parallel to the filter membrane, while a much lower filtrate flow rate passes through the membrane. This method induces large shear forces near the membrane surface and thus

reduces both the concentration polarization region and membrane fouling. Filtration membranes are generally stacked in order to provide large areas, on the order of a few square meters, to further limit filter fouling. The method allows processing of large volumes of water to isolate colloids in significant quantities without reduced filtration rates (Whitehouse et al., 1986, 1990; Kuwabara & Harvey, 1990; Marley et al., 1991; Hoffmann et al., 2000)

A new and very powerful method of colloid size and composition analysis is field-flow fractionation (Giddings, 1993; Beckett, 2000). This method, which is analogous to chromatography, provides continuous high resolution size separations. Various subtechniques of field-flow fractionation exist that allow analysis of particles ranging in size from 0.001 to 50 microns. Because this method elutes the fractionated particles, collected fractions can be further analyzed for their composition. In many cases online coupling of a specific detector to FFF allows determination of composition distributions as a function of colloid size. Examples include characterization of humic substances using TOC detection (Thang et al., 2001), investigations of colloid composition and mineral surface coatings using ICP-MS (Ranville et al., 1999; Chen et al., 1999). For example, Fig. 7–10 shows the particle size and element composition distributions of mobile colloids collected during a field study of flow through soil macropores (Ranville & Beckett, 2000). Note that Fe- and Al-containing colloids exhibit slightly shifted colloid diameter maximum in the fractogram. This technique also has been shown to be useful in laboratory studies to study colloid-pollutant interactions (Beckett et al., 1990). Recently FFF has been used to investigate the effect of size on transport of polydisperse colloids in laboratory sand columns (Dawson et al., 2001).

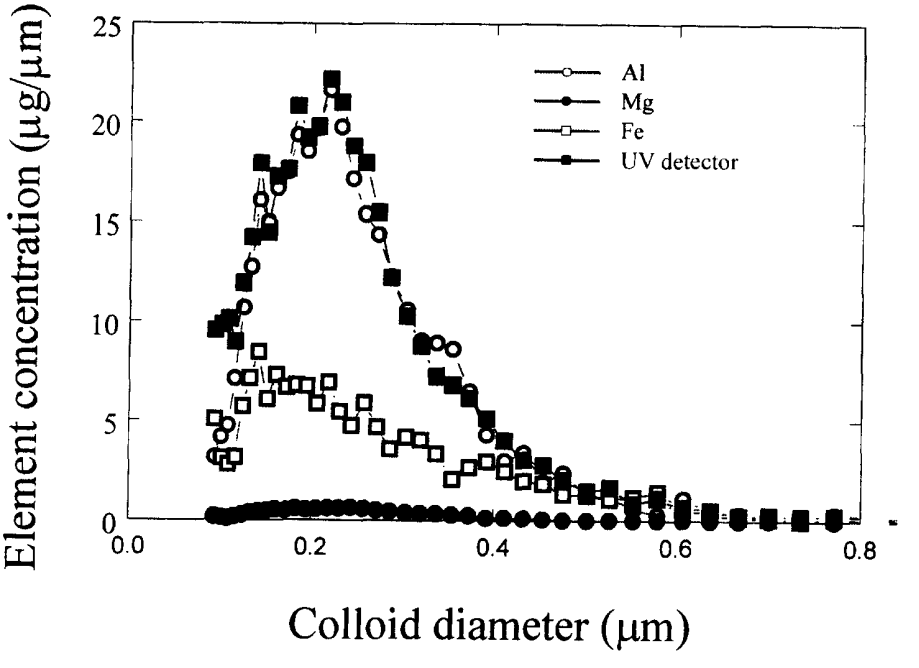

Fig. 7-10 Particle size distribution of mass (UV response) and element composition (Al, Fe) obtained by FFF-ICP-MS for a sample of colloids transported through soil macropores. In principle, integration under the UV detector response curve should yield the mass of colloidal particles. Similarly, integration of the elemental concentration curves (mg mm^{-1}) should yield the mass of the element in the colloids.

Colloid and Immobile-Phase Types

Data from the field suggests that in most cases colloids are derived from the existing IP materials and limited evidence suggests that the chemical heterogeneity of IP and colloidal materials is similar (Grolimund et al., 1996). While there is some evidence that mineral surfaces as a group behave relatively similarly when sorption data are normalized to specific site concentration or surface area, e.g., Pabalan et al. (1998), the extent to which such observations can be generalized to include surfaces that are not those of inorganic minerals. Indeed, the systems likely to be of greatest concern for colloid facilitated radionuclide transport, or retention for that matter, are systems for which the colloid phase is of a different chemical character than the immobile phase, i.e., asymmetrical systems.

Figure 7–11 is a comparison of the pH-potentiometric titration behavior of three surface archetypes: (Fig. 7–11a) a colloidal metal oxide–hematite (α-Fe_2O_3); (Fig. 7–11b) a natural organic matter (NOM): Suwannee River humic acid, and (Fig. 7–11c) a Gram-negative bacteria (*Desulfovibrio vulgaris*). While there are many other examples that might be brought to bear as representative colloid types, the three colloids described here exhibit the range of characteristics of colloids that can be found in systems of environmental relevance. These three surface types also will be discussed in the Colloid Generation, Transport and Deposition section.

The hematite presents classical amphoteric behavior, i.e., surface groups that can act as both acids and bases. The pH_{pzse} (point of zero salt effect) occurs at a pH value of approximately 9.2. Because the hematite does not have permanent structural charge, as do the clay groups illite, vermiculite, and smectite, the pH_{pzc} (point of Zero charge) coincides with the pH_{pzse} (Sposito, 1989). At pH values smaller that the pH_{pzc} the hematite surface will have a net positive charge; at pH values greater than pH_{pzc} the hematite will be net negatively charged. The response of the titrations to changes in ionic strength are characteristic of metals oxides. In this case, the data set was simulated using the Triple Layer Model of Davis et al. (1978).

The Suwannee River humic acid has been extensively studied as a model NOM. In general, for purposes here, the humic acid is composed of a suite of weak acid groups (typically considered carboxylic and phenolic according to the average pK_a values derived from titrations). The Suwannee River humic acid is negatively charged throughout the pH range of the titrations. The titration data were simulated (Lenhart & Honeyman, 1999) by treating the humic acid as being composed of a suite of monoprotic acids (after Westall et al., 1995).

The last example is a biocolloid. *Desulfovibrio vulgaris* is a Gram-negative sulfate-reducing bacteria. Under certain conditions it can use U(VI) as a terminal electron acceptor, reducing the U(VI) to U(IV) (Spear et al., 1999). For the titration analysis (Landkamer et al., 1999), the bacteria were in a resting state. Gram-negative bacteria have as part of their cell surface a lipopolysaccharide layer with O-specific side chains extending 50 to 500 Å into solution. Protons also are able to diffuse into a periplasmic space through special proteins called porins. The result is a kinetically-complex system. A comparison of the titration data for the NOM and bacteria shows that the response of the titration curves to changes in ionic strength is similar; however, the magnitude of the response for the *Desulfovibrio*

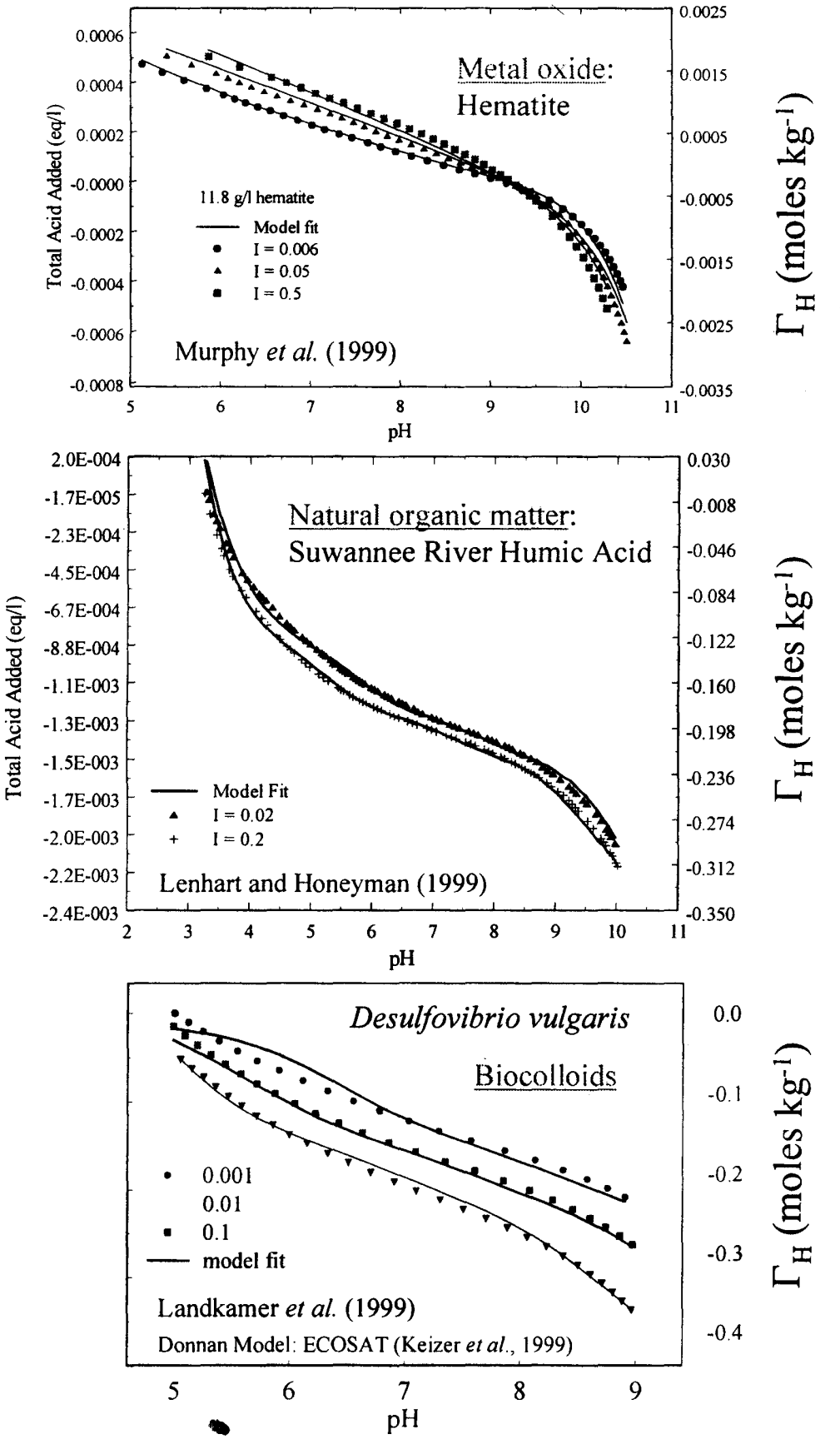

Fig. 7-11. Comparison of the potentiometric titration behavior of colloid archytypes: (a) hematite (α-Fe_2O_3), a metal oxide (Murphy et al., 1999); (b) Suwannee River humic acid (Lenhart & Honeyman, 1999); and (c) *Desulfovibrio vulgaris*, a Gram-negative bacterium (Landkamer et al., 1999).

vulgaris is much greater than for the humic acid. While both sets of titration curves were simulated as the deprotonation of weak acid groups, the *Desulfovibrio vulgaris* required the application of a Donnan model (Keizer & van Riemsdijk, 1998) to accurately capture the titration behavior.

Figure 7–12 is a comparison of the U(VI) sorptive behavior of three surface types. Sorption data are normalized to surface sites $P = [U(VI)_{sorbed}]/\{[U(VI)_{solution}][\text{colloid sites}]\}$. Note that: (i) the surfaces dominate the sorption of U(VI) at different pH values and (ii) the surfaces are markedly different in their ability to sorb U(VI). Because the relative ability of a surface to compete against other sorbents for a radionuclide is a function of the product of the interaction parameter (e.g., P or K_c) and the site concentration (e.g., Eq. [2]), Fig. 7–12 suggests, for example, that *Desulfovibrio vulgaris* could be an effective colloidal transport agent at substantially lower concentrations than in the cases of the NOM and hematite.

One problem with trying to ascertain the relative radionuclide-complexing ability of different environmental surfaces is a lack of consistency in the framework that is used for evaluating sorption (complexation) among surface types. Metal oxides (including clays) have been the subject of a vast amount of experimental research and modeling. While both natural organic matter and microbial surfaces have received attention for their ability to accumulate metal ion (bacteria and viruses much less so), there has been relatively little work done on the simulation of metal–NOM and metal–bacteria interactions in a manner that is consistent with the surface complexation (SC) approach used for metal oxides. Examples of the application of SC to NOM and bacteria are Westall et al. (1995), and Fein et al. (1997), respectively. As a consequence, it is difficult to predict competition between environmental surface types for radionuclides.

Table 7–2 provides a comparison of metal oxides and select biosurfaces. One problem with evaluating the properties of bacteria and other biosurfaces is that a consensus has yet to develop on methodologies for evaluating surface characteris-

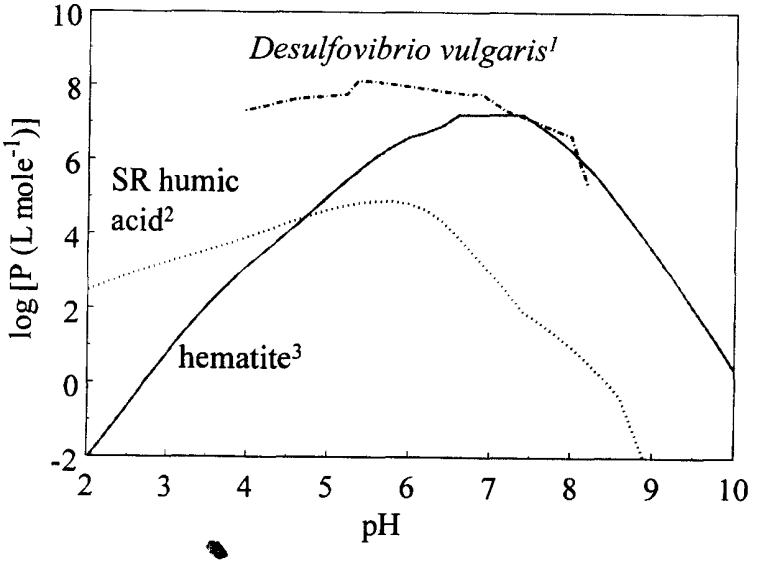

Fig. 7–12. Comparison of U(VI) binding to three surface types, as a function of pH. I = 0.01 *M*. Relative sorption intensity is expressed in terms of partitioning coefficient in which the data are normalized to site concentration (L mole^{-1}). *Desulfovibrio vulgaris:* a Gram-negative bacteria in a resting stage (from Landkamer et al., 2000, unpublished data); Suwannee River humic acid (data from Lenhart, 1997); hematite (data from Lenhart & Honeyman, 1999).

Table 7–2. Comparison of metal oxide and bacterial surfaces.

Mineral–bacteria	S_a	n_s (sites nm^{-2})	Source
Metal oxides: colloidal, crystalline	1–20	1–20 (2.3)	Various, Davis & Kent, 1990
Metal oxides: amorphous	Several hundred	Approx. 1 mole per mole M	Various
Kaolinite	10–20	1–5	Various
Smectite	20–80†	6–12	Various
Bacillus subtilis (Gram +)	140 (wet wt.)	carboxyl:0.53; phosphonate:0.19; hydroxyl:0.27	Fein et al., 1997
Bacillus sp. *Strain SG-1 spores*	74.5‡; 6.86§, 6.27¶	18.3	He &Tebo, 1998
Five species of Gram + bacteria	Cell wall isolates	4.21–26 (not including amine groups: +20–25 %)	van der Wal et al., 1997
Desulfovibrio vulgaris (Gram –)	6.2¶ (dry wt.)	Carboxyl + phosphonate: 3.6; amine:1.8	Landkamer et al., 1999

÷ External sites.
‡ Methylene blue.
§ BET
¶ Geometric.

tics. As a result, the literature base that does exist provides a range of microbe characteristics that to a great extent are the consequence of the nature of the evaluation technique rather than necessarily differences in the microbes, themselves.

Although the existence of natural organic matter (NOM) colloids in soil and groundwaters has been recognized for many decades, the role of NOM in contaminant transport has been relatively under-studied compared to mineral colloids. To a certain extent, the de-emphasis of NOM on contaminant transport is due to a general belief that NOM acts to enhance metal-ion binding to mineral surfaces; however, emerging evidence indicates that NOM, in many instances, may be a effective means of transporting metal ion and radionuclides through subsurface systems (McCarthy et al., 1998), not only through the direct transport of metal ions in the form of metal-ion/NOM complexes (e.g., Schüssler et al., 2000; Sakamoto et al., 2000) but also indirectly through the ability of NOM to stabilize inorganic colloids with respect to deposition (Deguelder et al., 2000; Liang & Morgan, 1990). Additionally, recent data (Buckau et al., 2001) indicates that fulvic acid may remain stable in solution for thousands of years.

Two different conceptual models of trace metal complexation by organic ligands in aquatic systems emerged during that last two decades. One model focuses on the existence of trace metal complexing organic ligands of low concentration but high metal-binding specificity and affinity that have their origin in the evolution of biological systems (i.e., siderophores and phytochelatins). A consequence of this model is that the bulk of dissolved organic carbon (DOC) is relatively unimportant in sequestering metals. Kinetic effects are consequently due to slow attainment of equilibrium as metal ions are distributed between several high affinity ligands (e.g., Hering & Morel, 1989).

In the second model, the availability of trace metals is governed not by ligands with a high affinity for the metal but by steric constraints due to trapping of metals within colloidal aggregates. In these situations, metal lability is governed primarily by mass transport limitations (e.g., Mackey & Zirino, 1994: the onion model of organic matter complexation of trace metals). As a consequence, the composition and physical confirmation of the bulk of the colloidal organic matter becomes of great importance.

To a certain extent, the relative roles of bulk NOM properties to constituent ligands have yet to be resolved. Bulk properties are likely to govern the deposition of high molecular weight organic colloids onto immobile-phase materials (e.g., Scheutjens & Fleer, 1979) although it possible to simulate the sorption of low molecular weight NOM (e.g., fulvic acid) by mineral surfaces by mathematically-treating the NOM as a suite of monoprotic acids (Lenhart & Honeyman, 1999); however, it also is increasingly evident that subfractions of NOM have primarily responsibility for complexing trace metals. This property of NOM is shown in Fig. 7–13 where the polysaccharide fraction is the component that dominates Th complexation.

COLLOID GENERATION, TRANSPORT, AND DEPOSITION

Several excellent reviews on colloid generation, deposition, and transport are available in the literature (e.g., Kretzchmar et al., 1999; Ryan & Elimelech, 1996).

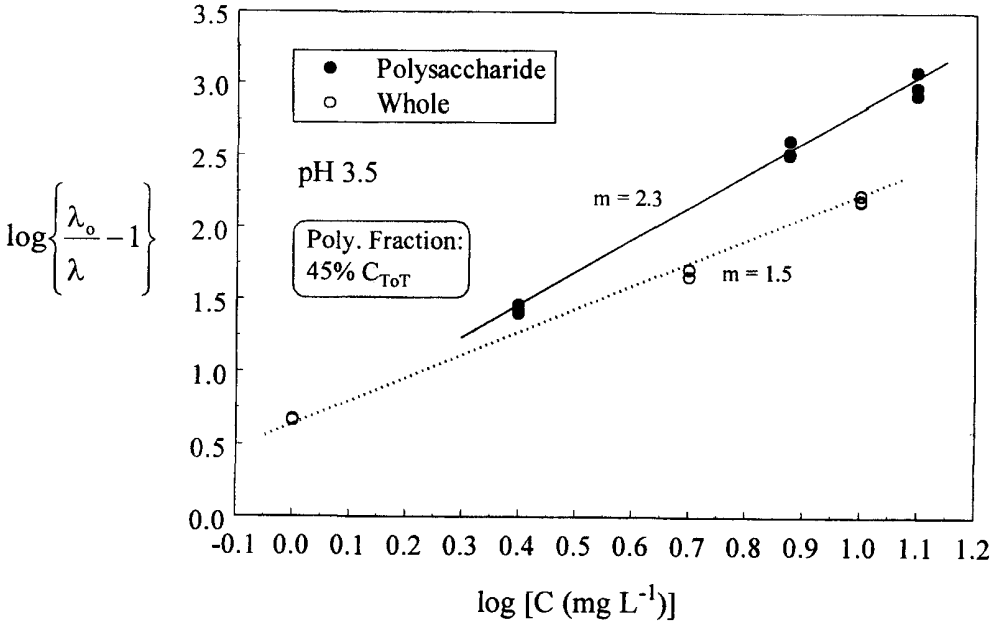

Fig. 7–13. Comparison of Th(IV) binding to whole marine colloidal organic matter and the acid polysaccharide fraction (data from Murphy, 2000). The data are plotted in the form of a classic Schubert plot (Schubert, 1948). The analytical method is a ligand competition, liquid–liquid extraction technique using HDEHP (di-2-ethylhexyl phosphoric acid) in toluene to compete against the colloidal organic matter (COM) in an aqueous phase. λ_o is the toluene/aqueous phase distribution of the Th in the absence of the COM; λ is the partitioning in the presence of the COM.

Most studies of colloid behavior have focused on inorganic colloids, although organic macromolecules and biocolloids have been studied to a limited extent.

Colloid Generation–Release

Inorganic colloids are generated by two primary mechanisms: (i) in situ precipitation and (ii) the mobilization of existing colloids. As pointed out by Ryan and Elimelech (1996), the former mechanism is relatively uncommon for natural systems, although it may be a dominant process in the near-field of waste repositories where gradients in pH and E_H may be expected. In addition, bacteria may under certain circumstances produce inorganic colloids as in the reductive precipitation of U(VI) to U(IV) by some sulfate-reducing bacteria (Fig. 7–14). Under constant physical and chemical conditions, the release rates of existing inorganic colloids are relatively small. Unlike the case for colloid deposition, where theory is relatively well developed, models for the release of inorganic colloids are few. In general, inorganic colloids are released through DLVO effects; colloid release is regulated by system conditions that affect mineral surface charge (pH, ionic strength, the specific sorption of solutes). Colloids also may be generated through chemical processes that destroy cementing agents (Ryan & Gschwend, 1994) or through hydrodynamic effects such as shear brought on by rapid pumping.

Biocolloid deposition and release also is be regulated by DLVO type interactions [e.g., Ryan et al., (1999) or through nonelectrostatic mechanisms (hydrophobic bonding in the case of viruses]. Bacteria can attach to immobile surfaces through excreted biopolymers (e.g., Extended DLVO theory); subsequent destruc-

tion of the biopolymers can result in bacterial release. Bacteria also may produce organic macromolecules, such as acid polysaccharides, which are strong complexants for actinides (Murphy, 2000). Such molecules may themselves attach to immobile surfaces thereby retarding associated radionuclides or, under other system conditions, act to facilitate radionuclide transport.

A variety of processes–mechanisms have been proposed to explain the sorption of NOM by mineral surfaces. These sorption processes include ligand exchange (Parfitt et al., 1977; Davis, 1982; Murphy et al., 1992; Gu et al., 1994; Murphy et al., 1999; Lenhart & Honeyman, 1999), cation bridging (Baham & Sposito, 1989), entropy driven physical adsorption (Jardine et al., 1989) and hydrophobic repulsion (e.g., Jardine et al., 1989; Schlautman & Morgan, 1994). In addition, the following mechanisms–processes also have been postulated: cation exchange, proton exchange, anion exchange, water bridging, hydrogen bonding, and van der Waals interactions (Sposito, 1989). These remain postulated processes, however, as there is little direct evidence as a basis for selecting between them (Baham & Sposito, 1994). Because many of these processes are, at least in principle, reversible, NOM sorbed by mineral surfaces, along with its complexed trace metals and radionuclides, can be released in response to changes in system conditions.

Figure 7–15 (Ranville et al., 2000) illustrates the possibility for another mechanism of soil colloid generation. The data are for ^{239,240}Pu-contaminated soil

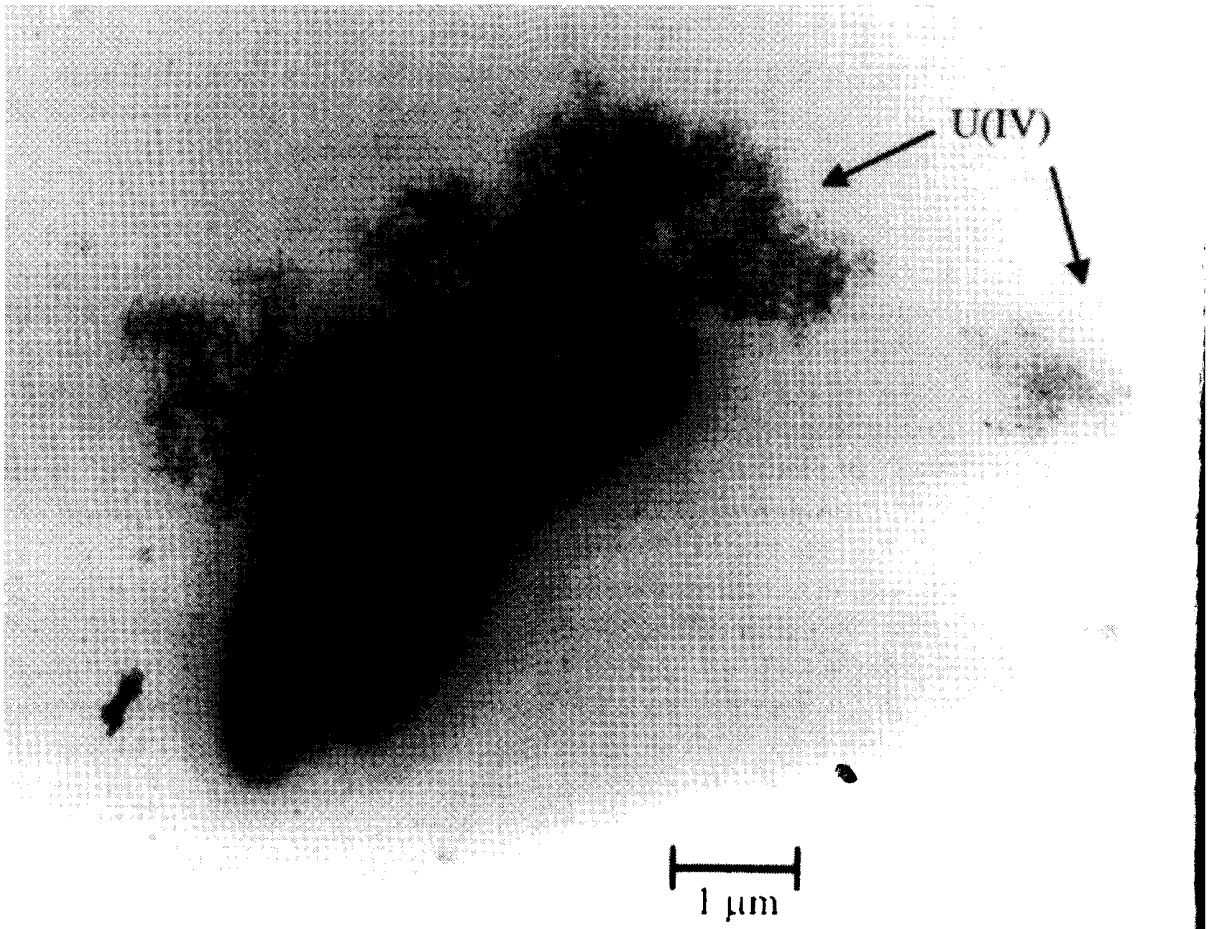

Fig. 7–14. TEM photo of a mixed culture of sulfate-reducing bacteria after 4 h of exposure to 1 μ*M* uranyl acetate illustrating the production of U(IV) intrinsic colloids. Spear et al. (1999).

from Rocky Flats, CO. Figure 7–15a shows the distribution of selected soil characteristics as a function of soil size fraction, for soil isolates suspended in deionized water. Also shown is the distribution of ^{239,240}Pu, both as % of total ^{239,240}Pu and as specific activity (pCi g^{-1}). Figure 7–15b shows the distribution of the same soil properties, and soil ^{239,240}Pu, after the addition of 3 to 5% hydrogen peroxide (H_2O_2). Studies have shown that 3 to 5% H_2O_2 solutions are effective at destroy-

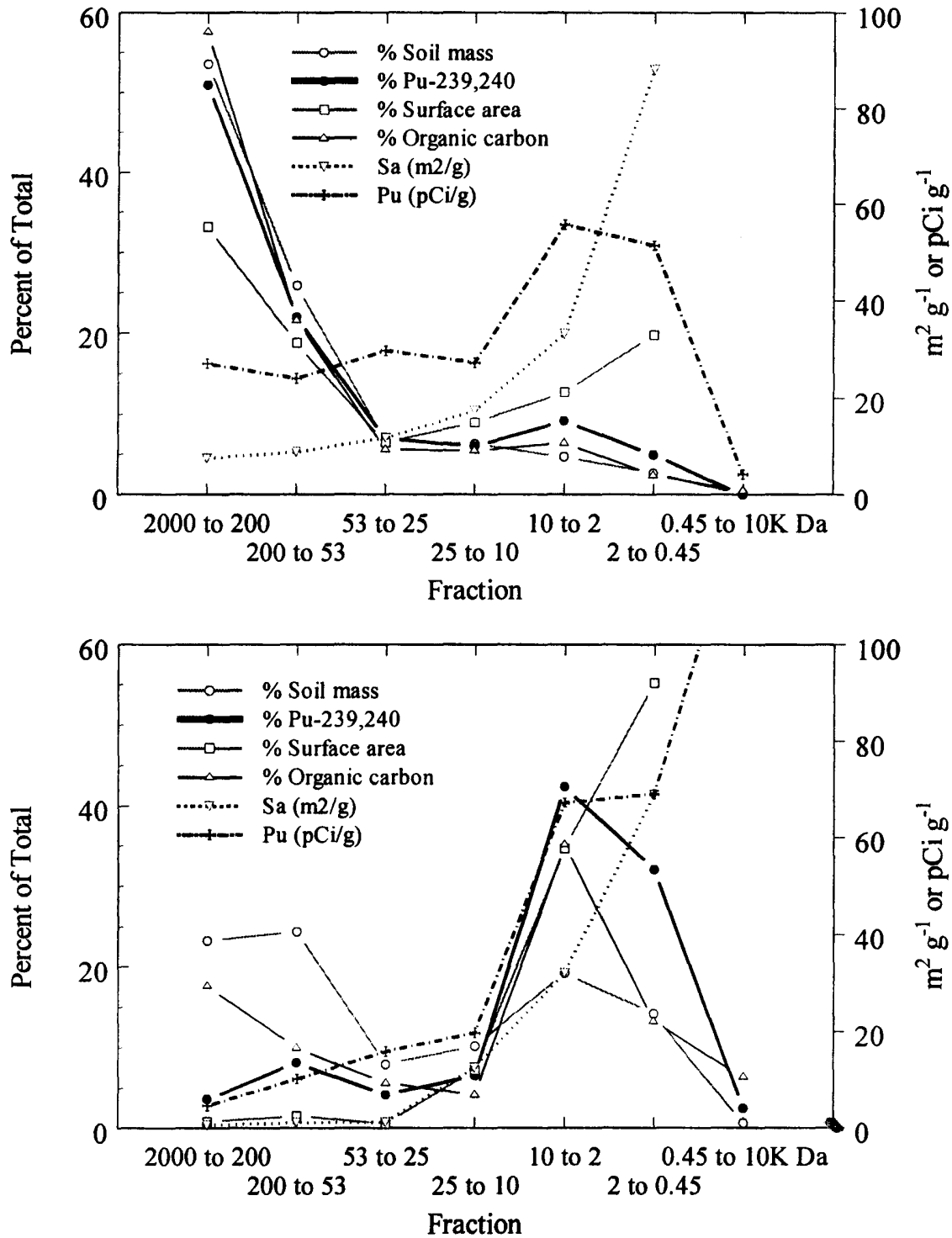

Fig. 7–15. Distribution of : soil mass, % ^{239,240}Pu, %surface area, % organic carbon % Specific surface area (m^2 g^{-1}), ^{239,240}Pu as a function of soil size fraction (2000 μm – 10 K Da): (a) suspension in DI water and (b) after destruction of organic matter with peroxide (Ranville et al., 2000).

ing surface-associated organic matter but that it does not attack organic matter that has penetrated the inner layers of clay minerals (Righi et al., 1995). Addition of the H_2O_2 results in a shift in the distribution of Pu to the finest fractions. If the organic matter in undisturbed soil acts to create soil aggregates through interparticle bridging or regulation of DLVO-type interactions, processes that destroy the organic matter (microbial activity, mechanical mixing of the soil, intense surface fires) may create a colloidal radionuclide fraction.

Figure 7–16 shows the distribution of ^{239,240}Pu in the dissolved phase of an aqueous suspension of ^{239,240}Pu-contaminated soil from Rocky Flats, CO (Honeyman et al., 1999). The experiment was conducted under conditions open to the atmosphere and for a contact time of approximately 3 wk. An Amicon Mini-Tan ultrafiltration cell was used with a 10 K Da membrane. The analysis aliquots were approximately 250 mL in volume and the activity balance, total dissolved (<0.45 μm) ^{239,240}Pu compared with the sum of the colloidal (0.45 μm to10 K Da) plus ultrafiltrate (<10K Da) ^{239,240}Pu fractions is complete). Note that $f_{c/d}$ is approximately equal to 0.7 [–] and that the fraction of total ^{239,240}Pu in the colloid fraction, f_c, is 1.1×10^{-3} [–].

Colloid Deposition

By far, the greatest amount of theoretical and experimental work on colloid attachment or deposition has as its roots DLVO theory (e.g., Kretzchmar et al., 1999; Ryan & Elimelech, 1996; and references therein). Filtration theory (e.g., Yao et al., 1971), which is usually expressed in terms of a single collector (i.e., the immobile phase) efficiency, works well for systems with well-defined geometry and in which repulsive double layer interactions are absent, that is, for fast deposition. Although filtration theory quickly evolved to include DLVO type interactions (i.e., repulsive forces and slow deposition), large discrepancies between experimental results and theory typically arise if double-layer interactions are required (e.g., Elimelech & O'Melia, 1990). As a consequence, predicting colloid deposition in response to

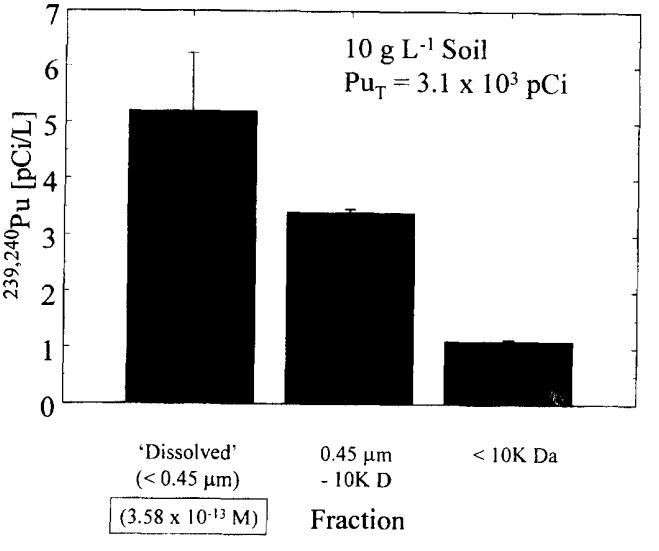

Fig. 7–16. Ultrafiltration of water in equilibrium with suspended Rocky Flats, CO, soil isolates. Total dissolved ^{239,240}Pu is approximately 3.6×10^{-13} M. Error bars represent an estimate of the total propagated error (e.g., extraction and counting; Honeyman et al., 1999).

changes in ionic strength, pH (for surfaces where the proton is a potential-determining ion) or other surface-charge regulating processes is problematic with filtration theory as typically applied.

An additional problem with applying models of colloid deposition to the field is the inherent heterogeneity of systems of interest. Although there are a number of aspects to the heterogeneity problem as it applies to colloid transport, recent advances in understanding the role of geochemical heterogeneity in colloid deposition and release suggest a promising avenue for understanding and predicting colloid transport in real systems (e.g., Sun et al., 2001).

Figure 7–17 (Kretzchmar et al., 1995) illustrates one part of the dynamic heterogeneity problem: deposition site blockage by deposited colloids. In this example (Fig. 7–17a), natural soil colloids are injected until breakthrough occurs. Water is injected and no colloids are released. A second pulse of injected colloids is eluted coincident with a conservative tracer suggesting that sites for colloid deposition are already occupied. A lower concentration of injected colloids (Fig. 7–17b) results in a slower rate of breakthrough as it takes longer in the experimental runs with a lower colloid concentration for the colloids to occupy favorable colloid deposition sites.

The deposition of colloids onto immobile-phase sites favorable to the deposition of colloids, and the eventual filling up of those sites by the deposited colloids, will, in principle, result in the eventual fostering of colloid facilitated contaminant transport. Dynamic blocking functions have been developed to account for the decrease in deposition rate with increasing fractional coverage of favorable deposition sites by colloids (Johnson et al., 1996).

Collector surfaces in real systems contain a mixture of favorable and unfavorable sites for colloid deposition. Which category a site falls into depends on the nature of the colloid. For example, Fe oxide colloids would probably be favorably deposited onto negatively-charged immobile-phase surfaces such as quartz (i.e., under circum-neutral pH conditions). While geochemical heterogeneity has been

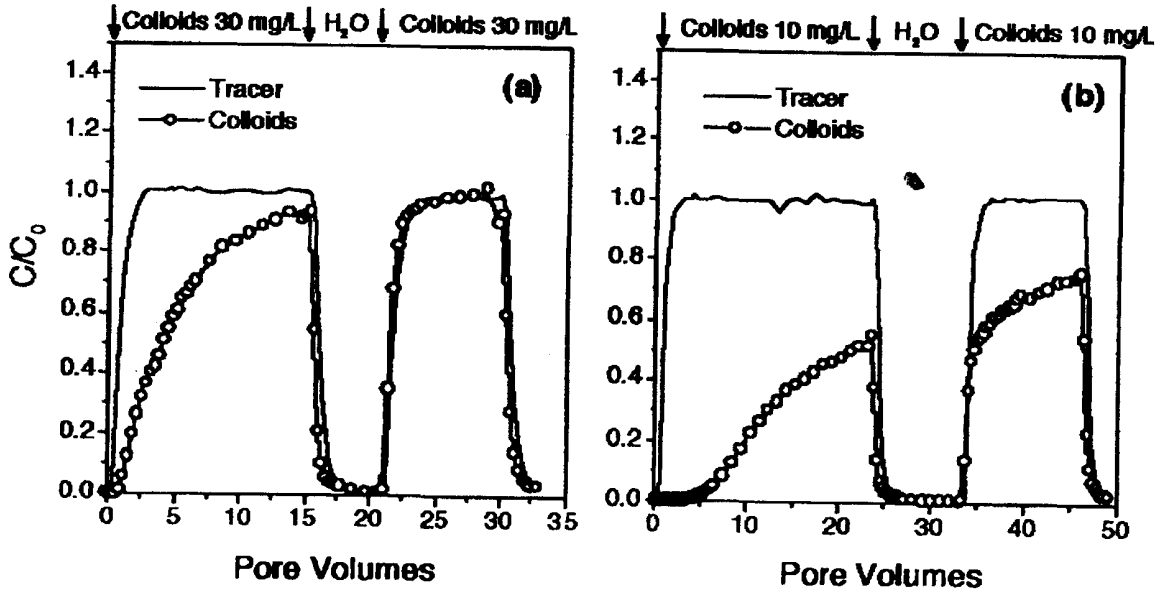

Fig. 7-17. Experimental evidence of colloid deposition site blocking. The data are for the transport of natural soil colloids through undisturbed saprolite columns (from Kretzchmar et al., 1995).

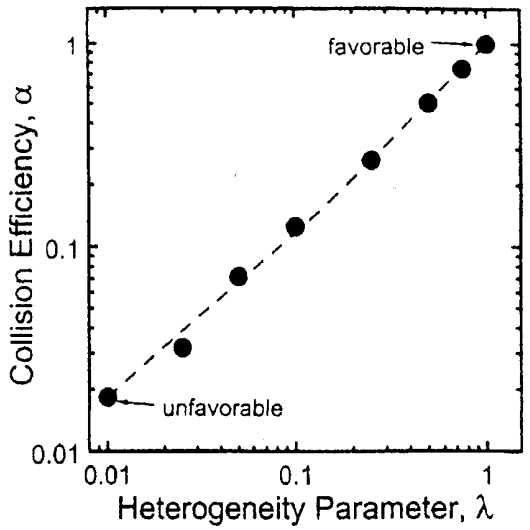

Fig. 7–18. Comparison of experimental data and modeling results (Elimelech et al., 2000) showing that the overall collision efficiency is linearly dependent on the degree of chemical heterogeneity. The surface of the quartz sand collector phase was modified with aminosilane, which created favorable deposition sites for quartz colloids. I is the fraction of favorable colloid deposition sites.

identified as an important parameter for predicting colloid deposition, evaluating heterogeneity is more elusive. Relatively few studies exist in which the nature of sorbent (for adsorption) or collector (for colloid deposition) has been systematically ascertained. Indeed, a framework for characterizing collector heterogeneity has yet to be thoroughly developed. For example, suggestions are that the extent of heterogeneity is relatively narrow (a few percent: Ryan et al., 1999); however, the nature of the distribution of the heterogeneity (regularly-distributed or randon) appears to be as important as extent of the heterogeneity, itself. Furthermore, it appears that techniques such as measuring the average ζ-(zeta) potential of a collector leads to problems with theoretical predictions of colloid deposition (Elimelech et al., 2000).

Figure 7–18 shows experimental results from Elimelech et al. (2000), demonstrating that colloid depostion kinetics is linearly related to the degree of chemical heterogeneity. In this case, silica microspheres were injected into columns containing quartz sand with varying modification of the sand surface with aminosilane. The heterogeneity parameter, λ, is the fraction of the sand surface modified by the aminosilane. The aminosilane-modified sand surfaces are positively charged whereas the unmodified sand surface has a net negative surface charge. The collision (attchement) efficiency, α, is the ratio of the single collector efficiency at λ_I to the single collector efficiency under conditions of favorable deposition (i.e., $\lambda = 1$). As is evident from Fig. 7–18, the overall collision efficiency is linearly dependent on the degree of chemical heterogeneity.

CONCLUSIONS REGARDING COLLOID-FACILITATED RADIONUCLIDE TRANSPORT

Evidence for colloid-facilitated radionuclide or metal ion transport come primarily from two sources: (i) the deduction that a mobile colloid-phase must be present to explain the apparent enhanced transport of otherwise highly retarded species (e.g., Buddemeier & Hunt, 1988); and (ii) laboratory studies of model systems (e.g.,

Grolimund et al., 1996). Evidence from field experiments is essentially nonexistent and many field examples of colloid-facilitated contaminant transport remain deductions from actinide–colloid associations (e.g., Kersting et al., 1999).

That colloid-facilitated radionuclide transport should take place is a straightforward deduction from the component parts of the problem: (i) highly-retarded radionuclides will strongly sorb to colloidal materials; (ii) colloids exist in most groundwater environments in relatively high concentrations; and (iii) colloids can be transported through the subsurface over appreciable distances. Why then is the debate over the significance colloid-facilitated radionuclide transport at the field scale still considerable?

The Principles of Colloid Facilitated Radionuclide Transport outlined in the first section support the conclusion that colloid facilitated radionuclide transport is a phenomenon that will probably take place only under limited system conditions. Systems that we define here as being symmetrical are probably the dominant systems under natural conditions; they also are the systems for which colloid-facilitated radionuclide transport will be minimal. In addition, radionuclides that are subject to colloid-facilitated transport have a dissolved phase component that is, in many cases, negligible. Kersting et al. (1999), for example, evaluated Pu at levels of around $10^{-14}M$. Laboratory studies provide incontrovertible examples that colloidal materials can enhance the transport of low-solubility radionuclide species but field studies remain ambiguous because the colloids, themselves, are not traced.

Most systems of interest as sites for nuclear waste repositories will be symmetrical, at least in the far field. Near field systems are likely to become asymmetrical with time. Colloid-facilitated radionuclide transport in symmetrical systems will probably be minimal. The uncertainty over the importance of colloid-facilitated radionuclide transport is associated with a substantial lack of knowledge of system heterogeneity.

A great need exists for the evaluation of colloid-facilitated transport under field conditions, not simply observations of radionuclide–colloid association but large-scale field experiments. More data sets are needed for developing and testing models and potentially asymmetric systems need to be identified. In particular, increased understanding is needed on the role of chemical and physical heterogeneity on colloid-facilitated radionuclide transport, with a particular emphasis on the immobile phase and the influence of minor system components. Finally, a greater emphasis needs to be placed on organic- and bio-colloids.

ACKNOWLEDGMENTS

Time for writing this chapter was supported in part by an National Science Foundation grant to Bruce D. Honeyman (ERA-9909477). We also thank Dr. Sam Traina for his review of the manuscript.

REFERENCES

Backhus, D.A., P.M. Gschwend, and M.D. Reynolds. 1986. Sampling colloids in groundwater. EOS. 67:954.

Baham, J., and G. Sposito. 1994. Adsorption of dissolved organic carbon extracted from Sewage sludge on montmorillonite and kaolinite in the presence of metal ions. J. Environ. Qual. 23:147–153.

Batley, G.E. 1990. Physiochemical separation methods for trace element speciation in aquatic samples. p 43–76. *In* G.E. Batley (ed.) Trace element speciation: Analytical methods and problems. CRC Press, Boca Raton, FL.

Beckett, R. 2000. Overview of environmental applications. p. 489–496. *In* M. Schimpf et al. (ed.) Field-flow fractionation handbook. John Wiley & Sons, New York.

Beckett, R., D.M. Hotchin, and B.T. Hart. 1990. The use of field-flow fractionation to study pollutant-colloid interactions. J. Chromatog. 517:435–477.

Borkovec, M., Q. Wu, G. Degovics, P. Laggner, and H. Sticher. 1993. Surface area and size distributions of soil particles. Colloids Surf., A. 73:65–76.

Buckau, G., C. Deguelder, and A.B. Kersting. 2001. Impact of colloids on long-term safety in performance assessment of nuclear waste disposal. GEOTRAP V, Oskarshamn, Sweden, 7–7 May.

Buddemeier, R.W., and J.R. Hunt. 1988. Transport of colloidal contaminant in groundwater: Radionuclide migration at the Nevada test site. Appl. Geochem. 3:535–548.

Buffle, J., and G.G. Leppard. 1995. Characterization of aquatic colloids and macromolecules: 2. Key role of physical structure on analytical results. Environ. Sci. Technol. 29:2176–2184.

Buffle, J., D. Perret, and M. Newman. 1992. The use of filtration and ultrafiltration for size fractionation of aquatic particles, colloids, and macromolecules. p. 171–230. *In* J. Buffle and H. van Leeuwen (ed.) Environmental particles. Vol. 1. Lewis Publ., Boca Raton, FL.

Bundschuh, T., W. Hauser, J.L. Kim, R. Knopp, and F.J. Scherbaum. 2001. Determination of colloid size by two-dimensional optical detection of laser induced plasma. Coll. Surf. A, 180:285–293.

Chen, B., F. Shanks, and R. Beckett. 1999. Determination of phosphorous distributions in environmental colloids using SdFFF-ICP-HR-MS. Abstract, FFF 1999, Paris, France. Sept. 5–8.

Contardi, J.S., D.R. Turner, and T.M. Ahn. 2001. Modeling colloid transport for performance assessment. J. Contam. Hydrol. 47:323–333.

Corarcioglu, M.Y., S. Jiang, and S.-H. Kim. 1999. Comparison of kinetic and hybrid-equilibrium models for simulating colloid-facilitated contaminant transport in porous media. Transp. Porous Media. 36:373–390.

Davis, J.A. 1982. Adsorption of natural dissolved organic matter at the oxide–water interface. Geochim. Cosmochim. Acta. 46:2381–2393.

Davis, J.A. 1984. Complexation of trace metals by adsorbed natural organic matter. Geochim. Cosmochim. Acta. 48:679–691.

Davis, J.A., R.O. James, and J.O. Leckie. 1978. Surface ionization and complexation at the oxide–water interface: I. Computation of electrical double layer properties in simple electrolytes. J. Collod Interf. Sci. 63:480–499.

Davis, J.A., and D.B. Kent. 1990. Surface complexation modeling in aqueous systems. p. 177–260. *In* M.F. Hochella, Jr., and A.F. White (ed.) Mineral–water interface geochemistry. Mineral. Soc. of Am., Washington, DC.

Dawson, D.J., J.F. Ranville, B. Jackson, B.D. Honeyman, and J. Seaman. 2001. Particle size distributions of soil colloids: Comparison of sizing methods and influence on transport in porous media. 9 Int. Conf. on Field Flow Fractionation, Golden CO, June 26–29, 2001.

Deerlove, J.P.L., G. Longworth, M.J.I. Ivanovich, B. Delakowitz, and P. Zeh. 1991. A study of groundwater-colloids and their geochemical interactions with natural radionuclides in Gorleben aquifer systems. Radiochimica Acta 52/53:83–89.

Deguelder, C., G. Longworth, V. Moulin, P. Vilks, C. Ross, G. Bidoglio, A. Cremers, J. Kim, J. Pieri, J. Ramsay, B. Salbu, and U. Vuorinen. 1989. Grimsel colloid exercise: An international intercomparison exercise on the sampling and characterization of groundwater colloids. Int. Rep. TM-36. Paul Sherrer Inst., Wûrenlingen and Villingen, Switzerland.

Deguelder, C., I. Triay, J.-I. Kim, P. Wilks, M. Laaksoharju, and N. Miekeley. 2000. Groundwater colloid properties:a global approach. Appl. Geochem. 15:1043–1051.

Elimelech, M., and C.R. O'Melia. 1990. Kinetics of deposition of colloidal particles in porous media. Environ. Sci. Technol. 24:1528–1536.

Elimelech, M., M. Nagai, C.-H. Ko, and J.N. Ryan. 2000. Relative insignificance of mineral zeta potential to colloid transport in geochemically heterogeneous porous media. Environ. Sci. Technol. 34:2143–2148.

Fein, J.B., C.J. Daughney, N. Yee, and T.A. Davis. 1997. A chemical equilibrium model for metal adsoaprion onto bacterial surfaces. Geochim. Cosmochim. Acta.61:3319–3327.

Giddings, J.C. 1993. Field-flow fractionation: Separation and characterization of macromolecular-colloidal-particulate materials. Science (Washington, DC) 260:1456–1465.

Grolimund, D., M. Borkovec, K. Barmettler, and H. Sticher. 1996. Colloid facilitated transport of strongly sorbing contaminants in natural porous media. Environ. Sci. Technol. 30:3118–3123.

Gu, B., J. Schmitt, Z. Chen, L. Liang, and J.F. McCarthy. 1994. Adsorption and desorption of natural organic matter on iron oxide: Mechanisms and models. Environ. Sci. Technol. 28:38–46.

Gutmam, R.G. 1987. Membrane filtration: The technology of pressure driven crossflow processes. Adam Hilger, Bristol, England.

Harnish, R.A., D.M. McKnight, and J.F. Ranville. 1994. Particulate, colloidal, and dissolved phase associations of plutonium and americium in a water sample from well 1587 at the Rocky Flats Plant, Colorado. U.S. Geol. Surv. WRI Rep. 93-4175. U.S. Geol. Surv., Reston, VA.

He, L.M., and B.M. Tebo. 1998. Surface charge properties of and Cu(II) adsorption by spores of the marine *Bacillus* sp. Strain SG-1. Appl. Environ. Microbiol. 3:1123–1129.

Hering, J., and F.M.M. Morel. 1989. Slow coordination reactions in seawater. Geochim. Cosmochim. Acta. 53:611–618.

Hoffmann, S.R., M.M. Shafer, and D.E. Armstrong. 2000. A critical evaluation of tangential-flow ultrafiltration for trace metal studies in freshwater systems: 1. Organic carbon. Environ. Sci. Technol. 34:3420.

Honeyman, B.D. 1999a. Colloid properties and their effects on actinide transport through soils and sediments. *In* 91st Annual Meeting of the Soil Sci. Soc. of Am., Salt Lake City, UT, Oct. 31–Nov. 4, 1999.

Honeyman, B.D. 1999b. Colloidal culprits in contamination. Nature 397:23–24.

Honeyman, B.D., L.S. Balistrieri, and J.W. Murray. 1988. Oceanic trace metal scavenging: The importance of particle concentration. Deep Sea Res. 35:227–246.

Honeyman, B.D., R.A. Harnish, T. McKibben, J.R. Spear, and S. Winkler. 1999. Actinide migration studies at the Rocky Flats Environmental Technology Site: The effect of soil-water redox potential on ^{239,240}Pu solubility. Report to Kaiser-Hill, Rocky Flats Environ. Technol. Site.

Honeyman, B.D., and P.H. Santschi. 1989. A Brownian-pumping model for trace metal scavenging: Evidence from Th isotopes. J. Mar. Res. 47:951–992.

Honeyman, B.D., and P.H. Santschi. 1991. Coupling adsorption and particle aggregation: Laboratory studies of "colloidal pumping" using ^{59}Fe-labeled hematite. Environ. Sci. Technol. 25:1739–1746.

Jardine, P.M., N.L. Weber, and J.F. McCarthy. 1989. Mechanisms of dissolved organic carbon adsorption on soil. Soil Sci. Soc. Am. J. 53:1378–1385.

Johnson, P.R., N. Sun, and M. Elimelech. 1996. Colloid transport in geochemically heterogeneous porous media: Modeling and measurement. Environ. Sci. Technol 30:3284–3293.

Kersting, A.B., D.W. Efurd, D.L. Finnegan, D.J. Rokop, D.K. Smith, and J.L. Thompson. 1999. Nature 397:56–59.

Keizer, M.G., and W.H. von Riemsdijk. 1998. ECOSAT: A computer program for the calculation of speciation and transport in soil-water systems. Dep. of Environ. Sci., Wageningen Agricultural University, the Netherlands.

Kennedy, V.C., G.W. Zellweger, and B.F. Jones. 1974. Filter pore-size effects on the analysis of Al, Fe, Mn, and Ti in water. Water Resour. Res. 10:785–790.

Kim, J.I., P. Zeh, and B. Delakowitz. 1992. Chemical interactions of actinide ions with groundwater colloids in Gorleben aquifer systems. Radiochim. Acta. 58/59:147–154.

Kingston, W., and M. Whitbeck 1991. Characterization of colloids found in various groundwater environments in central and southern Nevada. Water Resour. Ctr. Publ. 45083. Desert Res. Inst., Las Vegas, NV.

Kohler, M., G.P. Curtis, D.B. Kent, and J.A. Davis. 1996. Experimental investigation and modeling of uranium(VI) transport under variable chemical conditions. Wat. Res. Res. 32:3539–3551.

Kretzschmar, R., M. Borkovec, D. Grollimund, and M. Elimelech. 1999. Mobile subsurface colloids and their role in contaminant transport. Adv. Agron. 66:121–194.

Kretzchmar, R., W.P. Robarge, and A. Amoozegar. 1995. Influence of natural organic matter on transport of soil colloids through saprolite. Wat. Resour. Res. 31:435–445.

Kuwabara, J.S., and R.W. Harvey. 1990. Application of hollow fiber, tangential flow device for sampling suspended bacteria and particles from natural waters. J. Environ. Qual. 19:625–629.

Landkamer, L., B.D. Honeyman, and L. Figueroa. 1999. Modeling the sorption of uranium (VI) to gram-negative bacteria. Poster presentation at Migration '99 Sept. 26–Oct. 1, Lake Tahoe, CA. U.S. Geol. Surv., Reston, VA.

Leppard, G.G. 1992. Evaluation of electron microscope techniques for the description of aquatic colloids. p. 231–290. *In* J. Buffle and H.P. van Leeuwen (ed.) Environmental particles. Vol. 1. Lewis Publ., Boca Raton, FL.

Lenhart, J.J. 1997. Surface chemical modeling of U(VI) sorption onto hematite in the presence of humic and fulvic acids. Ph.D. diss. Environ. Sci. and Eng. Div., Colorado School of Mines, Golden.

Lenhart, J.J., and B.D. Honeyman. 1999. Uranium(VI) sorption to hematite in the presence of humic acid. Geochim. Cosmochim. Acta. 63:2819–2901.

Liang, L., and J.J. Morgan. 1990. Chemical aspects of iron oxide coagulation in water: Laboratory studies and implications for natural systems. Aquatic Sci. 52:32–55.

Lieser, K.H., and R. Hill, R. 1992. Chemistry of thorium in the hydrosphere and in the geosphere. Radiochimica Acta. 56:141–151.

Mackey, D.J., and A. Zirino. 1994. Comments on trace metal speciation in seawater or do "onions" grow in the sea? Anal. Chimica Acta. 284:635–647.

Marley, N.A., J.S. Gaffney, K.A. Orlandini, and C.P. Dugue. 1991. An evaluation of an automated hollow-fiber ultrafiltration apparatus for the isolation of colloidal materials in natural waters. Hydrol. Process. 5:291–299.

McCarthy, J.F., K.R. Czerwinski, W.E. Sanford, P.M. Jardine, and J.D. Marsh. 1998. Mobilization of transuranic radionuclides from disposal trenches by natural organic matter. J. Contam. Hydrol. 30:49–77.

McCarthy, J.F., and C. Deguelder. 1993. Sampling and characterization of colloids and particles in groundwater for studying their role in contaminant transport. *In* J. Buffle and H.P. van Leeuwen (ed.) Environmental particles. Vol. 2. Lewis Publ., Boca Ratton, FL.

McCarthy, J.F., and J.M. Zachara. 1989. Subsurface transport of contaminants. Environ. Sci. Technol. 23:496–502.

Murphy, E.M., J.M. Zachara, S.C. Smith, and J.L. Phillips. 1992. The sorption of humic acids to mineral surfaces and their role in contaminant binding. Sci. Total Environ. 117/118:413–423.

Murphy, R.J. 2000. Thorium (IV) binding to organic and inorganic ligands: Marine colloidal organic matter, marine polysaccharides and hematite. Environ. Sci. Eng. Div., Colorado School of Mines, Golden.

Murphy, R.J. J.J. Lenhart, and B.D. Honeyman. 1999. The sorption of thorium and uranium by hematite in the presence of natural organic matter. Colloids and surfaces. A. Physicochem. Eng. Aspects. 157:47–62.

Nomizu, T., K. Goto, and A. Mizuike. 1988. Electron microscopy of nanometer particles in freshwater. Anal. Chem. 60:2653–2656.

Östhals, E., J. Bruno, and I. Grenthe 1994. On the influence of carbonate on mineral dissolution: III. The solubility of microcrystalline ThO_2 in CO_2–H_2O media. Geochim. Cosmochim. Acta. 58:613–624.

Pabalan, R., D. Turner, F. Bertetti, and J. Prikryl. 1998. Uranium(VI) adsorption onto selected mineral surfaces. *In* E. Jenne (ed.) Adsorption of metals by geomedia. Academic Press, New York.

Parfitt, R.L., A.R. Fraser, and V.C. Farmer. 1977. Adsorption on hydrous oxides: III. Fulvic acid and humic acid on goethite, gibbsite and imogolite. J. Soil Sci. 28:289–296.

Puls, R.W., J.H. Eychaner, and R.M. Powell. 1990. Colloid-facilitated transport of inorganic contaminants in groundwater: Part I. Sampling considerations. Environmental Research Brief, EPA/600/M-90/023. U.S. Environmental Protection Agency, Washington, DC.

Puls, R.W., R.M. Powell, D.A. Clark, and C.J. Paul. 1991. Facilitated transport of inorganic contaminants in groundwater: Part II. Colloid transport. Environmental Research Brief, EPA/600/M-91/040. U.S. Environmental Protection Agency, Washington, DC.

Quigley, M.S., B.D. Honeyman, and P.H. Santschi. 1996. Thorium sorption in the marine environment: Equilibrium partitioning at the hematite–water interface, sorption–desorption kinetics and particle tracing. Aquatic Geochem. 1:277–301.

Ranville, J.F., and R. Beckett. 2000. Recent applications of field-flow fractionation to the study of elements associated with aquatic and soil colloids. Abstract. Am. Chemical Soc. Fall 2000 National Meeting, Washington, DC., Aug. 20–24, 2000.

Ranville, J.F., D.J. Chittleborough, F. Doss, T. Harris, R. Morrison, and R. Beckett. 1999. Development of sedimentation field-flow fractionation-inductively coupled plasma-mass spectrometry for the analysis of soil colloids. Anal. Chimica. Acta. 381:315–329.

Ranville, J.F., R.A. Harnish, S. Winkler, and B.D. Honeyman. 2000. Soil aggregation and its influence on $^{239,240}Pu$ particle-size distributions of soils collected from rocky Flats, CO. Report to Region VIII. U.S. Environmental Protection Agency, Washington, DC.

Righi, D., H. Dinel, H.R. Schulten, and M. Schnitzer. 1995. Characterization of clay-organic matter complexes resistant to oxidation by peroxide. Eur. J. Soil Sci. 46:423–429.

Ryan, J.N., and M. Elimelech. 1996. Colloid mobilization and transport in groundwater. Colloids Surf. 107:1–56.

Ryan, J.N., M. Elimelech, R.A. Ard, R.W. Harvey, and P.R. Johnson. 1999. Bacteriophage PRD1 and solica colloid transport and recovery in an iron oxide-coated sand aquifer. Environ. Sci. Technol. 33:63–73.

Ryan, J.N., and P.M. Gschwend. 1994. Effect of solution chemistry on clay colloid release from an iron oxide-coated aquifer sand. Environ. Sci. Technol. 28:1717–1726.

Ryan, J.N., and P.M. Gschwend. 1990. Colloid mobilization in two Atlantic coastal plain aquifers: Field studies. Water Resour. Res. 26:307–322.

Sakamoto, Y., S. Nagao, H. Ogawa, and R.R. Rao. 2000. The migration behavior of Np(V) in sandy soil and granite media in the presence of humic substances. Radiochimica Acta. 88:651–656.

Salbu, B., H.E. Bjørnstad, N.S. Lindstrøm, E. Lydersen, E.M. Brevik, J.P. Rambaek, and P.E. Paus. 1985. Size fractionation techniques in the determination of elements associated with particulate or colloidal material in natural fresh waters. Talanta 32:907–913.

Seaman, J.C. 2000. Thin-foil analysis of sol and groundwater colloids: Reducing instrument and operator bias. Environ. Sci. Technol. 34:187–191.

Schlautman, M.A., and J.J. Morgan. 1994. Adsorption of aquatic humic substances on colloidal-size aluminum oxide particles: Influence of solution chemistry. Geochim. Cosmochim. Acta. 58:4293–4303.

Schubert, J. 1948. The use of ion exchangers for the determination of physical-chemical properties of substances, particularly radiotracers, in solution. I. J. Coll. Phys. Chem. 52:340–356.

Schurtenberger, P., and M.E. Neuman. 1993. Characterization of biological and environmental particles using static and dynamic light scattering. p. 37–115. *In* J. Buffle and H.P. van Leeuwen (ed.) Environmental particles. Vol. 2. Lewis Publishers, Chelsea, MI.

Schûssler, W., R. Artinger, B. Kienzler, and J.L. Kim. 2000. Conceptual modeling of the humic colloid-bourne americium(III) migration by a kinetic approach. Environ. Sci. Technol. 34:2608–2611.

Scheutjens, J.M.H.M., and G.H. Fleer. 1979. Statistical theory of the adsorption of interacting chain molecules: I. Partition function, segment density distribution and adsorption isotherm. J. Phys. Chem. 83:1619.

Spear, J.R., L.A. Figueroa, and B.D. Honeyman. 1999. Modeling the removal of U(VI) from aqueous solutions in the presence of sulfate-reducing bacteria. Environ. Sci. Technol. 33:2667–2675.

Sposito, G. 1989. The chemistry of soils. Oxford University Press, New York.

Sun, N, N.-Z. Sun, M. Elimelech, and J.N. Ryan. 2001. Sensitivity analysis and parameter identifyibility for colloid transport in geochemically heterogeneous porous media. Water Resour. Res. 37:209–222.

Tanizaki, Y., T. Shimokawa, and M. Nakamura. 1992. Physiochemical separation of trace elements in river waters by size fractionation. Environ. Sci. Techol. 26:1433–1444.

Thang, N.M., H. Geckis, J.L. Kim, and H.P. Beck. 2001. Application of the flow field flow fractionation (FFFF) to the characterization of aquatic humic colloids: Evaluation and optimization of the method. Coll. Surf, A.. 181:289–301.

Van der Wal, A., W. Norde, A. Zehnder, and J. Lyklema. 1997. Determination of the total charge in cell walls of Gram-positive bacteria. Coll. Surf. B.: Biointerfaces. 9:81–100.

Vilks, P., and M.-H. Baik. 2001. Laboratory migration experiments with radionuclides and natural colloids in a granite fracture. J. Contam. Hydrol. 47:197–210.

Vilks, P., F. Caron, and M. Haas. 1998. Potential for the formation and migration of colloidal material from a near-surface waste disposal site. Appl. Geochem. 13:31–42.

Westall, C., J.D. Jones, G.D. Turner, and J.M. Zachara. 1995. Models for association of metal ions with heterogeneous sorbents. Environ. Sci. Technol. 29:951–959.

Whitehouse, B.G., G. Petrick, and M. Ehrhardt. 1986. Crossflow filtration of colloids from Baltic Sea water. Water Res. 20:1599–1601.

Whitehouse, B.G., P.A. Yeats, and P.M. Strain. 1990. Cross-flow filtration of colloids from aquatic environments. Limnol. Oceanogr. 35:1368–1375.

Yao, K.M., M.T. Habibian, and C.R. O'Melia. 1971. Water and wastewater filtration: Concepts and applications. Environ. Sci. Technol. 5:1105–1112.

Yeh, G.T., S.L. Carpenter, P.L. Hopkins, and M.D. Siegel. 1995. LEGHC: A Lagrangian-Eulerian finite element model of hydrogeochemical transport. Tech. Rep. Sand95-1121. Sandia Natl. Lab., Albuquerque, NM

8 Soil Radionuclide Plumes

Patrick V. Brady, Carlos F. Jové-Colon, and Gabe Carr

Sandia National Laboratories
Albuquerque, New Mexico

Frank Huang

New Mexico Institute of Mining and Technology
Socorro, New Mexico

ABSTRACT

Radionuclide plumes have been generated by U mining and milling, wastewater discharges, dumping of low-level waste, and weapons testing. Also there are natural plumes of dissolved U associated with U ore deposits. Plume lengths tend to cluster reflecting common, contaminant-specific attenuation mechanisms. Of the more common radioactive contaminants, tritium and ^{129}I move the farthest in the subsurface. Uranium plumes on average tend to be <5 km in length; ^{99}Tc plumes can exceed a kilometer in length; ^{90}Sr plumes are typically shorter than 100 to 200 m, and ^{137}Cs plumes rarely exceed 10 to 20 m in length. Macroscopic analysis of the nature and extent of radioactive contamination in soils provides a critical perspective on the potential health risk posed by specific radionuclides. Considering the areal extent of radionuclide plumes emanating from point sources also allows a very clear assessment of the general controls over radionuclide transport. It also should constitute the basis for developing effective long-term monitoring approaches.

Society routinely confronts macroscopic expressions of soil–radionuclide interactions in the form of contaminant plumes—roughly two or three-dimensional distributions of concentrated radionuclides that pose a risk to groundwater and/or constitute a human health risk associated with particulate exposure. To minimize risk, the plume must be isolated by preventing human access, through, e.g., wellhead protection efforts or capping of contaminated soils or, better yet, removed altogether. In theory, a fundamental understanding of the underlying microscopic chemical, biological, and physical processes—such as that outlined in previous chapters—might point to a ready means for accurately predicting the long-term fate of contaminant plumes (i.e., a fate and transport model), and (possibly), efficient in situ techniques for treating or removing radioactive contaminants. An earlier chapter (Davis et al., 2002, this publication) illustrated how a number of these microscopic processes have been integrated to explain macroscopic plume behavior at the Koongarra Site in Australia. A subsequent chapter (Turner et al., 2002, this publication) describes how the same integration might be applied to predict the behav-

 Geochemistry of Soil Radionuclides. SSSA Special Publication no. 59.

ior of a hypothetical plume emanating from the proposed high-level nuclear waste repository at Yucca Mountain, Nevada, sometime in the future.

This chapter moves toward an alternate objective and dwells primarily on the macroscopic imprint of radionuclide plumes. Specifically, we proceed on the hypothesis that quantifying such macroscopic characteristics as plume dimensionality, length, and persistence might provide useful information about the primary soil processes that control the fate and transport of radioactive contaminants and the overall risk posed by radionuclide contaminant plumes. This approach is termed a *historical case analysis*. It builds on the molecular approach described in earlier chapters and provides some guidance to how standard fate and transport models might be modified to reflect better mechanistic process understanding. Specifically, a historical case analysis sets some bounds on what fate and transport models should predict.

Historical case analyses that focus on radionuclides take advantage of a long and rich history of natural analogue studies. The motivation for working out the behavior of radionuclide plumes emanating from ore bodies and the like has been to put some bounds on the ultimate fate of high level nuclear waste. Our intention is to use much of the same data to say something about the long-term persistence and risk associated with existing plumes. It is useful to begin by first outlining the general plume behavior of more numerous nonradioactive contaminants.

HISTORICAL CASE ANALYSES

Soil contaminant plumes are tragic, but ubiquitous, features of the industrial landscape that often pose long-term threats to human and environmental health. Direct human health risks arise from either drinking of contaminated groundwater from a plume or from exposure to contaminated solids present in the surficial layer of soils. In short, contaminants that neither sorb, nor form insoluble solids in the soil zone tend to partition into the aqueous phase and spread to form three-dimensional plumes. Contaminants that are retarded in the soil zone through sorption or mineral precipitation form vertically restricted two-dimensional plumes. The human health risk of three-dimensional plumes is largely associated with the drinking water pathway. Human health risks from two-dimensional plumes are primarily linked to ingestion of soil particulates. There is some overlap though. Often three-dimensional plumes have an associated hot-spot of separated phase contamination in the soil zone. Similarly, two-dimensional plumes can "bleed" contaminants into underlying groundwater. Additionally, fractures, utility lines, and other soil pathways can impart a three-dimensional structure to what would otherwise be a two-dimensional plume.

Conceptually, contaminant plumes emanating from a point source can be expected to have the highest dissolved contaminant levels near the source, and progressively lower levels down-gradient. In theory, the direction of maximum advance of contaminants should be parallel to the hydrologic gradient and reflect the influence of diffusion, advection and longitudinal dispersion. Once the source term is removed, or treated to stop further transport of contaminant to the groundwater (e.g., with a landfill cap), dilution by fresh recharge should lead to a decrease in dissolved

phase concentrations. Indeed, dilution along the leading edge of a plume alone might ultimately arrest subsequent advance. Note though that in the absence of chemical removal mechanisms (natural or engineered), the contaminant mass in a plume is unaffected by dilution. Natural mechanisms that reduce the bioavailable mass of contaminant in soil solutions include biodegradation, reversible and/or irreversible sorption, and chemical transformation (i.e, reduction or oxidation to less soluble forms).

Obvious examples of three-dimensional plumes include the contaminated zones that often emanate from leaking underground fuel tanks. The U.S. Environmental Protection Agency once estimated roughly 300 000 leaking underground fuel tanks to exist in the USA, mostly in well populated areas. There are several thousand three-dimensional plumes in the USA containing industrial solvent components such as trichlororethylene (TCE) and perchloroethylene (PCE) as well. Chlorinated organics, such as TCE and PCE, along with fuel hydrocarbon components (benzene, toluene, ethylbenzene, and xylene) dominate the cleanup activities mandated by Comprehensive Environmental Response, Compensation, and Liability Act (CERCLA) and Resource Conservation and Recovery Act (RCRA)—the primary statutes that guide soil and groundwater cleanup in the USA. Because these contaminants are relatively soluble and sorb only sparingly, their passage through soils is often rapid and the plumes they subsequently form are large, often exceeding a kilometer in length. Note also that many of these contaminants possess Henry's Law constants that allow significant vapor phase transport in permeable or fractures media.

The ultimate extent of plume advance is controlled to an extent by a combination of chemical and physical factors, primarily biodegradation and dilution–dispersion. In particular, rapid biodegradation apparently sets sharp limits on the growth of plumes containing fuel hydrocarbon components (see McNab & Narasimhan, 1995; Rice et al., 1995). Sporadic and/or minor biodegradation is often unable to prevent the expansion of chlorinated organic plumes until they are quite large in many cases though (McNab & Rice, 2001). The difference in plume advance can be ascribed to the sharply differing susceptibilities of respectively fuel hydrocarbons and chlorinated organics to attenuation in most soils and groundwaters (McNab & Rice, 2001). The physical characteristics of the latter play an important role as well, but the chemical characteristics of the breakdown reaction are central.

Two-dimensional zones of soil contamination typically contain PAHs, PCBs, Pb, Cd, and other metals. Common to these contaminants is a high tendency to sorb to soil solids and/or a strong tendency to form their own insoluble solids. Nonpolar PAHs and PCBs tend to adhere to organic matter disseminated in the soil. The inorganic contaminants sorb to Fe (and Mn) hydroxides when present, but also to clays, and ionizable functional groups found on some soil organics. For these contaminants the combined effect of solubility and sorption prevents large-scale plume development in the vertical dimension, which ultimately limits the impact on groundwater in many cases. Though otherwise immobile contaminants in two-dimensional plumes can provide a flux of colloidal material surface and groundwaters—see the preceding chapter by Honeyman and Ranville (2002, this publication). The risk of two-dimensional plumes to humans comes largely from ingestion of

solids-associated contaminants and depends upon an explicit estimate of contaminant bioavailability in the digestive tract (see Ruby et al., 1996).

There is some overlap that complicates the two-dimensional vs. three-dimensional ranking scheme outlined above. For example, although chromate sorbs sparingly and therefore is capable of forming large three-dimensional plumes, it is often subsequently reduced to form insoluble Cr(III)-bearing solids—see, e.g., Fendorf et al. (2002, this publication), the case study of chromate attenuation by Henderson (1994). Two-dimensional plume contaminants such as Pb can form three-dimensional plumes if the chemical state of the host soil zone is such that it fosters mobility of inorganic contaminants. For example, reducing conditions, such as often prevail in waste dump leachates or in waterlogged soils, can lead to dissolution of iron hydroxide hosts and liberate to solution inorganic contaminants that would otherwise remain sorbed (see Litaor & Ibrahim, 1996). Similarly, the presence of chelating ligands in hazardous waste dumps can dramatically enhance dissolved phase transport of contaminants that would otherwise be immobile (see Means et al., 1978, 1980). An understanding of the site-specific major component chemistry (redox behavior, pH, and others) and its effect on trace component solubility and sorption is thus critical to assessing the potential impact of a plume on health risk.

Before considering soil radionuclide plumes in the framework that has been described thus far a few points must be made about the persistence of nonradionuclide plumes in the face of natural processes and engineered remediation efforts—as they apply to radionuclides as well. Perhaps the most important point is that plume remediation is exceedingly difficult—fewer than 10% of the contaminated sites in the USA have been cleaned up. Considering that several billion dollars have been spent on the effort since CERCLA (the Superfund law) was passed in 1980 and that cleanup outlays are not predicted to increase substantially in the future (also, the majority of the funds go to activities other than cleanup), one can't help but predict that the various organic and inorganic contaminant plumes that dot the landscape now will do so well into the future, barring some dramatic increase in remediation efficiencies. There are some exceptions though. Natural biodegradation of fuel hydrocarbons apparently causes many of these plumes to collapse and vanish over time. Sometimes geochemical conditions favor ambient biodegradation of chlorinated organics as well. Some two-dimensional plumes, if limited in areal extent, can be dug up or covered up. The contaminant plumes that remain though—and this almost certainly constitutes the majority—must be considered semi-permanent features that need to be managed to minimize risk.

A critical first step to managing plumes, in addition to the unraveling of the various fate and transport mechanisms at the microscopic level, is the development of a natural history of contaminant plumes—that is, a macroscopic understanding of how plumes behave in time and space (10s to 1000s of meters). Often regulators and the general public must deal solely with the macroscopic side of the picture. Moreover, although it is countless microscopic steps that control macroscopic plume behavior, the integration of the one to accurately predict the other is often impossible at present to achieve. Until the two are unambiguously bridged, the soil science of radionuclide contamination is forced to communicate to the public with macroscopic terms—namely in the language of plumes (i.e., How big is the plume? How big will it get? Will it reach my well? etc.). The objectives of this chapter are

therefore to: briefly review the chemical and biological controls over radionuclide movement in soils; to describe the historical behavior of as many radionuclide plumes as space allows; and to use these observations to set some broad limits on the potential impact of radionuclide soil plumes. Far more comprehensive accountings of radionuclide releases to the environment can be found elsewhere (see e.g., http://home.acadia.net/cbm/Rad8.html).

RADIONUCLIDE PLUMES

Compared with the hundreds of thousands of fuel hydrocarbon, chlorinated organic, and the various inorganic plumes, plumes containing radioactive contaminants are relatively rare. No more than a few dozen radionuclide plumes are the object of the vast majority of remedial activities. In the USA most of these can be directly or indirectly related to defense activities that began with the Manhattan Project and continued through the Cold War, or with the mining and processing of U for the commercial nuclear power industry. The defense-related activities and the associated contaminant plumes were largely the work of the U.S. Department of Energy and its predecessors—ERDA (the Energy Research and Development Agency) and the AEC (the Atomic Energy Commission). These radionuclide plumes loom very large in the general public's perception of aggregate risk. Moreover, the volumes of contaminated material are staggering (U.S. Department. of Energy, 1997), including: approximately 79 million cubic meters of contaminated solids—95% of which is soil, 70% of which is contaminated with radionuclides; nearly 1.8 billion cubic meters of contaminated groundwater—86% of which is contaminated with radionuclides. Figure 8–1 lists the radioelements of concern in relative frequency of occurrence at contaminated U.S. Department of Energy sites (Riley et al., 1992). The long-lived nature of many radionuclides, their association with nuclear weapons and cancer, and the fact that a number of them had literally never been seen on Earth before the middle of the 20th Century makes radioactive contaminants special in the eyes of the public.

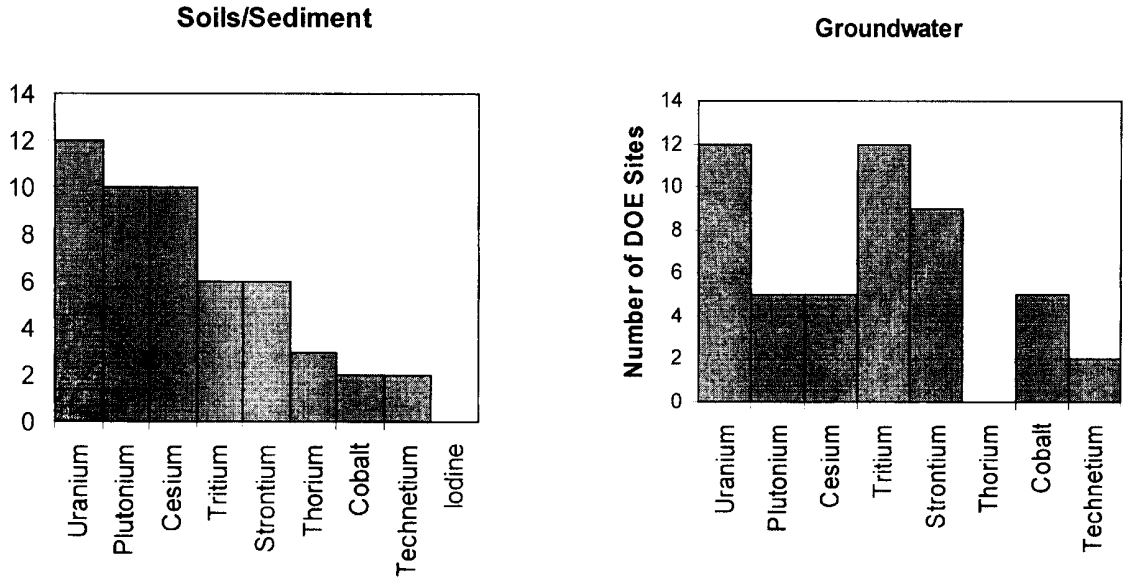

Fig. 8–1. Frequency of occurrence of selected radionuclides in groundwater and soils/sediments at U.S. Department of Energy facilities (from Riley et al., 1992).

In spite of their special place in environmental threats perceived by the public, the chemical controls on soil radionuclide plumes are mostly the same as those of nonradioactive plumes—though there are some twists. The fact that radionuclides possess precisely measured decay half-lives constrains radionuclide plumes somewhat to finite existences. The rule of thumb is that 10 half-lives must elapse before a decaying contaminant can be considered to be gone; e.g., if people can be prevented from drinking from a ^{90}Sr (half-life = 29 yr)—contaminated aquifer for ~300 yr the latter's health impact is minimized. Although 300 yr is obviously a long time, there are presently few remedial techniques, outside of physical removal or leaching with corrosive chemicals, that achieve removal of sorbing radionuclides appreciably faster than radioactive decay—particularly if the radionuclides have been dispersed any significant distance. With the exception of tritium (^{3}H) (half-life = 12.3 yr), and in many cases $^{129}I^-$ (half-life = 1.6 million yr) and $^{99}TcO_4^-$(half-life = 210 thousand yr), many of the soil radionuclides of concern are complexly bound up in the soil fabric making their engineered extraction exceedingly difficult—if not impossible. Another outcome of pervasive radionuclide–soil surface interactions is that radionuclide plumes, with few exceptions (e.g., tritium and occasionally U), should become two-dimensional and relatively stable (nonexpanding) after an initial pulse. The approach below is to consider plumes by contaminant beginning with U—a contaminant that tends to be three-dimensional—that is, it sometimes spreads vertically down below the soil zone. The focus is primarily on plumes existing in North America and that exist in soils or groundwaters (surface water spread of radionuclides has been neglected).

Although decay of ^{238}U, because of its long half-life of 4.5 billion yr, plays almost no role in U plume attenuation, soil transport of U is affected by most of the processes that control transport of other radionuclides (sorption, indirect effects of biologic activity, etc.); hence consideration of U plumes is a useful starting place. After an overview describing U plume sources, a general review of U chemistry and transport is presented, which is itself followed by a description of plume case studies. The sequence of source identification, fate and transport, and plume description will be the path followed for subsequent treatment of ^{90}Sr, ^{137}Cs (half-life = 30.1 yr), ^{99}Tc, Pu, and tritium.

Uranium

Uranium plumes in groundwater have been produced through mining, processing, weapons testing and from natural ore bodies, and include: Uranium Mill Tailings Remedial Action (UMTRA) sites in the USA—sites where U ore was processed; sites where U was released during explosive testing or nuclear waste storage activities; and natural U ore deposits. Much of the discussion below comes from the review of Jové-Colon et al. (2001).

Chemical Controls on Uranium Fate and Transport

Movement of U dissolved from igneous source rocks typically occurs under oxidizing conditions when U is present as the uranyl ion U(VI) (UO_2^{+2}). Uranium is less soluble under reducing conditions, when it is typically present as aqueous

$U(OH)_4$. Figure 8–2 shows uranyl speciation under oxidizing conditions ($pO_2 = 0.2$ atm) and $pCO_2 = 10^{-3.5}$ atm. Note the prevalence of UO_2^{++}-carbonate complexes at pH ≥ 7. In the absence of CO_2, but at the same fO_2, uranyl-hydroxy ions predominate at pH > 5 in most natural waters.

Subsurface accumulations of U—ore bodies—tend to occur at redox fronts where oxidizing, U-rich solutions encounter electron-donating solids, typically organics, that are able to reduce soluble U(VI) to insoluble U(IV)-containing minerals (An exception is formation of insoluble uranyl vanadates). The most common U(IV)-bearing phases found in ore deposits are uraninite (UO_2), pitchblende (highly impure uraninite), coffinite ($USiO_4 \times nH_2O$), and Brannerite [(U,Ca, Y, Ce)(Ti, $Fe)_2O_6(OH)$]. Other common uranyl phases, such as uranophane ($Ca(UO_2)_2(SiO_3OH)_2(H_2O)_5$), are limited in association to the presence of altered nuclear fuel rods and naturally weathered uraninite.

Microorganisms can affect the transport and deposition of U by, producing dissolved compounds (e.g., organic acids) capable of chelating U (Francis, 1998) and forming poorly sorbing anionic complexes, by reducing uranyl to less soluble U(IV) minerals, or by providing a substrate (bacterial cell walls) on which U can sorb (Fowle et al., 2000).

After precipitation, adsorption is the most important sink for U in natural systems. Uranium sorption in soils is primarily controlled by pH and carbonate levels (see Davis et al., 2002, this publication). At high pHs, where anionic uranyl-carbonate complexes predominate, U is only weakly sorbed due to electrostatic repulsion by negatively charged mineral surfaces. When carbonate concentrations are low or absent uranyl-hydroxy surface complexes are observed to form. Minor irreversible sorption of U typically occurs when Fe and Mn oxides are present. Colloidal transport appears to be a less important transport mechanism for U relative to other actinides (see review of Jové Colon et al., 2001).

Plumes

The better studied U plumes are those at UMTRA sites, weapons test and waste storage facilities, and surrounding ore bodies. The UMTRA sites served as

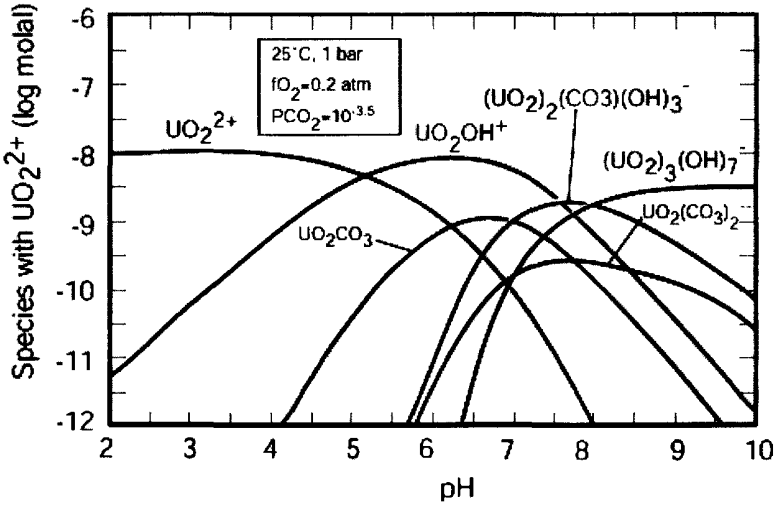

Fig. 8–2. Uranyl speciation at 25°C and 1 bar under oxidizing conditions; $fO_2 = 0.2$ atm and $pCO_2 = 10^{-3.5}$ atm. Uranium speciation data is from the Geochemical Workbench (GWB) software package (Bethke, 1998) (from Jové Colon et al., 2001, with permission).

U ore processing and milling plants and typically witnessed the use of acid–alkaline leaching, sand–slime separation, and ion-exchange recovery processes (lime, sulfuric acid, nitric acid, sodium carbonate, kerosene, and ammonia gas were often used as part of the leaching processes). The UMTRA sites are classified in two types: Title I and Title II. There are 24 Title I UMTRA sites located mostly in the western USA. Most were established in the 1950s and comprise the bulk of the U-plume data obtained as many of them have been the subject of recent (~15 years) monitoring and remediation. In general, these sites contained piles of mill tailings and other contaminated material forming alluvium-like surface deposits where the majority have been removed and relocated elsewhere in specially engineered repositories. On the other hand, other UMTRA sites (Title II) still have their mill tailings in place that typically contribute high levels of U to aquifers near the tailing source. This appears to result in longer plumes. The Title II sites will be discussed briefly because temporal monitoring of groundwater chemistry is scarce and evaluation of existing literature data is still in progress.

Natural recharge through tailings piles is (or was) the primary source of dissolved U. Most of the aquifers beneath mill piles are contaminated exceeding safe levels. Additional contaminants in the effluent include Pb, Cd, Mo, nitrate, ammonium, and Se.

White et al. (1984) envisioned three general transport mechanisms for U, which may well apply to all UMTRA sites: (i) initial dewatering of the slurry material in the tailings pile and concomitant downward flow soon following deposition, (ii) mixing and dilution of the tailing pore waters with local ground and seepage waters, and (iii) periodic meteoric water recharge into the tailing pile by precipitation or snowmelt. Subsequent U transport through the alluvium will be highly dependent upon solution chemistry (i.e., pH, ionic strength, and composition) and redox state of the system as it affects both sorption and precipitation. Dilution and sorption are the most likely mechanisms responsible for lowering U concentrations away from the plume source.

Natural U ore deposits are often used as analogues for long-term high level nuclear waste repositories but also are useful analogues for existing contaminant plumes. The principal U ore source mineral in these deposits is reduced U oxide (UO_2) that is subsequently altered during fluid-mineral interaction under oxidizing conditions to uranyl—oxides, phosphates, and silicates. Most of the U migration away from the concentrated U ore occurred after oxidation, through groundwater mass transport. Subsequently, U became incorporated into surrounding rock through sorption and precipitation of weathering phases. The fate and transport of U at these sites has been most recently reviewed by Jové-Colon et al. (2001).

Maximum plume axial lengths—defined here as the maximum spread of the 10 to 20 ppb contour—were estimated from visual inspection of contour maps by Jové-Colon et al. (2001) and are listed in Table 8–1. The 10 to 20 ppb contour was chosen for convenience. Note that the numbers in Table 8–1 are approximate because of: limited monitoring data, the highly distorted morphology of groundwater plumes, the presence of daughter plumes, and the presence of background U. There also is little data to provide a clear picture of the vertical extent of plumes. The general lack of temporal data for time periods longer than 5 yr for most sites also represents a source of uncertainty as does the fact that many of the sites pos-

Table 8–1. Summary of estimated maximum axial plume lengths and their site characteristics (from Jové-Colon et al., 2001, with permission).

Site	Type	Max. axial plume length	Min. axial plume length†	Sampled depth	Comments
		km		m	
Canonsburg, PA	UMTRA Title I	0.3–0.37	--	2–8	Groundwater table can be found at shallow depths in the fill. Humid continental climate.
Crow Butte Uranium Mine Unit 1, Nebraska	In situ leaching	0.63	0.07	--	Preoperational/baseline maximum plume length measured to ~ 20 ppb. Post-operational ISL mining caused [U] to be orders of magnitude larger in monitoring groundwater wells.
Falls City, TX	UMTRA (Title I)	4.95	3.94	--	Plume analysis comprises tailings pile areas 1, 2, 3, 4, 5, 6, and 7. Largest UMTRA plume.
Fernald Processing Site, Ohio	UMTRA (Title I)	1.3	0.61–0.78	--	Private well monitoring locations (1992–1996)
Grand Junction, CO	UMTRA (Title I)	2.5	0.47–0.6	--	Bulk groundwater composition is SO_4^- rich and relatively HCO_3^- poor. Close to saturation with respect to calcite.
Gunnison, CO	UMTRA (Title I)	2	0.4	50–150	Lindgren (1999) reported a plume length value of 1.5 km interpolated distance to [U]=40 ppb.
Hanford (WA) 300 Area process trench, Washington	UMTRA (Title I)	0.79	0.52	50–150	Plume bounded by the Columbia River
Kennecott Uranium Facility, Wyoming	UMTRA Mine (Title II)	0.69	0.26	~15	Highly irregular plume shape. Maximum plume length measured to ~8 pCi/L
Konigstein Mine, Germany	In situ leaching	3.6–4.0	~1.5	~15–350	In situ leaching of U with sulfuric acid (H_2SO_4). Longest plume measured.
LLNL Plume 1 Pit 4-5, California	Explosive Activity	0.43	0.08	--	Sampled 2nd quarter 1994; plume length measured to the [^{234}U + ^{238}U]=10 pCi/L (~30 ppb) contour.
Maybell, CO	UMTRA (Title I)	0.4	0.15	40–50	U/TDS ratio indicates that soluble salts move further than U beyond the mill tailing limits.
Monticello Millsite, Colorado	UMTRA (Title I)	2.2–2.4	0.42	--	Plume length distance measured to a ^{234}U + ^{238}U concentration level of ~18 pCi L^{-1} (~54 ppb).
Monument Valley, Arizona	UMTRA (Title I)	1.4	1.1	17–47	Plume length for the$[U]_T$>44 ppb region (deep De Chelly aquifer) is ~0.7 km. Max. plume length determined for the alluvial aquifer.
Naturita, CO	UMTRA (Title I)	0.7	0.2	3–76	Plume length may be larger than estimated value. Groundwater sampling restricted to the shallow river alluvium.
New Rifle, CO	UMTRA (Title I)	1.6	0.6	30–95	U/TDS ratio is similar in all sampling wells suggesting that U salts and U migrate at the same rate.
Rio Algom, Moab-Lisbon Facility, Utah	UMTRA Mine (Title II)	2.52	1.71	13–45	Maximum plume length measured to 10–20 pCi/L natural U sampling well–among the largest Title II plumes
Riverton, WY	UMTRA (Title I)	1.7	1.2	7–8	Lindgren (1999) reported a plume length value of 0.9 km interpolated distance to the 44 ppb [U] point

(continued on next page)

Table 8–1. Continued.

Site	Type	Max. axial plume length	Min. axial plume length†	Sampled depth	Comments
		km		m	
Slick Rock (NC), CO	UMTRA (Title I)	0.24	0.12	20–50	Sampling restricted to tailings pile. Plume may be bigger than estimated. Monitoring wells at plume boundary show [U] 900–1000 ppb.
Slick Rock (UC), Colorado	UMTRA (Title I)	0.5	0.2	20–50	Site is bounded by a topographic high and a river.
Sohio Western L-Bar, New Mexico	UMTRA - Mine (Title II)	1.34	0.96	--	Maximum and minimum. plume lengths are approximate; few wells available for measuring natural U sampling
Split Rock (Wyoming) Northwest Valley	UMTRA (Title II)	2.63	0.75	0–30	Mill tailings still remain in place. Long plume length for an UMTRA site.
Split Rock (Wyoming) Southwest Valley	UMTRA (Title II)	2.51	0.86	0–30	Mill tailings still remain in place. Long plume length for an UMTRA site.
Split Rock (Wyoming) Between Northwest and Southwest Valley	UMTRA (Title II)	2	--	0–30	Mill tailings still remain in place. Plume length measured between two valleys containing the mill processing plants and tailings.
Tuba City, AZ	UMTRA (Title I)	1.12	0.5	15–18	Maximum plume length measured to [U] 40 ppb.
Weldon Springs Site, Missouri (WSOW)	UMTRA (Title I)	0.6	--	--	Plume length value is very approximate. [U] well data is very heterogeneous. Multiple plumes observed. Very localized plume lengths with [U]>15 pCi/L (~45 ppb) are only reported.
Weldon Springs Site, Missouri (WSCP)	UMTRA (Title I)	1.1	--	--	Multiple plumes observed. Same explanation as above.
Koongarra ore deposit, Alligator River Uranium Field, Australia	Natural Analogue	0.48–0.5	0.38	13–25	Presence of a weathered zoned. Uranyl- carbonate complexes predominant due to high HCO_{3-} concentration in deeper groundwater.
Bangombe, Oklo natural reactors, Gabon	Natural Analogue	0.25	--	25–500	Presence of a weathered zone. Groundwater chemistry controlled by the $Fe^{2+}/Fe(OH)_3$ equilibria. Fluids are not enriched in CO_2.
Okelobondo, Oklo natural reactors, Gabon	Natural Analogue	0.9–1.0	--	6–100	Presence of a weathered zone. Groundwater chemistry controlled by the $Fe^{2+}/Fe(OH)_3$ (reduced) and $Mn^{2+}/MnOOH$ (oxidized) equilibria. The latter is richer in CO_2.
Osamu Utsumi, Poços de Caldas, Brazil	Natural Analogue	0.5–0.6	--	0–125	Presence of a weathered zone. Pyrite oxidation induces reduction of fluids and subsequent UO_2 precipitation in the redox front.
Morro do Ferro, Poços de Caldas, Brazil	Natural Analogue	0.15	--	0–85	Presence of a weathered zone. Th rich deposit. Th presence in groundwater is probably associated to colloids. Ore zone is very close to the surface.
Cigar Lake ore deposit, Canada	Natural Analogue	0.4	--	0–500	Deep (~430 m) and concealed unconformity type U deposit. Capped by an impermeable quartz barrier. Considered a closed system.

† Minimum axial lengths are measured perpendicular to maximum axial length.

sessed a very large (hundreds of meters across) and disperse source term. The width of the source term is implicitly counted in the maximum plume axial length measurement. In other words, if the actual plume advance were modeled as emanating from a point source, the calculated plume lengths would be a great deal less. In some cases, particularly for the large scale natural analogues (e.g., Poços de Caldas and Oklo), the plume lengths were estimated based on a vertical profile using a linear monitoring well transect. Many of the UMTRA sites are located within 2 or 3 km of rivers. There are a few cases where groundwater plumes were truncated by discharge into rivers, as might be expected where rivers are fed by groundwater. In arid regions, though, rivers often lose water to adjacent aquifers and many of the plumes were observed to spread parallel to, or away from, nearby rivers, suggesting that measured plume lengths reflect groundwater transport.

The frequency distribution of maximum axial plume lengths for all sites listed in Table 8–1 is shown in Fig. 8–3, and suggests that the maximum observed distance of migration is a little >3 km. Note again that this distance is the maximum observed spread of the 10 to 20 ppb U plume contour, and that it includes both upgradient and downgradient limbs of the plume. In other words, the downgradient (maximum) reach of plumes from the source is substantially <3 km. An anomalous, long outlier is the plume associated with the Konigstein mine (Biehler & Falck, 1999; Nitzsche & Merkel, 1999), located 25 km southeast of the city of Dresden, Germany and the UMTRA site Falls City, TX. In situ leaching (ISL) was conducted in the Konigstein mine using periodic inputs of sulfuric acid (H_2SO_4) that mixed and diluted with local groundwater needing further additions of the acid to continue the leaching process (Biehler & Falck, 1999). Leached contaminants have therefore been spread further than they would otherwise go. Note lastly that Title II sites, where source removal has often been less complete than at Title I sites, will possess longer plumes than the bulk shown in Fig. 8–3.

Natural plumes from ores that have been weathered and subjected to periodic meteoric inputs for long periods of time do not migrate appreciably beyond their

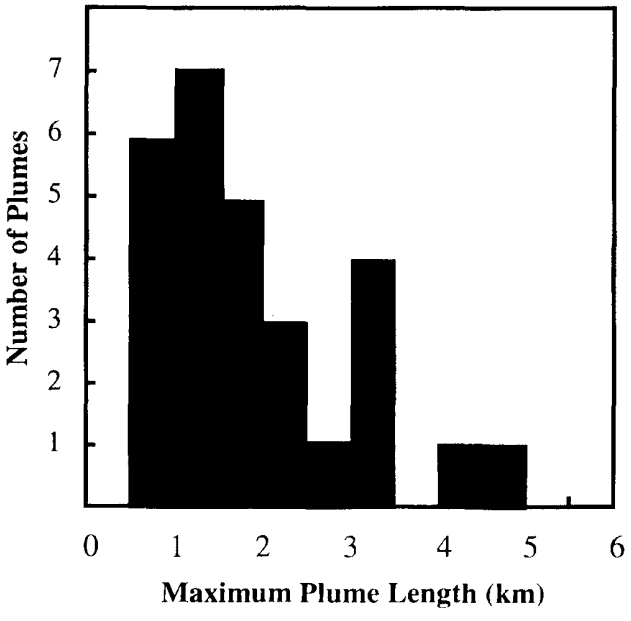

Fig. 8–3. Histogram of maximum plume lengths for U plumes (from Jové-Colon et al., 2001, with permission).

known natural barriers, even during mining. Similarly, the UMTRA sites do not show a significant dispersion of contaminants beyond the limits of the contaminated area if the source term is removed, even though these are not as deeply buried and are in more porous strata than those found in the natural analogues and ore U mining sites. The plume length and the U concentration in monitoring wells remain relatively constant or change insignificantly for time periods approaching 15 yr in some cases (Lindgren, 1999), thus it appears that sorption, dilution, and mineral precipitation are sufficiently effective sinks to limit short-term (years to decades) advances of artificial U plumes. In long-term situations (thousands to millions of years), weathering processes and secondary precipitation of oxidized uranyl phases appears to limit the advance of natural plumes. Lastly, the fact that plume advances vary minimally, despite the fact that hydrologic conductivities, K_ds, and original contaminant source masses for the various sites probably vary by orders of magnitude, suggest the possibly dominant role of chemistry in plume movement.

^{90}Strontium and ^{137}Cesium

^{90}Sr and ^{137}Cs are ubiquitous in the processing of nuclear fuel and, subsequently, in low-level radioactive wastes. ^{90}Sr and ^{137}Cs also were released during the Chernobyl accident. In groundwater, dissolved Cs tends to be present in the Cs^+ form. Cesium sorbs strongly to the clay fraction in soils (K_d are typically >1000 mL g^{-1}) and often the fraction that can be subsequently desorbed is small—around 15%—see the review of Brady et al. (1999). Strontium behaves similarly to Ca in soils and sorbs appreciably to soil components—a median value for soil K_d of 27 mL g^{-1} has been proposed (Baes & Sharp, 1983). This value is similar to that measured at the Hanford Site. The irreversibly sorbed fraction (i.e., the nonexchangeable fraction of soil Sr) is rarely >15% and often 0—see the literature review of Brady et al. (1999).

Some of the better studied sites contaminated with ^{90}Sr and ^{137}Cs include: (i) The Nitrate Disposal Pit at Chalk River Nuclear Laboratory in Ontario, Canada; (ii) The A Disposal area at Chalk River; the 100-K and 100-N area at the Hanford Site in Washington; the 200 East area at Hanford, the 600 area at Hanford; the Maxey Flats Low Level Waste (LLW) Site in Kentucky; the West Valley LLW Site in New York, the Sheffield LLW Site in Illinois; and the Barnwell LLW site in South Carolina. Barnwell is the only active LLW disposal site among those listed above. Surface water and soil contamination by ^{90}Sr and ^{137}Cs exists at Oak Ridge National Laboratory in Tennessee. There also is an apparently stable ^{90}Sr plume at Brookhaven National Laboratory on Long Island.

At the Nitrate Disposal Pit at Chalk River approximately 3800 L of acidic ammonium nitrate solution containing roughly 700 to 1000 curies of ^{90}Sr and 200 to 300 curies ^{137}Cs was disposed of in a limestone-lined pit (Robertson et al., 1987). This occurred from 1953 to 1954. The pit was approximately 55 m^2 and its base was 7 to 8 m above the water table. The surficial sediments consist of unconsolidated sand and silt made up of quartz and feldspar, hornblende, and mica. Groundwater recharge occurs primarily through precipitation—77 cm yr^{-1}. Monitoring began at the site in 1955 and by 1957, ^{90}Sr was detected 150 m downgradient from the source; however, between 1957 and 1961, the plume front advanced only an ad-

ditional 50 m further downgradient from the source at about 1.5% of the groundwater velocity. A study conducted in 1984 (Robertson et al., 1987) indicated that the plume had migrated 350 m in a narrow path from the disposal pit. The initial rapid movement of ^{90}Sr from the site was thought to be caused by the Ca^{2+} produced by neutralization of the waste by the limestone lining. Competition of Ca^{2+} for sorption sites reduced ^{90}Sr retention initially, but over time this effect diminished. At least three specific ^{90}Sr uptake mechanisms were proposed: rapid, reversible ion exchange onto feldspars, slow sorption onto Fe oxyhydroxide coatings, and slow/irreversible fixation to the ferromagnesian fraction of the sand (Melnyk et al., 1984). ^{137}Cs was bound rapidly to the micaceous fraction of the sand and remained in the close vicinity <15 m from the disposal pit. Trace quantities of slowly remobilized, particulate-associated ^{137}Cs were detected 100 and 400 m away from the source though (Robertson et al., 1987).

The A Disposal area at Chalk River saw burial of solid radioactive waste beginning in 1946 in three phases. From 1952 to 1955 4.6 million L of emergency cooling water containing 1000 curies each of ^{90}Sr and ^{137}Cs (as well as other fission products) were discharged into unlined shallow trenches. Beginning in 1954 (and continuing for 6 yr) 7000 L of acidified liquid waste and 2300 kg of ammonium nitrate plus 60 curies of ^{90}Sr and 70 curies of ^{137}Cs were disposed of into a pit lined with lime and dolomite. Beginning in 1955 (and continuing for 5.5 yr) 50 000 L of acidified liquid waste containing 300 curies of ^{90}Sr and 250 curies of ^{137}Cs were discharged into an unlined shallow pit. The geology of the site consists of interbedded silts, sands, and clays overlying a till or crystalline bedrock having low permeability. The saturated thickness varies between 2.4 and 24 m and the primary path of groundwater movement is through the surficial sand units. The latter are made up primarily of quartz and feldspar with minor mica, hornblende, *k*-feldspar and magnetite. Groundwater monitoring began in 1956. As of 1961 (Parsons, 1961):

1. The initial pulse of ^{90}Sr and ^{137}Cs disposed of beginning in 1952 and associated with cooling water appeared to have remained close to the trench area.
2. The second pulse that began in 1954 resulted in rapid migration of both ^{90}Sr and ^{137}Cs to respectively ~170 and 80 m, as well as some remobilization of the initial pulse.
3. The third pulse that began in 1955 resulted in two layers of spreading ^{90}Sr that extended 160 and 175 m from the pit. Only trace quantities of ^{137}Cs were detected.

From 1961 to 1975, the plumes from the second pulse slowed and the ^{90}Sr advanced only an additional 50 m. The ^{137}Cs advanced an additional 10 m (Jackson & Inch, 1980). ^{90}Sr and ^{137}Cs were calculated to be moving at respectively 3 and 0.3% of the groundwater velocity. Ultimately the upper 1955 plume merged with the 1954 plume. Measurements conducted in 1985–1986 (Robertson et al., 1989) indicated that the 1954 and 1955 plumes had advanced ~350 m downgradient from the disposal pit in a relatively narrow (50–120 m) band (based on the 1000 *p*Ci/L vertically averaged contour). ^{137}Cs was projected to have moved only several meters from 1976 to 1985 reaching a total distance of ~130 m from the source.

^{90}Sr movement following the 1954 and 1955 disposals was thought to be aided by the reduced pH of the plume (long-term plume pH was found to be slightly acidic—5.4 to 6.6—relative to the ambient), high NH_4^+ levels from the waste, and high Ca^{2+} levels from the pit lining (Robertson et al., 1989). ^{137}Cs movement was attributed to the presence of NH_4^+ that competed with ^{137}Cs for sorption sites. Indeed Cs K_ds were measured in column tests to decrease from 420 to 30 mg L^{-1} as NH_4^+ levels were raised from 0 to 10 mg L^{-1} (Robertson et al., 1989). As acidity, Ca^{2+}, and NH_4^+ levels decreased over time migration of ^{90}Sr and ^{137}Cs slowed and the sorption mechanisms seen at the Nitrate Disposal area were believed to prevail. Jackson and Inch (1980) showed that ~80% of the ^{90}Sr was exchangeable and largely associated with feldspars. ^{137}Cs was again associated with the micaceous fraction.

There are several ^{90}Sr plumes in the 100-K, 100-N, 200-East, and 600 areas of the Hanford Site in eastern Washington. The 100-K and 100-N areas contain former Pu production reactors and related waste disposal facilities. The 200-East area is dedicated to fuel reprocessing, waste processing, and disposal activities. In the 100-K area the source of the ^{90}Sr plume near the K-East fuel-storage basin is believed to be the basin itself and the 116-KE-3 injection well–drain field that was used to received effluent from the basin. The K-East basin was used to store irradiated fuel rods from 1955 to 1971 (Pacific Northwest National Laboratory, 1999). In the 100-N area, the sources of ^{90}Sr, which is concentrated between the 1301-N facility and the Columbia River, are probably the 1301-N and 1325-N liquid waste disposal facilities. The 1301-N facility was in operation from 1963 to 1985 whereas the 1325-N facility ran from 1983 to 1991. Discharge into both was dominated by N-reactor cooling water that contained radioactive fission and activation products (Pacific Northwest National Laboratory, 1999). Approximately 27.9 curies of ^{90}Sr and 27.5 curies of ^{137}Cs were disposed of below the water table at the 216-B-5 injection well in the 200-East area from 1945 to 1947 (Pacific Northwest National Laboratory, 1993; Pacific Northwest National Laboratory, 1999). In the 600 Area, the Gable Mountain Pond received liquid waste from the 200-East Area from 1957 to 1987, as well as approximately 100 000 curies of fission products from an unplanned release of cooling water from the PUREX plant (Pacific Northwest National Laboratory, 1999).

The geology beneath the 100-K Area consists of eolian silty sand, the Hanford Formation (a mixture of gravel and sand), Unit E of the Ringold Formation (sand and gravel), and Ringold Formation paleosols and overbank deposits of silt and sand. In the K-East storage basin area the unconfined aquifer is located primarily in Unit E of the Ringold Formation. The water table is approximately 22 m below the ground surface and the thickness of the unconfined aquifer is about 25 m. Groundwater in the unconfined aquifer generally flows from the southeast to the northwest toward the river, except during high river stages. Locally, pump and treat efforts affect the water table as well. In the 100-N Area, the unconfined aquifer resides in Unit E of the Ringold Formation and the depth to the water table varies from <1 m near the Columbia River to approximately 21 m farther inland. The base of the unconfined aquifer is a clay-rich unit ~12 m beneath the water table. Groundwater normally flows toward the northwest beneath the 1301-N facility and towards the north beneath the 1325-N facility. Sediments in the 200-East area include the Hanford and Ringold Formations. The depth to the water table varies from 65 to

100 m. The thickness of the saturated zone above the top of the basalt bedrock varies from 0 m in the north to ~80 m in the south. Groundwater around the area of the 216-B-5 injection well flows primarily to the northwest (Pacific Northwest National Laboratory, 1999). In the Gable Mountain Pond area, groundwater is shallow and flows toward the northwest. Groundwater chemistry is dominated by Ca and Mg (cations) and bicarbonate and sulfate (anions). Near the Columbia River, compositions are most dilute. Wastewaters were in many cases very dilute as well.

In general, ^{90}Sr and ^{137}Cs plume attenuation at the Hanford site is dominated by ion exchange–uptake onto clays in the various horizons. Plumes have in many cases slowed soon after disposal ceased, though remobilization has occurred locally where high river stages have exposed radionuclides otherwise stranded in the vadose zone to water. At the 100-K Area, the ^{90}Sr plume around the 116-KE-3 injection well–drain appears to be stagnant and to extend ~75 m (determined from the 100 *p*Ci/L contour) from the source. In the 200-East Area ^{90}Sr contamination extends to at least 150 m northwest of the source (Pacific Northwest National Laboratory, 1999). ^{137}Cs from the 216-B-5 injection well appears to be restricted to the immediate vicinity of the well. ^{90}Sr from the Gable Mountain Pond has migrated through the sedimentary column to groundwater and extends >350 m (based on the 100 *p*Ci/L contour) from the perimeter of the pond (Pacific Northwest National Laboratory, 1999).

At the 100-N area the bulk of the plume has made it to the river and only the tail remains. The plume no longer appears to be moving though large amounts of ^{90}Sr remain in the vadose zone. The K_d describing ^{90}Sr uptake is ~15 to 30 mg L^{-1} and sorption is largely reversible and rapid and ultimately controlled by competition between ^{90}Sr and other cations (Serne & LeGore, 1996). ^{90}Sr levels in the 100-N plume are estimated to be approximately 10^{-12} *M*, compared with ~ 3.5×10^{-6} *M* natural Sr (and ~10^{-3} *M* Ca+Mg).

The low absolute levels of ^{90}Sr in many of these plumes sets some very severe constraints on the success that remedial technologies might achieve. Specifically, in situ cleanup approaches, that rely on the specific chemistry of Sr, will in all likelihood treat at least a million atoms of nonradioactive Sr for each atom of ^{90}Sr that is either extracted or immobilized. Moreover, many of the chemical techniques that might be applied to Sr contamination (e.g., chelation, formation of metal phosphates, reactive barriers containing ion-exchange material) might end up affecting chemically similar Ca and Mg instead—decreasing the odds for the in situ chemical treatment further from the factor of one in a million set by the natural background of Sr at the site. It should be kept in mind that the moderately high K_d at the site and the moderately low decay half-life of ^{90}Sr tends to prevent large-scale plume advance. In effect, an in situ reactive barrier already exists at the site that engineered approaches might be judged against.

Numerous ^{90}Sr and ^{137}Cs plumes apparently emanate from leaks in high-level waste tanks at Hanford. Typically the tanks contain waste sludges and residual caustic solutions. Movement of ^{90}Sr and ^{137}Cs through the vadose zone beneath the tanks might have been aided by direct and indirect action of the caustic solutions on aqueous speciation and the surface reactivity of otherwise sorptive phases that exist at depth. Colloidal transport probably also plays a role in contaminant transport. A recently initiated vadose zone monitoring effort will hopefully provide a clear pic-

ture of the extent and relative velocity of ^{90}Sr and ^{137}Cs plumes (see http://www.doegjpo.com/programs/hanf/HTFVZ.html). Early indications point to vertical transport of a few dozen meters at most for both. ^{90}Sr appears to move further than ^{137}Cs.

Maxey Flats is a LLW disposal site in Kentucky that consists of trenches ~90 m long, 7.5 m wide, and 7.5 m deep occupying an area of about 0.8 km^2. It received the bulk of the waste from 1963 to 1978. The site is located on a plateau 90 to 120 m above the surrounding valleys. Trenches were excavated in nonporous shale underlain by sandstone beds. The saturated zone reaches the upper portions of the shale. Groundwater transport is largely through fractures and joints. The site is humid and receives ~117 cm of rainfall a year. Water accumulation in the trenches and microbial degradation of organic matter ultimately led to anoxic conditions—low dissolved O_2 and sulfate, high alkalinity, high Fe^{2+}, and high ammonia in the trenches. Some surface runoff transport of ^{137}Cs has been detected at the site. Minor groundwater transport of ^{90}Sr and ^{137}Cs is thought to occur through mobilization by organic acids (Dayal et al., 1986).

The West Valley LLW disposal site operated from 1963 to 1975 and received roughly 67 000 m^3 of waste. Burial trenches were excavated in fine-grained, clay-rich till. Quartz and illite constitute >50% of the till minerals, the remainder being calcite, kaolinite, and feldspar. The till is ~28 m thick and overlies a fine sand plus silt that is itself underlain by a layer of silty clay till having very low permeability. Average annual precipitation is ~100 cm. Because of the low hydraulic conductivity of the material, very little water infiltrates vertically through the till. Trench waters have pH values between 6.5 and 7.7 and are anoxic. Although organic complexation, brought on by degradation of wastes, has been observed, ^{90}Sr and ^{137}Cs were found to be confined to the trenches (Prudic, 1986). Plume attenuation is dominated by the low hydraulic conductivity and the high ionic exchange capacity of the material (Prudic, 1986).

The Sheffield LLW disposal site in the state of Illinois received >61 000 curies of radioactive wastes—consisting mostly of tritium, ^{90}Sr, ^{137}Cs, and ^{60}Co—between 1967 and 1978 (Murphy & Bergeron, 1991). Wastes were disposed of in burial trenches excavated in glacial loess of silts and clays possessing interbedded sand lens. The average depth to groundwater at the site is ~7.6 m. The soil is relatively permeable and average precipitation is about 89 cm yr^{-1}. Because of the relatively high soil permeability, trenches rarely accumulated leachate and the soil solution remained oxic and the pH remained between 6.2 and 8.5. ^{90}Sr and ^{137}Cs have occasionally been observed in trench waters but no general migration has been detected (Murphy & Bergeron, 1991).

The Barnwell LLW disposal site in South Carolina began accepting LLW in 1971 and continues to operate. Burial trenches in unconsolidated coastal plain sediment of gravel, sand, silt, clay, and limestone are made up of approximately 85% quartz and <10% kaolinite and mica. Sediments are relatively permeable and the water table is generally between 10 and 15 m of the surface. Precipitation is around 120 cm yr^{-1} and roughly 30% of this recharges into the aquifer (Pietrzak et al., 1982). Trench waters have high redox potentials and pHs range from 5.8 to 7.6. Little water

accumulates in the trenches because of the relatively high permeability. ^{90}Sr is restricted to the immediate area of the trenches (Pietrzak et al., 1982).

Lastly, the large amounts of ^{90}Sr and ^{137}Cs released by the accident at the Chernobyl Nuclear Power Plant (ChNPP; Kiev, Ukraine) and that have subsequently accumulated in soil bodies in large parts of central and eastern Europe (see Golosov et al., 1999; Kryshev, 1995; Matsunaga et al., 1998; and references therein) shed some insights on their relative mobility in soils. Recent examinations of soils from central Russia (Golosov et al., 1999), Hungary (Szerbin et al., 1999), Ireland (Rafferty et al., 2000), Sweden (Isaksson & Erlandsson, 1998; Rosen et al., 1999), Croatia (Barisic et al., 1999), Belarus (Arapis et al., 1997), Poland (Zygmunt et al., 1998), and southern England (Owens et al., 1996) reveal that the maximum activity of ^{137}Cs is primarily restricted to a depth range from 0–1 to ~6 cm in the top areas of the soil profile. In some cases, the maximum ^{137}Cs activity could be larger in slightly deeper parts of the profile possibly due to active sedimentation, vegetation–plant activity, and the presence of large-scale porosity (Owens et al., 1996). Interestingly, the overall vertical distributions of ^{137}Cs activity observed in soil profiles situated relatively close to the ChNPP are very similar to the above-mentioned cases located away from the source (Agapkina et al., 1995; Ivanov et al., 1996, 1997); even when the relative activity of ^{137}Cs is somewhat different. A soil extraction study (Krouglov et al., 1998) in contaminated soils not far from the ChNPP confirms the exchangeable behavior of ^{90}Sr and the strong association of ^{137}Cs with soil mineral phases that may be enhanced with time. In general, ^{90}Sr tends to migrate deeper than ^{137}Cs (see Ivanov et al., 1997); a feature also observed in subsurface radionuclide plumes. Field-scale observations in soils nearby the ChNNP (Agapkina et al., 1995) suggests a relationship of ^{137}Cs and ^{90}Sr transport facilitated through organic material. Other studies suggest a role of plant activity in mediating and facilitating radionuclide transport throughout the soil profile (Sanford et al., 1998).

Table 8–2 provides estimates of ^{90}Sr and ^{137}Cs plume lengths. In some cases the lengths are different than cited above because different contour lines were used for delineation. There are no entries for Sheffield, Barnwell, West Valley, and Maxey Flats as ^{90}Sr and ^{137}Cs do not appear to have left the immediate vicinity of the disposal sites. As with the U plume analysis, there is a fair bit of uncertainty involved in the estimated plume lengths, particularly because of spatial and temporal monitoring gaps. Nevertheless, they present a reasonably clear picture of ^{90}Sr and ^{137}Cs advance. Specifically, there are several cases where ^{90}Sr plumes have moved a dozen meters or less; seven or eight cases where plumes have gone up to 0.5 km; and one case where a plume has exceeded 1 km—the 100-N plume at Hanford. The spread in plume advance may say more about the size of the original ^{90}Sr source than anything else, i.e., larger sources resulted in larger plumes. Although no similar source term control over U plume length was argued for earlier, there may be such an effect. Resolving the question would require comparing the estimated masses of solid-phase U at each site—an effort that has not been made. ^{137}Cs plumes are less in number than ^{90}Sr plumes and appear not to exceed ~20 meters. Attenuation mechanisms such as sorption tend to be more effective for ^{137}Cs than ^{90}Sr, and the smaller ^{137}Cs plumes may reflect this. The source term for both ^{137}Cs and ^{90}Sr was similar at the Chalk River Plumes, yet ^{90}Sr traveled farther.

Table 8–2. Summary of estimated maximum axial plume lengths for ^{90}Sr and ^{137}Cs sites and their site characteristics.

Site	Type	Max. axial plume length	Min. axial plume length	Sampled depth	Sources	Comments
		m	mm	m		
Chalk River Nuclear Laboratory , lower Perch Lake Basin, Ontario, Canada	Vitrified nuclear waste	3 m for ^{137}Cs and 12.8 m for ^{90}Sr	0.7 m for ^{137}Cs and 0.8 m for ^{90}Sr	--	Lyon et al. (1985)	Leaching experiment where vitrified nuclear waste was buried beneath the groundwater table to monitor radionuclide transport.
Chalk River Nuclear Laboratory, ACS waste pits, Ontario, Canada	Nuclear Waste Disposal	125 m for ^{90}Sr		5–9	King & Killey (1992)	Acid-Chemical-Solvent (ACS) pits were used for 5 yr for disposal activities. Plume was estimated to a [^{90}Sr] ~0.1 Bq g^{-1} gamma log in soil.
Chalk River Nuclear Laboratory, Waste Management Area B, Ontario, Canada	Nuclear Waste Disposal	~170 m for ^{90}Sr	~100 m	--	Buckley et al. (1992)	Dominant radionuclide contaminant is ^{90}Sr. Subsurface plume estimated to ^{90}Sr concentrations of 3000–4500 Bq L^{-1}. Surface water [^{90}Sr] exceed a spreading distance of ~460 m.
Chalk River Nuclear Laboratory, Waste Vicinity of disposal Area A, Ontario, Canada	Nuclear Waste Disposal	260– 283 m for ^{90}Sr	26–30 m	6–12	Jackson & Inch (1983)	Plume boundary measured to counts of 1000 dpm g^{-1} in the borehole.
Savannah River Site, F Area Retention Basin, South Carolina	Nuclear Waste Disposal	~47 m for ^{137}Cs	30.5 m for ^{137}Cs	2–8	Lockwood et al. (1997)	Plume measured to either a ^{137}Cs concentration of 0.1–10 pCi g^{-1} in soil.

Hanford, 100-K area, unconfined aquifer, KW basin, Washington	Nuclear Waste Disposal	~338 m for ^{90}Sr	~154 m	--	Johnson et al. (1998)	Plumes are estimated to a [^{90}Sr] of ~0.9 pCi/L.
Hanford, 100-K area, unconfined aquifer, KE basin, Washington	Nuclear Waste Disposal	~385 m for ^{90}Sr	~230 m	--	Johnson et al. (1998)	Plumes are estimated to a [^{90}Sr] of ~0.8 pCi/L. KW basin was used for storage of irradiated fuel material.
Hanford, WA, 100-K area, unconfined aquifer, plume close to southernmost tip of 116-K-2 liquid waste disposal trench	Nuclear Waste Disposal	~510 m for ^{90}Sr	~310 m	--	Johnson et al. (1998)	Plumes are estimated to a [^{90}Sr] of ~0.8 pCi/L. Plumes is cut-off by the Columbia River. Liquid waste disposal trench is located ~380 m from the Columbia River.
Hanford, WA 100-K area, unconfined aquifer, plume close to northernmost tip of 116-K-2 liquid waste disposal trench	Nuclear Waste Disposal	~340 m for ^{90}Sr	~308 m	--	Johnson et al. (1998)	Plumes are estimated to a [^{90}Sr] of ~0.3 pCi/L. Plumes is cut-off by the Columbia River. Liquid waste disposal trench is located ~380 m from the Columbia River.
Hanford, WA, 100-N area, uppermost aquifer	Nuclear Waste Disposal	~1100 to 1400 m for ^{90}Sr	~880 m	--	Earth and Environmental Services (1996).	Plumes are estimated to a [^{90}Sr] of ~0.5 pCi/L. Plumes is cut-off by the Columbia River. Plume comprises reactor and liquid waste disposal trench areas. Liquid waste disposal trench 1325-N is located ~700 m from the Columbia River.

* Minimum axial lengths are measured perpendicular to maximum axial length.

^{99}Technetium and ^{129}Iodine

^{99}Tc is generated in nuclear power plants as a fission product and in medical laboratories and academic institutions. In the processing of nuclear materials, ^{99}Tc and ^{129}I are found in wastes from a wide range of processes, including ion-exchange resins, filter sludges, evaporator bottoms, cartridge filters, trash, and decommissioning wastes. ^{99}Tc and ^{129}I tend to dominate performance assessment calculations that are used to predict doses that might result from radionuclide releases from high and low-level waste facilities. Realistic models of subsurface fate and transport tend to predict sorption and/or decay of most of the other radionuclides. Because ^{99}Tc and ^{129}I are anionic and form no insoluble solids under oxidizing conditions, they are predicted to move fastest and farthest when they are expected in a waste site point source.

In soils, I is present mainly as nonsorbing iodide. The pertechnetate ion (TcO_4^-) is the dominant chemical form of dissolved Tc(VII) and total Tc in the environment. The anionic pertechnetate does not form complexes with chelating agents nor does it coprecipitate with particles unless it is first reduced to a lower valence state such as Tc(IV), which precipitates solids such as TcO_2 or $TcO_2 \cdot 2H_2O$. As the redox potential decreases, TcO_2 becomes the dominant solubility control for dissolved technetium. TcO_2 is typically sparingly soluble in water (the formation of Tc(VI)-CO_3 complexes may have some role in solubility and transport). Under reducing conditions, TcS_2 may form as well.

Three ^{99}Tc plumes exists at the Paducah Gaseous Diffusion Plant (PGDP) in western Kentucky (see e.g., http://www.bechteljacobs.com/pad/1998-4.pdf and http://web.ead.anl.gov/TechCon/Projects/tce/description/index.cfm). The PGDP site overlies roughly 20 m of clay-rich soil. At ~18.3 m depth there exists a thick gravel deposit that forms a regional aquifer (RGA, the Regional Gravel Aquifer), and the pathway for ^{99}Tc (and commingled TCE) contamination. The saturated zone lies roughly 3 to 7 m below ground surface. ^{99}Tc levels range from the detection limit (~25 *p*Ci/L) to 40 000 *p*Ci/L (the regulated level is 900 *p*Ci/L). ^{99}Tc is present in both the vadose and saturated zone. It is retarded by shallow silt and clay units, but plumes extend between 0.5 and 5.3 km offsite towards the Ohio River. Groundwater wells are being pumped to inhibit plume movement. ^{99}Tc plumes exist at the Hanford Site at the 200-East Area, the 600 Area, and the 200-West Area. The last plume is the largest.

^{129}I plumes existing at the Hanford site are largely confined to the 200 Areas where it was discharged to subsurface drains. The highest concentrations observed onsite are downgradient from the PUREX and REDOX Plants in the 200-East and 200-West Areas, respectively. The ^{129}I plume at the latter area is coincident with tritium and nitrate plumes and appears to be moving at the same velocity, suggesting that essentially no retardation of ^{129}I is occurring.

Tritium

The primary source of tritium in the environment has been radioactive fallout from testing of thermonuclear weapons (i.e., hydrogen bombs) and discharges from nuclear power plants. Tritium also is used in industrial thickness gauges, luminous paints, nonpowered (self-luminous) light sources, fusion research, as a ra-

dioactive tracer in geology, chemistry and biological experiments, and in production of nuclear weapons. Plumes containing tritium are, in a geochemical sense, a great deal less interesting than the other radionuclide-bearing contaminant plumes simply because there are for all intents and purposes no retardation reactions that affect tritium—other than its decay. Tritium also suffers from the same problem noted for ^{90}Sr—namely, any remediation will probably have to treat millions of molecules of water for every tritium molecule affected. Tritium moves through soils at the same velocity as water. Consequently, tritium plumes can become rather large. Treatment techniques focus primarily on isolation of the tritiated water through physical means until sufficient decay has occurred. Tritium plumes exist at the Savannah River Site, Brookhaven National Laboratory, the Hanford Site, among others.

Plutonium

Except for trace quantities of Pu in pitchblende and small amounts produced in natural reactors (e.g., the Oklo natural reactor in Gabon), Pu does not exist as a naturally occurring element. Significant quantities of Pu have been released into the environment, primarily as radioactive fallout from nuclear weapons testing and accidental releases (e.g., the Windscale accident in 1957 and the Chernobyl accident in 1986). Plutonium has four possible oxidation states (i.e., +3, +4, +5, and +6). The +4 state is the most stable one in soils, and Pu in this form sorbs to Fe hydroxides and forms sparingly soluble hydroxides as well. Plutonium mobility in soils appears to depend on pH, clay content, the presence of calcium carbonate, and organic matter. Microbial activity also may enhance the movement of Pu and Pu moves as a colloid (see Honeyman & Ranville, 2002, this publication). In general, Pu binds very strongly to soils, and very little can be desorbed. Coughtrey et al. (1986) estimate the latter to be <1%. Litaor and Ibrahim (1996) used 0.01 *M* $CaCl_2$ as an extractant and measured Pu in Rocky Flats soil to be 0.04 to 0.08% exchangeable. Bunzl et al. (1995) measured exchangeable $^{239+240}Pu$ (0.5 to 1%) from fallout-contaminated soils in Germany using 1 *M* NH_4OAc as the extractant.

Pu contamination of soils at the Rocky Flats Facility is one of the more widely publicized occurrences. Litaor and Ibrahim (1996) showed that Pu, which was largely bound to soil metal hydroxides, became more mobile when soil saturation led to reducing conditions and Pu desorption. Overall, strong sorption prevents Pu plumes from forming in all but the most anomalous settings, e.g., the Nevada Test Site, where underground testing of nuclear weapons was carried out for decades and where Pu-contaminated waters can be found. Note though that very few parts of the world are tested as thoroughly for Pu as at the Nevada Test Site. On the other hand, the extreme difficulty of Pu remobilization, combined with its singular toxicity make removal of waste Pu from contaminated soils extraordinarily difficult. The same is true, but to a lesser extent, for ^{137}Cs.

SUMMARY DISCUSSION

Figure 8-4 is a schematic of the relative lengths of maximum plume advance observed for the various radionuclides in soils and groundwaters. At the low end

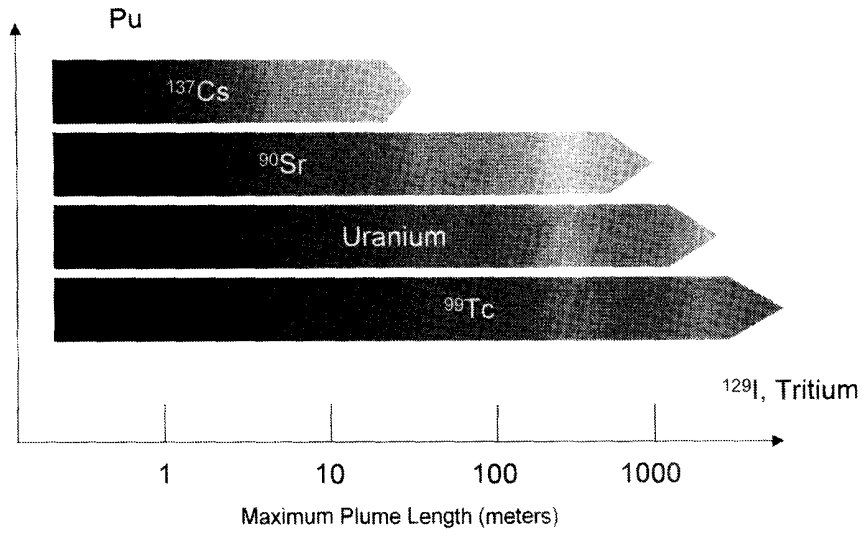

Fig. 8–4. Schematic summary of radionuclide plume lengths at steady-state (see text).

is Pu, which is strongly associated with soil particulates and is rarely seen to move any great distance in the dissolved phase. At the other end of the spectrum are tritium, which is never retarded relative to water, and ^{129}I and ^{99}Tc, which tend to move as fast as tritium does. In between are U, ^{90}Sr, and ^{137}Cs in order of decreasing plume length. Note that several processes contribute to the sequence—some quantifiable, such as tendency to sorb, others, such as original source magnitude—are less clear. Presumably, plume lengths represent a combination of the two (and probably other factors as well). Figure 8–4 seeks simply to collect and describe the approximate lengths of observed plumes independent of any mechanistic interpretation. It says what plume lengths are without addressing the why. Nevertheless, Fig. 8–4 might be used to consider potential health risk from a plume by allowing the filtering out of unlikely transport predictions. For example, predictions of kilometer-scale ^{90}Sr advance would probably require some very persuasive site-specific evidence. The only one found above to have reached this distance (and beyond) is the 100-N Area at Hanford and it possessed some very special attributes, namely enormous water fluxes and a very sizeable source term. A prediction of ^{137}Cs transport beyond 100 m should carry with it some very strong arguments outlining why it is so far beyond the norm. Hypothetically, such arguments might include fast pathways (e.g., fractures) and possibly colloids. A transport model that predicts appreciable dissolved Pu, as opposed to colloidal Pu, in a plume would be at odds with the overwhelming majority of macroscopic observations. To our knowledge, no dissolved phase Pu plumes exist.

Obviously knowing the collective history of plumes of a given contaminant type might constitute a persuasive tool with which to communicate with scientists and nonscientists alike. Its power is a direct function of the number of plumes that have been considered and the technical detail involved in the effort. The initial analysis above should be expanded, particularly to include non-North American sites, for greater impact.

Most of the plumes described above have been in the ground for decades and, in the absence of dramatic improvements in cleanup technologies, will likely remain there for the foreseeable future. We therefore close this chapter by returning to the question of how to scientifically manage radionuclide plumes. Although some of the contaminant plumes described above may be advancing, most have slowed. Some have stopped altogether. Plume attenuation is most clearly seen for those contaminants that sorb appreciably to soils. Nevertheless, until radioactive decay, dilution, and possibly irreversible sorption have lowered concentrations to safe limits even arrested plumes that pose a human and an ecological risk that must be guarded against. How to do so? Obviously better methods for accurately predicting trajectories of individual plumes are needed. A first step is then to consider U plumes separately from the rest since U is often a major component of soil and groundwaters; the other isotopes are only present at trace levels. A second step is to include **all** of the relevant chemical processes, in particular—colloidal transport, irreversible sorption, and surface complexation, in transport predictions. Lastly, predictions of plume advance should always be validated against the common element-specific behavior observed in actual plumes.

Because U is often a major component of ground and soil waters; hence its fate and transport tends to depend, at least to some extent, on large-scale dissolution and precipitation of solubility-limiting U-bearing solids. There exists a clear and well-agreed upon method for describing the thermodynamics and kinetics of mineral solubility and aqueous speciation in natural systems. This framework can likewise be applied to predict the likely reaction paths followed by major elements such as U in contaminated systems. These scenarios can subsequently be compared back against natural analogues and some confidence gained as to their validity. Substantial credence comes from the ability of geochemists to use standard geochemical models to accurately predict such natural features as, for example, the speciation of seawater and diagenetic phase relations. Note though that all of the other radionuclides exist at trace levels in natural waters; hence their transport depends on sorption, ion exchange, possible inclusion in surface solid solutions, and/or transport as colloids (tritium is an exception). There is some overlap at the outer fringes of the haloes that surround uranium ore bodies. Trace isotope plumes are roughly equivalent to ore bodies without the primary ore or secondary phases.

No equivalent framework exists for predicting the outcome of the accumulated processes that control trace radionuclide transport. The preceding chapters point to a wealth of mechanistic understanding of sorption, ion exchange, and colloidal transport, yet there is a relative absence of cases where submodels have been calibrated against natural features. For this reason, the same level of credence is not given to trace-element transport predictions as is routinely given to major-element estimations. More often than not, the trace element problem is treated in, for example, performance assessment by using a K_d model, which is known to be mechanistically flawed (Reardon, 1981; Bethke & Brady, 2000), to model processes that probably do not occur in nature, i.e., completely reversible sorption of cationic radionuclides. In many cases it is impossible to account for existing plumes using a K_d model, which neglects irreversible sorption. The next generation of fate and

transport models should not include K_ds and should include irreversible uptake, and they should be calibrated against real plumes.

ACKNOWLEDGMENTS

We appreciate helpful reviews by Richard Metcalf and Nathan Yee. We also acknowledge funding over the years from the U.S. NRC, DOE-EM40, and the Sandia LDRD Office. Our gratitude is not to imply that the views expressed here are those of our sponsors or reviewers.

REFERENCES

Agapkina, G.I., F.A. Tikhomirov, A.I. Shcheglov, W. Kracke, and K. Bunzl. 1995. Association of Chernobyl-derived Pu-239+240; Am-241; Sr-90; and Cs-137 with organic-matter in the soil solution. J. Environ. Radioactivity 29(3):257–269.

Arapis, G., E. Petrayev, E. Shagalova, O. Zhukova, G. Sokolik, and T. Ivanova. 1997. Effective migration velocity of Cs-137 and Sr-90 as a function of the type of soils in Belarus. J. Environ. Radioactivity 34(2):171–185.

Baes, C.F.I., and R.D. Sharp. 1983. A proposal for estimation of soil leaching and leaching constants for use in assessment models. J Environ. Qual. 12:17–28.

Barisic, D., A. Vertacnik, and S. Lulic. 1999. Caesium contamination and vertical distribution in undisturbed soils in Croatia. J. Environ. Radioactivity. 46(3):361–374.

Bethke, C.M. 1998. The Geochemist's Workbench Release 3.0: A users software guide to Rxn, Act2, Tact, React, and Gtplot. Hydrogeology Program. Univ. of Illinois, Urbana-Champaign.

Bethke, C.M., and P.V. Brady. 2000. How the K_d approach undermines ground water cleanup. Ground Water 321:435–442.

Biehler, D., and W.E. Falck. 1999. Simulation of the effects of geochemical reactions on groundwater quality during planned flooding of the Konigstein uranium mine, Saxony, Germany. Hydrogeol. J. 7(3):284–293.

Brady, P.V., B.P. Spalding, K.M. Krupka, R.D. Waters, P. Zhang, D.J. Borns, and W.D. Brady. 1999. Site screening and technical guidance for monitored natural attenuation at DOE sites. SAND 99-0464. Sandia Natl. Lab., Albuquerque, NM.

Buckley, K.R., and W.D. Vijayan. 1992. A process for contaminant removal and waste volume reduction to remediate groundwater containing certain radionuclides, toxic metals, and organics. U.S. Department of Energy DOE/CH-9201 Final Rep. Contract no. 02112415. U.S. Department of Energy, Washington, DC.

Bunzl, K., H. Flessa, W. Kracke, and W. Schimmack. 1995. Association of fallout 239+240Pu and 241Am with various soil components in successive layers of a grassland soil. Environ. Sci. Technol. 29:2513–2518.

Coughtrey, P.J., D. Jackson, C.H. Jones, P. Kane, and M.C. Thorne. 1986. Radionuclide distribution and transport in terrestrial and aquatic systems. Vol. 6. A. A. Balkema.

Dayal, R., R.F. Pietrzak, and J.H. Clinton. 1986. Oxidation-induced geochemical changes in trench leachates from the Maxey Flats low-level radioactive waste disposal site. Nuclear Technol. 72:184–193.

Davis, J.A., T.E. Payne, and T.D. Waite. 2002. Simulating the pH and pCO_2 dependence of uranium(VI) adsorption by a weathered schist with surface complexation models. p. 61–86. *In* P. Zhang and P.V. Brady (ed.) Geochemistry of soil radionuclides. SSSA Spec. Publ. 59. SSSA, Madison, WI.

Earth and Environmental Services, Westinghouse Hanford Company. 1996. Annual Report for RCRA Groundwater Monitoring Projects at Hanford Facilities for 1995. DOE/RL-96-01. Revision 0 UC-702. U.S. Department of Energy, Washington, DC.

Fendorf, S., C.M. Hansel, B. Wielinga, and S. Miller. 2002. Operative pathways of chromate and uranyl reduction within soils and sediments. p. 111–129. *In* P. Zhang and P.V. Brady (ed.) Geochemistry of soil radionuclides. SSSA Spec. Publ. 59. SSSA, Madison, WI.

Fowle, D.A., J.B. Fein, and A.M. Martin. 2000. Experimental study of uranyl adsorption onto *Bacillus subtilis*. Environ. Sci. Technol. 34:3737–3741.

Francis, A.J. 1998. Biotransformation of uranium and other actinides in radioactive wastes. J. Alloys Compounds 271:78–84.

Golosov, V.N., D.E. Walling, A.V. Panin, E.D. Stukin, E.V. Kvasnikova, and N.N. Ivanova. 1999. The spatial variability of Chernobyl-derived Cs-137 inventories in a small agricultural drainage basin in central Russia. Appl. Radiation Isotopes 51(3):341–352.

Henderson, T. 1994. Geochemical reduction of hexavalent chromium in the Trinity Sand Aquifer. Ground Water 32:477–486.

Honeyman, B.D., and J.F. Ranville. 2002. Colloid properties and their effects on radionuclide transort through soils and groundwaters. p. 131–163. *In* P. Zhang and P.V. Brady (ed.) Geochemistry of soil radionuclides. SSSA Spec. Publ. 59. SSSA, Madison, WI.

Isaksson, M., and B. Erlandsson. 1998. Models for the vertical migration of Cs-137 in the ground: A field study. J. Environ. Radioactivity 41(2):163–182.

Ivanov, Y.A., V.A. Kashparov, S.E. Levchuk, and S.I. Zvarich. 1996. Vertical migration of radionuclides from CNPP accident in soils: 1. Long-term dynamics of redistribution of radionuclides along soil profile in situ. Radiochemistry 38(3):250–256.

Ivanov, Y.A., N. Lewyckyj, S.E. Levchuk, B.S. Prister, S.K. Firsakova, N.P. Arkhipov, A.N. Arkhipov, S.V. Kruglov, R.M. Alexakhin, J. Sandalls, and S. Askbrant. 1997. Migration of Cs-137 and Sr-90 from Chernobyl fallout in Ukrainian: Belarussian and Russian soils. J. Environ. Radioactivity 35(1):1–21.

Jackson, R.F., and K.J. Inch. 1980. Hydrogeochemical processes affecting the migration of radionuclides in a fluvial sand aquifer at the Chalk River Nuclear Laboratories. National Hydrology Research Institute.

Jackson, R.E., and K.J. Inch.1983. Partitioning of strontium-90 among aqueous and mineral species in a contaminated aquifer. Environ. Sci. Technol. 17:231–237.

Johnson, V.G., C.J. Chou, M.J. Hartman, and W.D. Webber. 1998. Groundwater monitor the 100-K fuel-storage basins: July 1996 through April 1998. PNNL Rep. PNNL-12023.

Jové-Colon, C.F., P.V. Brady, M.D. Siegel, and E.R. Lindgren. 2001. Historical case analysis of uranium plume attenuation. Soil Sediment Contam. 10:71–115.

King, K.J., and R.W.D. Killey. 1992. An assessment of chemical and radiological contamination in the vicinity of the acid chemical solvent pits. AECL Res. Rep. TR-550.

Krouglov, S.V., A.D. Kurinov, and R.M. Alexakhin. 1998. Chemical fractionation of Sr-90; Ru-106; Cs-137; and Ce-144 in Chernobyl-contaminated soils: an evolution in the course of time. J. Environ. Radioactivity 38(1):59–76.

Kryshev, I.I. 1995. Radioactive contamination of aquatic ecosystems following the Chernobyl Accident. J. Environ. Radioactivity 27(3):207–219.

Lindgren, E. 1999. Natural attenuation of uranium groundwater plumes at UMTRA sites: A one dimensional analysis of historical data. Sandia National Laboratories, Albuquerque, NM.

Litaor, M.I., and S.A. Ibrahim. 1996. Plutonium association with selected solid phases in soils of Rocky Flats, Colorado, using sequential extraction technique. J. Environ. Qual. 25:1144–1152.

Lockwood, G.J., R.A. Normann, and C.V. Williams. 1997. A final report of the environmental measurement-while-drilling-gamma ray spectrometer system technology demonstration at the Savannah River Site F area retention basin. Sandia Natl. Lab. Rep. SAND97-2028 UC-600.

Lyon, K.E., and R.J. Patterson. 1985. Retention of ^{137}Cs and ^{90}Sr by mineral sorbents surrounding vitrified nuclear waste. Can. Inland Water Branch Sci. Serv. 148:1–19.

Matsunaga, T., T. Ueno, H. Amano, Y. Tkatchenko, A. Kovalyov, M. Watanabe, and Y. Onuma. 1998. Characteristics of Chernobyl-derived radionuclides in particulate form in surface waters in the exclusion zone around the Chernobyl Nuclear Power Plant. J. Contam. Hydrol. 35(1–3):101–113.

McNab, W.W.J., and T.N. Narasimhan. 1995. Reactive transport of petroleum hydrocarbon constituents in shallow aquifer: Modeling geochemical interactions between organic and inorganic species. Water Resour. Res. 31:2027–2033.

McNab, W.W.J., and D. Rice. 2001. Ascertaining the effect of reductive dehalogenation on chlorinated hydrocarbon plume lengths in groundwater: Analyses of multisite data. Soil Sediment Contam. 10:1–19.

Means, J.L., D.A. Crerar, and J.O. Duguid. 1978. Migration of radioactive wastes: radionuclide mobilization by completing agents. Science (Washington, DC) 200:1477–1481.

Means, J.L., T. Kucak, and D.A. Crerar. 1980. Relative degradation rates of NTA, EDTA and DTPA and environmental implications. Environ. Pollut. Ser. B. 1:45–60.

Melnyk, T.W., F.B. Walton, and L.H. Johnson. 1984. High-level waste glass field burial test: Leaching and migration of fission products. Nucl. Chem. Waste Manage. 5:49–62.

Murphy, E.M. and M.P. Bergeron. 1991. A review of environmental conditions and performance of the commercial low-level radioactive waste disposal facility near Sheffield, Illinois. U.S. National Research Council, Washington, DC.

Nitzsche, O., and B. Merkel. 1999. Reactive transport modeling of uranium 238 and radium 226 in groundwater of the Konigstein uranium mine; Germany. Hydrogeol. J. 7(5):423–430.

Pacific Northwest National Laboratory. 1993. Hanford site environmental report for calendar year 1992.

Pacific Northwest National Laboratory. 1999. Hanford site groundwater monitoring for fiscal year 1998.

Parsons, P.J. 1961. Movement of radioactive waste through soil III: Investigating the migration of fission products from high-ionic liquids deposited in soil. p. 45. Chalk River Nuclear Laboratories.

Pietrzak, R., K.S. Czyscinski, and A.J. Weiss. 1982. Evaluation of isotope migration—land burial: Water chemistry at commercially operated low-level radioactive waste disposal sites. U.S. National Research Council, Washington, DC.

Prudic, D.E. 1986. Ground-water hydrology and subsurface migration of radionuclides at a commercial radioactive-waste burial site, West Valley, Cattaraugus County, New York. U.S. Geological Society,

Owens, P.N., D.E. Walling, and Q.P. He. 1996. The behaviour of bomb-derived caesium-137 fallout in catchment soils. J. Environ. Radioactivity 32(3):169–191.

Rafferty, B., M. Brennan, D. Dawson, and D. Dowding. 2000. Mechanisms of Cs-137 migration in coniferous forest soils. J. Environ. Radioactivity 48(2):131–143.

Reardon, E.J. 1981. K_d's -can they be used to describe reversible ion sorption reactions in contaminant transport. Ground Water 19:279–286.

Rice, D.W., B.P. Dooher, S.J. Cullen, L.G. Everett, W.E. Kastenberg, R.D. Grose, and M.A. Marino. 1995. Recommendations to improve the cleanup process for California's leaking underground fuel tanks. Lawrence Livermore National Laboratory Report UCRL-AR-121762.

Riley, R.G., J.M. Zachara, and F.J. Wobber. 1992. Chemical contaminants on DOE lands and selection of contaminant mixtures for subsurface science research. U.S. Department of Energy, Washington, DC.

Robertson, D.E., M.P. Bergeron, D. Holford, K.H. Abel, C.W. Thomas, D.A. Myers, R.C.D., Killey, G.L. Moltanyer, J.L. Young, and T. Ohnuki. 1989. Demonstration of performance modeling of a low-level waste shallow-land burial site: A comparison of predictive radionuclide transport modeling versus field observations at the "A" Disposal Area, Chalk River Nuclear Laboratories. U.S. National Research Council, Washington, DC.

Robertson, D.E., M.P. Bergeron, P.A. Myers, K.H. Abul, L.W. Thomas, D.R. Champ, R. Killey G.L. Moltanyer, and J.L. Young. 1987. Demonstration of performance modeling of a low-level waste shallow-land burial site: A comparison of predictive radionuclide transport modeling versus field observations at the nitrate disposal pit site, Chalk River Nuclear Laboratories. U.S. National Research Council, Washington, DC.

Rosen, K., I. Oborn, and H. Lonsjo. 1999. Migration of radiocaesium in Swedish soil profiles after the Chernobyl accident: 1987–1995. J. Environ. Radioactivity 46(1):45–66.

Ruby, M.V., A. Davis, R. Schoof, S. Eberle, and C.M. Sellstone. 1996. Estimation of lead and arsenic bioavailability using a physiologically based extraction test. Environ. Sci. Technol. 30:422–430.

Sanford, W.E., I.L. Larsen, J.W. McConnell, and R.D. Rogers. 1998. Upward migration of radio-cesium and strontium in a sand-filled lysimeter. J. Environ. Radioactivity 41(2):147–162.

Serne, R.J., and V.L. LeGore. 1996. Strontium-90 adsorption properties and sediment characterization at the 100-N area.

Szerbin, P., E. KoblingerBokori, L. Koblinger, I. Vegvari, and A. Ugron. 1999. Caesium-137 migration in Hungarian soils. Sci. Total Environ. 227(2–3):215–227.

Turner, D.R., F.P. Bertetti, and R.T. Pabalan. 2002. Role of radionuclide sorption in high-level waste performance assessment: Approaches for the abstraction of detailed models. p. 211–252. *In* P. Zhang and P.V. Brady (ed.) Geochemistry of soil radionuclides. SSSA Spec. Publ. 59. SSSA, Madison, WI.

U.S. Department of Energy. 1997. Linking legacies: Connecting the Cold War nuclear weapons production process to their environmental consequences. U.S. Department of Energy, Washington, DC.

White, A.F., J.M. Delany, T.N. Narasimhan, and A. Smith. 1984. Groundwater contamination from an inactive uranium mill tailings pile: 1. Application of a chemical mixing model. Water Resour. Res. 20:1743–1752.

Zygmunt, J., S. Chibowski, and Z. Klimowicz. 1998. The effect of sorption properties of soil minerals on the vertical migration rate of cesium in soil. J. Radioanalytical Nucl. Chem. 231(1–2):57–62.

9 Soil Mineral Backfills and Radionuclide Retention

James L. Krumhansl, Patrick V. Brady, and Peng-Chu Zhang

Sandia National Laboratories
Albuquerque, New Mexico

ABSTRACT

Mineral-based, chemically reactive barriers are a useful means for limiting the impact of stored, or spilled, radionuclides on the biosphere. Reliance on reactive barriers for passive treatment of hazardous wastes involves placing permeable curtains of a reactive material in the paths of a migrating contaminant plume. Flow of contaminated groundwater through the barrier and reaction of the contaminant with the active component of the barrier would cause either conversion to a less hazardous substance, or, as in the case of some radioisotopes, their removal from the groundwater through sorption–sequestration. The key is identifying reactive components that are effective for long periods of time under soil conditions. Radioisotope retention is mineral-specific, yet also depends on the geochemistry of adjacent soils and groundwaters. Soil geochemistry determines absolute amounts of contaminant uptake as well as the long-term stability of chemical barriers. This chapter considers the soil science aspects of reactive components of barriers intended to scavenge contaminant radionuclides. Typically, these are minerals and mineral-like materials, including clays and metal oxides and hydroxides. Clays, zeolites, and hydrous ferric oxide (HFO) are effective cation sorbers whose behavior is reasonably predictable in the subsurface. In many cases HFO significantly retards Np, U(VI), $SeO_3^{=}$ (but not $SeO_4^{=}$) and Pu (V and VI). Sr, Ni, and Co are typically less retarded by HFO. Clays and zeolites are effective sorbers of Sr and Cs. Apatite-group materials are effective sequestering agents for a broad range of contaminants, though the uptake mechanisms are often poorly understood. Anion retention is a particularly desirable characteristic of chemical barriers, as TcO_4^- and I^- are often calculated to be primary dose components, particularly from low-level waste facilities. Anion sorption can be engineered using insoluble oxides and hydroxides, and sulfides of divalent metals such as Cu. Iron metal also is an effective sorber of TcO_4^-.

Radionuclides contaminate large volumes of soils and groundwaters, primarily in the USA, Europe, and the nations of the former Soviet Union (see the chapter by Brady et al., 2002, this publication). To the extent that it is possible to do so, radionuclide-contaminated soils and groundwater plumes at U.S. DOE facilities will be removed and isolated for long-term storage, typically in low-level waste landfills. Higher level radioactive waste in the USA will probably be shipped to either the Waste Isolation Pilot Plant (WIPP)—a facility in southeastern New Mexico in-

 Geochemistry of Soil Radionuclides. SSSA Special Publication no. 59.

tended for storage of transuranic wastes, or possibly to Yucca Mountain—a proposed final resting place for radioactive waste from civilian nuclear power plants. Ultimate disposal of high level waste (HLW) in France is expected to be in one of three geologic sites being investigated: two clay units (the East and Gard sites in, respectively, the Meus and Gard Departments) and a granite (the Vienne site in the south of the Vienne Department). Low-level and intermediate short-lived waste in France will be stabilized in a concrete matrix, deposited in concrete bins covered with concrete or gravel, and overlain with a clay layer. Low level waste (LLW) in Germany is being disposed of in a rock salt formation at Morsleben. Intermediate level waste and HLW in Germany may ultimately be disposed of in a salt dome near Gorleben. Japanese HLW may be buried in a deep geologic formation in the presence of concrete and a bentonite backfill. Korean LLW and Intermediate level waste (ILW) are expected to be disposed of in either rock caverns or vaults along with backfill materials and/or grout. Korean HLW is envisioned to involve geologic disposal in crystalline rock and multiple barriers. Belgian HLW will probably be disposed of in the Boom Clay. Likewise, Swedish waste will be embedded in a dense Na-bentonite. Switzerland's storage of Swiss LLW and ILW is expected to be at Wolfenschiessen, Nidwalden. Disposal will be in caverns, or silos–tunnels, depending on its half-life, and will rely on a cementitious backfill. Disposal of Swiss HLW, while not planned for several decades, is expected to be in geologic repositories in crystalline rock or the Opalinus Clay.

Backfills are needed to maintain the physical integrity of waste repositories, but also are increasingly considered specifically for their chemical characteristics. To assure isolation of radionuclides at low-level, high-level, and transuranic waste sites, considerable effort has been expended by a number of countries to develop *getters*—solids that might be added to backfills to retard the movement of the most labile radionuclides into the environment. Chemical barriers also are being used to arrest the movement of existing radionuclide-bearing plumes in the subsurface before they can impact drinking water supplies. This application of chemical barriers can only be expected to receive more attention in the future, as the alternative—in situ extraction of subsurface contaminants—is increasingly seen as a near-impossible task (National Research Council, 1994). Figure 9–1 schematically illustrates chemical barrier placement in a repository and downgradient of a contaminant plume. Note that while physical backfills may impede, or divert the flow of water, chemical backfills have as their object the actual cleansing of contaminated fluids.

Although the motivations behind the use of chemical barriers are fairly straightforward, the specific chemical reactions that must be engineered are often

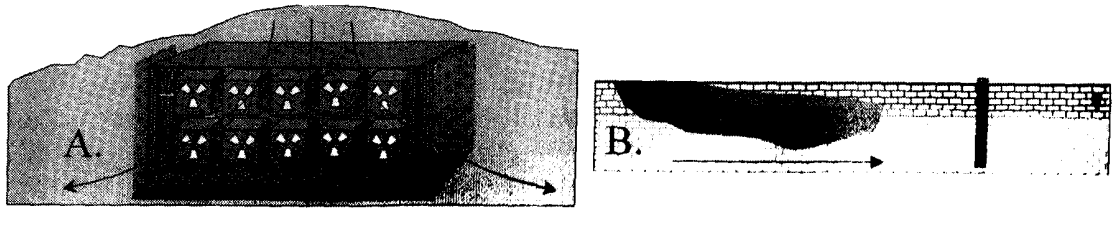

Fig. 9–1. Chemical barriers. (A) Backfill, and (B) Reactive barrier. Arrows show presumed paths of fluid movement.

complex, and the design specifications formidable. Barriers must remain structurally robust, sometimes for hundreds of years. Moreover, the reactive component of the backfill must perform reliably, even if the ambient groundwater chemistry changes. By choosing minerals or mineral-like materials as the reactive component, it may be possible to demonstrate a longevity that is not possible with compounds such as organic ion exchange resins or zero-valent Fe. Furthermore, natural materials may be available at a fraction of the cost of synthetics and do not produce environmentally undesirable degradation products. Because the number of materials that can impede the movement of problem radionuclides is limited, the critical step in barrier implementation has been the identification of the chemically reactive component. A number of these components have been proposed in recent years, and the mechanistic controls on their function have become clearer, though much work remains; however, the state of the science has now evolved to the point where chemical barriers can be tailor-made to target specific elements and particular hydrogeologic settings. Here we identify families of chemical barriers that effectively sequester specific radioisotopes of concern under a spectrum of hydrogeologic conditions, and outline the general logic underlying the use of chemical barriers for radionuclide retention.

In many low-level waste repositories, the small absolute size of the initial inventory prevents solubility limits from being exceeded. All waste repositories are subject to eventual transport of contaminant-laden fluids into the surrounding rock and soil, and dilution to levels below solubility limits (if not in the immediate near-field, certainly in the far-field, see Brady & Kozak, 1995). Radionuclide sorption is therefore a primary control over radionuclide movement. If sorption to aquifer material is strong, decay to less dangerous isotopes might occur before a potential receptor is impacted. Alternatively, lack of binding would result in more rapid groundwater transport of radioactive elements to the biosphere.

The isotopes that are predicted to leave repositories rapidly, or that are most common in subsurface plumes are: ^{129}I, ^{137}Cs, ^{99}Tc, ^{79}Se, ^{90}Sr, ^{239,240,241}Pu, and ^{235,238}U. Some problem isotopes such as ^{129}I, ^{99}Tc, and ^{79}Se do not sorb to most soils, hence their transport through the environment is relatively fast. Others, for example, ^{239,240,241}Pu, are toxic at low levels, so even minimal environmental transport is bad. Still others, e.g., ^{137}Cs and ^{90}Sr , are the result of atmospheric deposition and contaminate relatively large quantities of water.

In discussing radionuclide retardation it is necessary to bring together traditional soil chemical approaches with those used by the community of scientists and engineers working on nuclear waste disposal issues. One point of conflict that inevitably arises in such a meeting is the reliance of the performance assessment (PA) community on K_ds as a numerical tool to describe sorption in lieu of more mechanistically rigorous surface complexation approaches. K_ds describe the equilibrium partitioning of a particular constituent of interest between the dissolved and solid phases. In actuality, experimentally measured K_ds are operative quantities that may subsume multiple reactions and, therefore, possess little mechanistic meaning (see Davis & Kent, 1990). K_ds also tend to be poor descriptors of contaminant movement (Bethke & Brady, 2000; Reardon, 1981). Nevertheless, PA uses K_ds because they are numerically convenient and performance assessments are the driving force for most studies of radioactive contaminants in groundwaters. Hence, the

bulk of the literature on potentially useful materials is tabulated in the form of K_d values, though often the actual scavenging mechanism is unknown. Because of the ubiquity of K_ds, and because they do provide a rough measure of mineral-isotope affinity, particularly when isotopes are present at trace levels (well below solubility limits and the number of available surface sites) we consider them here. A more mechanistically valid examination of reactive transport is presented in the chapter by Davis et al. (2002, this publication).

At the core of the K_d concept is the equilibrium between an empty sorbing site, with concentration [*S*-] and a dissolved component, concentration [A_{aq}], that then partitions onto the site [*S*-*A*] in a manner that can be computed using an equilibrium constant, K_{eq}:

$$S\text{-} + A_{aq} \Leftrightarrow S\text{-}A \quad [1]$$

$$K_{eq} = [S\text{-}A]/[S\text{-}][A_{aq}] \quad [2]$$

$$K_d = [S\text{-}A]/[A_{aq}] = K_{eq}[S\text{-}] \quad [3]$$

As long as only a very small fraction of the sites are occupied, [*S*-] remains essentially constant, as does the K_d value; however, as soon as saturation of the sites is approached the K_d will appear to decrease with increased loading. Thus, if a constant K_d value is used in planning construction of a reactive barrier, it must be verified that the sorption sites on the material will not approach saturation with the target radionuclide. In the real world, radionuclides would probably be a minor component compared with the other groundwater constituents (Na^+, K^+, Ca^{++}, Mg^{++}, HCO_3^-, $SO_4^=$, Cl^-). Whether or not these major constituents are strongly sorbed onto a particular material determines whether [*S*-] changes much in different groundwaters and, hence, whether K_d values will be portable or can be extrapolated from one field site to another, or from a laboratory experiment to a field setting.

Where surface complexation reactions are the main radionuclide scavenging mechanisms the groundwater pH also will be a key factor in determining the portability of a K_d value. The zero point of charge (ZPC) and isoelectric point (IEP) both denote reference pHs where the net charge of a particular surface is zero, i.e., that pH unique to a mineral where the total number of negatively charged sites is balanced by that of positively charged sites (see Stumm & Morgan, 1996). At normal groundwater pH values, the hydrogen ion release by hydrated surfaces of soil minerals is such that the surfaces have net negative charges (Table 9–1). Cation sorption is therefore favored. Consequently, cationic radionuclides do not tend to migrate far from the source of the pollution before they are immobilized by interactions with normal soil components (Colloidal transport is an exception to this and is covered in the chapter by Honeyman & Ranville, 2002, this publication); however, it is also evident that a few oxides do not follow this general rule and these could be useful in retarding anions rather than cations.

The other ion exchange mechanism that is of importance in natural system involves fixed residual charge in a crystal lattice on, for example, basal planes of clays.

Table 9–1. Selected minerals ZPCs and IEPs.

Mineral	ZPC/IEP	
Quartz	2.9†	2.0‡
Mica, Feldspars	5–8	2–2.4
Maghemite	--	6.7
Goethite [FeOOH]	7.3	7.8
$Fe(OH)_3$–amorphous	--	8.5
Fe_3O_4	--	6.5
Calcite	9.3	--
CuO	--	9.5
Boehmite [AlO(OH)]	9.1–10.4§	8.2
Gibbsite [$Al(OH)_3$]	9.6–10§	--
Montmorillonite	--	5.0
Kaolinite	5	4.6

† Sposito, 1984.
‡ Stumm and Morgan, 1970.
§ Goldberg et al., 1996.

$$S\text{-}B + A_{aq} \Leftrightarrow S\text{-}A + B_{aq} \quad [4]$$

$$K_{eq} = [B_{aq}][S\text{-}A]/[A_{aq}][S\text{-}B] \quad [5]$$

$$K_d = [S\text{-}A]/[A_{aq}] = K_{eq}[S\text{-}B]/[B_{aq}] \quad [6]$$

On clays, cation exchange occurs to compensate for charge imbalance deep within the crystal lattice rather than onto a broken, unsatisfied bond on the mineral surface. Hence, even at low concentrations, common groundwater solutes can compete with H^+ (or hydroxide) ions and occupy most sorption sites. In this simple example, as long as B_{aq} is concentrated enough to keep the number of *S-B* sites large, changes in K_d with variations in pH, or other groundwater ions, would not be expected and the K_d should be relatively portable.

Clays and zeolites are well-known examples where the lattice has a net negative charge and the counter-cations can exchange to reflect cation concentrations in a coexisting solution; however, clay edge sites more closely resemble the surfaces of other silicate minerals, and can be described using surface complexation models (Arnold et al., 2001; Fletcher & Sposito, 1989) Natural materials with residual positive lattice charge are much less common but are of particular interest because they might be used as reactive barrier components for anionic contaminants (see below). Imogolite (an amorphous hydrous aluminum silicate) and hydrotalcites ($Mg_6Al_2(CO_3)(OH)_{16\bullet} \bullet 4H_2O$ fall into this category.

Where the K_d formalism is supported by the physical chemistry of the radionuclide scavenging process, it is possible to estimate the theoretical efficiency of a reactive barrier based on simple mass balance relationships. Specifically, the total capacity (mg contaminant g^{-1} of barrier material) of a reactive barrier is equal to the product: K_d(mL g^{-1}) × C_o (mg mL^{-1}). The total number of volumes that can pass through a unit area of the barrier until contaminant breakthrough occurs is equal to the product K_d(mL g^{-1}) × Mass in column (g)/Column pore volume (mL). The retardation of contaminant velocity (V_c) relative to the normal groundwater veloc-

Table 9–2. General range of soil/mineral K_ds.

Radionuclide	K_d range†‡
Pu	11–300000†
^{90}Sr	0.15–3300†
^{137}Cs	10–52000†
$^{235,238}U$	10.5–4400†
^{226}Ra	1000‡
^{60}Co	0.2–3800†
^{241}Am	1–47230†
^{79}Se	0
^{129}I	0†
^{99}Tc	0†

† Agricultural soils, pH 4.5 and 9; Baes and Sharp, 1983.
‡ Brady and Kozak, 1995.

ity (V) while the fluid is in the reactive barrier is given by: $V/V_c = [1 + xK_d]$, $x = 4$ to 10 for normal packing of earth materials (Freeze & Cherry, 1979).

Table 9–2 represents ranges of K_d values found in normal soils and rocks. The great variability in Table 9–2 suggests that Pu, Sr, Cs, U, Ra, and Am might be immobilized with a host of natural materials. In contrast, Se, I, and Tc, which commonly exist as anions, will be more difficult to immobilize. This suggests a natural division in selecting materials for reactive barriers. Common materials should work for the first group of elements while relatively exotic materials may be required to slow the progress of Se, I, and Tc.

The reactive component of most soils consists of Fe(III)-oxides, organic matter, clays, and carbonate minerals. Typically, the surfaces of these solids possess a negative charge that becomes most negative at high pH. Contaminants that are cationic (e.g., UO_2^{+2}, Sr^{2+}, Cs^{+}, PuO_2^{+}, Ra^{2+}) are attracted to these sites by electrostatic forces and uptake is greatest at high pH, except when ligands stable at high pH (e.g., carbonate) form anionic complexes. This high pH desorption is most clearly seen for uranyl. Uptake of cations by clay minerals is different and depends less on pH and more on the abundance of competing cations in soil solutions and between the clay layers.

The anion exchange potential of most soils is less significant and anionic radioisotopes, such as $^{129}I^{-}$ and $^{99}TcO_4^{-}$, tend to be repelled electrostatically from negatively charged mineral surface sites, resulting in low K_ds. The predictable outcome is that release of ^{129}I and/or ^{99}Tc is routinely identified as a primary risk driver for radwaste repositories, whereas cationic radioisotopes are generally predicted to sorb. Designing a safe repository is occasionally a matter of identifying a chemical barrier that can sorb anions. Most soil components are effective chemical barriers for cationic contaminants.

Hydrous Iron Oxides

Commonly, hydrous iron oxide (HFO) is the most important sorber in soils. The surface chemistry of HFO and its predicted behavior in soils is therefore a useful starting point from which to consider chemical barriers and backfills. Many of the important equilibrium relationships involving HFO have been abstracted into

Table 9–3. Groundwater chemistry at some contaminated U.S. Department of Energy sites.

Component	Hanford†	NTS–J-13‡	Rocky Flats§	ORNL¶	SRS††
	mg L^{-1}				
Ca^{++}	67.5	14	160	32	5
Fe^{++}	3	0.04	--	0.013	0.18
K^{+}	3	4.9	3.6	0.1	1.0
Mg^{++}	16.4	2.1	44	20	0.9
Na^{+}	27.6	51	140	0.56	1.2
Si (SiO_{2aq})	16.2 (34.7)	31.0 (66.4)	--	(64)	(12)
Cl^{-}	22	7.5	85	1	1.4
NO_3^{-}	1.7	5.6	8.0	--	0.27
$SO_4^{=}$	108	22	590	2	14.1
HCO_3^{-}	137.3	120	180	183	10.5
pH	8.46	7.1	8.1	8.3	6.3

† Kaplan et al., 1996.
‡ Guzowski et al., 1982.
§ Anderson, 1998.
¶ Toran and Saunders, 1999.
†† Marine, 1976.

databases (Dzombak & Morel, 1990) and reaction path codes (Bethke, 1998) that permit convenient bounding assessments of the performance of HFO-containing materials under soil conditions. The following example uses the REACT code (Bethke, 1998) to develop a picture of the comparative sorption of various radionuclides onto Fe oxide from different contaminated groundwaters. REACT uses the HFO database of Dzombak and Morel (1990) to consider surface complexation (actinide complexation constants are from Dzombak & Morel, 1990). To facilitate easy comparisons, all of the radionuclides are assumed to be present initially at concentrations of 10^{-8} molar. Water chemistries are summarized for a variety of U.S. Department of Energy sites in Table 9–3. Each of these sites possesses large-scale soil and groundwater contamination. Rocky Flats is located outside of Denver, CO, in the semi-arid high plains. The ORNL (Oak Ridge National Laboratory) water comes from a dolomite aquifer (hence its mildly basic character) in eastern Tennessee, while the Savannah River (SRS) groundwater was derived from a sandy aquifer with little buffering capacity in a region of high organic productivity in South Carolina. Hence, it has quit a low pH, a very low overall level of total dissolved solids and minimal pH buffering capacity.

In assessing HFO for use in a reactive barrier, it is important to consider the evolution of the barrier chemistry over time. Initially the sorption sites will reflect the occupancy at the time the material was placed in the ground. In this example, 1 g of HFO is initially equilibrated with 1 L of groundwater containing 10^{-8} molar concentrations of Sr, Pu(V), Pu(VI), U(VI), Np(V), Se(VI), and Se(IV). The 1 g of HFO is assumed to be the reactive fraction of the soil, i.e., all other sorbing minerals are ignored. The computation starts by saturating the sites with radionuclides at concentrations that are trivial compared with those in the contaminated groundwaters. As the calculation progresses, aliquots of groundwater are brought in contact with 1 g of HFO until a total of 500 L has passed. As this happens, the radionuclide concentration builds up on the solids in a manner that reflects the scavenging ability of the Fe oxide. At the same time, the major groundwater compo-

Table 9–4. Primary surface Species (log *M*).

Species	Rocky Flats	Savannah River
	Log *M*	
>(w)FeOH	−2.19	−2.14
>(w)FeO^-	−3.61	−3.72
>(w)$FeOH_2^+$	−3.64	−3.80
>(s)FeOH	−6.09	−5.21
>(s)FeO^-	−6.80	−6.00
>(s)$FeOH_2^+$	−7.02	−6.07
Calcium occupied sites		
>(w)$FeOCa^+$	−3.77	−5.19
>(s)$FeOHCa^{++}$	−4.36	−4.77
$SO_4^=$ occupied sites		
>(w)$FeOHSO_4^-$	−4.22	−5.46
>(w)$FeSO_4^-$	−5.46	−6.64

nents also load onto the Fe oxide, changing the major site occupancy and distribution. In this case, the database considers competitive sorption of sulfate and Ca, but not silica or bicarbonate. Note also that the database considers two basic types of sorption sites, strong (s) and weak (w), and that the abundance of strong sites is set for illustrative purposes to 10% of the weak sites. REACT was run in the flush mode that sequentially adds aliquots of fluid while displacing a fraction of the reacted portion of the previous aliquot. Two waters from Table 9–3 were used as input: Savannah River waters, because they are representative of dilute, low-pH groundwater that might be found in many areas of the northeastern USA, and Rocky Flats water because it is saline, has a higher pH and could represent surface waters in many areas of the western USA. Tables 9–4 and 9–5 show surface site occupancies calculated to exist at completion.

Calcium and sulfate occupy more strong and weak sites when the input water is that of Rocky Flats. The number of unoccupied (more numerous) weak sites is, however, almost identical for the two groundwaters. This reflects the fact that even in the Rocky Flats groundwater only a very small fraction of the weak sites are occupied so the total number of weak sites available to scavenge radionuclides is similar in both fluids. The opposite is true with the strong sites. Here, the more concentrated Rocky Flats fluid results in a significant proportion of the strong sites being filled with Ca, leaving far fewer strong sites to sorb radionuclides. The dif-

Table 9–5. Radionuclide-occupied sites (log *M*).

Component	Rocky Flats Log *M*		Savannah River Log *M*	
Pu(V)	>(w)$FeOPuO_2$	−5.7058	>(s)$FeOPuO_2$	−5.4303
Pu(VI)	>(w)$FeOPuO_2$	−6.4723	>(s)$FeOPuO_2^+$	−5.4808
Np	>(w)$FeONpO_2$	−5.4316	>(s)$FeONpO_2$	−5.4341
U	>(w)$FeOUO_2^+$	−8.2860	>(s)$FeOUO_2^+$	−5.5683
Se(IV)	>(w)$FeOHSeO_3^=$	−5.7086	>(w)$FeOHSeO_3^=$	−5.5676
Se(VI)	>(w)$FeOHSeO_4^=$	−13.8991	>(w)$FeOHSeO_4^=$	−9.6414
Sr	>(s)$FeOHSr^{++}$	−9.9244	>(s)$FeOHSr^{++}$	−8.8255
Ni	>(s)$FeONi^+$	−13.7215	>(s)$FeONi^+$	−12.9406
Co	>(s)$FeOCo^+$	−23.4639	>(s)$FeOCo^+$	−22.6830

ference in availability of strong sites between the two groundwaters has a major impact on the predicted final state of the barrier (Table 9–5). From Rocky Flats groundwaters most radionuclides (except Sr, Co, and Ni) sorb to weak sites. From Savannah River groundwaters most sorb to strong sites.

Actual site loading reflects not only the competition for sites by major groundwater components but also the complexing ability of different groundwaters. For example, formation of anionic Pu(VI) carbonate complexes prevents attachment of the latter to negatively charged mineral surfaces (note slight excess of negative sites over positive sites in Table 9–4). Stronger carbonate complexation in the Rocky Flats groundwater causes decreased Pu (VI) sorption relative to Savannah River groundwater. Carbonate complexation of U(VI) causes an even sharper difference. Appreciable Np uptake is predicted for both groundwaters. For other radionuclides, however, details of the environment, such as groundwater redox state, need to be considered. For example, mildly reducing conditions increase the chances of successfully sequestering Se and Pu. Lastly, it must be emphasized that, while the example above outlines general inputs and outputs of a reaction-transport code assessment of barrier performance, actual application of a reaction-transport code at a particular site requires the use of site-specific input data. In particular, considerable effort should be expended to determine appropriate fluid composition inputs as well as site-specific sorption parameters. Sr, Co, and Ni are predicted to be less retarded under the conditions considered here. Subtle shifts in pH and/or carbonate concentrations might reverse the situation, causing Sr, Co, and Ni to be more retarded than the actinides. Such changes could be accounted for with a properly calibrated surface complexation model. Reliance on the K_d model, on the other hand, would necessitate prior determination of K_ds under each of the expected solution compositions.

Immobilization of ^{137}Cs and ^{90}Sr

From the earliest days of the nuclear fuel cycle, handling of ^{137}Cs and ^{90}Sr-containing wastes constituted an important problem. Consequently, a vast literature exists on the use of natural and synthetic clays and zeolites to scavenge Cs and Sr from wastewaters. Indeed, a detailed review of the zeolite literature would alone constitute a separate volume. Ion exchange arises from three types of sites: (i) frayed edge sites that are Cs–K specific (Smith & Comans, 1996); (ii) interlayer ion exchange due to a net negative charge on the covalently-bonded lattic layers; and (iii) surface complexation reactions arising from broken bonds on the layer edges (Fletcher & Sposito, 1989). Much of the environmental focus has been on clinoptilolite—$(Na,K,Ca)_3$–$Al_3(Al,Si)_2Si_{13}O_{36}$•$12(H_2O)$, named from the Greek *klino* oblique; *ptylon* feather; and *lithos* stone. Clinoptilolite forms typically from the alteration of volcanic glass and has subsequently been considered for use both as a repository backfill, and as a reactive barrier. At the time of this writing, clinoptilolite barriers had been placed at the Oak Ridge National Laboratory in Tennessee, and at Chalk River in Canada, in each case to intercept ^{90}Sr plumes.

Krupka et al. (1999) reviewed strontium K_d values for a variety of clay-containing sediments and found that, for pH 5 to 8 groundwaters and sediments containing 4 to 40% clay, K_d values ranged from 15 to 200 mL g^{-1}. In more basic so-

lutions, values up to 300 mL g^{-1} were noted. In sediments consisting of between 20 and 60% clay, K_d values ranged from 200 to 1600 mL g^{-1} in the pH range from 5 to 8. In more basic fluids, K_d values up to 1700 mL g^{-1} were seen. Despite considerable scatter, K_ds appear to increase with cation exchange capacity. Typically Sr exchange reactions on and off of clays are readily reversible so it is unlikely that irreversible sorption would boost the performance of a clay-based reactive barrier being used to retard ^{90}Sr.

Cs K_ds possess little pH dependence. The literature survey of Krupka et al. (1999) indicates that sediment K_ds for sediments having 4 to 20% clay had K_ds from 30 to 9000 mL g^{-1}. Sediments having 20 to 60% clay content had K_ds of 80 to 26 700 mL g^{-1}. When >5% mica was present, K_d values ranged between 70 and 22 000 mL g^{-1} for 4 to 20% clay and 210 to 66 700 mL g^{-1} when the sediments contained between 20 and 60% clay. Cs concentrations in these experiments were generally $<10^{-9}$ *M* (0.14 ppm).

Tamura (1972) provided a more detailed analysis of Cs K_d values on clay-like minerals. In descending order, Cs selectivity was experimentally determined to be: illite > biotite > hydrobiotite > montmorillonite > kaolinite. A factor of 10^3 separates the low-K_d (kaolinite) from the high-K_d (illite) clays. A linear inverse correlation between aqueous Na concentration and K_d also was observed. In 0.02 *M* Na^+ solutions, the K_d for illite was about 2×10^4 mL g^{-1} while in 2 *M* Na^+ the K_d was an order of magnitude less. K_ds for other types of clay were even more strongly affected by Na.

Radionuclide retention in a sorptive reactive barrier after passage of a contaminant plume can be a significant concern. In theory, movement of contaminant-free solutions through a barrier holding a sorbed contaminant would tend to favor release of the latter back into solution assuming that the sorption reactions are completely reversible. In fact, many radionuclide-sorption reactions are highly irreversible (e.g., Brady & Borns, 1997; Brady et al., 1997). Although the release of Sr is readily reversible, the slow release of ^{137}Cs may play a significant role in its ultimate disposal given that its half life is only 30.2 yr. Smith and Comans (1996) suggest that the release of strongly held fallout ^{137}Cs has a half-life of about 10 yr (0.014% per day). These general rates were confirmed in laboratory studies where clays were loaded with excess Cs, washed free of readily exchangeable Cs using Li chloride and nitrate solutions, then washed free of Li salts, and finally placed in dialysis bags so that the release of Cs into deionized water could be monitored (Krumhansl et al., 2001). Clays made up of paired octahedral and tetrahedral sheets (TO clays) (KGa-1 and KGa-2 kaolinites) lost a significant percentage of their residual Cs in the early stages of dialysis while the smectite and mica clays retained most of their Cs. Release rates for clays made up of octahedral layers between two tetrahedral layers (TOT clays) for 75 to 139 d after the initiation of dialysis were in the range of 0.017 to 0.022% per day. At the end of the experiment, the ratio of the concentrations of Cs on the clay and in the solution suggested K_d values of 1.4×10^4 for Fithian illite, 2.6×10^3 for K metabentonite and 9.1×10^3 mL g^{-1} for SWy-1 bentonite. In terms of overall Cs retention, the K metabentonite was the most effective, so this would be the optimal clay for inclusion in a reactive barrier. Long-term Cs release is proportional to the residual loading remaining on the clay (Fig. 9–2). The linear correlation in Fig. 9–2 suggests that the site involved in sorption

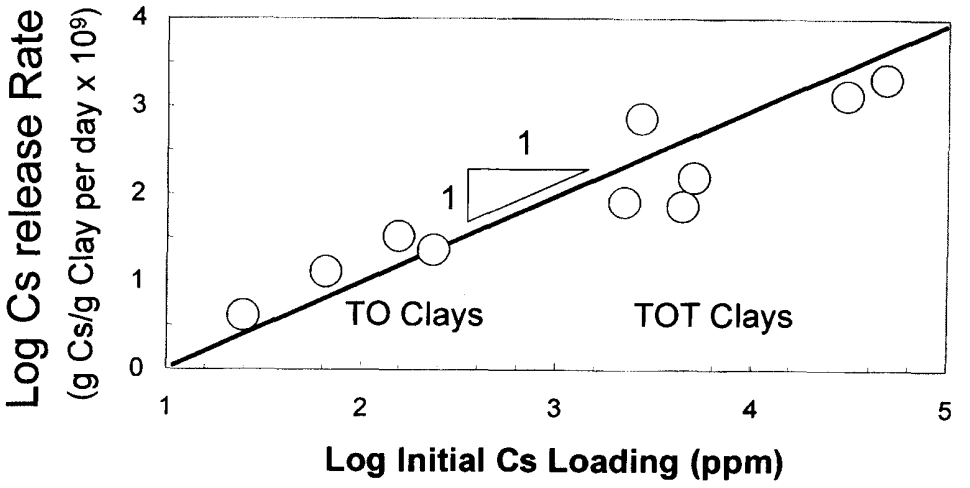

Fig. 9–2. Cs release rates from common clays.

is the same in both types of clays. The only reactive sites that are common to both TO and TOT clays are edge sites. On kaolinite these may be associated with smectite impurities. Presumably, the one to one correlation seen in Fig. 9–2 represents sorption on these frayed edge sites.

Apatite

Sedimentary apatites are notably enriched in trace elements, presumably because of an ability to remove the latter effectively from adjacent solutions some time in the past. This implies that apatite-group minerals might be ideal reactive barrier candidates. The low solubility of Ca-hydroxyapatite; $K_{sp} = [Ca^{2+}]^5[PO_4^{3-}]^3[OH^-] = 10^{-58}$, and the inclusion of trace cations in a phosphate lattice should tend to limit coexisting aqueous concentrations to very low levels (see Arey et al., 1999). In the presence of apatite, the minerals saleeite [$Mg(UO_2)_2(PO_4)_2 \cdot 9H_2O$] and meta-autunite [$Ca(UO_2)_2(PO_4)_2 \cdot 6H_2O$] form at ambient temperature (Gauglitz et al., 1992). Sorption of U(VI), Pb(II), and Cd(II) to phosphate minerals appears to be element-dependent (Jeanjean et al., 1995). Apatite dissolution in the presence of U(VI)-bearing solids leads to formation of an amorphous or microcystalline U(VI) phosphate phase. Pb may become incorporated into the apatite (Jeanjean et al., 1995). The primary uptake mechanism for Cd appears to be the formation of solid $Cd_5H_2(PO_4)_4$. Although U(VI), Pb and Cd can be effectively removed from solution by addition of hydroxyapatite, the sorbed quantities vary in the order Pb > U > Cd.

An additional benefit of the dissolution-reprecipitation process is that, typically, the entrapped metal becomes nonbioavailable. For example, bioavailability of Cd, Pb, Cu, Zn, and As to vegetation in contaminated soils was observed to be significantly reduced by addition of apatite (Laperche et al., 1996). Presumably, the cations substitute for Ca sites, whereas As substitutes as an oxyanion in to the anion sites. Not only did apatite addition reduce the Pb content in *sudax* shoot tissue from 170 to 3 mg kg^{-1}, the accumulated Pb in the plant root was stabilized by formation of pyromorphite ($Pb_5(PO_4)_3Cl$) (Laperche et al., 1996). Consequently, phosphate soil amendments have received considerable attention for contaminant immobi-

Table 9–6. K_ds for apatites and related phosphatic materials (from Anderson, 1998).

Element	K_d Range
Sr	5–88
Se	1–540
Cs	0.1–32
Tc	0.1–40
U	4300–35 000
Am	115–100
Pu	1500–115 000

lization and reclamation of exposed soils (Cotter-Howells & Caporn, 1996; Ying Ma et al., 1993).

Because of the U-apatite association observed in natural phosphatic materials (Read, 1992), various nuclear agencies have considered apatite as a site remediation option in the construction of reactive barriers (see Morrison & Spangler, 1992). Hydroxyapatite also has been considered as a reactive barrier material for U-contaminated waters at the U.S. Department of Energy facility at Fernald, and as a backfill in the WIPP. Hydroxyapatite also has been examined as a candidate backfill for rock salt-based radioactive waste disposal (e.g., Gorleben, Germany). Anderson (1998) assessed the removal efficiency of a variety of natural and synthetic apatites with regard to Sr, Se, Cs, Tc, U, Am, and Pu (Table 9–6) in a synthetic Rocky Flats groundwater (Table 9–3). While hydroxyapatite is apparently not an effective Sr scavenger, it appears that tricalcium phosphate is, possibly because the latter reacts slowly to make hydroxyapatite.

Studies of actinide [Am, Np, Pu (V), and U(VI)] removal by apatite across a range of pH values in concentrated WIPP brines (Table 9–7) indicate much lower uranium K_d values than those of Anderson (1998) (Table 9–8). These results, however, probably reflect carbonate complexing in the mildly basic conditions (pH 8.5 to 10) under which the brine-matrix experiments were performed. In all cases the

Table 9–7. Chemistry of WIPP brines (from Molecke, 1983).

Component	Brine A (*M*)	ERDA-6 (*M*)
Na^+	1.83	6.09
K^+	0.77	0.12
Mg^{++}	1.44	0.011
Ca^{++}	0.02	0.009
Cl^-	5.35	5.08
$SO_4^=$	0.04	0.15
BO_3^{-3}	0.02	0.07
HCO_3^-	0.01	0.029
Br^-	0.01	0.009
Initial pH	6.5	7.0

Table 9–8. Apatite K_d values in WIPP brine A.

	Am	Np	U	Pu
Hydroxyapatite (Fischer)	>462	>59 000	25	>270
Idaho phosphate rock	>300	11	76	>137
Florida phosphate rock	>265	533		> 16

best performer was reagent-grade hydroxyapatite; followed by Florida phosphate rock, and then Idaho phosphate rock. Bone meal generally performed even more poorly than Idaho phosphate rock. The possibility of great variability between seemingly similar materials also was observed in an early study with Np in WIPP brine. In the case of Np, highly variable results were observed, with K_d values >59 000 mL g^{-1} for hydroxyapatite, 553 mL g^{-1} for Florida phosphate rock and 11 mL g^{-1} for Idaho phosphate rock.

Sr removal by apatite probably involves exchange or substitution for Ca and is not particularly surprising. Cs is sorbed to a negligible degree except by phosphate rock, where it is likely that a small amount of clay impurity is actually the active agent. No removal of TcO_4^- was observed, except for bone char (a mixture of activated C and Ca phosphate), where compounds other than apatite may account for uptake (see below). High Se K_d values probably indicate exchange of surface phosphate groups, leading to a maximum K_d at about a pH of 8 (Monteil-Rivera et al., 2000).

To summarize, apatite—like Fe oxide—appears to hold promise as a broad-spectrum sorbent for many radionuclides though its reactivity depends on the radionuclide as well as the surface chemistry of the material.

Iodine and Technetium Retention

Although I^- and TcO_4^- have very different chemistries, the formal problems associated with their immobilization are similar. At normal groundwater pH, the common silicate and oxide minerals have negative surface charges and so repel anions rather than sorbing them. Also, neither ion forms insoluble compounds in oxidized groundwaters; however, under reducing conditions, Tc tends to be reduced to insoluble forms. A barrier of metallic Fe can temporally achieve this effect (see Vandergraaf et al., 1984), but if the Fe is oxidized, Tc may potentially return to TcO_4^- and become mobile again—assuming it is not buried in the rind of oxidation products. Thus, for both I^- and TcO_4^-, the key issue to reactive barrier construction is finding exceptions to the rules that normally govern the mobility of anions in nature.

A few compounds, notably hydrotalcite and imogolite, have residual positive lattice charges analogous, but opposite in sign, to those possessed by the clays. Here, the issue is specificity, since radioisotopes are generally a trace species in a soup of far more abundant, common groundwater anions that also will be attracted to a positive surface charge. Some forms of Al and Cu oxide appear to retain positive surface charges to around pH 9 (Table 9–1), making them potentially useful as anion scavengers in typical groundwaters.

Balsley et al. (1996, 1998) surveyed a variety of potential iodide sorbers. CuO has a high ZPC (Table 9–1), which should favor iodide sorption. Indeed, most copper-containing minerals appear to sorb iodide. Copper oxides exhibit iodide K_d values of about 300 mL g^{-1} (Balsley et al., 1996). For copper sulfides, the K_d values range up to 1000 mL g^{-1} at pH values below 8 (Table 9–9 and Fig. 9–3). Earlier studies identified chalcopyrite, $CuFeS_2$; galena, PbS (Huie et al., 1988); and cinnabar, HgS (Ikeda et al., 1994); as having an affinity for iodide. From pH 4 to 11, Ca monosulfate aluminate (CMSA) K_ds for iodide declined steadily with in-

Table 9–9. K_ds for iodide sorption on candidate barriers (from Balsley et al., 1998).

Mineral	K_d
	mL g^{-1}
CMSA	29–108
Imogolite soil	39–231
Zn-Hydrotalcite†	25–389
Zn-Hydrotalcite‡	50–289
Zn-Hydrotalcite§	34–61
Lignite coal	0–518
Subbituminous coal	26–884
Cinnabar	69–3399
Covellite (CuS)	145–1375
Chalcocite (Cu_2S)	58–1285
Cuprite (CuO)	453
Tenorite (Cu_2O)	380

† Cl^-substituted.
‡ SO_4^{2-} substituted.
§ CO_3^{2-} substituted.

creasing pH. High K_ds of imogolite soil are restricted to pH values <6. Strong sorption of iodide is observed on lignite coal at pH 3.9, but sorption tends to decrease over time to zero. K_ds tend to decrease with increasing pH (see Fig. 9–3).

TcO_4^- mobility might be reduced through: (i) reduction of Tc^{+7} to the lower solubility Tc^{+4}; however, Eriksen et al., (1992) found that hydroxide and carbonate complexation can enhance Tc^{+4} solubilities); (ii) anion exchange on those few minerals that retain a net positive residual charge in their lattices; and (iii) surface complexation on those materials that have a high zero point of charge. Table 9–10 shows measured pertechnetate K_ds for a variety of materials. Coals are a long-lived, readily available, material that might reductively sorb Tc. Copper sulfides, CMSA, imogolite, and hydrotalcites were considered because of their ability to scavenge iodide (Balsley et al., 1998). Bone char was considered because Anderson (1998)

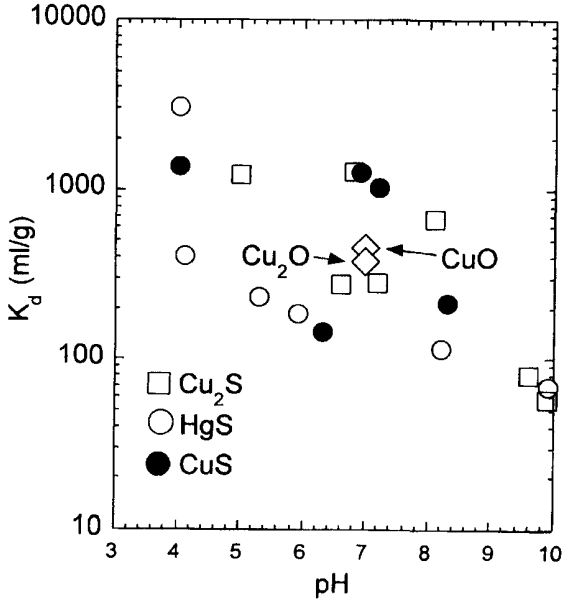

Fig. 9-3. Metal sulfide and metal oxdie K_ds for iodide.

Table 9–10. Tracer TcO_4^- batch K_d values: initial $^{95m}Tc = 7.89 \times 10^{-13}$ *M*.

Material	pH range	Ks_d 2 h	Ks_d 6 h	Ks_d 24 h
Hydrotalcite, CO_3	6.6–8.4	5.7–3.7	1.3–0.8	1.1–0.8
Hydrotalcite, Cl	5.3–7.4	58–29	37–20	17–14
Hydrotalcite, SO_4	6.6–7.1	118–179	113–89	61–43
Imogolite rich soil	6.0–7.0	15–13	16–15	18–15
Synthetic imogolite	6.4	41	23	23
Subbituminous coal	6.8–9.0	29–18	24–4.4	29–3.7
Lignite	7.1–10.5	84–30	98–31	128–35
FeOOH	6.3–8.5	30–36	26–32	24–30
CuS	5.4	93	114	67
Cu_2S	8.6	41	47	31
CuO	6.8	39	46	43
Cu_2O	7.1	56	63	55

noted its ability to scavenge TcO_4^- from Rocky Flats groundwater. Hydrous aluminum oxide also has been investigated because of its relatively high zero point of charge, and because synthesis studies of various Al-rich Hanford tank sludges demonstrated TcO_4^- removal (along with ReO_4^- and SeO_4^{2-}) when boehmite was precipitated from acidic waste simulate solutions (Zhang et al., 2000).

NpO_2^+ sorption was measured on the same materials (See Table 9–11). Neptunium release is considered to be one of the primary contributors to risk at the proposed repository at Yucca Mountain. Radionuclides leaving breached waste packages at Yucca Mountain. are likely to encounter large quantities (roughly 20 tons per waste package) of degradation products of the steel components, most likely goethite or hematite. Also, several kilograms of Cu oxides and sulfides are predicted to form due to the degradation of individual waste packages and other engineered materials. The K_d values in Tables 9–10 and 9–11 suggests that the presence of both Fe and Cu oxides inside and beneath breached waste packages may exert a powerful control over pertechnetate and neptunium migration.

Table 9–11. Tracer NpO_2^+ batch K_d values, initial $^{239}Np = 1.28 \times 10^{-13}$ *M* (analyses courtesy of Fred Marsh, Sandia National Laboratories.)

Material	pH range	K_d 2 h	K_d 6 h	K_d 24 h
Hydrotalcite, CO_3	6.6–8.4	232–>2811	342–>2688	584–>2700
Hydrotalcite, Cl	5.3–7.4	1344–2685	2278–3148	>5488–3778
Hydrotalcite, SO_4	6.6–7.1	1879–>6079	2871–>5506	> 4863–>4372
Imogolite rich soil	6.0–7.0	88–400	147–692	211–1927
Synthetic imogolite	6.4	82	50	51
Subbituminous coal	6.8–9.0	352–551	301–596	306–766
Lignite	7.1–10.5	614–842	595–1087	810–1828
FeOOH	6.3–8.5	1078–>3128	1048–>3149	974–3128
CuS	5.4	3.6	1.7	0.7
Cu_2S	8.6	7.6	91	661
CuO	6.8	20	22	33
Cu_2O	7.1	15	32	786
CMSA	11.7	>10 728	>11 405	>10 390

Table 9–12. TcO_4^- K_d values for Bone Char. A. K_d values in 10% DSSF-7† fluid.

Tc mg L^{-1}	K_d at 1–2 d	K_d at 14 d	K_d at 32 d	K_d at 47 d
0.1	1.6	4.5	5.1	--
0.5	1.6	3.3	3.7	3.8
1.0	1.6	3.3	3.4	--
5.0	1.5	2.5	2.5	2.5
5.0‡	3.2	3.0	2.9	2.8
5.0§	2.6	1.9	1.2	0.9
20	1.2	2.3	2.3	2.2

† 1 L of DSSF-7 fluid contains approximately 1.16 moles of $NaNO_3$, 0.20 moles of KNO_3, 0.75 moles of KOH, 0.008 moles of Na_2SO_4, 0.014 moles of $Na_2HPO_4 \cdot H_2O$, 3.89 moles of NaOH, 0.72 moles of $Al(NO_3)_3 \cdot 9H_2O$, 0.147 moles of Na_2CO_3,0.10 moles of NaCl and 1.51 moles of $NaNO_2$.

‡ As received, not ground.

§ 2 g of solid to 20 g of fluid, all others were 10 g of solid to 20 g of fluid.

Simulated Waste Tank Fluids

At the other end of the spectrum from dilute groundwaters are the highly caustic sodium nitrate–nitrite–aluminate solutions stored in underground tanks at Hanford and Savannah River. Unfortunately, the tanks occasionally leak and all of the contents in the tanks will eventually need to be processed before permanent disposal of the radioactive inventory. Thus, the development of chemical barriers to the migration of Tc will have applications that go beyond remediation of contaminated groundwaters. Not only is the ionic strength extreme in these fluids (often in excess of 10 *M*), but Tc concentrations may be in the 1 to 10 mg L^{-1} range. The high nitrate content and strong oxidizing capacity of these fluids preclude using Fe or the various coals tested previously. Although boehmite is present in considerable amounts in the tanks (Liu et al., 1999), its ability to scavenge Tc vanishes at these high pHs. Hydrotalcites hold little promise in high hydroxide-carbonate fluids because other anions should not be able to compete successfully for the interlayer exchange sites (Miyata, 1983). Hydroxyapatite is described as a minor component in tank sludges (Liu et al., 1999). This observation, along with the report by Anderson (1998), suggested that bone char might scavenge TcO_4^- from leaked tank fluids. A generic high nitrate–nitrite–hydroxide–sodium aluminate Hanford tank leachate fluid (DSSF-7) was diluted with nine parts deionized water to simulate the initial contact of a leaked tank fluid with ground water. TcO_4^- K_d values were assessed across a range of Tc concentrations (Table 9–12) and suggest that bone char might perform effectively as a pertechnetate sorber under the extreme conditions likely to prevail in contact with HLW tank effluents. Note that if bone char sorbs by ion exchange, reversible desorption of pertechnetate might occur once dilute fluids encountered the material, and a degree of irreversibility has been observed experimentally.

Table 9–13 indicates which compounds possess at least a limited capacity for sorbing TcO_4^- and iodide under a variety of soil conditions. Thus, in performance assessment calculations involving transport over significant distances (and hence substantial dilution ratios) it is likely that assuming a K_d of 0 is overly conservative. Note though that the absolute capacity of each material should be determined before relying on it in a chemical backfill.

Table 9–13. Candidate Tc getters for differing environments.

Material	Near HLW tanks	Groundwater oxidizing	Groundwater reducing
Iron metal	X	X (see text)	X
CuS			X
CuO		X	
Imogolite		X	X
Lignite		X	X
Hydrotalcite, SO_4		X	
Bone Char	X	X	X
Boehmite	?	X	X

CONCLUSIONS

Minerals have been identified that can effectively sorb each of the important radioisotopes under most soil or repository settings. Moreover, a growing number of permeable reactive barriers (PRBs) have already been used to remediate actual radionuclide plumes. PRBs containing Fe metal have been used to reduce U from its soluble hexavalent state to its relatively insoluble quadrivalent form at Fry Canyon, Utah; Monticello, UT; Rocky Flats, CO; and Oak Ridge National Laboratories, Tennessee. Sorptive uptake of U by hydroxyapatite and Fe hydroxide was tested at Fry Canyon, UT as well (see http://www.epa.gov/radiation/cleanup/docs/frycan_techdemo_interim_040201.pdf).

With few exceptions, the subject of radionuclide desorption has been avoided in this chapter. If a barrier is left in place, desorption by contaminant-free groundwater will ultimately occur to some degree after the pollution plume has passed. The release may be so slow that release of contamination into post-plume groundwater never violates regulatory standards due to radioactive decay and dilution. Unlike the forward loading step, release process(es) cannot generally be predicted ahead of time and, instead must be measured (see Eick et al., 2001). Partially because of this knowledge gap, long-term monitoring will be required at all reactive barrier sites. Indeed the results of future research on long-term desorption of contaminants from PRBs may determine the extent to which they are ultimately relied upon.

ACKNOWLEDGMENTS

We are profoundly grateful to Carol Stein and David Fowle for their helpful comments on improving this manuscript. We appreciate the early help of Hans W. Papenguth. We also appreciate funding over the years from the Hanford ILAW project, DOE-EMSP, and the Sandia National Laboratories LDRD Office.

REFERENCES

Anderson C.L. (1998) Removal of metals and radionuclides using apatite and other natural sorbants. M.S. thesis. Univ. of New Mexico, Albuquerque.

Arey, J.S., J.C. Seaman, and P.M. Bertsch. 1999. Immobilization of uranium in contaminated sediments by hydroxyapatite addition. Environ. Sci. Technol. 33(2):337–342.

Arnold, T., T. Zorn, H. Zanker, G. Bernhard, and H. Nitsche. 2001. Sorption behavior of U(VI) on phyllite: Experiments and modeling. J. Contam. Hydrol. 47:219–231.

Baes, C.F.I., and R.D. Sharp. 1983. A proposal for estimation of soil leaching and leaching constants for use in assessment models. J. Environ. Qual. 12:17–28.

Balsley, S.D., P.V. Brady, and J.L. Krumhansl. 1996. Iodide retention by metal sulfide surfaces: Cinnabar (HgS) and Chalcocite (Cu_2S). Environ. Sci. Technol. 30:3025–3027.

Balsley, S.D., P.V. Brady, J.L. Krumhansl, and H.L. Anderson. 1998. Anion scavengers for low level radioactive waste backfills. J. Soil Contam. 7:125–141.

Bethke, C.M. 1998. The geochemist's workbench. Release 3.0. A users software guide to Rxn, Act2, Tact, React, and Gtplot. Hydrogeology Program. Univ. of Illinois, Urbana-Champaign.

Bethke, C.M., and P.V. Brady. 2000. How the K_d approach undermines ground water cleanup. Groundwater 321:435–442.

Brady, P.V., and D.J. Borns. 1997. Natural attenuation of metals and radionuclides: Report from a workshop held by Sandia National Laboratories, SAND97-2727. Sandia National Laboratories, Albuquerque, NM.

Brady, P.V., M.V. Brady, and D.J. Borns. 1997. Natural attenuation: CERCLA, RBCAs, and the future of environmental remediation. Lewis Publishers, Boca Raton, FL.

Brady, P.V., C.F. Jové Colon, F. Huang, and G. Carr. 2002. Soil radionuclide plumes. p. 165–190. *In*. P. Zhang and P.V. Brady (ed.) Geochemistry of soil radionuclides. SSSA Spec. Publ. 59. SSSA, Madison, WI.

Brady, P.V., and M.W. Kozak. 1995. Geochemical engineering of low level radioactive waste in cementitious environments. Waste Manage. 15:293–301.

Cotter-Howells, J.D., and S. Caporn. 1996. Remediation of contaminated land by formation of heavy metal phosphates. Appl. Geochem. 11:335–342.

Davis, J.A., and D.B. Kent. 1990. Surface complexation modeling in aqueous chemistry. p.77–260. *In* M.F. Hochella and A.F. White. (ed.) Mineral-interface geochemistry. Mineral. Soc. of Am., Washington, DC.

Davis, J.A., T.E. Payne, and T.D. Waite. 2002. Simulating the pH and pCO_2 dependence of uranium(IV) adsorption by a weathered schist with surface complexation models. p. 61–86. *In* Geochemistry of soil radionuclides. SSSA Spec. Publ. 59. SSSA, Madison, WI.

Dzombak, D.A., and F.M.M. Morel. 1990. Surface complexation modeling: Hydrous ferric oxide. John Wiley & Sons, New York.

Eick, M.J., B.R. Naprstek,, P.V. Brady. 2001. Kinetics of Ni(II) sorption and desorption on kaolinite: Residence time effects. Soil Sci. 166:11–17.

Eriksen, T.E., P. Ndalamba, J. Bruno, and M. Caceci. 1992. The solubility of TcO2 • *n*H2O in neutral to alkaline solutions under constant *p*CO2. Radiochim. Acta 58(8):67–70.

Fletcher, P., and G. Sposito. 1989. The chemical modelling of clay/electrolyte interactions for montmorillonite. Clay Mineral. 24:375–391.

Freeze, R.A., and J.A. Cherry. 1979. Groundwater. Prentice-Hall,

Gauglitz, R.M., W. Holterdorf, W. Franke, and G. Marx. 1992. Immobilization of heavy metals by hydroxylapatite. Radiochim. Acta. 58/59:253–257.

Goldberg, S., J.A. Davis, and J.D. Hem. 1996. The surface chemistry of aluminum oxides and hydroxides. p. 271–332. *In* G. Sposito (ed.) The environmental chemistry of aluminum. 2nd ed. CRC Lewis Publ., Boca Raton, FL.

Guzowski, F.B., F.B. Nimik, M.D. Siegel, and N.C. Finley. 1982. Repository site data report for tuff: Yucca Mountain, Nevada. Sandia Natl. Lab., Albuquerque, NM.

Honeyman, B.D., and J.F. Ranville. 2002. Colloid properties and their effects on radionuclide transport through soils and groundwaters. p. 131–163. *In* Geochemistry of soil radionuclides. SSSA Spec. Publ. 59. SSSA, Madison, WI.

Huie, Z., Z. Jishu, and Z. Lanying. 1988. Sorption of radionuclides technetium and iodine on minerals. Radiochim. Acta 44/45:143–145.

Ikeda, Y., M. Sazarashi, M. Tsuji, R. Seki, and H. Yoshikawa. 1994. Adsorption of I^- ions on cinnabar for ^{129}I waste management. Radiochim. Acta 65:195–198.

Jeanjean, J., J.C. Rouchard, L. Tran, and M. Fedoroff. 1995. Sorption of uranium and other heavy metals on hydroxyapatite. J. Radioanal. Nucl. Chem. 201:1108–1116.

Kaplan, D., and et al. 1996. Radionuclide adsorption distribution coefficients measured in Hanford sediments for the low level waste performance assessment project. Pacific Northwest Natl. Lab., Richland, WA.

Krumhansl, J.L., P.V. Brady., and H.L. Anderson. 2001. Reactive barriers for Cs-137 retention. J. Contam. Hydrol. 47:233–240.

Krupka, K.M., D.I. Kaplan, G. Whelan, R.J. Serne, and S.V. Mattigod. 1999. Understanding variation in partition coefficient, K_d, values. Vol. II. Review of geochemistry and available K_d values for cadmium, cesium, chromium, lead, plutonium, radon, strontium, thorium, tritium (^3H), and uranium. U.S. Environmental Protection Agency, Richland, WA.

Laperche, V., S.J. Traina, P. Gaddam, and T.J. Logan. 1996. Chemical and mineralogical characterizations of Pb in a contaminated soil: Reactions with synthetic apatite. Environ. Sci. Technol. 30:3321–3326.

Liu, J., J. Lumetta, G.L. Graff, N.G. Colton, B.C. Bunker, and J.L. Krumhansl. 1999. Characterization of colloidal phases in tank wastes. Proc. Am. Chem. Soc. 218:164.

Marine, I.W. 1976. Geochemistry of ground water at the Savannah River Plant. DP-1356. U.S. DOE, Washington, DC.

Miyata, S. 1983. Anion-exchange properties of hydrotalcite-like compounds. Clays Clay Miner. 31(4):305–311.

Molecke, M.A. 1983. A comparison of brines relevant to nuclear waste experimentation. Sandia Natl. Lab., Albuquerque, NM.

Monteil-Rivera, F., M. Fedoroff, J. Jeanjean, L. Minel, M.-G. Barthes, and J. Dumonceau. 2000. Sorption of selenite SeO_3^{-2} on hydroxyapatite: An exchange process. J. Colloid Interface Sci. 221:291–300.

Morrison, S.J., and R.R. Spangler. 1992. Extraction of uranium and molybdenum from aqueous solutions: A survey of industrial materials for use in chemical barriers for uranium mill tailings remediation. Environ. Sci. Technol. 26.

National Research Council. 1994. Alternatives for groundwater cleanup. Natl. Academy Press, Washington, DC.

Read, D. 1992. Geochemical modeling of uranium redistribution in the Osamu Utsumi mine, Pocos de Caldas. J. Geochem. Exploration 451(3):503–520.

Reardon, E.J. 1981. K_ds: Can they be used to describe reversible ion sorption reactions in contaminant transport. Ground Water 19:279–286.

Smith, J.T., and R.N.J. Comans. 1996. Modeling the diffuse transport and remobilization of ^{137}Cs in sediments: The effects of sorption kinetics and reversibility. Geochim. Cosmochim. Acta 60:995–1004.

Sposito, G. 1984. The surface chemistry of soils. Oxford Univ. Press, Oxford.

Stumm, W., and J.J. Morgan. 1970. Aquatic chemistry. Wiley-Interscience, New York.

Stumm, W., and J.J. Morgan. 1996. Aquatic chemistry. Wiley-Interscience, New York.

Tamura, T. 1972. Sorption phenomena significant in radioactive waste disposal. p. 318–330. *In* Underground waste management and environmental implications. Vol. 18. Am. Assoc. of Petroleum Geol., Tulsa, OK.

Toran, L.E., and J.A. Saunders. 1999. Modeling alternative paths of chemical evolution of Na_HCO_3-type groundwater near Oak Ridge, Tennessee, USA. Hydrogeol. J. 7:355–364.

Vandergraaf, T.T., K.V. Ticknor, and I.M. George. 1984. Reactions between technetium in solution and iron-containing minerals under oxic and anoxic conditions. Am. Chem. Soc. Symp. Ser. 246:25–43.

Ying, Ma Q., S.J. Traina, T.L. Logan, and J.A. Ryan. 1993. In situ lead immobilization by apatite. Environ. Sci. Technol. 27:1803–1810.

Zhang, P.C., J.L. Krumhansl, and P.V. Brady. 2000. Boehmite sorbs perrheehnate and pertechnetate. Radiochim. Acta 88:369–373.

10 Role of Radionuclide Sorption in High-Level Waste Performance Assessment: Approaches for the Abstraction of Detailed Models

David R. Turner, F. Paul Bertetti, and Roberto T. Pabalan

Southwest Research Institute
San Antonio, Texas

ABSTRACT

Sorption in the geosphere may help to mitigate radionuclide transport from the proposed high-level radioactive waste repository at Yucca Mountain, Nevada. Probabilistic performance assessment (PA) models typically use a constant sorption coefficient (K_d) for each radionuclide and each hydrostratigraphic unit. Approaches have been developed that include aspects of mechanistic sorption models into PA calculations. Simplified surface complexation models are calibrated against laboratory experiments and used to calculate actinide transport parameters. In one approach, parameter distributions are calculated based on site-specific water chemistry from the Yucca Mountain vicinity. Model results are used to provide limits on K_d probability distribution functions as input into PA. Under the groundwater chemical conditions observed at Yucca Mountain, calculated sorption parameters can range across many orders of magnitude. Another approach uses the simplified surface complexation model to calculate actinide sorption behavior for a wide range in geochemical parameters. Response surfaces for actinide sorption as a function of pH and pCO_2 are developed. The approaches outlined in this study can be adapted readily to current PA efforts.

Many countries are currently investigating long-term geologic disposal of high-level nuclear waste (HLW) (National Research Council, 1999; Nuclear Energy Agency, 1998). In the U.S. HLW program, the Nuclear Waste Policy Act of 1982 (as amended 1987) charges the U.S. Department of Energy with characterizing and evaluating Yucca Mountain, Nevada, as a potential site for a geologic HLW repository. A multiple barrier approach that includes both engineered and natural barriers to radionuclide release is typically endorsed. In this approach, HLW (spent nuclear fuel, defense waste) is placed in engineered waste packages and placed in an underground mined repository. When the repository is full, the drifts are closed and the repository sealed. The engineered barriers (waste form, waste canister, backfill) are designed to provide waste isolation for an extended period of time. In addition to providing a suitable environment for the waste packages and other engineered

 Geochemistry of Soil Radionuclides. SSSA Special Publication no. 59.

barrier components, the geosphere surrounding the repository is expected to provide additional isolation to reduce exposure at receptor locations. The conceptual model assumes that after failure of the engineered barrier, radionuclides are released and transported in the groundwater. Understanding the means by which radionuclides migrate in the subsurface is therefore a critical part of PA calculations that attempt to assess the safety of the repository concept. Processes such as sorption that serve to reduce radionuclide concentrations or retard radionuclide migration are considered to be favorable to repository performance.

Experimental and modeling studies indicate that sorption behavior, and the sorption coefficient (K_d) that is used to describe it, is strongly dependent on solution and mineral properties along transport paths. Without an abundance of site-specific chemical and mineralogical data, it is difficult to extrapolate K_d values beyond experimental conditions with any quantifiable certainty in PA calculations; however, because experimental evidence indicates that K_ds vary in a systematic fashion that can be modeled using well-established geochemical approaches, there is an underlying link, dependent on variations in the chemistry of the system at Yucca Mountain, that may be used to correlate the sorption behavior of different radioelements. The purpose of this study is to outline an approach that incorporates aspects of detailed geochemical models in estimating sorption and radionuclide transport parameters for radionuclide transport at Yucca Mountain, and to describe how this approach may be implemented in PA. The focus is on identifying geochemical parameters that exert the most control on radionuclide sorption, and incorporating the effects of those parameters in a way that lends itself to the simplification (abstraction) process used in PA for the proposed repository. In this way, PA models can represent chemical effects on sorption behavior more accurately.

BACKGROUND

A number of countries are investigating geologic disposal of HLW, including the USA, Sweden, Finland, Germany, and Japan, (National Research Council, 1999; Nuclear Energy Agency, 1998). Although the details of the different national programs are different, there are many similarities. The following section provides a brief discussion of the HLW disposal program in the USA, the role of the different government agencies, and an outline of how PA is used in licensing decisions.

Introduction to the U.S. High-Level Nuclear Waste Management Program

The proposed site at Yucca Mountain is located approximately 175 km northwest of Las Vegas, NV (Fig. 10–1). If the site is found to be suitable, approved, and licensed, the repository would be located in a thick sequence of Tertiary volcanic tuffs. Although a number of basins have been identified in the region, groundwater flow through the area is generally from recharge areas to the north through a series of aquifers, including both tuffs and regional Paleozoic carbonates, with discharge from springs, seeps, and agricultural and domestic wells to the south of Yucca Mountain (Winograd & Thordarson, 1975). The proposed regulatory framework (U.S. Nuclear Regulatory Commission, 1999a) establishes criteria for repository

performance. When finalized, these criteria will conform to the public health and environmental radiation protection standards established for Yucca Mountain by the U.S. Environmental Protection Agency (U.S. Environmental Protection Agency, 2001). Specifically, the quantitative measure of repository performance is based on radiation dose to a hypothetical reasonably maximally exposed individual located in the accessible environment about 18 km south (downgradient) from the proposed repository. There also is a groundwater protection aspect of the regulatory standard

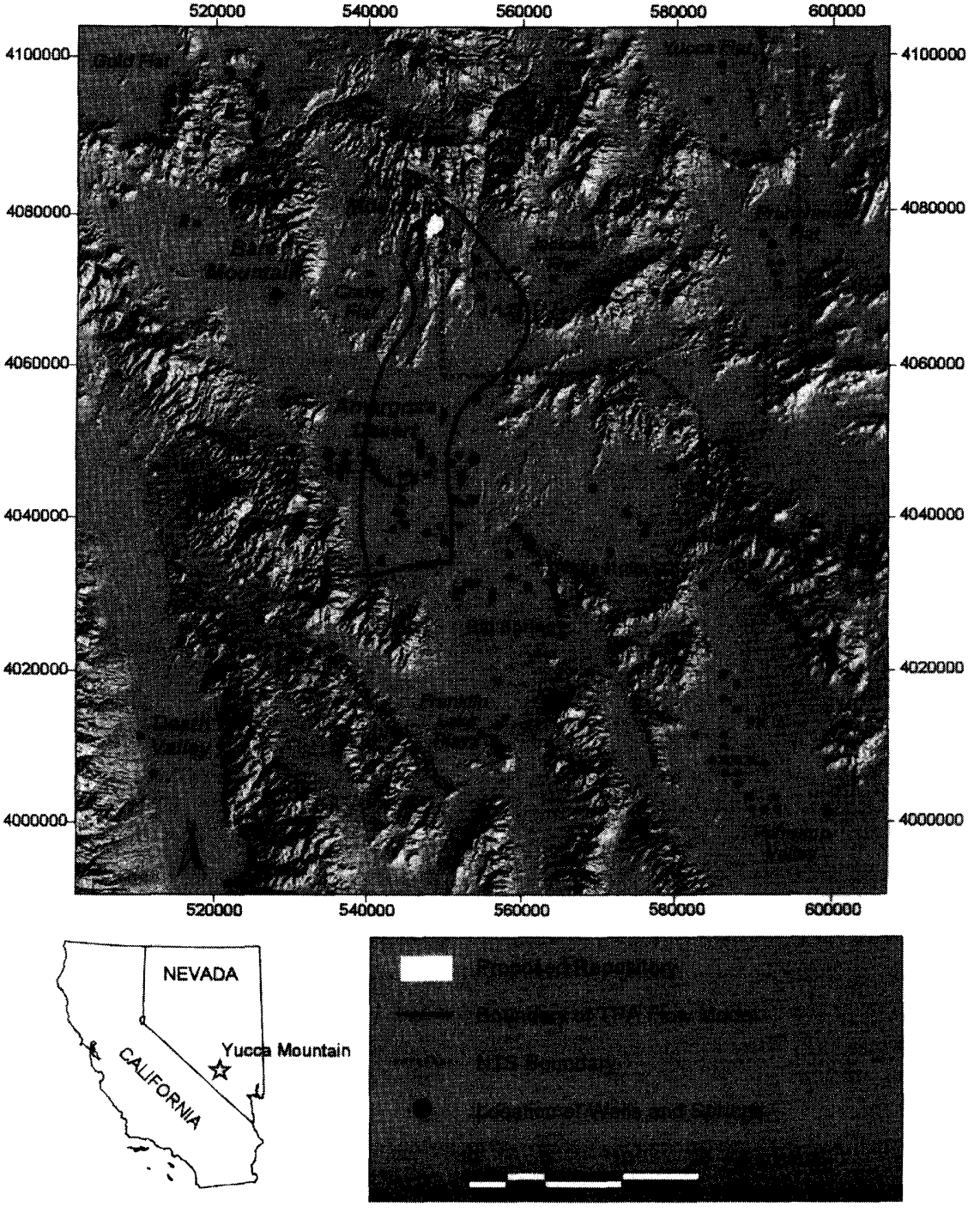

Fig. 10-1. Location of the proposed repository at Yucca Mountain, NV. Groundwater sample locations and geographical features discussed in the text are identified. The flow regime outline is from the TPA 3.1 model (U.S. Nuclear Regulatory Commission 1999b).

that requires estimates of dissolved radionuclide concentrations. The time period of interest to performance is 10 000 yr after permanent closure.

In the U.S. HLW program, the U.S. Department of Energy is the license applicant. The U.S. Nuclear Regulatory Commission (NRC) evaluates the U.S. Department of Energy license application against its regulations. An important part of the proposed NRC regulations (10 CFR Part 63, U.S. Nuclear Regulatory Commission, 1999a) governing the licensing, construction, operation, and permanent closure of the proposed repository at Yucca Mountain is the use of PA calculations to evaluate the performance of the different barriers to waste containment and migration over long time periods (10 CFR 63.114). These PA analyses are intended to represent the degree of knowledge of the Yucca Mountain site, and at the same time, represent the uncertainty in both our conceptual and mathematical models of the site.

Role of Total System Performance Assessment in High-Level Nuclear Waste Management

The multiple barrier approach to geologic disposal of HLW at Yucca Mountain relies on the geologic setting to provide a degree of isolation in addition to that provided by the engineered barrier system for a period of 10 000 yr or more. Complex coupled computer models have been developed to evaluate the suitability of Yucca Mountain through a series of site-specific PA calculations. In the U.S. Department of Energy program, these PA calculations are carried out under an iterative series of total system performance assessments (TSPA) that are updated as site characterization proceeds and repository design evolves (Civilian Radioactive Waste Management System, Management, and Operating Contractor, 1998, 2000a; U.S. Department of Energy, 1998). The NRC also has developed an independent capability in PA, including the iterative performance assessment (IPA) (Wescott et al., 1995) and total-system performance assessment (TPA) (U.S. Nuclear Regulatory Commission 1999b,c).

In the U.S. Department of Energy Repository Safety Strategy (Civilian Radioactive Waste Management System, Management, and Operating Contractor, 2000b), a fundamental quantity of interest in TSPA calculations is the rate of radionuclide transport from the proposed repository through the subsurface to the biosphere and potential receptor(s). Reduction in radionuclide concentrations and delay in arrival times during radionuclide transport are identified by the U.S. Department of Energy as key attributes that need to be tested in any suitability demonstration for the proposed repository at Yucca Mountain. As part of the geological setting, sorption processes can retard radionuclide transport, delaying arrival times at the receptor location(s), and can reduce radionuclide concentrations at the point of exposure.

TSPA calculations for the natural barrier system at Yucca Mountain require linking a number of geological, geochemical, and hydrological models. Because of the long simulation period and the heterogeneous geochemical and hydrological systems at Yucca Mountain, simplification of complex process models is necessary to reduce the computational burden for PA calculations. In PA, the process of simplification is called model abstraction. Sorption modeling is an example where

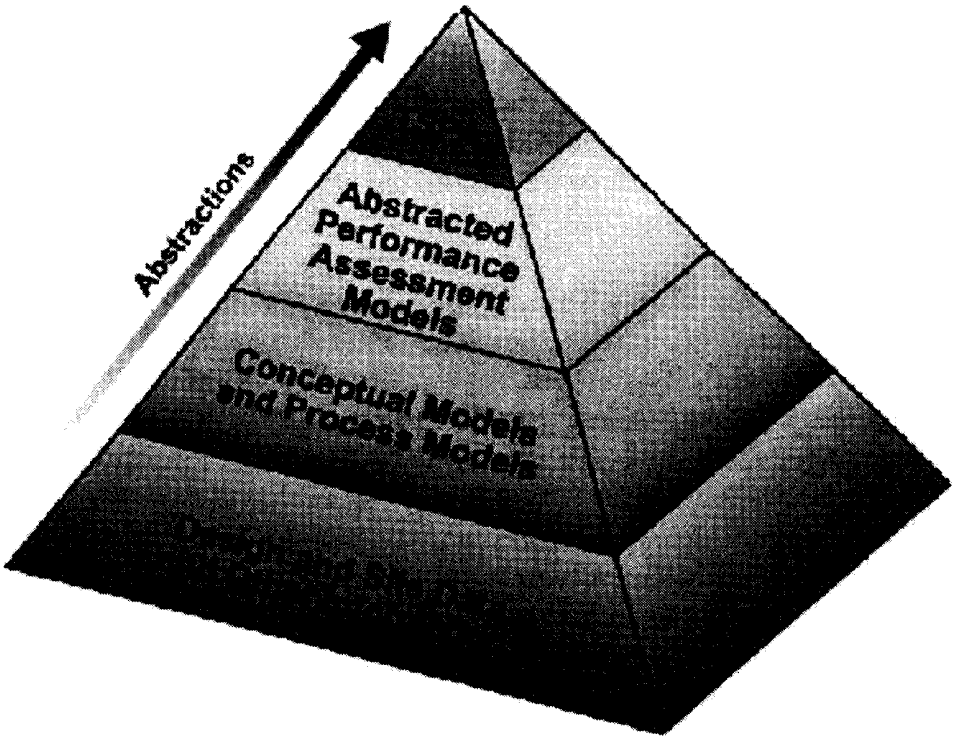

Fig. 10–2. The Total System Performance Assessment pyramid representing the technical basis for the abstraction process (from Civilian Radioactive Waste Management System, Management, and Operating Contractor, 2000a).

detailed geochemical models are available for simulating reactive transport (e.g., Yeh & Tripathi, 1989, 1991), but are not suited for incorporation in the current generation of PA codes.

During the abstraction process, critical aspects controlling a given process are identified, conceptual models are developed, parameters are defined, and uncertainties estimated. The PA abstraction is supported by a combination of site and laboratory data, more detailed process models, and in some cases expert judgement (Fig. 10–2). The purpose of this study is to outline approaches that can be used to abstract the results from geochemical sorption models for use in PA.

Overview of the Role of Radionuclide Sorption in the Yucca Mountain Total System Performance Assessments

One of the initial reasons for proposing Yucca Mountain as a location for the repository is the existence of a deep regional water table. The proposed repository will be located some 250 m below the ground surface and approximately 300 m above the regional water table (Civilian Radioactive Waste Management System, Management, and Operating Contractor, 2000a,c). Geologic HLW disposal at Yucca Mountain is unique in this respect, in that the repository would be located in the unsaturated zone under oxidizing conditions. Conceptual models of the proposed Yucca Mountain repository include vertical transport through fractures and matrix in the volcanic tuff of the unsaturated zone followed by lateral transport through the saturated zone to the receptor location. The first part of the saturated zone transport leg is anticipated to be through fractured volcanic tuff, with the last part of the transport through saturated alluvium. There is some current uncertainty

in the length of the flow path through the alluvium, and this is treated as a sampled parameter in the U.S. Department of Energy TSPA.

The U.S. Department of Energy has been conducting TSPA analyses of the proposed repository at Yucca Mountain since 1991. As considered in TSPA, sorption is a general term for describing a combination of chemical interactions between the dissolved radionuclides and the solid phases (Civilian Radioactive Waste Management System, Management, and Operating Contractor, 2000a). Sorption, characterized by a single K_d value, reduces the rate of radionuclide advective transport and amplifies the effects of matrix diffusion through its potential effect on increasing concentration gradients. This lumped approach of incorporating all potential retardation mechanisms in a single K_d is readily incorporated into existing transport codes and simplifies the numerical simulation of radionuclide migration. It does not, however, distinguish between different sorption processes and geochemical interactions, such as surface adsorption, precipitation, and ion exchange.

Batch sorption experiments are used to identify the overall partitioning between the aqueous and solid phase, and establish limits on K_d. The magnitude of K_d is a function of the chemical element, the rock type involved in the interaction, and the geochemical conditions of the water contacting the rock. In PA calculations, K_d is considered to be an uncertain parameter. The uncertainty is defined using a probability distribution function (PDF) that places upper and lower limits on K_d and, if possible, identifies the central tendency of the PDF. The PDFs are sampled to obtain multiple realizations to generate a family of complementary cumulative distribution functions (CCDF) for radionuclide release (Wilson et al., 1994). Because it is impractical to perform batch experiments under all anticipated conditions, the PDFs are typically developed either formally or informally by a group of one or more experts who consider the sorption behavior of the critical radionuclides and the anticipated variability in water and mineral chemistry over the transport path. During TSPA calculations, each PDF is sampled in multiple realizations that are used to generate statistics of the estimated dose to the receptor(s) (Civilian Radioactive Waste Management System, Management, and Operating Contractor, 2000a; U.S. Nuclear Regulatory Commission, 1999b,c).

The approach outlined above has been applied to modeling radionuclide sorption in the porous matrix and alluvium at Yucca Mountain. In the U.S. Department of Energy TSPA analyses, eight radioelements are transported through four basic types of hydrostratigraphic units at Yucca Mountain: devitrified tuff, vitric tuff, zeolitic tuff, and alluvium (Civilian Radioactive Waste Management System, Management, and Operating Contractor, 2000a). Each rock type or hydrostratigraphic unit is assigned a K_d PDF for each radionuclide of interest. The NRC TPA analyses track 16 radioelements through eight separate hydrostratigraphic units (U.S. Nuclear Regulatory Commission, 1999b,c). This approach rapidly leads to a large number of parameters for sorption and transport in the matrix. In TSPA simulations, it is assumed that each sampled K_d value is constant for a given hydrostratigraphic unit and over the entire time. It is further assumed in the sampling procedures used in some PA models (Civilian Radioactive Waste Management System, Management, and Operating Contractor, 2000a,b,c; U.S. Nuclear Regulatory Commission, 1999b,c) that the sorption parameters for the radionuclides of concern are statistically independent of one another.

The amount of retardation that sorption in the matrix contributes under actual transport conditions is a function of both K_d and the transport paths. For example, in the U.S. Department of Energy TSPA analyses, the majority of the flow is through fractures in the devitrified tuff, and flow tends to bypass the zeolitic tuff because of its low permeability (Civilian Radioactive Waste Management System, Management, and Operating Contractor, 2000a,b,c). Sorption is most effective in the vitric tuff and its effectiveness in the devitrified tuff is tied to the degree to which matrix diffusion moves radionuclides out of fractures and into the rock matrix where there are assumed to be more available sorption sites.

Sorption also is a potential retardation mechanism for radionuclide transport through fractures. The surfaces of fractures are often lined with minerals that may be capable of sorbing some of the radionuclides; however, there is limited characterization of the extent and distribution of fracture-lining minerals along potential flow paths (Carlos et al., 1995). In the conceptual model used for Yucca Mountain, it is conservatively assumed that there is no sorption (i.e., $K_d = 0$) in fractured tuff for radionuclides being tracked in PA (Civilian Radioactive Waste Management System, Management, and Operating Contractor, 2000a,b,c; U.S. Nuclear Regulatory Commission, 1999b,c). In the saturated alluvium, porous media transport behavior is assumed, and all radionuclides are subject to sorption as described by the K_d PDF.

Both the U.S. Department of Energy and the NRC use sensitivity analyses to examine the importance of sorption to repository performance (Civilian Radioactive Waste Management System, Management, and Operating Contractor, 1998, 2000a; U.S. Nuclear Regulatory Commission, 1999b,c). Although the specific results vary, the most significant contributors to dose typically include radionuclides such as ^{99}Tc, ^{129}I, and sorbing ^{237}Np that are anticipated to be highly soluble and weakly sorbing under the geochemical conditions expected and anticipated at Yucca Mountain (e.g., oxidizing, Na-bicarbonate solutions). Other radionuclides are predicted to be important either due to colloid transport, high inventory, or a high dose-conversion factor (^{239}Pu, ^{241}Am, ^{238}U, and ^{230}Th) (Civilian Radioactive Waste Management System, Management, and Operating Contractor, 1998).

RADIONUCLIDE SORPTION BEHAVIOR

Improving the ability to address the geochemical controls on sorption in PA abstractions depends on understanding the key parameters controlling radionuclide sorption behavior. The approaches outlined below are focused on actinides (U, Np, Pu, Th, Am), but are general enough to be applied to other radionuclides of interest in PA.

Key Geochemical Parameters-Actinides

The distribution (or sorption) coefficient (K_d) is a convenient empirical ratio for representing batch sorption data and is commonly used in transport models in PA. The K_d (mL × g^{-1}) can be defined as:

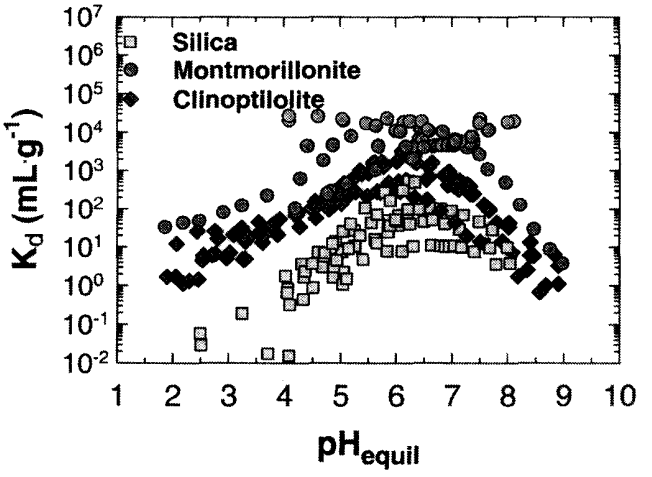

Fig. 10–3. Effects of pH on U(VI) sorption on different silicate and aluminosilicate minerals in the presence of atmospheric CO_2 ($PCO_2 = 10^{-3.5}$ atm). Data from Zachara and McKinley (1993), McKinley et al. (1995), and Pabalan et al. (1998).

$$K_d\ (\text{mL} \times \text{g}^{-1}) = \frac{\text{equilibrium mass of radionuclide sorbed on solid}}{\text{equilibrium mass of radionuclide in solution}} \times (V/M) \quad [1]$$

where V is the volume of experimental solution in mL and M is the mass of solid in g. The use of K_d normalizes sorption data to the solid-mass to solution-volume (M/V) ratio used in laboratory batch experiments and provides a means of accounting for the change in solution concentration that occurs during the course of the experiment.

For actinides, sorption behavior typically varies as a function of its aqueous speciation (Fig. 10–3), with a close correspondence between the pH dependence of sorption behavior, the predominance field of actinide-hydroxy complexes, and the presence of complexing ligands such as carbonate (Bertetti et al., 1998; Pabalan et al., 1998). Under low pH conditions, actinide sorption tends to be weak, except under low ionic strength conditions for cation exchangers such as montmorillonite and, to a lesser extent, clinoptilolite (e.g., McKinley et al., 1995; Pabalan et al., 1993; Turner et al., 1996; Zachara & McKinley, 1993). With increasing pH, actinide sorption increases, with a maximum typically in the pH range where the hydroxy complexes are important. In carbonate-free laboratory systems, actinide sorption continues to increase with increasing pH and increasing hydrolysis (e.g., Allard et al., 1984; Hsi & Langmuir, 1985; McKinley et al., 1995; Turner et al., 1998), but actinide sorption behavior is sensitive to the presence of carbonate or other ligands in solution that affect aqueous speciation. For example, in carbonate-bearing systems, actinide sorption tends to decrease with increasing pH and/or increasing carbonate concentration (Fig. 10–4) (Bertetti et al., 1998; LaFlamme & Murray, 1987; Pabalan et al., 1998; Sanchez et al., 1985).

In contrast to the relatively pronounced effects of aqueous speciation on actinide sorption, the similarity in the pH-dependence of actinide sorption on a wide variety of minerals such as quartz, α-alumina, clinoptilolite, montmorillonite, amorphous silica, kaolinite, and titanium oxide suggests a relative insensitivity to surface charge characteristics of the sorbent as compared with the effect of changing the total number of available sites. For example, the data in Fig. 10–3 demon-

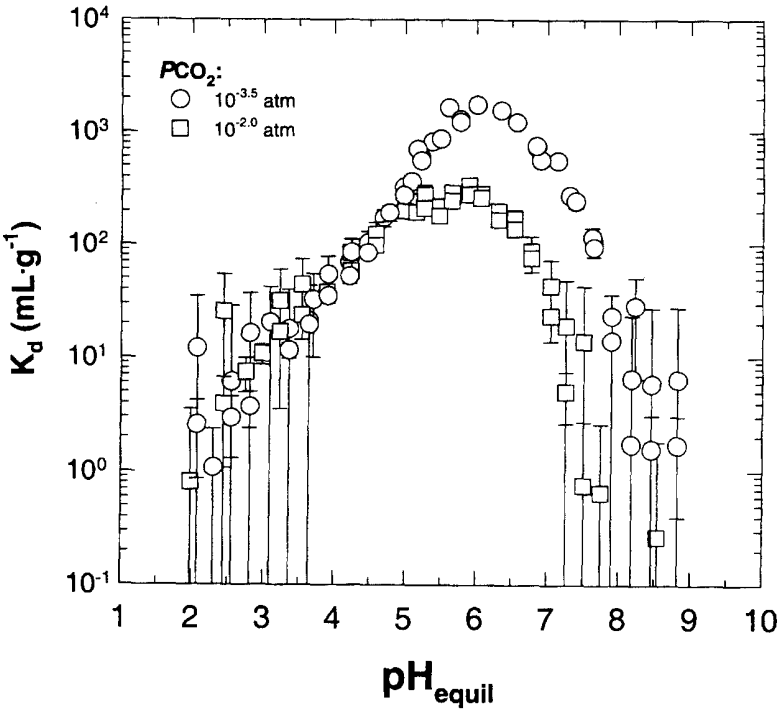

Fig. 10–4. Effects of variable PCO_2 on U(VI) sorption on clinoptilolite (data from Pabalan et al., 1998).

strate that U(VI) sorption on quartz, α-alumina, clinoptilolite, and montmorillonite in the presence of atmospheric CO_2 ($PCO_2 = 10^{-3.5}$ atm) is strongly affected by solution pH (Pabalan et al., 1998). Although the minerals used in the experiments have different mineralogic and surface properties, U(VI) sorption on these minerals is similar with respect to dependence on pH. In all cases, U sorption is at a maximum at near neutral pH (~6.0 to ~6.8) and decreases sharply towards more acidic or more alkaline conditions. In experiments, ionic strength effects up to about 1 *M* seem to be limited for actinide surface complexation reactions (Pabalan et al., 1998), although these effects can be important if ion exchange is the predominant sorption mechanism (Turner et al., 1996). Elevated ionic strength also may stabilize aqueous complexes that can affect actinide sorption behavior.

Experimental sorption results are typically plotted in terms of percent sorbed versus pH (Fig. 10–5a). In the U(VI)–H_2O–CO_2 system, the amount of U(VI) sorbed (in percent) relative to the initial amount of U(VI) in solution increases with increasing *M/V* ratio, giving a broader sorption envelope. The apparent *M/V* effect, however, is mostly eliminated if the results are plotted in terms of K_d (Fig. 10– 5b). As demonstrated in Pabalan et al. (1998), U(VI) sorption on quartz, α-alumina, clinoptilolite, and montmorillonite is similar with respect to pH dependence; however, the K_d values for the different minerals vary over three orders of magnitude. This variation is an artifact of normalizing the data to the sorbent mass and representing sorption data in terms of K_d. Similar observations were reported for Np(V) sorption (Bertetti et al., 1998).

Surface areas measured by gas adsorption (e.g., N_2-BET) methods are a relative index of the number of sorption sites on the mineral surface and it may be more useful to represent sorption data normalized to the specific surface area of the mineral sorbent (Bertetti et al., 1998; Pabalan et al., 1998; Smith & Schafer, 1999). Fig-

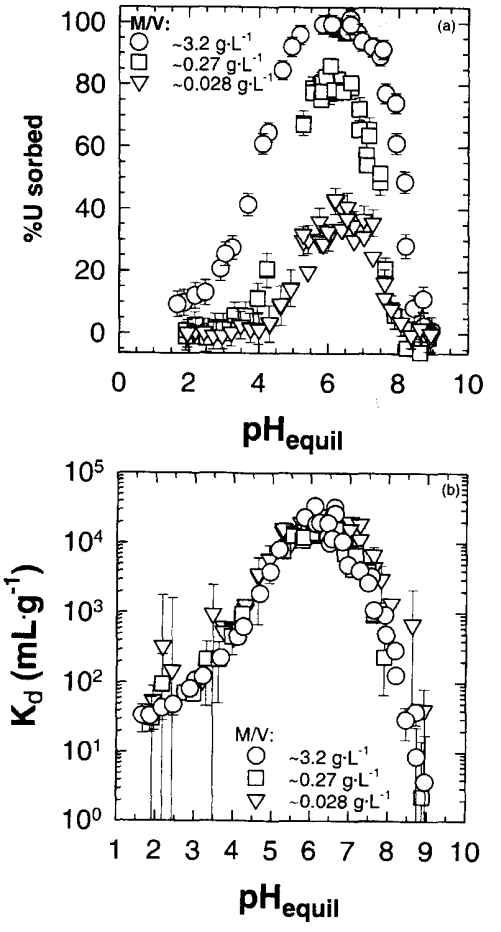

Fig. 10–5. Effects of M/V ratio on U(VI) sorption on montmorillonite expressed in terms of (a) percent U(VI) sorbed; (b) K_d (mL × g^{-1}) (data from Pabalan et al., 1998).

ure 10–6a presents the results of U(VI) sorption on quartz, α-alumina, clinoptilolite, and montmorillonite, plotted in terms of K_d. In contrast, Fig. 10–6b presents the same U(VI) sorption data replotted in terms of K_a (mL × m^{-2}), where K_a is K_d normalized to the mineral's N_2-BET specific surface area (S_a, $m^2 \times g^{-1}$) (i.e., $K_a = K_d/S_a$). As shown in Fig. 10–6b, surface area normalized sorption data for clinoptilolite and montmorillonite are indistinguishable, whereas surface area normalized sorption data for quartz and α-alumina are almost coincident. The α-alumina K_a are slightly lower than those of quartz due to the higher initial U concentration of the α-alumina experiments (Pabalan et al., 1998).

Surface areas determined by N_2-BET methods most likely overestimate the amount of sorption sites on layered silicates such as montmorillonite and zeolitic minerals such as clinoptilolite. For example, it is believed that surface complex formation of U(VI) on montmorillonite occurs on the hydroxylated edge sites of the mineral (Zachara & McKinley, 1993; Turner et al., 1996). Wanner et al. (1994) estimated that only 10% of the N_2-BET specific surface area is accounted for by the crystallite edges of montmorillonite. Assuming that the effective surface area (S_{ea}) for montmorillonite and clinoptilolite is equivalent to about 10% of the measured S_a, sorption data for montmorillonite and clinoptilolite can be recast in terms of $K_{a'}$, where $K_{a'}$ is K_d normalized to the mineral's S_{ea} (i.e., $K_{a'} = K_d/S_{ea}$). For nonlayered and nonporous minerals such as quartz and α-alumina, $K_a = K_{a'}$. Figure 10–7 plots

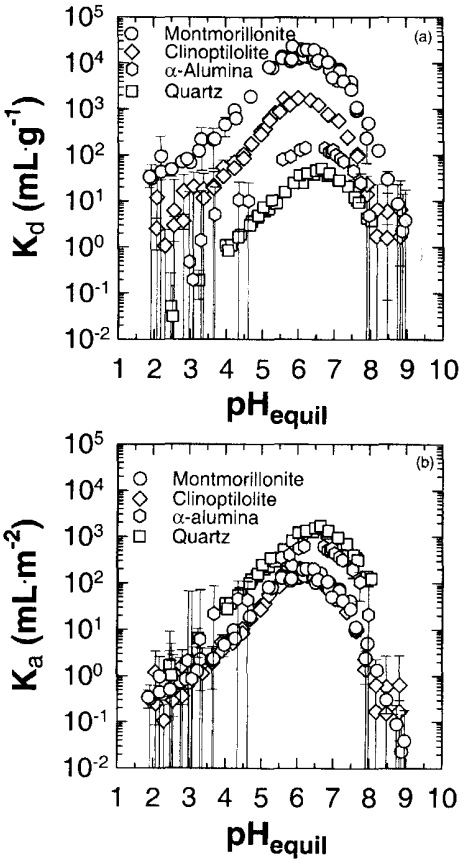

Fig. 10–6. Sorption of U(VI) on different silicate and aluminosilicate minerals expressed in terms of (a) K_d (mL × g^{-1}); (b) K_a (mL × m^{-2}) (data from Pabalan et al., 1998).

$K_{a'}$ values for quartz, clinoptilolite, and montmorillonite. As shown in the figure, U(VI) sorption on these minerals, which have distinct mineralogic and surface properties, are essentially equivalent when recast in terms of $K_{a'}$. This suggests that at least for aluminosilicate minerals, expressing sorption in terms of $K_{a'}$ provides a generalized basis for PA transport calculations. The K_d values for a given hydrostratigraphic unit can then be backed out assuming an effective specific surface area

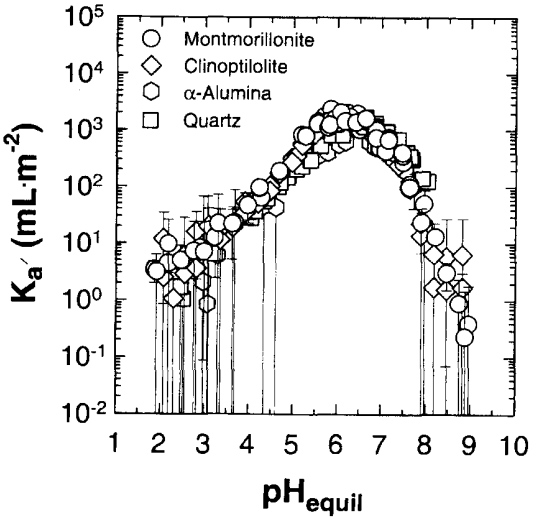

Fig. 10–7. Sorption data from Fig. 10–6 expressed in terms of $K_{a'} = K_d/S_{ca}$. See text for detailed discussion.

and the relationship $K_d = K_{a'} \times S_{ea}$. Similar results have been demonstrated for Np(V) (Bertetti et al., 1998); however, limited data and incomplete description of experimental conditions precludes examining these trends for all actinide–mineral systems of interest in HLW disposal. Therefore, an assumption underlying the approaches developed in this study is that other actinides will exhibit similar behavior.

Modeling Sorption Behavior-Surface Complexation Approaches

The pronounced effects of aqueous chemistry on actinide sorption behavior suggest that sorption modeling should account for changing physicochemical conditions. A number of different modeling approaches of varying complexity can be used to incorporate the effects of chemistry on radionuclide sorption. A class of models that has been used with success in modeling pH-dependent sorption for actinides and other metals is the electrostatic surface complexation model (SCM). These models are equilibrium representations of sorption at the mineral–water interface and are discussed in detail elsewhere (Davis & Kent, 1990; Dzombak & Morel, 1990; Hayes et al., 1991; Serne et al., 1990; Turner, 1995), with only a brief overview presented here.

Model Description

Applying SCMs requires assuming analogous behavior between aqueous speciation in the bulk solution away from the mineral-interface and the formation of complexes with functional binding sites at the mineral surface. Surface reactions are postulated and the related mass action and mass balance relations are used to simulate sorption at the mineral surface as a function of system chemistry. SCMs account for the pH dependence of surface charge development at the mineral–water interface through the use of electrostatic terms. Of the different SCMs, the diffuse-layer model (DLM) is perhaps the simplest, using a two-layer representation of the mineral–water interface (Dzombak & Morel, 1990). In contrast to more complex multilayer models, the DLM assumes that supporting electrolytes such as Na^+ and Cl^- do not interact with the surface, and does not specifically address the effects of ionic strength on sorption except through the charge-potential relationship (Davis & Kent, 1990; Dzombak & Morel, 1990).

The sorption of actinides on a variably charged surface sorption site can be represented as a function of pH in a generalized surface reaction demonstrated here with Np(V):

$$> XOH^\circ + pNpO_2^+ + nH_2O$$

$$\Leftrightarrow [> XOH_q - (NpO_2)_p\,(OH)_n]^{p+q-n-1} + (1 + n - q)H^+ \qquad [2]$$

where q is the protonation state of the sorption site ($q = 0$, 1, or 2 for deprotonated, neutral, and protonated, respectively), and p and n are the reaction coefficients for NpO_2^+ and H_2O. NpO_2^+ represents the aqueous Np(V) species and $[>XOH_q - (NpO_2)_p(OH)_n]^{p+q-n-1}$ represents the Np(V) surface complex. In the SCM approach, a coulombic correction is incorporated into the mass action expressions for

surface reactions to extract the intrinsic equilibrium constants. Similar reactions can be written for other actinides such as U and Pu.

In a general sense, the observed dependence of actinide sorption on pH and PCO_2 is a consequence of mass action effects and equilibrium chemistry in the surface reaction represented by Eq. [2]. An increase in the activity of NpO_2^+ drives the equilibrium reaction forward towards increasing sorption. Complexing ligands such as dissolved carbonate in a CO_2 atmosphere tend to form aqueous actinide-carbonate complexes in competition with the sorbing surface. Carbonate competition for the available actinide increases with increasing pH, reducing the aqueous actinide activity and driving the reaction in Eq. [2] to the left (decreasing sorption). This explanation is, of course, simplistic due to the synergistic effects between solution chemistry, sorption site protonation state, and speciation of the aqueous and surface actinide complexes.

Sorption Modeling-Diffuse-Layer Model Parameters

Several computer codes exist with the capability of modeling pH-dependent actinide sorption (PHREEQC, HYDRAQL, MINTEQA2) (Allison et al., 1991; Papelis et al., 1988; Parkhurst & Appelo, 1999). Applying geochemical models to radionuclide sorption requires thermodynamic data for the aqueous speciation of the radionuclide of interest and SCM parameters consistent with these data. The database for the geochemical equilibrium speciation code MINTEQA2, Version 3.11 (Allison et al., 1991) has been modified to include aqueous thermodynamic data for a number of radioelements important to HLW management (Turner et al., 1993). Postulated sorption reactions and DLM parameters (Table 10–1) were derived in previous reports (Pabalan et al., 1998; Turner, 1995; Turner et al., 1993, 1998) by interpreting available actinide sorption data using a simplified uniform DLM approach (Turner, 1995).

For the purposes of this study, five actinide elements are considered: Am(III), Np(V), Pu(V), Th(IV), and U(VI). All five of these radionuclides are an important part of the radionuclide inventory intended for Yucca Mountain (Kerrisk, 1985; Oversby, 1987). With the exception of Pu, all are considered to be strongly dominated by a single oxidation state in the oxidizing groundwaters assumed for Yucca Mountain. Although the redox chemistry of Pu is very complex, U.S. Department of Energy research on radionuclide speciation and solubility indicates that Pu(V) is the dominant oxidation state for Pu in water from wells J-13 and UE-25 p#1 (Nitsche et al., 1993; Triay et al., 1997). Plutonium also may be present in the +4 and +6 oxidation states, but only Pu(V) is considered here.

The DLM has specific limitations that may affect its applicability across a broad range of conditions or mineralogy, and the extent of chemical and physical conditions over which the model can be applied should be considered carefully. The DLM parameters (i.e., binding constant and surface reactions modeled) are based on a limited number of sorption experiments conducted over a limited range of PCO_2, M/V, and actinide concentrations (Pabalan & Turner, 1997; Pabalan et al., 1998; Righetto et al., 1988, 1991; Turner, 1995; Turner et al., 1998). For simplicity, ion exchange reactions were not included in the model and only surface complexation was considered. Also, it is important to note that, although full aqueous

Table 10–1. DLM model parameters used in this study.

Radioelement–Mineral	Surface complex	Binding constant	Reference
Np(V)-montmorillonite	$>AlO^-$	−9.73	Turner et al., 1998
	$>AlOH_2^+$	8.33	Turner et al., 1998
	>SiO–	−7.20	Turner et al., 1998
	$>AlO–NpO_2(OH)^-$	−13.79	Turner et al., 1998
	$>SiOH\text{-}NpO_2^+$	4.05	Turner et al., 1998
U(VI)-montmorillonite	$>AlO^-$	−9.73	Pabalan & Turner, 1997
	$>AlOH_2^+$	8.33	Pabalan & Turner, 1997
	$>SiO^-$	−7.20	Pabalan & Turner, 1997
	$>AlO\text{-}UO_2^+$	2.70	Pabalan & Turner, 1997
	$>SiO\text{-}UO_2^+$	2.60	Pabalan & Turner, 1997
	$>AlO\text{-}(UO_2)_3(OH)_5^0$	−14.95	Pabalan & Turner, 1997
	$>SiO\text{-}(UO_2)_3(OH)_5^0$	−15.29	Pabalan & Turner, 1997
Am(III)-γ alumina	$>AlO^-$	−9.73	Turner & Sassman, 1996
	$>AlOH_2^+$	8.33	Turner & Sassman, 1996
	$>AlO\text{-}Am^{2+}$	4.66	This study [modified Turner, 1995]
Pu(V)-γ alumina	$>AlO^-$	−9.73	Turner & Sassman, 1996
	$>AlOH_2^+$	8.33	Turner & Sassman, 1996
	$>AlO\text{-}PuO_2^0$	−2.18	This study [modified Turner, 1995]
Th(IV)-γ alumina	$>AlO^-$	−9.73	Turner & Sassman, 1996
	$>AlOH_2^+$	8.33	Turner & Sassman, 1996
	$>AlO\text{-}Th^{3+}$	15.3	This study [modified Turner, 1995]

speciation is incorporated in the model, the only surface reactions considered are protonation–deprotonation of surface sites and actinide sorption reactions. Direct competition for available surface sites with other radioelements or major and minor groundwater constituents is neglected. Calculated changes in sorption behavior are therefore limited to those resulting from changes in aqueous speciation of the radionuclide due to complexing with ligands in the groundwater. This may have an impact on how the effects of carbonate on sorption are considered in the model. If aqueous carbonate complexation of a given actinide is either considered to be small or neglected in the thermodynamic database, then carbonate will have only a small or negligible effect on sorption behavior. For example, the database adopted from the U.S. Department of Energy (GEMBOCHS.V2-EQ8-DATA0.COM.R2) does not include Th-carbonate complexes. The effects of carbonate complexation on the modeling results for Th sorption behavior are therefore negligible.

PRELIMINARY APPROACHES FOR ADDRESSING CHEMICAL EFFECTS IN PERFORMANCE ASSESSMENT TRANSPORT/SORPTION MODELS

Computational requirements limit direct incorporation of geochemical sorption models into current PA codes, and it is likely that the use of PDFs for K_ds will continue in the next generation of PA codes. One approach to incorporating detailed model results in PA is to use them off-line to provide constraints on parameter uncertainty and account for site-specific geochemical variability. Two approaches are

described in this report and demonstrated using DLM sorption modeling with hydrochemical information specific to Yucca Mountain.

Estimating Sorption Parameter Probability Distribution Functions

One approach to accounting for geochemical effects on sorption behavior in PA is to develop the uncertainties represented by the K_d PDFs using process models to simulate sorption under observed variability in hydrochemistry in the vicinity of Yucca Mountain. A detailed description of the method as applied to Np(V) and U(VI) sorption is provided in Turner and Pabalan (1999). The approach has been extended to include Am(III), Th(IV), and Pu(V) DLM results. This approach offers the immediate advantage of being compatible with the approaches to K_d uncertainty that are used in the current generation of PA codes (Civilian Radioactive Waste Management System, Management, and Operating Contractor, 1998; U.S. Nuclear Regulatory Commission, 1999b,c). A summary is provided here.

Gathering Hydrochemical Data

Evaluating the effects of geochemistry on sorption at Yucca Mountain requires an understanding of the expected variability in key geochemical parameters. A convenient and comprehensive source of regional hydrochemistry data in the Yucca Mountain vicinity is the U.S. Geological Survey (USGS) report of Perfect et al. (1995) that compiles >4700 analyses from USGS reports and U.S. Department of Energy reports and the USGS National Water Information Service database. Perfect et al. (1995) describes an editing philosophy to evaluate the raw data, remove duplicates, make chemical data entries consistent, and calculate charge balance. The editing philosophy is described in detail in the report.

It is assumed that the ranges of values of the chemical parameters reported in Perfect et al. (1995) represent the total variation that can be expected along potential flow paths in the Yucca Mountain hydrologic system during the 10 000 yr postclosure period. The extent of the effects of the thermal loading of the repository is a design issue that is still under consideration by the U.S. Department of Energy(Civilian Radioactive Waste Management System, Management, and Operating Contractor, 2000b, 2001), and potential changes to the chemistry of the Yucca Mountain region due to the heat generated by the HLW are neglected. Because of limitations in the source data, it is likely that the water chemistries reported for wells are from a mixture of several producing zones. Perfect (1994) used cluster analysis to identify nine separate water chemistries related to lithology, but the sorption modeling approach described here was applied to the total range in hydrochemistry represented by all of the samples. Detailed sorption modeling using these data is therefore assumed to represent the total range in a parameter such as K_d (or $K_{a'}$) due to geochemical effects.

To prepare the site-specific hydrochemistry for geochemical sorption modeling, Turner and Pabalan (1999) screened the data of Perfect et al. (1995) using geochemical criteria presented in Hitchon and Brulotte (1994). Uncertainties in sampling and measurement of key geochemical parameters such as pH suggested the need for additional examination of the data. For example, Hem (1985) noted that

field pH measurements prior to the early 1950s are uncertain due to equipment or methodology. Turner and Pabalan (1999) therefore included an additional screening criterion limiting the dataset to post-1960 analyses on the assumption that more recent analyses are more traceable and reliable than older analyses. The final screening step was to limit the area covered to the vicinity of Yucca Mountain (Turner & Pabalan, 1999). The area (100 × 100 km) is much larger than the flow model used in typical PA calculations for Yucca Mountain (Civilian Radioactive Waste Management System, Management, and Operating Contractor, 2000a; U.S. Nuclear Regulatory Commission 1999b,c), but it includes the most plausible flow paths to the location of likely receptor(s) 10 to 30 km downgradient from Yucca Mountain (Winograd & Thordarson, 1975) and to natural discharge and paleodischarge points to the southeast (Waddell, 1982; Paces et al., 1993). The final dataset contains 460 water analyses collected from 238 separate locations (Turner & Pabalan, 1999). In addition to spatial variability, the dataset also offers the opportunity to examine changes in hydrochemistry (and potentially radionuclide sorption) over a time period of several decades.

The database of water chemistries can be used to identify ranges and distribution types for key geochemical parameters in the ambient hydrochemical system at Yucca Mountain. For example, in the dataset, pH varied from 6.3 to 9.6 showing a normal distribution (or a log normal distribution with respect to H activity). Inorganic carbon (C_T) showed a large range from 6.8 to >10 000 mg × L^{-1} (Turner & Pabalan, 1999). Although the bulk of the data show C_T < 1000 mg × L^{-1}, however, the C_T data are skewed by a small number (10 out of 460) evaporative brines collected from playas >50 km SW of Yucca Mountain that show extremes in C_T. Although these high C_T concentration samples meet the screening criteria of Hitchon and Brulotte (1994), they are not likely to be representative of deep regional groundwaters or fracture waters. Without significant treatment, the brines also are unusable as a potable water source, and would not likely contribute to receptor doses. Omitting these samples would result in a smaller range in C_T, but because they meet the screening criteria, they were retained in the modeling exercise to evaluate the effects of observed extremes in C_T on potential radionuclide sorption.

Because of a lack of vertical control on sampling intervals, local horizons of different chemistries may not be distinguishable. There also is a general lack of information on the redox condition of the water (e.g., Eh, dissolved O_2, pe, Fe^{3+}/Fe^{2+}), leaving a potentially critical parameter unconstrained. This uncertainty may be especially important for redox sensitive elements such as the actinides. The approach used by both U.S. Department of Energy and NRC in PA at Yucca Mountain assumes oxidizing conditions along the entire flow path (Civilian Radioactive Waste Management System, Management, and Operating Contractor, 2000a; U.S. Nuclear Regulatory Commission, 1999b,c). This is considered to be conservative with regard to performance because most of the radionuclides (e.g., Np, U) are much more soluble and thought to be weaker sorbers under oxidizing conditions.

Using Yucca Mountain Hydrochemical Data in Sorption Modeling

For each of the 460 separate analyses, values of pH and the concentrations of the major species Ca^{2+}, Mg^{2+}, Na^{+}, K^{+}, HCO_3^-, CO_3^{2-}, SO_4^{2-}, Cl^-, F^-, Fe, and

Table 10–2. Descriptive statistics for calculated sorption coefficient PDFs (expressed as log $K_{a'}$ in mL × m^{-2}) using the DLM approach outlined in the text.

log $K_{a'}$ (mL × m^{-2})	Am(III)	Np(V)	Pu(V)	Th(IV)	U(VI)
Mean	6.549	0.742	2.707	4.248	–0.032
Median	6.539	0.773	2.715	4.330	0.002
Mode	6.337	0.738	2.650	4.439	–0.158
Standard deviation	0.748	0.422	0.305	0.583	0.975
Kurtosis	1.924	26.576	5.055	34.228	12.928
Skewness	0.118	–3.556	–0.148	–4.414	–2.318
Range	5.958	5.140	2.974	7.715	9.407
Minimum	3.160	–3.264	0.906	–1.780	–6.837
Maximum	9.119	1.876	3.881	5.935	2.570
Count	460	460	460	460	460

SiO_2(aq) were written to an input file formatted for use with MINTEQA2, Version 3.11 (Allison et al., 1991). Temperature and pH were fixed at the measured values, Eh was unspecified due to a lack of measured data in the dataset, and measured Fe was assumed to be entirely Fe^{3+} (oxidizing conditions). Surface sorption reactions for the actinide–H_2O–CO_2–mineral system using the parameters listed in Table 10–1 were added to the major element hydrochemistry in the MINTEQA2 input file. As noted previously, only a single oxidation state was modeled for each radionuclide because of a lack of redox information. Also, the model was further simplified by neglecting the potential effects of competitive sorption by groundwater cations such as Ca^{2+}, Mg^{2+}.

The MINTEQA2 output was used to establish mean, minimum, and maximum values for sorption and related transport parameter PDFs for PA input (Table 10–2). In the model results, a lognormal distribution seems to describe the calculated variability (Fig. 10–8). Mean and median log values are similar for each radioelement considered here (Table 10–2), suggesting that although there is some skewing of the distribution, the central tendency is not overly affected by extreme water chemistry values. In addition to constraining PDFs for a given radioelement, this approach provides a means of developing a multivariate correlation among sorption parameter PDFs that reflects the underlying effects of geochemistry on sorption (Table 10–3). For example, calculating a distribution for Np(V) and U(VI) sorption coefficient can provide a bivariate correlation between Np(V) and U(VI) sorption behavior that results from the effects of site-specific chemical variability. The correlation coefficient for Log K_d calculated for Np(V) and U(VI) is about 0.6, indicating a positive correlation in sorption behavior for these two actinides due to geochemical effects alone (Fig. 10– 9). The correlation is weak ($r^2 = 0.37$), however, due to the different speciation behavior of these two actinides, and also is probably influenced by a few outlier points.

Correlation coefficients calculated in a similar manner for multiple pairings of radioelements can be included as input into the PA sampling routine, allowing the value selected for one radioelement sorption parameter to be conditioned by its geochemical relationship to the other radioelements. Theoretically, for a given water composition, sorption coefficients of two or more radioelements should be determinate based on the geochemical controls on their sorption behavior. In this sense, the sorption coefficients are deterministically correlated. These types of cor-

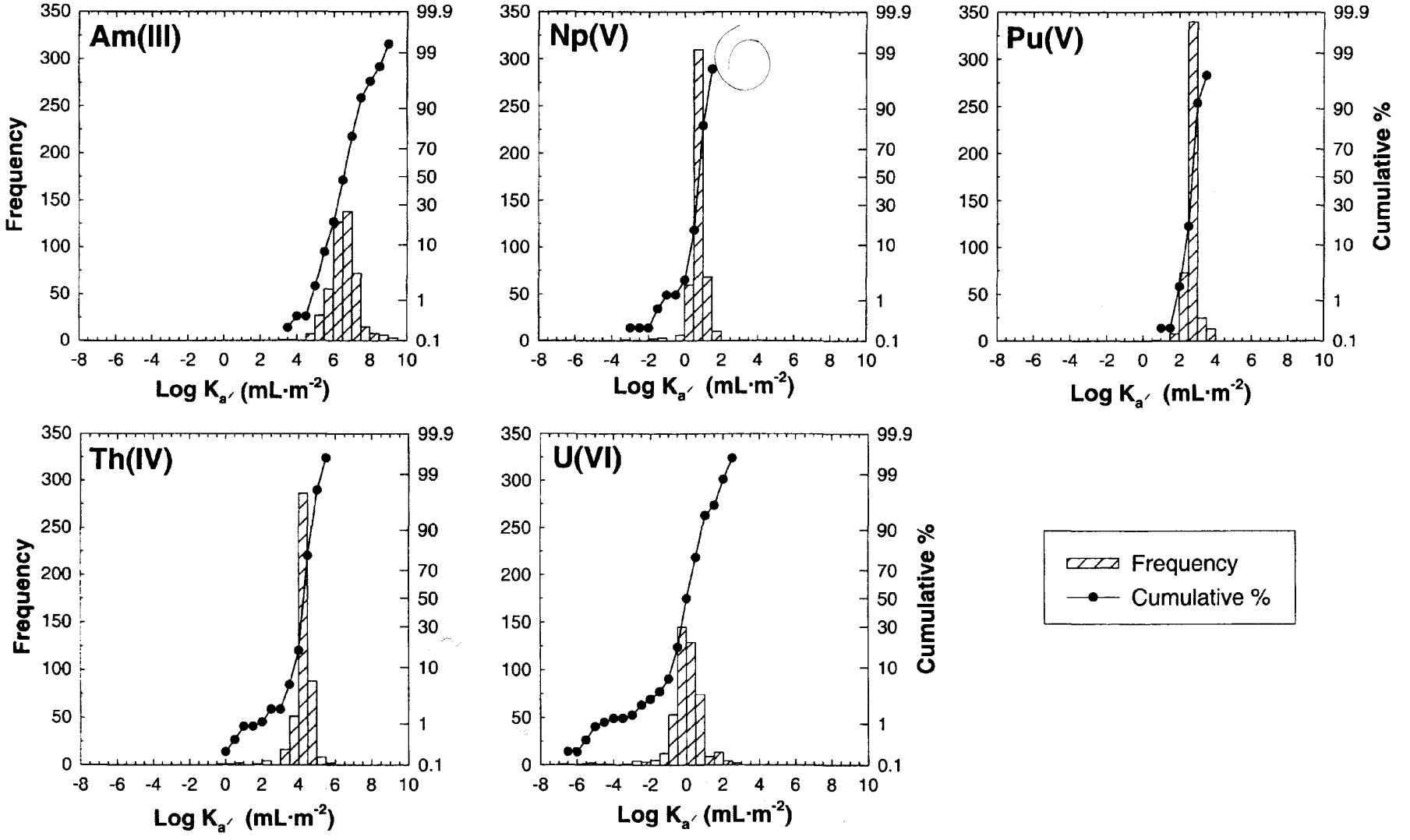

Fig. 10–8. Calculated sorption parameter PDFs. DLM parameters are from Table 10–1 with hydrochemical data from Perfect et al. (1995). See text for detailed discussion.

Table 10–3. Correlation coefficients among log $K_{a'}$ (mL × m^{-2}) values calculated using DLM parameters in Table 10–1 and hydrochemistry data from Perfect et al. (1995).

log $K_{a'}$ (mL × m^{-2})	Am(III)	Np(V)	Pu(V)	Th(IV)	U(VI)
Am(III)	1				
Np(V)	0.837	1			
Pu(V)	0.964	0.881	1		
Th(IV)	0.112	0.260	0.109	1	
U(VI)	0.346	0.610	0.489	0.165	1

relations, however, offer an effective way to indirectly represent the effects of geochemistry in the structure of current PA approaches (U.S. Nuclear Regulatory Commission, 1999b; Civilian Radioactive Waste Management System, Management and Operating Contractor, 2000a).

The spatial variability in hydrochemistry in the vicinity of Yucca Mountain is reflected in the large range in calculated sorption parameters (Table 10–2). One means of showing the variability in geochemical and sorption parameters is through the use of contour plots. Turner et al. (1999) created a geographic information system (GIS) coverage to show the spatial variation in potential radionuclide sorption that may have an effect on PA calculations (Fig. 10–10). Calculated K_d for Np(V) is in the range of 25 to 100 mL × g^{-1} for most of the region downgradient from Yucca Mountain. In general, trends in potential sorption parallel trends in pH and PCO_2 along the axis of Amargosa Valley. Contour plots of a derived parameter such as K_d should be used carefully given the large number of groundwater properties that

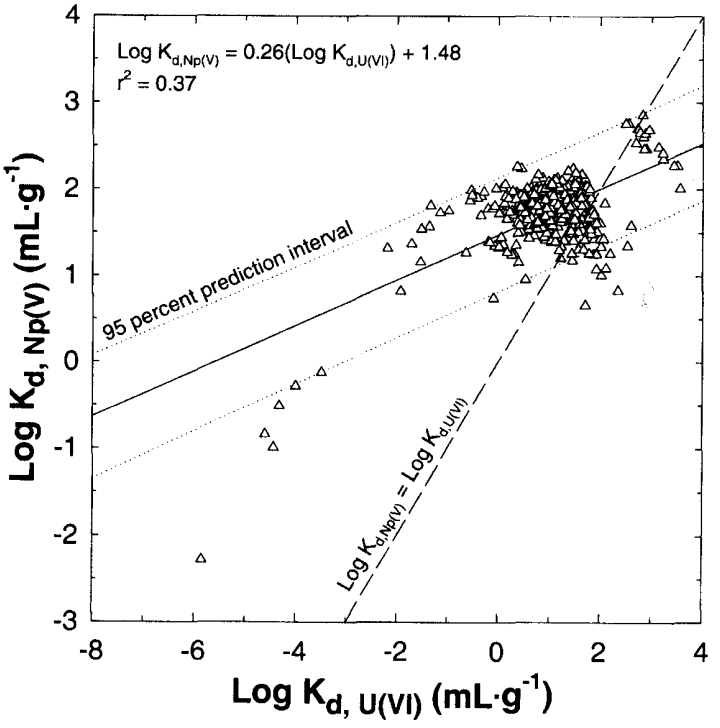

Fig. 10–9. Corresponding Np(V)- and U(VI)-montmorillonite sorption coefficients (K_d in mL × g^{-1}) calculated with MINTEQA2 using DLM parameters given in Table 10–1. Solid line shows linear regression to the data with 95% prediction limits (dotted lines). Dashed line shows Log $K_{d,U(VI)}$ = Log $K_{d,Np(V)}$ for reference. Water chemistry based on 460 analyses developed from the data of Perfect et al. (1995).

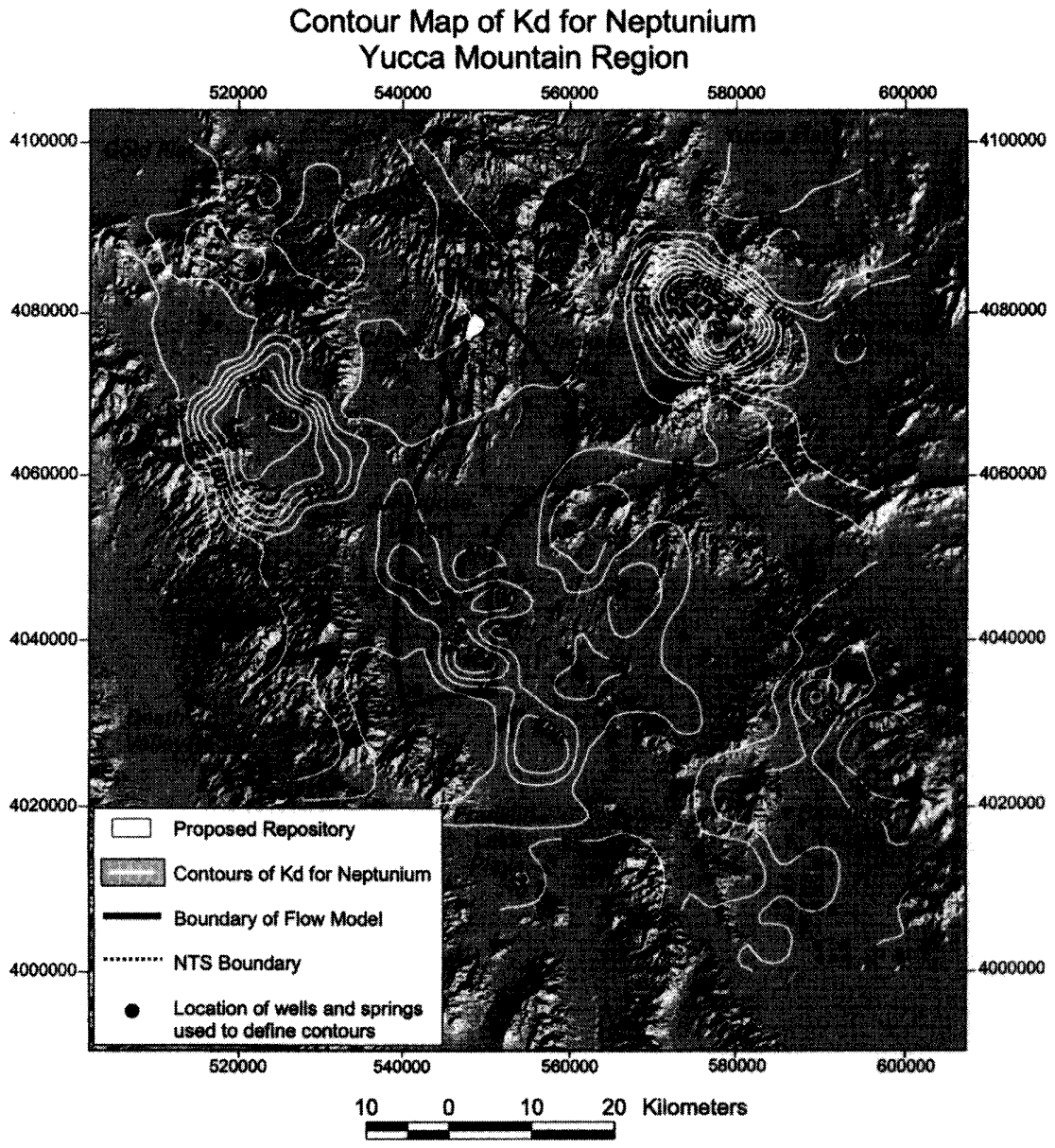

Fig. 10–10. Contour map of Np(V)-montmorillonite K_d (mL × g^{-1}) calculated using the DLM with parameters from Table 10–1 and hydrochemistry from Perfect et al. (1995). Contour interval is 25 mL × g^{-1}. Heavy outline shows the flow model from Yucca Mountain (white) used in NRC TPA calculations (U.S. Nuclear Regulatory Commission, 1999b,c).

may potentially affect the model calculations. In this particular example, the field K_d values were determined assuming that aluminosilicates will dominate sorption, and using a constant effective surface area (S_{ea}) to transform K_a, calculated using a SCM calibrated to experimental data to K_d.

Although it seems straightforward, estimating S_{ea} at the field scale is difficult. One approach is to establish relationships between S_{ea} and field hydrostratigraphic properties such as permeability and porosity. Arthur (1996) proposed a relationship among porosity, dry density, and pore radius to determine S_{ea}. Smith and Schafer (1999) also proposed a method relating porosity, permeability, and tortuosity. For the purposes of the analysis presented here, the approach of Arthur (1996) was used with constant parameter values taken from the input file for TPA

3.1 (U.S. Nuclear Regulatory Commission, 1999b). The calculated surface areas ranged from 2.7 to 8.8 $m^2 \times g^{-1}$ agreed well with measured surface areas (2.6 to 10 $m^2 \times g^{-1}$) reported for total surface areas of tuff samples in Triay et al. (1997).

Assuming a constant value for S_{ea} is perhaps not inherently satisfying given arguments such as those presented by Smith and Shafer (1999) for anisotropic behavior of this property. Because of flow dynamics and complex mineralogies, S_{ea} is one of the more difficult uncertainties to address at the field scale. It may be possible to treat S_{ea} as an uncertain parameter to be sampled during the PA analysis. This would lead to the problem of creating the necessary PDFs for S_{ea}, but it might be possible to use the relationships of Arthur (1996) or Smith and Shafer (1999) to create a PDF that is internally consistent with the rest of the transport abstraction in the PA code. The contour map also shows that even with 238 separate sample locations, sampling density is concentrated in a few areas, and generally sparse over much of the region of interest. One way to address the sparse sample distribution is through the use of geostatistical techniques to show potential correlation lengths and directional anisotropy resulting from geochemical variability (Painter et al., 2001).

Performance Assessment Results and Sensitivity Analyses

The transport parameter PDFs and correlation coefficients developed using this approach were provided as input to the NRC TPA 3.1 code (U.S. Nuclear Regulatory Commission 1999b,c). Due to computational requirements, these correlations were only implemented for the Saturated Zone Alluvium unit (SAV) in the TPA input file. K_d values were converted to retardation factors (R_d) using the relationship:

$$R_d = 1 + (\rho_b K_d/\theta) \quad [3]$$

where ρ_b is bulk density (g cm^{-3}) and θ is porosity (unitless). In calculating the R_d, ρ_b, and θ are held constant at values used for alluvium in the TPA code. Only the sorption coefficient is treated as an uncertain parameter, so the variability of the retardation factor should reflect the variability in K_d. Sensitivity analyses are used to determine (i) whether the correlation coefficients were correctly implemented in TPA 3.1 sampling of the PDFs; (ii) the effects of correlated K_ds (or R_d) on dose as compared with the noncorrelated K_ds of previous versions of the TPA code.

For the sensitivity analyses, total effective dose equivalent (TEDE) was calculated for individual radionuclides at 50 000 yr for a receptor group 20 km downgradient from the proposed repository. A total of 250 realizations were used to represent the range in TEDE resulting from parameter uncertainty.

Five transport parameters for the saturated alluvium were treated as variable, including R_d values for Am, Np, Pu, Th, and U. The PDFs for these R_d values were unchanged from the TPA 3.1 base case dataset, and runs were made either with or without correlation coefficients. All other parameters were held at the base case values. An initial check of the K_d parameters sampled in the 250 realizations indicate that the TPA code is correctly including the correlation coefficients (Fig. 10–11).

Preliminary sensitivity analyses results suggest that incorporation of correlation among K_ds does have an effect on predicted TEDE for these five radioele-

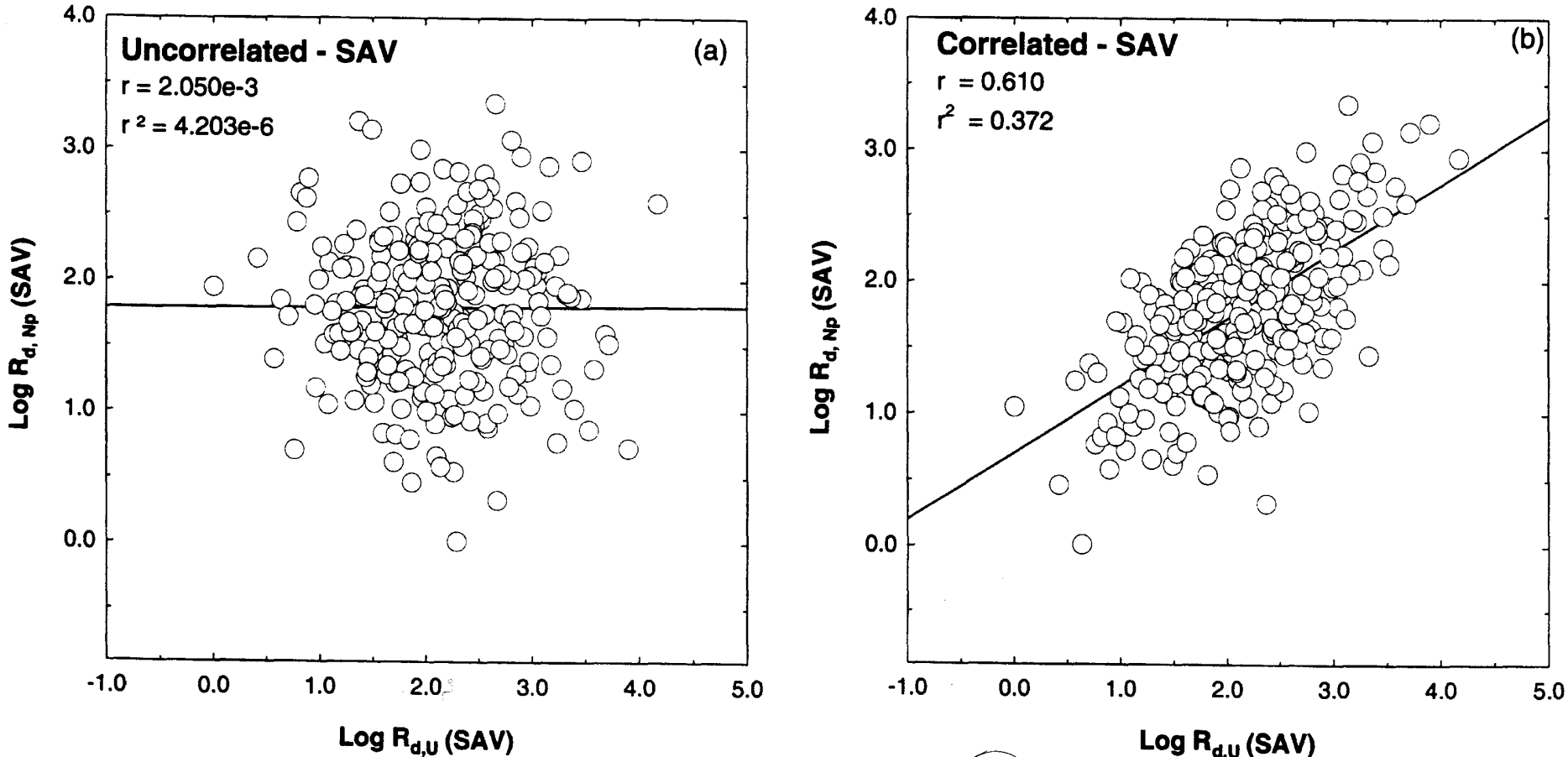

Fig. 10–11. Checking TPA 3.1 (U.S. Nuclear Regulatory Commission, 1999b,c) sampled radionuclide transport parameters for U and Np (250 realizations). (a) Sampling from uncorrelated transport parameters ($r^2 = 4.2 \times 10^{-6}$). (b) Sampling from correlated transport parameters [$r^2 = 0.372$ as compared with 0.37 calculated using DLM and the hydrochemical data of Perfect et al. (1995)].

ments relative to doses calculated assuming uncorrelated K_ds (Fig. 10–12). As expected, the radionuclides most affected include those with correlations: ^{238}U, ^{237}Np, ^{230}Th, ^{241}Am. Other radionuclides (e.g., ^{226}Ra and ^{210}Pb) present in TPA 3.1 in the decay chain from $^{234}U \rightarrow {}^{230}Th \rightarrow {}^{226}Ra \rightarrow {}^{210}Pb$ also exhibit similar correlation effects on TEDE (Fig. 10–12). The effect, however, does not appear to be systematic. For 250 realizations, calculated peak dose for all radionuclides assuming correlation among K_ds for can be either higher or lower than the uncorrelated case. Although individual realizations for a given radionuclide may be quite different, the predicted peak mean dose (all radionuclides) is essentially unchanged at 10 000 yr (about 5% higher for the correlated case). The small effect is due in large part to the relatively robust waste packages predicted in the TPA 3.1 base case (U.S. Nuclear Regulatory Commission, 1999b,c), and the dominant contribution to dose of the high solubility, nonsorbing radionuclides ^{99}Tc and ^{129}I. Also, correlations are limited to a subset of the radionuclides tracked in TPA, and have only been considered for transport through the saturated alluvium. The expected dose curves for the correlated and uncorrelated case begin to diverge at longer times, after more waste packages have begun to fail and the contaminant plume reaches the saturated zone. The preliminary results suggest an additional level of uncertainty that should be considered in PA as correlations are developed for other radionuclides and implemented along the entire flow and transport pathway.

The U.S. Department of Energy has recently entered into a series of agreements with the NRC to provide the technical basis for its sorption coefficients (U.S. Nuclear Regulatory Commission, 2001). Detailed sorption modeling and correlation among K_d PDFs may provide useful insights for evaluating the justification for using chemical analogues in PA to supplement limited sorption data for some radionuclides. To limit the potential for pairing chemically unreasonable sorption coefficients between different radioelements during parameter sampling, the correlation of sorption coefficients should be examined and included, as appropriate, as part of the technical basis for transport parameter PDFs.

Sorption Response Surfaces

While using the DLM to constrain transport parameters PDFs is an approach that is quickly adapted to current PA approaches, it does not reduce the number of sampled parameters. Also, correlating among the different PDFs to reflect underlying geochemical effects on sorption is not efficient and brings a high computational burden to the PA calculations. Moreover, although the PDF method represents the variability of geochemical conditions, it does not represent the variation in a spatial sense. Site-specific values for geochemical and mineralogical properties could be used to better represent conditions along an expected flow path even if explicit geochemical coupling is not available in PA. This type of approach, not yet implemented in PA, would use the DLM to generate a response surface that represented sorption as a function of several key parameters (e.g., pH and PCO_2) (Fig. 10–13). With this method, measured site-specific values could be used in a more direct fashion. These parameters and their field-measured PDFs could be assigned to appropriate locations and stratigraphic horizons included in the PA model and sampled to determine the appropriate K_d values, based on SCM calculations, for

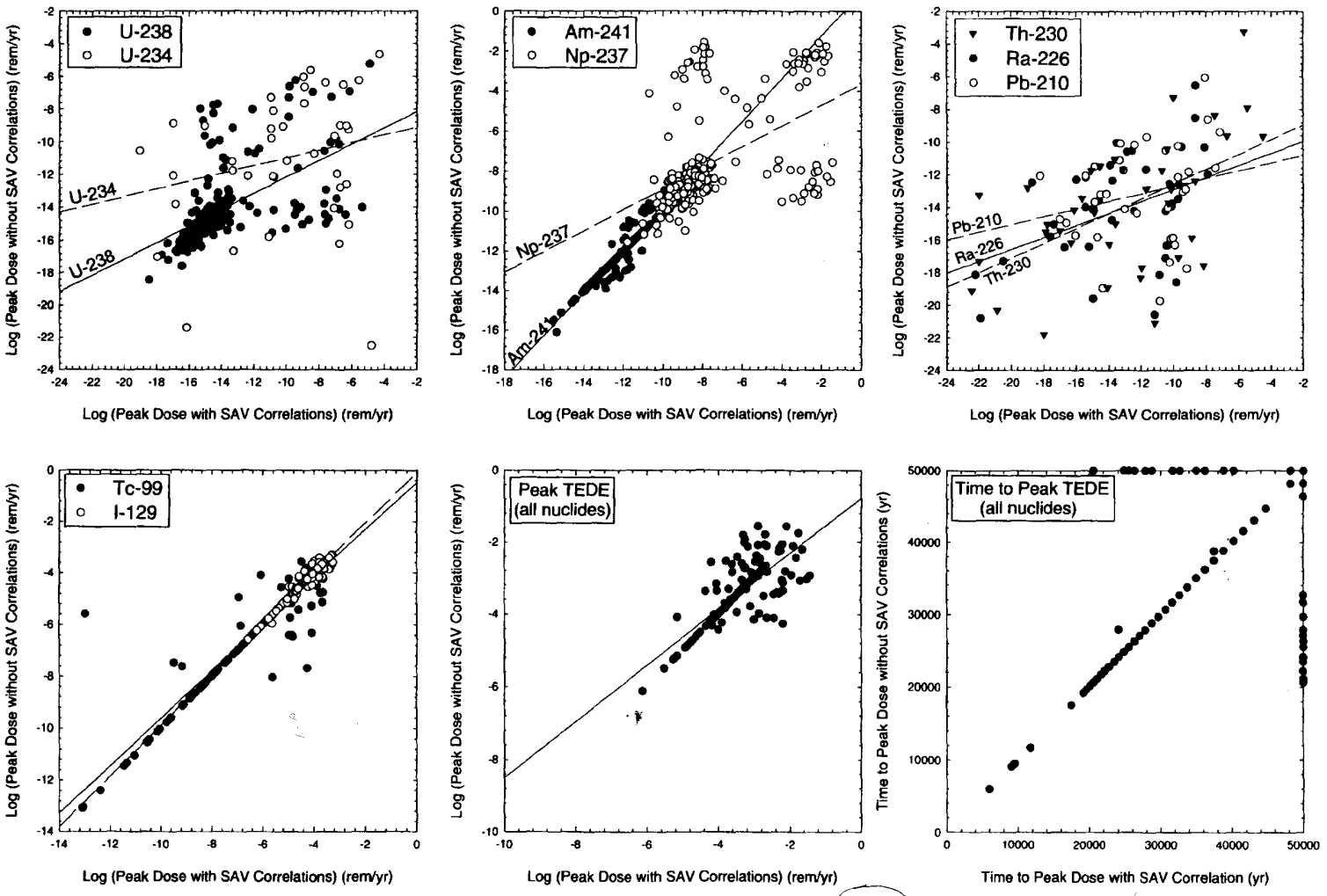

Fig. 10–12. TPA 3.1 calculated peak dose (rem × yr^{-1}) for specific radionuclides to receptor group at 20 km. Comparison of results using uncorrelated and correlated alluvium sorption parameters for Am(III), Np(V), Pu(V), Th(IV), and U(VI). Lines represent regression to data for each nuclide, as indicated. Correlation coefficients listed in Table 10–3. All other parameters set at baseline values and PDFs (U.S. Nuclear Regulatory Commission, 1999b,c).

the transport paths within each realization. While this is still not an explicit incorporation of geochemistry in the transport calculations, it does provide a step toward a more sound theoretical basis for sorption modeling in PA. It also has the benefit of reducing the number of sampled parameters for each PA run.

Demonstrating the Response Surface for Np(V)

Since Np(V) sorption is known to be sensitive to a variety of system physicochemical conditions, several model simulations were conducted to assess the sensitivity of the model to system variables. DLM simulations were conducted using parameters in Table 10–1 across a range of pH, PCO_2, M/V, and Np(V) concentration. The range in simulated conditions are summarized in Table 10–4. In general, for each model simulation, PCO_2 was held constant while pH was varied throughout a range from 2 to 11.75.

Following the simulations, the DLM-generated data were analyzed to identify important variables and evaluate significant trends and consistencies. Surface plots of results were generated. An effort was then made to evaluate the best approach to reproducing the sorption coefficient or response surface.

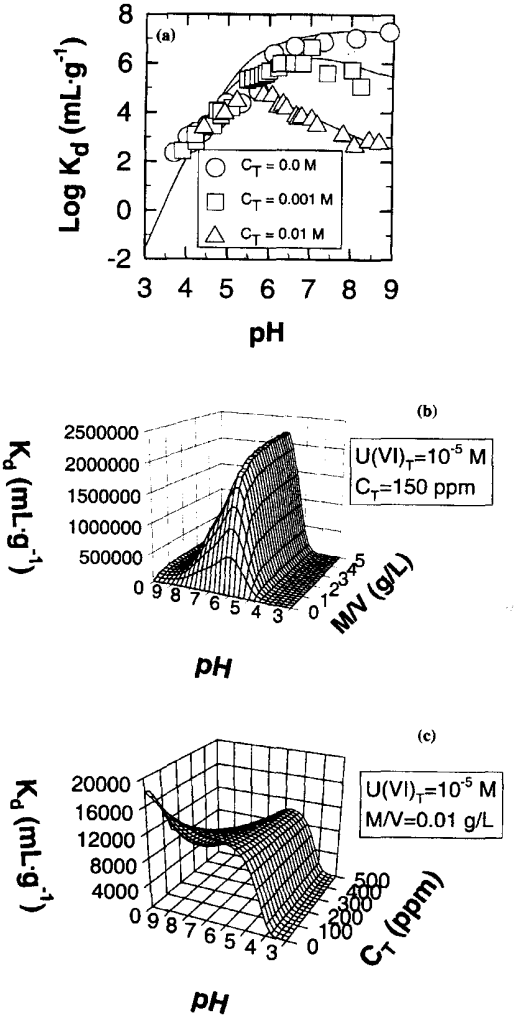

Fig. 10–13. Schematic diagram showing steps to developing a response surface for radionuclide sorption. (a) Model calibration against experimental data; (b) Sorption variability as a function of pH and M/V; (c) Sorption variability as a function of pH and C_T.

Table 10–4. Summary of conditions modeled using the DLM approach described in the text.

Run	pH range	PCO_2 (atm)	$Np(V)_{total}$	M/V ($g \times L^{-1}$)
1	2 to 11.75 in 0.25 increments	no CO_2, 10^{-7} through 10^{-2} atm in $10^{0.5}$ atm increments	8.9×10^{-7} M	4
2	2 to 11.75 in 0.25 increments	no CO_2, 10^{-7} through 10^{-2} atm in $10^{0.5}$ atm increments	2.0×10^{-11} M	4
3	2 to 11.75 in 0.25 increments	no CO_2, 10^{-7} atm, $10^{-3.5}$ atm	8.9×10^{-7} M	40
4	2 to 11.75 in 0.25 increments	no CO_2, 10^{-7} atm, $10^{-3.5}$ atm	8.9×10^{-7} M	400
5	2 to 11.75 in 0.25 increments	no CO_2, 10^{-7} atm, $10^{-3.5}$ atm	8.9×10^{-7} M	2000
6	2 to 11.75 in 0.25 increments	no CO_2, 10^{-7} atm, $10^{-3.5}$ atm	1.0×10^{-14} M	4
7	2 to 11.75 in 0.25 increments	no CO_2, 10^{-7} atm, $10^{-3.5}$ atm	1.0×10^{-18} M	4

Sensitivity Analyses using Response Surfaces

Sensitivity of the Model to Variation in pH. Previous experimental results demonstrate that Np(V) sorption is sensitive to solution pH, and that Np(V) sorption follows a trend similar to the hydrolysis of the NpO_2^+ species in solution (Bertetti et al., 1996, 1998; Turner et al., 1998). The DLM reproduces the expected (Bertetti et al., 1998) pH dependency well (Fig. 10–14). This behavior is consistent with that of other actinides (Allard et al., 1984; Hsi & Langmuir, 1985; McKinley et al., 1995; Turner et al., 1998).

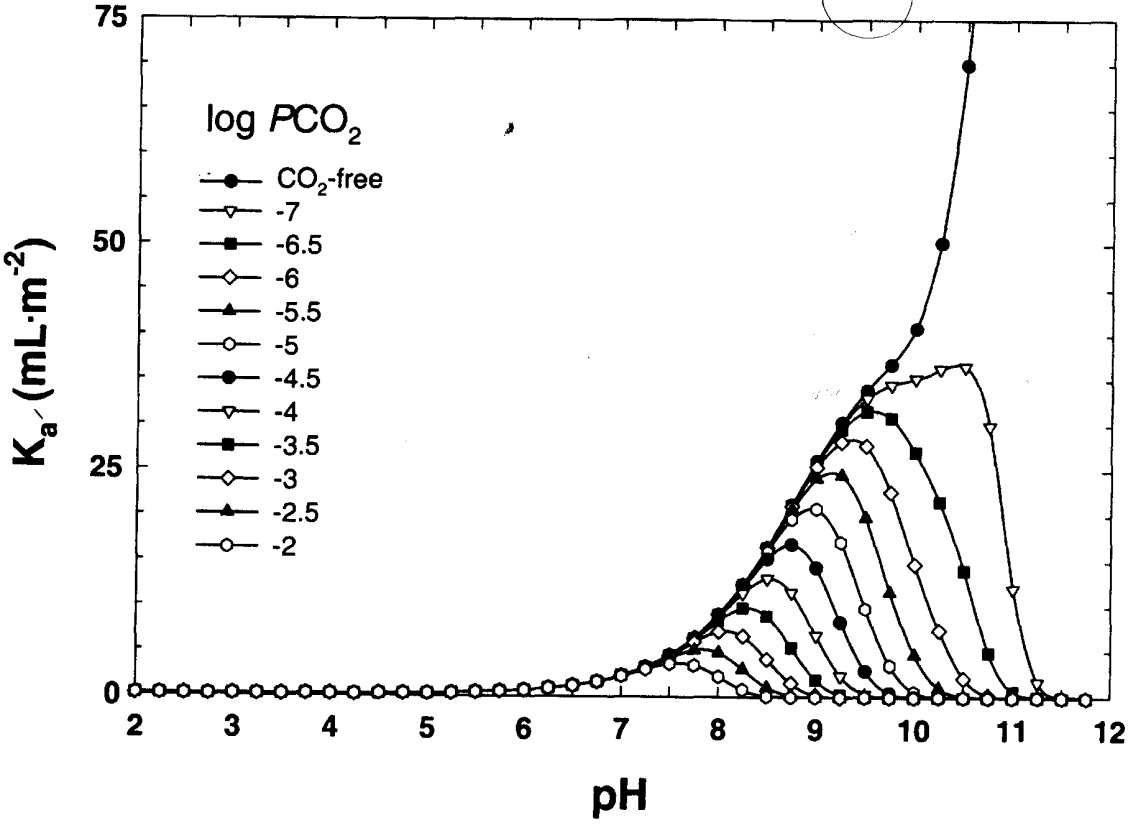

Fig. 10–14. DLM results of Np(V) sorption plotted over a range of PCO_2 and pH. $Np(V)_{total} = 1 \times 10^{-6}$ M, $M/V = 4$ g × L^{-1}. DLM parameters are from Table 10–1.

Sensitivity of the Model to Variations in PCO_2. Because they are linked through the aqueous carbonate system, the PCO_2 in the model system also has a significant effect on the pH range and magnitude of Np(V) sorption (Fig. 10–14). As PCO_2 increases, the pH at which Np(V) sorption reaches a maximum occurs at progressively lower pH values and the range of pH across which sorption is observed diminishes. The results are consistent with previous experimental results (Bertetti et al., 1998; Turner et al., 1998), but it is important to note that the model slightly underpredicts the magnitude of sorption at high pH values when CO_2 is present. This may be due to a lack of consideration of the sorption of Np-carbonate complexes or an overestimate of the presence of Np-carbonate complexes in solution. (Turner et al., 1998). For completeness, the pH and PCO_2 shown in Fig. 10–14 covers a range that is likely to be much broader than that expected in the vicinity of Yucca Mountain. Current ambient limits can be established using a database such as Perfect et al. (1995). Subsequent changes, such as those that might be expected during the thermal phase of the repository (Civilian Radioactive Waste Management System, Management, and Operating Contractor, 2001) could be established in other parts of the PA abstraction and extended to the transport analysis.

Sensitivity of the Model to Variation in *M/V*. As expected, the model is not particularly sensitive to variations in *M/V* (Fig. 10–15). This occurs primarily because representation of results in terms of K_d, and subsequently $K_{a'}$, normalizes the data for differences in *M/V*. At very high *M/V* ratios, the high calculated surface areas effectively limit sorption as represented by $K_{a'}$. Additionally, for the low radionuclide concentrations expected, there is always an excess of available sorption sites,

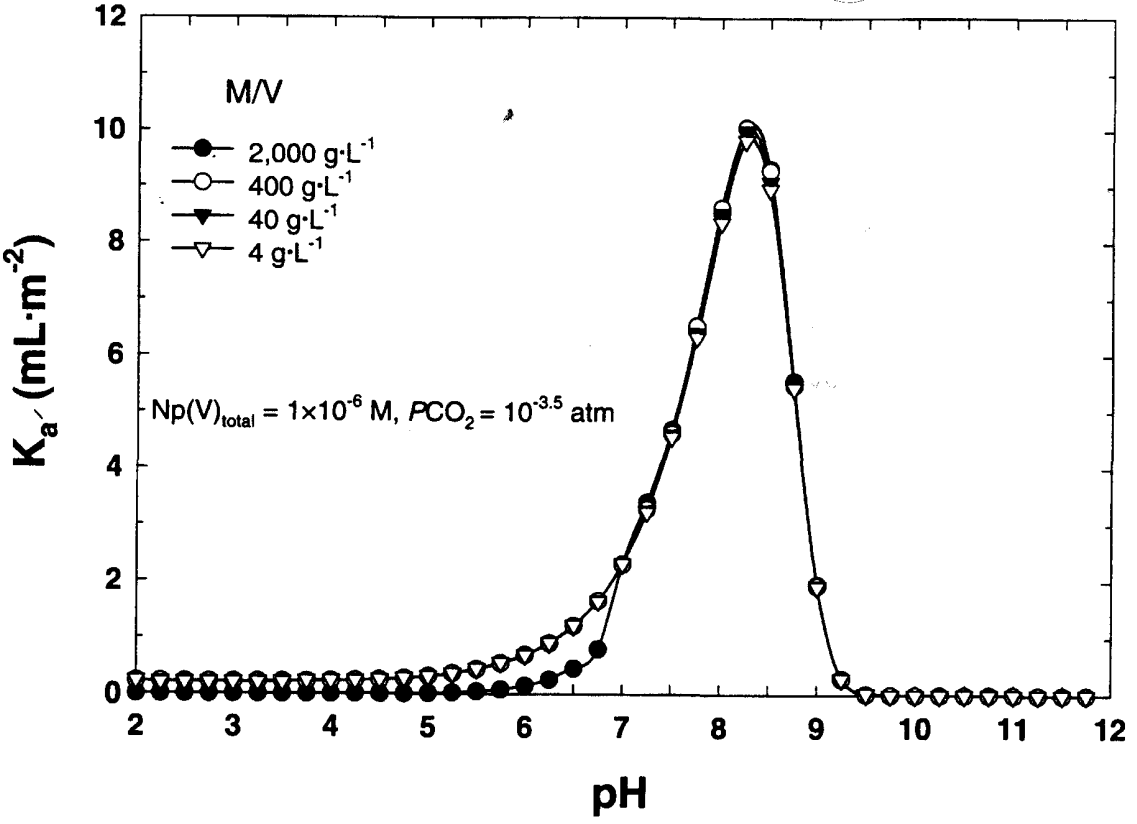

Fig. 10–15. DLM results for Np(V) sorption at various *M/V* values under atmospheric CO_2 (PCO_2 = $10^{-3.5}$ atm) $Np(V)_{total} = 1 \times 10^{-6}$ *M*. DLM parameters are from Table 10–1.

even at low *M/V* ratios. It is important to note, however, that the simplified modeling approach presented here does not include competitive sorption by groundwater constituents such as Ca^{2+} or Mg^{2+} that might be present at much higher concentrations.

Sensitivity of the Model to Variation in Np(V) Concentration. The model results are not sensitive to variances in the Np(V) concentration, even across large range of concentrations examined (Fig. 10–16). These results agree with experimentally derived results of Np(V) sorption (e.g., Girvin et al., 1991; Righetto et al., 1991; Bertetti et al., 1998).

These DLM sensitivity analyses suggest that actinide sorption is most sensitive to changes in pH and PCO_2. Therefore, pH and PCO_2 would be the most useful parameters to use in construction of a representative response surface for Np(V) sorption. Fig. 10–17 is a three-dimensional response surface depicting the variation in $K_{a'}$ across a range of pH and PCO_2 (*M/V* and Np(V) concentration are held constant). The response surface represents values of $K_{a'}$ which are based on detailed DLM calculations, that can be quickly derived for PA using available site-specific geochemical parameters (i.e., pH and PCO_2). Because pH and PCO_2 are linked through the carbonate aqueous chemistry, selection of one parameter provides constraints on the value of the other. Implementing the response surface approach for PA should be designed such that sampling pH and PCO_2 preserves the carbonate chemistry linkage in determining the piercing point on the $K_{a'}$ surface.

This approach carries a number of simplifying assumptions embedded in the detailed sorption model. Notwithstanding the limitations of the model, the approach

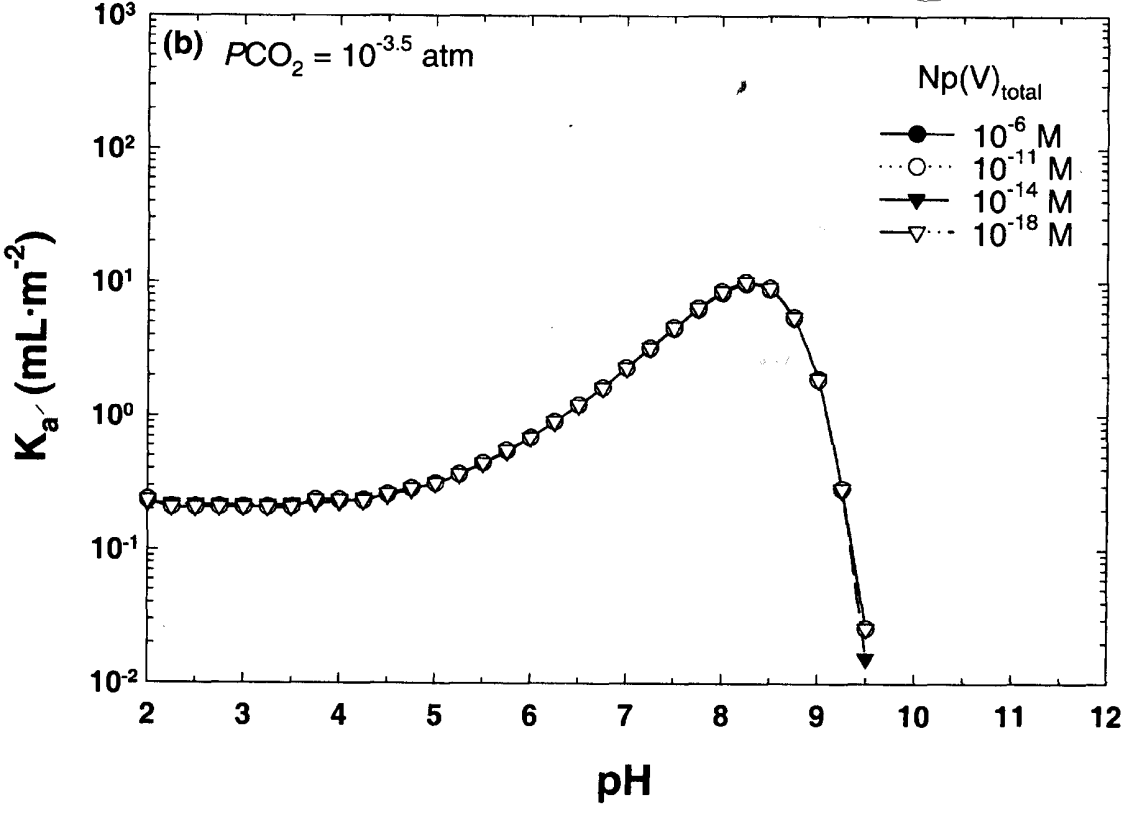

Fig. 10–16. DLM results for Np(V) sorption at various Np(V) concentrations under atmospheric CO_2 ($PCO_2 = 10^{-3.5}$ atm). $M/V = 4$ g × L^{-1}. DLM parameters are from Table 10–1.

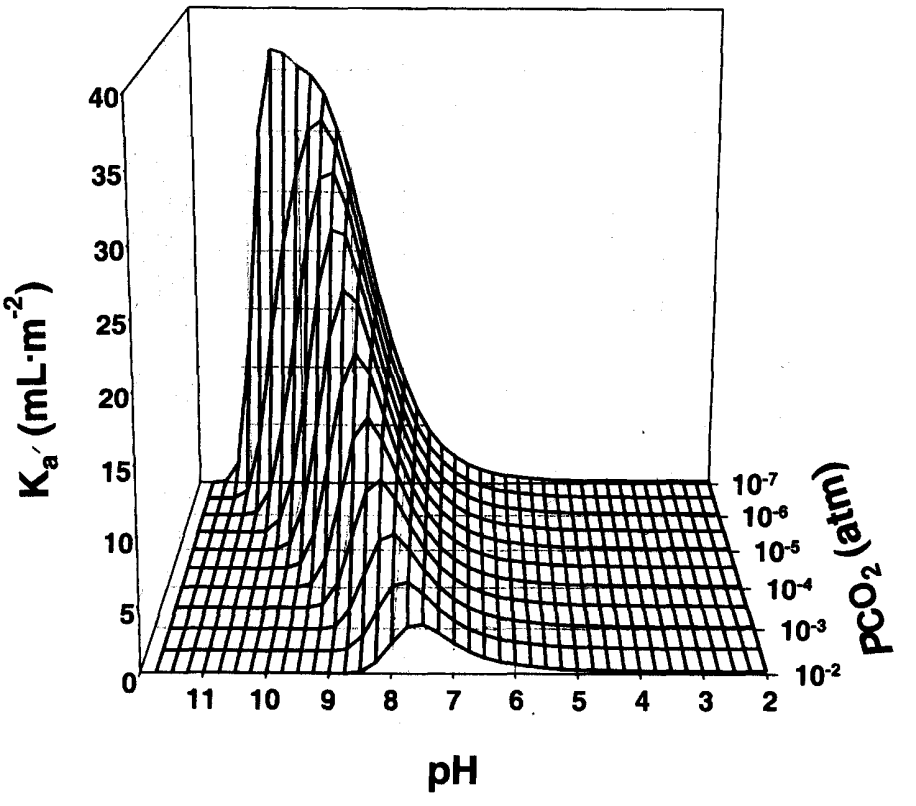

Fig. 10–17. Response surface for Np(V) sorption calculated using the DLM. Data are plotted from 10^{-7} to 10^{-2} atm (CO_2-free results not shown for clarity). $Np(V)_{total}$ ~1 × 10^{-6} *M*, *M*/*V* = 4 g × L^{-1}. DLM parameters are from Table 10–1.

has potential for application as part of the PA. There are several options for incorporating the sorption coefficient response surface. The response surface or an interpolated version of the surface can be generated as a database or look-up table with indices of the appropriate geochemical parameters (e.g., pH and PCO_2). Alternatively, a mathematical representation of the response surface may be generated so that pH and PCO_2 could be entered into a function that would produce a sorption parameter output. Finally, a combination of the look-up table and mathematical representation of the DLM-generated response surface can be developed and applied using site-specific data.

Look-up Table or Interpolated Surface

The modeled Np(V) sorption surface shown in Fig. 10–17 is a noninterpolated mesh consisting only of model generated data (mesh intersections). Representing the appropriate K_a' for pH and PCO_2 values between the model points requires some form of interpolation. Use of computer-generated interpolated meshes to represent the data is often unsatisfactory, and specific interpolation between discrete points can be a computational burden. Interpolation may be, in part, avoided by producing a model data set on a finer scale (smaller grid size). Alternatively, input from site-specific data can be limited (through rounding, for instance) to values that correspond to the grid. In ether case, a look-up table in the form demonstrated by Table 10–5 (or some other matrix format suitable to PA) represents a simple and fast mechanism for extracting site-specific K_a' values. Disadvantages include main-

Table 10–5. Sample look-up table for Np(V) sorption response surface ($K_{a'}$ in mL × m^{-2}). $Np(V)_{total} = 10^{-6}$ molal, $M/V = 4$ g × L^{-1}.

	Log PCO_2 (atm)											
pH	no CO_2	−7.00	−6.50	−6.00	−5.50	−5.00	−4.50	−4.00	−3.50	−3.00	− 2.50	−2.00
2.00	0.2341	0.2341	0.2341	0.2341	0.2341	0.2341	0.2341	0.2341	0.2341	0.2341	0. 2341	0.2341
2.25	0.2079	0.2079	0.2079	0.2079	0.2079	0.2079	0.2079	0.2079	0.2079	0.2079	0.2079	0.2079
2.50	0.2079	0.2079	0.2079	0.2079	0.2079	0.2079	0.2079	0.2079	0.2079	0.2079	0.2079	0.2079
2.75	0.2079	0.2079	0.2079	0.2079	0.2079	0.2079	0.2079	0.2079	0.2079	0.2079	0.2079	0.2079
3.00	0.2079	0.2079	0.2079	0.2079	0.2079	0.2079	0.2079	0.2079	0.2079	0.2079	0.2079	0.2079
3.25	0.2079	0.2079	0.2079	0.2079	0.2079	0.2079	0.2079	0.2079	0.2079	0.2079	0.2079	0.2079
3.50	0.2079	0.2079	0.2079	0.2079	0.2079	0.2079	0.2079	0.2079	0.2079	0.2079	0.2079	0.2079
3.75	0.2341	0.2341	0.2341	0.2341	0.2341	0.2341	0.2341	0.2341	0.2341	0.2341	0.2341	0.2341
4.00	0.2341	0.2341	0.2341	0.2341	0.2341	0.2341	0.2341	0.2341	0.2341	0.2341	0.2341	0.2341
4.25	0.2341	0.2341	0.2341	0.2341	0.2341	0.2341	0.2341	0.2341	0.2341	0.2341	0.2341	0.2341
4.50	0.2603	0.2603	0.2603	0.2603	0.2603	0.2603	0.2603	0.2603	0.2603	0.2603	0.2603	0.2603
4.75	0.2867	0.2867	0.2867	0.2867	0.2867	0.2867	0.2867	0.2867	0.2867	0.2867	0.2867	0.2867
5.00	0.3130	0.3130	0.3130	0.3130	0.3130	0.3130	0.3130	0.3130	0.3130	0.3130	0.3130	0.3130
5.25	0.3660	0.3660	0.3660	0.3660	0.3660	0.3660	0.3660	0.3660	0.3660	0.3660	0.3660	0.3660
5.50	0.4457	0.4457	0.4457	0.4457	0.4457	0.4457	0.4457	0.4457	0.4457	0.4457	0.4457	0.4457
5.75	0.5529	0.5529	0.5529	0.5529	0.5529	0.5529	0.5529	0.5529	0.5529	0.5529	0.5529	0.5529
6.00	0.6880	0.6880	0.6880	0.6880	0.6880	0.6880	0.6880	0.6880	0.6880	0.6880	0.6880	0.6880
6.25	0.9071	0.9071	0.9071	0.9071	0.9071	0.9071	0.9071	0.9071	0.9071	0.9071	0.9071	0.9071
6.50	1.2144	1.2144	1.2144	1.2144	1.2144	1.2144	1.2144	1.2144	1.2144	1.2144	1.2144	1.1862
6.75	1.6451	1.6451	1.6451	1.6451	1.6451	1.6451	1.6451	1.6451	1.6451	1.6451	1.6451	1.6451
7.00	2.3022	2.3022	2.3022	2.3022	2.3022	2.3022	2.3022	2.3022	2.3022	2.2716	2.2716	2.2412
7.25	3.2507	3.2507	3.2507	3.2507	3.2507	3.2507	3.2180	3.2180	3.2180	3.2180	3.1530	2.9915
7.50	4.5839	4.5839	4.5839	4.5839	4.5839	4.5839	4.5839	4.5839	4.5482	4.4770	4.2305	3.6147
7.75	6.4836	6.4836	6.4836	6.4836	6.4836	6.4836	6.4836	6.4433	6.3229	6.0063	5.1299	3.4481
8.00	9.1026	9.1026	9.1026	9.1026	9.1026	9.0555	9.0084	8.8682	8.3635	7.1849	4.8363	2.2107
8.25	12.4660	12.4660	12.4660	12.4660	12.4093	12.3528	12.1286	11.4713	9.8251	6.6868	3.0559	0.7971
8.50	16.5473	16.5473	16.5473	16.5473	16.4088	16.1344	15.3324	13.1591	8.9616	4.1608	1.1019	0.1035
8.75	21.2582	21.2582	21.1725	21.0872	20.7488	19.6822	16.8977	11.5793	5.4292	1.5000	0.1556	0.0000
9.00	26.0843	25.9802	25.8765	25.4658	24.1749	20.8329	14.3720	6.8099	1.9102	0.2079	0.0000	0.0000
9.25	30.3776	30.1340	29.6530	28.2587	24.5651	17.1821	8.2733	2.3635	0.2867	0.0000	0.0000	0.0000
9.50	33.8870	33.0697	31.6281	27.8093	19.8431	9.7760	2.8637	0.3395	0.0258	0.0000	0.0000	0.0000
9.75	36.7831	34.5856	30.8712	22.6727	11.6335	3.4813	0.4457	0.0258	0.0000	0.0000	0.0000	0.0000
10.00	40.8242	35.3007	27.1492	14.7507	4.6556	0.6067	0.0258	0.0000	0.0000	0.0000	0.0000	0.0000

tenance of a potentially large number of data tables for all radionuclides of interest and an additional level of uncertainty added in the interpolation.

Three-dimensional Mathematical Representation

A second approach to incorporating the $K_{a'}$ response surface in PA would be to represent the surface with an equation or set of equations. Mathematical descriptions of the response surface would have the advantage of representing a continuous range of values over the desired intervals of pH and PCO_2. Using the response surface shown in Fig. 10–17, an attempt was made to fit a three-dimensional function to the surface using the three-dimensional curve fitting software (Table Curve three-dimensional, Jandel Scientific). Unfortunately, the resulting fits did not adequately reproduce the surface for the purposes of this study. Omitting the extreme ranges where sorption is effectively zero, and restricting the range of pH and PCO_2 values considered to those areas where sorption was most pronounced did not result in an improved fit. Although other response surfaces may be well represented mathematically, efforts to fit the Np(V) data were not continued.

Combination of Look-Up and Mathematical Representation

A combination of mathematical modeling of the response surface and use of discrete look-up values may offer a reasonable solution for PA. Fig. 10–18 shows the Np(V)-DLM results as a series of pH-dependent sorption curves for each PCO_2 modeled. Similarities in the shape of the sorption curves as a function of pH suggest that one equation form might be capable of fitting the curves. To test this, the pH-sorption curves were fit using Table Curve Two-Dimensional (Jandel Scientific) to generate equations for the curves at each value of PCO_2. The range of data fit

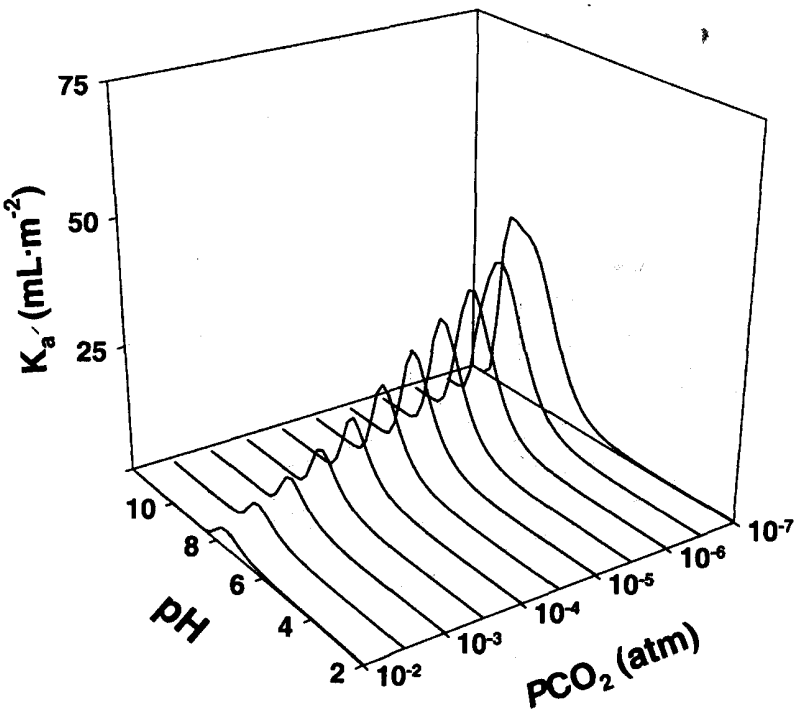

Fig. 10–18. Plot of DLM predictions of Np(V) sorption at discrete PCO_2 values. $Np(V)_{total} \sim 1 \times 10^{-6}$ *M*, *M/V* = 4 g × L^{-1}. DLM parameters are from Table 10–1.

for each curve was limited to regions where sorption was predicted to be greater than zero. A relatively simple equation:

$$\ln(y) = a + bx + cx^2 + dx^3 + ex^4 + fx^5 \quad [4]$$

where y represents the sorption parameter of interest and a, b, c, d, and e are constants; adequately reproduces the model predicted sorption curves across the desired pH range for each value of PCO_2. Coefficients and goodness-of-fit values for each curve are given in Table 10–6, and the fits are graphically represented in Fig. 10–19. The fits are excellent, except for some deviations at low values of PCO_2, which are not reasonably expected in the field. The fitting exercise was limited to one equation form to simplify eventual inclusion into PA. Alternative or multiple equations could be used to improve fits, but would add complexity to the modeling process. One advantage of this technique of incorporating the response surface is that only one parameter need be interpolated or restricted based on grid spacing to generate an appropriate sorption coefficient (K_d or $K_{a'}$). Since pH is typically measured with greater certainty, PCO_2 was selected to be the interpolated parameter. Similar response surfaces can be developed for other radionuclides (Fig. 10–20). One drawback to the polynomial form of Eq. [4] is that extrapolation beyond the fitted range (Table 10–6) can result in unreasonable sorption behavior.

A sample flow chart is presented using the combination look-up table and mathematical representation of the response surface (Fig. 10–21). Required data for the sorption module include solution pH, PCO_2 (or equivalent), and S_{ea}. The chart shows those areas where additional modeling detail may be included (e.g., ion exchange) and where conservative assumptions of no sorption ($K_d = 0$) can be used. The proposed approach is flexible enough to be used with other modeling approaches and not limited to the DLM demonstrated here. Because the modeling is done off-line, additional detail (e.g., ion exchange) can be included without affecting the PA computation time.

Sampling Key Geochemical Parameters

Using K_d response surfaces in PA requires some means of sampling key geochemical parameters such as pH and C_T (or log PCO_2) and associating them with proper hydrostratigraphic units and spatial distributions. In the vicinity of Yucca Mountain, water chemistry databases such as those of Perfect et al. (1995) for saturated zone waters and Yang et al. (1996; 1998) for unsaturated zone waters provide a source of information for establishing PDFs for these parameters. Because of the link through carbonate aqueous chemistry, log PCO_2 and pH would be expected to be correlated; this information should be used in constraining sampling these geochemical parameters in PA. Other parameters like ionic strength or Na/Ca ratios might be more appropriate as sampled parameters for response surfaces developed using other modeling approaches, such as ion exchange. If data are available, the flow paths could be partitioned with respect to geochemical parameters. This type of refinement may be unwarranted for PA, however, given the uncertainty in changing geochemical conditions over the long times of interest and the sparseness of geochemical data for the flow and transport pathway.

Table 10–6. Equation parameters and summary of fit results for model curves at discrete PCO_2. $Np(V)_{total} = 10^{-6}$ molal, $M/V = 4\ g \times L^{-1}$.

PCO_2 (atm)	Coefficients: [ln ($K_{a'}$, in mL × m^{-2}) = $a + bx + cx^2 + dx^3 + ex^4 + fx^5$]							
	a	*b*	*c*	*d*	*e*	*f*	r^2 value	pH range used for fit
$10^{-2.0}$	−323.7345	151.4137	−17.3990	−1.7541	0.4728	−0.0248	0.9999	6–9.25
$10^{-2.5}$	−441.4873	226.8171	−37.7489	1.2089	0.2378	−0.0167	0.9999	6–9.25
$10^{-3.0}$	148.2266	−173.8279	69.4791	−12.8694	1.1394	−0.0391	0.9999	6–9.50
$10^{-3.5}$	604.4445	−474.5178	147.2075	−22.6668	1.7365	−0.0529	0.9999	6–9.50
$10^{-4.0}$	847.1362	−620.1545	180.5362	−26.2031	1.8993	−0.0550	0.9999	6–10.00
$10^{-4.5}$	925.7299	−652.8079	183.1898	−25.6434	1.7940	−0.0502	0.9999	6–10.25
$10^{-5.0}$	923.2319	−632.0906	172.1421	−23.3804	1.5873	−0.0431	0.9999	6–10.50
$10^{-5.5}$	672.7843	−452.9837	121.1472	−16.1548	1.0778	−0.0288	0.9999	6–11.00
$10^{-6.0}$	393.8475	−258.6709	67.3401	−8.7496	0.5711	−0.0150	0.9999	6–11.25
$10^{-6.5}$	722.6946	−436.2311	104.2139	−12.3724	0.7340	−0.0175	0.9978	6–11.50
$10^{-7.0}$	2202.1902	−1290.5774	299.2739	−34.3782	1.9602	−0.0444	0.9816	6–11.75
no CO_2	1211.3978	−705.8275	161.4080	−18.1364	1.0037	−0.0219	0.9996	6–11.75

Surface areas, which are required to convert response surface $K_{a'}$ values to K_ds, are theoretically measurable, but in practice are difficult to determine with certainty. One way to address this uncertainty is to develop S_a PDFs based on laboratory and field measurements. For example, Triay et al. (1997) report measured N_2-BET S_a values of 2.6 to 10 $m^2 \times g^{-1}$ for tuff samples from the vicinity of Yucca Mountain. A number of recent studies also develop theoretical relationships between reactive S_a and hydrologic parameters such as porosity, permeability, density, and pore radius (Arthur, 1996; Smith & Schafer, 1999). Appropriate values could then be associated with geologic and hydrologic unit models (Civilian Radioactive Waste Management System, Management, and Operating Contractor, 2000d,e; U.S. Nuclear Regulatory Commission, 1999b,c) already used in PA.

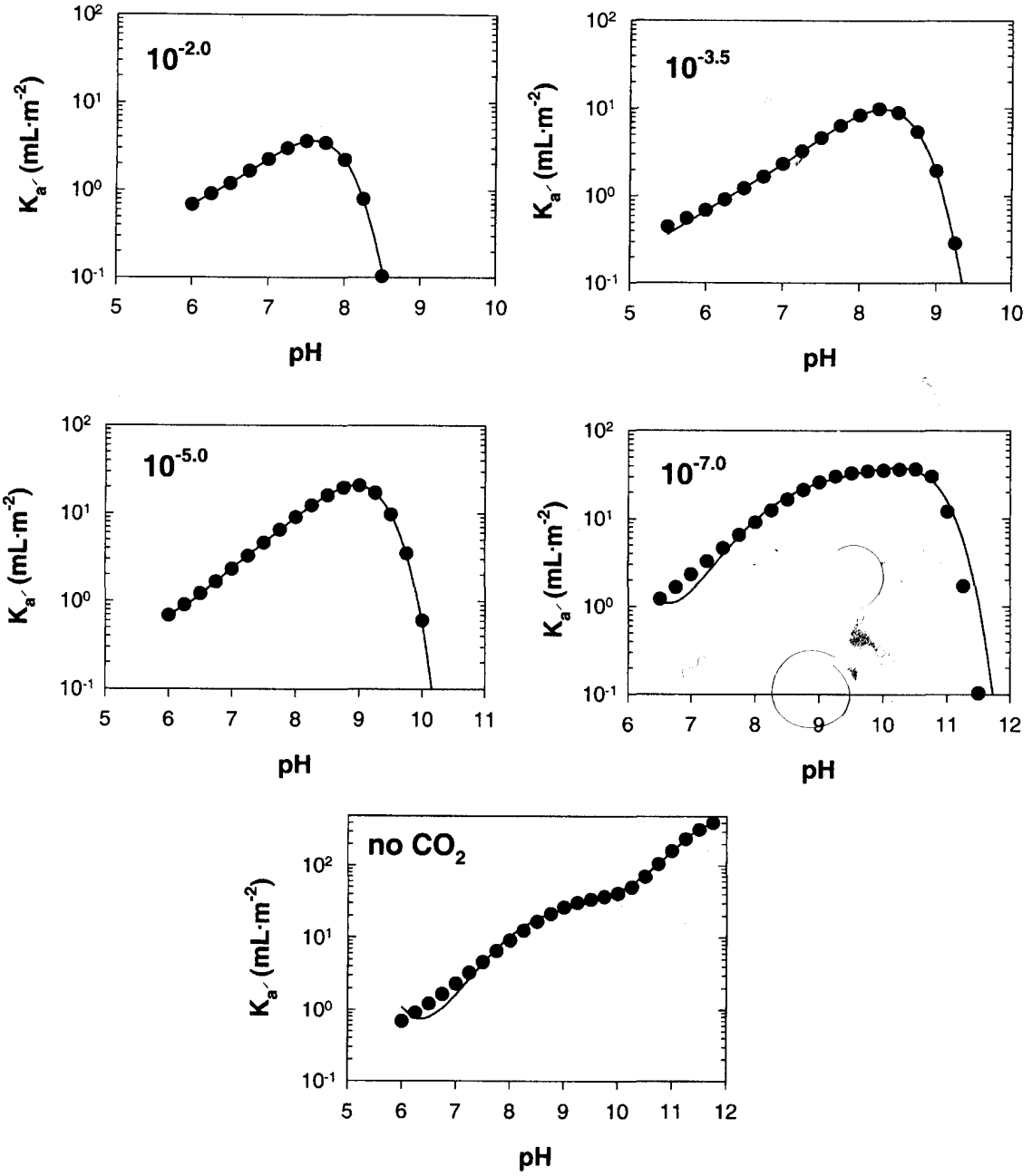

Fig. 10–19. Plots of polynomial fits to DLM $K_{a'}$s (points) for selected discrete values of PCO_2. Polynomial coefficients are given in Table 10–6. Values listed in the upper left hand corner of each plot show PCO_2 in atm for the particular data set and fit. DLM parameters are from Table 10–1.

DISCUSSION

Certain geochemical processes can both retard the transport of radionuclides, delaying arrival times at the receptor location(s), and reduce radionuclide concentrations at the point of exposure. An understanding of geochemical processes that influence radionuclide transport may be used to compensate for uncertainties in hydrologic models of the Yucca Mountain system (Simmons et al., 1995).

Both of the SCM-based approaches applied here have several limitations. Models have been calibrated and tested against relatively small sorption datasets, particularly for Am(III), Th(IV), and Pu(V), and the models also focus on a surface complexation mechanism and neglect other potential mechanisms such as ion

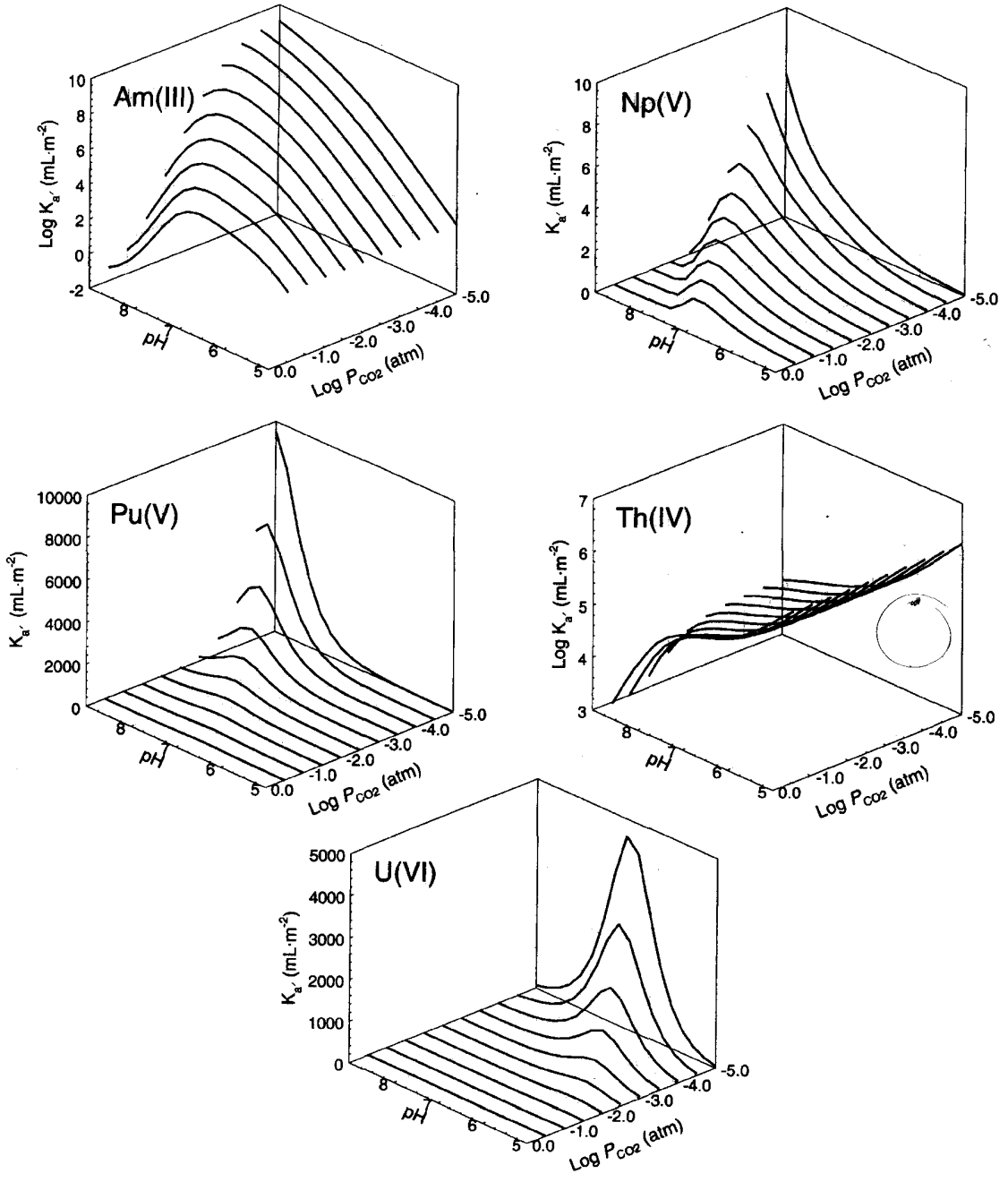

Fig. 10-20. Plot of DLM predictions of important HLW radionuclides at discrete PCO_2 values. DLM parameters are from Table 10-1.

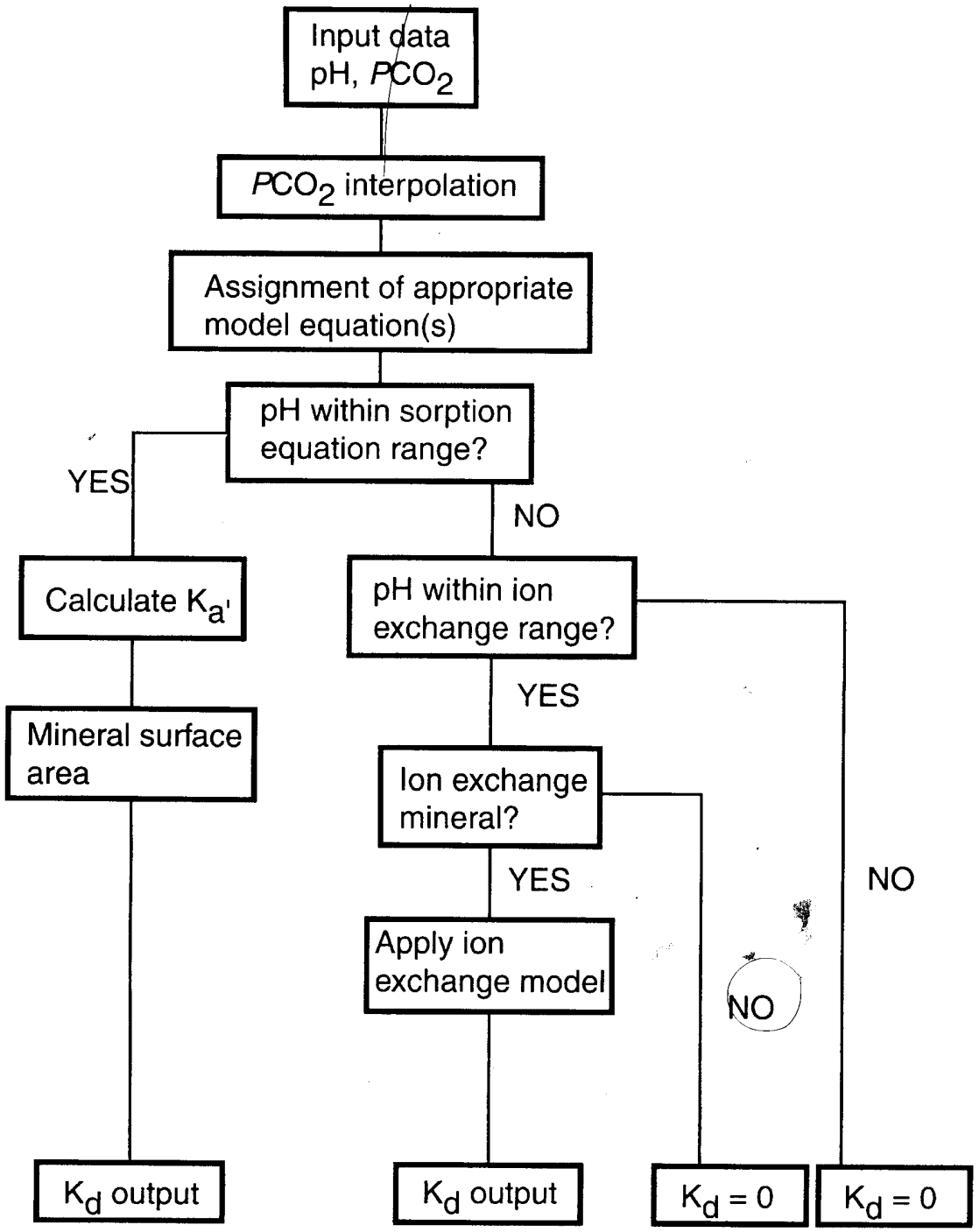

Fig. 10–21. Flow diagram showing an approach that can be used to incorporate geochemical sorption models in PA.

exchange. The DLM approach discussed here has many underlying simplifications including: (i) a constant site density (2.3 sites nm^{-2}), (ii) representation of sorption on aluminosilicate minerals by a combination of aluminol ($>AlOH^0$) and silanol ($>SiOH^0$) sites (Turner, 1995), and (iii) surface reactions that are postulated and used on the basis of the simplest reaction(s) to reproduce the observed data. Other potential difficulties are in the uncertainty in SCM electrostatic terms for natural materials and applying models based on single mineral experiments to complex nat-

ural mineral assemblages (Davis, 2001). For example, Davis et al. (1998) have developed a nonelectrostatic sorption model to address this uncertainty for U transport.

There also remains a considerable degree of uncertainty in the aqueous thermodynamic data for a number of radionuclides of interest in HLW management. The Nuclear Energy Agency (NEA) Thermodynamic Data Base Project has produced volumes on U (Wanner & Forest, 1992), Am (Silva et al., 1995) and Tc (Rard et al., 1999). An additional volume in Np and Pu has only recently become available (Lemire et al., 2001), and was not used in this study. And even for those volumes published, a number of key minerals and species may not be well constrained. For example, the NEA database for U does not include data for many key U-silicate minerals such as uranophane, haiweeite, and soddyite, and the equilibrium constant for the neutral aqueous species $UO_2(OH)_2^0$ is only bounded at an upper limit.

Still, the simplified SCM approach used here with the DLM accurately reproduces experimental data over the ranges on which the model is based and appears to be applicable for more than one mineral type. Mineral surface or rock surface areas may be used to normalize sorption data and the similar nature of sorption behavior suggests that the model has the potential for applicability to a number of minerals, especially silicates. Comparisons to data from similar mineral types conducted across a broader range of conditions show the model is able to represent changes in sorption behavior owing to modifications in system chemistry (e.g., pH and PCO_2). The relative insensitivity to M/V and Np(V) concentration within the model suggests that a relatively limited number of variables need to be tracked in PA.

Ideally, mechanistic sorption models such as SCMs or ion exchange would be directly incorporated into PA calculations using reactive transport codes. While hydrogeochemical transport codes may be used to examine particular aspects of reactive transport, however, the additional computational burden that results from coupling equations for geochemistry and fluid flow may be excessive for PA. This is even more important for stochastic approaches that rely on sampling techniques and many realizations to generate CCDFs and population statistics. It may be possible to use detailed sorption models such as the DLM off-line to support K_d selection and assess the effect of critical parameters such as pH and PCO_2 for site-specific conditions.

One approach is to use existing site-specific information on the physical–chemical system at Yucca Mountain to constrain variability in sorption behavior. The compilation of Perfect et al. (1995) is assumed to represent likely variations in regional hydrochemistry in the vicinity of Yucca Mountain during the regulatory time period. A simplified DLM is used with this hydrochemistry data to provide realistic constraints on the PDFs used in PA to describe radionuclide sorption. The model results suggest that lognormal distributions of actinide sorption coefficients are appropriate; the total ranges in calculated sorption parameters are as much as nine orders of magnitude due to changes in observed hydrochemistry alone, but much of the lower part of the range is skewed by a relatively small set of carbonate-rich groundwaters. The statistical relationship between the calculated K_d PDFs also provides a demonstration of calculating correlation coefficients among ra-

dioelement sorption parameters that can be used to indirectly include the effects of geochemistry in PA calculations.

An alternative method for using detailed sorption models is to apply the model across a wide range of geochemical conditions and develop a sorption response surface as a function of key parameters. Unlike K_d, which is a derived value, geochemical parameters such as pH are properties of the physicochemical system that can either be measured or assigned bounding limits. The calculated sorbed and aqueous concentrations can be used to develop a range in K_d values predicted as a function of these variables. While this is not an explicit incorporation of geochemistry in the transport calculations, it does provide a step toward a more theoretical basis for sorption modeling in PA.

The approaches outlined here are not limited either to Yucca Mountain, or to a specific type of mechanistic geochemical sorption model. They do provide a means of incorporating aspects of detailed model results into current PA codes. Considerations for future work in the application of these approaches to PA should include (i) evaluation of available data to apply similar approaches for other radionuclides, (ii) application of single mineral sorption models to natural mineral assemblages, (iii) extension of modeling to incorporate more than one set of experiments for development of surface reactions and binding constants, (iv) evaluation of the utility of incorporating ion exchange, as appropriate, and (v) development of experiments that would aid in model validation.

ACKNOWLEDGMENTS

The authors would like to thank Jim Prikryl and Alka Jain for their efforts in obtaining Center for Nuclear Waste Regulatory Analyses (CNWRA) laboratory results reported. This manuscript has benefitted greatly from the thorough reviews and valuable recommendations of Lauren Browning, Budhi Sagar, Bill Dam, John Bradbury, and two anonymous reviewers. Arturo Ramos and Lee Selvey provided assistance in preparing this manuscript. This manuscript was prepared to document work performed by the CNWRA for the Nuclear Regulatory Commission (NRC) under Contract no. NRC-02-97-009. The activities reported here were performed on behalf of the NRC Office of Nuclear Material Safety and Safeguards, Division of Waste Management. The report is an independent product of the CNWRA and does not necessarily reflect the view or regulatory position of the NRC. The MINTEQA2, Version 3.11 computer code is controlled under CNWRA Software Configuration Procedures. The spreadsheet software Microsoft Excel 97, and the curve-fitting software TableCurve 2-D and TableCurve 3-D from Jandel Scientific were used to fit data presented here. These are commercial software packages and only the object codes are available to the CNWRA.

REFERENCES

Allard, B., U. Olofsson, and B. Torstenfelt. 1984. Environmental actinide chemistry. Inorgan. Chim. Acta 94:205–221.

Allison, J.D., D.S. Brown, and K.J. Novo-Gradac. 1991. MINTEQA2/PRODEFA2, a geochemical assessment model for environmental systems: Version 3.0 user's manual. USEPA/600/3-91/021. U.S. Environmental Protection Agency, Athens, GA.

Arthur, R.C. 1996. SITE-94: Adaptation of mechanistic sorption models for performance assessment calculations. SKI Report 96:34. Swed. Nucl. Power Inspectorate, Stockholm.

Bertetti, F.P., R.T. Pabalan, and M.G. Almendarez. 1998. Studies of neptunium^{V} sorption on quartz, clinoptilolite, montmorillonite, and α-alumina. p. 131–148. *In* E.A. Jenne (ed.) Adsorption of metals by geomedia. Academic Press, New York.

Carlos, B.A., S.J. Chipera, and D.L. Bish. 1995. Distribution and chemistry of fracture-lining minerals at Yucca Mountain, Nevada. LA-12977-MS. Los Alamos National Laboratory, Los Alamos, NM.

Civilian Radioactive Waste Management System, Management, and Operating Contractor. 1998. Total system performance assessment-viability assessment (TSPA-VA) analyses technical basis document. B00000000-01717-4301 REV 01. Civilian Radioactive Waste Management System, Management and Operating Contractor, Las Vegas.

Civilian Radioactive Waste Management System, Management, and Operating Contractor. 2000a. Total system performance assessment for the site recommendation. TDF-WIS-PA-00001 REV 00. Civilian Radioactive Waste Management System, Management and Operating Contractor, Las Vegas.

Civilian Radioactive Waste Management System, Management, and Operating Contractor. 2000b. Repository safety strategy: Plan to prepare the safety case to support yucca mountain site recommendation and licensing considerations. TDR-WIS-RL-000001 REV04 ICN01. Civilian Radioactive Waste Management System, Management, and Operating Contractor, Las Vegas.

Civilian Radioactive Waste Management System, Management, and Operating Contractor. 2000c. Unsaturated zone flow and transport model process model report. TDR-NBS-HS-000002 REV00 ICN02. Civilian Radioactive Waste Management System, Management, and Operating Contractor, Las Vegas.

Civilian Radioactive Waste Management System, Management, and Operating Contractor. 2000d. Hydrogeologic framework model for the saturated-zone site-scale flow and transport model. ANL-NBS-HS-000033. Revision 00. Civilian Radioactive Waste Management, System, Management and Operating Contractor, Las Vegas.

Civilian Radioactive Waste Management System, Management, and Operating Contractor. 2000e. Geologic framework model (GFM3.1). MDL-NBS-GS-000002. Revision 00. Civilian Radioactive Waste Management System, Management, and Operating Contractor, Las Vegas.

Civilian Radioactive Waste Management System, Management, and Operating Contractor. 2001. FY 01 supplemental science and performance analyses. TDR-MGR-MD-000007. Revision 00. Civilian Radioactive Waste Management System, Management, and Operating Contractor, Las Vegas.

Davis, J.A. 2001. Surface complexation modeling of uranium(VI) adsorption on natural mineral assemblages. NUREG/CR-6708. U.S. Nuclear Regulatory Commission, Washington, DC.

Davis, J.A., J.A. Coston, D.B. Kent, and C.C. Fuller CC. 1998. Application of the surface complexation concept to complex mineral assemblages. Environ. Sci. Technol. 32:2820–2828.

Davis, J.A., and D.B. Kent. 1990. Surface complexation modeling in aqueous geochemistry. p. 177–260. *In* M.F. Hochella, Jr., and A.F. White (ed.) Reviews in mineralogy. Vol. 23. Mineral–Water Interface Geochemistry. Mineral. Soc. Am., Washington, DC.

Dzombak, D.A., and F.M.M. Morel. 1990. Surface complexation modeling: Hydrous ferric oxide. John Wiley & Sons, New York.

Girvin, D.C., L.L. Ames, A.P. Schwab, and J.E. McGarrah. 1991. Neptunium adsorption on synthetic amorphous iron oxyhydroxide. J. Colloid Interface Sci. 141:67–78.

Hayes, K.F., G. Redden, W. Ela, and J.O. Leckie. 1991. Surface complexation models: An evaluation of model parameter estimation using FITEQL and oxide mineral titration data. J. Colloid Interface Sci. 142:448–469.

Hem, J.D. 1985. Study and interpretation of the chemical characteristics of natural waters. U.S. Geol. Surv. Water Supply Pap. 2254. U.S. Geol. Surv., Washington, DC.

Hitchon, B., and M. Brulotte. 1994. Culling criteria for "standard" formation water analyses. Appl. Geochem. 9:637–645.

Hsi, C-K.D., and D. Langmuir. 1985. Adsorption of uranyl onto ferric oxyhydroxides: Application of the surface complexation site-binding model. Geochim. Cosmochim. Acta 49:1931–1941.

Kerrisk, J.F. 1985. An assessment of the important radionuclides in nuclear waste. LA-10414-MS. Los Alamos Natl. Lab., Los Alamos, NM.

LaFlamme, B.D.,and J.W. Murray. 1987. Solid–solution interaction: The effect of carbonate alkalinity on adsorbed thorium. Geochim. Cosmochim. Acta 51:243–250.

Lemire, R.J., J.Fuger, H. Nitsche, P. Potter, M.H. Rand, J. Rydberg, K. Spahiu, J.C. Sullivan, W.J. Ullman, P. Vitorge, and H. Wanner. 2001. Chemical thermodynamics series. Vol. 4. Chemical thermodynamics of neptunium and plutonium. Nuclear Energy Agency, Org. Econom. Coop. Develop. Elsevier, New York.

McKinley J.P., J.M. Zachara, S.C. Smith, and G.D. Turner. 1995. The influence of hydrolysis and multiple site-binding reactions on adsorption of U(VI) to montmorillonite. Clays Clay Miner. 43:586–598.

National Research Council. 1999. Disposition of high-level radioactive waste through geological isolation: Development, current status, and technical and policy challenges. Natl. Academy Press, Washington, DC.

Nitsche, H., R.C. Gatti, E.M. Standifer, S.C. Lee, A. Müller, T. Prussin, R.S. Deinhammer, H. Maurer, K. Becraft, S. Leung, and S.A. Carpenter. 1993. Measured solubilities and speciations of neptunium, plutonium, and americium in a typical groundwater (J-13) from the Yucca Mountain region: Milestone Rep. 3010-WBS 1.2.3.4.1.3.1. LA-12562-MS. Los Alamos Natl. Lab., Los Alamos, NM.

Nuclear Energy Agency. 1998. Update on waste management policies and programmes. Nuclear Waste Bull. no. 13. Nuclear Energy Agency, Issy-les-Moulineaux, France.

Oversby, V.M. 1987. Important radionuclides in high level nuclear waste disposal: Determination using a comparison of the U.S. EPA and NRC regulations. Nucl. Chem. Waste Manage. 7:149–161.

Pabalan, R.T., and D.R. Turner. 1997. Uranium(6+) sorption on montmorillonite: Experimental and surface complexation modeling study. Aqueous Geochem. 2:203–226.

Pabalan, R.T., J.D. Prikryl, P.M. Muller, and T.B. Dietrich. 1993. Experimental study of uranium(6+) sorption on the zeolite mineral clinoptilolite. p. 777–782. *In* C. Interrante and R. Pabalan (ed.) MRS Symp. Proc. Vol. 294. Scientific Basis for Nuclear Waste Management-XVI. Mat. Res. Soc., Pittsburgh, PA.

Pabalan, R.T., D.R. Turner, F.P. Bertetti, and J.D. Prikryl. 1998. Uranium^{VI} sorption onto selected mineral surfaces. p. 199–130. *In* E.A. Jenne (ed.) Adsorption of metals by geomedia. Academic Press, New York.

Paces, J.B., E.M. Taylor, and C.A. Bush. 1993. Late quaternary history and uranium isotopic compositions of ground water discharge deposits, Crater Flat, Nevada. p. 1573–1580. *In* Proc. from the 4th Int. Conf. on High Level Radioactive Waste Management. Am. Nucl. Soc., La Grange Park, IL.

Painter, S., V. Cvetkovic, and D.R. Turner. 2001. Effect of heterogeneity on radionuclide retardation in the alluvial aquifer near Yucca Mountain, Nevada. Groundwater 39:326–338.

Papelis, C., K.F. Hayes, and J.O. Leckie. 1988. HYDRAQL: A program for the computation of chemical equilibrium composition of aqueous batch systems including surface complexation modeling of ion adsorption at the oxide–solution interface. Tech. Rep. 306. Dep. Civil. Eng., Stanford Univ., Stanford, CA.

Parkhurst, D.L., and C.A.J. Appelo. 1999. User's guide to PHREEQC (Version 2)-A computer program for speciation, batch-reaction, one-dimensional transport, and inverse geochemical calculations. U.S. Geol. Surv. Water Resour. Investigations Rep. 99-4259. U.S. Geol. Surv., Denver, CO.

Perfect, D.L. 1994. Creation and analysis of a hydrochemical data base for the Death Valley region, Nevada and California. M.S. thesis. Colorado School of Mines, Golden.

Perfect, D.L., C.C. Faunt, W.C. Steinkampf, and A.K. Turner. 1995. Hydrochemical data base for the Death Valley region, Nevada and California. U.S. Geol. Surv. Open-File Rep. 94-305. U.S. Geol. Surv., Denver, CO.

Rard, J.A., M.H. Rand, G. Anderegg, and H. Wanner. 1999. Chemical thermodynamics series, Vol. 3. Chemical thermodynamics of technetium. Nucl. Energy Agency, Org. Econ. Coop. Dev. Elsevier, New York.

Righetto, L., G. Bidoglio, G. Azimonti, and I.R. Bellobono. 1991. Competitive actinide interactions in colloidal humic acid-mineral oxide systems. Environ. Sci. Technol. 25:1913–1919.

Righetto, L., G. Bidoglio, B. Marcandalli, and I.R. Bellobono. 1988. Surface interactions of actinides with alumina colloids. Radiochim. Acta 44/45:73–75.

Sanchez, A.L., J.W. Murray, and T.H. Sibley. 1985. The adsorption of plutonium IV and V on goethite. Geochim. Cosmochim. Acta 49:2297–2307.

Serne, R.J., R.C. Arthur, and K.M. Krupka. 1990. Review of geochemical processes and codes for assessment of radionuclide migration potential at commercial LLW sites. PNL-7285. Pacific Northwest Lab., Richland, WA.

Silva, R.J., G. Bidoglio, M.H. Rand, P.B. Robouch, H. Wanner, and I. Puigdomenich. 1995. Chemical thermodynamics series. Vol. 2. Chemical thermodynamics of americium. Nucl. Energy Agency, Org. Econom. Coop. Develop. Elsevier, New York.

Simmons, A.M., S.T. Nelson, P.L. Cloke, T.R. Crump, C.J. Duffy, W.E. Glassley, Z.E. Peterman, M.D. Siegel, D. Stahl, W.C. Steinkampf, and B.E. Viani. 1995. The critical role of geochemistry in the program approach. Dep. Energy Letter Rep. U.S. Department of Energy, Washington, DC.

Smith, R.W., and A.L. Schafer. 1999. Effective reactive surface area: An isotropic property of physically and chemically heterogeneous porous media. p. 1051–1058. *In* J. Lee and D. Wronkiewicz (ed.) MRS Symp. Proc. Vol. 556. Scientific Basis for Nuclear Waste Management XXII. Mat. Res. Soc., Pittsburgh, PA.

Triay, I.R., A. Meijer, J.L. Conca, K.S. Kung, R.S. Rundberg, E.A. Strietelmeier, C.D. Tait, D.L. Clark, M.P. Neu, and D.E. Hobart. 1997. Summary and synthesis report on radionuclide retardation for the Yucca Mountain Site Characterization Project. Milestone 3784M. LA-13262-MS. Chem. Sci. and Technol. Div., Los Alamos Natl. Lab., Los Alamos, NM.

Turner, D.R. 1995. A uniform approach to surface complexation modeling of radionuclide sorption. CNWRA 95-001. Ctr. Nucl. Waste Regulatory Analyses, San Antonio, TX.

Turner, D.R., T. Griffin, and T.B. Dietrich. 1993. Radionuclide sorption modeling using the MINTEQA2 speciation code. p. 783–789. *In* C. Interrante and R. Pabalan (ed.) MRS Symp. Proc. Vol. 294. Scientific Basis for Nuclear Waste Management XVI. Mat. Res. Soc., Pittsburgh, PA.

Turner, D.R., and R.T. Pabalan. 1999. Abstraction of mechanistic sorption model results for performance assessment calculations at Yucca Mountain, Nevada. Waste Manage. 19:375–388.

Turner, D.R., R.T. Pabalan, and F.P. Bertetti. 1998. Neptunium(V) sorption on montmorillonite: An experimental and surface complexation modeling study. Clays Clay Miner. 46:256–269.

Turner, D.R., R.T. Pabalan, J.D. Prikryl, and F.P. Bertetti. 1999. Radionuclide sorption at Yucca Mountain, Nevada: Demonstration of an alternative approach for performance assessment. p. 583–590. *In* J. Lee and D. Wronkiewicz (ed.) MRS Symp. Proc. Vol. 556. Scientific Basis for Nuclear Waste Management XXII. Mat. Res. Soc., Pittsburgh, PA.

Turner, D.R., and S.A. Sassman. 1996. Approaches to sorption modeling for high-level waste performance assessment. J. Contam. Hydrol. 21:311–332.

Turner, G.D., J.M. Zachara, J.P. McKinley, and S.C. Smith. 1996. Surface-charge properties and UO_2^{2+} adsorption of a surface smectite. Geochim. Cosmochim. Acta 60:3399–3414.

U.S. Department of Energy. 1998. Viability assessment of a repository at Yucca Mountain. DOE/RW-0508. U.S. Department of Energy, Office of Civilian Radioactive Waste Management, Las Vegas.

U.S. Environmental Protection Agency. 2001. 40 CFR Part 197. Public health and environmental radiation protection standards for Yucca Mountain, NV; Final rule. Fed. Reg. 66:32074–32135.

U.S. Nuclear Regulatory Commission. 1999a. 10 CFR Part 19 et al. Disposal of high-level radioactive wastes in a proposed geological repository at Yucca Mountain, Nevada; Proposed rule. Fed. Reg. 64:8640–8679.

U.S. Nuclear Regulatory Commission. 1999b. NRC sensitivity and uncertainty analyses for a proposed HLW repository at Yucca Mountain, Nevada, using TPA 3.1. Conceptual models and data. NUREG-1668. Vol. 1. U.S. Nuclear Regulatory Commission, Washington, DC.

U.S. Nuclear Regulatory Commission. 1999c. NRC sensitivity and uncertainty analyses for a proposed HLW repository at Yucca Mountain, Nevada, using TPA 3.1 Results and Conclusions. NUREG-1668. Vol. 2. U.S. Nuclear Regulatory Commission, Washington, DC.

U.S. Nuclear Regulatory Commission. 2001. Summary of the resolution of the key technical issue on radionuclide transport. Available at http://www.nrc.gov/NMSS/DWM/120500agreement.htm.

Waddell, R.K. 1982. Two-dimensional, steady-state model of ground-water flow, Nevada Test Site and vicinity, Nevada–California. U.S. Geol. Surv. Water Resources Investigations Rep. 82-4085. U.S. Geol. Surv., Denver, CO.

Wanner, H., Y. Albinsson, O. Karnl, E. Wieland, P. Wersin, and L. Charlet. 1994. The acid–base chemistry of montmorillonite. Radiochim. Acta 66/67:733–738.

Wanner, H., and I. Forest. 1992. Chemical thermodynamics series. Vol. 1. Chemical thermodynamics of uranium. Nuclear Energy Agency, Org. Econom. Coop. Develop. Elsevier, New York.

Wescott, R.G., M.P. Lee, N.A. Eisenberg, and T.J. McCartin. 1995. NRC iterative performance assessment Phase 2: Development of capabilities for review of a performance assessment for a high-level waste repository. NUREG-1464. U.S. Nuclear Regulatory Commission, Washington, DC.

Wilson, M.L., J.H. Gauthier, R.W. Barnard, G.E. Barr, and H.A. Dockery, E. Dunn, R.R. Eaton, D.C. Guerin, N. Lu, M.J. Martinez, R. Nilson, C.A. Rautman, T.H. Robey, B. Ross, E.E. Ryder, A.R. Schenker, S.A. Shannon, L.H. Skinner, W.G. Halsey, J.D. Gansemer, L.C. Lewis, A.D. Lamont, I.R. Triay, A. Meijer, D.E. Morris. 1994. Total-system performance assessment for Yucca Mountain SNL Second Iteration (TSPA-1993). Vol. 2. SAND93-2675. Sandia Natl. Lab., Albuquerque, NM.

Winograd, I.J., and W. Thordarson. 1975. Hydrogeologic and hydrochemical framework, south-central Great Basin, Nevada–California with special reference to the Nevada Test Site. U.S. Geol. Surv. Prof. Pap. 712-C. U.S. Geol. Surv., Washington, DC.

Yang, I.C., G.W. Rattray, P. Yu.. 1996. Interpretation of chemical and isotopic data from boreholes in the unsaturated zone at Yucca Mountain, Nevada. U.S. Geol. Surv. Water Resour. Investigations Rep. 96-4058. U.S. Geol. Surv., Denver, CO.

Yang, I.C., P, Yu, G.W. Rattray, J.S. Ferarese, and J.N. Ryan, 1998. Hydrochemical investigations in characterizing the unsaturated zone at Yucca Mountain, Nevada. U.S. Geol. Surv. Water Resour. Investigations Rep. 98-4132. U.S. Geol. Surv., Denver, CO.

Yeh, G.T., and V.S. Tripathi. 1989. A critical evaluation of recent developments in hydrogeochemical transport models of reactive multichemical components. Water Resour. Res. 25:93–108.

Yeh, G.T., and V.S. Tripathi. 1991 A model for simulating transport of reactive multispecies components: Model development and demonstration. Water Resour. Res. 27:3075–3094.

Zachara, J.M., and J.P. McKinley. 1993. Influence of hydrolysis on the sorption of metal cations by smectites: Importance of edge coordination reactions. Aquatic Sci. 55:250–261.